ADVANCES IN MAGNETISM OF SOILS AND SEDIMENTS

EDITED BY: Sara Satolli, Eric C. Ferre, Myriam Kars, Sarah P. Slotznick and Ricardo I. F. Trindade

PUBLISHED IN: Frontiers in Earth Science

frontiers Research Topics

frontiers

ISSN 1664-8714
ISBN 978-2-88971-265-6
DOI 10.3389/978-2-88971-265-6

About Frontiers

Frontiers is more than just an open-access publisher of scholarly articles: it is a pioneering approach to the world of academia, radically improving the way scholarly research is managed. The grand vision of Frontiers is a world where all people have an equal opportunity to seek, share and generate knowledge. Frontiers provides immediate and permanent online open access to all its publications, but this alone is not enough to realize our grand goals.

Frontiers Journal Series

The Frontiers Journal Series is a multi-tier and interdisciplinary set of open-access, online journals, promising a paradigm shift from the current review, selection and dissemination processes in academic publishing. All Frontiers journals are driven by researchers for researchers; therefore, they constitute a service to the scholarly community. At the same time, the Frontiers Journal Series operates on a revolutionary invention, the tiered publishing system, initially addressing specific communities of scholars, and gradually climbing up to broader public understanding, thus serving the interests of the lay society, too.

Dedication to Quality

Each Frontiers article is a landmark of the highest quality, thanks to genuinely collaborative interactions between authors and review editors, who include some of the world's best academicians. Research must be certified by peers before entering a stream of knowledge that may eventually reach the public - and shape society; therefore, Frontiers only applies the most rigorous and unbiased reviews.
Frontiers revolutionizes research publishing by freely delivering the most outstanding research, evaluated with no bias from both the academic and social point of view. By applying the most advanced information technologies, Frontiers is catapulting scholarly publishing into a new generation.

What are Frontiers Research Topics?

Frontiers Research Topics are very popular trademarks of the Frontiers Journals Series: they are collections of at least ten articles, all centered on a particular subject. With their unique mix of varied contributions from Original Research to Review Articles, Frontiers Research Topics unify the most influential researchers, the latest key findings and historical advances in a hot research area! Find out more on how to host your own Frontiers Research Topic or contribute to one as an author by contacting the Frontiers Editorial Office: frontiersin.org/about/contact

ADVANCES IN MAGNETISM OF SOILS AND SEDIMENTS

Topic Editors:
Sara Satolli, G. d'Annunzio University of Chieti and Pescara, Italy
Eric C. Ferre, University of Louisiana at Lafayette, United States
Myriam Kars, Kōchi University, Japan
Sarah P. Slotznick, Dartmouth College, United States
Ricardo I. F. Trindade, University of São Paulo, Brazil

Citation: Satolli, S., Ferre, E. C., Kars, M., Slotznick, S. P., Trindade, R. I. F., eds. (2021). Advances in Magnetism of Soils and Sediments. Lausanne: Frontiers Media SA. doi: 10.3389/978-2-88971-265-6

Table of Contents

frontiers in Earth Science

EDITORIAL
published: 29 June 2021
doi: 10.3389/feart.2021.722670

Editorial: Advances in Magnetism of Soils and Sediments

Sara Satolli[1]*, *Eric C. Ferré*[2], *Myriam Kars*[3], *Sarah P. Slotznick*[4] and *Ricardo I. F. Trindade*[5]

[1]Department of Engineering and Geology, G. d'Annunzio University of Chieti and Pescara, Chieti, Italy, [2]University of Louisiana at Lafayette, Lafayette, LA, United States, [3]Kōchi University, Kochi, Japan, [4]Dartmouth College, Hanover, NH, United States, [5]University of São Paulo, São Paulo, Brazil

Keywords: sediment, soil, environment, magnetic, process

Editorial on the Research Topic

Advances in Magnetism of Soils and Sediments

Our understanding of how rock magnetism records sedimentary and environmental processes, along with the refinement of analytical methods, has substantially improved in the last decade. In addition, there is an increasing appreciation of the strong interaction between (bio)geochemical and physical systems and their preservation in the sedimentary record. These developments hold great promise for a better comprehension of the evolution of our planet through time. In this Special Issue, we highlight some of the most significant advances to the topic of sedimentary and soil magnetism and their impact on several related domains.

The Advances in Magnetism of Soil and Sediments Special Issue focuses on identifying and assessing the impact of processes that occur throughout the entire sedimentary and soil cycle on rock magnetic, paleomagnetic, and environmental records (**Figure 1**). Magnetic mineral assemblages are affected by a wide range of chemical, physical and biological processes at different scales in depth and through time, and therefore are good indicators of environmental changes. In terrestrial environments (e.g., soil, sediment, speleothem), the magnetic mineralogy is dominated by detrital particles, mostly iron oxy-hydroxides and iron oxides, which are eroded and transported by wind or water. Some of these minerals are further altered by weathering and diagenetic processes at depth, related to the degradation and fermentation of the organic matter. Biological activity is responsible for the formation of authigenic minerals, either intracellularly or extracellularly, in oxic sedimentary environment. Other constituents of the magnetic assemblage can include atmospheric particles from volcanic ash and anthropogenic aerosols, and to a lesser extent extraterrestrial input. Particles from land are then transported and deposited in aqueous environments and constitute the main magnetic component in marine sediments. Eolian particles (dust), volcanic ash, biogenic magnetic particles from biomineralization, and extraterrestrial input also contribute to magnetic minerals in marine sediments. Post-depositional alteration due to burial, diagenetic processes or fluid and gas circulation, in anoxic conditions, leads to a drastic change in the magnetic mineral assemblages with the reduction of iron oxy-hydroxides and iron oxides to form iron sulfides. Because of magnetic minerals sensitivity to (bio)geochemical conditions, investigating the changes in the magnetic mineral assemblages and associated mechanisms in a diversity of environments leads to new insights on past environmental and paleoceanographic conditions.

With that perspective in mind, a broad range of natural materials are investigated by fourteen original contributions: speleothems, ocean surface and deep sediments, methane- and gas hydrate-bearing sediments, estuarine sediments, sandstone, particulate matter, ice cores, plant ash, soil, paleosols, and microbialites.

Rock magnetic and paleomagnetic approaches can provide highly sensitive and unique information on mineral changes, particularly in fine grained materials, and constrain the relative timing and duration of mineralogical processes during sedimentation and their impact on the environment. In this Volume, classic rock magnetic and paleomagnetic techniques, are combined

OPEN ACCESS

Edited and reviewed by:
Kenneth Philip Kodama, Lehigh University, United States

***Correspondence:**
Sara Satolli
sara.satolli@unich.it

Specialty section:
This article was submitted to Geomagnetism and Paleomagnetism, a section of the journal Frontiers in Earth Science

Received: *09 June 2021*
Accepted: *18 June 2021*
Published: *29 June 2021*

Citation:
Satolli S, Ferré EC, Kars M, Slotznick SP and Trindade RIF (2021) Editorial: Advances in Magnetism of Soils and Sediments. Front. Earth Sci. 9:722670. doi: 10.3389/feart.2021.722670

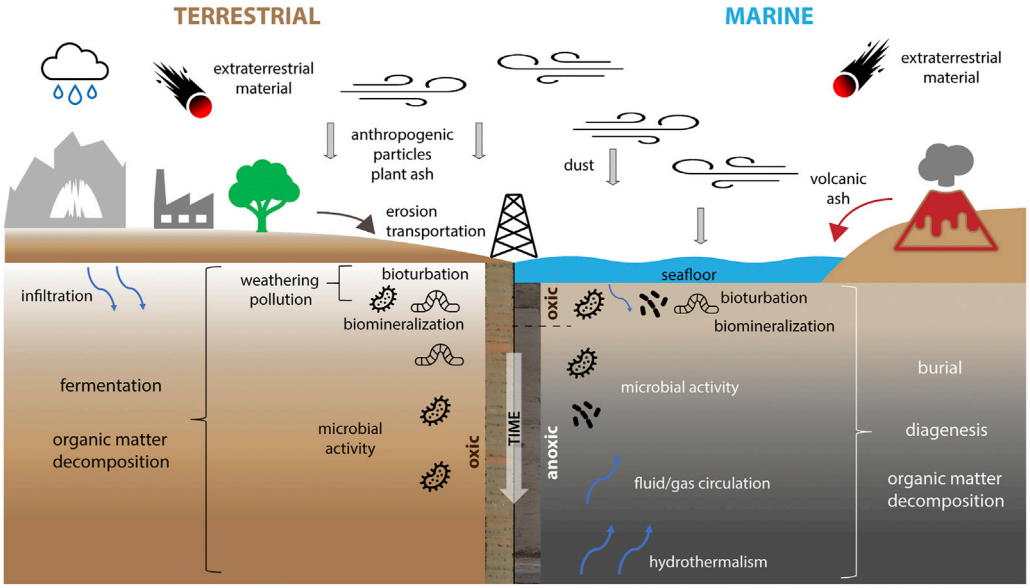

FIGURE 1 | Graphical synthesis of contributions to this Special Issue, highlighting the main sources of magnetic material in terrestrial and marine environments, the physiochemical conditions at the burial site, and the depositional and post-depositional processes that affect the magnetic signal in the geological environment.

with other analytical methods (i.e., Quantum Diamond Microscope magnetic field imaging, electron microscopy, Mössbauer and X-ray spectroscopy, X-ray and electron diffraction, geochemical analyses) yielding strong constraints on several processes, including climatic conditions, diagenesis, post-depositional effects, chemical magnetization, and their effect on the magnetic signal.

Two contributions discuss the advances in the characterization of magnetic minerals in sediments, combining classic rock magnetism with new techniques. Fu et al. show new methods to investigate the magnetic mineralogy of speleothems using magnetic microscopy via Quantum Diamond Microscope magnetic field imaging. This recently developed technique provides high-resolution time-series of detrital input which the authors associate to paleoprecipitation, thus providing useful paleoenvironmental information. Li et al. report a case where deep-sea surface sediments show a complex magnetic mineralogy indicating multiple different sources (distal and local igneous rocks as well as minor magnetofossil and superparamagnetic contributions) identified by scanning and transmission electron microscopy and magnetic methods.

Three contributions explore diagenesis in the context of methanogenesis. Amiel et al. connect early diagenetic processes and sedimentary magnetism using a composite high-resolution sedimentary record of pore-water chemistry, solid phase chemical measurements and mineral-magnetic parameters; they note a strong correlation between increase in the magnetic signal and the precipitation of authigenic magnetic minerals. Badesab et al. integrate rock magnetic, mineralogical, and microscopic analyses to investigate the linkage between greigite magnetism, methane seepage dynamics, and evolution of shallow gas hydrate system. Finally, Kars et al. investigate authigenic ferrimagnetic iron sulfides in gas-hydrate-bearing marine sediments, highlighting a close linkage between greigite, methane hydrate and microbial activity.

Another two contributions explore post-depositional effects on the magnetic mineralogy.

Ahn et al. is related to diagenetic effects on environmental magnetic parameters in an estuarine setting. They support rock magnetic analysis with electron microscopy to evaluate paleoenvironmental proxies and highlight a set of potentially robust magnetic proxies for sea-level change in the Holocene. Ejembi et al. show the profound effects of secondary, post-depositional fluid flow on the magnetic fabric of sandstones using anisotropy of magnetic susceptibility, rock magnetism and electron microscopy.

Three contributions detail advances in measurements of atmospheric magnetic particulate matter. Lanci et al. explore the nature and provenance of dust in Antarctic ice cores, finding undocumented complex behavior possibly due to post-depositional alteration. Till et al. deal with a usually neglected source of magnetic particles in atmosphetic dust, which is plant ash. They investigate through rock magnetic and geochemical characterization factors affecting the soils magnetic response to fire. Shin et al. show the importance of volcanic contributions to sedimentary magnetism, pointing out the close relation between magnetic susceptibility and volcanic proportions in terrigenous sediments.

Another two contributions explore advances in the magnetism of soils and paleosols. In particular, von Dobeneck et al. illustrate

that ground magnetic surveys can delineate the structural characteristics of an intrusive basaltic dike, and also reflect the subsurface deformation of its weathering products. Stine et al. analyze the effects of weathering on paleosol magnetic properties using rock-magnetic experiments, scanning electron microscopy, and Mössbauer spectroscopy. These detailed analyses were able to build on prior geochemical and magnetic analyses and suggest complicated interactions between changing provenance and precipitation levels affecting the magnetic signals.

The last two contributions bear on advances in the paleomagnetism of sediments. These papers deal with the quality of the paleomagnetic record in sedimentary rocks. Jung and Bowles investigate the potential of microbialites as a paleomagnetic recorder, proving modern microbialites and an ancient example can carry a consistent magnetization with timing of acquisition close to that of sediment deposition. Finally, Dallanave and Kirscher assess the reliability of the sedimentary record for paleogeographic reconstructions. By simulating geomagnetic directions at different latitudes, they highlight the value of utilizing anisotropy of magnetic susceptibility to assess sedimentary paleomagnetic data before use in paleogeographic reconstructions.

Although open to the larger community, the Special Issue stems from an engaging session on the topic of soil and sediment magnetism during American Geophysical Union's Fall Meeting in 2019. The diversity of the field as it stands now are shown throughout this collection along with the promise of new directions for the future.

AUTHOR CONTRIBUTIONS

All Authors have equally contributed to the Editorial.

Conflict of Interest: The authors declare that the research was conducted in the absence of any commercial or financial relationships that could be construed as a potential conflict of interest.

frontiers in Earth Science

ORIGINAL RESEARCH
published: 30 June 2020
doi: 10.3389/feart.2020.00258

Insight Into Provenance and Variability of Atmospheric Dust in Antarctic Ice Cores During the Late Pleistocene From Magnetic Measurements

Luca Lanci[1], Barbara Delmonte[2], Maria Cristina Salvatore[3,4] and Carlo Baroni[3,4]*

[1] Department of Pure and Applied Science, University of Urbino, Urbino, Italy, [2] Department of Environmental Science, University of Milano-Bicocca, Milan, Italy, [3] Department of Earth Science, University of Pisa, Pisa, Italy, [4] CNR-IGG, Institute of Geoscience and Earth Resources, Pisa, Italy

OPEN ACCESS

Edited by:
Sara Satolli, G. d'Annunzio University of Chieti and Pescara, Italy

Reviewed by:
Simo Spassov, Royal Meteorological Institute of Belgium, Belgium
Stefanie Brachfeld, Montclair State University, United States

***Correspondence:**
Luca Lanci
luca.lanci@uniurb.it

Specialty section:
This article was submitted to Geomagnetism and Paleomagnetism, a section of the journal Frontiers in Earth Science

Received: *04 April 2020*
Accepted: *09 June 2020*
Published: *30 June 2020*

Citation:
Lanci L, Delmonte B, Salvatore MC and Baroni C (2020) Insight Into Provenance and Variability of Atmospheric Dust in Antarctic Ice Cores During the Late Pleistocene From Magnetic Measurements. Front. Earth Sci. 8:258. doi: 10.3389/feart.2020.00258

We measured saturation isothermal remanent magnetization (SIRM), coercivity of remanence (H_{cr}), and insoluble dust mass concentration (IDC) of 49 ice samples from Vostok and EPICA Dome-C ice cores (Antarctica) as a measure of magnetic properties of the aerosol dust trapped in the ice. Samples range in age from marine isotopic stage (MIS) 7 to 19 in EPICA Dome-C ice core and from MIS 1 to 11 in Vostok ice core. Data from ice samples were compared with 86 samples from possible source areas (PSA) from East Antarctica, including 11 samples from South America and New Zealand. Previous results from MIS 1 to MIS 6 found that magnetic properties of aerosol dust could be divided in two distinct groups characterized by high-H_{cr} and low-$SIRM_{dust}$ for glacial samples, and low-H_{cr} and high-$SIRM_{dust}$, for interglacial samples. The new data from older ice samples highlighted several discrepancies from this expectation with significant differences between Vostok and Dome-C sites. Magnetic properties of Antarctic PSA sample show a large variability, however, PSA samples from Victoria Land and few other, have magnetic properties compatible with that of the glacial dust, or more precisely with samples characterized by high dust flux. The new data from Pleistocene ice and from PSA samples confirm South American and Antarctic provenance of the largest atmospheric dust load typical of glacial stages. On the other hand, we did not found any PSA sample with properties compatible with the highly magnetic samples (mostly from interglacial stages), which are characterized by low IDC. These samples from the oldest and deepest part of the cores revealed a more complex picture than previously outlined from the analysis of MIS 1–6, and show unusual magnetic properties which can be tentatively attributed to post-depositional alteration occurring into the ice.

Keywords: isothermal remanent magnetization, magnetic properties, Atmospheric dust concentration, Antarctic ice cores, dust source area

INTRODUCTION

The provenance of wind-blown dust and its characteristics are key issues to understand climate, atmospheric and environmental changes. Vostok (VK) and EPICA Dome-C (EDC) ice cores, drilled in the interior of the Antarctic ice sheet (**Figure 1**), provide the best known and longest dust records from Antarctica. VK gave the first dust record of the last 420,000 years (Petit et al., 1999) and revealed that the dust input to Antarctica was highest during glacial periods, lower during stadial and interstadial stages, and lowest in interglacial stages. The EDC ice core confirmed earlier findings from Vostok and, extended the dust record into the last ca. 800,000 years (Community Members EPICA, 2004; Jouzel et al., 2007), the longest polar ice core record.

The concentration of dust trapped in polar ice, its grain size and physical properties are modulated by synergistic factors related to climatic conditions and vary over orbital timescales. Therefore, the identification of dust provenance and its characteristics are important for understanding climate, atmospheric and environmental changes, and potentially provides key constraints to dust transport processes.

Many traditional geochemical methods for dust source tracking are not relevant to Antarctic ice cores because of their low dust concentration, spanning from a few ng/g during warm interglacial periods to a few hundreds of ng/g during relatively dustier glacial periods. The Sr-Nd and Pb radiogenic isotope composition of mineral dust in ice cores are the most widely-used technique for dust source tracking, however, the intrinsic limitations related to the extremely low dust abundance during interglacial stages restrict the geochemical data availability for interglacial stages to the Holocene and marine isotopic stage (MIS) 5. Magnetic measurements are not subject to this limitation since extremely low values of remanent magnetization can be precisely measured using SQUIDs magnetometers. The high sensitivity makes it possible to measure rock-magnetic properties of mineral dust directly in small ice samples (30–40 *g* mass) even for typical interglacial dust concentrations, overcoming the intrinsic limitations of traditional geochemical methods related to dust abundance. The intensity of isothermal remanent magnetization (IRM) and coercivity of remanence (H_{cr}) give information about remanence-carrying minerals in the dust. They generally consist of iron oxides and in particular hematite (γ–Fe_2O_3), maghemite (α–Fe_2O_3), and magnetite (Fe_3O_4), which are the most common and chemically stable natural iron oxides. Hence, magnetic properties of natural ice reflect the concentration and the type of iron oxides entrapped in the dust (e.g., Lanci et al., 2012).

Eolian dust from VK, EDC, and other sites from the interior of the East Antarctic plateau have been extensively studied for dust concentration (e.g., Lambert et al., 2008; Petit and Delmonte, 2009) and radiogenic isotope composition (Grousset et al., 1992; Basile et al., 1997; Delmonte et al., 2008, 2010a), which was compared with that of samples from possible source areas (PSA) in the Southern hemisphere to gather information on dust provenance (Revel-Rolland et al., 2006; Gaiero, 2007; Gaiero et al., 2007). Geographic provenance of aeolian mineral dust during the last climate cycle, suggests a dominant source from southern South America during glacials with an open question for the Holocene, which displays signatures and properties that are somewhat different wih respect to the glacial and variable in time. In central East Antarctica there is a general consensus on a significant contribution from different dust sources during the Holocene (Gabrielli et al., 2010) including Fe-rich local (Antarctic) sources as well (Wegner et al., 2012; Vallelonga et al., 2013). However, Paleari et al. (2019) on the basis of dust mineralogy suggested that South America is the primary dust source to Antarctica during both glacial and interglacial stages and that an additional Antarctic contribution is not required, coherently with conclusions based on Pb isotopic data from Gili et al. (2016). Sr and Nd isotope data from different ice cores confirmed a broadly uniform isotopic signature during all glacial periods of Pleistocene. Some minor differences, apparently correlated to the dust influx onto the Plateau, have been observed and interpreted as related to the activation of a secondary, still unidentified, dust source during dustier glacial stages (Delmonte et al., 2010a).

Geochemical data from interglacial ice are rather scarce. Gabrielli et al. (2010) studied aeolian dust composition using Rare Earth Elements concentration in EDC from 2.9 to 33.7 kyr BP, measuring a large number of samples from both climate stages. They found a homogeneous crustal-like composition during the last glacial stage consistent with dust from heterogeneous sources located in different areas or within the same region (e.g., South America). Starting at about 15 kyr BP, they found a major change in dust composition, which was characterized by a larger variability, and that persisted throughout the Holocene. They interpreted this variable character as the alternation of different dust sources during the Holocene.

Magnetic measurements on Antarctic ice cores from MIS 1–6 in EDC and MIS 1–2 in VK (Lanci et al., 2004, 2007, 2008b, 2012), found that ice magnetic properties show a significant difference between glacial and interglacial stages, with the notable exception of MIS 1 (Holocene) in VK, which shows magnetic properties very similar to MIS 2. According to its magnetic properties the aerosol dust was divided into two distinct groups characterized by high-H_{cr} and low-$SIRM_{dust}$ for glacial samples, and low-H_{cr} and high-$SIRM_{dust}$, for interglacial samples. It is also been observed that the glacial/interglacial difference is more pronounced at EDC compared to VK, and it is even larger at the external site of Talos dome (Lanci and Delmonte, 2013). To explain the above-mentioned differences between VK, EDC, and Talos Dome it has been hypothesized that the presence of local sources, active during interglacials, distribute the dust unevenly. Furthermore, these local sources had to be highly magnetic in order to explain the observed data, which suggested a volcanic origin. All these observations were found in general good agreement with geochemical data.

In this paper we extend the investigation of the magnetic properties of glacial and interglacial ice from EDC and VK ice cores to the late Pleistocene and compare ice measurements with magnetic measurements of PSA samples. They provide, for

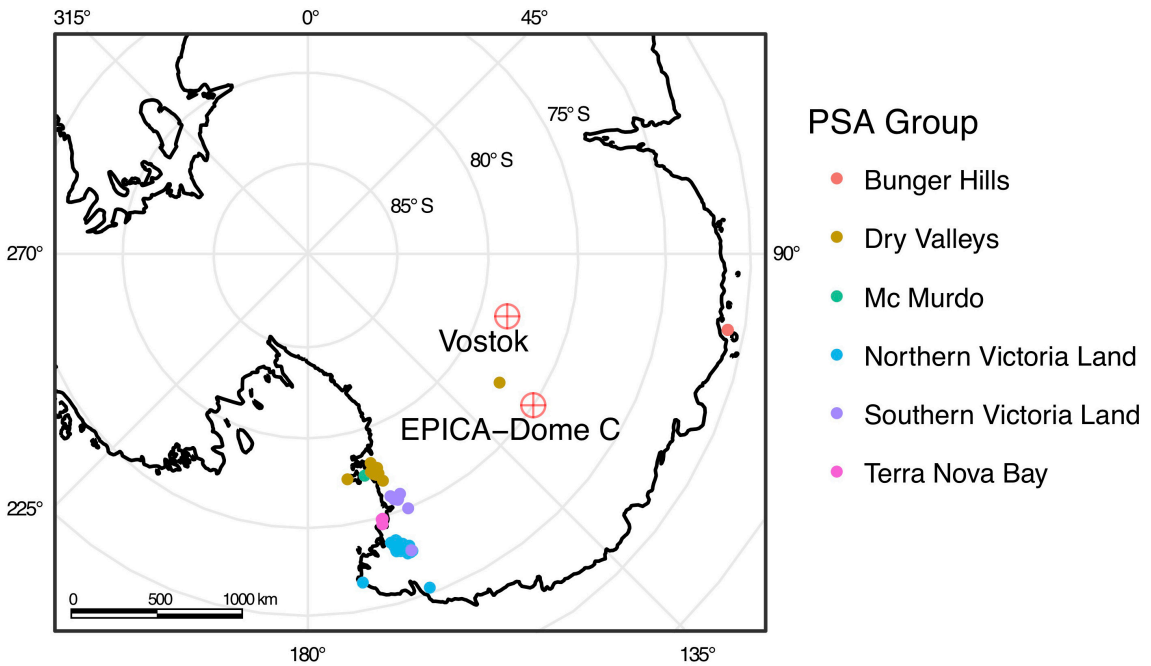

FIGURE 1 | Location map of the Vostok and EPICA Dome-C ice cores sites and PSA samples studied for magnetic properties (see **Supplementary Material** for details on PSA).

the first time, insights of dust origin during interglacial stages prior than MIS 6.

MATERIALS AND METHODS

Ice Samples

We analyzed ice samples from EDC and VK ice cores taken from glacial and interglacial stages in MIS 7 to MIS 19, corresponding to core depth from 2,289 m to 3,180 m, in EDC core, and from Holocene to MIS 11, corresponding to core depth from 183 m to 3,300 m, in VK core. A total of 28 ice samples from EDC and 21 samples from VK were measured. Samples consisted of approximately cubic pieces of ice weighting from ca. 30 *g* to 40 *g*. The standard preparation of the samples that includes the core cutting, decontamination, and measurement procedures, are equivalent to that described in previous papers (e.g., Lanci et al., 2012). Samples were decontaminated with ultra-pure water in a class 10,000 clean room using standard procedures and IRMs were induced in whole-ice samples at low temperature (∼100 K). Cooling at low temperature before IRM acquisition is necessary to avoid physical reorientation of magnetic grains in the ice matrix (Lanci et al., 2001; Dash et al., 2006). IRM was induced with a pulse magnetizer and measured using a 2G superconducting magnetometer with DC-SQUID sensors at the ALP laboratory. The measurements were performed quickly to avoid significant re-warming of the samples and their temperature was set back to 100 K after each measurement. IRM acquisition curves for most ice samples from both sites, are shown in **Figure 2**.

Since all ice samples were saturated, or nearly saturated, at the maximum field of 1 T we consider the IRM at 1 T equivalent to the saturation IRM (SIRM). Backfield demagnetization of the SIRM was performed at 100 K using 10 mT steps, and was used to compute H_{cr} and the exact field value of H_{cr} was linearly interpolated between zero-crossing IRM magnetizations. The SIRM that was first measured at ∼100 K was then remeasured after allowing the samples to re-equilibrate to the freezer temperature (∼255 K) for several hours in order to remove the remanent magnetization due to superparamagnetic particles (Lanci and Kent, 2006). We refer to the SIRM that remains after warming to ca. 255 K simply as $SIRM_{ice}$ meaning that such SIRM is computed with respect to the mass of the ice sample. The SIRM measured at 255 K is generally smaller than that measured at ∼100 K, which includes a superparamagnetic fraction part of which is carried by nanometer-sized particles of extraterrestrial origin (Lanci et al., 2012). The rewarming has the main purpose of discarding this superparamagnetic fraction because of its different origin, but the temperature transit of the samples through the Verwey transition and through the magnetite isotropic point, both around 120 K, could further reduce the remanent magnetization of multi-domain grains. This underestimate the SIRM of the dust trapped in ice compared to an ideal measurement, but this error is balanced out in the comparison with PSA samples since both measurements were performed using the same procedure.

Insoluble dust concentration (IDC) was measured in the same ice samples analyzed for magnetic properties, after additional decontamination in the clean room and melting at room temperature. Insoluble microparticles were measured by Coulter

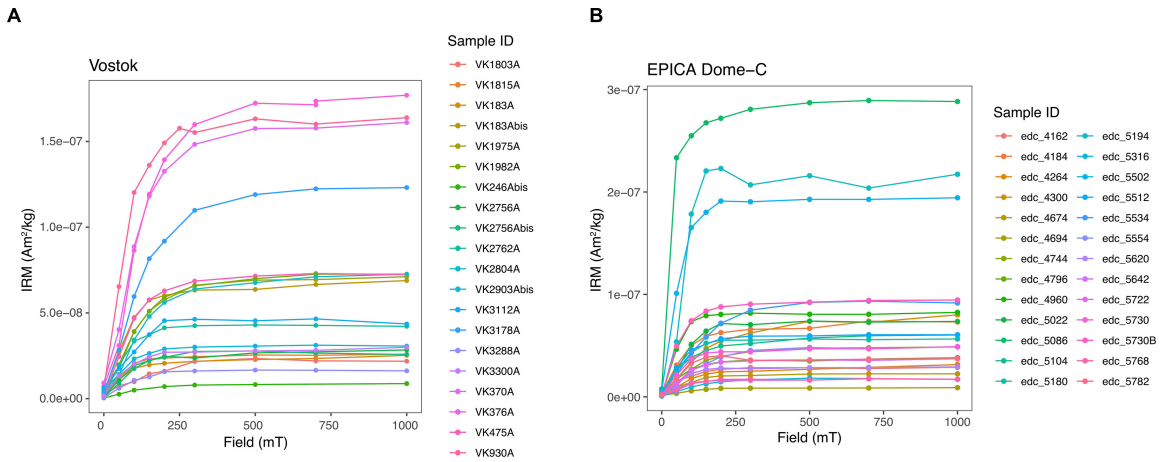

FIGURE 2 | IRM acquisition of ice samples from **(A)** Vostok and **(B)** EPICA Dome-C ice cores. IRM is measured at 100 K and expressed as magnetic moment per unit of mass of the whole ice samples. Therefore this is the magnetization of the dust diluted within the ice. IRM acquisition curves are of good quality considering the extremely low intensity of the ice magnetization and testify to the reliability of the measurements.

Counter, which detects insoluble particles with equivalent spherical diameters ranging from ca. 1 μm to about 30 μm. The dust mass was then calculated assuming that mineral grains have an average density of 2.5 g/cm^3, which is the standard average density for eolian dust used in the literature (e.g., Delmonte et al., 2004, and references therein).

Our IDC data, shown in **Figure 3**, are generally compatible with the extensive measurements performed on the same cores (Petit et al., 1999; Ruth et al., 2008). However, we notice that some samples, whose stable isotope profile belongs to the full glacial (MIS 8, 10, 12, and 18 in EDC and MIS 4 in VK), show a IDC significantly lower than previous measurements. We assume that the lower IDC of our discrete samples are a consequence of the natural variability of IDC during glacial stages.

The magnetization of the dust trapped in ice samples ($SIRM_{dust}$) was computed by dividing the samples magnetic moment by the mass of the dust measured in the same samples, or equivalently dividing the $SIRM_{ice}$ by the IDC mass. Analytical errors of the combined magnetic and IDC measurements were discussed in Lanci and Delmonte (2013). Probably the most important factor affecting the precision of $SIRM_{dust}$ is the uncertainty of the mass loss of the soluble aerosol fraction during Coulter Counter measurements. We do not have a direct estimate of this error that would result in an overestimate of $SIRM_{dust}$ but we assume that is proportional to the IDC, practically meaning that the $SIRM_{dust}$ could be overestimated by a small constant factor.

Possible Source Area Samples

We analyzed 86 samples from PSA from Antarctica each one consisting of ca. 3 grams of pristine fine sands and silt, sieved keeping the granulometric fraction <62 μm. Several of these samples have been studied previously (Lanza and Zanella, 1993; Gore et al., 2001; Delmonte et al., 2010b, 2013; Bristow et al., 2011; Blakowski et al., 2016). Antarctic PSA samples were studied to examine the possible influence of local sources of dust and were collected in unconsolidated sediments mostly from the Dry Valley and Victoria Land regions. These samples were integrated with 11 PSA samples from classic source area (South America and New Zealand) previously studied for isotopic analysis (Delmonte et al., 2004). Measurements on PSA samples were performed following the same protocol used for ice samples in order to allow a proper comparison. We decided to use the relatively coarse (<62 μm) granulometric fraction of PSA samples after a pilote experiment made with the fine-grained fraction on a set of 5 Argentinian PSA samples. Measurements on the fine fraction gave inconsistent results suggesting that the sedimentation procedure used for separation introduced relevant artifacts in the magnetic properties. We are aware that the different granulometry could cause some discrepancy in the magnetic properties of the PSA samples and airborne dust, however, the results obtained from a analogous experiment in North GRIP ice core (Lanci et al., 2004) and from laboratory experiments using natural and artificial sediments (Valet et al., 2017) suggest that such a discrepancy can be small compared to the large natural variability of the magnetic properties of PSA samples and of dust trapped in ice.

The study of PSA samples is aimed to constrain the provenance area of aerosol dust. The problem of dust provenance is traditionally addressed using radiogenic isotopes studies, magnetic methods are probably not as selective in detecting the provenance area but they are simpler to perform and have provided a larger amount of data. As for isotopic data, the assumption is that magnetic properties of PSA samples will be similar to that of aerosol dust if they share the same provenance. This reasonable assumption is supported by results from NGRIP ice core where dust magnetization is similar to that of pristine loess samples from Chinese Loess Plateau (Lanci et al., 2004). The PSA location is shown in **Figure 1** and a table with their magnetic properties and other available information can be found in the **Supplementary Material**.

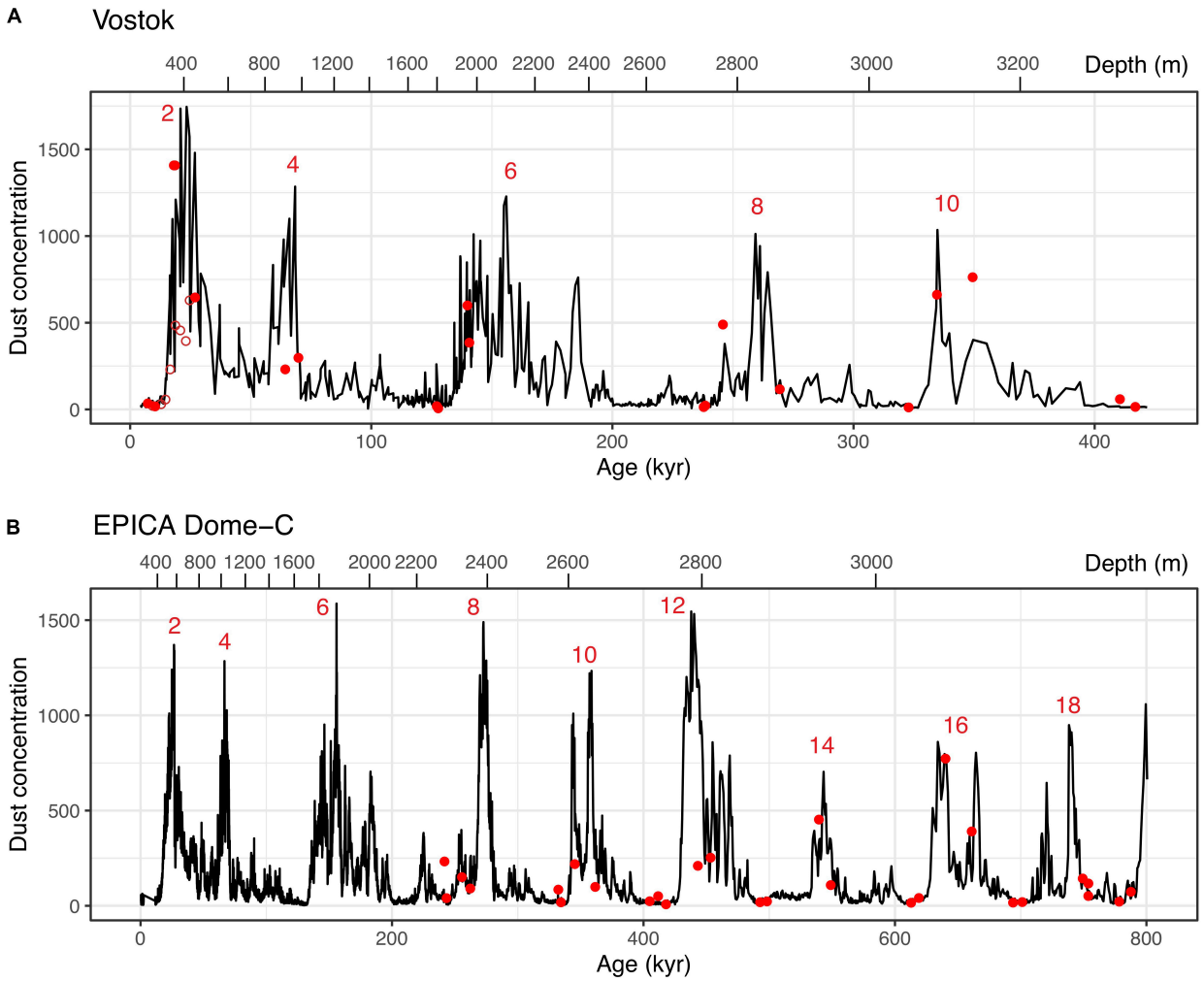

FIGURE 3 | IDC measurements of individual samples (solid red circles) from Vostok and Epica Dome C (**A** and **B**, respectively) compared with extensive measurements on the same cores (black line) from Petit et al. (1999) and Ruth et al. (2008). Vostok samples includes additional samples from Lanci et al. (2007) shown with open symbols, see section "**Appendix**." Red numbers indicate the glacial marine isotopic stages and scales on the top axis report the core depth. Note that all EDC samples are taken at depth >2,200 m.

RESULTS

Ice Samples

An overview of the magnetization of ice samples, divided in glacial and interglacial stages and by sites, are shown in the log-log diagrams of IDC versus $SIRM_{ice}$ (**Figures 4A,B**). Samples from VK (**Figure 4A**) suggest a main linear trend indicating a proportionality between IDC and $SIRM_{ice}$. The linear trend can be computed by fitting either a line passing through the origin whose slope represents the average $SIRM_{dust}$ (gray dashed line in **Figure 4A**) or as a line with an offset (which is not rectilinear in the log-log plot, the green dashed line in **Figure 4A**). The latter can be interpreted as a linear model with a contribution to $SIRM_{ice}$ proportional to IDC plus a constant contribution independent from IDC. Both linear models have a high correlation coefficient (R^2 = 0.85 and R^2 = 0.78, respectively) and are significant at the 99% confidence level according to a *t*-test. Prominent outliers belongs to MIS 7, MIS 9 and MIS 11, and are sampled at depth > 2,500 m.

EPICA Dome-C samples (**Figure 4B**), which are all taken in the deepest part of the core (depth > 2,200 m), do not show the same clear linear relationship. Especially samples from interglacial stages deviates significantly from the VK proportionality line because of a much higher magnetization, which suggests a much higher concentration of magnetic minerals. The difference between VK and EDC interglacial $SIRM_{ice}$ is evident also in the distribution density estimates shown in the marginal plots. Glacial and interglacial distribution of $SIRM_{ice}$ are well distinct in VK and very similar in EDC, to a minor extent also ICD distributions have a larger overlap in EDC.

The semilogarithmic diagram of $SIRM_{dust}/H_{cr}$ (**Figures 5A,B**) have been used to characterize the magnetic properties of the dust trapped in the ice (e.g., Lanci et al., 2012). The $SIRM_{dust}$

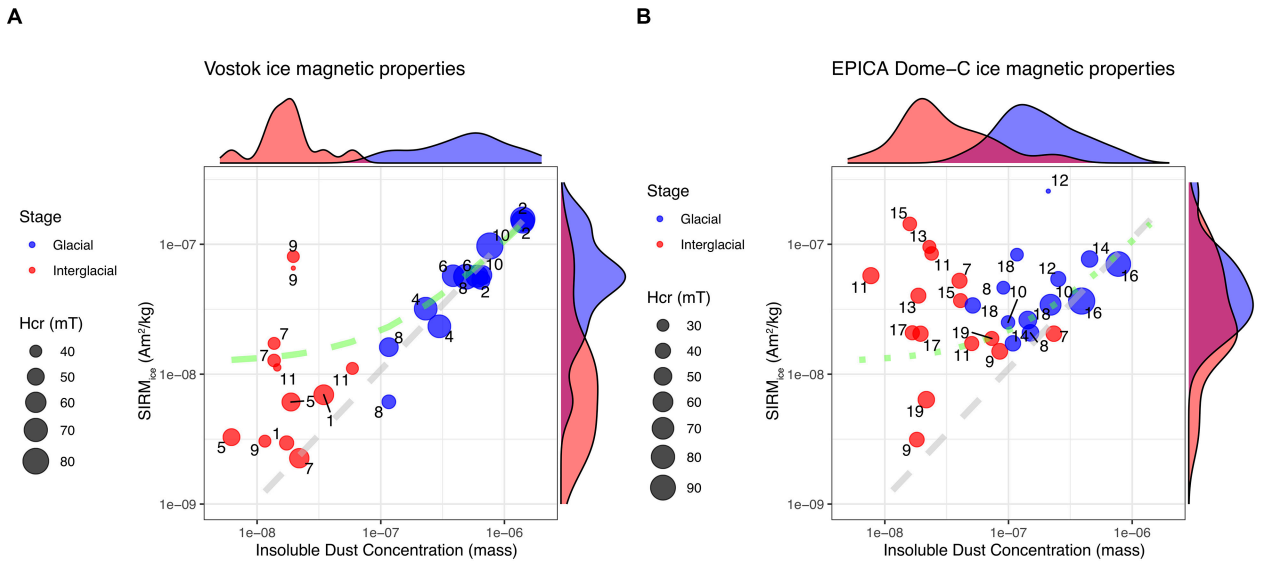

FIGURE 4 | Log-log diagram of IDC and $SIRM_{ice}$ of the EDC and VK datasets. Samples are grouped by color in glacial and interglacial stages with numbers indicating the isotopic stage (MIS) of each sample, symbols size is proportional to H_{cr}. Estimated distribution densities are shown in the marginal plots. **(A)** In VK samples the distributions of glacial and interglacial $SIRM_{ice}$ are distinct and most of the samples do not deviate significantly from a linear relationship between IDC and $SIRM_{ice}$. The best-fit lines (not rectilinear in the log-log diagram) represents the following models: $SIRM_{ice} = 0.108 \times IDC + e_i$ (gray) and $SIRM_{ice} = 0.0935 \times IDC + 1.23 \times 10^{-8} + e_i$ (green) where e_i are random variables representing the deviations of the data from the best-fit line. **(B)** Compared to VK, EDC samples shows significant differences in the distribution of $SIRM_{ice}$. EDC ice samples from interglacial stages are much more magnetic than VK and the same linear relationship found in VK (here reported for comparison) is not maintained.

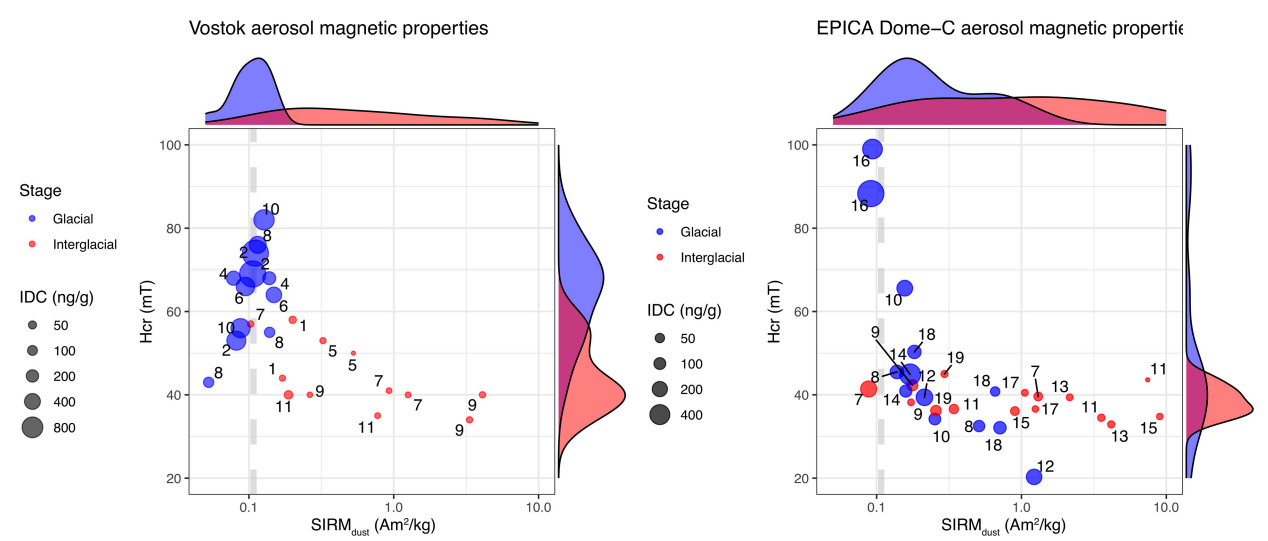

FIGURE 5 | Semi-logaritmic $SIRM/H_{cr}$ diagram. Samples are grouped by color in glacial and interglacial stages with numbers indicating the isotopic stage (MIS) of each sample, symbols size are proportional to IDC. Vertical line at 0.11 A m^2/kg represents the average $SIRM_{dust}$ computed by the best-fit line. **(A)** The magnetic properties of VK are distributed along the vertical line of constant SIRM. Some low IDC samples from interglacial stages 5, 7, 9, and 11 plot in the lower-right part of the $SIRM/H_{cr}$ diagram. **(B)** Only two EDC samples from MIS 16 exhibit true glacial magnetic properties and plots in the upper-left portion of the $SIRM/H_{cr}$ diagram. Most samples are characterized by low H_{cr} and high SIRM irrespective of climatic stage. Note, however, that no EDC samples prior to MIS 6 are present in this dataset.

of glacial samples from VK are well-grouped around an average value of ca. 0.1 A m^2/kg corresponding to the slope of the linear models above. The $SIRM_{dust}$ of interglacial samples is generally higher and occasionally extremely high. We further notice that samples with high $SIRM_{dust}$ generally exhibit low H_{cr} suggesting that their remanent magnetization is carried by low-coercivity

ferrimagnetic minerals such as magnetite or maghemite. In samples from EDC the groups of glacial and interglacial samples have a broader overlap and especially the latter displays extremely large $SIRM_{dust}$ values. The natural variability of both $SIRM_{dust}$ and H_{cr} can be large even within the same MIS.

Extremely high $SIRM_{dust}$ values (>1 A m^2/kg), were occasionally observed in some interglacial samples from the previous EDC dataset (Lanci et al., 2008b) and Talos Dome (Lanci and Delmonte, 2013). In the new dataset they are much more frequent and, in EDC, not limited to interglacial stages; in fact only samples from MIS 16 have shown "typical" glacial magnetic properties similar to that previously observed in MIS 2, MIS 4, and MIS 6 (Lanci et al., 2008b). In **Table 1** we have summarized the data from VK and EDC ice cores listing the averaged values (within each MIS) of all the available magnetic data, including this study, the amended Vostok dataset from Lanci et al. (2007); see section "**Appendix**", and the EDC dataset from Lanci et al. (2008b).

Possible Source Area Samples

Magnetic properties of PSA samples, which include Fe-rich magmatic rocks, are summarized in **Figures 6A,B** using the semilogaritmic $SIRM/H_{cr}$ diagram. PSA data are compared to all the available aerosol dust data from VK and EDC ice cores, which include data from Lanci et al. (2007) and Lanci et al. (2008b; section "**Appendix**"); the complete dataset is included in the **Supplementary Information Tables**. To avoid cluttering the diagram, the aerosol dust data are summarized using their two-dimensions distribution density estimates, computed with the method described in Venables and Ripley (2002). Aerosol distribution density are computed separately for samples with high IDC (IDC $\geq$ 100 ng/g), which comprise mostly glacial samples, and low IDC (IDC $<$ 100 ng/g) that comprise interglacial samples.

The complete set of PSA samples (**Figure 6A**) shows a very large scatter in the magnetic properties. Magnetic properties of Argentinian samples are sufficiently similar to that of interglacial aerosol, although their SIRM is slightly lower. This could be a consequence of the underestimate of IDC due to the soluble dust fraction that result in an overestimate of $SIRM_{dust}$. Overall we believe that magnetic properties confirm the affinity suggested by isotopic analysis (Gaiero, 2007; Gili et al., 2016) in Argentinian samples while New Zealand PSA samples, instead, are mostly incompatible from the point of view of magnetic properties. Within the set of Antarctic PSA samples the variability of magnetic properties is surprisingly large, however, some of them and in particular the sample group from dry Valleys and Victoria Land, have magnetic properties that are similar to that of glacial dust (**Figure 6B**). The map inset in **Figure 6B** shows that compatible PSA samples likely originate all in a restricted area and derived from, the bedrock with a high concentration of magnetic minerals. Our results from PSA samples are in general agreement with magnetic measurements of the rock from the Dry Valleys (Brachfeld et al., 2013), although some caution is needed comparing the two sets because of the different measurement procedures. In particular the difference in H_{cr} that in the data from Brachfeld et al. (2013) have, on average, lower values, could be a consequence of measurements at room temperature instead of 100 K. In comparing these data lower SIRM in the PSA set can also be expected because of their transition through the Verwey transition or magnetite isotropic point after magnetization. A subset of Brachfeld et al. (2013) data, which falls near the distribution of dust, are presented in **Figure 7**.

DISCUSSION

The magnetic properties of Pleistocene ice have emphasized the differences between EDC and VK previously observed during the most recent (MIS 1–6) climatic stages (Lanci and Delmonte, 2013). If the aerosol record of Antarctic ice cores were a perfect record of long range atmospheric transport one would expect minimal differences between the two sites, hence Lanci and Delmonte (2013) resorted to short distance (i.e., local) sources to explain the observed data. Regrettably, the even larger differences observed in the new dataset are much more difficult to explain, especially in light of the results from PSA samples.

The analysis of PSA samples gave two main results: first they show that, in general agreement with the literature (Delmonte et al., 2010a), Argentinian PSA samples are similar, hence compatible, with glacial aerosols. They also showed that there is a group of Antarctic PSA samples that are equally compatible with glacial aerosol from the point of view of magnetic properties. This group of samples originates in a relatively restricted area. Based on our results it can be safely concluded that the aerosol dust entrapped in ice samples from glacial periods is compatible with a mixture of South American (Argentinian) and Antarctic contributions.

A second important result is that none of the measured PSA sample has magnetic properties that can explain the distribution density of the interglacial samples (IDC $<$ 100 ng/g), in particular none of them reach the very large $SIRM_{dust}$ observed in these samples. Although our PSA dataset is not exhaustive, this observation is confirmed by the rock magnetic data from the Dry Valleys (Brachfeld et al., 2013) and cast doubts on the existence of a local (i.e., Antarctic) source of highly magnetic dust capable to explain the magnetic properties of these samples and therefore do not support the hypothesis of their origin from a local source. Without a local source capable of supplying enough magnetic minerals to justify the strong magnetization of interglacial dust, the observed differences between EDC and VK are difficult to explain as original depositional features.

The nature of the magnetic particles responsible for the very high $SIRM_{dust}$ values found especially in interglacial samples (IDC $<$ 100 ng/g) and particularly in several EDC samples from MIS 11, 13, and 15 and VK samples from MIS 9 is puzzling. A compatible local source was not found and, more generally, terrestrial rocks with such a large SIRM are not common. In fact, to find similar SIRM we had to resort to the Antarctic micrometeorite collection of Suavet et al. (2009; **Figure 7**). However, a direct flux of micrometeorites cannot account for the high $SIRM_{dust}$ for two reasons: (i) a uniform micrometeorite flux cannot explain the difference between relatively close sites of

TABLE 1 | Summary of available magnetic data from Vostok and EPICA Dome-C, averaged over their climatic stages.

Vostok					EPICA Dome-C				
M.I.S.	**N**	**Mean H_{cr} (mT)**	**Mean $SIRM_{dust}$ ($A\ m^2/kg$)**	**I.D.C. (ng/g)**	**M.I.S.**	**N**	**Mean H_{cr} (mT)**	**Mean $SIRM_{dust}$ ($A\ m^2/kg$)**	**I.D.C. (ng/g)**
1	7	63 ± 13.1	0.167 ± 0.029	64.9	1	8	46 ± 3.7	0.733 ± 0.462	70.1
2	8	79 ± 14.7	0.119 ± 0.026	775	2	8	85 ± 12.2	0.086 ± 0.040	567
3		—	—		3	7	66 ± 7.7	0.203 ± 0.140	130
4	2	68 ± 0	0.108 ± 0.030	264	4	3	82 ± 11.7	0.088 ± 0.002	342
5	2	52 ± 1.5	0.426 ± 0.101	12.5	5	7	46 ± 5.0	0.689 ± 0.521	18.3
6	2	65 ± 1.0	0.122 ± 0.027	492	6	9	82 ± 16.0	0.110 ± 0.058	253
7	3	46 ± 9.5	0.763 ± 0.595	16.5	7	2	41 ± 0.9	0.738 ± 0.567	80.1
8	3	58 ± 16.7	0.102 ± 0.045	303	8	2	39 ± 6.5	0.324 ± 0.186	121
9	3	38 ± 3.5	2.568 ± 2.032	16.9	9	2	40 ± 2.0	0.175 ± 0.002	51.6
10	2	69 ± 13.0	0.107 ± 0.020	712	10	2	50 ± 15.7	0.204 ± 0.048	159
11	2	38 ± 2.5	0.481 ± 0.293	36.8	11	3	38 ± 4.8	3.725 ± 3.628	41.9
12		—	—		12	2	30 ± 9.6	0.718 ± 0.505	231
					13	2	36 ± 3.2	3.161 ± 1.007	20.8
					14	2	43 ± 2.0	0.165 ± 0.006	281
					15	2	36 ± 0.7	4.956 ± 4.056	28.4
					16	2	94 ± 5.3	0.092 ± 0.001	582
					17	2	39 ± 1.9	1.152 ± 0.097	18.1
					18	3	41 ± 9.1	0.517 ± 0.291	104
					19	2	41 ± 4.4	0.276 ± 0.019	47.5

Magnetic data from EDC, MIS 1–6 are taken from Lanci et al. (2008a), VK data from MIS 1–2 are integrated with data from Lanci et al. (2007). The errors (s) represent the sample variability within each group, not the measurement error.

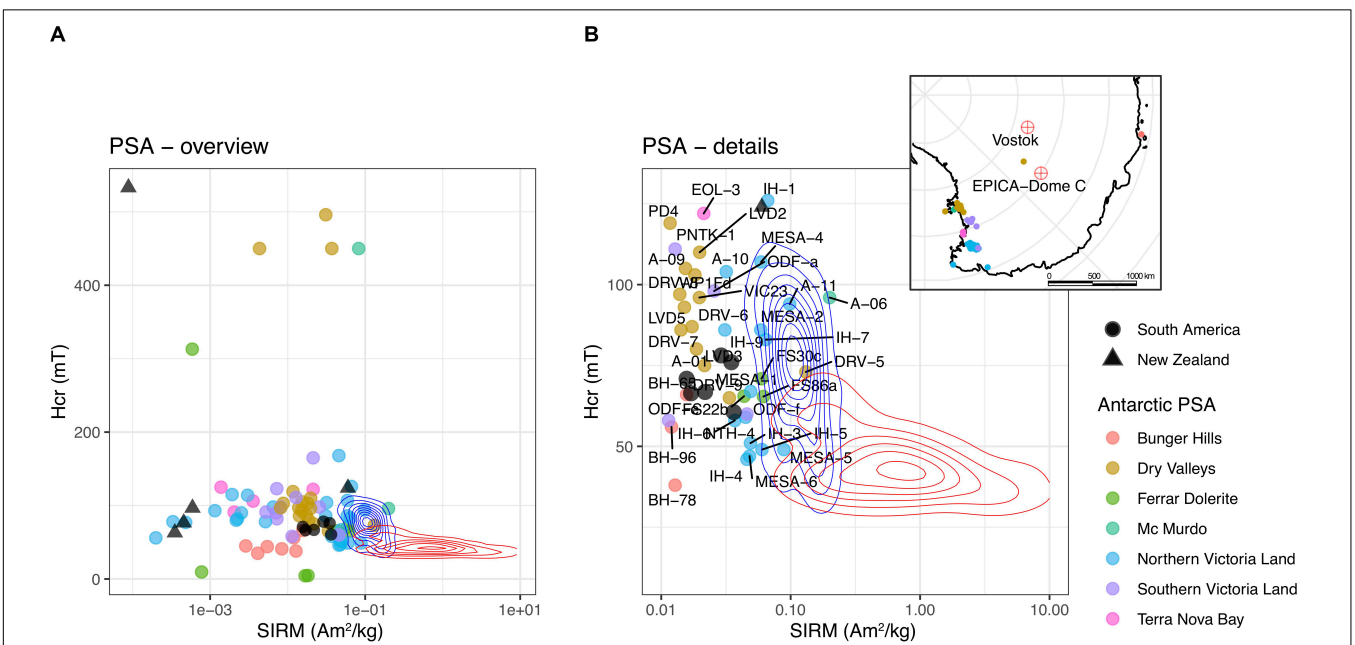

FIGURE 6 | Magnetic properties of PSA samples in the semi-logaritmic SIRM/H_{cr} diagram. The $SIRM_{dust}$ data from ice cores, including the dataset from Lanci et al. (2008a), are reported for comparison using their distribution density estimates computed according to Venables and Ripley (2002). $SIRM_{dust}$ data are divided in glacial (IDC ≥ 100 ng/g) and interglacial (IDC < 100 ng/g) groups whose distribution is indicated with blue and red lines, respectively. Isolines shows the same level of density of $SIRM_{dust}$ data. The whole dataset used to compute the distribution is available in the **Supplementary Material**. **(A)** All available PSA samples divided in groups based on provenance area. **(B)** Close-up view of the PSA samples that shows properties similar to that of ice dust. Information on individual PSA samples can be found in the **Supplementary Information**. Despite the large natural variability of magnetic properties of PSA samples, none of them can explain the properties of interglacial aerosol dust.

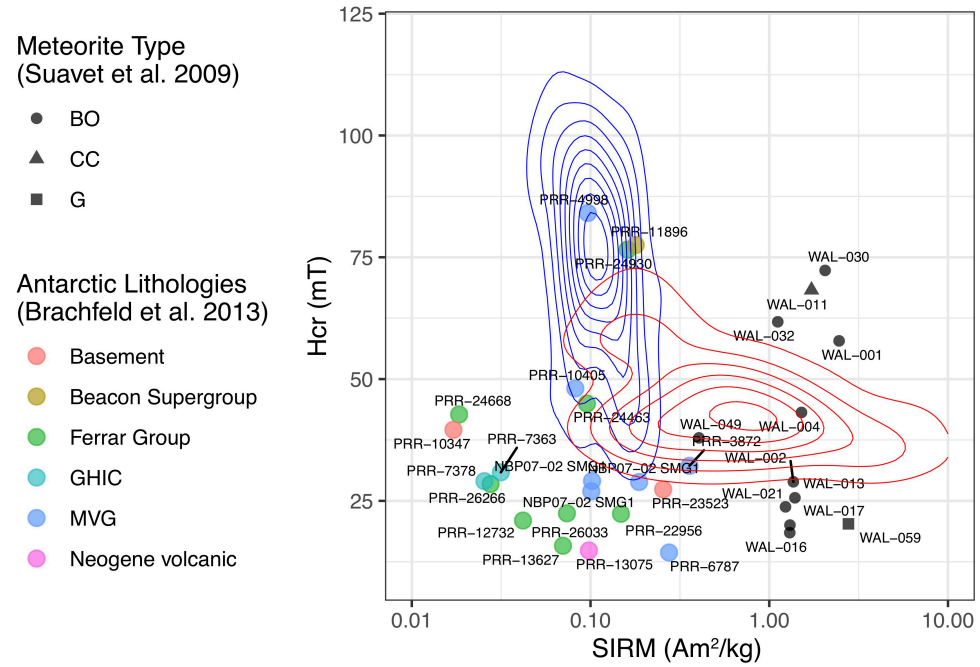

FIGURE 7 | Semi-logaritmic SIRM/H_{cr} diagram of rock-magnetic data from the Dry Valley (Brachfeld et al., 2013) and of micrometeorite samples from Suavet et al. (2009). Samples labels and groups correspond to that of original data, micrometeorite groups are divided in BO (Barred Olivine), CC (Cryptocrystalline), and G (G-type cosmic spherules). The $SIRM_{dust}$ data from ice cores are reported for comparison as their density estimates as in **Figure 6**. SIRM of Dry Valley rocks are not significantly different from that of PSA samples from the same area and are compatible with glacial dust but they have, on average, a lower H_{cr}, Magnetic properties of micrometeorites are compatible with that of interglacial aerosol dust except for the larger variability of H_{cr}. However, to explain the total amount of magnetic minerals found in the ice would require a micrometeorite flux ranging from 2×10^{-7} to 2×10^{-6} (kg/m^2 year). Extrapolated to the whole Earth surface (5.1×10^{14} m^2) this corresponds to a total flux from ca. 102 to ca. 1020 (kt/year), which is orders of magnitudes higher than current estimates of ca. 160 ± 60 t/year (Prasad et al., 2013).

EDC and VK, and (ii) more importantly, the required particles flux exceed by at least two orders of magnitude micrometeorites influx estimates (Prasad et al., 2013).

Furthermore, we notice that highly magnetic samples pertain to a part of the core, below 2,500 m depth, where post-depositional physical processes affecting the mineral dust have been observed (Lambert et al., 2008).

These results do not identify the origin of interglacial dust, but they suggest that samples with $SIRM_{dust}$ larger than ca. 1 A m^2/kg are unlikely to represent the pristine magnetic properties of natural atmospheric dust. In fact, it seem reasonable to expect that the properties of interglacial airborne dust cannot be too different from those of the PSA samples and therefore, ultimately not very different from the magnetic properties of the glacial dust. This, incidentally, is what had emerged from an earlier study in Holocene samples from VK (Lanci et al., 2007), and suggests that most of the observed glacial/interglacial difference could be the results of post-depositional alteration of the original aerosol. Post-depositional processes in mineral dust are known to occur in the deepest part of Talos Dome ice core (Baccolo et al., 2018), although these results cannot be directly applied to EDC and VK.

Based on these observations we tentatively define an index of alteration of magnetic minerals computed as the absolute value of the difference between the actual $SIRM_{dust}$ and the pristine $SIRM_{dust}$ normalized to unity,

$$I = \frac{|SIRM_{dust} - SIRM_{pristine}|}{SIRM_{dust}}$$

The pristine $SIRM_{dust}$ is not known but based on the above consideration we assume that the magnetic properties of the VK Holocene ice are the best available for pristine interglacial dust. The pristine $SIRM_{dust}$ value is then estimated as the linear fit of $SIRM_{ice}$ versus IDC, similar to that shown in **Figure 4**, but computed using only VK samples from MIS 1 and MIS 2 that are assumed to be the least altered, This set of samples can be extracted from the table "complete set" in the **Supplementary Material**. The coefficients of this linear fit (intercept = 4.37×10^{-9} slope = 0.1052), which are highly significant according to a *t*-test, are used to compute the pristine $SIRM_{dust}$ of other samples using MIS-averaged IDC data listed in **Table 1** as $SIRM_{pristine} = 4.37 \times 10^{-9} + 0.1052 \cdot \mathrm{IDC}$. The results (**Figure 8**) show that no glacial stages from VK show relevant alteration and the only large alteration index are obtained in interglacials MIS 7 and MIS 9. High index values are found only at a depth > 2,000 m and MIS > 6 in both sites, with the exception of MIS 5 at EDC. Most of the older MIS from EDC (depth > 2,000 m) have a large index.

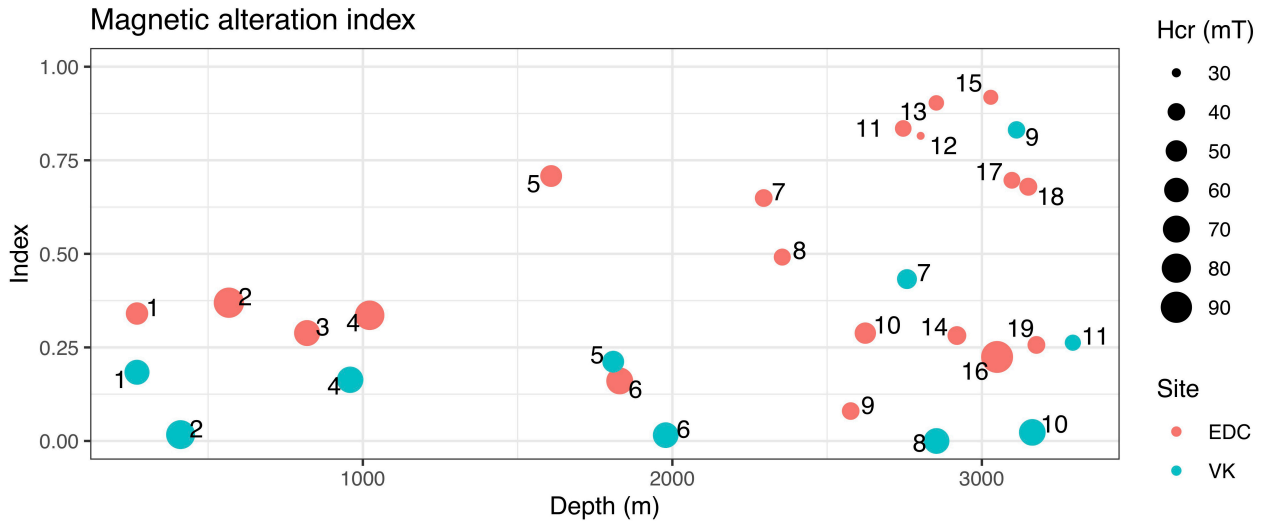

FIGURE 8 | Alteration index representing the normalized absolute difference between $SIRM_{dust}$ and its estimated pristine value, which is computed from IDC data averaged within each MIS (**Table 1**), see text for details. Alteration index close to zero indicates a $SIRM_{dust}$ similar to that measured in the Holocene and LGM samples at VK. Values close to unity indicates anomalously large $SIRM_{dust}$ that could not be explained by the magnetization of PSA samples. Symbols size is proportional to H_{cr} and numbers indicate the M.I.S. from which one can deduce the average age of the group of samples (**Table 1**).

This summarizes previous observations suggesting that: (i) alteration processes are more common in samples deposited during interglacial periods, (ii) large alteration indexes become very frequent below ca. 2,000 m depth, where mineral dust is more likely to be affected by post-depositional processes, (iii) lowest H_{cr} (smaller symbols in **Figure 8**) are often associated with higher indexes suggesting that alteration affects the magnetic mineralogy, and (iv) regardless of other factors, the alteration is more pronounced at EDC than at VK.

CONCLUSION

According to a widely accepted interpretation of the Antarctic dust record based on the study of the lasted climatic stages, during glacial conditions dust deposition is dominated by a large load of long-distance transported dust, while during interglacial conditions other, unknown, contributions became significantly large compared to the much smaller atmospheric dust load. In this conceptual model the magnetic properties of wind-blown dust in Antarctica are expected to oscillate between two clusters which were identified with the interglacial cluster dominated by dust with low-H_{cr} and high-$SIRM_{dust}$ and glacial cluster characterized by high-H_{cr} and low-$SIRM_{dust}$. Our result, instead, shows that this model does not hold very well when older climatic stages of VK and EDC are analyzed. Moreover, the difference between VK and EDC sites, which could be considered minor during MIS 1–6, became larger in older stages during both glacial and interglacial periods.

Results from PSA samples support the provenance of glacial aerosols from Argentina and found compatible Antarctic samples from Victoria Land. However, magnetic properties of PSA samples are incompatible with that of interglacial aerosol, hence, the origin of the source responsible for the low-H_{cr} and high-$SIRM_{dust}$ measured in interglacial samples remains enigmatic. The properties of these samples, and in particular their $SIRM_{dust}$ are unusual in terrestrial rocks and we had to resource to data from Antarctic micrometeorites to find similar SIRM. Nonetheless the required micrometeorite flux exceed the current estimates by orders of magnitude and this mechanism would not explain the difference between VK and EDC.

With the lack of plausible sources for the low-H_{cr} and high-$SIRM_{dust}$ aerosol, the differences observed between EDC and VK ice cores are difficult to explain as original depositional features and it is suggested that they could originate from post-depositional alteration occurring in the deepest part of the Antarctic ice sheet. In any case our results indicate that the properties of interglacial Antarctic dust from the deepest layers of ice cores, do not represent a reliable sample of the pristine atmospheric aerosol composition. In this respect VK dust record seems to provide a less biased record than EDC.

DATA AVAILABILITY STATEMENT

The raw data supporting the conclusions of this article will be made available by the authors, without undue reservation.

AUTHOR CONTRIBUTIONS

LL contributed to conception and design of the study, performed laboratory measurements and data analysis, wrote the first draft

of the manuscript. BD contributed to conception and design of the study, performed laboratory measurements, provided ice sample, and contributed to data analysis and interpretation. MS and CB provided PSA samples and contributed to data interpretation. All authors contributed to manuscript revision, read and approved the submitted version.

FUNDING

This work is a contribution to the PRIN 2009 research project "Variability and geographic provenance of eolian dust in Antarctica during the late Quaternary: a multi-parametric approach with the use of cutting-edge techniques" and partial supported by University of Urbino and DiSPeA research project 2019.

ACKNOWLEDGMENTS

The reviews from SS and SB, as well as the discussion with Dennis V. Kent helped to improve the manuscript. Jean-Robert Petit is acknowledged for kindly providing ice samples and some PSA samples, Paul Augustinus kindly provided PSA samples from Bunger Hills, and Roberto Lanza provided PSA samples of Ferrar dolerite.

SUPPLEMENTARY MATERIAL

The Supplementary Material for this article can be found online at: https://www.frontiersin.org/articles/10.3389/feart.2020.00258/full#supplementary-material

REFERENCES

Baccolo, G., Cibin, G., Delmonte, B., Hampai, D., Marcelli, A., Di Stefano, E., et al. (2018). The contribution of synchrotron light for the characterization of atmospheric mineral dust in deep ice cores: preliminary results from the talos dome ice core (East Antarctica). *Condens. Matter.* 3:25. doi: 10.3390/condmat3030025

Basile, I., Grousset, F. E., Revel, M., Petit, J.-R., Biscaye, P. E., and Barkov, N. I. (1997). Patagonian origin of glacial dust deposited in East Antarctica (Vostok and Dome C) during glacial stages 2, 4 and 6. *Earth Planet. Sci. Lett.* 146, 573–589. doi: 10.1016/s0012-821x(96)00255-5

Blakowski, M. A., Aciego, S. M., Delmonte, B., Baroni, C., Salvatore, M. C., and Simms, K. W. W. (2016). A Sr-Nd- Hf isotope characterization of dust source areas in Victoria Land and the McMurdo Sound sector of Antarctica. *Quat. Sci. Rev.* 141, 26–37. doi: 10.1016/j.quascirev.2016.03.023

Brachfeld, S., Pinzon, J., Darley, J., Sagnotti, L., Kuhn, G., Florindo, F., et al. (2013). Magnetic tracers of ice sheet extent and sediment provenance in the ANDRILL AND-1B drill core, Ross Sea, Antarctica. *Glob. Planet. Chang.* 110, 420–433. doi: 10.1016/j.gloplacha.2013.09.015

Bristow, C. S., Augustinus, P., Rhodes, E. J., Wallis, I. C., and Jol, M. H. (2011). Is climate change affecting rates of dune migration in Antarctica? *Geology* 39, 831–834. doi: 10.1130/G32212.1

Community Members EPICA (2004). Eight glacial cycles from an antarctic ice core. *Nature* 429, 623–628. doi: 10.1038/nature02599

Dash, J. G., Rempel, A. W., and Wettlaufer, J. S. (2006). The physics of premelted ice and its geophysical consequences. *Rev. Mod. Phys.* 78:695. doi: 10.1103/RevModPhys.78.695

Delmonte, B., Andersson, P. S., Hansson, M., Schoberg, H., Petit, J.-R., Basile-Doelsch, I., et al. (2008). Aeolian dust in East Antarctica (EPICA-Dome C and Vostok): provenance during glacial ages over the last 800 Kyr. *Geophys. Res. Lett.* 35:L07703.

Delmonte, B., Andersson, P. S., Schöberg, H., Hansson, M., Petit, J.-R., Delmas, R., et al. (2010a). Geographic provenance of aeolian dust in East Antarctica during pleistocene glaciations: preliminary results from talos dome and comparison with East Antarctic and New Andean Ice core data. *Quat. Sci. Rev.* 29, 256–264. doi: 10.1016/j.quascirev.2009.05.010

Delmonte, B., Baroni, C., Andersson, P. S., Narcisi, B., Salvatore, M. C., Petit, J. R., et al. (2010b). Aeolian dust in the Talos Dome ice core (East Antarctica, Pacific/Ross Sea sector): Victoria Land versus remote sources over the last two climate cycles. *J. Quat. Sci.* 25, 1327–1337. doi: 10.1002/jqs.1418

Delmonte, B., Baroni, C., Andersson, P. S., Narcisi, B., Salvatore, M. C., Petit, J. R., et al. (2013). Modern and Holocene aeolian dust variability from Talos Dome (Northern Victoria Land) to the interior of the Antarctic ice sheet. *Quat. Sci. Rev.* 64, 76–89. doi: 10.1016/j.quascirev.2012.11.033

Delmonte, B., Basile-Doelsch, I., Petit, J. R., Maggi, V., Revel-Rolland, M., Michard, A., et al. (2004). Comparing the Epica and Vostok dust records during the last 220,000 years: stratigraphical correlation and provenance in glacial periods. *Earth Sci. Rev.* 66, 63–87. doi: 10.1016/j.earscirev.2003.10.004

Gabrielli, P., Wegner, A., Petit, J.-R., Delmonte, B., De Deckker, P., Gaspari, V., et al. (2010). A major glacial-interglacial change in Aeolian dust composition inferred from rare earth elements in Antarctic Ice. *Quat. Sci. Rev.* 29, 265–273. doi: 10.1016/j.quascirev.2009.09.002

Gaiero, D. M. (2007). Dust provenance in Antarctic Ice during glacial periods: from where in Southern South America? *Geophys. Res. Lett.* 34:L17707. doi: 10.1029/2007GL030520

Gaiero, D. M., Brunet, F., Probst, J.-L., and Depetris, P. J. (2007). A uniform isotopic and chemical signature of dust exported from patagonia: rock sources and occurrence in southern environment. *Chem. Geol.* 238, 107–120. doi: 10.1016/j.chemgeo.2006.11.003

Gili, S., Gaiero, D. M., Goldstein, S. L., Chemale, F., Koester, E., Jweda, J., et al. (2016). Provenance of dust to antarctica: a lead isotopic perspective. *Geophys. Res. Lett.* 43, 2291–2298. doi: 10.1002/2016GL068244

Gore, D. B., Rhodes, E. J., Augustinus, P. C., Leishman, M. R., Colhoun, E. A., and Rees-Jones, J. (2001). Bunger Hills, East Antarctica: ice free at the last glacial maximum. *Geology* 29, 1103–1106.

Grousset, F. E., Biscaye, P. E., Revel, M., Petit, J.-R., Pye, K., Joussaume, S., et al. (1992). Antarctic (Dome C) ice core dusts at 18ky B.P.: isotopic constraints on origins and atmospheric circulation. *Earth Planet. Sci. Lett.* 111, 175–182. doi: 10.1016/0012-821x(92)90177-w

Jouzel, J., Masson-Delmotte, V., Cattani, O., Dreyfus, G., Falourd, S., Hoffmann, G., et al. (2007). Orbital and millennial Antarctic climate variability over the past 800,000 Years. *Science* 317, 793–796.

Lambert, F., Delmonte, B., Petit, J.-R., Bigler, M., Kaufmann, P. R., Hutterli, M. A., et al. (2008). New constraints on the Aeolian dust cycle from an 800,000-year Antarctic Ice core record. *Nature* 452, 616–619.

Lanci, L., and Delmonte, B. (2013). Magnetic properties of Aerosol dust in peripheral and inner Antarctic ice cores as a proxy for dust provenance. *Glob. Planet. Chang.* 110, 414–419. doi: 10.1016/j.gloplacha.2013.05.003

Lanci, L., Delmonte, B., Kent, D. V., Maggi, V., Biscaye, P. E., and Petit, J.-R. (2012). Magnetization of Polar Ice: a measurement of terrestrial dust and extraterrestrial fallout. *Quat. Sci. Rev.* 33, 20–31. doi: 10.1016/j.quascirev.2011.11.023

Lanci, L., Delmonte, B., Maggi, V., Petit, J.-R., and Kent, D. V. (2008a). Ice magnetization in the EPICA-dome C Ice core: implication for dust sources during glacial and interglacial periods. *J. Geophys. Res. Atmos.* 113:D14207. doi: 10.1029/2007JD009678

Lanci, L., Delmonte, B., Maggi, V., Petit, J. R., and Kent, D. V. (2008b). Ice magnetization in the EPICA-dome C Ice core: preliminary results. *Terra Antartica Rep.* 14, 83–88.

Lanci, L., and Kent, D. V. (2006). Meteoric smoke fallout revealed by superparamagnetism in Greenland Ice. *Geophys. Res. Lett.* 33:L13308. doi: 10.1029/2006GL026480

Lanci, L., Kent, D. V., and Biscaye, P. E. (2007). Meteoric smoke concentration in the Vostok Ice core estimated from superparamagnetic relaxation and some consequences for estimates of earth accretion rate. *Geophys. Res. Lett.* 34:L10803. doi: 10.1029/2007GL029811

Lanci, L., Kent, D. V., Biscaye, P. E., and Bory, A. (2001). Isothermal remanent magnetization of Greenland Ice: preliminary results. *Geophys. Res. Lett.* 28, 1639–1642. doi: 10.1029/2000GL012594

Lanci, L., Kent, D. V., Biscaye, P. E., and Steffensen, J. P. (2004). Magnetization of Greenland Ice and its relationship with dust content. *J. Geophys. Res. D Atmos.* 34:L10803. doi: 10.1029/2003JD004433

Lanza, R., and Zanella, E. (1993). Palaeomagnetism of the Ferrar dolerite in the northern Prince Albert Mountains (Victoria Land, Antarctica). *Geophys. J. Int.* 114, 501–511. doi: 10.1111/j.1365-246X.1993.tb06983.x

Paleari, C. I., Delmonte, B., Andò, S., Garzanti, E., Petit, J.-R., and Maggi, V. (2019). Aeolian dust provenance in central East Antarctica during the holocene: environmental constraints from single-grain raman spectroscopy. *Geophys. Res. Lett.* 46, 9968–9979. doi: 10.1029/2019GL083402

Petit, J.-R., and Delmonte, B. (2009). A model for large glacial–interglacial climate-induced changes in dust and sea salt concentrations in deep ice cores (Central Antarctica): palaeoclimatic implications and prospects for refining ice core chronologies. *Tellus* 61, 768–790. doi: 10.1111/j.1600-0889.2009.00437.x

Petit, J.-R., Jouzel, J., Raynaud, D., Barkov, N. I., Barnola, J.-M., Basile, I., et al. (1999). Climate and atmospheric history of the past 420,000 years from the Vostok Ice Core, Antarctica. *Nature* 399, 429–436. doi: 10.1038/20859

Prasad, M. S., Rudraswami, N. G., and Panda, D. K. (2013). Micrometeorite flux on earth during the last ˜50,000 years. *J. Geophys. Res. E Planet.* 118, 2381–2399. doi: 10.1002/2013JE004460

Revel-Rolland, M., De Deckker, P., Delmonte, B., Hesse, P. P., Magee, J. W., Basile-Doelsch, I., et al. (2006). Eastern Australia: a possible source of dust in East Antarctica interglacial ice. *Earth Planet. Sci. Lett.* 249, 1–13. doi: 10.1016/j.epsl.2006.06.028

Ruth, U., Barbante, C., Bigler, M., Delmonte, B., Fischer, H., Gabrielli, P., et al. (2008). Proxies and measurement techniques for mineral dust in Antarctic ice cores. *Environ. Sci. Technol.* 42, 5675–5681. doi: 10.1021/es703078z

Suavet, C. P., Gattaceca, J., Rochette, P., Perchiazzi, N., Folco, L., Duprat, J., et al. (2009). Magnetic properties of micrometeorites. *J. Geophys. Res.* 114:B04102.

Valet, J. P., Tanty, C., and Carlut, J. (2017). Detrital magnetization of laboratory-redeposited sediments. *Geophys. J. Int.* 210, 34–41. doi: 10.1093/gji/ggx139

Vallelonga, P., Barbante, C., Cozzi, G., Gabrieli, J., Schüpbach, S., Spolaor, A., et al. (2013). Iron fluxes to talos dome, Antarctica, over the Past 200 Kyr. *Clim. Past* 9, 597–604. doi: 10.5194/cp-9-597-2013

Venables, W. N., and Ripley, B. D. (2002). *Modern Applied Statistics with S*, 4th Edn. New York, NY: Springer, doi: 10.2307/2685660

Wegner, A., Gabrielli, P., Wilhelms-Dick, D., Ruth, U., Kriews, M., De Deckker, P., et al. (2012). Change in dust variability in the Atlantic sector of Antarctica at the end of the last deglaciation. *Clim. Past* 8, 135–147. doi: 10.5194/cp-8-135-2012

Conflict of Interest: The authors declare that the research was conducted in the absence of any commercial or financial relationships that could be construed as a potential conflict of interest.

The handling editor declared a past co-authorship with one of the authors LL.

APPENDIX

Integration With Previous Data From Vostok

The new measurements were integrated with unpublished H_{cr} data from VK ice core, based on measurements performed during a previous study (Lanci et al., 2007).

This dataset consisted in 10 groups of specimens from Vostok ice core published in Lanci et al. (2007), taken at depth from ∼144 m to ∼481 m belonging to MIS 1 and MIS 2. In each group of samples the mean $SIRM_{ice}$ and $SIRM_{dust}$ was computed in order to average out the imprecision in the IDC data, which were taken from the literature. Here we processed the unpublished backfield IRM demagnetization measurements and computed the mean H_{cr} for each group. IRM demagnetizations were not available for all samples and the mean values were computed on a different number of specimens, as summarized in **Table A1**.

In 8 groups of samples out of 10, we have a minimum of 4 H_{cr} measurements that allowed to compute reliable mean H_{cr} values.

TABLE A1 | Integrated dataset from Lanci et al. (2007).

Depth (m)	M.I.S.	Mean H_{cr} (mT)	N	Mean $SIRM_{dust}$ (A m^2/kg)	*N*
225.15	1	56 ± 8.7	4	0.1400	7
292.85	1	62 ± 13.4	7	0.2046	10
323.18	1	76 ± 14.1	5	0.1630	8
351.19	1	79 ± 6.4	4	0.1242	4
377.42	2	94 ± 11.7	6	0.1112	8
402.4	2	85 ± 4.5	6	0.1367	6
429.5	2	85 ± 15.6	4	0.1706	9
447.55	2	93 ± 10.8	5	0.1106	6

The mean $SIRM_{dust}$ measurements are from Lanci et al. (2007), H_{cr} data are computed from unpublished measurements. The errors (s) of the mean H_{cr} represent the variability within each group of samples, not the measurement error.

frontiers in Earth Science

ORIGINAL RESEARCH
published: 17 July 2020
doi: 10.3389/feart.2020.00300

High Potency of Volcanic Contribution to the ∼400 kyr Sedimentary Magnetic Record in the Northwest Pacific

Ji Young Shin[1], Wonnyon Kim[1] and Kiseong Hyeong[2]*

[1] Deep-Sea and Seabed Mineral Resource Research Center, Korea Institute of Ocean Science and Technology, Busan, South Korea, [2] Global Ocean Research Center, Korea Institute of Ocean Science and Technology, Busan, South Korea

As the northwest Pacific has been subject to varying terrigenous input linked to paleoclimate change, the concentration of magnetic minerals in deep-sea sediments is often utilized as a proxy to reconstruct the past atmospheric circulation in the Northern hemisphere. Volcanic materials account for a significant portion of the terrigenous input, but their contribution to sedimentary magnetic properties has not been carefully investigated. This study reveals the magnetic contribution and characteristics of volcanic materials, based on particle-size specific magnetic measurements on sediments that span the last 400 kyr for five size-fractions, including ranges typically attributed to fine eolian (<2 and 2–8 μm) and coarse volcanic (8–31 and 31–63 μm) sediments. Such detrital origins were confirmed by SEM observations. Magnetic concentration (i.e., saturation isothermal remanent magnetization) of the coarse fractions is found to have a positive relationship with bulk values, making up a 23–68% portion. The volcanic contribution is more pronounced on the concentration of hard (>100 mT) magnetic minerals, showing an increased portion of 32–74%. From coercivity spectra analysis, the coarse volcanic fractions are characterized by an abundance of the ∼100 mT coercivity minerals, which can result in an increased average coercivity of bulk sediments. Around the study area, magnetic susceptibility records show synchronized variations with volcanic proportions in terrigenous sediments, validating their close relationship. Consequently, our results indicate that volcanic materials have a high potency of magnetic concentration, which can control bulk sedimentary signals in the northwest Pacific.

Keywords: volcanic materials, terrigenous input, particle size fraction, magnetic concentration, northwest Pacific

OPEN ACCESS

Edited by:
Myriam Kars,
Kôchi University, Japan

Reviewed by:
Qingsong Liu,
Chinese Academy of Sciences (CAS), China
Brendan Thomas Reilly,
University of California, San Diego, United States

****Correspondence:***
Wonnyon Kim
wkim@kiost.ac.kr

Specialty section:
This article was submitted to Geomagnetism and Paleomagnetism, a section of the journal Frontiers in Earth Science

Received: *07 May 2020*
Accepted: *26 June 2020*
Published: *17 July 2020*

Citation:
Shin JY, Kim W and Hyeong K (2020) High Potency of Volcanic Contribution to the ∼400 kyr Sedimentary Magnetic Record in the Northwest Pacific. Front. Earth Sci. 8:300. doi: 10.3389/feart.2020.00300

INTRODUCTION

Mineral dust in the North Pacific, including iron oxides, is transported mainly from the Asian inland by westerly winds (Rea et al., 1998). In agreement with the geochemical behaviors of mineral dust, the physical properties of magnetic particles (e.g., concentration and composition) in deep-sea sediments have shown long-term dependence on Cenozoic global cooling. For example, an increased concentration of magnetic minerals in sediments, particularly of high coercivity minerals

(e.g., hematite), has been an indicator of the intensified Asian dust input by source aridification (e.g., Yamazaki and Ioka, 1997; Bailey et al., 2011; Zhang et al., 2018). On orbital timescales, magnetic mineral concentration in North Pacific sediments shows a good correlation with the global oxygen isotope stack (e.g., LR04; Lisiecki and Raymo, 2005) during the Pleistocene, with its decrease or increase during colder or warmer periods, respectively (e.g., Yamazaki, 1999; Yamamoto et al., 2007; Kars et al., 2017). As an explanation for the cyclicity of the magnetic concentration, various factors have been suggested: glacial enhancement of dust input with high coercivity minerals (Doh et al., 1988), fossilized biogenic magnetite contribution relative to dust input (Yamazaki, 2009), and non-steady state diagenesis with glacial magnetite dissolution (Korff et al., 2016; Shin et al., 2018). However, the relationship between terrigenous input and magnetic concentration in orbital timescales is still unclear.

In the northwest Pacific, the atmospheric transport of volcanic materials from nearby arcs (e.g., Japan and the Kurile Islands) makes a vital part of terrigenous input (Nakai et al., 1993). The geochemical isotopic composition of terrigenous sediments provides a simple binary mixing feature between eolian and volcanic components (Pettke et al., 2000; Bory et al., 2003; Chen et al., 2007). Volcanic materials generally comprise more than 10–30 percentages of terrigenous input in the northwest Pacific (e.g., Nakai et al., 1993; Serno et al., 2014). Most magnetic studies on volcanic materials have identified that intercalated tephra layers in northwest Pacific sediments are characterized by strong magnetization (e.g., Yamamoto et al., 2007; Korff et al., 2016). In addition, a good relationship between magnetic signal and volcanic ash contribution during the last ∼800 kyr has been reported from abyssal sediments at a western marginal site (Urbat and Pletsch, 2003).

The development of methods to unmix magnetic signals helps discriminate magnetic mineral assemblages in bulk sediments, such as detrital/biogenic magnetite and hematite (e.g., Kruiver and Passier, 2001; Egli et al., 2010; Heslop, 2015). The magnetic contribution of biogenic magnetite, which significantly contributes to the bulk magnetic signals of northwest Pacific sediments, is readily decomposed by its non-interacting magnetic signature, such as a low and narrow coercivity distribution (Roberts et al., 2000; Egli, 2004). Meanwhile, detrital magnetite and hematite can be identified by a broader spectrum and their intrinsic coercivity (Egli, 2004). However, it is often difficult to decompose detrital magnetic minerals of different origins, such as eolian and volcanic components, from bulk magnetic signals. In this case, the combination of physical particle size separation and magnetic measurements provide useful insight to sediment transport mechanisms linked to particle size distribution (e.g., Bailey et al., 2011; Hatfield, 2014; Hatfield et al., 2017). In this study, the particle size separation approach is applied to isolate the magnetic properties of northwest Pacific sediments. From the particle size-dependent magnetic properties, we investigate the magnetic contribution of volcanic materials and its relationship with the climate-related magnetic variations since 400 ka.

MATERIALS AND METHODS

Materials

Sediment samples were taken from the core NPGP1302-1B (32°17.550N, 158°13.570E; **Figure 1**) on the South High of the Shatsky Rise studied by Shin et al. (2018). Terrigenous sediments of the Shatsky Rise area are mainly composed of eolian dust from Asian deserts (e.g., the Taklimakan and Gobi deserts) and volcanic materials from the nearby Japanese arcs (Natland, 1993; Zhao et al., 2006). In terms of magnetic minerals, the terrigenous fractions have experienced post-depositional alteration (i.e., magnetite dissolutions) during glacial periods, as indicated by abruptly reduced magnetizations in glacial-stage sediments (Korff et al., 2016; Shin et al., 2018). For the studied core, Shin et al. (2018) reported that magnetic minerals experienced weak alteration during Marine Isotope Stage (MIS) 2 and severe dissolution during MIS 6, 8, and 10.

To identify particle size dependence on rock magnetic properties, 20 bulk sediment samples were selected from core NGP1302-1B and physically separated into five particle size fractions (<2, 2–8, 8–31, 31–63, and >63 μm). Sample selection was based on sediment ages of NPGP1302-1B (Shin et al., 2018), covering periods of MIS 1–10. Shin et al. (2018) constructed the sediment age model through correlations of magnetic susceptibility and Ba/Ti (Ba/Al) records with adjacent cores. Radiocarbon dates spanning the last ∼20 kyr were also combined. From a total of 23 age–depth points, the average sedimentation rate was calculated as 1.60 cm/kyr, with the bottom age of 394 ka at 603 cm depth.

Particle Size Separation

Particle size separation was made following the Atterberg method (Atterberg, 1912). A bulk sediment sample of ∼2.5 g dry weight was mixed with 25 ml of a 2% Calgon solution (sodium hexametaphosphate) and distilled water and stirred sufficiently. The >63 μm fraction was extracted by sieving. Next, the sediment solution was separated into four size-fractions on the basis of Stroke's Law, in sequence from coarse to fine fractions (31–63, 8–31, 2–8, and <2 μm), by siphoning suspended sediments after deposition time of respective particle size fractions. The extraction process of each fraction was repeated at least twice to obtain purer particle size fractions. The size-separated samples were oven-dried at a temperature of ∼50°C and measured as dry masses. For the <2 μm fraction, the mass of Calgon was corrected.

Magnetic Measurements

For a total of 100 size-fractionated samples, concentration-related magnetic parameters were measured: saturation isothermal remanent magnetization (SIRM), anhysteretic remanent magnetization (ARM), and backward IRM at 100 and 300 mT in the opposite direction to the SIRM (IRM_{-100mT} and IRM_{-300mT}, respectively). Hard IRMs (HIRMs) were calculated as follows: $HIRM_{100} = 0.5 \times (SIRM + IRM_{-100mT})$ and $HIRM_{300} = 0.5 \times (SIRM + IRM_{-300mT})$.

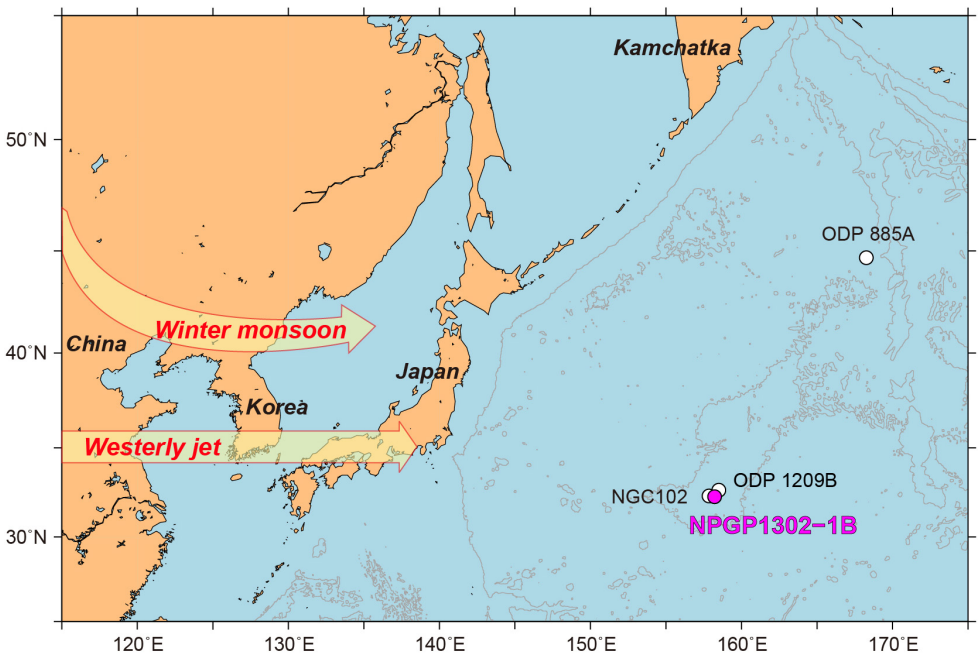

FIGURE 1 | A map showing the location of the studied core NPGP1302-1B. Cores referred in this study are also shown. In the North Pacific, eolian dust and volcanic materials are transported by the Westerly jet and the East Asian winter monsoon (yellow shaded arrows).

SIRM and ARM represent magnetizations of all grains and fine-grained ferrimagnetic minerals (e.g., magnetite), respectively (Evans and Heller, 2003). $HIRM_{100}$ and $HIRM_{300}$ reflect concentrations of magnetic minerals with >100 mT (e.g., partially oxidized magnetite) and >300 mT coercivities (e.g., hematite), respectively. S-ratios (S_{100} and S_{300}) were calculated using $S_{100} = 0.5 \times (1 - IRM_{-100mT}/SIRM)$ and $S_{300} = 0.5 \times (1 - IRM_{-300mT}/SIRM)$. S_{100} and S_{300} are applied to estimate the relative significance of magnetic minerals with <100 mT and <300 mT coercivities, respectively, among all magnetic minerals (Evans and Heller, 2003). All remanent magnetization values were measured using a Agico JR-6A spinner magnetometer.

For selected size-fractionated samples, IRM acquisition and backfield demagnetization curves were obtained using a Princeton MicroMag 3900 vibrating sample magnetometer in the Center for Advanced Marine Core Research, Kochi University, Japan. IRMs were acquired by applying DC fields of up to 1 T, with 140 nonlinear field steps. From stepwise backfield IRM demagnetization, remanence coercivity (B_{cr}) was estimated as the field reduced the remanence to zero. Based on IRM acquisition behavior, principal component analysis on coercivity distribution was performed using a fitting program (Kruiver and Passier, 2001).

Electron Microscope Observations

Scanning electron microscopy (SEM) observations were carried out for magnetic mineral extracts from selected size-fractionated samples and a volcanic ash layer. After magnetic measurements, samples were dispersed into distilled water under ultrasonication for 5 min. The sediment solution was slowly dropped into a glass vial filled with distilled water, and magnetic minerals were extracted by a rare earth magnet of 1 T which was placed next to the vial. This procedure was repeated several times to gather purer magnetic extracts. The extracted samples were dried at ~50°C in an oven overnight. Finally, the dried magnetic extracts were mounted using a carbon tape, and then coated with carbon. SEM observations were performed with a JEOL analytical field emission SEM (JSM-7610F) coupled with energy dispersive X-ray spectroscopy (EDS) at Gyeongsang National University, South Korea.

RESULTS

Magnetic concentration parameters (SIRM, ARM, $HIRM_{100}$, and $HIRM_{300}$) of size-fractionated samples were normalized by mass, and then multiplied by each mass fraction (f); representing mass-normalized and mass-weighted values, respectively. The mass-normalized values are generally higher in coarser fractions which take small portions in total mass (**Supplementary Figure S1**), indicating higher magnetic concentration. In order to take account into mass contribution together, the mass-weighted values were adopted in this study (**Figure 2**) and relative abundance of magnetic minerals in each size fraction was evaluated (e.g., Razik et al., 2014). By normalizing the mass-weighted values with bulk values, the percentage magnetic contribution (PMC) was also calculated.

The calculated parameters for the sized fractions in this study are compared with the results obtained from bulk samples in

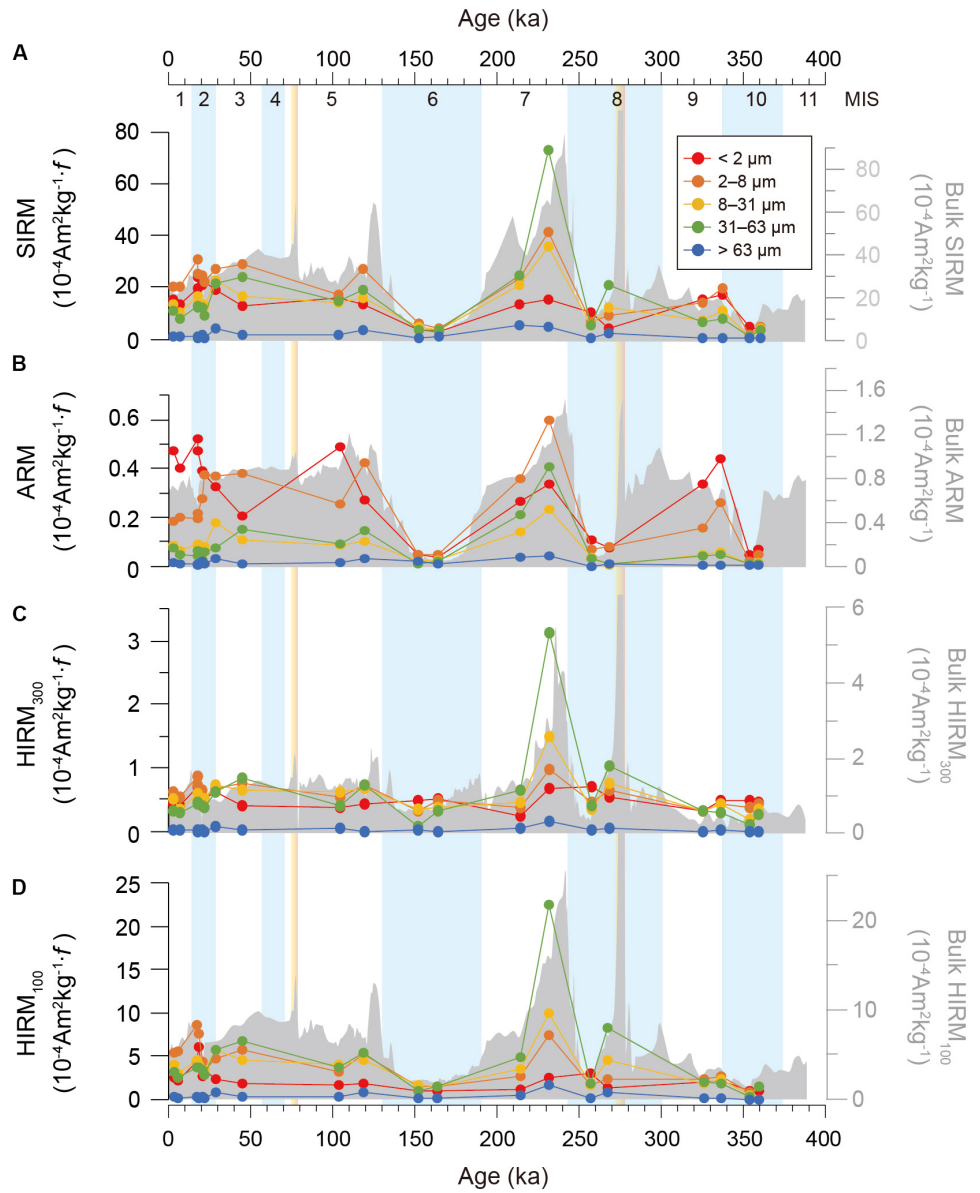

FIGURE 2 | Magnetic concentration parameters of bulk and size-fractionated samples from NPGP1302-1B. **(A)** Saturation isothermal remanent magnetization (SIRM); **(B)** anhysteretic remanent magnetization (ARM); **(C)** hard (>300 mT) IRM ($HIRM_{300}$); and **(D)** hard (>100 mT) IRM ($HIRM_{100}$). Values are mass-weighted by multiplying fractional abundance (%). For comparison, the bulk values from Shin et al. (2018) are shown as gray shaded area. Marine Isotope Stages (MIS) are labeled as numbers on the top. Volcanic ash layers at ~80 and ~270 ka are marked by orange bars.

the previous study (Shin et al., 2018). In addition, the relative significance composition of low and high coercivity minerals was estimated by comparison of S-ratios.

SIRM and ARM

SIRM values of the sized fractions display similar variations to bulk SIRM, showing markedly low values in all fractions during MIS 6, 8, and 10 (**Figure 2A**). Of the five fractions, the 2–8 μm fraction has relatively high SIRM values with the highest average PMC of 31% (**Figure 2A** and **Table 1**), revealing higher contribution (36–38%) during MIS 1 and 9, and lower contribution (19–27%) during MIS 7 and 8 (**Figure 3A**). The finest fraction (<2 μm) does not show distinctively high SIRM values (**Figure 2A**), and the average PMC (25%) is lower than the 2–8 μm fraction (**Table 1**). Although coarser fractions (8–31 and 31–63 μm) have slightly lower average PMC values of 21 and 22%, respectively (**Table 1**), they occasionally show significantly high SIRM values and PMC up to 43% (**Figures 2A**, **3A**). In particular, the 31–63 μm fraction exhibits the maximum SIRM values with PMC of 28–43% during MIS 7 and around a volcanic ash layer at ~270 ka (**Figures 2A**, **3A**). The coarsest fraction (>63 μm) contributes a small portion to the bulk SIRM

TABLE 1 | Percentage Magnetic Contribution (PMC) of each particle size fraction to bulk magnetic concentration parameters.

(μm)	(%)	SIRM	ARM	$HIRM_{300}$	$HIRM_{100}$
<2	Mean PMC (range)	25 (8–55)	44 (21–63)	26 (10–43)	18 (6–36)
2–8	Mean PMC (range)	31 (22–38)	33 (22–46)	27 (15–34)	28 (14–42)
8–31	Mean PMC (range)	21 (13–27)	11 (2–18)	24 (16–31)	25 (18–31)
31–63	Mean PMC (range)	22 (10–43)	10 (3–25)	22 (6–49)	27 (14–51)
>63	Mean PMC (range)	2 (0.2–6)	2 (0.1–13)	1 (0–3)	2 (0.2–4)

(**Figure 3A** and **Table 1**) and could reflect inclusions of magnetic grains in host minerals, such as silicates (e.g., Chang et al., 2016; Chen et al., 2017).

Fine fractions (<2 and 2–8 μm) have high ARM values (**Figure 2B**), which is consistent with ARM being more sensitive to the presence of finer magnetic grains. Their average PMC dominates the bulk ARM, accounting for 44 and 33%, respectively (**Table 1**). The two dominant fractions show opposing fluctuations in some periods (**Figure 2B**), which probably reflects fine magnetite of different origins (e.g., biogenic vs. detrital magnetite). ARM values of coarser fractions (8–31 and 31–63 μm), similarly, vary with those of the 2–8 μm fraction (**Figure 2B**), but their average PMC is generally as low as 11 and 10%, for 8–31 and 31–63 μm fractions, respectively (**Table 1**).

HIRMs and S-Ratios

Bulk $HIRM_{300}$ and $HIRM_{100}$ variations resemble that of SIRM, reflecting a similar input mechanism for both high and low coercivity minerals (**Figures 2C,D**). Of the measured parameters, the bulk $HIRM_{300}$ does not show a noticeable decrease during MIS 6, 8, and 10 (**Figure 2C**) since high coercivity minerals (e.g., hematite) are resistant to dissolutions (Roberts, 2015). Fine fractions of <2 and 2–8 μm have relatively constant $HIRM_{300}$ values (**Figure 2C**), with average PMC values of 26 and 27%, respectively (**Table 1**). The PMC generally increases during glacials (MIS 2, 6, 8, and 10) (**Figure 3C**). On the other hand, the coarser fractions, 8–31 and 31–63 μm, display a relatively large fluctuation in $HIRM_{300}$ values (**Figure 2C**) with average PMC values of 24 and 22%, respectively (**Table 1**). Strikingly, the coarse fractions dominate the bulk $HIRM_{300}$ with peak values in MIS 7, as in SIRM, showing PMC of 62–74% (**Figures 2C**, **3C**).

Compared to the bulk $HIRM_{300}$, $HIRM_{100}$ variation is more similar to SIRM variation (**Figures 2A,C,D**). However, the <2 μm fraction has relatively low $HIRM_{100}$ values, with an average PMC of 18% (**Figure 2D** and **Table 1**). Meanwhile, $HIRM_{100}$ values of coarser fractions of 8–31 and 31–63 μm dominate the bulk values (**Figure 2D**), showing average PMC values of 25 and 26%, respectively (**Table 1**). The PMC of the coarse fractions to $HIRM_{100}$, exhibiting ∼50–80% together, is distinctively higher than to other parameters (**Figure 3**).

The sized fractions have relatively constant S_{300} ratios in the range of ∼0.95–0.98, except for significant decreases during MIS 6, 8, and 10. This indicates the dominance of low coercivity minerals (<300 mT) in all fractions. As shown by relative fluctuations in SIRM instead of $HIRM_{300}$ (**Figure 4**), the S_{300} decreases during MIS 6, 8, and 10 are associated with a decrease in low coercivity minerals. The lowest S_{300} in the <2 μm fraction supports the preferential dissolution of fine magnetites (e.g., Roberts, 2015). S_{100} of the sized fractions, similarly, changes with S_{300}, showing decreases during MIS 6, 8, and 10. However, more distinctly, S_{100} is lower in the coarse fractions (8–31 and 31–63 μm), reflecting the greater contribution of high coercivity minerals (>100 mT). This is consistent with relatively high PMC to the bulk $HIRM_{100}$ in the coarse fractions (**Figures 3D**, **4A**).

SEM Observations

SEM photos of magnetic extracts for the <2 μm and 8–31 μm fractions of 231 ka (361 cm depth) in **Figure 5**. For the <2 μm fraction (**Figures 5A,B**), magnetic particles show various morphologies with frequent occurrences of subangular–euhedral and cuboidal shapes with smooth surfaces. EDS analysis reveals that most of the particles are identified as iron-oxides showing distinctive Fe and O peaks (**Supplementary Figure S2**). Most of <100 nm particles are observed as cuboidal iron-oxides aggregated each other (lower panels of **Supplementary Figure S2**). On the other hand, magnetic extracts for the 8–31 μm fraction show angular, irregular, and vesicular morphologies with 10–30 μm particle sizes (**Figures 5C,D**). Such typical morphologies are characteristics of volcanic ashes (e.g., Riley et al., 2003). Within large alumino-silicates composed mainly of Al, Ca, and Si, iron-oxides are observed as submicron sized inclusions (**Figure 5D** and **Supplementary Figure S3**). Notably, the iron-oxide inclusions also have Ti as a major element.

For comparison, magnetic extracts for a volcanic ash layer (275 ka, 470 cm depth) were observed (**Figures 5E,F**). As expected, all the particles observed show similar morphologies to those in the 8–31 μm fraction. Ti-rich iron-oxides occur in the large alumino-silicate host (**Supplementary Figure S4**). Such morphological and compositional similarities indicate that most of large particles (>8 μm) including iron-oxides are probably in volcanic origin.

DISCUSSION

Climate Dependence of Volcanic Fraction

For the past ∼500 kyr, terrigenous sediments of ODP 1209B site on the South High of the Shatsky Rise, where our study core was collected at ∼50 km away (**Figure 1**), have shown a bimodal particle size distribution, with modes of ∼4 and ∼20 μm accounting for ∼60–100% and ∼0–40% of the terrigenous fraction, respectively (Zhang et al., 2019). The major components of the 4 and 20 μm modes have been identified as eolian dust and volcanic materials, respectively, based on their Nd isotopic (ε_{Nd}) and geochemical (La-Sc-Th) compositions (Zhang et al., 2019). In the ODP 1209B core, ε_{Nd} varied systematically with relative proportion of two size modes, in which ε_{Nd} increased toward volcanic end member composition

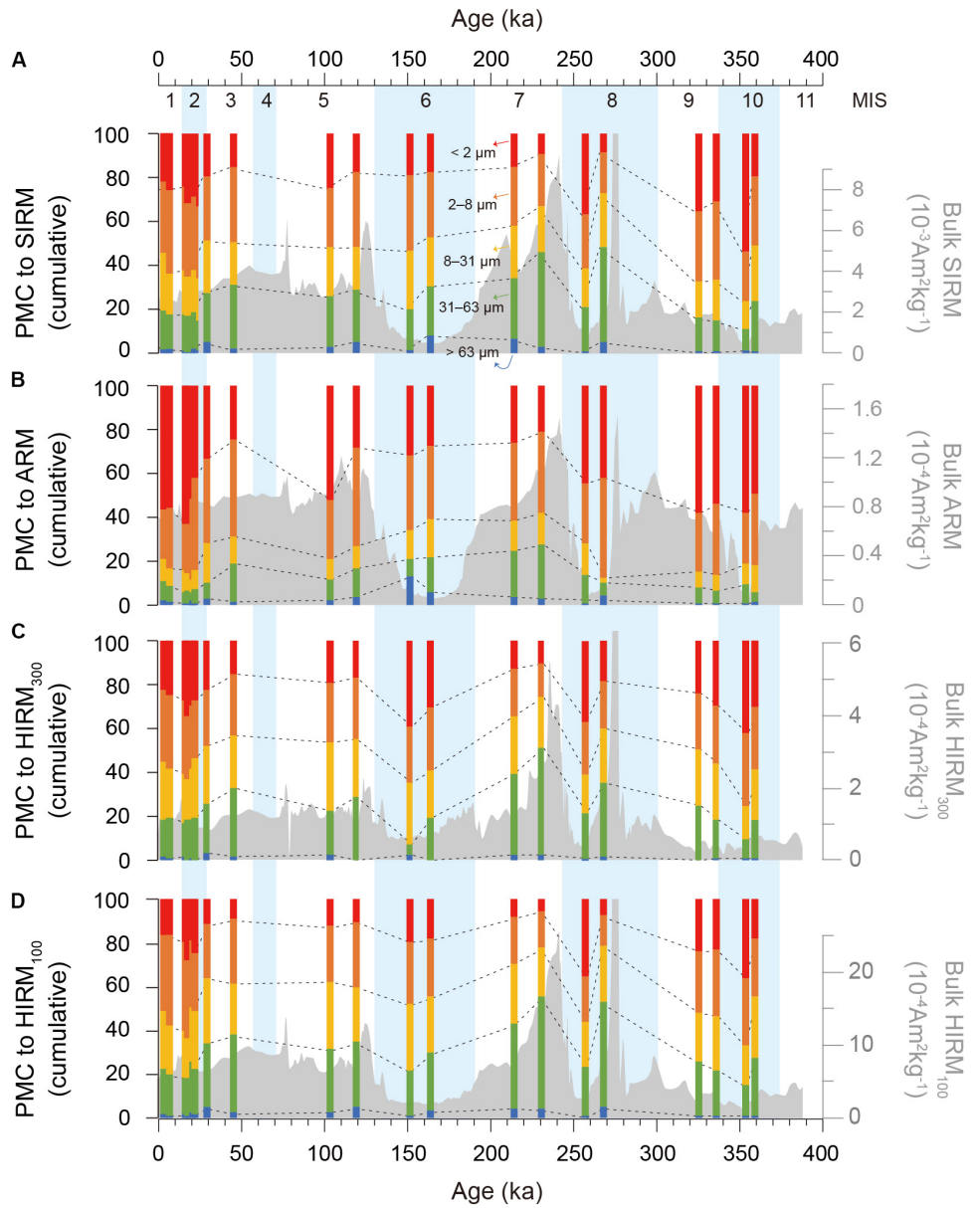

FIGURE 3 | Percentage magnetic contribution (PMC) of the size-fractionated samples to bulk magnetic parameters of **(A)** SIRM, **(B)** ARM, **(C)** $HIRM_{300}$, and **(D)** $HIRM_{100}$. PMC of each fraction is illustrated as cumulative bar chart. The color index is the same as in **Figure 2**.

with increasing proportion of 20 μm mode size fraction. The SEM observation results of our size-fractionated samples clearly confirmed the two main detrital origins, showing differences in morphologies of magnetic particles (**Figure 5**). Thus, the 2–8 and 8–31 μm samples of this study are expected to represent magnetic signals of the eolian and volcanic components, respectively. In addition, finer (<2 μm) and coarser (31–63 μm) fractions probably retain the extended magnetic properties of the two components.

SIRM reflects the total magnetic mineral concentration, and average PMC of fine fractions (<2 and 2–8 μm) dominantly contribute to the bulk values (**Table 1**). Given the dominant fine eolian component in the pelagic setting (Maher, 2011), it is natural that the fine fractions make a high magnetic contribution. However, coarse fractions (8–31 and 31–63 μm) show a significant PMC of >50% in some cases. For example, the coarse fractions in MIS 7 make up greater than 60% of bulk SIRM, with high mass-weighted SIRM values (**Figures 2A**, **3A**), implying significant contribution of volcanic particles to bulk magnetic concentration as confirmed by SEM observations (**Figures 5C,D**). Notably, the PMC of the coarse fractions is more distinctive in HIRMs than SIRM (**Figure 3** and **Table 1**).

Interestingly, the temporal change in the bulk SIRM and HIRMs shows positive correlations with PMCs of the coarse

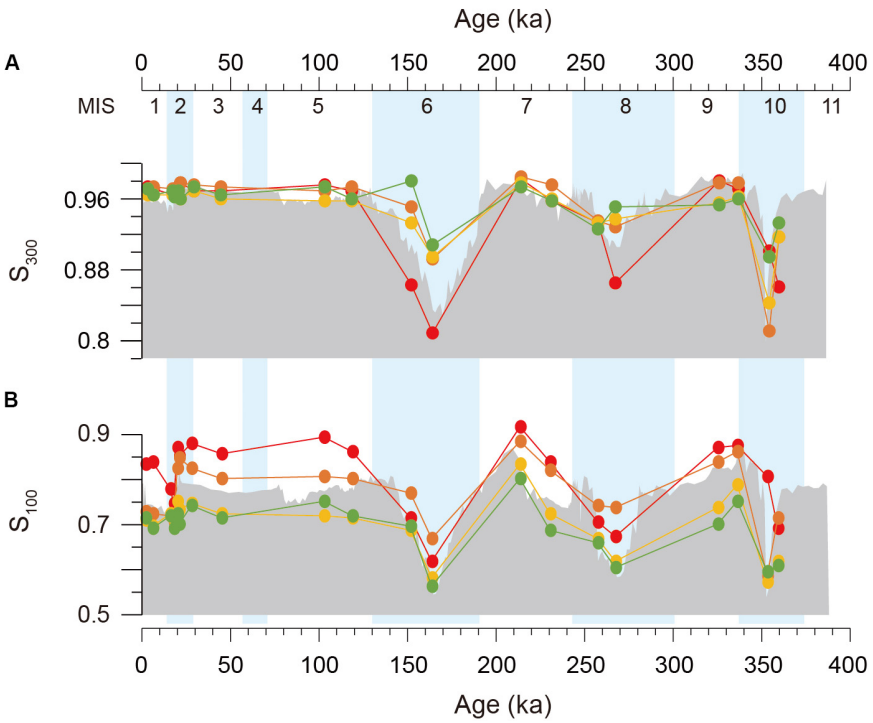

FIGURE 4 | (A) S_{300} and **(B)** S_{100} of bulk and size-fractionated samples. The lower S-ratios indicates greater contribution of high coercivity magnetic minerals. The color index is the same as in **Figure 2**.

fractions (8–31 and 31–63 μm), while the fine fractions (<2 and 2–8 μm) reveal negative correlations (**Figure 6**). Except for highly altered MIS 6, 8, and 10 samples that probably suffered magnetite dissolutions (Shin et al., 2018), PMC of the coarse fractions show a high correlation coefficient (r^2) of 0.87 for SIRM (**Figure 6A**). This strongly indicates that volcanic contribution has a close relationship with temporal changes of magnetic concentration. Such significance of volcanic contribution on magnetic signal is consistently found in the nearby core ODP site 1209B (**Figure 1**). As shown in **Figure 7**, Zhang et al. (2019) reported that relative changes in volcanic particle contribution of the ∼20 μm mode component at the site 1209B mimics the global oxygen isotope stack (LR04; Lisiecki and Raymo, 2005) during the last ∼500 kyr. When we compare this volcanic component with magnetic susceptibility from the site 1209B (Westerhold and Röhl, 2006), the two records show concurrent variations. This implies that volcanic particle contribution, rather than eolian dust, is the critical cause of the magnetic susceptibility variations. Moreover, the two records are very analogous to bulk magnetic susceptibility records of the studied core NPGP1302-1B (Shin et al., 2018) and a nearby core NGC102 (Yamamoto et al., 2007). Yamamoto et al. (2007) also stratigraphically correlated similar magnetic susceptibility changes of cores around the Shatsky Rise. All these consistent records indicate that bulk magnetic signals (i.e., magnetic mineral concentration) of northwest Pacific sediments sensitively responded to volcanic particle contribution.

As Zhang et al. (2019) suggested, the climate-dependence of volcanic particle contribution can be explained as the relative effect of dilution by evolving eolian dust flux, as dust input is enhanced during glacials (e.g., Hovan et al., 1991; Lambert et al., 2008; Jacobel et al., 2017); volcanic activities alone cannot directly paced to climate change. Of course, it should be noted that glacial magnetic signals represent the concentration of remaining magnetic minerals after magnetite dissolution (Shin et al., 2018). All particle fractions have low mass-concentration of magnetic minerals during MIS 6, 8, and 10 (**Supplementary Figure S1**) with low S-ratios (**Figure 4**), suggesting that magnetic minerals were primarily dissolved. Nevertheless, stronger contribution of eolian dust is likely well-reflected in higher PMC to $HIRM_{300}$ of fine fractions during glacials (**Figure 3**). Conclusively, our results provide a more comprehensive understanding of the cause of climate-dependent magnetic variations: volcanic coarse particles have strong potency to magnetic concentration parameters of both low and high coercivity minerals and thus acted as the main controller of bulk magnetic records in relation to terrigenous input. Volcanic materials, thus, should be considered as an essential factor for the interpretation of magnetic signals in the northwest Pacific, even though they account for a relatively small portion in sediments than dust.

Magnetic Characterization of the Volcanic Component

Magnetic properties of volcanic materials deposited in the northwest Pacific have been identified mostly from intercalated ash layers in bulk sediments. In general, the volcanic ash

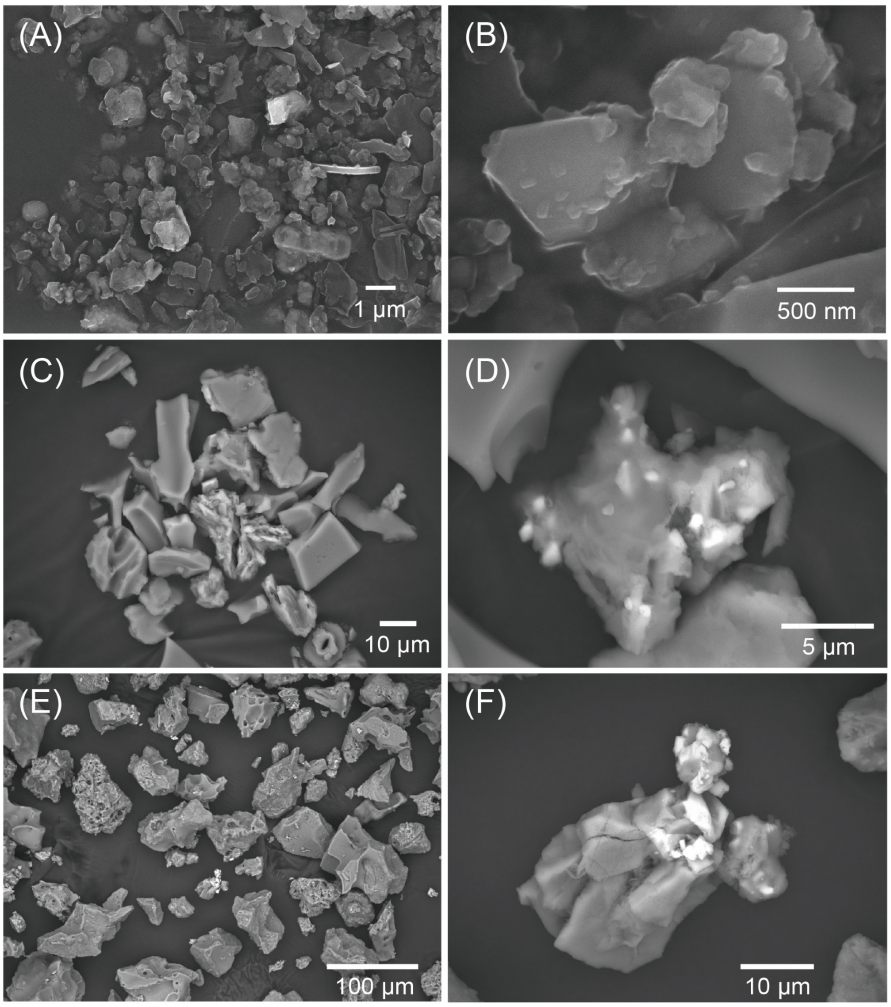

FIGURE 5 | Scanning electron microscopy (SEM) photos of magnetic extracts for **(A,B)** the <2 μm and **(C,D)** the 8–31 μm fractions of the 231 ka (361 cm depth) sample. **(E,F)** SEM photos for volcanic ash layer (275 ka, 470 cm depth) are presented for comparison. Representative chemical compositions are shown in **Supplementary Figures S2–S4**.

layers are characterized by magnetic spikes, associated with deposition of abundant magnetic minerals by short-term events (e.g., Yamamoto et al., 2007; Korff et al., 2016; Shin et al., 2018). Detailed magnetic analyses on the volcanic ash layers have also reported their magnetic features, such as rare antiferromagnetic minerals (Natland, 1993) and abundant ultrafine superparamagnetic particles (Bailey et al., 2011). In particular, Zhang et al. (2018) verified that volcanic ash layers deposited at a northern Pacific site (ODP site 885A; **Figure 1**) rarely contain pedogenic hematite and goethite, commonly present in eolian dust from arid regions, based on diffuse reflectance spectroscopy (DRS) signals. They also specified abundant high coercivity (80–100 mT) ferrimagnetic minerals in the ash layers from coercivity distribution. Along with these achievements, the particle size separation approach in this study can further provide magnetic information on the long-term airborne input of coarse volcanogenic particles in the northwest Pacific.

Considering the magnetic features of volcanic ash layers, coercivity distribution of fine (<2 and 2–8 μm) and coarse (8–31 and 31–63 μm) fractions could provide useful information on eolian- and volcanic-related magnetic signals, respectively. IRM component analysis for selected interglacial bulk samples and their sized fractions, avoiding glacial magnetic alteration, was performed (**Figure 8** and **Supplementary Figure S5**). Coercivity spectra of the four sized fractions are all dominated by component 2, with low coercivity ($B_{1/2}$ of 45–54 mT; **Figures 8C–F**). In the coercivity range, a narrow dispersion parameter (DP) of ∼0.2 in the finest fraction (<2 μm) is typical for biogenic magnetite, while wider DP in the other fractions corresponds to detrital magnetite (Egli, 2004; Yamazaki, 2009). Despite the dominant contribution of component 2, component 3, with a $B_{1/2}$ of 93–145 mT, is prominent in the coarse fractions with ∼22.5% contribution to SIRM (**Figures 6E,F**). On the other hand, component 4, which exhibits a higher coercivity ($B_{1/2}$ of 427–501 mT), is negligible in the coarse fractions.

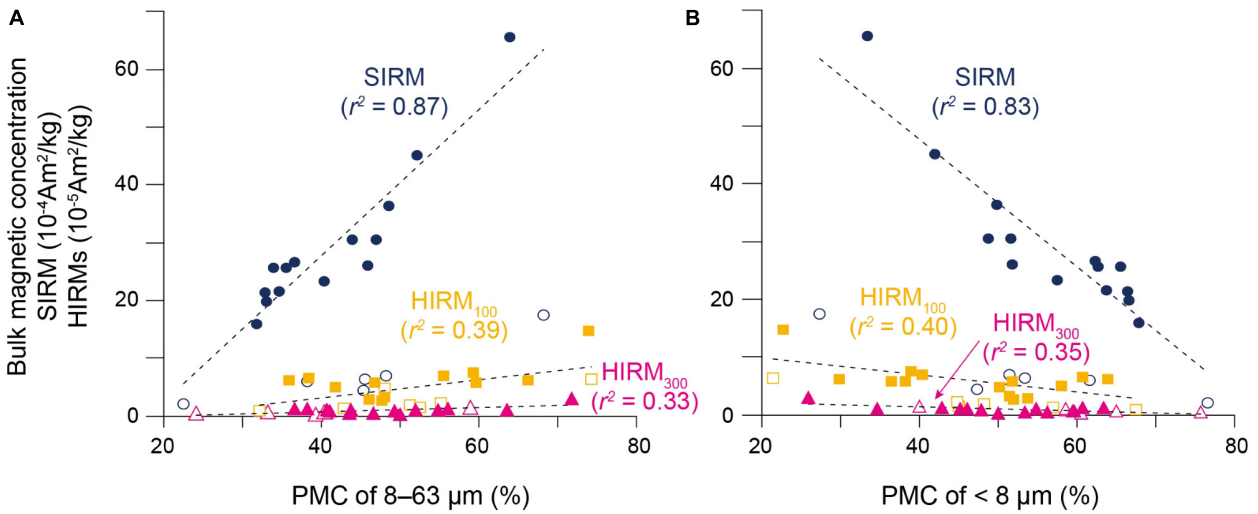

FIGURE 6 | Correlation between bulk magnetic concentration (SIRM, $HIRM_{300}$, and $HIRM_{100}$) and PMCs of **(A)** coarse (8–31 and 31–63 μm) and **(B)** fine (<2 and 2–8 μm) fractions. Glacial samples (MIS 6, 8, and 10), suspected to be altered (open symbols), were excepted for the correlation. PMCs of coarse and fine fractions reveal positive and negative correlations, respectively, with bulk concentration parameters.

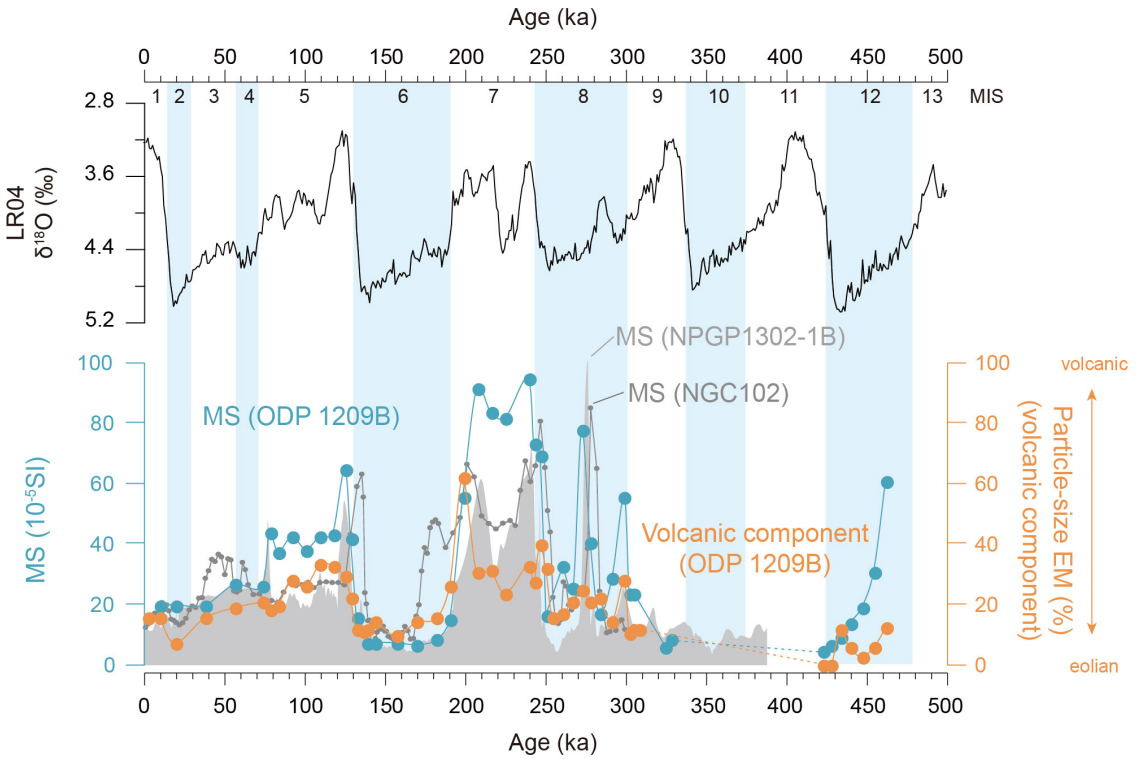

FIGURE 7 | Comparison of global oxygen isotope (LR04; Lisiecki and Raymo, 2005), magnetic susceptibility (MS) of ODP site 1209B (blue; Westerhold and Röhl, 2006; Bordiga et al., 2013 for age construction), particle size endmember (EM) contribution in ODP site 1209B (orange; Zhang et al., 2019), and MS records of NGC102 (dark gray; Yamamoto et al., 2007) and NPGP1302-1B (gray shaded; Shin et al., 2018). The EM corresponds to volcanic component relative to eolian dust in terrigenous fraction of ODP site 1209B.

In contrast, the fine fractions display high-field tails in the IRM acquisition curves (**Figure 8A**), indicating the presence of high coercivity antiferromagnetic minerals, such as hematite, in eolian dust. The high coercivity signal in the fine fractions could be useful to trace the eolian contribution as demonstrated using DRS parameters by Zhang et al. (2018). Taken together,

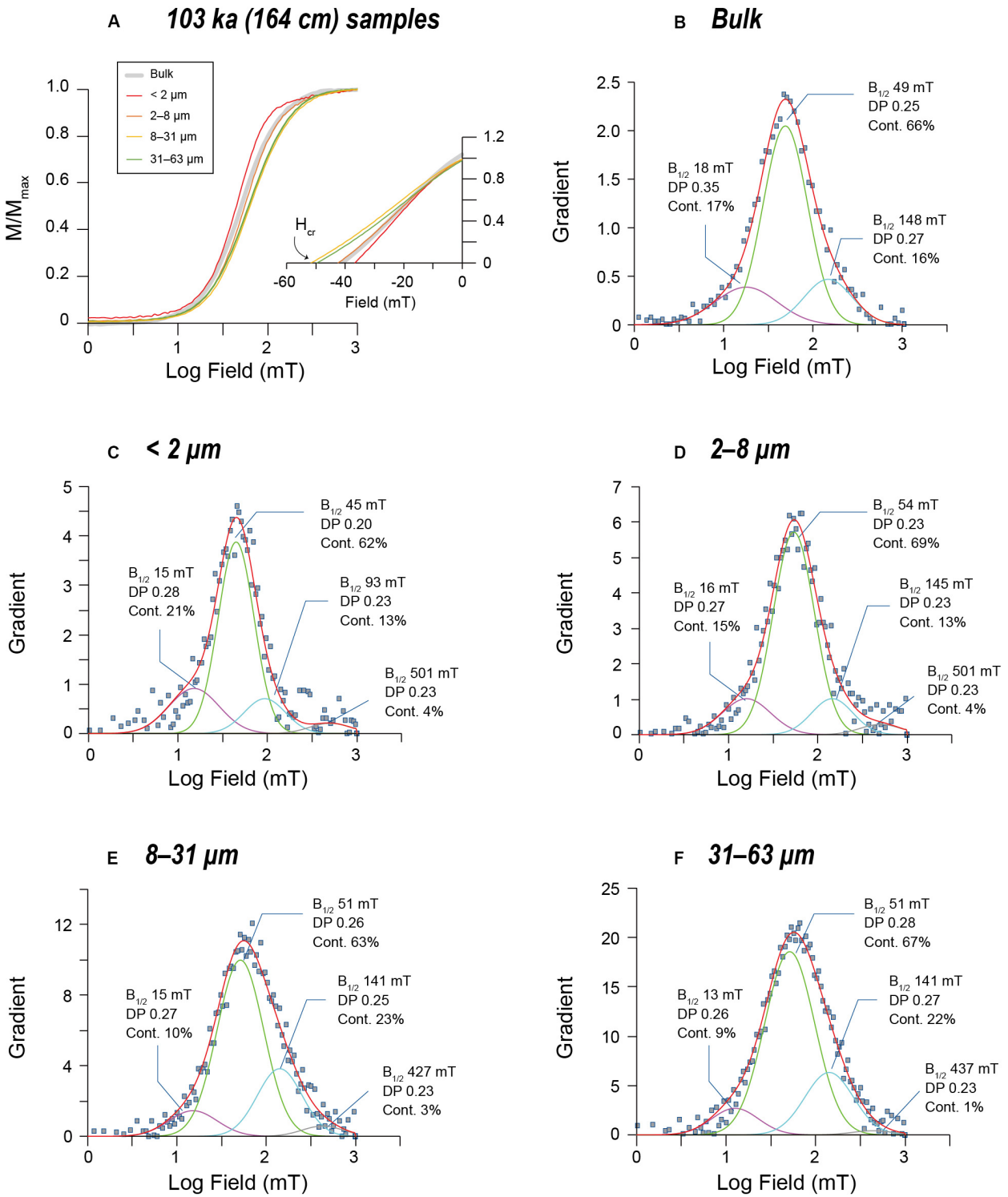

FIGURE 8 | Remanence acquisition and gradient plots for the 103 ka (164 cm depth) samples. **(A)** IRM acquisition and backfield decay curves for bulk and sized fractions altogether; **(B–F)** coercivity spectra of bulk and each sized fractions. In coercivity spectra, raw data points are indicated by squares; coercivity components are marked as purple (component 1), green (component 2), blue (component 3), and gray (component 4) lines; and sum of components are red lines fitted to the raw data. For each coercivity component, mean coercivity ($B_{1/2}$), dispersion parameters (DP), and contribution to SIRM (cont.%) are specified.

from the coercivity behaviors of the coarse fractions, volcanic materials can be characterized by abundant ferrimagnetic minerals of intermediate coercivity (∼100 mT). Although this coercivity range is slightly higher than the results from the ash layers originating from the Kamchatka-Aleutian arcs (i.e., the site 885A; Zhang et al., 2018), the coercivity distribution of our coarse fractions may be somewhat different depending on the relic of antiferromagnetic minerals in eolian dust (**Supplementary Figure S5**).

The IRM acquisition behavior of the bulk sample is similar to that of the 2–8 μm sample, particularly in the low coercivity range (**Figure 8A**). However, as shown in the bulk coercivity spectra (**Figure 8B**), the large dispersion of component 2 and the significant contribution of component 3 are more related to the coercivity distribution of the coarse fractions (**Figures 6E,F**). This confirms volcanic particles as an essential supply source of magnetic minerals. In particular, the abundant intermediate coercivity minerals (i.e., component 3) in volcanic particles can yield relatively high coercivity, as consistently presented by higher B_{cr} and lower S-ratios in the coarse fractions (**Figures 4**, **6A**, respectively). This implies that some proxies for higher coercivity fractions in bulk sediments (e.g., S-ratios and HIRMs) can be influenced by volcanic contribution. Thus, the use of such conventional eolian proxies for bulk sediments should be accompanied by consideration of volcanic contribution in coarse fraction in the northwest Pacific. In that respect, the magnetic analysis combined with particle size separation is a useful tool for characterizing volcanic and eolian contribution on bulk sediments.

CONCLUSION

Based on particle size-dependent magnetic properties, magnetic characteristics of volcanic materials and their contribution to bulk magnetic concentration was evaluated in ∼400 kyr sediments from the northwest Pacific. Magnetic properties of fine (<2 and 2–8 μm) and coarse (8–31 and 31–63 μm) fractions were isolated as eolian- and volcanic-related, respectively. SIRM and HIRMs ($HIRM_{300}$ and $HIRM_{100}$) were significantly contributed to by the coarse fractions, often showing >50% (up to 74%) of PMC. Moreover, the PMC of the coarse fractions generally varies in sync with the respective bulk values of SIRM and HIRMs, implying a close relationship between volcanic particle contribution and bulk magnetic concentration. Such a relationship is validated by covariation between magnetic susceptibility records and the relative proportion of volcanic components in the terrigenous fraction. Thus, we suggest volcanic materials as an important factor of magnetic concentration in the northwest Pacific, related to climate change. In addition, coercivity spectra of the coarse fractions reveal that volcanic materials contain abundant intermediate coercivity (∼100 mT) minerals, which can significantly influence high coercivity fraction parameters (e.g., S-ratios and HIRMs). Therefore, traditional coercivity proxies should be carefully interpreted in the northwest Pacific, in consideration with the volcanic contribution.

DATA AVAILABILITY STATEMENT

All datasets generated for this study are included in the article/**Supplementary Material**.

AUTHOR CONTRIBUTIONS

WK designed the sampling, reviewed the manuscript, and contributed to visualization and organization. JS designed the study, carried out analyses, and wrote the manuscript. KH contributed to the discussion. All authors contributed to the article and approved the submitted version.

FUNDING

This study was financially supported by the Ministry of Oceans and Fisheries (20160099) and the Korea Institute of Ocean Science and Technology (PE99824).

ACKNOWLEDGMENTS

We appreciate the editor MK for handling the paper and the two reviewers QL and BR for improving the manuscript significantly. We would like to thank Dr. S. J. Pak for his advice on SEM observations. IRM curves were acquired at the paleomagnetism laboratory of the Center for Advanced Marine Core Research (CMCR), Kochi University. We would like to thank Editage (http://www.editage.co.kr) for English language editing.

SUPPLEMENTARY MATERIAL

The Supplementary Material for this article can be found online at: https://www.frontiersin.org/articles/10.3389/feart.2020.00300/full#supplementary-material

REFERENCES

Atterberg, A. (1912). Die mechanische Bodenanalyse und die klassifikation der mineral böden sechwedens. *Int. Mitt. Bodenk.* 2, 312–342.

Bailey, I., Liu, Q., Swann, G. E. A., Jiang, Z., Sun, Y., Zhao, X., et al. (2011). Iron fertilisation and biogeochemical cycles in the sub-Arctic northwest Pacific during the late Pliocene intensification of northern hemisphere glaciation. *Earth Planet. Sci. Lett.* 307, 253–265. doi: 10.1016/j.epsl.2011.05.029

Bordiga, M., Beaufort, L., Cobianchi, M., Lupi, C., Mancin, N., Luciani, V., et al. (2013). Calcareous plankton and geochemistry from the ODP site 1209B in the NW Pacific Ocean (Shatsky Rise): new data to interpret calcite dissolution and paleoproductivity changes of the last 450ka. *Palaeogeogr. Palaeoclimatol. Palaeoecol.* 371, 93–108. doi: 10.1016/j.palaeo.2012.12.021

Bory, A. J. M., Biscaye, P. E., and Grousset, F. E. (2003). Two distinct seasonal Asian source regions for mineral dust deposited in Greenland (NorthGRIP). *Geophys. Res. Lett.* 30, 1–4. doi: 10.1029/2002GL016446

Chang, L., Roberts, A. P., Heslop, D., Hayashida, A., Li, J., Zhao, X., et al. (2016). Widespread occurrence of silicate-hosted magnetic mineral inclusions in marine sediments and their contribution to paleomagnetic recording. *J. Geophys. Res. Solid Earth* 121, 8415–8431. doi: 10.1002/2016JB013109

Chen, J., Li, G., Yang, J., Rao, W., Lu, H., Balsam, W., et al. (2007). Nd and Sr isotopic characteristics of Chinese deserts: implications for the provenances of Asian dust. *Geochim. Cosmochim. Acta* 71, 3904–3914. doi: 10.1016/j.gca.2007.04.033

Chen, L., Heslop, D., Roberts, A. P., Chang, L., Zhao, X., McGregor, H. V., et al. (2017). Remanence acquisition efficiency in biogenic and detrital magnetite and recording of geomagnetic paleointensity. *Geochem. Geophys. Geosyst.* 18, 1435–1450. doi: 10.1002/2016GC006753

Doh, S.-J., King, J. W., and Leinen, M. (1988). A rock-magnetic study of giant piston core LL44-GPC3 from the central North Pacific and its paleoceanographic implications. *Paleoceanography* 3, 89–111. doi: 10.1029/PA003i001p00089

Egli, R. (2004). Characterization of individual rock magnetic components by analysis of remanence curves, 1. unmixing natural sediments. *Stud. Geophys. Geod.* 48, 391–446. doi: 10.1023/B:SGEG.0000020839.45304.6d

Egli, R., Chen, A. P., Winklhofer, M., Kodama, K. P., and Horng, C.-S. (2010). Detection of noninteracting single domain particles using first-order reversal curve diagrams. *Geochem. Geophys. Geosyst.* 11:Q01Z11. doi: 10.1029/2009GC002916

Evans, M., and Heller, F. (2003). *Environmental Magnetism: Principles and Applications of Enviromagnetics*. Amsterdam: Elsevier.

Hatfield, R. (2014). Particle size-specific magnetic measurements as a tool for enhancing our understanding of the bulk magnetic properties of sediments. *Minerals* 4, 758–787. doi: 10.3390/min4040758

Hatfield, R. G., Stoner, J. S., Reilly, B. T., Tepley, F. J., Wheeler, B. H., and Housen, B. A. (2017). Grain size dependent magnetic discrimination of Iceland and South Greenland terrestrial sediments in the northern North Atlantic sediment record. *Earth Planet. Sci. Lett.* 474, 474–489. doi: 10.1016/j.epsl.2017.06.042

Heslop, D. (2015). Numerical strategies for magnetic mineral unmixing. *Earth Sci. Rev.* 150, 256–284. doi: 10.1016/j.earscirev.2015.07.007

Hovan, S. A., Rea, D. K., and Pisias, N. G. (1991). Late pleistocene continental climate and oceanic variability recorded in Northwest Pacific Sediments. *Paleoceanography* 6, 349–370. doi: 10.1029/91PA00559

Jacobel, A. W., McManus, J. F., Anderson, R. F., and Winckler, G. (2017). Climate-related response of dust flux to the central equatorial Pacific over the past 150 kyr. *Earth Planet. Sci. Lett.* 457, 160–172. doi: 10.1016/j.epsl.2016.09.042

Kars, M., Musgrave, R. J., Kodama, K., Jonas, A.-S., Bordiga, M., Ruebsam, W., et al. (2017). Impact of climate change on the magnetic mineral assemblage in marine sediments from Izu rear arc, NW Pacific Ocean, over the last 1 Myr. *Palaeogeogr. Palaeoclimatol. Palaeoecol.* 480, 53–69. doi: 10.1016/j.palaeo.2017.05.016

Korff, L., von Dobeneck, T., Frederichs, T., Kasten, S., Kuhn, G., Gersonde, R., et al. (2016). Cyclic magnetite dissolution in Pleistocene sediments of the abyssal northwest Pacific Ocean: evidence for glacial oxygen depletion and carbon trapping. *Paleoceanography* 31, 600–624. doi: 10.1002/2015PA002882

Kruiver, P. P., and Passier, H. F. (2001). Coercivity analysis of magnetic phases in sapropel S1 related to variations in redox conditions, including an investigation of the S ratio. *Geochem. Geophys. Geosyst.* 2:181. doi: 10.1029/2001GC000181

Lambert, F., Delmonte, B., Petit, J. R., Bigler, M., Kaufmann, P. R., Hutterli, M. A., et al. (2008). Dust-climate couplings over the past 800,000 years from the EPICA Dome C ice core. *Nature* 452, 616–619. doi: 10.1038/nature06763

Lisiecki, L. E., and Raymo, M. E. (2005). A Pliocene-Pleistocene stack of 57 globally distributed benthic $\delta^{18}O$ records. *Paleoceanography* 20:PA1003. doi: 10.1029/2004PA001071

Maher, B. A. (2011). The magnetic properties of Quaternary aeolian dusts and sediments, and their palaeoclimatic significance. *Aeolian Res.* 3, 87–144. doi: 10.1016/j.aeolia.2011.01.005

Nakai, S., Halliday, A. N., and Rea, D. K. (1993). Provenance of dust in the Pacific Ocean. *Earth Planet. Sci. Lett.* 119, 143–157. doi: 10.1016/0012-821X(93)90012-X

Natland, J. (1993). "Volcanic ash and pumice at shatsky rise: sources, mechanisms of transport, and bearing on atmospheric circulation," in *Proceedings of the Ocean Drilling Program, 132 Scientific Results*, (College Station, TX: Ocean Drilling Program), 57–66. doi: 10.2973/odp.proc.sr.132.301.1993

Pettke, T., Halliday, A. N., Hall, C. M., and Rea, D. K. (2000). Dust production and deposition in Asia and the north Pacific Ocean over the past 12 Myr. *Earth Planet. Sci. Lett.* 178, 397–413. doi: 10.1016/S0012-821X(00)00083-2

Razik, S., Dekkers, M. J., and von Dobeneck, T. (2014). How environmental magnetism can enhance the interpretational value of grain-size analysis: a time-slice study on sediment export to the NW African margin in Heinrich Stadial 1 and Mid Holocene. *Palaeogeogr. Palaeoclimatol. Palaeoecol.* 406, 33–48. doi: 10.1016/j.palaeo.2014.04.009

Rea, D. K., Snoeckx, H., and Joseph, L. H. (1998). Late Cenozoic Eolian deposition in the North Pacific: Asian drying, Tibetan uplift, and cooling of the northern hemisphere. *Paleoceanography* 13, 215–224. doi: 10.1029/98PA00123

Riley, C. M., Rose, W. I., and Bluth, G. J. S. (2003). Quantitative shape measurements of distal volcanic ash. *J. Geophys. Res. Solid Earth* 108, 1–15. doi: 10.1029/2001jb000818

Roberts, A. P. (2015). Magnetic mineral diagenesis. *Earth Sci. Rev.* 151, 1–47. doi: 10.1016/j.earscirev.2015.09.010

Roberts, A. P., Pike, C. R., and Verosub, K. L. (2000). First-order reversal curve diagrams: a new tool for characterizing the magnetic properties of natural samples. *J. Geophys. Res. Solid Earth* 105, 28461–28475. doi: 10.1029/2000JB900326

Serno, S., Winckler, G., Anderson, R. F., Hayes, C. T., McGee, D., Machalett, B., et al. (2014). Eolian dust input to the Subarctic North Pacific. *Earth Planet. Sci. Lett.* 387, 252–263. doi: 10.1016/j.epsl.2013.11.008

Shin, J. Y., Yu, Y., Seo, I., Hyeong, K., Lim, D., and Kim, W. (2018). Magnetic properties of deep−sea sediments from the North Pacific: a proxy of glacial deep−water ventilation. *Geochem. Geophys. Geosyst.* 19, 4433–4443. doi: 10.1029/2018GC007735

Urbat, M., and Pletsch, T. (2003). "Pleistocene deep-sea sediment in ODP hole 1149A, Nadezhda Basin: sources, alteration, and age controls (0–800 ka)," in *Proceedings of the Ocean Drilling Program, 185 Scientific Results*, (College Station, TX: Ocean Drilling Program), doi: 10.2973/odp.proc.sr.185.012.2003

Westerhold, T., and Röhl, U. (2006). "Data report: revised composite depth records for Shatsky rise sites 1209, 1210, and 1211," in *Proceedings of the Ocean Drilling Program, 198 Scientific Results*, (College Station, TX: Ocean Drilling Program), doi: 10.2973/odp.proc.sr.198.122.2006

Yamamoto, Y., Yamazaki, T., Kanamatsu, T., Ioka, N., and Mishima, T. (2007). Relative paleointensity stack during the last 250 kyr in the northwest Pacific. *J. Geophys. Res.* 112:B01104. doi: 10.1029/2006JB004477

Yamazaki, T. (1999). Relative paleointensity of the geomagnetic field during Brunhes Chron recorded in North Pacific deep-sea sediment cores: orbital influence? *Earth Planet. Sci. Lett.* 169, 23–35. doi: 10.1016/S0012-821X(99)00064-3

Yamazaki, T. (2009). Environmental magnetism of Pleistocene sediments in the North Pacific and Ontong-Java Plateau: temporal variations of detrital and biogenic components. *Geochem. Geophys. Geosyst.* 10:Q07Z04. doi: 10.1029/2009GC002413

Yamazaki, T., and Ioka, N. (1997). Environmental rock-magnetism of pelagic clay: implications for Asian eolian input to the North Pacific since the Pliocene. *Paleoceanography* 12, 111–124. doi: 10.1029/96PA02757

Zhang, Q., Liu, Q., Li, J., and Sun, Y. (2018). An integrated study of the Eolian dust in pelagic sediments from the North Pacific Ocean based on environmental magnetism, transmission electron microscopy, and diffuse reflectance spectroscopy. *J. Geophys. Res. Solid Earth* 123, 3358–3376. doi: 10.1002/2017JB014951

Zhang, W., Li, G., and Chen, J. (2019). The application of Neodymium isotope as a chronostratigraphic tool in North Pacific sediments. *Geol. Mag.* 157, 768–776. doi: 10.1017/S001675681900089X

Zhao, T. L., Gong, S. L., Zhang, X. Y., Blanchet, J.-P., McKendry, I. G., and Zhou, Z. J. (2006). A simulated climatology of Asian Dust Aerosol and its trans-pacific transport. Part I: mean climate and validation. *J. Clim.* 19, 88–103. doi: 10.1175/JCLI3605.1

Conflict of Interest: The authors declare that the research was conducted in the absence of any commercial or financial relationships that could be construed as a potential conflict of interest.

frontiers in Earth Science

ORIGINAL RESEARCH
published: 28 July 2020
doi: 10.3389/feart.2020.00283

The Effect of Early Diagenesis in Methanic Sediments on Sedimentary Magnetic Properties: Case Study From the SE Mediterranean Continental Shelf

Nitai Amiel[1]*†, *Ron Shaar*[2] *and Orit Sivan*[1]

[1] The Department of Geological and Environmental Sciences, Ben-Gurion University of the Negev, Beersheba, Israel, [2] The Institute of Earth Sciences, The Hebrew University of Jerusalem, Jerusalem, Israel

OPEN ACCESS

Edited by:
Myriam Kars,
Kôchi University, Japan

Reviewed by:
Janna Just,
University of Bremen, Germany
Natascha Riedinger,
Oklahoma State University,
United States

***Correspondence:**
Nitai Amiel
Nitai.amiel@weizmann.ac.il

†Present address:
Nitai Amiel,
Department of Earth and Planetary Sciences, Weizmann Institute of Science, Rehovot, Israel

Specialty section:
This article was submitted to Sedimentology, Stratigraphy and Diagenesis, a section of the journal Frontiers in Earth Science

Received: 24 March 2020
Accepted: 18 June 2020
Published: 28 July 2020

Citation:
Amiel N, Shaar R and Sivan O (2020) The Effect of Early Diagenesis in Methanic Sediments on Sedimentary Magnetic Properties: Case Study From the SE Mediterranean Continental Shelf. Front. Earth Sci. 8:283. doi: 10.3389/feart.2020.00283

Microbial respiration in marine sediment can affect the magnetic properties of the sediment through a complicated interplay between reductive dissolution and authigenic precipitation of iron-bearing magnetic minerals. However, a direct link between the main diagenetic zones in the upper sedimentary column and sedimentary magnetic properties using high resolution multi parameter profiles has been demonstrated only in few studies. Here, we directly correlate early diagenetic processes and sedimentary magnetism using a composite high-resolution sedimentary record of pore water chemistry, solid phase chemical measurements and mineral-magnetic parameters. Measurements along the profiles include the entire redox cascade, from the water-sediment interface, down through the deep methanic zone, on a six-meter sediment core collected from the Southern Eastern Mediterranean continental shelf. The uppermost part of the sediment core, associated with oxic, nitrous, manganous, ferruginous, and sulfate reduction zones, is characterized by high ferrous iron and sulfate concentrations and high values of the measured magnetic parameters [susceptibility, Isothermal remanent magnetization (IRM) and Anhysteretic remanent magnetization (ARM)]. This layer is underlain by a sulfate-methane transition zone (SMTZ) that shows a significant decrease in magnetic parameters due to the dissolution of magnetic minerals. Below the SMTZ, the methanic zone has been assumed to be magnetically inactive under steady-state conditions. However, we observe in the upper methanic zone an increase in microbial iron reduction, coupled to an abrupt increase in magnetic parameters. Our data indicate that the observed increase in the magnetic signal is related to the precipitation of authigenic magnetic minerals. These diagenetic changes should be considered when interpreting paleomagnetic data, and highlight the potential to use high-resolution magnetic data as a proxy for identifying diagenetic processes.

Keywords: early diagenesis, sedimentary magnetism, porewater chemistry, methanogenesis, iron reduction

INTRODUCTION

Microbial respiration of organic debris in sediments is coupled to the reduction of electron acceptors along a cascade of decreasing free energy yield from oxygen reduction, followed by nitrate reduction, manganese and iron oxide reduction, then sulfate reduction, and finally, methanogenesis (Froelich et al., 1979). This respiration order predicts that the more favorable processes (with more negative Gibbs energy) would occur at shallower depths (Jorgensen, 2000). Therefore, these respiration processes define diagenetic zones associated with change in the chemical composition of the pore water (Berner, 1980; Canfield and Thamdrup, 2009).

The change in pore water chemistry due to the microbial respiration processes can cause also diagenetic changes in the mineralogy of the sediment. This can include dissolution and precipitation of iron-bearing magnetic minerals, which leave traceable magnetic fingerprints (signals) in the sediment (Lovley, 1991; Liu, 2004; Maloof et al., 2007; Rowan et al., 2009; Roberts, 2015). Thus, understanding and characterizing the link between geochemical pore water profiles, diagenetic zones, and sedimentary magnetic changes, is necessary for adequate interpretation of magnetic sedimentary data, and vice versa can enable new insights into the microbial activity in sediments.

Magnetic properties of the sediment and the assemblage of its magnetic particles can vary as a response to changes in sediment transport and deposition regime, but also due to diagenetic reactions, which evolve with burial (Liu et al., 2012). In the oxic zone, surface oxidation of detrital iron minerals, mainly maghemitization of magnetite, commonly occurs (Smirnov and Tarduno, 2000; Torii, 2011). In addition, iron-bearing minerals can precipitate in the oxic, nitrogenous, and manganous zones (which can overlap) as dissolved ferrous iron from underlying zones diffuses upward and reacts with dissolved oxygen, nitrate, or with oxide minerals, to form oxyhydroxides (Lovley et al., 1990; Cornell and Schwertmann, 2003). In the ferruginous zone, iron minerals undergo reductive dissolution by iron reducing bacteria oxidizing organic substrates, releasing ferrous iron into the pore water and triggering the precipitation of authigenic and/or biogenic minerals, mainly magnetite (Channell et al., 1982; Chang et al., 1987; Karlin et al., 1987; Lovley et al., 1987). Ferric iron appears in most aquatic systems as low-solubility iron oxide minerals. Thus, its reduction is a challenge to microorganisms, which need to breathe those minerals, rendering many of them effectively unavailable for reduction deep in sedimentary environments, and leading to the dominance of sulfate reducing bacteria at a certain depth (Shi et al., 2007). In the sulfate reduction zone, sulfide, the product of bacterial sulfate reduction, reacts also with the remnant of the ferric iron oxides, which have survived the dissolution in the upper sediment. This causes oxidation of the sulfide to sulfur intermediates (and then to sulfate and sulfide by disproportionation), reductive dissolution of the detritus iron oxides and liberation of dissolved ferrous iron into the porewater (Rickard and Luther, 2007). The excess sulfide and the dissolved ferrous iron precipitate as authigenic iron-sulfide minerals, first as iron-monosulfide, altering to pyrite, the most stable iron-sulfide mineral, as sulfide concentration increases (Berner, 1984; Canfield and Berner, 1987; Roberts, 1995; Rowan et al., 2009).

Once sulfate is depleted, methane production by methanogens (Archaea), traditionally serves as the terminal process anchoring carbon remineralization. When the produced methane comes into contact with an available electron acceptor, it can be consumed by it through microbial oxidation (methanotrophy), the main process by which methane is prevented from escaping to the atmosphere. In marine sediments (the main natural reservoir of methane), up to 90% of the upward methane flux is consumed anaerobically by sulfate (Valentine, 2002), wherein established (diffusive) profiles it occurs within a distinct sulfate-methane transition zone (SMTZ). According to the classical view, minor magnetic changes are expected below the SMTZ with regard to the iron mineral assemblages in the sediments. A significant iron reduction has been recently reported below the SMTZ, in the methanic zone of marine sediments, where the release of dissolved ferrous iron often coincides with a decrease in methane concentrations (Jørgensen et al., 2004; März et al., 2008; Slomp et al., 2013; Riedinger et al., 2014; Treude et al., 2014; Egger et al., 2015). These observations suggest the possibility of a "deep" diagenetic zone associated with the reduction of iron minerals that have survived the upper reduction zones and potentially the formation of magnetic authigenic minerals.

Several studies have explored the relationship between porewater chemistry, sediment chemistry, and sedimentary magnetism (Kasten et al., 1998; Liu, 2004; Riedinger et al., 2005; Kawamura et al., 2007, 2012; Larrasoaña et al., 2007; Fu et al., 2008; März et al., 2008; Rao et al., 2008; Cruz et al., 2018). However, a direct link between depth profiles of chemical composition of the porewater and the magnetic parameters throughout the diagenetic zones has been only partly established (Garming et al., 2005; Fu et al., 2008). Here, we explore the coupling between porewater chemistry and sedimentary magnetism in marine sediments and investigate the entire diagenetic profile from the oxic zone down to the deep methanic zone.

MATERIALS AND METHODS

Study Site

The sediment core was collected from Station SG-1 (32°57.83′N 34°55.29′E), located on the continental shelf of Israel, 20 km offshore Acre, at a water depth of 85 m (**Figure 1**). The sediments in this area mainly correspond to input from the Nile River, which has been delivering a massive load of siliciclastic clays through counter-clockwise currents parallel to the coast since sea level stabilization at 6000–7000 years BP (Nir, 1984; Lambeck and Purcell, 2005; Schattner et al., 2010). The sediment extending 3–5 km from the shore is mainly composed of sand and silt, while further, the sediment is composed of muddy clayey sediments derived from the Nile. The most abundant clay mineral is montmorillonite (with a smaller fraction of illite and kaolinite), which makes silica, alumina, and ferric iron oxides the main chemical components in the bulk sediment (Nir, 1984). Although methane is not expected in the upper several meters

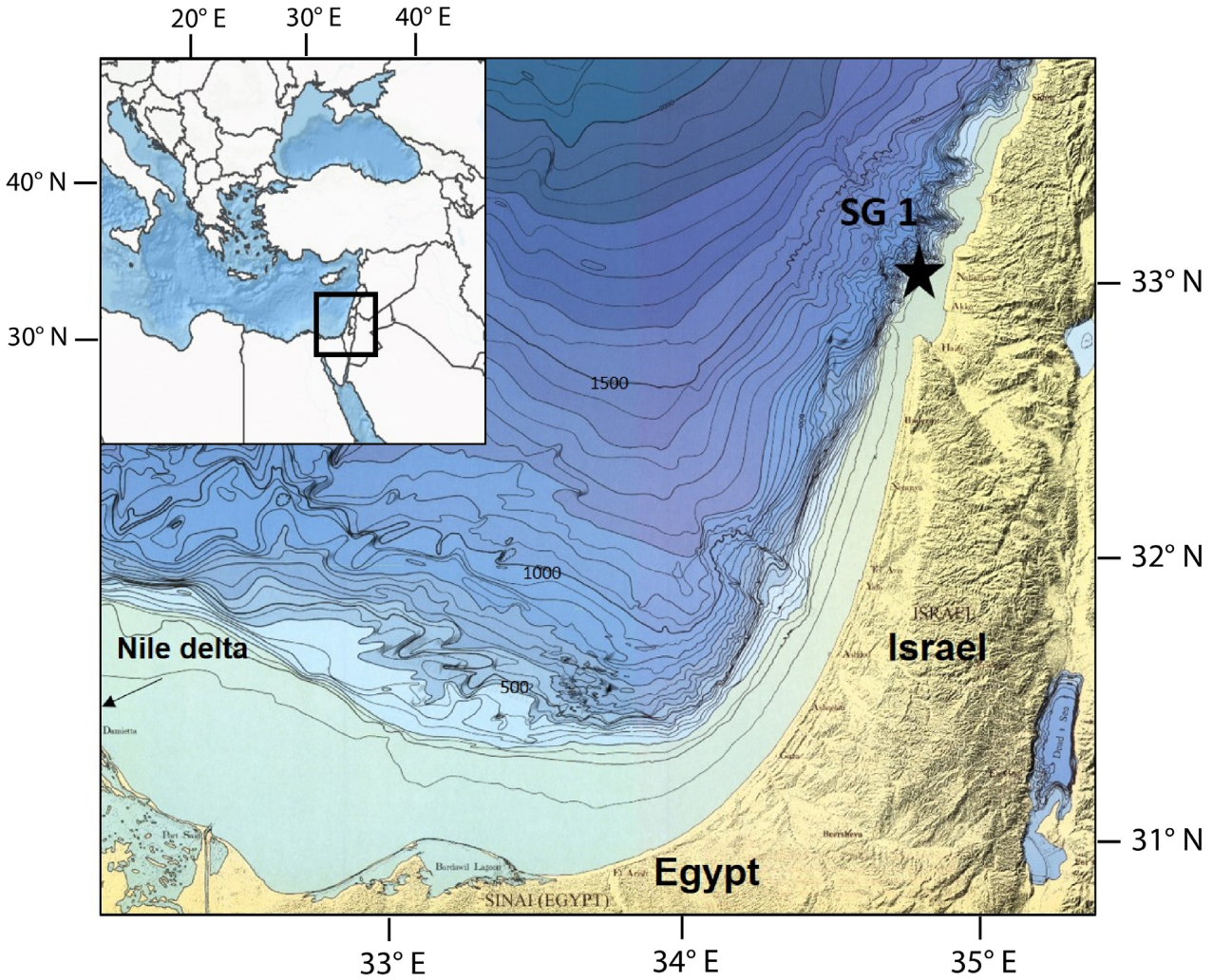

FIGURE 1 | Location map of Station SG-1 in the Southern Eastern Mediterranean Sea continental shelf.

of the sediments due to the oligotrophic characteristics the SE Mediterranean Sea surface water, methane was observed in several cores collected from SG-1 (Sela-Adler et al., 2015; Vigderovich et al., 2019; Wurgaft et al., 2019). They identified the SMTZ in the upper few meters of the sediments, conducted an isotopic analysis of the methane and concluded that most of the methane is from biogenic source and that it is being produced *in situ*. Yet, it is possible some methane gas might diffuse upward from a deeper biogenic methane gas pocket, which was observed by seismic surveys at depths of 40–110 m (Schattner et al., 2012).

Sampling

A 6 m long sediment core was collected from Station SG-1 using a piston corer during a cruise on the *R. V. Bat-Galim* in January 2017. The sediment core was sliced onboard at intervals of 30 cm within minutes of core collection. For headspace measurements of CH_4, approximately 1.5 mL of sediment was taken from the top of each sediment slice. This sediment was transferred immediately into N_2-flushed crimped bottles containing 5 mL of 1.5 N NaOH. Sediment samples from the top 5 cm of each sediment slice were transferred to vials under anaerobic conditions, and porewater was extracted from them on the same day by centrifugation at 4°C under an N_2 atmosphere. The supernatant was filtered through a 0.22 μm filter and was analyzed for dissolved Fe^{2+}, sulfide, and sulfate. The sediment was dried in an ambient temperate under N_2 atmosphere, the dry sediment was analyzed for different iron minerals fractions following the sequential extraction protocol from Poulton and Canfield (2005). The 30 cm core segments were split along their length and sampled for magnetic analysis by pushing non-magnetic plastic sampling boxes of 23 × 23 × 19 mm into the split halves at ∼5 cm intervals. Magnetic mineral extractions for scanning electron microscopy (SEM) were prepared from a mixture of 2–3 g of sediment and alcohol, using a strong hand magnet within a plastic probe (Nowaczyk, 2011). The extracts were dried in ambient temperature, half of the dried sediment was characterized by X-Ray Diffraction (XRD) measurement, the other half tapped on a conductive polycarbonate tape for

electron microscopy imaging and elemental analyses, using high-resolution SEM with an integrated energy dispersive X-ray spectroscopy (EDS).

Chemical Measurements

Headspace methane concentrations were measured on a Thermo Scientific gas chromatograph (GC) equipped with a flame ionization detector (FID) at a precision of 2 $\mu mol \cdot L^{-1}$. Sulfate concentrations were analyzed by inductively coupled plasma-atomic emission spectroscopy (ICP-OES-720-ES, VRIAN) with a precision of 2%. Ferrous iron was fixed immediately using Ferrozine solution, and its absorbance in 562 nm was measured on a spectrophotometer (Stookey, 1970), with an error of less than 7 $\mu mol \cdot L^{-1}$. Sulfide was measured using the Cline method (Cline, 1969), and 1.5 mL filtered porewater was inserted into a 15 mL falcon tube with 0.1 mL of ZnAc (200 $g \cdot L^{-1}$). Then, 120 μL of the diamine reagent was added into the solution, and the sample was stored in the dark for 30 min before measuring. Sulfide concentration was measured photometrically at 665 nm wavelength with a precision of $\pm$ 2%. The measurements of different iron minerals in the solid phase were performed on chemical extractions of four Fe fractions (Fe_{carb}- siderite and ankerite, Fe_{ox1}- ferrihydrite and lepidocrocite, Fe_{ox2}- goethite, hematite and akageneite, and Fe_{mag}- magnetite), following the Poulton and Canfield (2005) sequential extraction protocol. A 0.5 g dry sediment was inserted into a centrifuge tube with 10mL of a specific extractant at every stage. The fluids were separated from the sediment by centrifugation and removed from the tube after every extraction stage. At the end of each extraction stage, the extractant was transferred into a falcon tube containing ferrozine solution, and then it was measured spectrophotometrically. Fe_{Carb} was extracted by adding 1 M sodium acetate at pH 4.5 to the samples for 24 h. Fe_{ox1} was extracted by adding 1 M hydroxylamine- HCl in 25% [v/v] acetic acid to the samples for 48 h. Fe_{ox2} was extracted by adding 50 $g \cdot L^{-1}$ sodium dithionite buffered to pH 4.8 with 0.35 M acetic acid or 0.2 M sodium citrate for 2 h. Fe_{mag} was extracted by adding 0.2 M ammonium acetate solution at pH 3.2 for 6 h.

Magnetic Measurements

Magnetization measurements were carried out using a three-axial 2G-750 Superconducting Rock Magnetometer (SRM) system with an in-line two-axial AF unit and an axial anhysteretic remanent magnetization (ARM) coil. IRM was acquired using ASC pulse magnetizer and was measured using AGICO JR-6 spinner. Each sample was subjected to the following procedure: AF demagnetization of the NRM; ARM acquisition in 100 mT AC field and 0.1 mT bias field; AF demagnetization of the ARM using the same steps as the NRM demagnetization; IRM acquisition in 1.5 T. Demagnetization experiments were done in 11 steps (5, 10, 15, 20, 30, 40, 50, 65, 80, 100, 110, and 120 mT). Demagnetization data were analyzed using the PmagPy software package (Tauxe et al., 2016). Characteristic remanent magnetization (ChrM) directions were calculated from principal component analysis (PCA) following Kirschvink (1980). To detect the presence of gyro-remanent magnetization (GRM), typical to SD greigite (Snowball, 1997; Roberts et al., 2011) we calculate a GRM(%) parameter as described in eq. 1:

$$GRM(\%) = 100 \cdot \frac{m_{120\ mT} - m_{min}}{NRM} \quad (1)$$

Where $m_{120\ mT}$ is the magnetic moment after the 120mT step and m_{min} is the minimum moment measured during the AF demagnetization process.

Bulk low frequency (χlf) and high frequency (χhf) susceptibility were measured using an AGICO MFK-1 kappabridge at frequency of 976 and 15616 Hz, respectively. Frequency-dependent susceptibility (χfd) was calculated using the percentage of the normalized difference in susceptibility, as shown in eq. 2:

$$\chi_{fd}(\%) = 100 \cdot \frac{\chi_{lf} - \chi_{hf}}{\chi_{lf}} \quad (2)$$

High-temperature susceptibility thermomagnetic curves were measured on selected samples from depths 160, 280, 340, and 550 cm with the kappabridge using a CS4 furnace at temperatures ranging from ambient temperature to 700°C in Argon atmosphere. Low-temperature zero field cooling (ZFC) heating curves were measured on samples from depths 54, 150, 240, 350, 450, and 560 cm using Quantum Design MPMS by heating the samples under 10 mT magnetic field from 5K to room temperature after cooling them in zero field.

Electron Microscopy

Imaging of magnetic minerals, extracted from depths 84, 160, and 280 cm, was done using a FEI Magellan TM 400L field emission XHR-SEM (Oxford Instruments, United Kingdom) at 10–15 kV and 0.2 nA using a Secondary electron detector (ETD) and High contrast retractable solid-state detector (vCD). Elemental composition measurement was carried out using an energy dispersive X-ray spectroscopy (EDS) silicon drift detector Oxford X-Max (Oxford Instruments, United Kingdom). Imaging was conducted at the center of Nanoscience and Nanotechnology at the Hebrew University, Jerusalem, Israel.

X-Ray Diffraction

Sample characterization was performed by X-Ray Powder Diffraction method. Data were collected on Panalytical Empyrean Powder Diffractometer equipped with position sensitive detector (PSD) PIXCEL and Graphite monochromator on the diffracted beam The Cu K_α radiation (α = 1.541 Å) was used at operation conditions (voltage and current) 40 kV and 30 mA. The usual Bragg-Brentano q/2q was employed. q/2q scans were run for 15 min in a 2q range of 5–60° with step equal to ∼0.026°. Phase identification was performed by using the Match computer search/match program coupled with the ICDD (International Centre for Diffraction Data) Powder Diffraction File database (2015).

RESULTS

Sediment Composition

The sediment is composed of homogenous dark-gray clay and silt. Neither changes in grain size, nor in sediment color are visible. The XRD results (**Supplementary Figure S1**) indicate that the sediment is composed of quartz, calcite, clays, and albite. All four samples, collected from different depths, show an identical composition. Wurgaft et al. (2019) determined the content of calcite, clays, and quartz, in a different core collected from the same station, by 4–6%, 50–70%, and 15–25%, respectively. Measurements of iron fractions using chemical extractions (**Figure 2D**) show that goethite, hematite and akageneite (Fe_{ox2}) are the most abundant Fe minerals in the sediment, with concentrations of 2.2% wt/dry sediment at the top of the sediment, decreasing to 1.4% wt/dry sediment at 500 cm depth. Ferrihydrite and lepidocrocite (Fe_{ox1}) and siderite and ankerite (Fe_{carb}) concentrations at the sediment-water interface are 0.5 and 0.3% wt/dry sediment, respectively. Fe_{Ox1} concentration increases to 0.65% wt/dry sediment at 250 cm depth and then decreases to its initial value, while Fe_{carb} concentrations increase with depth to a value of 0.48% wt/dry sediment at 500 cm depth. Magnetite (Fe_{mag}) concentration decreases from 0.14% wt/dry sediment at the top of the sediment to 0.08% wt/dry sediment at 200 cm depth, then it rises to ∼0.18% wt/dry sediment between 220 and 260 cm, and decreases back to 0.1% wt/dry sediment below that.

Porewater Chemistry

Figures 2A–C shows the porewater chemistry depths profiles. Dissolved ferrous iron concentrations at the top 90 cm of the core are 20–90 μM, between 190 to 290 cm depth the concentrations are 20–70 μM, and at the rest of the core they are below 5 μM (with one exception at 480 cm depth) (**Figure 2A**). Sulfate concentrations are 34 mM at the top of the core, and gradually decrease to zero at 180 cm depth (**Figure 2B**). Methane starts to accumulate below 100 cm to ∼2.7 mM at 450 cm depth, where it remains stable with depth (**Figure 2C**).

According to the porewater chemistry data (**Figure 2**), the ferruginous zone is located at depths of 10–100 cm; the sulfidic zone is at the upper 180 cm; the SMTZ is located at depth of 105–180 cm, with a decrement in sulfate concentration parallel to the rise in methane concentrations; and the methanic zone is below 180cm with some peaks of iron reduction (see Discussion).

Rock Magnetism

Depth profiles of selected bulk rock magnetic parameters are shown in **Figures 2E–J**. For a detailed review of each of these parameters, see Liu et al. (2012). The Mass normalized low-frequency susceptibility χlf (**Figure 2E**, see section "Materials and Methods") is sensitive to the mineralogy and the concentration

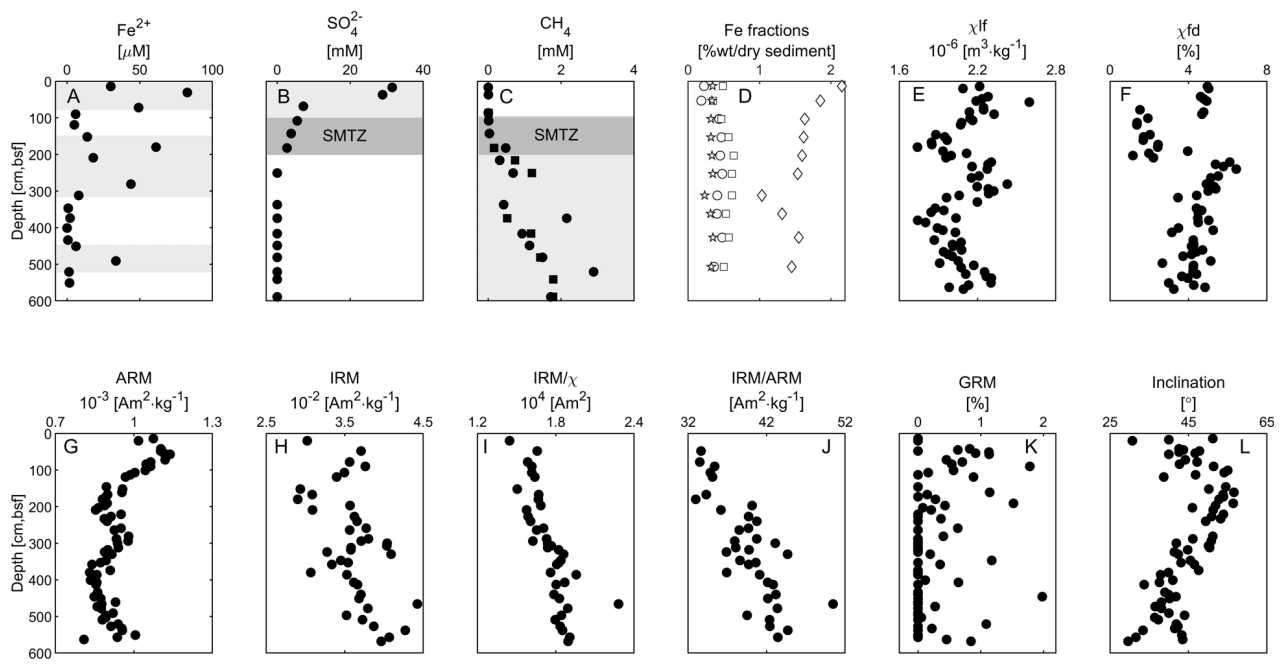

FIGURE 2 | Depth profiles of porewater geochemistry, Fe fractions, and magnetic data. **(A)** Porewater ferrous iron concentrations. **(B)** Porewater sulfate concentrations. **(C)** Porewater methane concentrations. **(D)** Sediment Fe fraction concentration. Fe_{carb} (siderite and ankerite) - Circles. Fe_{ox1} (ferrihydrite and lepidocrocite)- Squares, Fe_{ox2} (goethite, hematite, and akageneite)- Diamonds, Femag- Stars. **(E)** Low-frequency susceptibility. **(F)** Frequency dependent susceptibility. **(G)** Anhysteretic remanent magnetization (ARM), **(H)** Isothermal remanent magnetization (IRM). **(I)** IRM to low-frequency susceptibility ratio. **(J)** IRM to ARM ratio. **(K)** Gyroremanent magnetization (GRM%). **(L)** Inclination. The data in panels **(A–C)** represent the average of duplicates with error values smaller than the sample symbol, except the methane profile, in which the two duplicates are shown (in squares and circles). Iron and sulfate reduction and methanic zones are marked with gray background. The SMTZ is marked with dark gray background.

of all the magnetic phases. χlf shows a zigzagged pattern with two maxima at the top 100 cm and between ∼200–300 cm, and two minima at ∼150 cm and ∼380. The mass normalized ARM and IRM magnetizations (see Methods, **Figures 2G,H**) are sensitive to the mineralogy, grain size, and concentration of the ferromagnetic phase, and they show similar trends of changes as χlf. This indicates that the depth variations in the susceptibility and magnetization curves are affected mainly by changes in the properties of low coercivity ferromagnetic particles capable of recording both ARM at 100mT and IRM at 1.5T. χfd (**Figure 2F**) - the difference between the low-frequency and high-frequency susceptibilities (see Methods) - is sensitive to concentration of small sub-micrometer scale ferromagnetic particles across the superparamagnetic (SP) – single domain (SD) transition. The χfd shows a similar trend as χlf in the top 300 cm, but with more abrupt change at ∼100 cm and 210 cm. This indicates a sudden drop in the concentration of the smallest ferromagnetic particles below the upper 100 cm, and recovery of small particles below 210 cm. The ratio between IRM and ARM (**Figure 2J**) increases with depth, suggesting a steady increase in the grain size of the ferromagnetic particles below the SMTZ. The ratio between IRM and χlf (**Figure 2I**), which is sensitive to SD ferromagnetic mineralogy, and also used as an indicator to greigite (Roberts, 1995; Sagnotti and Winkler, 1999) also shows a steady increase with no abrupt changes. The AF median destructive field (MDF) of the ARM (not shown in **Figure 2**) ranges between 17.1mT and 19.0mT. We could not see any correlation between the MDF values and the rest of the magnetic parameters.

The thermomagnetic curves of all four measured samples show very similar patterns (**Figure 3**). The susceptibility values gradually decrease above 400°C, with sharp drops between 400°C and 500°C and near 580°C. This indicates the presence of magnetite and titanomagnetite.

The ZFC curves (**Figure 4**) can help identify the presence of stoichiometric magnetite using the Verwey transition, the change in magnetite magnetization due to a crystallographic phase transition from an inverse cubic spinel to monoclinic, which occurs at 124 k (Verwey, 1939). The curves (**Figures 4A–F**) show similar trends, dominated by a paramagnetic signal that apparently masks small changes in magnetization. An increase in magnetization between 25K to 50K is observed in all samples. In order to detect small changes in magnetization around the Verwey transition temperature, which are not clearly visible in **Figures 4A–F**, we show in **Figure 4G** the first derivative of the ZFC curves. A peak in the derivative near the Verwey transition temperature, which is indicative for the presence

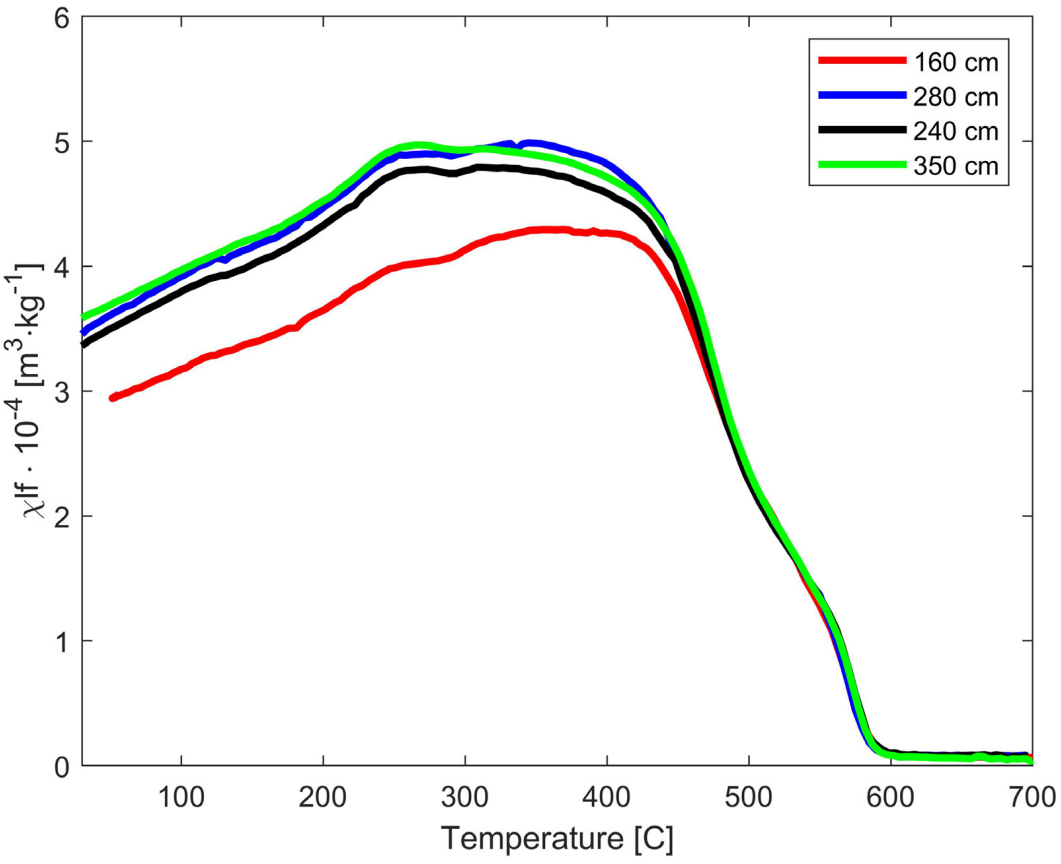

FIGURE 3 | Susceptibility thermomagnetic heating curves.

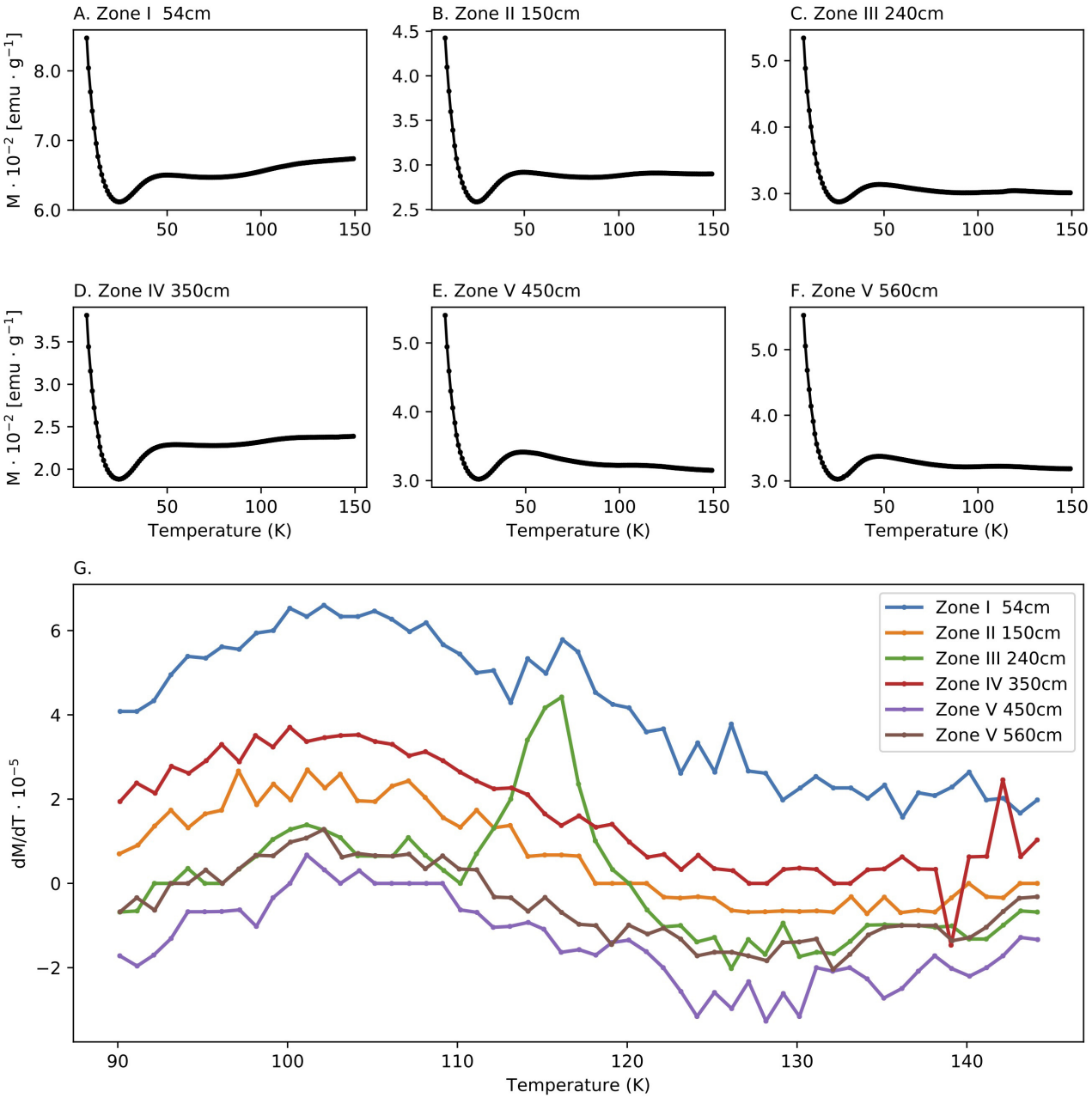

FIGURE 4 | Low temperature measurements. **(A–F)** Zero field cooling (ZFC) curves of samples collected from the five diagenetic zones defines in **(G)** First derivative of the curves shown in **(A–F)** around the Verwey transition temperature.

of stoichiometric magnetite, is observed only at depth of 350 cm. This may suggest low concentration of stoichiometric magnetite in this depth.

Paleomagnetic Directions

Demagnetization of the NRM yielded straight univectorial Zijderveld diagrams with straight lines converging to the origin. ChRM component calculated between 10 mT and 80mT yielded MAD values (Kirschvink, 1980) below 5, typically less than 2, and DANG values (Tauxe and Staudigel, 2004) below 3 (except one specimen). The low MAD indicates low scatter of the data points, and the low DANG values indicate convergence to the origin, which together implies high quality of magnetic recording. We did not observe any correlation between the MAD values and the geochemical zones. To detect the presence of gyro-remanent magnetization (GRM), typical to SD greigite (Snowball, 1997; Roberts et al., 2011) we calculate a GRM(%) parameter (see section "Materials and Methods"). Most of the GRM(%) values (**Figure 2K**) are equal to zero, and except one sample, all values are lower than 2%, indicating no GRM effect in this dataset.

The inclination values (**Figure 2L**) range between 30° and 57°, where the geocentric axial dipole (GAD) inclination in the study area is 52.4°. Thus, the directions fall within the expected secular variation range.

DISCUSSION

Study Site Conditions

Sela-Adler et al. (2015) collected several cores from nearby stations, at water depths of 80–88, across a 10 km N-S trending strip in the vicinity of SG-1 station. In all cores, they identified the SMTZ in the top 4 m of the sediment and a clear signature of *in situ* methane. Following their findings, we investigated in details SG-1, in an attempt to better define the diagenesis zones in the upper sediment and correlate them with the magnetic properties of the sediment. Our interpretations of the new geochemical and magnetic data are based on the assumptions of a steady state condition, that is semi-constant delivery of sediments with similar properties. Generally speaking, there are a number of non-steady state mechanisms that can potentially violate our working assumption. One possible scenario is an abrupt change in the sedimentation rate, which can cause migration of the SMTZ (e.g., Riedinger et al., 2005; Fu et al., 2008). In addition, temporal changes in the organic matter load into the sediment can affect the depths of the different respiration processes (e.g., Larrasoaña et al., 2003; Rowan et al., 2009). Also, changes in the grain size and composition can lead to the accumulation of magnetic minerals in the sediment and change in the magnetic parameters. These mechanisms require time-variations in the flux of the sediment from Nile river, which is the main source of sediments to the studied area. Indeed, the Nile has experienced several environmental changes in the Holocene. The African Humid Period (AHP), which extended from 10–6 kyr was associated with an increased runoff of the Nile river and enhanced supply of organic-rich sediment. The outcome of these changes is the deposition of dark organic-rich sapropel layer (Rossignol-Strick et al., 1982). Yet, the sapropel layer is located at much greater depths below our investigated core. Also, while the Nile river water discharge in the last 6 kyr has changed several times, mainly due to shifts in the Inter-Tropical Convergence Zone (ITCZ), potential changes in the sedimentation rate of the SE Mediterranean have not been observed since by the last sapropel (e.g., Blanchet et al., 2013 for the last 7 kyr).

A number of observations support the steady state assumption. The entire core comprises homogenous lithology of silts and clays (Wurgaft et al., 2019), and the XRD analysis indicates nearly identical composition at all depths (**Supplementary Figure S1**). In addition, the thermomagnetic curves are also nearly identical, supporting the assumption of no significant change in the bulk properties of the sediment source. A physical disturbance of the sediments seems unlikely as the core was collected from a stable part of the continental shelf, where mass transports and turbidity currents do not play a significant role. Indeed, the paleomagnetic data show a stable paleomagnetic recording mechanism and all the paleomagnetic directions fall within the expected range of geomagnetic secular variation. This excludes the possibility of sediment disturbance from currents or slumps.

The sediment in SG-1 site was not dated, and the sequence lacks any chronological marker that enable estimation of the sedimentation rate and the age span of the core. Yet, based on previous analysis of cores from similar depths (Bareket et al., 2016), the estimated deposition rate is around 1 mm/year. To better constrain the age of the core, we show in **Figure 5** the prediction of global geomagnetic models (**Figure 5A**) compared to the paleomagnetic inclination in SG-1 (**Figure 5B**). We used the SHA.DIF.14k geomagnetic model of Pavón-carrasco et al. (2014) that covers the past 14,000 years because it spans through sufficient time interval. The paleomagnetic inclination profile in SG-1 shows a steady decrease in inclination from 200 cm down to the bottom of the core. This trend in SG-1 inclination fits the decrease in inclination from ∼3000 BP to ∼7000 BP. Also, the increase in geomagnetic inclination from ∼9000 BP to the beginning of the Holocene, is not observed in SG-1. This provides us a rough constraint for the maximum age of the magnetic acquisition in SG-1, placing it before ∼9000 BP, likely around ∼6000 BP. The paleomagnetic data support our assumption that the sediments were deposited after the last sapropel in Mediterranean.

From the overall observations we base our interpretation of the data on the assumption that the observed depth-variations in the magnetic parameters, which are sensitive to small changes in the mineralogy and grain-size of the ferromagnetic phase, reflect dissolution and precipitation processes related to diagenesis rather than changes in the sediment supply. While we cannot rule out the possibility of other factors affecting the magnetic properties of the sediment, it seems more likely that that the changes in the magnetic parameters that occur in parallel to changes in the pore water geochemical data are associated with diagenesis. In the following parts, we interpret the combined magnetic-geochemical data in view of early diagenesis zones under steady state conditions.

Microbial Respiration Pathways and Magnetic Diagenetic Zones

Based on the geochemical and magnetic results, the sedimentary column can be divided roughly into five diagenetic zones. These zones are shown in **Figure 6**, with the main geochemical-magnetic depth profiles.

Zone I (0–100 cm depth) is the uppermost part of the sediment. It includes an overlap between the ferruginous and the sulfidic zones, as indicated by the high concentrations of dissolved ferrous iron (**Figure 6A**) and a steady decrease of sulfate concentrations with depth (**Figure 6B**). Based on the results of a previous study on an adjacent core, organoclastic sulfate reduction (OSR) is the main mechanism for sulfate reduction in this zone (Wurgaft et al., 2019). Dissolved sulfide concentrations are below the detection limit there and throughout the sediment core, probably due to precipitation of ferrous iron- sulfide minerals (Wurgaft et al., 2019). Indeed, pyrite framboids were observed in this zone (**Figure 7A**), supporting the presence of sulfide in this depth. The magnetic parameters χlf, χfd, ARM,

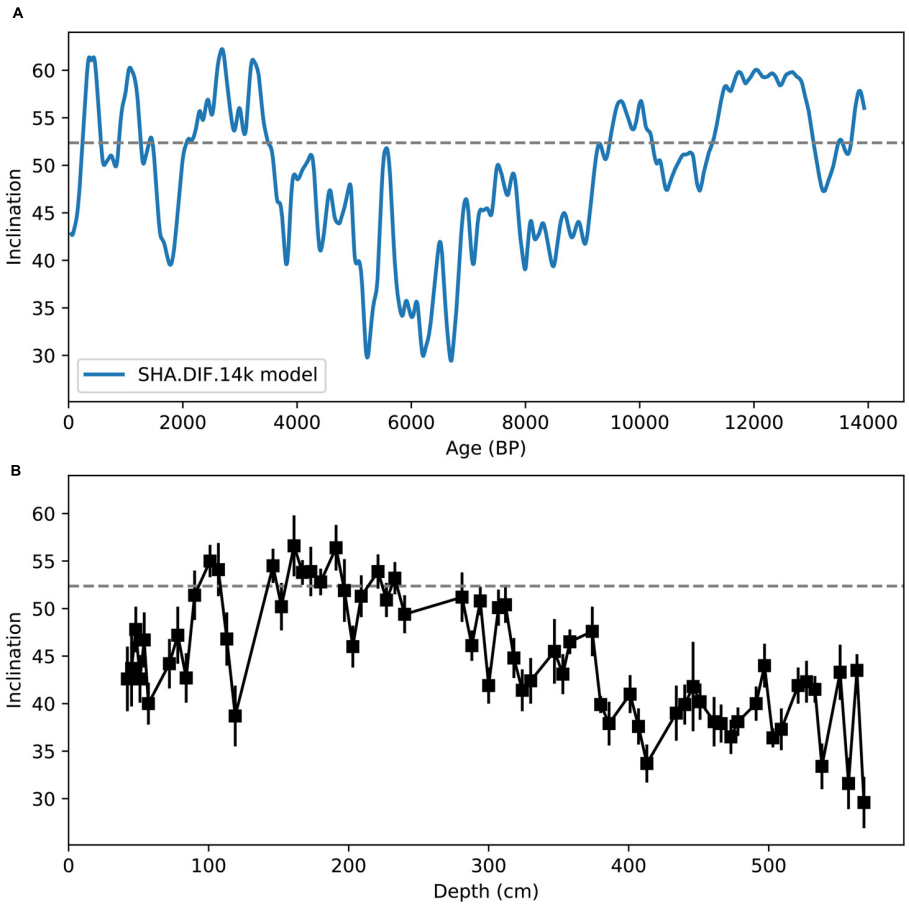

FIGURE 5 | Paleomagnetic inclination. **(A)** Geomagnetic inclination predicted by SHA.DIF.14k model (Pavón-carrasco et al., 2014) at the sampling site. **(B)** Depth profile of paleomagnetic inclinations in SG-1.

and IRM (**Figures 6E–H**) in zone I are high compared to the underlying zones, due to the relatively high concentration of detrital titanomagnetite (**Figure 7B**). A slight increase in the ARM (from 0 to 50 cm) and IRM (from 0 to 90 cm) suggest enhancement of the magnetic parameters, which could potentially be explained by precipitation of ferrimagnetic greigite, or remnants of precursor greigite in pyrite framboids (Ebert et al., 2018), or precipitation biogenic and/or authigenic magnetite (Chang et al., 1987; Karlin et al., 1987; Lovley et al., 1987; Roberts, 2015; Roberts et al., 2018).

Zone II (100–180 cm depth) is the SMTZ, where sulfate concentrations are low and methane concentrations are already measurable. This zone is characterized by intensive sulfate reduction by both anaerobic oxidation of methane (S-AOM) and OSR, which results in sulfide formation (Wurgaft et al., 2019). The sulfide reacts with iron oxides, leading to reductive dissolution of detritus ferric iron minerals and precipitation of the produced dissolved ferrous iron with the excess sulfide, as in Zone I (**Figure 6**). The observed steep decrease in all magnetic parameters in this zone is due to the intense reductive dissolution of iron-bearing magnetic minerals and the precipitation of paramagnetic pyrite (Canfield and Berner, 1987; Rowan and Roberts, 2006; Rowan et al., 2009; Roberts, 2015; Roberts et al., 2018). The frequency dependent susceptibility decreases at a shallower depth than χlf, suggesting that the smaller SD and superparamagnetic (SP) particles dissolve first. The effect of this process on the iron-bearing minerals is displayed in **Figures 7B,C**, showing titanomagnetite with partial dissolution marks and a pyrite framboid.

Zone III (180–310 cm depth) is the upper methanic zone, where sulfate is already depleted, and methane continues to increase with depth. Here we observed another increase in dissolved ferrous iron concentrations, as shown in other methanic sediments (Kawamura et al., 2007; Slomp et al., 2013; Riedinger et al., 2014; Egger et al., 2015). The significant increase in magnetic susceptibility and IRM indicates precipitation of authigenic ferrimagnetic minerals. The sharp increase in frequency-dependent susceptibility indicates a contribution from a large fraction of SP/SD particles. Interestingly, the ARM does not increase as sharply as the susceptibility and the IRM, suggesting that the newly formed particles may be in the non-interacting SD range. As we do not have any direct measurements of this authigenic phase, we can only

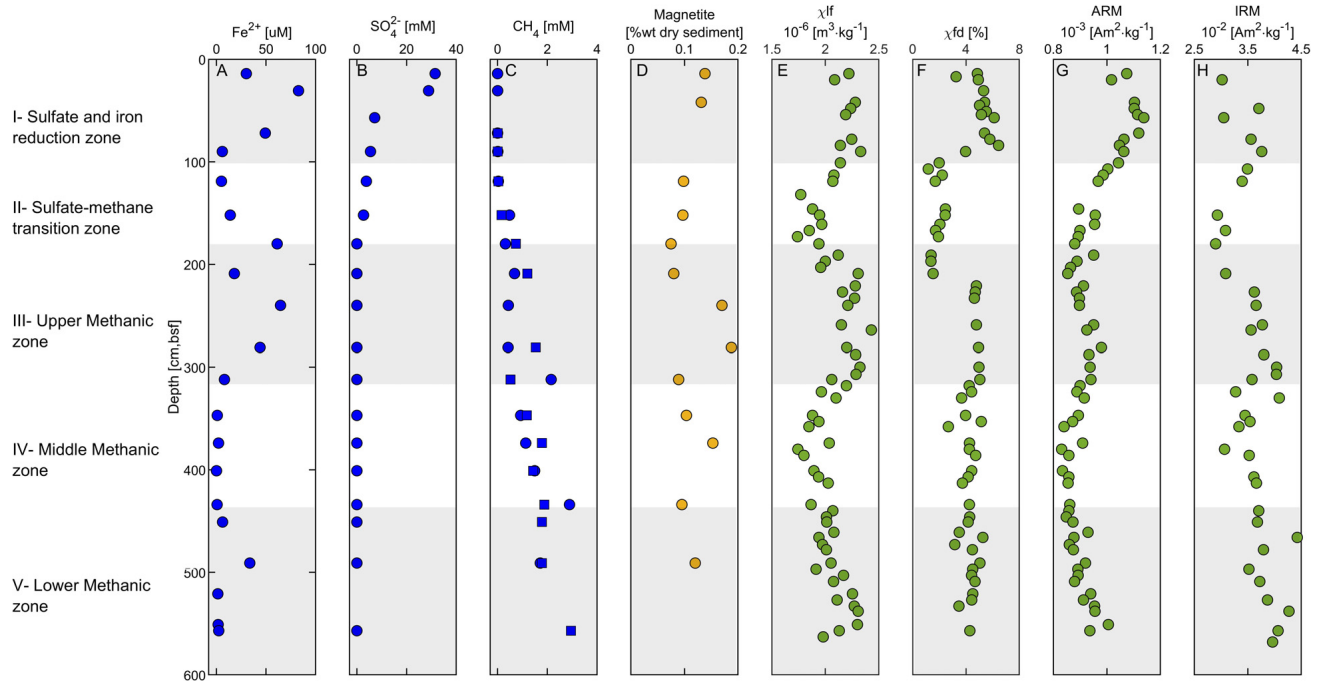

FIGURE 6 | Geochemical – magnetic depth profiles. **(A)** Porewater ferrous iron concentrations. **(B)** Porewater sulfate concentrations. **(C)** Porewater methane concentrations. **(D)** sediment magnetite concentration [following extractions of Poulton and Canfield (2005) protocol]. **(E)** Low-frequency susceptibility, **(F)** Frequency dependent susceptibility. **(G)** Anhysteretic remanent magnetization (ARM). **(H)** Isothermal remanent magnetization (IRM). The data in panels **(A–C)** represent the average of duplicates with error values smaller than the sample symbol, except the methane profile, in which the two duplicates are shown (in squares and circles). The five diagenetic zones are marked with white and gray backgrounds.

hypothesize, in this stage their mineralogy. One possibility is greigite (Larrasoaña et al., 2007; Chang et al., 2008; Rowan et al., 2009; Roberts et al., 2011) or pyrrhotite (Larrasoaña et al., 2007; Roberts, 2015; Horng, 2018; Roberts et al., 2018). Also, authigenic magnetite can explain this type of magnetic pattern, as was shown in the suboxic ferruginous interface (Moskowitz et al., 1989, 1993; Lovley, 1991). The precipitation of authigenic magnetite in this zone is supported by higher magnetite concentrations (**Figure 6D**) and by the largest drop in magnetization next to the Verwey Transition at 120°K (**Figure 4G**). Shang et al. (2020) showed that magnetite can precipitate in anaerobic environments by methanogenic archaeon *Methanosarcina barkeri*, supporting this possibility. The mechanism for its formation remains unknown, although evidence in that work supports the extracellular reduction of ferrihydrite. Electron microscopy from 160 cm depth shows pyrite particles (**Figures 7D,E**) and partly dissolved titanomagnetite (**Figure 7F**), indicating that only part of the detrital titanomagnetite has been dissolved in the SMTZ. Thus, due to the fast sedimentation rate, a significant portion of the detrital ferromagnetic particles survive the SMTZ and can contribute to this diagenetic reaction.

Zone IV (310–575 cm depth) is the middle methanic zone. Here, there are negligible ferrous iron concentrations, methane concentrations still slightly increase with depth, and sulfate is absent. A moderate decrease in χlf, IRM, and ARM is interpreted as further growth and coarsening of the authigenic precipitated magnetic minerals in this zone (Peters and Dekkers, 2003). This can be similar to the results found by Rowan et al. (2009), which suggested that greigite particles in marine sediments grow with depth from superparamagnetic particles through the SD blocking volume.

Zone V (440–575 cm depth) is the lower methanic zone. Ferrous iron concentrations show an increase in one point at 490 cm depth, and methane concentration stops increasing with depth. These observed concertation trends indicate a reduction of ferric iron potentially related to AOM, as previously observed and modeled in the deep methanic depth of marine and freshwater sediments (Sivan et al., 2007, 2011; Riedinger et al., 2014; Egger et al., 2015, 2017; Bar-Or et al., 2017).

The ZFC curves show an increase in the derivative near the Verwey transition temperature mostly in Zone III, indicating the presence of magnetite in a small amount. The occurrence of magnetite could be explained also by greigite oxidation to magnetite following the sediment core extraction. Yet, this does not explain why the Verwey transition is not observed in other zones. Alternatively, it can be a result of direct precipitation of a small fraction of the authigenic magnetite. Interestingly, Verwey transition is not observed in the underlying Zones IV and V, deeper in the methanic zones, suggesting that this magnetite might undergo dissolution at greater depths, fitting the major role of magnetite reduction observed in iron-coupled AOM (Bar-Or et al., 2017). Dissolution can explain the decrease in the magnetic parameters in Zone IV.

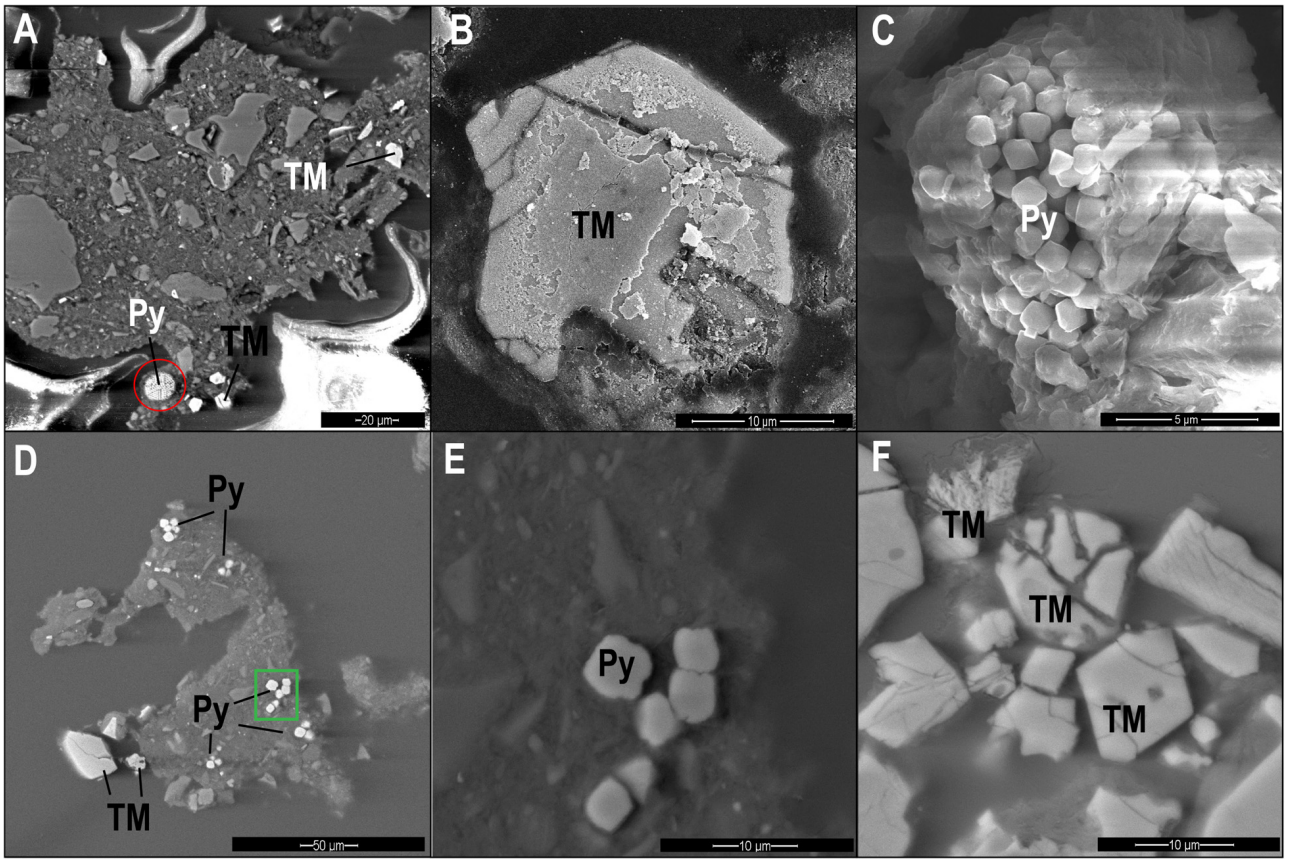

FIGURE 7 | SEM images of pyrite (Py) and titanomagnetite (TM) particles from different diagenetic zones. **(A)** Backscattered electron (BSE) image of pyrite framboid (red circle) and titanomagnetite from Zone I (84 cm depth). **(B)** Secondary electron (SE) image of titanomagnetite with dissolution marks from Zone II (160 cm). **(C)** SE image of a pyrite framboid from Zone II (160 cm). **(D,E)** BSE image of pyrite and titanomagnetite particles from Zone III (280 cm). **(E)** is an enlarged picture of the pyrite region marked with green frame. **(F)** BSE image of partly dissolved titanomagnetite from Zone III (280 cm).

Diagenetic Processes in the Methanic Zone and Their Impact on Magnetic Signals

Microbial iron reduction within the methanic zone has been observed in this area by incubation experiments that included also dead controls (Vigderovich et al., 2019), as well as in other marine provinces (Jørgensen et al., 2004; März et al., 2008; Slomp et al., 2013; Riedinger et al., 2014; Treude et al., 2014; Egger et al., 2015). This means reactivation of iron oxides with low solubility and more crystalline structure, that have "survived" the sulfidic zone at the previously assumed inactive zone, probably in relation to the methane cycling. It is still neither clear why iron oxides are 'reactivated' by the microbes and reduced in these deep methanogenic sediments nor what the link is to methane. However, theoretically, it can be due to the following: (a) Inhibition of methanogenesis by succession competition of iron-reducing bacteria over methanogens at the deeper part due to changes in environmental conditions of processes with close $\Delta G°$ (Jorgensen, 2000; Thamdrup, 2000; Roden et al., 2007). Iron reduction, in this case uses acetate, hydrogen or sulfide, either at low dissolved levels (Vigderovich et al., 2019) or as pyrite or FeS (Bottrell et al., 2000); (b) Direct iron utilization by archaeal methanogens that are abundant in this depth and can reactivate and reduce these low solubility minerals due to their specific advantages in electron transferring (Bond and Lovley, 2002; Van Bodegom et al., 2004; Zhang et al., 2012; Yamada et al., 2014; Sivan et al., 2016); (c) The use of methane, which is present in this zone, as an electron donor for iron reduction. This iron-coupled AOM process was suggested in other marine methanic sediments (Sivan et al., 2007; Riedinger et al., 2014; Treude et al., 2014; Egger et al., 2015, 2016).

The high abundance of iron-oxide minerals that have survived the sulfidic zone for reactivation at the methanic zone can be due to rapid sedimentation rate (Riedinger et al., 2005, 2014; Egger et al., 2017), non-steady state condition in eutrophication conditions (Egger et al., 2015), or intensive methanic zone that shallows the SMTZ zone (Sivan et al., 2007). In our study site, the combination of high sedimentation rates, and high methane fluxes (Vigderovich et al., 2019; Wurgaft et al., 2019) can explain the high concentration of iron-oxide minerals in the deep methanic zone.

The reactivation of iron minerals in the methanic zone means that the traditional view that this zone is magnetically inactive is

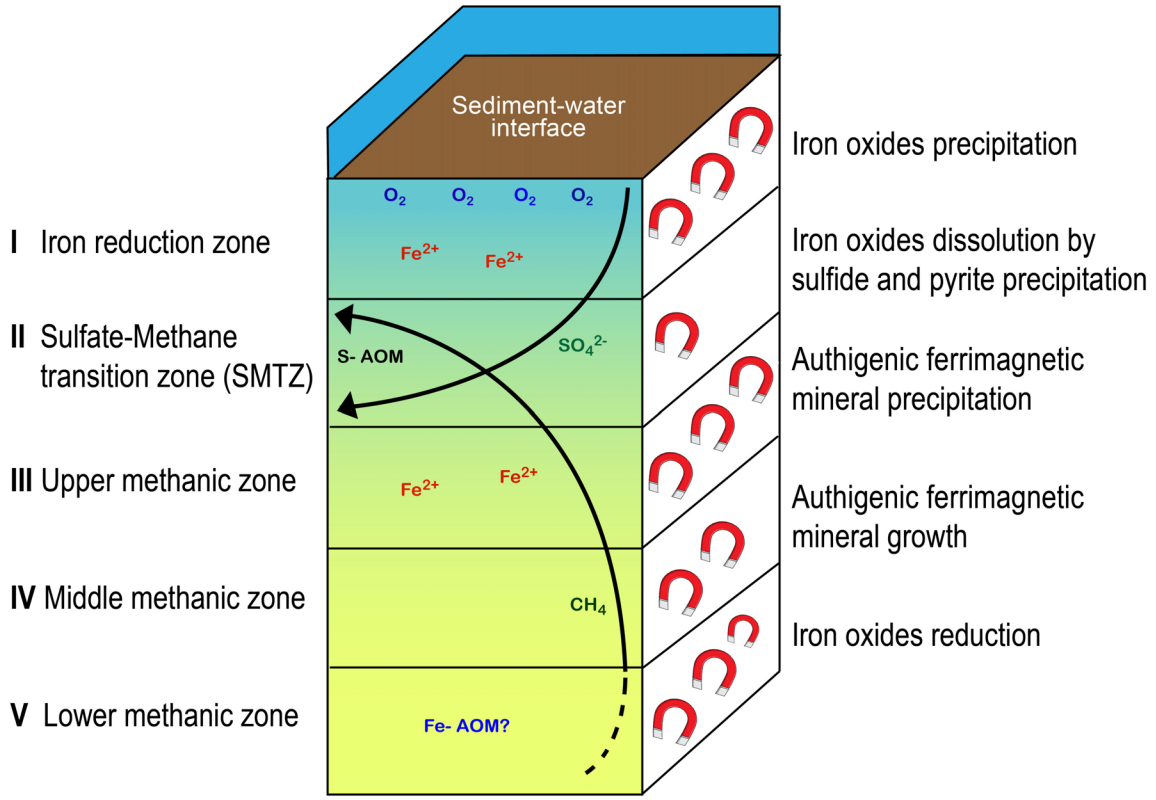

FIGURE 8 | Schematic illustration with a general scheme of the five diagenetic zones, the microbial processes and the resulting magnetic changes in the sedimentary column.

challenged. In this zone only paramagnetic minerals as siderite ($FeCO_3$) and vivianite [$Fe(II)_3(PO_4)\cdot 8H_2O$] were assumed to precipitate under elevated concentrations of dissolved ferrous-iron, if pore waters are saturated with respect to carbonate or phosphate, respectively (Berner, 1980; Slomp et al., 2013; Liu et al., 2018). However, several studies have suggested magnetic modification and mineral precipitation just below the SMTZ, mainly monosulfides, pyrrhotite, greigite and pyrite (Dekkers, 1989; Peters and Dekkers, 2003; Riedinger et al., 2005, 2014; Horng and Chen, 2006; Larrasoaña et al., 2007; Kars and Kodama, 2015; Shi et al., 2017; Horng, 2018; Roberts et al., 2018; Badesab et al., 2019). Here, we show clearly enhancement of the magnetic properties of the upper methanic zone due to precipitation of ferrimagnetic minerals. Sivan et al. (2016) and Shang et al. (2020) studies emphasize the ability of methanogens to reduce iron in anaerobic conditions close to the natural ones in the sediments and to precipitate magnetite as a by-product. These studies may give us a clue about the mechanism for iron reduction in our sediments and the significant precipitation of authigenic ferrimagnetic minerals as magnetite several meters below the surface of the sediments. This precipitation in this zone can cause smoothed remanence acquisition, partial remagnetization or even complete remagnetization (Roberts and Weaver, 2005; Larrasoaña et al., 2007; Rowan et al., 2009; Roberts et al., 2018).

SUMMARY AND CONCLUSION

Our data indicate that early diagenesis can have notable implications on the magnetic parameters of methanic marine sediments. **Figure 8** summarizes the coupling between porewater chemistry and magnetic parameters. Magnetic enhancement is observed first in the classic ferruginous zone. At the SMTZ, the reductive dissolution of magnetic iron minerals, followed by pyrite precipitation, cause a decrease of the magnetic imprint. In the upper methanic zone there is reactivation and reduction dissolution of iron minerals accompanied with intensive precipitation of authigenic ferrimagnetic minerals, enhancing the magnetic parameters of the sediment. In previous studies, pure culture anaerobic experiments close to the natural conditions of methanic sediments showed extracellular precipitation of magnetite, providing a possible explanation for the reactivation of iron minerals in the methanic zone and its potential precipitation there (Shang et al., 2020). This is by a direct switch of methanogens from methanogenesis to iron reduction due to their specific advantages in electron transferring [e.g., through their conductive methanophenazine (Sivan et al., 2016)] and precipitation of magnetite as a by-product. The diagenetic processes described here can potentially contribute

to partial re-magnetization of the sediment and might impact the interpretation of paleomagnetic data. In addition, our data support the understanding that high resolution profiles of rock magnetic parameters, such as IRM, ARM, and susceptibility, can be used to approximate the depth of the SMTZ and the methanic zone in methane-bearing sediments and provide important insights into the degree of magnetic alteration triggered by early diagenesis.

DATA AVAILABILITY STATEMENT

NRM measurements and demagnetization data are available in the MagIC database (earthref.org/MagIC/16844). Geochemical and magnetic depth profile data can be accessed at the PANGAEA repository (https://www.pangaea.de/) (Amiel et al., 2020).

AUTHOR CONTRIBUTIONS

NA wrote the manuscript and analyzed the data. RS and OS planned the research, assisted with data analysis, contributed to discussions, and provided feedback on the manuscript. All authors contributed to the article and approved the submitted version.

FUNDING

The project leading to this application has received funding from the European Union's Horizon 2020 Research and Innovation Program under Grant Agreement Nos. 818450 to OS and 804490 to RS. This project was also supported by the Mediterranean Sea Research Center of Israel to NA and ISF-NSFC grant (2561/16) to OS.

ACKNOWLEDGMENTS

We thank the crew of the RV Bat-Galim and Prof. B. Herut, the head of the Israel Oceanographic and Limnological Research Institute, for their assistance during field sampling and core handling. We also thank Prof. I. Felner from The Hebrew University of Jerusalem, Israel, for his assistance in conducting the low-temperature magnetic measurements, Dr. Valeria Boyko for her help in laboratory work, and Yael Ebert for her assistance with the paleomagnetic measurements.

SUPPLEMENTARY MATERIAL

The Supplementary Material for this article can be found online at: https://www.frontiersin.org/articles/10.3389/feart.2020.00283/full#supplementary-material

REFERENCES

Amiel, N., Shaar, R., and Sivan, O. (2020). Porewater chemistry and magnetic parameters of a sediment core from SG1 station in the South-Eastern Mediterranean Sea. *PANGAEA* doi: 10.1594/PANGAEA.919428

Badesab, F., Gaikwad, V., and Dewangan, P. (2019). Controls on Greigite preservation in a gas hydrate system of the Krishna-Godavari basin, Bay of Bengal. *Geo Mar. Lett.* 124, 4428–4451. doi: 10.1007/s00367-019-00604-z

Bareket, M. M., Bookman, R., Katsman, R., de Stigter, H., and Herut, B. (2016). The role of transport processes of particulate mercury in modifying marine anthropogenic secondary sources, the case of Haifa bay, Israel. *Mar. Pollut. Bull.* 105, 286–291. doi: 10.1016/j.marpolbul.2016.02.014

Bar-Or, I., Elvert, M., Eckert, W., Kushmaro, A., Vigderovich, H., Zhu, Q., et al. (2017). Iron-Coupled anaerobic oxidation of methane performed by a mixed bacterial-archaeal community based on poorly reactive minerals. *Environ. Sci. Technol.* 51, 12293–12301. doi: 10.1021/acs.est.7b03126

Berner, R. (1980). *Early Diagenesis: A Theoretical Approach (No. 1)*. Princeton, NJ: Princeton University Press.

Berner, R. A. (1984). Sedimentary pyrite formation. *Am. J. Sci.* 268, 1–23. doi: 10.2475/ajs.268.1.1

Blanchet, C. L., Tjallingii, R., Frank, M., Lorenzen, J., Reitz, A., Brown, K., et al. (2013). High- and low-latitude forcing of the Nile River regime during the Holocene inferred from laminated sediments of the Nile deep-sea fan. *Earth Planet. Sci. Lett.* 364, 98–110. doi: 10.1016/j.epsl.2013.01.009

Bond, D. R., and Lovley, D. R. (2002). Reduction of Fe(III) oxide by methanogens in the presence and absence of extracellular quinones. *Environ. Microbiol.* 4, 115–124. doi: 10.1046/j.1462-2920.2002.00279.x

Bottrell, S. H., Parkes, R. J., Cragg, B. A., and Raiswell, R. (2000). Isotopic evidence for anoxic pyrite oxidation and stimulation of bacterial sulphate reduction in marine sediments. *J. Geol. Soc.* 157, 711–714. doi: 10.1144/jgs.157.4.711

Canfield, D. E., and Berner, R. A. (1987). Dissolution and pyritization of magnetite in anoxic marine sediments. *Geochim. Cosmochim. Acta* 51, 645–659. doi: 10.1016/0016-7037(87)90076-7

Canfield, D. E., and Thamdrup, B. (2009). Towards a consistent classification scheme for geochemical environments, or, why we wish the term "suboxic" would go away: editorial. *Geobiology* 7, 385–392. doi: 10.1111/j.1472-4669.2009.00214.x

Chang, L., Roberts, A. P., Tang, Y., Rainford, B. D., Muxworthy, A. R., and Chen, Q. (2008). Fundamental magnetic parameters from pure synthetic greigite (Fe3S4). *J. Geophys. Res.* 113:B06104. doi: 10.1029/2007JB005502

Chang, S. B. R., Kirschvink, J. L., and Stolz, J. F. (1987). Biogenic magnetite as a primary remanence carrier in limestone deposits. *Phys. Earth Planet. Inter.* 46, 289–303. doi: 10.1016/0031-9201(87)90191-9

Channell, J. E. T., Freeman, R., Heller, F., and Lowrie, W. (1982). Timing of diagenetic haematite growth in red pelagic limestones from Gubbio (Italy). *Earth Planet. Sci. Lett.* 58, 189–201. doi: 10.1016/0012-821X(82)90193-5

Cline, J. D. (1969). Spectrophotometric determination of hydrogen sulfide in natural waters. *Limnol. Oceanogr.* 14, 454–458. doi: 10.4319/lo.1969.14.3.0454

Cornell, R. M., and Schwertmann, U. (2003). *The Iron Oxides*, 2nd Edn. Weinheim: John Wiley & Sons. doi: 10.1002/9783527613229.ch01

Cruz, A. P. S., Barbosa, C. F., Ayres-Neto, A., Munayco, P., Scorzelli, R. B., Amorim, N. S., et al. (2018). Geochemistry and magnetic sediment distribution at the western boundary upwelling system of southwest Atlantic. *Cont. Shelf Res.* 153, 64–74. doi: 10.1016/j.csr.2017.12.011

Dekkers, M. J. (1989). Magnetic properties of natural pyrrhotite. II. High- and low-temperature behaviour of Jrs and TRM as function of grain size. *Phys. Earth Planet. Inter.* 57, 266–283. doi: 10.1016/0031-9201(89)90116-7

Ebert, Y., Shaar, R., Emmanuel, S., Nowaczyk, N., and Stein, M. (2018). Overwriting of sedimentary magnetism by bacterially mediated mineral alteration. *Geology* 46, 2–5. doi: 10.1130/G39706.1

Egger, M., Hagens, M., Sapart, C. J., Dijkstra, N., van Helmond, N. A. G. M., Mogollón, J. M., et al. (2017). Iron oxide reduction in methane-rich deep Baltic Sea sediments. *Geochim. Cosmochim. Acta* 207, 256–276. doi: 10.1016/j.gca.2017.03.019

Egger, M., Kraal, P., Jilbert, T., Sulu-Gambari, F., Sapart, C. J., Röckmann, T., et al. (2016). Anaerobic oxidation of methane alters sediment records of sulfur, iron

and phosphorus in the Black Sea. *Biogeosciences* 13, 5333–5355. doi: 10.5194/bg-13-5333-2016

Egger, M., Rasigraf, O., Sapart, C. J., Jilbert, T., Jetten, M. S. M., Röckmann, T., et al. (2015). Iron-mediated anaerobic oxidation of methane in brackish coastal sediments. *Environ. Sci. Technol.* 49, 277–283. doi: 10.1021/es503663z

Froelich, P. N., Klinkhammer, G. P., Bender, M. L., Luedtke, N. A., Heath, G. R., Cullen, D., et al. (1979). Early oxidation of organic matter in pelagic sediments of the eastern equatorial Atlantic: suboxic diagenesis. *Geochim. Cosmochim. Acta* 43, 1075–1090. doi: 10.1016/0016-7037(79)90095-4

Fu, Y., von Dobeneck, T., Franke, C., Heslop, D., and Kasten, S. (2008). Rock magnetic identification and geochemical process models of greigite formation in Quaternary marine sediments from the Gulf of Mexico (IODP Hole U1319A). *Earth Planet. Sci. Lett.* 275, 233–245. doi: 10.1016/j.epsl.2008.07.034

Garming, J. F. L., Bleil, U., and Riedinger, N. (2005). Alteration of magnetic mineralogy at the sulfate-methane transition: analysis of sediments from the Argentine continental slope. *Phys. Earth Planet. Inter.* 151, 290–308. doi: 10.1016/j.pepi.2005.04.001

Horng, C. S. (2018). Unusual magnetic properties of sedimentary pyrrhotite in methane seepage sediments: comparison with metamorphic pyrrhotite and sedimentary greigite. *J. Geophys. Res.* 123, 4601–4617. doi: 10.1002/2017JB015262

Horng, C. S., and Chen, K. H. (2006). Complicated magnetic mineral assemblages in marine sediments offshore of southwestern Taiwan: possible influence of methane flux on the early diagenetic process. *Terr. Atmos. Ocean. Sci.* 17, 1009–1026. doi: 10.3319/TAO.2006.17.4.1009(GH)

Jorgensen, B. B. (2000). "Bacteria and marine biogeochemistry," in *Marine Geochemistry*, eds H. D. Schulz, and M. Zabel (Berlin: Springer-Verlag), 169–206. doi: 10.1007/3-540-32144-6_5

Jørgensen, B. B., Böttcher, M. E., Lüschen, H., Neretin, L. N., and Volkov, I. I. (2004). Anaerobic methane oxidation and a deep H2S sink generate isotopically heavy sulfides in Black Sea sediments. *Geochim. Cosmochim. Acta* 68, 2095–2118. doi: 10.1016/j.gca.2003.07.017

Karlin, R., Lyle, M., and Heath, G. R. (1987). Authigenic magnetite formation in suboxic marine sediments. *Nature* 326, 490–493. doi: 10.1038/326490a0

Kars, M., and Kodama, K. (2015). Authigenesis of magnetic minerals in gas hydrate-bearing sediments in the Nankai Trough, offshore Japan. *Geochem. Geophys. Geosyst.* 16, 947–961. doi: 10.1002/2014GC005614.Received

Kasten, S., Freudenthal, T., Gingele, F. X., and Schulz, H. D. (1998). Simultaneous formation of iron-rich layers at different redox boundaries in sediments of the Amazon deep-sea fan. *Geochim. Cosmochim. Acta* 62, 2253–2264. doi: 10.1016/S0016-7037(98)00093-3

Kawamura, N., Ishikawa, N., and Torii, M. (2012). Diagenetic alteration of magnetic minerals in Labrador sea sediments (IODP sites U1305, U1306, and U1307). *Geochem. Geophys. Geosyst.* 13:Q08013. doi: 10.1029/2012GC004213

Kawamura, N., Oda, H., Ikehara, K., Yamazaki, T., Shioi, K., and Taga, S. (2007). Diagenetic effect on magnetic properties of marine core sediments from the southern Okhotsk Sea. *Earth Planets Space* 59, 83–93. doi: 10.1186/bf03352680

Kirschvink, J. L. (1980). The least-squares line and plane and the analysis of palaeomagnetic data. *Geophys. J. Int.* 62, 699–718. doi: 10.1111/j.1365-246x.1980.tb02601.x

Lambeck, K., and Purcell, A. (2005). Sea-level change in the Mediterranean Sea since the LGM: model predictions for tectonically stable areas. *Quat. Sci. Rev.* 24, 1969–1988. doi: 10.1016/j.quascirev.2004.06.025

Larrasoaña, J. C., Roberts, A. P., Musgrave, R. J., Gràcia, E., Piñero, E., Vega, M., et al. (2007). Diagenetic formation of greigite and pyrrhotite in gas hydrate marine sedimentary systems. *Earth Planet. Sci. Lett.* 261, 350–366. doi: 10.1016/j.epsl.2007.06.032

Larrasoaña, J. C., Roberts, A. P., Stoner, J. S., Richter, C., and Wehausen, R. (2003). A new proxy for bottom-water ventilation in the eastern Mediterranean based on diagenetically controlled magnetic properties of sapropel-bearing sediments. *Palaeogeogr. Palaeoclimatol. Palaeoecol.* 190, 221–242. doi: 10.1016/S0031-0182(02)00607-7

Liu, J. (2004). High-resolution analysis of early diagenetic effects on magnetic minerals in post-middle-Holocene continental shelf sediments from the Korea Strait. *J. Geophys. Res.* 109:B03103. doi: 10.1029/2003JB002813

Liu, J., Izon, G., Wang, J., Antler, G., Wang, Z., Zhao, J., et al. (2018). Vivianite formation in methane-rich deep-sea sediments from the South China Sea. *Biogeosciences* 15, 6329–6348. doi: 10.5194/bg-15-6329-2018

Liu, Q., Roberts, A. P., Larrasoaa, J. C., Banerjee, S. K., Guyodo, Y., Tauxe, L., et al. (2012). Environmental magnetism: principles and applications. *Rev. Geophys.* 50:RG4002. doi: 10.1029/2012RG000393

Lovley, D. R. (1991). Dissimilatory Fe (III) and Mn (IV) reduction. *Microbiol. Mol. Biol. Rev.* 55, 259–287. doi: 10.1016/S0065-2911(04)49005-5

Lovley, D. R., Chapelle, F. H., and Phillips, E. J. P. (1990). Fe(III)-reducing bacteria in deeply buried sediments of the Atlantic Coastal Plain. *Geology* 18, 954–957.

Lovley, D. R., Stolz, J. F., Nord, G. L., and Phillips, E. J. P. (1987). Anaerobic production of magnetite by a dissimilatory iron-reducing microorganism. *Nature* 330, 252–254. doi: 10.1038/330252a0

Maloof, A. C., Kopp, R. E., Grotzinger, J. P., Fike, D. A., Bosak, T., Vali, H., et al. (2007). Sedimentary iron cycling and the origin and preservation of magnetization in platform carbonate muds, Andros Island, Bahamas. *Earth Planet. Sci. Lett.* 259, 581–598. doi: 10.1016/j.epsl.2007.05.021

März, C., Hoffmann, J., Bleil, U., de Lange, G. J., and Kasten, S. (2008). Diagenetic changes of magnetic and geochemical signals by anaerobic methane oxidation in sediments of the Zambezi deep-sea fan (SW Indian Ocean). *Mar. Geol.* 255, 118–130. doi: 10.1016/j.margeo.2008.05.013

Moskowitz, B. M., Frankel, R. B., and Bazylinski, D. A. (1993). Rock magnetic criteria for the detection of biogenic magnetite. *Earth Planet. Sci. Lett.* 120, 283–300. doi: 10.1016/0012-821X(93)90245-5

Moskowitz, B. M., Frankel, R. B., Bazylinski, D. A., Jannasch, H. W., and Lovley, D. R. (1989). A comparison of magnetite particles produced anaerobically by magnetotactic and dissimilatory iron-reducing bacteria. *Geophys. Res. Lett.* 16, 665–668. doi: 10.1029/GL016i007p00665

Nir, Y. (1984). *Recent Sediments of the Israel Mediterranean Continental Shelf and Slope*. Gothenburg: Goteborg University.

Nowaczyk, N. R. (2011). Dissolution of titanomagnetite and sulphidization in sediments from Lake Kinneret. Israel. *Geophys. J. Int.* 187, 34–44. doi: 10.1111/j.1365-246X.2011.05120.x

Pavón-carrasco, F. J., Luisa, M., Miquel, J., and De Santis, A. (2014). A geomagnetic field model for the Holocene based on archaeomagnetic and lava flow data. *Earth Planet. Sci. Lett.* 388, 98–109. doi: 10.1016/j.epsl.2013.11.046

Peters, C., and Dekkers, M. J. (2003). Selected room temperature magnetic parameters as a function of mineralogy, concentration and grain size. *Phys. Chem. Earth* 28, 659–667. doi: 10.1016/S1474-7065(03)00120-7

Poulton, S. W., and Canfield, D. E. (2005). Development of a sequential extraction procedure for iron: implications for iron partitioning in continentally derived particulates. *Chem. Geol.* 214, 209–221. doi: 10.1016/j.chemgeo.2004.09.003

Rao, V. P., Kessarkar, P. M., Patil, S. K., and Ahmad, S. M. (2008). Rock magnetic and geochemical record in a sediment core from the eastern Arabian Sea: diagenetic and environmental implications during the late Quaternary. *Palaeogeogr. Palaeoclimatol. Palaeoecol.* 270, 46–52. doi: 10.1016/j.palaeo.2008.08.011

Rickard, D., and Luther, W. G. (2007). Chemistry of iron sulfides. *Chem. Rev.* 107, 514–562. doi: 10.1021/cr0503658

Riedinger, N., Formolo, M. J., Lyons, T. W., Henkel, S., Beck, A., and Kasten, S. (2014). An inorganic geochemical argument for coupled anaerobic oxidation of methane and iron reduction in marine sediments. *Geobiology* 12, 172–181. doi: 10.1111/gbi.12077

Riedinger, N., Pfeifer, K., Kasten, S., Garming, J. F. L., Vogt, C., and Hensen, C. (2005). Diagenetic alteration of magnetic signals by anaerobic oxidation of methane related to a change in sedimentation rate. *Geochim. Cosmochim. Acta* 69, 4117–4126. doi: 10.1016/j.gca.2005.02.004

Roberts, A. P. (1995). Magnetic properties of sedimentary gregite (Fe3S4). *Earth Planet. Sci. Lett.* 134, 227–236. doi: 10.1016/0012-821X(95)00131-U

Roberts, A. P. (2015). Magnetic mineral diagenesis. *Earth Sci. Rev.* 151, 1–47. doi: 10.1016/j.earscirev.2015.09.010

Roberts, A. P., Chang, L., Rowan, C, J., Horng, C., and Florindo, F. (2011). Magnetic properties of sedimentary greigite (Fe3S4): an update. *Rev. Geophys.* 49:RG1002. doi: 10.1029/2010RG000336.1.INTRODUCTION

Roberts, A. P., and Weaver, R. (2005). Multiple mechanisms of remagnetization involving sedimentary greigite (Fe3S4). *Earth Planet. Sci. Lett.* 231, 263–277. doi: 10.1016/j.epsl.2004.11.024

Roberts, A. P., Zhao, X., Harrison, R. J., Heslop, D., Muxworthy, A. R., Rowan, C. J., et al. (2018). Signatures of reductive magnetic mineral diagenesis from

unmixing of first-order reversal curves. *J. Geophys. Res.* 123, 4500–4522. doi: 10.1029/2018JB015706

Roden, E. E., Wetzel, R. G., and Dec, N. (2007). Organic carbon oxidation and suppression of methane production by microbial Fe (III) oxide reduction in vegetated and unvegetated freshwater wetland sediments. *Limnology* 41, 1733–1748. doi: 10.4319/lo.1996.41.8.1733

Rossignol-Strick, M., Nesteroff, W., Olive, P., and Vergnaud-Grazzini, C. (1982). After the deluge: mediterranean stagnation and sapropel formation. *Nature* 295, 105–110. doi: 10.1038/295105a0

Rowan, C. J., and Roberts, A. P. (2006). Magnetite dissolution, diachronous greigite formation, and secondary magnetizations from pyrite oxidation: unravelling complex magnetizations in Neogene marine sediments from New Zealand. *Earth Planet. Sci. Lett.* 241, 119–137. doi: 10.1016/j.epsl.2005.10.017

Rowan, C. J., Roberts, A. P., and Broadbent, T. (2009). Reductive diagenesis, magnetite dissolution, greigite growth and paleomagnetic smoothing in marine sediments: a new view. *Earth Planet. Sci. Lett.* 277, 223–235. doi: 10.1016/j.epsl.2008.10.016

Sagnotti, L., and Winkler, A. (1999). Rock magnetism and palaeomagnetism of greigite-bearing mudstones in the Italian peninsula. *Earth Planet. Sci. Lett.* 165, 67–80. doi: 10.1016/s0012-821x(98)00248-9

Schattner, U., Lazar, M., Harari, D., and Waldmann, N. (2012). Active gas migration systems offshore northern Israel, first evidence from seafloor and subsurface data. *Cont. Shelf Res.* 48, 167–172. doi: 10.1016/j.csr.2012.08.003

Schattner, U., Lazar, M., Tibor, G., Ben-Avraham, Z., and Makovsky, Y. (2010). Filling up the shelf - a sedimentary response to the last post-glacial sea rise. *Mar. Geol.* 278, 165–176. doi: 10.1016/j.margeo.2010.10.006

Sela-Adler, M., Herut, B., Bar-Or, I., Antler, G., Eliani-Russak, E., Levy, E., et al. (2015). Geochemical evidence for biogenic methane production and consumption in the shallow sediments of the SE Mediterranean shelf (Israel). *Cont. Shelf Res.* 101, 117–124. doi: 10.1016/j.csr.2015.04.001

Shang, H., Daye, M., Sivan, O., Borlina, C. S., Tamura, N., Weiss, B. P., et al. (2020). Formation of zero-valent iron in iron-reducing cultures of *Methanosarcina barkeri*. *Environ. Sci. Technol.* 54, 7354–7365. doi: 10.1021/acs.est.0c01595

Shi, L., Squier, T. C., Zachara, J. M., and Fredrickson, J. K. (2007). Respiration of metal (hydr)oxides by Shewanella and Geobacter: a key role for multihaem c-type cytochromes. *Mol. Microbiol.* 65, 12–20. doi: 10.1111/j.1365-2958.2007.05783.x

Shi, M., Wu, H., Roberts, A. P., Zhang, S., Zhao, X., Li, H., et al. (2017). Tectonic, climatic, and diagenetic control of magnetic properties of sediments from Kumano Basin, Nankai margin, southwestern Japan. *Mar. Geol.* 391, 1–12. doi: 10.1016/j.margeo.2017.07.006

Sivan, O., Adler, M., Pearson, A., Gelman, F., Bar-Or, I., John, S., et al. (2011). Geochemical evidence for iron-mediated anaerobic oxidation of methane. *Limnol. Oceanogr.* 56, 1536–1544. doi: 10.4319/lo.2011.56.4.1536

Sivan, O., Schrag, D. P., and Murray, R. W. (2007). Rates of methanogenesis and methanotrophy in deep-sea sediments. *Geobiology* 5, 141–151. doi: 10.1111/j.1472-4669.2007.00098.x

Sivan, O., Shusta, S. S., and Valentine, D. L. (2016). Methanogens rapidly transition from methane production to iron reduction. *Geobiology* 14, 190–203. doi: 10.1111/gbi.12172

Slomp, C. P., Mort, H. P., Jilbert, T., Reed, D. C., Gustafsson, B. G., and Wolthers, M. (2013). Coupled dynamics of iron and phosphorus in sediments of an oligotrophic coastal basin and the impact of anaerobic oxidation of methane. *PLoS One* 8:e62386. doi: 10.1371/journal.pone.0062386

Smirnov, A. V., and Tarduno, J. A. (2000). Low-temperature magnetic properties of pelagic sediments (Ocean Drilling Program Site 805C): tracers of maghemitization and magnetic mineral reduction. *J. Geophys. Res.* 105, 16457–16471. doi: 10.1029/2000jb900140

Snowball, I. F. (1997). Gyroremanent magnetization and the magnetic properties of greigite-bearing clays in southern Sweden. *Geophys. J. Int.* 129, 624–636. doi: 10.1111/j.1365-246x.1997.tb04498.x

Stookey, L. L. (1970). Ferrozine-A new spectrophotometric reagent for iron. *Anal. Chem.* 42, 779–781. doi: 10.1021/ac60289a016

Tauxe, L., Shaar, R., Jonestrask, L., Minnett, R., Koppers, A. A. P., Constable, C. G., et al. (2016). PmagPy: software package for paleomagnetic data analysis and a bridge to the Magnetics Information Consortium (MagIC) Database. *Geochem. Geophys. Geosyst.* 17, 2450–2463. doi: 10.1002/2016GC006307.Received

Tauxe, L., and Staudigel, H. (2004). Strength of the geomagnetic field in the Cretaceous Normal Superchron: new data from submarine basaltic glass of the Troodos Ophiolite. *Geochem. Geophys. Geosyst.* 5:Q02H06. doi: 10.1029/2003GC000635

Thamdrup, B. (2000). Bacterial manganese and iron reduction in aquatic sediments. *Adv. Microb. Ecol.* 16, 41–84. doi: 10.1007/978-1-4615-4187-5_2

Torii, M. (2011). Low-temperature oxidation and subsequent downcore dissolution of magnetite in deep-sea sediments, ODP Leg 161 (Western Mediterranean). *J. Geomagn. Geoelect.* 49, 1233–1245. doi: 10.5636/jgg.49.1233

Treude, T., Krause, S., Maltby, J., Dale, A. W., Coffin, R., and Hamdan, L. J. (2014). Sulfate reduction and methane oxidation activity below the sulfate-methane transition zone in Alaskan Beaufort Sea continental margin sediments: implications for deep sulfur cycling. *Geochim. Cosmochim. Acta* 144, 217–237. doi: 10.1016/j.gca.2014.08.018

Valentine, D. L. (2002). Biogeochemistry and microbial ecology of methane oxidation in anoxic environments: a review. *Antonie Van Leeuwenhoek* 81, 271–282. doi: 10.1023/A:1020587206351

Van Bodegom, P. M., Scholten, J. C. M., and Stams, A. J. M. (2004). Direct inhibition of methanogenesis by ferric iron. *FEMS Microbiol. Ecol.* 49, 261–268. doi: 10.1016/j.femsec.2004.03.017

Verwey, E. J. W. (1939). Electronic conduction of magnetite (Fe_3O_4) and its transition point at low temperatures. *Nature* 144, 327–328. doi: 10.1038/144327b0

Vigderovich, H., Liang, L., Herut, B., Wang, F., Wurgaft, E., Rubin-Blum, M., et al. (2019). Evidence for microbial iron reduction in the methanogenic sediments of the oligotrophic SE Mediterranean continental shelf. *Biogeosciences* 16, 3165–3181. doi: 10.5194/bg-2019-21

Wurgaft, E., Findlay, A. J., Vigderovich, H., Herut, B., and Sivan, O. (2019). Sulfate reduction rates in the sediments of the Mediterranean continental shelf inferred from combined dissolved inorganic carbon and total alkalinity profiles. *Mar. Chem.* 211, 64–74. doi: 10.1016/j.marchem.2019.03.004

Yamada, C., Kato, S., Kimura, S., Ishii, M., and Igarashi, Y. (2014). Reduction of Fe(III) oxides by phylogenetically and physiologically diverse thermophilic methanogens. *FEMS Microbiol. Ecol.* 89, 637–645. doi: 10.1111/1574-6941.12365

Zhang, J., Dong, H., Liu, D., Fischer, T. B., Wang, S., and Huang, L. (2012). Microbial reduction of Fe(III) in illite-smectite minerals by methanogen *Methanosarcina mazei*. *Chem. Geol.* 292–293, 35–44. doi: 10.1016/j.chemgeo.2011.11.003

Conflict of Interest: The authors declare that the research was conducted in the absence of any commercial or financial relationships that could be construed as a potential conflict of interest.

frontiers in Earth Science

ORIGINAL RESEARCH
published: 23 November 2020
doi: 10.3389/feart.2020.592557

Magnetic Mineral Diagenesis in a Newly Discovered Active Cold Seep Site in the Bay of Bengal

F. Badesab, P. Dewangan and V. Gaikwad*

Geological Oceanography Division, CSIR- National Institute of Oceanography, Dona Paula, Goa, India

OPEN ACCESS

Edited by:
Sarah P. Slotznick,
Dartmouth College, United States

Reviewed by:
Satria Bijaksana,
Bandung Institute of Technology, Indonesia
Peter Aaron Selkin,
University of Washington Tacoma, United States
Liao Chang,
Peking University, China

****Correspondence:***
F. Badesab
firoz@nio.org

Specialty section:
This article was submitted to Geomagnetism and Paleomagnetism, a section of the journal Frontiers in Earth Science

Received: *07 August 2020*
Accepted: *26 October 2020*
Published: *23 November 2020*

Citation:
Badesab F, Dewangan P and Gaikwad V (2020) Magnetic Mineral Diagenesis in a Newly Discovered Active Cold Seep Site in the Bay of Bengal. Front. Earth Sci. 8:592557. doi: 10.3389/feart.2020.592557

Diagenetically formed magnetic minerals at marine methane seep sites are potential archive of past fluid flow and could provide important constraints on the evolution of past methane seepage dynamics and gas hydrate formation over geologic time. In this study, we carried out integrated rock magnetic, and mineralogical analyses, supported by electron microscope observations, on a seep impacted sediment core to unravel the linkage between greigite magnetism, methane seepage dynamics, and evolution of shallow gas hydrate system in the K-G basin. Three sediment magnetic zones (MZ-1, MZ-2, and MZ-3) have been identified based on the down-core variations in rock magnetic properties. Two events of intense methane seepage are identified. Repeated occurences of authigenic carbonates throughout the core indicate the episodic intensification of anaerobic oxidation of methane (AOM) at the studied site. Marked depletion in magnetic susceptibility manifested by the presence of chemosynthetic shells (*Calyptogena* Sp.), methane-derived authigenic carbonates, and abundant pyrite grains provide evidences on intense methane seepage events at this site. Fracture-controlled fluid transport supported the formation of gas hydrates (distributed and massive) at this site. Three greigite bearing sediment intervals (G1, G2, G3) within the magnetically depleted zone (MZ-2) are probably the paleo-gas hydrate (distributed-type vein filling) intervals. A strong linkage among clay content, formation of veined hydrate deposits, precipitation of authigenic carbonates and greigite preservation is evident. Hydrate crystallizes within faults/fractures formed as the methane gas migrates through the gas hydrate stability zone (GHSZ). Formation of authigenic carbonate layers coupled with clay deposits restricted the upward migrating methane, which led to the formation of distributed-type vein filling hydrate deposits. A closed system created by veined hydrates trapped the sulfide and limited its availability thereby, causing arrestation of pyritization and favored the formation and preservation of greigite in G1, G2, G3.

Keywords: cold, seep, methane hydrate, rock magnetism, diagenesis, Bay of Bengal

INTRODUCTION

Cold seep ecosystems are unique ecosystem characterized by ebullition of methane-rich fluids through the seafloor (Suess, 2014). At active seeps, sulfate reduction driven by anaerobic oxidation of methane (AOM) releases sufficient amount of hydrogen sulfide into the surrounding pore waters (Borowski et al., 1996; Jørgensen et al., 2004) to sustain chemosynthetic communities. The hydrogen sulfide also facilitate dissolution of primary detrital magnetic minerals and transform them into stable non-magnetic pyrite or intermediate ferrimagnetic greigite; thereby, generating secondary magnetic signals in the host sediments (Housen and Musgrave, 1996; Passier et al., 1998; Kasten et al., 2003; Neretin et al., 2004; Riedinger et al., 2005; Musgrave et al., 2006; Larrasoaña et al., 2007; Roberts et al., 2015). These magnetic minerals serve as an excellent geological archive to record past methane seepage, and help in understanding the geochemical processes that favor diagenesis of magnetic mineral and may also influence the gas hydrate dynamics (formation and dissociation) (Housen and Musgrave, 1996; Aharon et al., 1997; Musgrave et al., 2006; Larrasoaña et al., 2007; Bayon et al., 2013; Feng and Chen, 2015).

Active seeps are also associated with shallow gas hydrates deposits (Bohrmann et al., 1998; Greinert et al., 2001; Suess, 2014; Bayon et al., 2015). These deposits undergo several cycles of formation and dissociation to sustain themselves within the sediment column (Chuvilin et al., 2018). Destabilization of gas hydrates due to increase in pressure owing to sedimentation, burial and tectonic activities can release vast amount of methane; a fraction of which may rise up to seafloor and form cold seep (Haq, B.U, 1998; Henriet et al., 1998; Vogt and Jung, 2002; Sultan et al., 2004; Handwerger et al., 2017; Argentino et al., 2019). Diagenesis of magnetic minerals involves postdepositional changes either by altering the detrital magnetic mineral assemblages or through authigenic growth of secondary minerals (Roberts, 2015; Musgrave et al., 2019). Therefore, the sediment magnetic signals in marine sedimentary system represent the primary depositional and secondary diagenetic processes. In methane-rich sediments, hydrogen sulfide generated via AOM at the sulfate-methane transition zone (SMTZ) can cause dissolution of iron oxides and precipitation of iron sulfides including ferrimagnetic greigite, pyrrhotite and culminating toward formation of pyrite (Kasten et al., 1998; Jørgensen et al., 2004; Kao et al., 2004; Neretin et al., 2004). Greigite can survive the pyritization process in the regions containing limited sulfide concentration. For example in gas hydrate bearing sediments of Cascadia Margin and Nankai Trough, it was demonstrated that sulfide sometime gets trapped within hydrate itself causing further arrestation of pyritization processes and subsequent precipitation of greigite and pyrrhotite (Housen and Musgrave, 1996; Kars and Kodama, 2015). Therefore, ferrimagnetic iron sulfide minerals (greigite, pyrrhotite) formed during such processes are regarded as potential markers of fossil gas hydrate deposits, and identification of such magnetic minerals may also help in deciphering paleo-gas hydrate deposits in marine sediments (Larrasoaña et al., 2007).

The first evidence of active methane seepage and shallow methane hydrate from geological, geochemical and geophysical studies was reported by Mazumdar et al. (2019) in the Krishna-Godavari (K-G) basin. Gas hydrate exploration cruise (SSD-045) of CSIR-National Institute of Oceanography (CSIR-NIO) onboard R/V Sindhu Sadhana discovered this active seep and associated shallow gas hydrates in 2018 (**Figure 1A**). Fracture-filled gas hydrates were recovered from sediment depth interval of 305–315 cmbsf at this site (Stn-9), (**Figure 1B**). The seep occurs due to deformation structures (fault/fractures and diapirs) formed due to shale tectonism in K-G basin (Dewangan et al., 2010; Sriram et al., 2020). A high-resolution seismic data beneath the seep sites showed the presence of acoustic chimneys, and the overburden is heavily faulted (Dewangan et al., 2020). Deep-rooted faults provide a conducive environment for the migration of methane from deep-seated gas reservoir and led to the development of a cold seep ecosystem and formation of shallow fracture-filled gas hydrate deposits at the studied site (Dewangan et al., 2020; Mazumdar et al., 2019; Sriram et al., 2020). High methane flux and favourable P-T conditions supported the accumulation of gas hydrates (Mazumdar et al., 2019). A recent rock magnetic study by Badesab et al. (2019) on the long drilled sediment cores that overlie the deep-seated gas hydrate deposit provided the longest and most detailed sediment magnetic record in the K-G basin, Bay of Bengal. They successfully delineated the control of higher sedimentation events and shale tectonics on the development of fracture-filled gas hydrate deposit and magnetic mineral diagenesis in K-G basin. A magnetic based proxy to constrain paleo-methane seepage events in marine sediments was established. In the present study, we carried out integrated rock magnetic and mineralogical analyses along with electron microscope observations on the seep impacted sediment core (SSD-045/Stn-9/GC-01) to unravel the linkage between greigite magnetism, methane seepage dynamics, and evolution of shallow gas hydrate system in the K-G basin. This 3.16 m long sediment gravity core serves as a potential archive to constrain the methane seepage dynamics and to understand the processes governing the shallow gas hydrate formation/dissociation through recent geologic time.

GEOLOGICAL SETTING

The K-G basin is a pericratonic, petroliferous rift basin located in the eastern continental margin of India (Powell et al., 1988). The sediment thicknesses reported from K-G basin varies from 3 to 5 km in the onshore region to about 8 km in the offshore region (Prabhakar and Zutshi, 1993; Bastia, 2007). Majority of sediment load to the basin is delivered by the Krishna and Godavari rivers (Rao, 2001). Annual sediment transport of the Krishna and Godavari rivers is estimated to be around 67.7 and 170 × 106 t, respectively (Biksham and Subramanian, 1988; Ramesh and Subramanian, 1988). Sedimentary deposits in the K-G basin are dominated by smectite-bearing Godavari clay formations (Rao, 2001). Krishna and Godavari rivers and their tributaries originates in the Western Ghats and drains through the

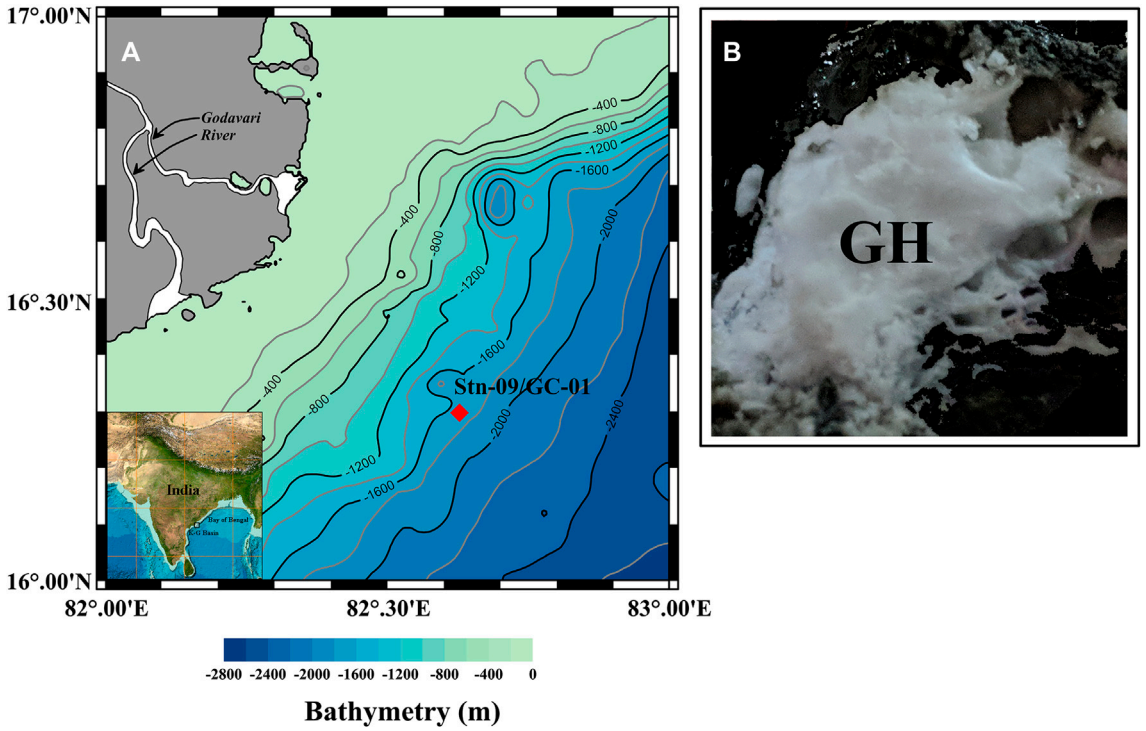

FIGURE 1 | (A) Map showing the location of sediment core (SSD-045/Stn-0/GC-01) in the Krishna-Godavari (K-G) basin, Bay of Bengal and **(B)** photograph of recovered gas hydrate (GH) sample. Bathymetry data of the studied area was obtained from GEBCO Compilation Group (2020) GEBCO 2020 Grid (doi: 10.5285/a29c5465-b138-234d-e053-6c86abc040b9).

provenance of Deccan trap basalts and Precambrian metamorphic rocks and created a thick sediment strata containing the dominant montmorillonite clay with traces of illite and kaolinite (Rao, 1991). Krishna and Godavari rivers are the major supplier of magnetite-rich detrital load to the K-G basin and hence provide an excellent opportunity to conduct studies related to environmental magnetism (Ramesh and Subramanian 1988; Sangode et al., 2007).

The K-G basin shows deformation structures in the form of shale bulges and toe-thrust faults due to ongoing gravity-driven shale tectonism (Choudhuri et al., 2010; Dewangan et al., 2010). One of the reasons for shale tectonism is rapid sedimentation during Paleocene and Eocene, which led to overpressured shale strata in the K-G basin (Rao and Mani, 1993; Singha and Chatterjee, 2014). The detrital load in the deltaic regions led to the movement of deeply buried shale strata and several geomorphic structures like bathymetric mounds, sedimentary ridges and toe-thrust faults formed on the sea floor. These deformed structures provide efficient migration pathway for methane-rich fluids through the deep-rooted faults, and hence these regions are preferred locales for the formation of gas hydrates deposits (Dewangan et al., 2010). The presence of sub-surface gas hydrate deposits in the K-G basin has been confirmed through well-logging, drilling and sediment coring activities, while paleo-methane seepage events are evident through the presence of methane derived authigenic carbonates and chemosynthetic community (Collett et al., 2008; Mazumdar et al., 2009, 2019).

MATERIALS AND METHODS

Coring Site, Sampling and Measurements

Gravity core (SSD-045/Stn-9/GC-01) was recovered onboard R/V Sindhu Sadhana (cruise no: SSD-045) from the K-G offshore basin (Latitude: 16°18.6027'N; Longitude: 82°37.9809'E; water depth: 1,673 m; core length: 3.16 m). The core was sub-sampled at the every 2 cm interval. Light gray to deep black colored soft sediments in this core yielded a strong odor of hydrogen sulfide after opening the sediment core onboard. The vertical sediment distribution in this core showed the dominance of clay and silt sized fractions. Numerous layers of light gray colored authigenic carbonates were found throughout the core. Dead shells of *Calyptogena* Sp. were found at 27 cmbsf and 51 cmbsf in the studied sediment core. Fracture-filled type gas hydrates were recovered from the core catcher and bottommost sediment interval at this site. Sediment sub-sampling for magnetic measurements were carried out in presence of high purity nitrogen flushing to avoid atmospheric conditions which could oxidize hydrogen sulfide or iron mono-sulfide present in the sediments. For rock magnetic analysis, 158 sub-wet sediment samples were weighed, and packed in a 25 mm cylindrical plastic sample bottles. Measurements were carried out

at the Paleomagnetic laboratory of CSIR-National Institute of Oceanography (NIO), Goa, India and Center for Advanced Marine Core Research (CMCR), Kochi University, Japan.

Rock Magnetic Analysis

Low-field low frequency (0.47 kHz) magnetic susceptibility (χ) was measured using a MS2B Bartington Instruments magnetic susceptibility meter. An anhysteretic remanent magnetization (ARM) was applied in a direct current bias field (50 μT) in the presence of 100 mT peak alternating field and the remanent magnetism was measured using an AGICO JR-6A automatic spinner magnetometer. An isothermal remanent magnetization (IRM) was applied in an inducing field of +1 T in the forward direction and was demagnetized by DC backfields at −20, −30, −100, and −300 mT using a MMPM10 pulse magnetizer. The respective remanences were measured using AGICO JR-6A automatic spinner magnetometer. Mass-normalized IRM acquired at a peak field of 1T is considered to be the saturation IRM (SIRM). *S*-ratio is calculated as the ratio between the IRM at −300 mT and SIRM ($IRM_{-300mT}/SIRM_{1T}$; Bloemendal et al., 1992). This ratio indicates the relative proportion of high coercivity minerals compared to soft ferrimagnetic minerals. Thermomagnetic measurements were carried out at Paleo and Rock Magnetism Laboratory of CMCR. About 12 selected dried sediment samples were analyzed on a Natsuhara Giken (Model NMB-89) magnetic balance (Range: Room temperature to 700°C) with a heating rate of 10°C/min in a 0.3-T field. Hysteresis loops, first-order reversal curves (FORC) and back-field demagnetization curves were also measured for 10 selected dried sediment samples with a saturating field of 1 T (averaging time of 200 ms, slew rate limit of 1 T/, and field increment of 4 mT) at the CMCR. FORC distributions were generally processed using a smoothing factor (SF) of 4, but SF = 6 was used where possible (Roberts et al., 2000). FORC diagrams (Pike et al., 1999) were processed using the FORCinel software (Harrison and Feinberg, 2008).

Low-temperature magnetic measurements were made on six selected dried sediment samples with a Quantum Design Magnetic Properties Measurement System at CMCR. A RT-SIRM was imparted at room temperature (300 K) in 2.5 T. Samples were later cooled to 5 K and warmed back to 300 K in a zero magnetic field. A LT-SIRM was then applied at 5 K in 2.5 T. Samples were warmed up to 300 K in a zero magnetic field (termed "ZFC" for zero field-cooled). Samples were then cooled to 5 K in the presence of a 2.5 T magnetic field. A LT-SIRM was again imparted at 5 K, and samples were warmed to 300 K in a zero magnetic field (termed "FC" for field-cooled). Magnetic parameters were normalized by sample mass. Derived parameters (δ_{FC} and δ_{ZFC}) were calculated following Moskowitz et al. (1993).

Sedimentological Analyses

Bulk Sediment Grain Size Measurements

Sediment grain size measurements were performed on a Laser Particle Size Analyzer (Malvern Mastersizer 2000) at CSIR-NIO. For removal of carbonate content, desalinated sediment samples were treated using dilute HCl (1N). Further, same suspensions were treated with 10% H_2O_2 to remove organic carbon content. The sediment dispersing agent (Na-hexametaphosphate) was added to the suspension before the analyses. Grain size values are presented as volume %.

Mineralogical Investigations

Magnetic particles were extracted from the bulk sediment following Petersen et al. (1986). A scanning electron microscope (SEM; JEOL JSM-5800 LV) captured the images of magnetic particles in a secondary electron imaging mode at energy levels between 15 and 20 keV. An energy dispersive X-ray spectroscopy (EDS) probe attached to the microscope was used to determine the composition of magnetic particles. The magnetic mineralogy of the selected samples from different sediment magnetic zones was determined using a Rigaku X-Ray Diffractometer (Ultima IV). The samples were run from 15° to 70° of 2θ at 1°/min scan speed using Cu Kα radiation (λ = 1.5414 Å).

Authigenic Carbonates and Chemosynthetic Community

Authigenic carbonates and chemosynthetic shells (*Calyptogena* sp.) were hand-picked during sub-sampling of the sediment core. These materials were washed and cleaned using a distilled water, and later dried at room temperature and stored in the plastic container.

RESULTS

Down-Core Changes in Magnetic Profile

We broadly classified the rock magnetic profile of the sediment core SSD-045/Stn-9/GC-01 into three distinct sediment magnetic zones: MZ-1 (uppermost 23.0 cmbsf), MZ-2 (25.0–265.0 cmbsf), and MZ-3 (267.0–315.0 cmbsf) based on the down core changes in the magnetic mineral concentration, composition and granulometry data. χ_{lf}, ARM, and SIRM (**Figures 2A–C**) are generally used as a diagnostic for magnetic mineral concentration. In MZ-1, a systematic decrease in these parameters from 1 to 5 cmbsf indicate down-core reduction in the magnetic mineral concentration (**Figures 2A–C**). MZ-1 showed higher values of χ_{lf}, ARM and SIRM suggesting high concentration of magnetic minerals while lower values are observed in MZ-2 and show uniform values except at certain intervals (**Figures 2A–C**). The beginning of MZ-2 is marked by an abrupt decrease in the magnetite concentration, and we refer this interval as the zone of reduced magnetic susceptibility (χ_{lf}). Within this zone (MZ-2), three distinct sediment intervals (G1, G2, G3) showed minor rise in χ_{lf}, ARM, SIRM, and SIRM/χ_{lf} indicating the dominance of fine-grained (SP-size) ferrimagnetic particles (**Figures 2A–C**,**E**; Tarduno, 1995; Rowan et al., 2009).

The SIRM/χ_{lf} ratio, an indicator of grain size of magnetic iron sulfides (Peters and Thompson, 1998; Peters and Dekkers, 2003) showed a linear decrease in MZ-1 and MZ-2 with a noticeable rise in G1, G2, G3 intervals and the bottommost sediment interval (303.0–315.0 cmbsf) in MZ-3 indicating the presence of fine-grained magnetic particles (**Figure 2E**). The variations in S-ratio can be linked to the changes in magnetic mineralogy, and

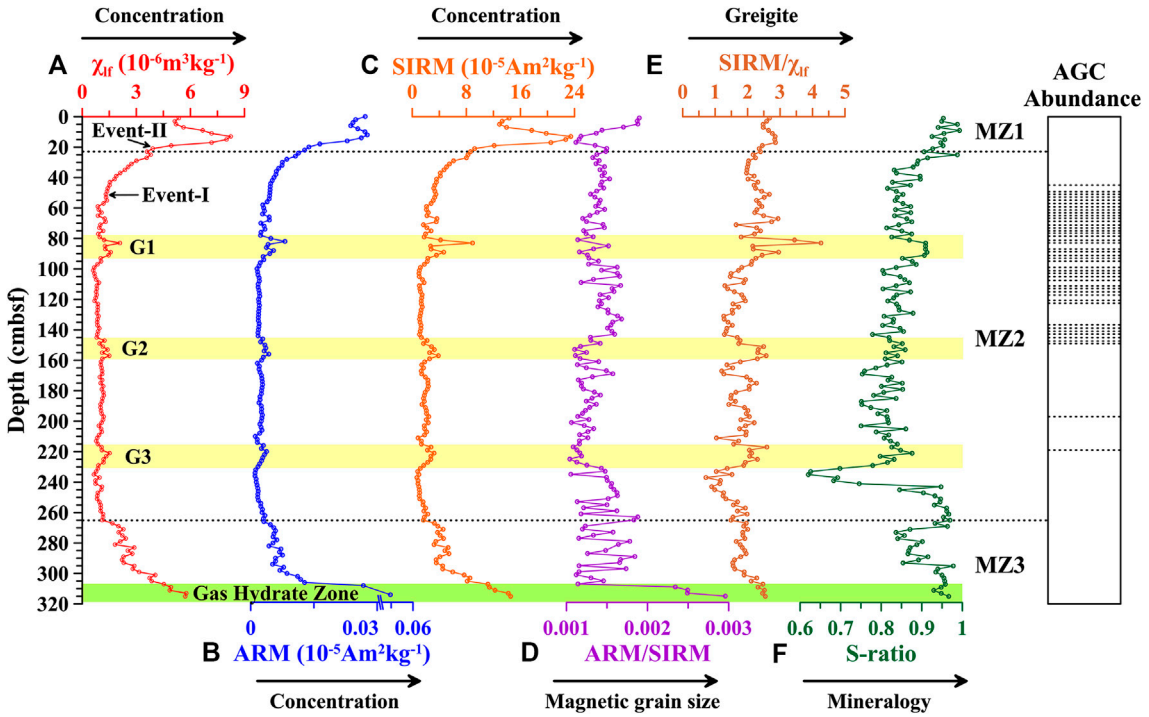

FIGURE 2 | Depth variations of selected rock magnetic data **(A–F)** for sediment core (SSD-045/Stn-9/GC-01). Data from discrete parameters are color-coded as magnetic susceptibility χ_{lf} (red), anhysteretic remanent magnetization (ARM) (blue), saturation isothermal remanent magnetization (SIRM) (orange), ARM/SIRM (purple), SIRM/χ_{lf} (brown), and S-ratio (green). Based on the variation in magnetic susceptibility, three sedimentary magneto-zones MZ-1, MZ-2, and MZ-3 are demarcated. Greigite bearing sediment intervals (G1, G2, and G3) are highlighted with yellow shading. Gas hydrate bearing bottom-most interval in MZ-3 is highlighted by green shading. AGC refers to authigenic carbonates.

is generally high and close to unity throughout the core (**Figure 2F**). A noticeable drop in S-ratio is observed between 229 cmbsf to 241 cmbsf suggesting the presence of either higher coercivity magnetic mineral (hematite, goethite) or ferrimagnetic magnetic iron sulfides (greigite, pyrrhotite) in this interval (**Figure 2F**) (Peters and Dekkers, 2003; Roberts et al., 2011).

Thermomagnetic Analyses

Thermomagnetic experiments on the representative sediment samples from MZ-1, MZ-2, MZ-3, G1, G2, and G3 are shown in **Figure 3**. A major drop in magnetization between 563°C and 595°C except on G3 sample (**Figure 3I**) suggest that the magnetite is the dominant magnetic mineral present in the sediments (Özdemir and Dunlop, 1997; **Figures 3A–J**). Increase in χ between 332°C and 480 °C can be attributed to the conversion of paramagnetic minerals into magnetite during heating process (Hirt et al., 1993; Passier et al., 2001; Philips, 2018; **Figures 3A–J**).

First-Order Reversal Curves Diagrams

FORC diagrams provided additional constraints on the domain states and mineralogy of the magnetic particles (**Figure 4**). In general, closed contours in all the plots suggest that the magnetic particles exhibit vortex state to multidomain (MD) type behavior (Roberts et al., 2000; Roberts et al., 2017). FORCs indicate that the magnetic mineralogy of samples from MZ-1, MZ-2, and MZ-3 could be dominated by the ferrimagnetic iron oxides (Vortex state-MD type magnetite) and sulfides (SP Greigite) (**Figures 4A–G**) (Muxworthy and Dunlop, 2002). In all the samples, FORC distributions are characterized by a peak at coercive field B_C ~ 10 mT with closed contours suggesting the dominance of vortex state behavior in magnetite (Lascu et al., 2018; Muxworthy and Dunlop, 2002; Roberts et al., 2017; **Figures 4A–I**). Greigite can exhibit both ultrafine-grained superparamagnetic (SP) (Rowan and Roberts, 2006; Rowan et al., 2009) and stable SD-type behavior (Roberts, 1995). Diagenetically reduced sediments enhances the formation of SP-size greigite particles (Tarduno, 1995; Rowan et al., 2009). Increase in SIRM/χ_{lf} in G1, G2 and G3 intervals confirms the presence of SP-sized greigite particles (**Figure 2E**; Maher and Thompson, 1999; Nowaczyk et al., 2012; Snowball and Thompson, 1990).

Low-Temperature Magnetic Measurements

Low-temperature magnetic measurements for representative samples selected from the different sediment magnetic zones MZ-1 (**Figure 5A**), MZ-2 (**Figure 5B**), MZ-3 (**Figure 5E**), G1 (**Figure 5C**), and G3 (**Figure 5D**) are presented. A well-developed Verwey (T_v 117–120 K) transition due to the presence of detrital magnetite is evident in RT-SIRM, ZFC-FC, and in the first derivative of magnetization curves (**Figures 5A,B,E**). During warming of RT-SIRM, remanence did not recover totally in these samples (MZ-1, MZ-2, and MZ-3) (Verwey, 1939;

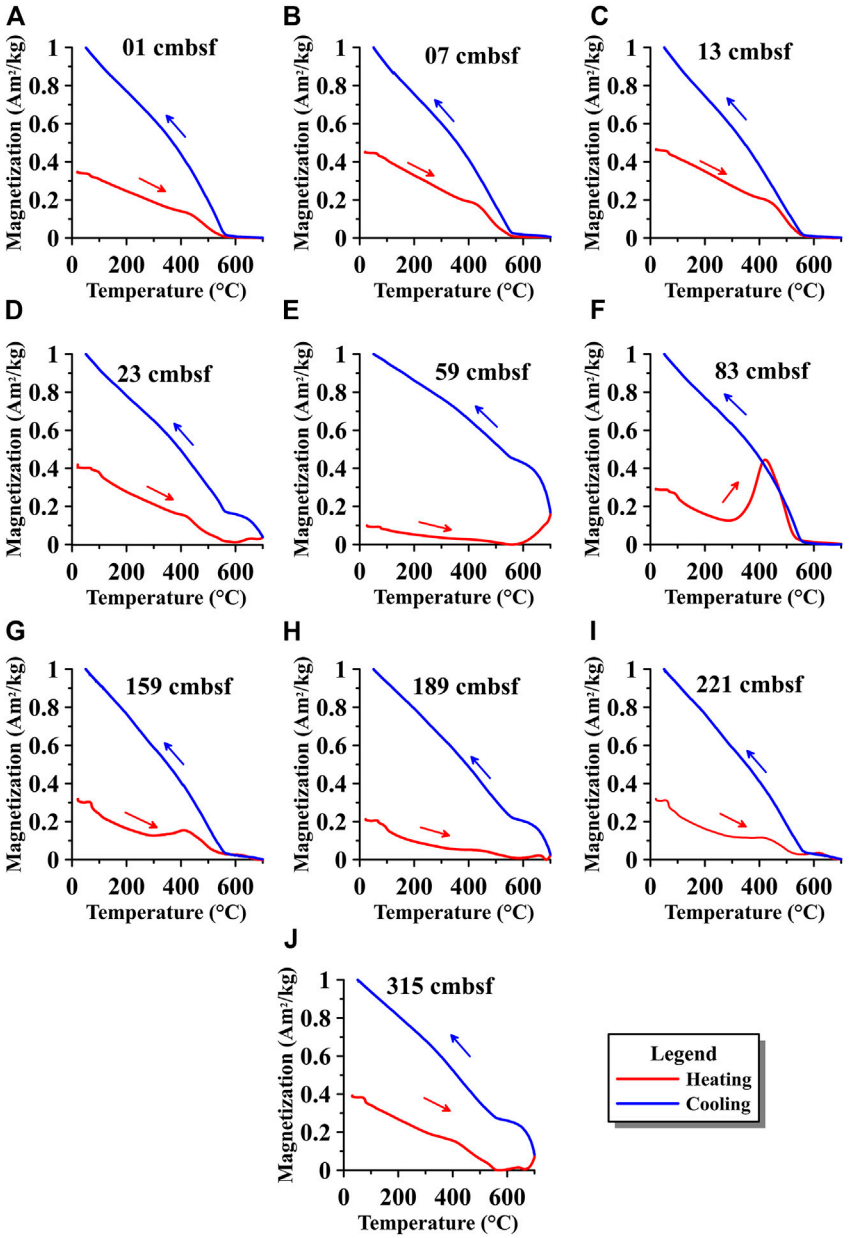

FIGURE 3 | (A–J) Thermomagnetic profiles of selected representative samples representing three sedimentary magnetic zones of the studied sediment core SSD-045/Stn-9/GC-01. Solid red lines indicate heating curves, and blue lines indicate cooling curves.

Muxworthy and McClelland, 2000; Özdemir et al., 2002; Chang et al., 2016). Samples (G1 and G3) from the zone of reduced magnetic susceptibility (MZ-2) did not show any indication of a Verwey transition in RT-SIRM, ZFC-FC, and the first derivative of magnetization curves (**Figures 5C**,D). We noticed that nearly 65% of the LT-SIRM imparted at 5K is lost during warming between 5 and 30 K (**Figures 5C**,D). This reflects the dominant presence of superparamagnetic (SP) magnetic particles in these samples (Tarduno et al., 1995; Passier and Dekkers, 2002). Kars and Kodama (2015) noticed a similar pattern of rapid decrease in LT-SIRM from 5 to ~30 K and ~50–60% loss of the imparted remanence in the sediment samples from Magesplay fault Zone of the Nankai Trough, offshore Japan. They attributed that the loss of remanence was due to the presence of SP particles which get unblocked very rapidly. The SP magnetic particles in these samples (G1 and G3) are most likely iron sulfides like greigite or pyrrhotite. These can be explained by the fact that fine-grained magnetic particles in these samples would get readily dissolved in the sulfidic environment (as seen through lowest χ_{lf} in MZ-2). In contrast, the SP greigite nanoparticles are thermodynamically more stable compared to the SP magnetite nanoparticles and would rather remain preserved (Rowan et al., 2009; Roberts et al.,

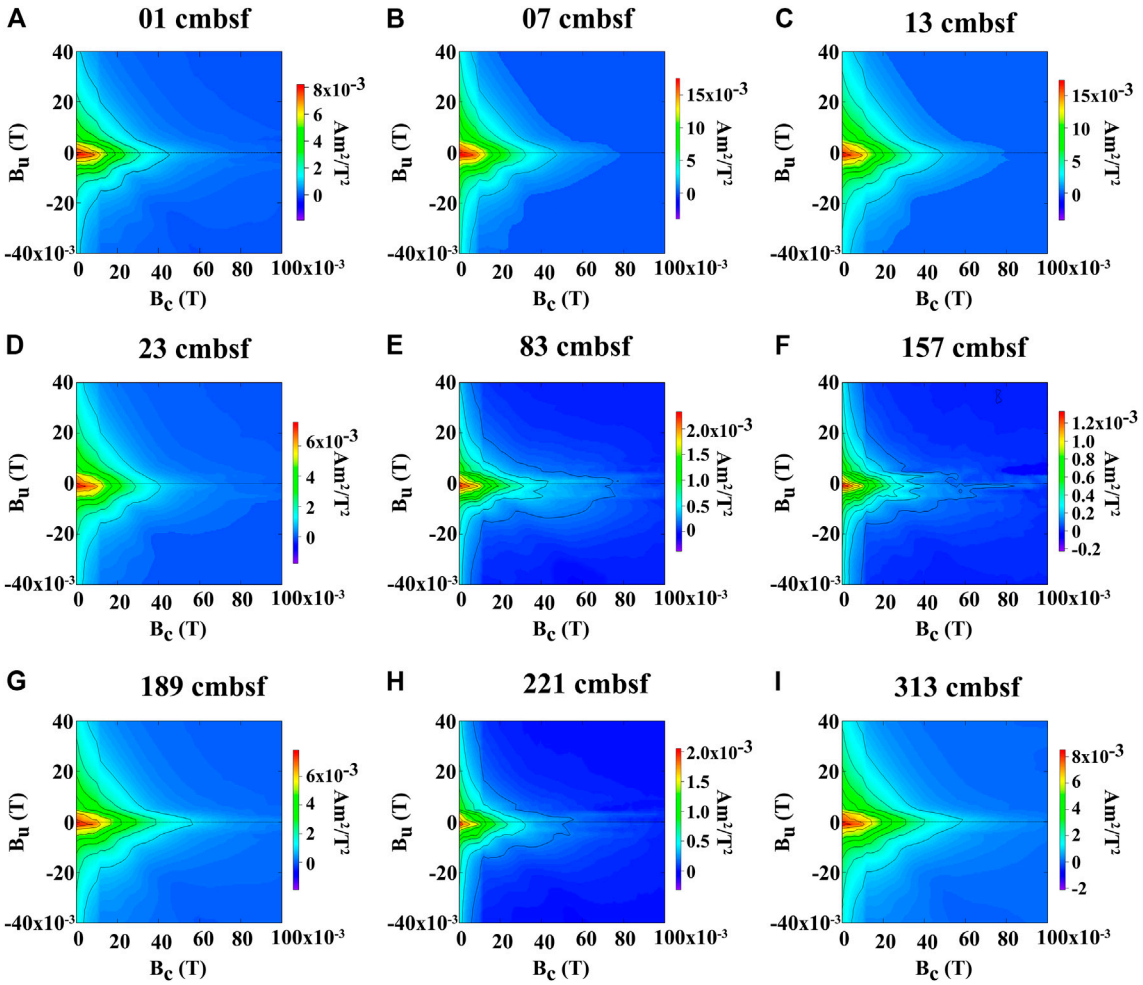

FIGURE 4 | (A–I) Representative first-order reversal curve diagrams for the three sedimentary magneto zones from core SSD-045/Stn-9/GC-01. All results are indicative of ferrimagnetic iron oxides, that is, titanomagnetite in the vortex state (Lascu et al., 2018; Roberts et al., 2017).

2018). Lack of LT transitions in the magnetization derivation curves in these samples (G1 and G3) is consistent and further confirms the presence of greigite (**Figures 5C**,D; Chang et al., 2009; Roberts et al., 2011).

Scanning Electron Microscope–Energy Dispersive X-ray Spectroscopy Observations of Magnetic Particles

In addition to rock magnetic parameters, SEM-EDS data confirm and support the interpretation on the magnetic mineralogy in core SSD-045/Stn-9/GC-01. Detrital origin ferrimagnetic iron oxides (titanomagnetite) of various sizes and shapes are found in all magnetic zones (**Figures 6A–L**). Magnetic zones (MZ-1, MZ-3) contain well-preserved titanomagnetite grains. EDS data for these grains indicate the presence of titanium, iron, and oxygen with minor amounts of calcium, silicon, aluminum, and manganese (**Figures 6B**,**K,L**).

Diagenetically formed iron sulfides are found to occur as sub-micron, spherical-shaped particles in MZ-1, MZ-2, G1, G2, and G3 (**Figures 6A,C,J**), and EDS spectra contain Fe and S peaks. Presence of such particles in the magnetic extracts from the zone of reduced χ_{lf} (G1, G2, G3) suggest that a ferrimagnetic iron sulfide i.e., greigite or pyrrhotite is the major constituent of the particles occurring as overgrowth on the paramagnetic host substrate such as pyrite (Rowan and Roberts, 2006). Sub-micron sized iron sulfide particles were also seen to occur as overgrowth on the large titanomagnetite grain in MZ-2 (**Figure 6E**). Several titanomagnetite grains of various sizes and shapes were found in the magnetically enhanced zone (MZ-3), and EDS spectra contain Ti, Fe, and O peaks (**Figures 6K,L**).

X-ray Diffraction (XRD) Analyses of Magnetic Minerals

Magnetic mineralogy is dominated by titanomagnetite, greigite, and pyrite particles occuring in varying proportion (**Figure 7**). XRD data confirms the dominant presence of pyrite along with minor peaks of greigite and titanomagnetite in G1, G2, and G3 (**Figures 7F**,I,K). Magnetically enhanced zone (MZ-3) contains titanomagnetite and pyrite (**Figures 7N,O**). Pyrite is the major

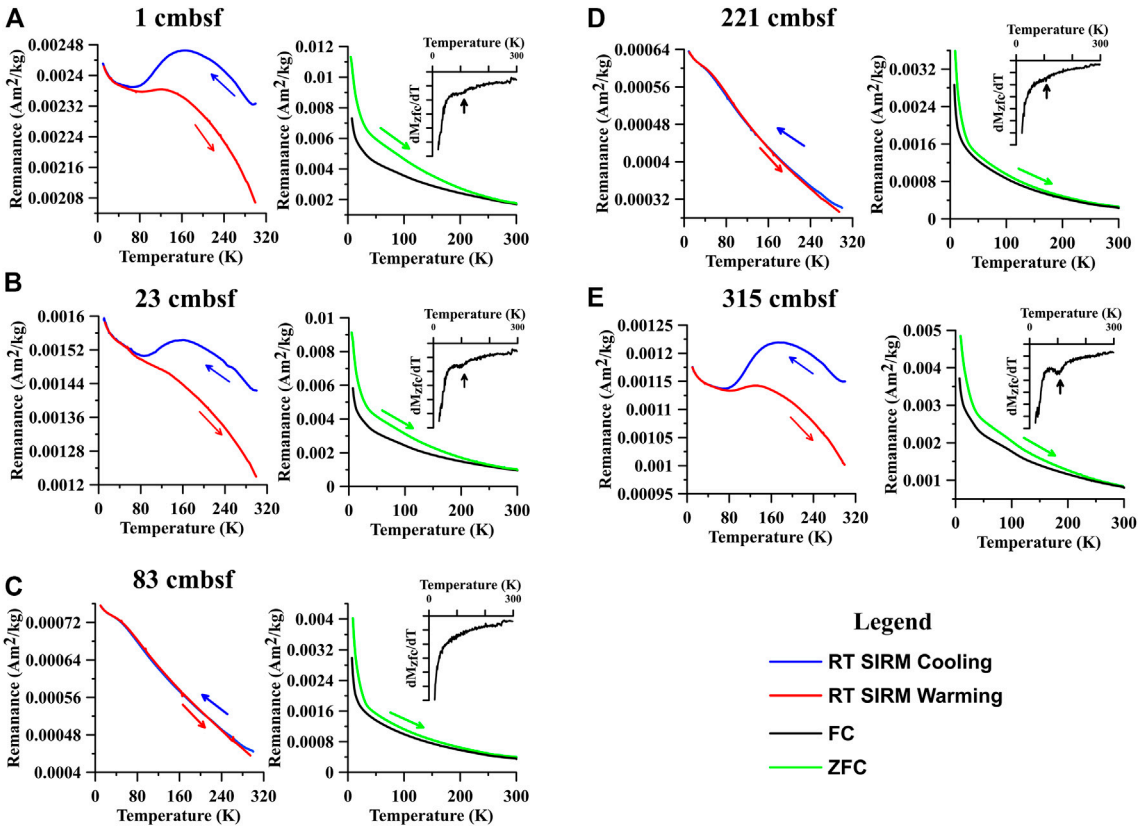

FIGURE 5 | (A–E) Low-temperature (<300 K) magnetization curves for representative samples from the three sedimentary magnetic zones identified in sediment core SSD-045/Stn-9/GC-01. FC, field-cooled; RTSIRM, saturation isothermal remanent magnetization at room temperature; ZFC, zero field-cooled.

magnetic mineral in the zone of reduced χ_{lf} (MZ-2) (**Figures 7C–M**). XRD peaks corresponding to quartz are seen in all the samples (**Figure 7**).

Authigenic Carbonates and Chemosynthetic Clams

Gray color authigenic carbonates of various sizes and morphologies are found predominantly throughout the core. Representative images of the carbonates found within the greigite-bearing (G1, G2, G3) sediment intervals are presented in **Figures 8A–I**. Two relict shells of *Calyptogena* (family: Vesicomydae) were found in the sediment depth intervals of 26–28 cmbsf and 50–52 cmbsf respectively (**Figures 8J,K**; **Table 1**).

Grain Size Distribution

Bulk sediment grain size in the core SSD-045/Stn-9/GC-01is dominated by the silt and clay sized fractions (**Figure 9**). Silt and clay content in this core varies from 14.56 to 52.29 vol% and 47.62–83.56 vol%, respectively. Down-core increase in sand content with distinct sediment intervals containing relatively higher sand concentrations at 83, 135, 197, 239, and 315 cmbsf are observed (**Figure 9**). Higher χ_{lf} were found in some of these sand layers in MZ-1 and MZ-3 suggesting the presence of coarse-grained magnetic particles (**Figure 9**).

Correlation Between Magnetic Parameter and Mean Grain Size

A good correlation between χ_{lf} and SIRM is observed in all the samples, but exhibits differences in their slope suggesting the presence of ferri-and paramagnetic mineral assemblages in the samples (**Figure 10A**). A cross plot of SIRM/χ_{lf} vs. χ_{lf} has been successfully utilized as a proxy for characterizing the magnetic mineral assemblages in the gas hydrate bearing sediments (Larrasoaña et al., 2007; Kars and Kodama, 2015; Badesab et al., 2019). We broadly classify the samples into three sub-groups (**Figure 10B**). Samples exhibiting higher χ_{lf} and SIRM/χ_{lf} values suggest the presence of fine-grained magnetite. Higher values of SIRM/χ_{lf} and relatively low χ_{lf} in the majority of samples indicate the dominance of ferri-and paramagnetic iron sulfides. Samples which lies within the intermediate range of SIRM/χ_{lf} and χ_{lf} values represent the mixture of magnetic iron sulfides and magnetite (**Figure 10B**). A good covariation between χ_{lf} and mineralogy diagnostic S-ratio is seen (**Figure 10C**). Samples exhibiting low S-ratio and relatively narrow range in χ_{lf} can be attributed to the presence of either higher coercivity magnetic

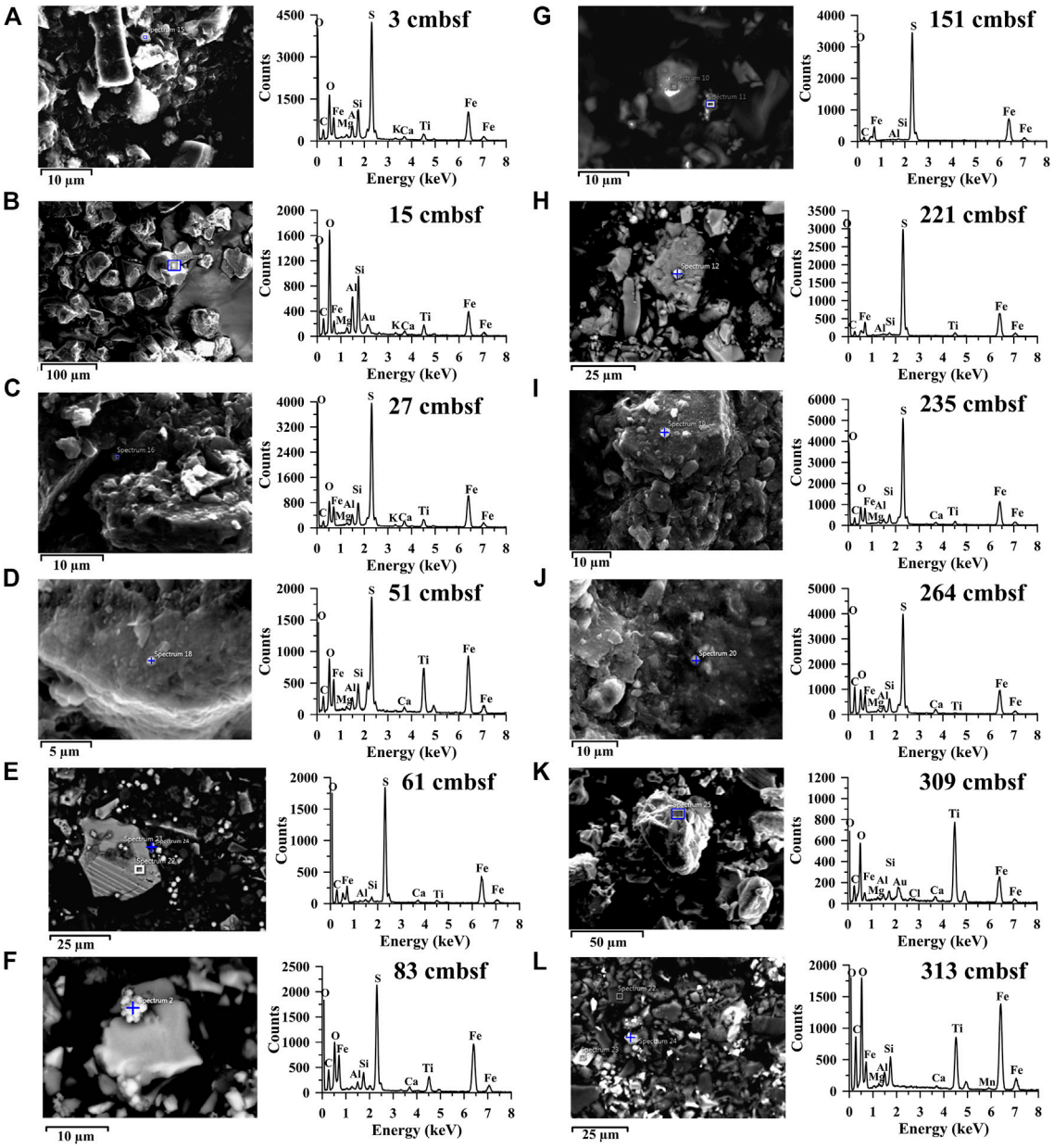

FIGURE 6 | (A–L) Scanning electron microscope images (secondary electron) on magnetic extracts from different sedimentary magnetic zones of core SSD045/Stn-9/GC-01. Energy dispersive X-ray spectroscopy spectra are placed adjacent to the respective images **(A–L)**. Iron (Fe), titanium (Ti), sulfur (S), oxygen (O), calcium (Ca), silicon (Si), carbon (C), aluminum (Al), magnesium (Mg), and manganese (Mn) peaks are indicated.

minerals or ferrimagnetic iron sulfides (**Figure 10C**) (Peters and Dekkers, 2003; Roberts et al., 2011).

Mineralogy diagnostic rock magnetic parameters indicated that the bulk magnetic mineralogy is dominated by the vortex state titanomagnetite. Moskowitz et al. (1993) demonstrated that the origin of magnetic mineral assemblages in the sediment samples can be characterized by δ_{ZFC} and δ_{FC}. In the analyzed samples, we noticed that δ_{FC}/δ_{ZFC} values are close to 1, which suggest that the titanomagnetites are of detrital origin (**Figure 10D**; Housen and Moskowitz, 2006). All data falls on a 1:1 line. Samples exhibiting low values δ_{ZFC} and δ_{FC} indicate the presence of diagenetically formed ferrimagnetic iron sulfides, while higher values of δ_{ZFC} and δ_{FC} indicates the presence of mixed-type (magnetite, pyrite) magnetic mineral assemblages (**Figure 10D**; Kars and Kodama, 2015; Badesab et al., 2019).

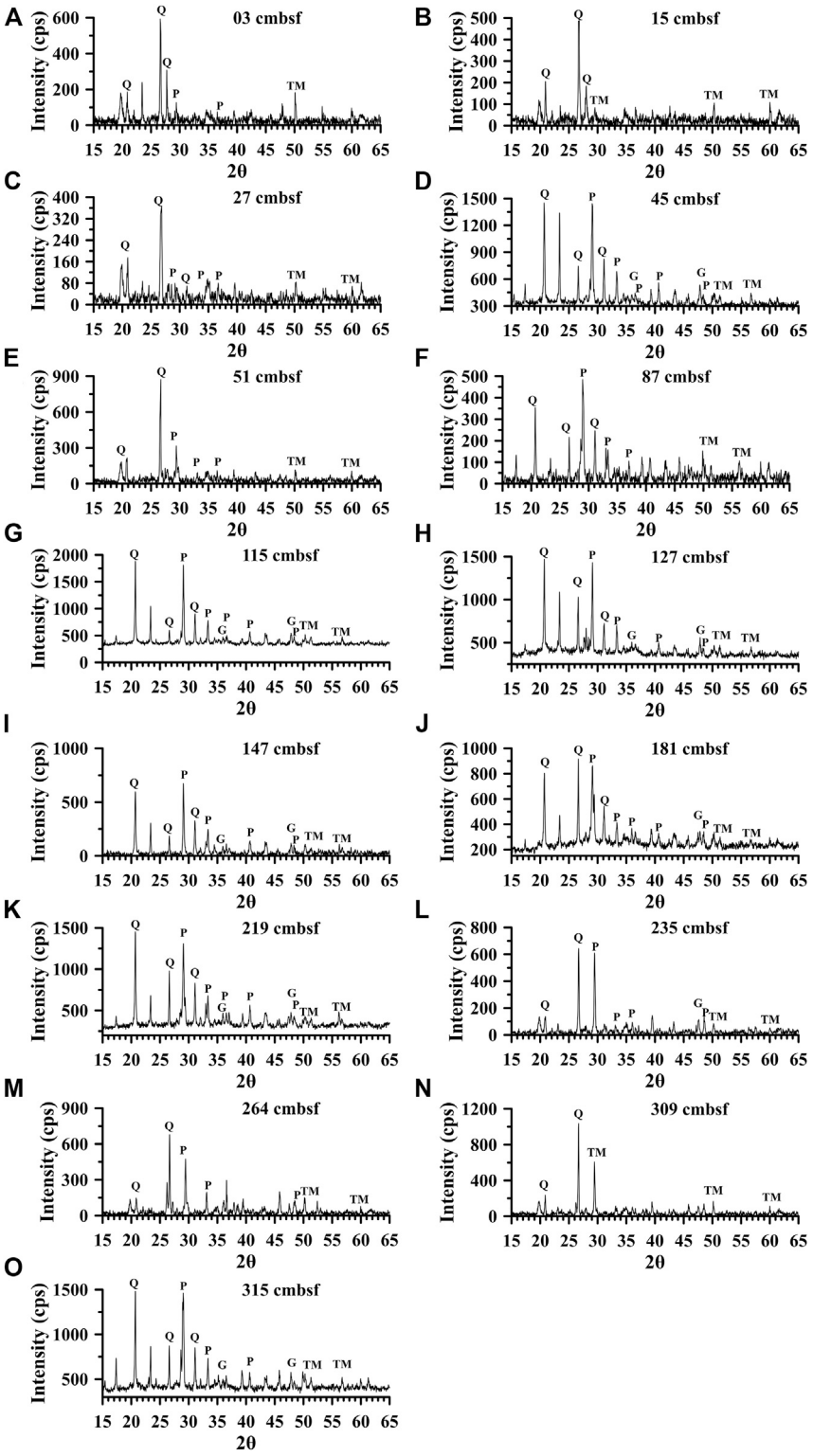

FIGURE 7 | (A–O) X-ray diffraction spectra for minerals extracted from different sedimentary magnetic zones of core SSD-045/Stn-9/GC-01 (a–o). TM, titanomagnetite; P, pyrite; Q, quartz; G, greigite.

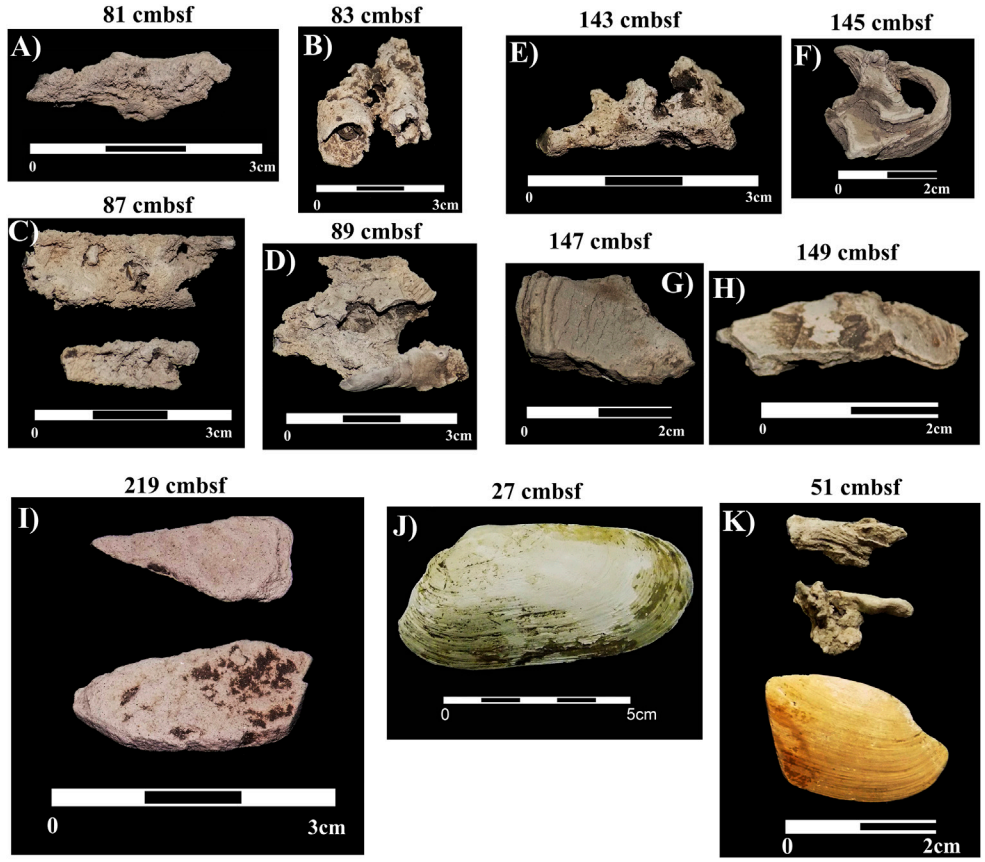

FIGURE 8 | (A–I) Photographs showing methane-derived authigenic carbonates found in greigite bearing intervals (G1, G2, and G3) in MZ-2, **(J)** *Calyptogena* sp. showing growth layers identified at 27 cmbsf and **(K)** authigenic carbonate together with *Calyptogena* sp identified at 51 cmbsf.

DISCUSSION

Paleo-Methane Seepage Events Constrained by Rock Magnetism, Authigenic Carbonates and Chemosynthetic Community

Variations in magnetic mineralogies (titanomagnetite, pyrite, greigite) and concentration governed the down-core changes in the magnetic properties. Primary magnetic minerals in the uppermost MZ-1 are dominated by titanomagnetite (vortex) with minor amount of pyrite (**Figures 2F**, **5A**, **6B**, **7A**,**B**). Gradual decrease of χ_{lf} in MZ-1 can be linked with the progressive dissolution of iron oxide and subsequent precipitation of iron sulfides. A distinct drop in χ_{lf}, ARM, and SIRM at the shallowest sediment interval (3–5 cmbsf) accompanied by the presence of pyrite and magnetite reflects the top-most dissolution front related to intense pyritization fueled by AOM-coupled sulfate reduction, and probably represent the depth of present-day SMTZ in the core SSD-045/Stn-9/GC-01 (**Figures 2A–C**, **6A**, **7A**). A systematic down-core increase in χ_{lf} and SIRM (from 7 to 17 cmbsf) manifested by the presence of magnetic particles below the proposed present-day SMTZ (3–5 cmbsf) indicate the period of weak AOM activity and minimum dissolution of the magnetic minerals (**Figures 2A**,**C**, **6B**, **7A**). Rapid burial and preservation of the detrital magnetic particles due to increased sedimentation specifically during this period is another possibility (Badesab et al., 2019). A marked depletion in χ_{lf} between 25–29 cmbsf and 43–52 cmbsf reflects the periods of increased magnetite dissolution and pyrite formation linked with at least two intense methane seepage events at the studied site (**Figures 2A**, **6C**,**D**, **7C**,**E**). These intervals most likely reflect paleo-SMTZ front, where upward migrating methane front interact with downward migrating sulfate front to trigger strong AOM.

The AOM increases the concentration of hydrogen sulfide in the pore-water and favor dissolution of primary magnetic mineral assemblages (Kasten et al., 1998; Jørgensen et al., 2004; Dewangan et al., 2013). Similar low χ_{lf} intervals due to paleo-methane expulsion events were reported from the K-G basin and South China Sea (Mazumdar et al., 2009; Peketi et al., 2012; Dewangan et al., 2013; Hu et al., 2019). The presence of chemosynthetic clams like *Callyptogena* sp. and methane derived authigenic carbonates provided further evidences of intense methane seepage events at these sediment intervals (**Figures 2A**, **6C**,**D**, **7C–E**, **8J**,K; **Table 1**). Fossil chemosynthetic community and authigenic carbonates were reported from site MD161/Stn-8 and NGHP-01–10D in K-G basin (Collett et al., 2008; Mazumdar et al., 2009, Peketi et al., 2012), Haima Seep, South China Sea

TABLE 1 | Depth-wise distribution of authigenic carbonates and shells in sediment core SSD- 045/Stn-09/GC-01.

Sr. No.	Authigenic carbonates ref. no.	Depth (cmbsf)	Other details
1	—	27	Shells
2	AGC-01	45	—
3	AGC-02	49	—
4	AGC-03	51	Shells + AGC
5	AGC-04	53	—
6	AGC-05	55	—
7	AGC-06	57	—
8	AGC-07	59	—
9	AGC-08	61	—
10	AGC-09	63	—
11	AGC-10	65	—
12	AGC-11	67	—
13	AGC-12	69	—
14	AGC-13	71	—
15	AGC-14	73	—
16	AGC-15	75	—
17	AGC-16	77	—
18	AGC-17	79	—
19	AGC-18	81	—
20	AGC-19	83	—
21	AGC-20	87	—
22	AGC-21	89	—
23	AGC-22	91	—
24	AGC-23	93	—
25	AGC-24	95	—
26	AGC-25	99	—
27	AGC-26	101	—
28	AGC-27	103	—
29	AGC-28	105	—
30	AGC-29	107	—
31	AGC-30	111	—
32	AGC-31	113	—
33	AGC-32	115	—
34	AGC-33	117	—
35	AGC-34	119	—
36	AGC-35	121	—
37	AGC-36	123	—
38	AGC-37	137	—
39	AGC-38	139	—
40	AGC-39	141	—
41	AGC-40	143	—
42	AGC-41	145	—
43	AGC-42	147	—
44	AGC-43	149	—
45	AGC-44	197	—
46	AGC-45	219	—

(Feng and Chen 2015; Liang et al., 2017), southwest Barents and Norwegian Sea (Crémière et al., 2016), Mediterranean Sea (Aloisi et al., 2000), and Gulf of Mexico (Bian et al., 2013). Downward decrease in ARM/SIRM (9–19 cmbsf in MZ-1) is followed by the consistent low χ_{lf} and ARM/SIRM values in MZ-2 (25–265 cmbsf; **Figures 2A**,D). As confirmed through the XRD (**Figures 7C–M**) and SEM-EDS (**Figures 6F**,H), the dominant magnetic mineral in MZ-2 is titanomagnetite (vortex) and pyrite. It is most likely that fine SD magnetite grains might have been preferentially removed by diagenetic dissolution (**Figures 2A–D**) owing to larger surface area (Karlin and Levi, 1983; Liu et al., 2004; Garming et al., 2005). The dominance of pyrite and titanomagnetite within 59–265 cmbsf interval of MZ-2 coupled with abundant occurrence of authigenic carbonates suggest that the strong SMTZ fronts sustained due to uniform supply of methane gas from the deep-seated reservoir (**Figures 2A, 6E–H,J, 7F–M**). It is interesting to note that a lower S-ratio interval (229–241 cmbsf) is observed in MZ-2. Horng, C.S. (2018) and Kars and Kodama (2015) reported that sedimentary pyrrhotite and greigite can have high coercivities which could result in low S-ratio. A dedicated rock-magnetic study conducted by Kars and Kodama (2015) on gas hydrate bearing sediments from Nankai trough reported that authigenically formed ferrimagnetic iron sulfides such as greigite

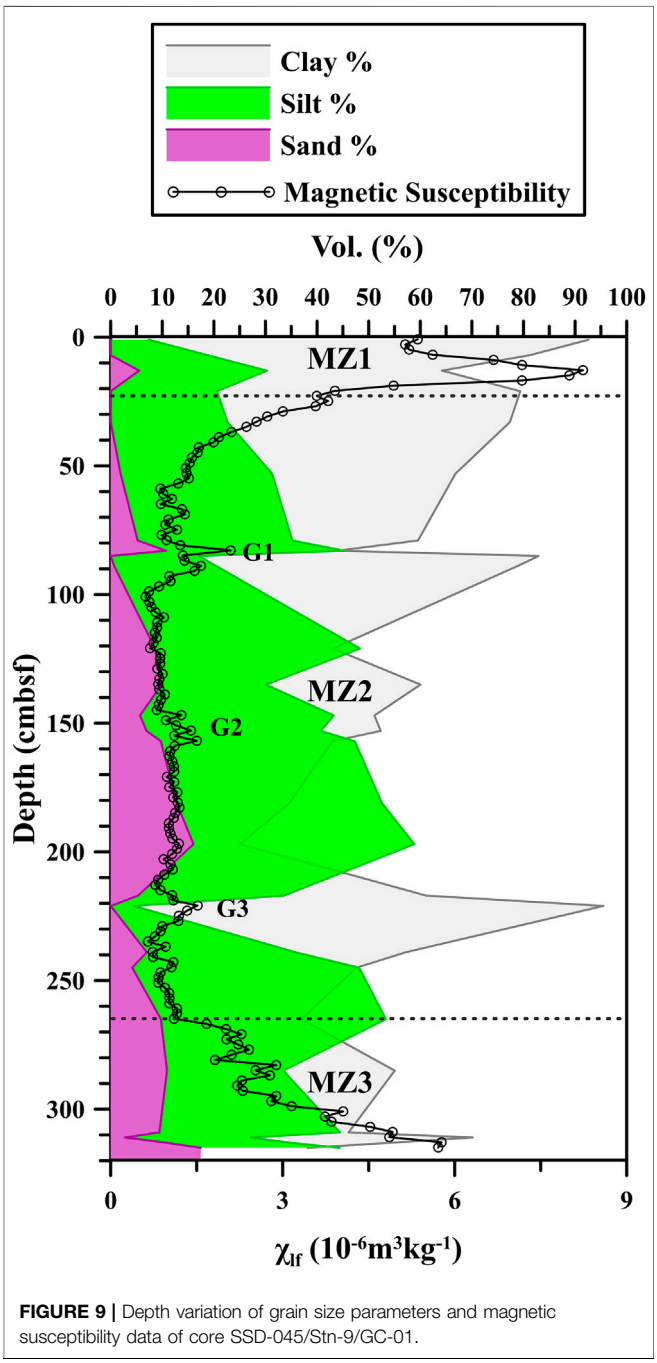

FIGURE 9 | Depth variation of grain size parameters and magnetic susceptibility data of core SSD-045/Stn-9/GC-01.

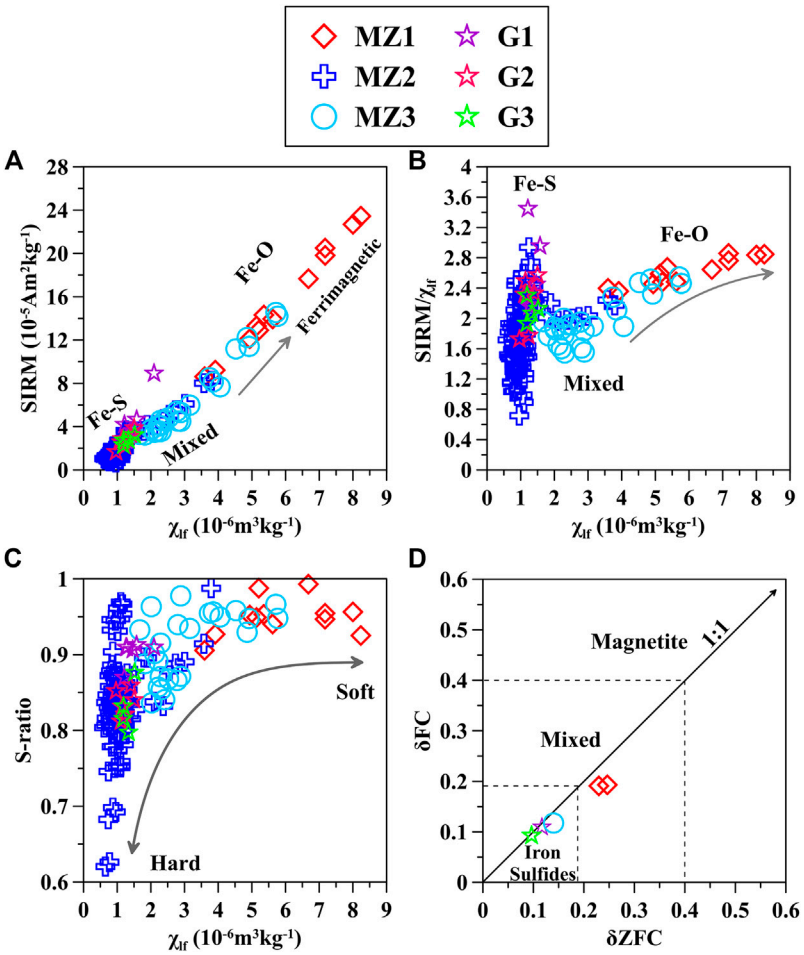

FIGURE 10 | (A–C) Scatterplots of magnetic parameters χ_{lf}, saturation isothermal remanent magnetization (SIRM), SIRM/χ, anhysteretic remanent magnetization (ARM)/SIRM), and S- for core SSD-045/Stn-9/GC-01. **(D)** δFC vs. δFC are derived from low-temperature measurements (Moskowitz et al., 1993) for core SSD-045/Stn-9/GC-01. Please note that gray color arrows in the scatter plots are used to highlight trends.

and pyrrhotite can exhibit high coercivities. The lower S-ratio interval observed in MZ-2 could be attributed to the presence of such ferrimagnetic iron sulfides (greigite/pyrrhotite) which were no longer stable and got converted into pyrite as evident through low χ_{lf} within 209–231 cmbsf, (**Figure 2A**) and SEM-EDS data (**Figures 6H,I**).

Lowermost sediment magnetic zone (MZ-3) is characterized by elevated χ_{lf}, ARM, SIRM, and contains the mixture of abundant detrital titanomagnetites and minor amount of diagenetically formed pyrite (**Figures 2A–C**, **5E**, **6K,L**, **7N**,O). High χ_{lf} accompanied by mixed trend of ARM/SIRM values could be attributed to the presence of both fine and coarse-grained detrital magnetic particle which probably survived diagenesis (**Figures 2A**,D). Fracture-filled gas hydrates deposits were recovered from MZ-3 (305–315 cmbsf, **Figure 1B**). Trapping of H_2S within the hydrate deposits hindered the pyritization processes (Housen and Musgrave, 1996), and lead to the preservation of detrital magnetite particles in MZ-3 (Riedinger et al., 2005) (**Figures 2A**, **4I**, **5E**, **6K,L**, **7N,O**). Rapid burial of magnetic particles is another important factor which can explain the existence of high χ_{lf} in gas hydrate bearing sediments (Badesab et al., 2019). We believe that both these processes hindered the diagenetic reactions and favored high χ_{lf} values in the gas hydrate bearing sediments at site Stn-9.

A dedicated magnetic study on pelagic sediments from western equatorial Pacific Ocean revealed that diagenetically reduced sediments could enhance the formation of SP-size greigite particles (Tarduno, 1995). Increase in SIRM/χ_{lf} in G1, G2, G3 intervals confirms the presence of SP-sized greigite particles (**Figure 2E**; Tarduno, 1995). FORC distributions from the same greigite bearing samples G1, G2 and G3 also showed closed contours indicative of vortex-type magnetic behavior (**Figures 4A–I**; Lascu et al., 2018; Muxworthy and Dunlop, 2002; Roberts et al., 2017). These observations suggests that magnetic particles in G1, G2, G3 and MZ-3 (313 cmbsf) in core SSD-045/Stn-9/GC-01 is dominated by SP greigite and vortex-state magnetite. Hence the minor rise in SIRM/χ_{lf} (**Figure 2E**) manifested by the presence of pyrite (**Figure 7O**) in MZ-3 (301–315 cmbsf) can be explained by the fact that ferrimagnetic greigite which was formed earlier

might have got transformed into more stable pyrite (Larrasoaña et al., 2007; Kars and Kodama 2015).

Occurrence of active methane seep are often associated with shallow gas hydrates and presence of seep-carbonates and has been well documented worldwide; for example offshore southwest Africa, Congo deep sea fan (Pierre and Fouquet, 2007), eastern Mediterranean Sea (Aloisi et al., 2000), northern Apennines and Tertiary Piedmont Basin of Italy (Dela Pierre et al., 2010; Argentino et al., 2019), Nyegga complex pockmark, Norwegian Sea (Mazzini et al., 2006), South China Sea (Tong et al., 2013; Han et al., 2014), Blake Ridge Diapir (Naehr et al., 2000), and Vestnesa Ridge, NW Svalbard (Schneider et al., 2018). At active seeps, methane gets consumed and this process generates dissolved bicarbonate, thereby increasing porewater alkalinity and favors precipitation of authigenic carbonate close to the seafloor (Boetius et al., 2000). Thus, the authigenically formed carbonates are considered as potential archives of past fluid flow (Aharon et al., 1997; Bayon et al., 2013; Feng and Chen, 2015). Repeated occurences of authigenic carbonates (**Figures 8A–K**; **Table 1**) from 45 to 219 cmbsf in core SSD-045/Stn-9/GC-01 indicate the episodic events of intense AOM due to enhanced methane flux. This also show the variability in past methane fluxes could be due to episodic ventilation of deep-seated methane gas or dissociation of gas hydrates or opening/closing of fault/fracture system driven by neo-tectonic activity (Dewangan et al., 2020).

Association of chemosynthetic communities with methane seepage has been reported from several cold seep locations (Sellanes and Krylova, 2005; Levin et al., 2016; Amon et al., 2017; Mazumdar et al., 2018). Evidence for the strong methane seepage events at 25–29 cmbsf and 43–52 cmbsf, and subsequently anaerobic oxidation of methane comes from the occurrence of authigenic carbonate nodules, chemosynthetic communities (*Calyptogena* sp.), and pyrite followed by distinct χ_{lf} drop at this intervals (**Figures 2A**, **8J**,K). Similar observations were reported from site MD161/Stn-8 in the K-G basin (Mazumdar et al., 2009; Dewangan et al., 2013). Variations of methane fluxes at seeps determine the migration of the SMTZ in marine sediments (Borowski et al., 1996). Delineation of SMTZ and the factors controlling its migration in a seep-impacted sediments could help in tracking the evolution of past methane seepage events. Previous studies employed various proxies to recognize the SMTZ and detect the past methane seepage events including Ba front (Dickens, 2001; Snyder et al., 2007), methane-derived authigenic carbonates, mineralogy and its carbon isotope composition (Teichert and Luppold, 2013; Kocherla et al., 2015), Sulfur isotope and Mo anomaly (Peketi et al., 2012) and magnetic susceptibility (Badesab et al., 2019). Fluctuations in methane fluxes in a complex gas hydrate bearing marine sedimentary system can also be tracked successfully using χ_{lf} records, for examples in K-G basin (Badesab et al., 2019; Dewangan et al., 2013; Usapkar et al., 2014), the Argentine continental slope (Garming et al., 2005), Nankai trough, Japan (Kars and Kodama, 2015), and Cascadia margin (Housen and Musgrave, 1996; Larrasoaña et al., 2007). Rock magnetic record of core SSD-045/Stn-9/GC-01 provides evidence of rapid SMTZ migration controlled by changing methane fluxes. Mineralogical analyses on the core revealed the presence of abundant diagenetically formed pyrite and minor amount of titanomagnetite within the zone (MZ-2) of reduced χ_{lf} (**Figures 7D–M**). Such phenomena can be attributed to the reducing environment associated with upward methane flux which enhances diagenesis of the highly magnetic detrital minerals such as titano-magnetite into nearly non-magnetic pyrite (Housen and Musgrave, 1996). In zone of reduced susceptibility (MZ-2), multiple episodes of seepage activities controlled the diagenetic alteration of magnetic minerals and hence have a direct impact on χ_{lf}. However, tracking paleo-SMTZ fronts can be challenging at times due to the differences in the rate of diagenesis constrained by changing methane fluxes. In such a scenario, the occurrence of authigenic carbonates would be useful in delineating the paleo-methane seepage activities. The abundant occurrence of authigenic carbonates in a depth range from 45 to 219 cmbsf within MZ-2 suggests that the SMTZ was quite variable in the past (**Figures 8A–I**; **Table 1**). We demonstrate that combination of rock magnetic and mineralogical (SEM-EDS, XRD) data together with authigenic carbonates are useful to identify the present and past SMTZ fronts fueled by methane seepages.

Possible Linkage Between Greigite Precipitation, Neo-Tectonic Events and Formation of Gas Hydrates (Disseminated-Type vs. Massive) in the Krishna-Godavari Basin

Fracture-controlled fluid migration has been well-reported at cold seeps, for example in Vestnesa Ridge (Yao et al., 2019), Harstad Basin, southwest Barents Sea (Vadakkepuliyambatta et al., 2013; Crémière et al., 2018), Hydrate Ridge (Torres et al., 2002; Weinberger and Brown, 2006), Blake Ridge (Egeberg and Dickens, 1999), and Central Chile (Geersen et al., 2016). Fractures/faults facilitate efficient transport of methane-rich fluids from greater depth to shallower depth, and sometimes methane escape from sediment-water interface as flares (Berndt et al., 2014; Sahling et al., 2014). In methanic sediments, interplay between availability of reactive iron supply and relative production of hydrogen sulfide (HS–) control the pyritization process (Wilkin and Barnes, 1997). In case of excess HS– and high availability of reactive iron, the pyritization process is complete and the metastable iron sulfides are eventually converted to pyrite (Berner, 1967). Under low HS– concentration greigite may preferentially be precipitated over pyrite and will lead to the preservation of greigite. Migration of methane-rich fluids is found to be associated with the authigenic ferrimagnetic iron sulfide minerals like greigite and/or pyrrhotite (Larrasoaña et al., 2007). Greigite formation is enhanced in the vicinity of gas hydrate deposits as observed in Hydrate Ridge (Larrasoaña et al., 2007) and Blake Ridge (Wellsbury et al., 2000). For greigite formation and preservation, either limited amount of hydrogen sulfide or increased supply of reactive iron is required to constrain the pyritization process in methanic sediments (Liu et al., 2004). For example, Kao et al., 2004 demonstrated that

widespread greigite preservation is likely if abundant reactive iron is available to react with sulfide during pyritization reactions. Roberts et al., 2011 suggested that the preservation of greigite depends on the balance between sulfide production and reactive iron concentration. In the studied core, three distinct greigite (G1, G2, and G3) bearing sediment intervals (81–93 cmbsf, 145–159 cmbsf, and 217–229 cmbsf) has been identified within the zone of reduced χ_{lf}. Presence of greigite has been further confirmed through rock magnetic (χ_{lf} and SIRM/χ_{lf}), SEM-EDS and XRD (**Figures 2A,E**, **6F–H**, **7I–K**). A general trend of downcore increase in magnetic grain size diagnostic proxy (ARM/SIRM) in MZ-2 is observed (**Figure 2D**; Maher and Thompson, 1999). ARM/IRM first decreases in MZ-1 because of preferential dissolution of fine-grained magnetite (Maher, 1988) in the upper part of the reduced zone, and rises downcore in response to the formation of fine-grained greigite in MZ-2. A rockmagnetic study conducted on a sediment core from Niger deep-sea fan by Dillon and Bleil (2006) observed that the iron redox boundary is very shallow (~3 mbsf) and below, a pervasive magnetite dissolution has taken place. Similar to our observations, they noticed minor increase in ARM/SIRM with depth after an initial drop. They attributed the steadily increasing ARM/SIRM ratio in the anoxic sulfidic zone with the small gradually growing SD fraction of magnetic sulfides, for example authigenic formation of greigite is most likely in such environment and similarly reported in Mediterranean sapropels (Roberts et al., 1999; Passier and Dekkers, 2002) and Korean Strait (Liu et al., 2004). Increase in SIRM/χ_{lf} in G1, G2 and G3 intervals also suggest the presence of authigenically formed SP-sized greigite particles in the studied core (**Figure 2E**). Within the zone of reduced χ_{lf} (MZ-2), elevated methane concentration might have allowed huge production of sulfide which enabled complete pyritization and restricted the greigite preservation as seen through lower and uniform values of χ_{lf}, SIRM and abundant presence of pyrite in MZ-2 (**Figures 2A,C**, **7C–M**). In contrast, decline in methane flux at G1, G2, and G3 intervals probably generated less sulfide, and favored the formation and preservation of greigite. Similar observation was made by Dewangan et al., 2013, where the presence of a thick authigenic carbonate layer beneath the SMTZ at site MD161/Stn-08 in K-G basin (Mazumdar et al., 2009) hindered the downward diffusion of sulfide favoring early arrest of the pyritization process and preservation of greigite. At the present site, low methane flux might have supported more distributed-type (vein-filling) hydrate deposits instead of massive deposits formed due to enhanced methane flux. We, therefore, propose that these three greigite bearing sediment intervals (G1, G2, and G3) are associated with distributed-type gas hydrate intervals at site Stn-9. However, we do not completely rule out the possibility of greigite formation due to increase in iron content in G1, G2, and G3.

A linkage between occurrence of greigite and increased clay content is evident (**Figure 9**). We propose a following plausible mechanism to explain the linkages between methane migration and formation of distributed-type (vein-filling gas hydrates), grain size and greigite formation and preservation. High resolution X-ray investigation conducted on the gas hydrates recovered from K-G basin revealed that hydraulic fractures created by upward migrating fluids was the dominant mechanism for the formation of veined-hydrate deposits at site NGHP-01–10 (Rees et al., 2011). At site Stn-9, it is highly possible that rapid migration of diffusive methane flux through the clay rich intervals in G1, G2, and G3 probably created multiple hydro-fractures which provided conducive environment for the formation of distributed–type (vein-filling) hydrates in these intervals. Growth of vein-filling hydrate network trapped the available sulfide within it and created a closed system by forming an impermeable layer which further restricted the supply of the downward diffusing sulfate (sea water) through the hydrate-bearing interval. A sulfide deficient zone is created which caused arrestation of pyritization and favored formation and preservation of greigite in G1, G2, and G3. Geochemical study conducted by Kao et al. (2004) on sediment cores from southwestern Taiwan reported that detrital minerals will survive in sediments if the methane fluxes are too small. At the studied site, fracture-filled gas hydrates were recovered from MZ-3 (305–315 cmbsf). Survival of detrital titanomagnetite particles in MZ-3 could be explained based on the fact that the lower methane (free) concentration in these intervals due to the presence of massive gas hydrate beneath this interval might have restricted the further diagenetic transformation of iron oxides into iron sulfides.

Grain size also provides important control on the gas hydrate formation in marine sedimentary system (Clennell et al., 1999; Torres et al., 2008). In Blake Ridge, high methane hydrate concentrations were found in sediment layers containing high silt content (Ginsburg et al., 2000; Lorenson, 2000). Overall, clay and silt dominate the bulk sediment grain size in the studied core (**Figure 9**). Marked peaks of decrease in silt content and concurrent rise in clay content more specifically within gas hydrate bearing intervals (G1, G2, G3 and bottom most: 305–315 cmbsf) suggest that distributed methane hydrate accumulation in veins/fracture preferentially occurs in the sediment intervals containing high clay content (**Figures 2A**, **9**).

Regulation of gas plumbing system due to opening/closing of the fractures/faults provides important constraints on the methane flux (Dewangan et al., 2011; Sriram et al., 2013; Mazumdar et al., 2019). Widespread occurrence (45–219 cmbsf) of authigenic carbonates in the studied core suggests that the multiple AOM driven by variability in paleo-methane fluxes is controlled by the opening and closing dynamics of the fracture/fault system due to prevailing shale tectonism (Dewangan et al., 2010; Gullapalli et al., 2019; Mazumdar et al., 2019). Sahling et al. (2014) also suggested that micro and macro fractures are often found associated with cold seep systems, wherein methane from deep-seated reservoir moves upward to sediment-water interface such as Hydrate Ridge (Torres et al., 2002) and Blake Ridge (Egeberg and Dickens 1999). At site Stn-9, fracture-controlled fluid transport supported the formation of gas hydrates (distributed and massive-type) (Mazumdar et al., 2019). We believe that hydrate crystallizes within the fault/fractures zone as methane gas migrate through GHSZ (You et al., 2019). It is interesting to note that several layers of hard authigenic carbonates are found above and within the proposed

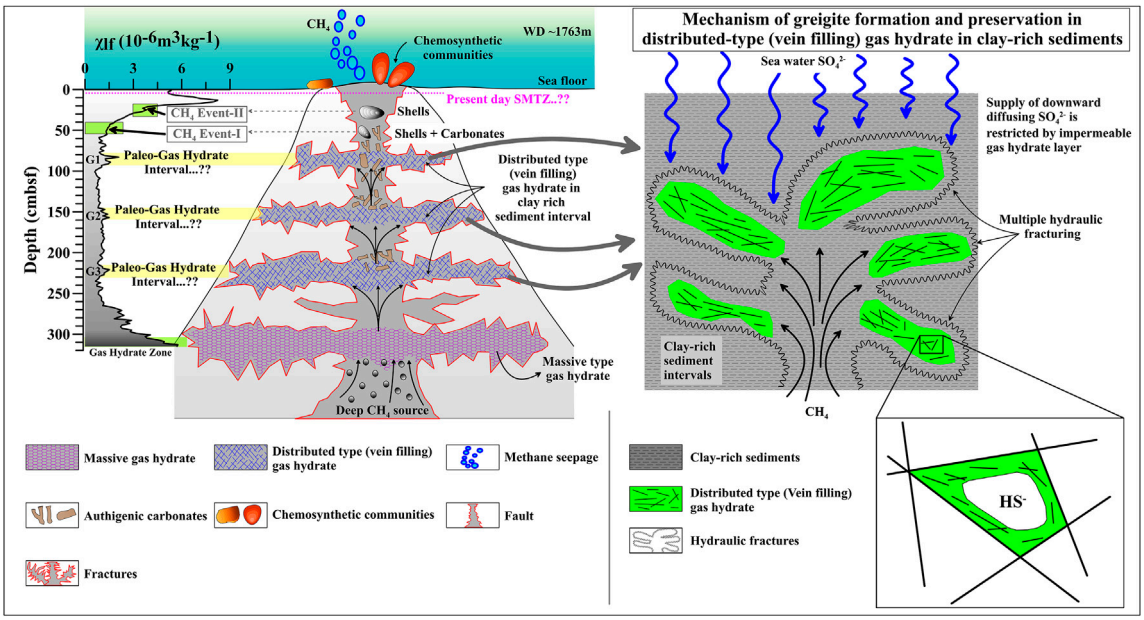

FIGURE 11 | Conceptual model explaining the mechanism controlling the shallow gas hydrate formation, greigite preservation and development of active cold seep system in the K-G basin.

distributed-type gas hydrate bearing intervals (G1, G2, G2) (**Table 1**). It may also be possible that formation of authigenic carbonate layers coupled with clay deposits restricted the upward migrating methane and led to the formation of distributed-type hydrate deposits. The distributed gas hydrate deposits build a closed system, which prevented the completion of pyritization process and thus, favored the formation and preservation of SP size greigite.

Evolution of Active Cold Seep System in Krishna-Godavari Basin: Constraints From Rock Magnetic, Microscopy and Mineralogical Proxies

We propose a plausible mechanism to explain the various features of an active cold seep system associated with shallow gas hydrates in the K-G basin (**Figure 11**). At active seep site, early diagenesis of magnetic minerals occurs very close to the sediment-water interface resulting in dissolution of primary detrital iron oxides and subsequent conversion to iron sulfides (pyrite). Distinct drop in concentration-dependent magnetic parameters manifested by the presence of diagenetically formed pyrite between 3 - 5 cmbsf represent the top-most dissolution front (recent) and can be attributed to the intense pyritization fueled by AOM-coupled sulfate reduction and probably represent the depth of present-day SMTZ in core SSD-045/Stn-9/GC-01. A couple of sediment intervals (25–29 cmbsf and 43–52 cmbsf) also show marked depletion in magnetic susceptibility and abundant presence of pyrite grains suggesting at least two events of huge H_2S build up by intense methane seepage events. Presence of chemosynthetic shells (*Calyptogena* Sp.), authigenic carbonates at these intervals confirm the paleo-methane seepage at site Stn-9. The existence of low and uniform magnetic susceptibility in MZ-2 (except G1, G2, and G3) reflects intense reductive diagenesis fueled by the elevated methane supply, which allowed the production of large concentration of sulfide, and led to transformation of primary iron-bearing magnetic minerals into paramagnetic pyrite. Repeated occurences of authigenic carbonates from 45 to 219 cmbsf in core SSD-045/Stn-9/GC-01 support multiple episodes of AOM intensification in the past. The opening/closing of fault/fractures due to neo-tectonic activities allowed migration of methane from deep-seated gas reservoir (Dewangan et al., 2011; Sriram et al., 2013; Dewangan et al., 2020; Mazumdar et al., 2019). Upon entering the shallow depths and encountering conducive P-T conditions, gas hydrates started crystallizing within the faults and fractures where methane concentration exceeded the solubility limit (You et al., 2019). We propose that the distributed-type gas hydrate formed in veins during periods of reduced methane flux at clay rich intervals (G1, G2, G3) arrested the pyritization process and favored the preservation of the intermediate iron sulfides minerals (greigite/pyrrhotite) (Larrasoaña et al., 2007).

High magnetic susceptibility in the bottom most sediment interval containing massive gas hydrate deposit (MZ-3) can be attributed to the survival of detrital magnetic grains due to both hinderance of diagenetic reactions due to trapping of H_2S within hydrate (Housen and Musgrave, 1996; Riedinger et al., 2005) and rapid burial and preservation of the detrital magnetic grains due to higher sedimentation events (Badesab et al., 2019). Such gas hydrates requires efficient methane migration from deep-seated reservoir through the fracture system as evident from the existence of seismic chimneys beneath this site (Dewangan et al., 2020). Some active faults may even transport methane to seafloor, which is observed as methane gas flares (Mazumdar et al., 2019).

CONCLUSION

Rock magnetic, sedimentological and mineralogical record of the sediment core SSD-045/Stn-9/GC-01 retrieved from a newly discovered active methane seep site in the K-G basin provided important constraints on the evolution of past methane seepage dynamics and gas hydrate formation over geologic time. Two events of intense methane seepage were identified in the studied core. Occurences of several layers of authigenic carbonates throughout the core followed by the presence of chemosynthetic shells (*Calyptogena* Sp.) at two distinct sediment depth intervals provided clues on the episodic intensification of AOM at the studied site. Three greigite bearing sediment intervals within the magnetically reduced sulfidic zone reflect the paleo-gas hydrate (distributed-type vein filling) intervals in the studied core. A linkage between increase clay content, formation of veined hydrate deposits, precipitation of authigenic carbonates and greigite preservation is evident. Our findings are summarized into a conceptual model (**Figure 11**) which explains the controls on the magnetic mineral diagenesis, methane seepage dynamics, and the evolution of shallow gas hydrate (distributed vein filling vs. massive-type) system in the K-G basin.

DATA AVAILABILITY STATEMENT

The datasets presented in this study can be found in online repositories. The names of the repository/repositories and accession number(s) can be found below: https://publication-data.nio.org/s/9DdiMtsnJGG7dTQ.

AUTHOR CONTRIBUTIONS

FB and PD developed the concept for the manuscript. PD and VG have contributed toward sediment core collection and sampling during the research expedition (SSD-045) onboard R/V Sindhu Sadhana. Analyses were performed by VG and FB. All authors contributed equally to the writing and editing of the manuscript and preparation of figures and table.

FUNDING

This work is a contribution to the GAP-2303 research project "Studies on Gas Hydrate Exploration and Technology Development for its exploitation" supported by Ministry of Earth Sciences. Govt. of India. Research visit of FB to Center for Advanced Marine Core Research (CMCR), Kochi University, Japan for carrying our specialized rock magnetic analyses at Paleomagnetic Laboratory were supported by DST-JSPS under the scheme JSPS Postdoctoral Fellowship for Overseas Researchers (Strategic Program; JSPS grant GR 17202) and Establishment of Young Researcher Fellowship Program 2017–2018 (IA/Indo-Japanese/F-1/2018) scheme awarded to FB.

ACKNOWLEDGMENTS

We thank the Director, CSIR–NIO, Secretary, MOES, and National Gas Hydrate Program (NGHP) for supporting this study. Aninda Mazumdar and participants of scientific cruise SSD-045 onboard research vessel R/V Sindhu Sadhana of CSIR-NIO and ship cell team are thanked for providing assistance in geological and geophysical data acquisition. We thank the Director of the Center for Advanced Marine Core Research (CMCR), Kochi University, Japan for access to the Paleomagnetic laboratory during a research visit of Firoz Badesab as a part of INSA-JSPS fellowship. Special thanks to Myriam Kars for providing timely guidance and research support to Dr Firoz Badesab during the fellowship period. We thank Chisa Nishimori for providing laboratory and technical support in Kochi. Thanks to Girish Prabhu, Areef Sardar, Aiswarya PV for providing assistance with XRD and SEM-EDS analysis. This is CSIR-NIO publication no. 6626.

REFERENCES

Aharon, P., Schwarcz, H. P., and Roberts, H. H. (1997). Radiometric dating of submarine hydrocarbon seeps in the Gulf of Mexico. *Geol. Soc. Am. Bull.* 109 (5), 568–579. doi:10.1130/0016-7606(1997)109<0568:RDOSHS>2.3.CO;2

Aloisi, G., Pierre, C., Rouchy, J. M., Foucher, J. P., and Woodside, J. (2000). Methane-related authigenic carbonates of eastern Mediterranean Sea mud volcanoes and their possible relation to gas hydrate destabilisation. *Earth Planet. Sci. Lett.* 184 (1), 321–338. doi:10.1016/S0012-821X(00)00322-8

Amon, D. J., Gobin, J., Van Dover, C. L., Levin, L. A., Marsh, L., and Raineault, N. A. (2017). Characterization of methane-seep communities in a deep-sea area designated for oil and natural gas exploitation off Trinidad and Tobago. *Front. Mar. Sci.* 4, 342. doi:10.3389/fmars.2017.00342

Argentino, C., Lugli, F., Cipriani, A., Conti, S., and Fontana, D. (2019). A deep fluid source of radiogenic Sr and highly dynamic seepage conditions recorded in Miocene seep carbonates of the northern Apennines (Italy). *Chem. Geol.* 522, 135–147. doi:10.1016/j.chemgeo.2019.05.029

Badesab, F., Dewangan, P., Gaikwad, V., Kars, M., Kocherla, M., Krishna, K. S., et al. (2019). Magnetic mineralogical approach for the exploration of gas hydrates in the Bay of Bengal. *J. Geophys. Res. Solid Earth.* 124, 4428–4451. doi:10.1029/2019JB01746

Bastia, R. (2007). *Geologic settings and petroleum systems of India's east coast offshore basins: concepts and applications*. Bangalore, India: Tech. Pub.

Bayon, G., Dupré, S., Ponzevera, E., Etoubleau, J., Chéron, S., Pierre, C., et al. (2013). Formation of carbonate chimneys in the Mediterranean Sea linked to deep-water oxygen depletion. *Nat. Geosci.* 6 (9), 755–760. doi:10.1038/ngeo1888

Bayon, G., Henderson, G. M., Etoubleau, J., Caprais, J. C., Ruffine, L., Marsset, T., et al. (2015). U-Th isotope constraints on gas hydrate and pockmark dynamics at the Niger delta margin. *Mar. Geol.* 370, 87–98. doi:10.1016/j.margeo.2015.10.012

Berndt, C., Feseker, T., Treude, T., Krastel, S., Liebetrau, V., Niemann, H., et al. (2014). Temporal constraints on hydrate-controlled methane seepage off Svalbard. *Science.* 343 (6168), 284–287. doi:10.1126/science.1246298

Berner, R. A. (1967). Thermodynamic stability of sedimentary iron sulfides. *Am. J. Sci.* 265 (9), 773–785. doi:10.2475/ajs.265.9.773

Bian, Y., Feng, D., Roberts, H. H., and Chen, D. (2013). Tracing the evolution of seep fluids from authigenic carbonates: Green Canyon, northern Gulf of Mexico. *Mar. Petrol. Geol.* 44, 71–81. doi:10.1016/j.marpetgeo.2013.03.010

Biksham, G., and Subramanian, V. (1988). Sediment transport of the Godavari River basin and its controlling factors. *J. Hydrol.* 101 (1–4), 275–290. doi:10.1016/0022-1694(88)90040-6

Bloemendal, J., King, J. W., Hall, F. R., and Doh, S. J. (1992). Rock magnetism of late Neogene and Pleistocene deep-sea sediments: relationship to sediment source, diagenetic processes, and sediment lithology. *J Geophys. Res. Solid Earth.* 96, 4361–4375. doi:10.1029/91JB03068

Boetius, A., Ravenschlag, K., Schubert, C. J., Rickert, D., Widdel, F., Gieseke, A., et al. (2000). A marine microbial consortium apparently mediating anaerobic oxidation of methane. *Nature.* 407 (6804), 623–626. doi:10.1038/35036572

Bohrmann, G., Greinert, J., Suess, E., and Torres, M. (1998). Authigenic carbonates from the Cascadia subduction zone and their relation to gas hydrate stability. *Geology.* 26 (7), 647–650. doi:10.1130/0091-7613(1998)026<0647:ACFTCS>2.3.CO;2

Borowski, W. S., Paull, C. K., and Ussler, W., III (1996). Marine pore-water sulfate profiles indicate *in situ* methane flux from underlying gas hydrate. *Geology.* 24 (7), 655–658. doi:10.1130/0091-7613(1996)024<0655:MPWSPI>2.3.CO;2.

Chang, L., Heslop, D., Roberts, A. P., Rey, D., and Mohamed, K. J. (2016). Discrimination of biogenic and detrital magnetite through a double Verwey transition temperature. *J. Geophys. Res. Solid Earth.* 121, 3–14. doi:10.1002/2015JB012485

Chang, L., Roberts, A. P., Rowan, C. J., Tang, Y., Pruner, P., Chen, Q., et al. (2009). Low-temperature magnetic properties of greigite (Fe3S4). *Geochem. Geophys. Geosys.* 10, Q01Y04. doi:10.1029/2008GC002276

Choudhuri, M., Guha, D., Dutta, A., Sinha, S., and Sinha, N. (2010). "Spatio-temporal variations and kinematics of shale mobility in the Krishna-Godavari basin, India," in AAPG Hedberg Conference, Port of Spain,Trinidad and Tobago, June 5–7, 2006.

Chuvilin, E., Bukhanov, B., Davletshina, D., Grebenkin, S., and Istomin, V. (2018). Dissociation and self-preservation of gas hydrates in permafrost. *Geosciences.* 8 (12), 431. doi:10.3390/geosciences8120431

Clennell, M. B., Hovland, M., Booth, P. H., and Winters, W. J. (1999). Formation of natural gas hydrates in marine sediments: 1. Conceptual model of gas hydrate growth conditioned by host sediment properties. *J. Geophys. Res. Solid Earth.* 104 (B10), 22985–22003. doi:10.1029/1999JB900175

Collett, T., Riedel, M., Cochran, J. R., Boswell, R., Presley, J., Kumar, P., et al. (2008). Indian national gas hydrate Program, expedition - 01, initial report. India: Directorate General of Hydrocarbons, Ministry of Petroleum and Natural Gas.

Crémière, A., Chand, S., Sahy, D., Thorsnes, T., Martma, T., Noble, S. R., et al. (2018). Structural controls on seepage of thermogenic and microbial methane since the last glacial maximum in the Harstad Basin, southwest Barents Sea. *Mar. Petrol. Geol.* 98, 569–581. doi:10.1016/j.marpetgeo.2018.07.010

Crémière, A., Lepland, A., Chand, S., Sahy, D., Condon, D. J., Noble, S. R., et al. (2016). Timescales of methane seepage on the Norwegian margin following collapse of the Scandinavian Ice Sheet. *Nat. Commun.* 7 (1), 1–10. doi:10.1038/ncomms11509

Dela Pierre, F., Martire, L., Natalicchio, M., Clari, P., and Petrea, C. (2010). Authigenic carbonates in Upper Miocene sediments of the Tertiary Piedmont Basin (NW Italy): vestiges of an ancient gas hydrate stability zone? *Geol. Soc. Am. Bull.* 122 (7–8), 994–1010. doi:10.1130/B30026.1

Dewangan, P., Basavaiah, N., Badesab, F. K., Usapkar, A., Mazumdar, A., Joshi, R., et al. (2013). Diagenesis of magnetic minerals in a gas hydrate/cold seep environment off the Krishna–Godavari basin, Bay of Bengal. *Mar. Geol.* 340, 57–70. doi:10.1016/j.margeo.2013.04.016

Dewangan, P., Ramprasad, T., Ramana, M. V., Mazumdar, A., Desa, M., and Badesab, F. K. (2010). Seabed morphology and gas venting features in the continental slope region of Krishna-Godavari basin, Bay of Bengal: implications in gas-hydrate exploration. *Mar. Petrol. Geol.* 27 (7), 1628–1641. doi:10.1016/j.marpetgeo.2010.03.015

Dewangan, P., Sriram, G., Kumar, A., Mazumdar, A., Peketi, A., Mahale, V. P., et al. (2020). Widespread occurrence of methane seeps in deep-water regions of Krishna-Godavari basin, Bay of Bengal. *Mar. Petrol. Geol., In Press, Journal Pre-proof.* doi:10.1016/j.marpetgeo.2020.104783

Dewangan, P., Sriram, G., Ramprasad, T., Ramana, M. V., and Jaiswal, P. (2011). Fault system and thermal regime in the vicinity of site NGHP-01-10, Krishna–Godavari basin, Bay of Bengal. *Mar. Petrol. Geol.* 28, 1899–1914. doi:10.1016/j.marpetgeo.2011.03.009

Dickens, G. R. (2001). Sulfate profiles and barium fronts in sediment on the Blake Ridge: present and past methane fluxes through a large gas hydrate reservoir. *Geochem. Cosmochim. Acta.* 65 (4), 529–543. doi:10.1016/S0016-7037(00)00556-1

Dillon, M., and Bleil, U. (2006). Rock magnetic signatures in diagenetically altered sediments from the Niger deep-sea fan. *J. Geophys. Res. Solid Earth.* 111 (B3), B03105. doi:10.1029/2004JB003540

Egeberg, P. K., and Dickens, G. R. (1999). Thermodynamic and pore water halogen constraints on gas hydrate distribution at ODP Site 997 (Blake Ridge). *Chem. Geol.* 153 (1), 53–79. doi:10.1016/S0009-2541(98)00152-1

Feng, D., and Chen, D. (2015). Authigenic carbonates from an active cold seep of the northern South China Sea: new insights into fluid sources and past seepage activity. *Deep Sea Res. II.* 122, 74–83. doi:10.1016/j.dsr2.2015.02.003

Garming, J. F. L., Bleil, U., and Riedinger, N. (2005). Alteration of magnetic mineralogy at the sulfate–methane transition: analysis of sediments from the Argentine continental slope. *Phys. Earth Planet. In.* 151 (3–4), 290–308. doi:10.1016/j.pepi.2005.04.001

Geersen, J., Scholz, F., Linke, P., Schmidt, M., Lange, D., Behrmann, J. H., et al. (2016). Fault zone controlled seafloor methane seepage in the rupture area of the 2010 M aule earthquake, Central Chile. *Geochem. Geophys. Geosys.* 17 (11), 4802–4813. doi:10.1002/2016GC006498

Ginsburg, G., Soloviev, V., Matveeva, T., and Andreeva, I. (2000). "24. Sediment grain-size control on gas hydrate presence, sites 994, 995 and 997," in Paper presented at the Proceedings of the Ocean Drilling Program, Scientific Results, College Station, TX.

Greinert, J., Bohrmann, G., and Suess, E. (2001). Gas hydrate-associated carbonates and methane-venting at Hydrate Ridge: classification, distribution and origin of authigenic lithologies. *AGU.* 124, 99–114. doi:10.1029/GM124p0099

Gullapalli, S., Dewangan, P., Kumar, A., Dakara, G., and Mishra, C. K. (2019). Seismic evidence of free gas migration through the gas hydrate stability zone (GHSZ) and active methane seep in Krishna-Godavari offshore basin. *Mar. Petrol. Geol.* 110, 695–705. doi:10.1016/j.marpetgeo.2019.07.052

Han, X., Suess, E., Liebetrau, V., Eisenhauer, A., and Huang, Y. (2014). Past methane release events and environmental conditions at the upper continental slope of the South China Sea: constraints by seep carbonates. *Int. J. Earth Sci.* 103 (7), 1873–1887. doi:10.1007/s00531-014-1018-5

Handwerger, A. L., Rempel, A. W., and Skarbek, R. M. (2017). Submarine landslides triggered by destabilization of high-saturation hydrate anomalies. *Geochem. Geophys. Geosys.* 18 (7), 2429–2445. doi:10.1002/2016GC006706

Haq, B. U. (1998). Natural gas hydrates: searching for the long-term climatic and slope-stability records. *Geol. Soc. Spec. Publ.* 137 (1), 303–318. doi:10.1144/GSL.SP.1998.137.01.24

Harrison, R. J., and Feinberg, J. M. (2008). FORCinel: an improved algorithm for calculating first order reversal curve distributions using locally weighted regression smoothing. *Geochem. Geophys. Geosys.* 9, Q05016. doi:10.1029/2008GC001987

Henriet, J. P., De Mol, B., Pillen, S. T., Vanneste, M., Van Rooij, D., Versteeg, W., et al. (1998). Gas hydrate crystals may help build reefs. *Nature.* 391 (6668), 648–649. doi:10.1038/35530

Hirt, A. M., Lowrie, W., Clendenen, W. S., and Kligfield, R. (1993). Correlation of strain and the anisotropy of magnetic susceptibility in the Onaping Formation: evidence for a near-circular origin of the Sudbury basin. *Tectonophysics.* 225 (4), 231–254. doi:10.1016/0040-1951(93)90300-9

Horng, C. S. (2018). Unusual magnetic properties of sedimentary pyrrhotite in methane-seepage sediments: comparison with metamorphic pyrrhotite and sedimentary greigite. *J. Geophys. Res. Solid Earth.* 123, 4601–4617. doi:10.1002/2017JB015262

Housen, B. A., and Moskowitz, B. M. (2006). Depth distribution of magnetofossils in near-surface sediments from the Blake/Bahama Outer Ridge, western North Atlantic Ocean, determined by low-temperature magnetism. *J. Geophys. Res Biogeo.* 111, G01005. doi:10.1029/2005JG000068

Housen, B. A., and Musgrave, R. J. (1996). Rock-magnetic signature of gas hydrates in accretionary prism sediments. *Earth Planet. Sci. Lett.* 139 (3–4), 509–519. doi:10.1016/0012-821X(95)00245-8

Hu, Y., Luo, M., Liang, Q., Chen, L., Feng, D., Yang, S., et al. (2019). Pore fluid compositions and inferred fluid flow patterns at the Haima cold seeps of the South China Sea. *Mar. Petrol. Geol.* 103, 29–40. doi:10.1016/j.marpetgeo.2019.01.007

Jørgensen, B. B., Böttcher, M. E., Lüschen, H., Neretin, L. N., and Volkov, I. I. (2004). Anaerobic methane oxidation and a deep H_2S sink generate isotopically heavy sulfides in Black Sea sediments. *Geochim. Cosmochim. Acta.* 68 (9), 2095–2118. doi:10.1016/j.gca.2003.07.017

Kao, S. J., Horng, C. S., Roberts, A. P., and Liu, K. K. (2004). Carbon–sulfur–iron relationships in sedimentary rocks from southwestern Taiwan: influence of geochemical environment on greigite and pyrrhotite formation. *Chem. Geol.* 203 (1–2), 153–168. doi:10.1016/j.chemgeo.2003.09.007

Karlin, R., and Levi, S. (1983). Diagenesis of magnetic minerals in recent haemipelagic sediments. *Nature.* 303 (5915), 327. doi:10.1038/303327a0

Kars, M., and Kodama, K. (2015). Rock magnetic characterization of ferrimagnetic iron sulfides in gas hydrate-bearing marine sediments at Site C0008, Nankai Trough, Pacific Ocean, off-coast Japan. *Earth Planets Space.* 67 (1), 118. doi:10.1186/s40623-015-0287-y

Kasten, S., Freudenthal, T., Gingele, F. X., and Schulz, H. D. (1998). Simultaneous formation of iron-rich layers at different redox boundaries in sediments of the Amazon deep-sea fan. *Geochim. Cosmochim. Acta.* 62, 2253–2264. doi:10.1016/S0016-7037(98)00093-3

Kasten, S., Zabel, M., Heuer, V., and Hensen, C. (2003). "Processes and signals of nonsteady-state diagenesis in deep-sea sediments and their pore waters," in *The South Atlantic in the late quaternary.* (Berlin, Heidelberg: Springer), 431–459. doi:10.1016/j.gca.2007.08.019

Kocherla, M., Teichert, B. M. A., Pillai, S., Satyanarayanan, M., Ramamurty, P. B., Patil, D. J., et al. (2015). Formation of methane-related authigenic carbonates in a highly dynamic biogeochemical system in the Krishna–Godavari Basin, Bay of Bengal. *Mar. Petrol. Geol.* 64, 324–333. doi:10.1016/j.marpetgeo.2015.02.034

Larrasoaña, J. C., Roberts, A. P., Musgrave, R. J., Gràcia, E., Piñero, E., Vega, M., et al. (2007). Diagenetic formation of greigite and pyrrhotite in gas hydrate marine sedimentary systems. *Earth Planet Sci. Lett.* 261 (3–4), 350–366. doi:10.1016/j.epsl.2007.06.032

Lascu, I., Einsle, J. F., Ball, M. R., and Harrison, R. J. (2018). The vortex state in geologicmaterials: a micromagnetic perspective. *J. Geophys. Res. Solid Earth.* 123, 7285–7304. doi:10.1029/2018JB015909

Levin, L. A., Baco, A. R., Bowden, D. A., Colaco, A., Cordes, E. E., Cunha, M. R., et al. (2016). Hydrothermal vents and methane seeps: rethinking the sphere of influence. *Front. Mar. Sci.* 3, 72. doi:10.3389/fmars.2016.00072

Liang, Q., Hu, Y., Feng, D., Peckmann, J., Chen, L., Yang, S., et al. (2017). Authigenic carbonates from newly discovered active cold seeps on the northwestern slope of the South China Sea: constraints on fluid sources, formation environments, and seepage dynamics. *Deep-Sea Res. I.* 124, 31–41. doi:10.1016/j.dsr.2017.04.015

Liu, J., Zhu, R., Roberts, A. P., Li, S., and Chang, J. H. (2004). High-resolution analysis of early diagenetic effects on magnetic minerals in post-middle-Holocene continental shelf sediments from the Korea Strait. *J. Geophys. Res. Solid Earth.* 109 (B3), B03130 (1-15). doi:10.1029/2003JB002813

Lorenson, T. (2000). "Microscopic character of marine sediment containing disseminated gas hydrate: examples from the Blake Ridge and the Middle America Trench," in *Gas hydrates: challenges for the future.* Editors G. D. Holder and P. R. Bishnoi (New York, NY: Academy of Sciences), Vol. 912, 189–194.

Maher, B. A. (1988). Magnetic properties of some synthetic sub-micron magnetites. *Geophys. J. Int.*, 94 (1), 83-96. doi:10.1111/j.1365-246X.1988.tb03429.x

Maher, B. A., and Thompson, R. (1999). *Quaternary climates, environments and magnetism.* Cambridge, UK: Cambridge University Press.

Mazumdar, A., Dewangan, P., Joäo, H. M., Peketi, A., Khosla, V. R., Kocherla, M., et al. (2009). Evidence of paleo–cold seep activity from the Bay of Bengal, offshore India. *Geochem. Geophys. Geosys.* 10, 10Q06005. doi:10.1029/2008GC002337

Mazumdar, A., Dewangan, P., Peketi, A., Gullapalli, S., Kalpana, M. S., Naik, G. P., et al. (2019). The first record of active methane (cold) seep ecosystem associated with shallow methane hydrate from the Indian EEZ. *J. Earth. Syst. Sci.* 128, 18. doi:10.1007/s12040-018-1044-y

Mazumdar, A., Dewangan, P., Peketi, A., Gullapalli, S., Sai PavanVolvoikar, S., et al. (2018). "Methane cold seep activity in the Indian EEZ: present is the key to the past."in Indian Geophysical Union, 55th Annual Convention on Changing Water Cycle and Water Resources, December 5–7, 2018, Bhopal: Rabindranath Tagore University.

Mazzini, A., Svensen, H., Hovland, M., and Planke, S. (2006). Comparison and implications from strikingly different authigenic carbonates in a Nyegga complex pockmark, G11, Norwegian Sea. *Mar. Geol.* 231 (1–4), 89–102. doi:10.1016/j.margeo.2006.05.012

Moskowitz, B. M., Frankel, R. B., and Bazylinski, D. A. (1993). Rock magnetic criteria for the detection of biogenic magnetite. *Earth Planet Sci. Lett.* 120 (3–4), 283–300. doi:10.1016/0012-821X(93)90245-5

Musgrave, R. J., Bangs, N. L., Larrasoaña, J. C., Gràcia, E., Hollamby, J. A., and Vega, M. E. (2006). Rise of the base of the gas hydrate zone since the last glacial recorded by rock magnetism. *Geology.* 34 (2), 117–120. doi:10.1130/G22008.1

Musgrave, R. J., Kars, M., and Vega, M. E. (2019). Progressive and punctuated magnetic mineral diagenesis: the rock magnetic record of multiple fluid inputs and progressive pyritization in a volcano-bounded basin, IODP site U1437, Izu rear arc. *J. Geophys. Res. Solid Earth.* 124 (6), 5357–5378. doi:10.1029/2018JB017277

Muxworthy, A. R., and Dunlop, D. J. (2002). First-order reversal curve (FORC) diagrams for pseudo-single-domain magnetites at high temperature. *Earth Planet Sci. Lett.* 203 (1), 369–382. doi:10.1016/S0012-821X(02)00880-4

Muxworthy, A. R., and McClelland, E. (2000). Review of the low-temperature magnetic properties of magnetite from a rock magnetic perspective. *Geophys. J. Int.* 140 (1), 101–114. doi:10.1046/j.1365-246x.2000.00999.x

Naehr, T. H., Rodriguez, N. M., Bohrmann, G., Paull, C. K., and Botz, R. (2000). "29. Methanederived authigenic carbonates associated with gas hydrate decomposition and fluid venting above the Blake Ridge Diapir," in Proceedings of the Ocean Drilling Program, Scientific Results, Vol. 164, 285–300.

Neretin, L. N., Böttcher, M. E., Jørgensen, B. B., Volkov, I. I., Lüschen, H., and Hilgenfeldt, K. (2004). Pyritization processes and greigite formation in the advancing sulfidization front in the upper Pleistocene sediments of the Black Sea 1. *Geochim. Cosmochim. Acta.* 68 (9), 2081–2093. doi:10.1016/S0016-7037(03)00450-2

Nowaczyk, N. R., Arz, H. W., Frank, U., Kind, J., and Plessen, B. (2012). Dynamics of the laschamp geomagnetic excursion from black sea sediments. *Earth Planet. Sc. Lett.* 351–352, 54–69. doi:10.1016/j.epsl.2012.06.050

Özdemir, Ö., and Dunlop, D. J. (1997). Effect of crystal defects and internal stress on the domain structure and magnetic properties of magnetite. *J. Geophys. Res. Solid Earth.* 102 (B9), 20211–20224. doi:10.1029/97JB01779

Özdemir, Ö., Dunlop, D. J., and Moskowitz, B. M. (2002). Changes in remanence, coercivity and domain state at low temperature in magnetite. *Earth Planet Sci. Lett.* 194 (3–4), 343–358. doi:10.1016/S0012-821X(01)00562-3

Passier, H. D., De Lange, G. J., and Dekkers, M. J. (2001). Magnetic properties and geochemistry of the active oxidation front and the youngest sapropel in the eastern Mediterranean Sea. *Geophys. J. Int.* 145 (3), 604–614. doi:10.1046/j.0956-540x.2001.01394.x

Passier, H. F., Dekkers, M. J., and de Lange, G. J. (1998). Sediment chemistry and magnetic properties in an anomalously reducing core from the eastern Mediterranean Sea. *Chem. Geol.* 152 (3–4), 287–306. doi:10.1016/S0009-2541(98)00121-1

Passier, H. F., and Dekkers, M. J. (2002). Iron oxide formation in the active oxidation front above sapropel S1 in the eastern Mediterranean Sea as derived from low-temperature magnetism. *Geophys. J. Int.* 150 (1), 230–240. doi:10.1046/j.1365-246X.2002.01704.x

Peketi, A., Mazumdar, A., Joshi, R. K., Patil, D. J., Srinivas, P. L., and Dayal, A. M. (2012). Tracing the paleo sulfate–methane transition zones and H_2S seepage events in marine sediments: an application of C-S-Mo systematic. *Geochem. Geophys. Geosys.* 13, Q10007. doi:10.1029/2012GC004288

Peters, C., and Dekkers, M. J. (2003). Selected room temperature magnetic parameters as a function of mineralogy, concentration and grain size. *Phys Chem Earth A/B/C.* 28 (16–19), 659–667. doi:10.1016/S1474-7065(03)00120-7

Peters, C., and Thompson, R. (1998). Magnetic identification of selected natural iron oxides and sulphides. *J. Magn. Magn. Mater.* 183 (3), 365–374. doi:10.1016/S0304-8853(97)01097-4

Petersen, N., Von Dobeneck, T., and Vali, H. (1986). Fossil bacterial magnetite in deep-sea sediments from the South Atlantic Ocean. *Nature.* 320, 611–615. doi:10.1038/320611a0

Philips, S. C. (2018). Diagenetic degradation of paleoenvironmental signals in magnetic susceptibility in the northern Bay of Bengal. *IRM Quart.* 27 (4).

Pierre, C., and Fouquet, Y. (2007). Authigenic carbonates from methane seeps of the Congo deep-sea fan. *Geo Mar. Lett.* 27 (2–4), 249–257. doi:10.1007/s00367-007-0081-3

Pike, C. R., Roberts, A. P., and Verosub, K. L. (1999). Characterizing interactions in fine magnetic particle systems using first order reversal curves. *J. Appl. Phys.* 85 (9), 6660–6667. doi:10.1063/1.370176

Powell, C. M., Roots, S. R., and Veevers, J. J. (1988). Pre-breakup continental extension in East Gondwanaland and the early opening of the eastern Indian Ocean. *Tectonophysics.* 155, 261–283. doi:10.1016/0040-1951(88)90269-7

Prabhakar, K. N., and Zutshi, P. L. (1993). Evolution of southern part of Indian East Coast basin. *J. Geol. Soc. India.* 41, 215–230.

Ramesh, R., and Subramanian, V. (1988). Temporal, spatial and size variation in the sediment transport in the Krishna River basin, India. *J Hydrol.* 98, 53–65. doi:10.1016/0022-1694(88)90205-3

Rao, G. N., and Mani, K. S. (1993). A study on generation of abnormal formation pressures in Krishna-Godavari Basin, India. *Indian J. Pet. geol.* 2, 20–30.

Rao, G. N. (2001). Sedimentation, stratigraphy, and petroleum potential of Krishna-Godavari basin, east coast of India. *Am. Assoc. Pet. Geol. Bull.* 85 (9), 1623–1643. doi:10.1306/8626CCDF-173B-11D7-8645000102C1865D

Rao, V. P. (1991). Clay mineral distribution in the continental shelf sediments from Krishna to Ganges river mouth, east coast of India. *Indian J. Mar. Sci.* 20, 7–12.

Rees, E. V. L., Priest, J. A., and Clayton, C. R. I. (2011). The structure of methane gas hydrate bearing sediments from the Krishna-Godavari Basin as seen from micro-CT scanning. *Mar. Petrol. Geol.* 28 (7), 1283–1293. doi:10.1016/j.marpetgeo.2011.03.015

Riedinger, N., Pfeifer, K., Kasten, S., Garming, J. F. L., Vogt, C., and Hensen, C. (2005). Diagenetic alteration of magnetic signals by anaerobic oxidation of methane related to a change in sedimentation rate. *Geochim. Cosmochim. Acta.* 69 (16), 4117–4126. doi:10.1016/j.gca.2005.02.004

Roberts, A. P., Almeida, T. P., Church, N. S., Harrison, R. J., Heslop, D., Li, Y., et al. (2017). Resolving the origin of pseudo-single domain magnetic behavior. *J. Geophys. Res. Solid Earth.* 122, 9534–9558. doi:10.1002/2017JB014860

Roberts, A. P., Chang, L., Rowan, C. J., Horng, C. S., and Florindo, F. (2011). Magnetic properties of sedimentary greigite (Fe_3S_4): an update. *Rev. Geophys.* 49, RG1002. doi:10.1029/2010RG000336

Roberts, A. P. (2015). Magnetic mineral diagenesis. *Earth Sci. Rev.* 151, 1–47. doi:10.1016/j.earscirev.2015.09.010

Roberts, A. P. (1995). Magnetic properties of sedimentary greigite (Fe_3S_4). *Earth Planet. Sci. Lett.* 134 (3), 227–236. doi:10.1016/0012-821X(95)00131-U

Roberts, A. P., Pike, C. R., and Verosub, K. L. (2000). First-order reversal curve diagrams: a new tool for characterizing the magnetic properties of natural samples. *J. Geophys. Res. Solid Earth.* 105 (B12), 28461–28475. doi:10.1029/2000JB900326

Roberts, A. P., Stoner, J. S., and Richter, C. (1999). Diagenetic magnetic enhancement of sapropels from the eastern Mediterranean Sea. *Mar. Geol.* 153 (1-4), 103-116. doi:10.1016/S0025-3227(98)00087-5

Roberts, A. P., Zhao, X., Harrison, R. J., Heslop, D., Muxworthy, A. R., Rowan, C. J., et al. (2018). Signatures of reductive magnetic mineral diagenesis from unmixing of first order reversal curves. *J. Geophys. Res. Solid Earth.* 123, 4500–4522. doi:10.1029/2018JB015706

Rowan, C. J., Roberts, A. P., and Broadbent, T. (2009). Reductive diagenesis, magnetite dissolution, greigite growth and paleomagnetic smoothing in marine sediments: a new view. *Earth Planet Sci. Lett.* 277 (1–2), 223–235. doi:10.1016/j.epsl.2008.10.016

Rowan, C. J., and Roberts, A. P. (2006). Magnetite dissolution, diachronous greigite formation, and secondary magnetizations from pyrite oxidation: unravelling complex magnetizations in Neogene marine sediments from New Zealand. *Earth Planet Sci. Lett.* 241 (1–2), 119–137. doi:10.1016/j.epsl.2005.10.017

Sahling, H., Römer, M., Pape, T., Bergès, B., dos Santos Fereirra, C., Boelmann, J., et al. (2014). Gas emissions at the continental margin west of Svalbard: mapping, sampling, and quantification. *Biogeosciences.* 11 (21), 6029–6046. doi:10.5194/bg-11-6029-2014

Sangode, S. J., Sinha, R., Phartiyal, B., Chauhan, O. S., Mazari, R. K., Bagati, T. N., et al. (2007). Environmental magnetic studies on some quaternary sediments of varied depositional settings in the Indian sub-continent. *Quat. Int.* 159, 102–118. doi:10.1016/j.quaint.2006.08.015

Schneider, A., Panieri, G., Lepland, A., Consolaro, C., Crémière, A., Forwick, M., et al. (2018). Methane seepage at Vestnesa Ridge (NW Svalbard) since the last glacial maximum. *Quat. Sci. Rev.* 193, 98–117. doi:10.1016/j.quascirev.2018.06.006

Sellanes, J., and Krylova, E. (2005). A new species of *Calyptogena* (Bivalvia: Vesicomyidae) from a recently discovered methane seepage area off Concepción Bay, Chile (~ 36 S). *J. Mar. Biolog. Assoc. U.K.* 85 (4), 969–976. doi:10.1017/S0025315405011963

Singha, D. K., and Chatterjee, R. (2014). Detection of overpressure zones and a statistical model for pore pressure estimation from well logs in the Krishna-Godavari Basin, India. *Geochem. Geophys. Geosys.* 15 (4), 1009–1020. doi:10.1002/2013GC005162

Snowball, I., and Thompson, R. (1990). A stable chemical remanence in Holocene sediments. *J. Geophys. Res. Solid Earth.* 95, 4471–4479. doi:10.1029/JB095iB04p04471

Snyder, G. T., Hiruta, A., Matsumoto, R., Dickens, G. R., Tomaru, H., Takeuchi, R., et al. (2007). Pore water profiles and authigenic mineralization in shallow marine sediments above the methane-charged system on Umitaka Spur, Japan Sea. *Deep-Sea Res. II.* 54 (11–13), 1216–1239. doi:10.1016/j.dsr2.2007.04.001

Sriram, G., Dewangan, P., Kumar, A., Mazumdar, A., Peketi, A., and Mahale, V. P. (2020). "Structural control on the methane seeps and shallow gas hydrate deposits in Krishna – Godavari Basin, Bay of Bengal," in 36th International Geological Congress, November 9–14, 2020.

Sriram, G., Dewangan, P., Ramprasad, T., and Rama Rao, P. (2013). Anisotropic amplitude variation of the bottom-simulating reflector beneath fracture-filled gas hydrate deposit. *J. Geophys. Res. Solid Earth.* 118 (5), 2258–2274. doi:10.1002/jgrb.50176

Suess, E. (2014). Marine cold seeps and their manifestations: geological control, biogeochemical criteria and environmental conditions. *Int. J. Earth Sci.* 103 (7), 1889–1916. doi:10.1007/s00531-014-1010-0

Sultan, N., Cochonat, P., Foucher, J. P., and Mienert, J. (2004). Effect of gas hydrates melting on seafloor slope instability. *Mar. Geol.* 213 (1), 379–401. doi:10.1016/j.margeo.2004.10.015

Tarduno, J. A., Sager, W. W., and Nogi, Y. (1995). "Early cretaceous magnetostratigraphy and paleolatitudes from the mid-pacific mountains: preliminary results bearing on guyot formation and pacific plate translation," in *Proc. ODP, Sci. Results*. Editors E. L. Winterer, W. W. Sager, J. V. Firth, and J. M. Sinton (College Station, TX: Ocean Drilling Program), Vol. 143, 395–398.

Tarduno, J. A. (1995). Superparamagnetism and reduction diagenesis in pelagic sediments: enhancement or depletion? *Geophys. Res. Lett.* 22 (11), 1337–1340. doi:10.1029/95GL00888

Teichert, B. M. A., and Luppold, F. W. (2013). Glendonites from an Early Jurassic methane seep-Climate or methane indicators? *Palaeogeogr. Palaeoclimatol. Palaeoecol.* 390, 81–93. doi:10.1016/j.palaeo.2013.03.001

Tong, H., Feng, D., Cheng, H., Yang, S., Wang, H., Min, A. G., et al. (2013). Authigenic carbonates from seeps on the northern continental slope of the South China Sea: new insights into fluid sources and geochronology. *Mar. Petrol. Geol.* 43, 260–271. doi:10.1016/j.marpetgeo.2013.01.011

Torres, M. E., McManus, J., Hammond, D. E., De Angelis, M. A., Heeschen, K. U., Colbert, S. L., et al. (2002). Fluid and chemical fluxes in and out of sediments hosting methane hydrate deposits on Hydrate Ridge, OR, I: hydrological provinces. *Earth Planet Sci. Lett.* 201 (3–4), 525–540. doi:10.1016/S0012-821X(02)00733-1

Torres, M. E., Trehu, A. M., Cespedes, N., Kastner, M., Wortmann, U. G., Kim, J. H., et al. (2008). Methane hydrate formation in turbidite sediments of northern Cascadia, IODP Expedition 311. *Earth Planet Sci. Lett.* 271, 170–180. doi:10.1016/j.epsl.2008.03.061

Usapkar, A., Dewangan, P., Kocherla, M., Ramprasad, T., Mazumdar, A., and Ramana, M. V. (2014). Enhanced methane flux event and sediment dispersal pattern in the Krishna–Godavari offshore basin: evidences from rock magnetic techniques. *Mar. Petrol. Geol.* 58, 461–475. doi:10.1016/j.marpetgeo.2014.08.008

Vadakkepuliyambatta, S., Bünz, S., Mienert, J., and Chand, S. (2013). Distribution of subsurface fluid-flow systems in the SW Barents Sea. *Mar. Petrol. Geol.* 43, 208–221. doi:10.1016/j.marpetgeo.2013.02.007

Verwey, E. J. W. (1939). Electronic conduction of magnetite (Fe_3O_4) and its transition point at low temperatures. *Nature.* 144 (3642), 327. doi:10.1038/144327b0

Vogt, P. R., and Jung, W. Y. (2002). Holocene mass wasting on upper non-Polar continental slopes—due to post-Glacial ocean warming and hydrate dissociation? *Geophy. Res. Lett.* 29 (9), 55–61. doi:10.1029/2001GL013488

Weinberger, J. L., and Brown, K. M. (2006). Fracture networks and hydrate distribution at Hydrate Ridge, Oregon. *Earth Planet Sci. Lett.* 245, 123–136. doi:10.1016/j.epsl.2006.03.012

Wellsbury, P., Goodman, K., Cragg, B. A., and Parkes, R. J. (2000). "The geomicrobiology of deep marine sediments from Blake Ridge containing methane hydrate (Sites 994, 995 and 997)," in Proceedings of the Ocean drilling program, Scientific results, College Station, TX: ODP, Vol. 164, 379–391. doi:10.1029/2001GL013488

Wilkin, R. T., and Barnes, H. L. (1997). Formation processes of framboidal pyrite. *Geochim. Cosmochim. Acta.* 61 (2), 323–339. doi:10.1016/S0016-7037(96)00320-1

Yao, H., Hong, W. L., Panieri, G., Sauer, S., Torres, M. E., Lehmann, M. F., et al. (2019). Fracture-controlled fluid transport supports microbial methane-oxidizing communities at Vestnesa Ridge. *Biogeosciences.* 16, 2221–2232. doi:10.5194/bg-16-2221-2019

You, K., Flemings, P. B., Malinverno, A., Collett, T. S., and Darnell, K. (2019). Mechanisms of methane hydrate formation in geological systems. *Rev. Geophys.* 57 (4), 1146–1196. doi:10.1029/2018RG000638

Conflict of Interest: The authors declare that the research was conducted in the absence of any commercial or financial relationships that could be construed as a potential conflict of interest.

frontiers in Earth Science

ORIGINAL RESEARCH
published: 07 December 2020
doi: 10.3389/feart.2020.601415

Post-Depositional Fluid Flow in Jurassic Sandstones of the Uncompahgre Uplift: Insights From Magnetic Fabrics

John I. Ejembi[1]*, *Eric C. Ferré*[2], *Sara Satolli*[3] and *Sarah A. Friedman*[4]

[1]Department of Geology, Southern Illinois University, Carbondale, IL, United States, [2]School of Geosciences, University of Louisiana at Lafayette, Lafayette, LA, United States, [3]Department of Engineering and Geology, University "G. d'Annunzio", Chieti-Pescara, Italy, [4]Department of Biological and Physical Sciences, Montana State University Billings, Billings, MT, United States

The anisotropy of magnetic susceptibility (AMS) in sedimentary rocks results from depositional, diagenetic, syn- and post-sedimentary processes that affect magnetic grains. Some studies have also shown the potential role played by post-depositional fluid flow in detrital and carbonate formations. Here we present a new case study of Middle-Upper Jurassic sandstones where secondary iron oxides, precipitated from fluids that migrated through pores, give rise to the AMS. These sandstones are well exposed in the Uncompahgre Uplift region of the Central Colorado Trough, Colorado. The magnetic foliation of these undeformed, subhorizontal strata consistently strike NE-SW over a large distance with an average 45° dip to the SE. This steep AMS fabric is oblique with respect to the regional subhorizontal bedding and therefore does not reflect the primary sedimentary fabric. Also, outcrop-scale and microscopic observations show a lack of post-depositional plastic (undulose extinction) or pressure-solution (stylolites) deformation microstructures in these sandstones, hence precluding a tectonic origin. The combination of magnetic hysteresis, isothermal remanent magnetization, and thermal demagnetization of the natural remanent magnetization indicate that these rocks carry a chemical remanent magnetization born primarily by hematite and goethite. High-field magnetic hysteresis and electron microscopy indicate that detrital magnetite and authigenic hematite are the main contributors to the AMS. These results show that post-depositional iron remobilization through these porous sandstones took place due to the action of percolating fluids which may have started as early as Late Cretaceous along with the Uncompahgre Uplift. The AMS fabric of porous sandstones does not systematically represent depositional or deformation processes, and caution is urged in the interpretation of magnetic fabrics in these types of reservoir rock. Conversely, understanding these fabrics may advance our knowledge of fluid flow in porous sandstones and may have applications in hydrocarbon exploration.

Keywords: anisotropy of magnetic susceptibility, fluid flow, Jurassic, Uncompahgre uplift, central Colorado, sediment

OPEN ACCESS

Edited by:
Yohan Guyodo, UMR7154 Institut de Physique du Globe de Paris (IPGP), France

Reviewed by:
Martin Chadima, Academy of Sciences of the Czech Republic (ASCR), Czechia
Bjarne Sven Gustav Almqvist, Uppsala University, Sweden

***Correspondence:**
John I. Ejembi
idokojj@gmail.com

Specialty section:
This article was submitted to Geomagnetism and Paleomagnetism, a section of the journal Frontiers in Earth Science

Received: *31 August 2020*
Accepted: *11 November 2020*
Published: *07 December 2020*

Citation:
Ejembi JI, Ferré EC, Satolli S and Friedman SA (2020) Post-Depositional Fluid Flow in Jurassic Sandstones of the Uncompahgre Uplift: Insights From Magnetic Fabrics. Front. Earth Sci. 8:601415. doi: 10.3389/feart.2020.601415

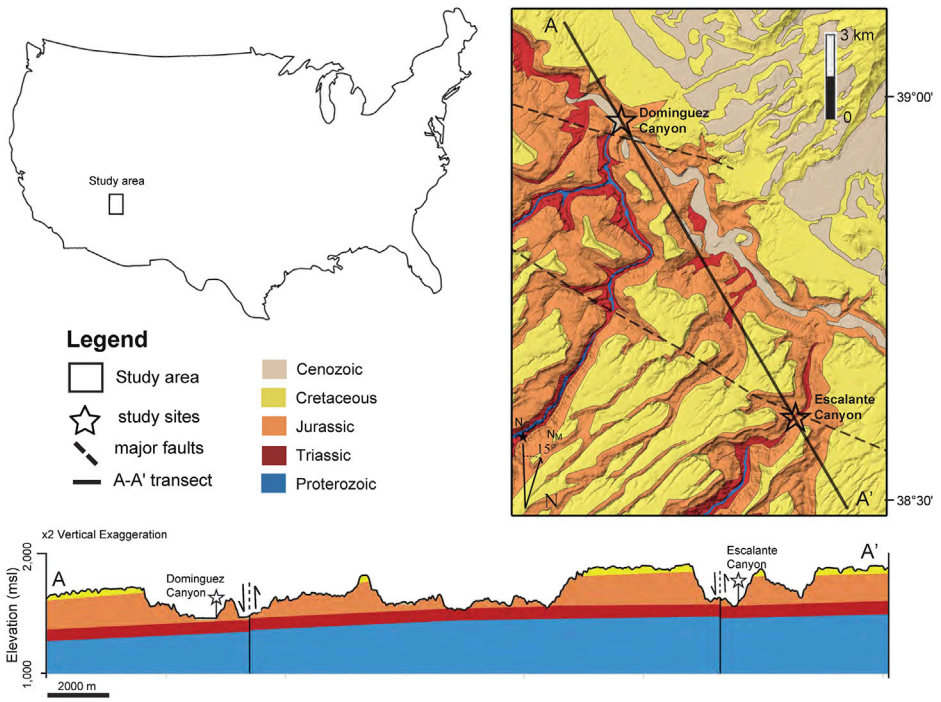

FIGURE 1 | Geologe map of the study area in western Colorado (after Tweto and Schoenfeld, 1979) and a northwest to southeast trending geologic cross-section of the study sites. The depth profile across section according to USGS DEM maps of area.

INTRODUCTION

Fluid-flow through permeable sandstones is a key process in multiple economically important geological processes such as, hydrocarbon migration (e.g., Oliver, 1986; Hunt, 1990; Ungerer et al., 1990), diagenetic alteration through fluid-rock interaction (Chan et al., 2000; Beitler et al., 2005; Potter and Chan, 2011; Potter-McIntyre et al., 2014), groundwater contamination of aquifers (e.g., Massei et al., 2002), or fluid-driven precipitation of ore minerals (e.g., Wilkinson, 2001). Common approaches to characterize regional fluid flow through rocks include fluid geochemistry (Musgrove and Banner, 1993) and hydrodynamic flow models (Wing and Ferry, 2007). For example, Musgrove and Banner (1993) used elemental and stable isotopic signatures in groundwater samples from a Cambro-Ordovician and Mississippian aquifer that were collected from different wells to evaluate the origin and mixing of meteoric and saline fluids in the United States Midcontinent. This approach relies on direct sampling of fluids for geochemical analysis and modeling whereas the hydrodynamic model approach requires multiple topographic relationships to be maintained for an accurate prediction of fluid-flow directions. These approaches, although generally successful, have limited application in ancient geologic systems particularly when fluid-flow is no longer active or when the original paleotopography has been modified either through erosion, alteration or tectonic activity.

In this study, we investigate the magnetic mineralogy, the origin and significance of the anisotropy of magnetic susceptibility (AMS), the NRM, and their implications regarding regional-scale fluid migration. The Jurassic sandstones of this study originate from two sites, located 12 km apart, along the southwest margin of the Central Colorado Trough, on the Eastern flank of the Uncompahgre Uplift: Escalante Canyon—EC and Dominguez Canyon, also known as Bridgeport—BP (**Figures 1**, **2**). The study area in the western Colorado Plateau consists primarily of Mesozoic sedimentary rocks underlain by deeply faulted Proterozoic crystalline basement blocks (**Figure 1**; e.g., Marshak et al., 2000). The Cenozoic and some Late Mesozoic sedimentary formations in this region have been eroded through successive uplifts (**Figures 1**, **2**; Pederson et al., 2002).

AMS has been an effective tool for tracking paleofluid flow in sedimentary rocks, magma flow in igneous provinces, and hydrothermal fluids caused by mantle upwelling (e.g., Schieber and Ellwood, 1993; Ferré et al., 2002; Sizaret et al., 2006; Essalhi et al., 2009). This method is sensitive to the petrofabric and crystallographic orientations of magnetic mineral grains (Tarling and Hrouda, 1993). The AMS of sediments has been successfully used to characterize syn- and post-depositional processes in sedimentary systems since its introduction by Ising (1942). Examples have been shown for geometry of pore spaces in siliciclastic rocks (Robion et al., 2014; Parés et al., 2016), flow mechanisms and nature of sediment deposition (Dall'Olio et al., 2013), and microscopic strain and deformational structures (e.g., Aubourg et al., 2004; Aubourg et al., 2010; Robion et al., 2007; Burmeister et al., 2009).

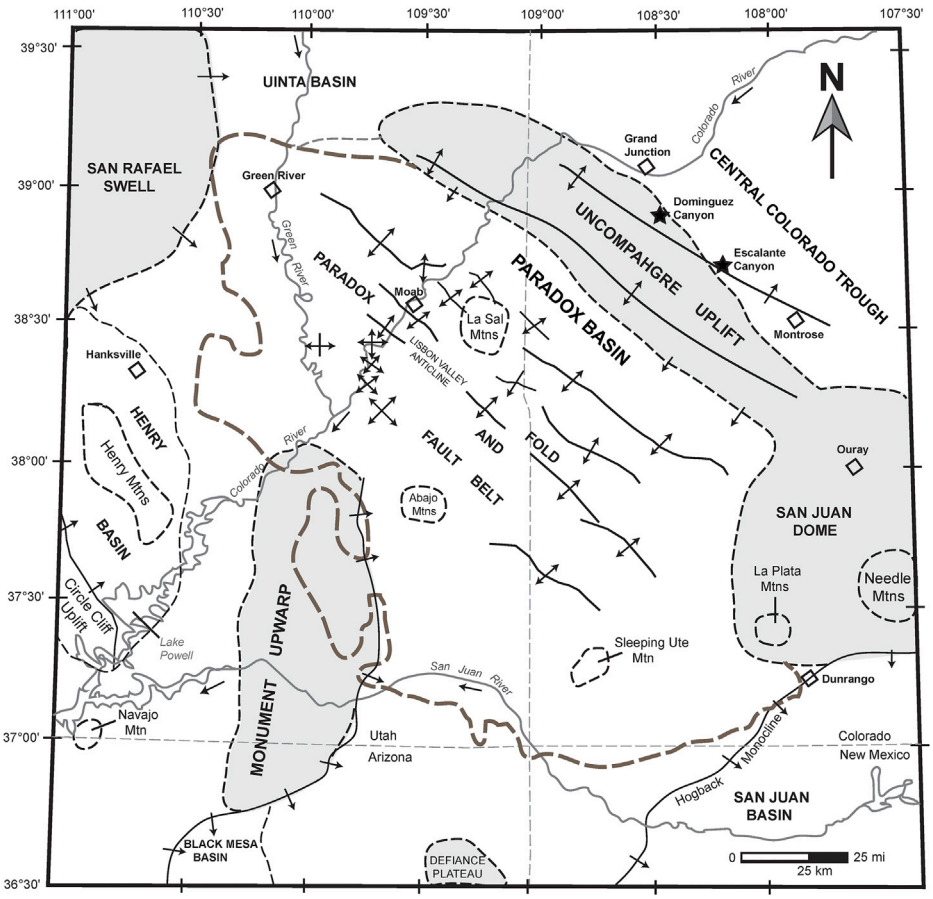

FIGURE 2 | Tectonic setting of the Paradox Basion and adjacent areas (after Kelley, 1958). Brown dashed line delineates the extent of the Paradox Basin. The Central Colorado Trough within the Paradox fold and thrust belt collected vast eolian and fluvio-lacustrine deposition during the Middle-Upper Jurassic.

The maroon, red, pink and in some cases, tan to grayish colors of the Middle-Late Jurassic sandstones of the Entrada Sandstone, Wanakah Formation, and Tidwell Member of the Morrison Formation in the Paradox Basin and adjacent areas are classic examples of secondary coloration acquired through fluid flow in permeable rocks (Parry et al., 2004; Beitler et al., 2005). The extent to which a primary and depositional fabric is preserved in these rocks, as opposed to a pervasive chemical overprint, constitutes the focus of this study. The magnetic mineralogy itself, along with the magnetic grain morphology, provide useful information on the syn- or post-depositional origin of the AMS. While radiometrically dating the development of the AMS is generally difficult, the paleomagnetic data acquired in our investigations could shed light on the type of AMS in these sandstones. The hypothesis we test using paleomagnetic data, combined with a well-established regional Jurassic-Cretaceous magnetostratigraphy, is that the AMS was acquired during or shortly after deposition, and therefore reflects primarily the sediment transport direction. The alternative hypothesis is that the AMS records a late stage precipitation event related to the downcutting of the Colorado and Gunnison Rivers (Hunt, 1969; Cook et al., 2009).

TECTONIC SETTING

The study area is situated on the northeastern margin along the Northeast flank of the Uncompahgre Plateau, west of the Central Colorado Trough (**Figure 2**). To the Southwest of the study area, the Paradox Basin formation began with crustal loading and downward lithospheric flexure during the contractional Pennsylvanian–Permian orogeny that formed the Ancestral Rocky Mountains (**Figure 2**; Kluth and Coney, 1981; Barbeau, 2003). Basin subsidence continued from the Triassic through Cretaceous. The Paradox Basin and other adjacent basins consist of Paleozoic through Cenozoic strata that unconformably overlie Proterozoic basement rocks that include granitic, high-grade metamorphic gneiss and schist (Tweto and Schoenfeld, 1979; **Figure 2**). Cretaceous rocks exposed on the Colorado Plateau have mostly been eroded away due to subsequent uplift and downcutting of major

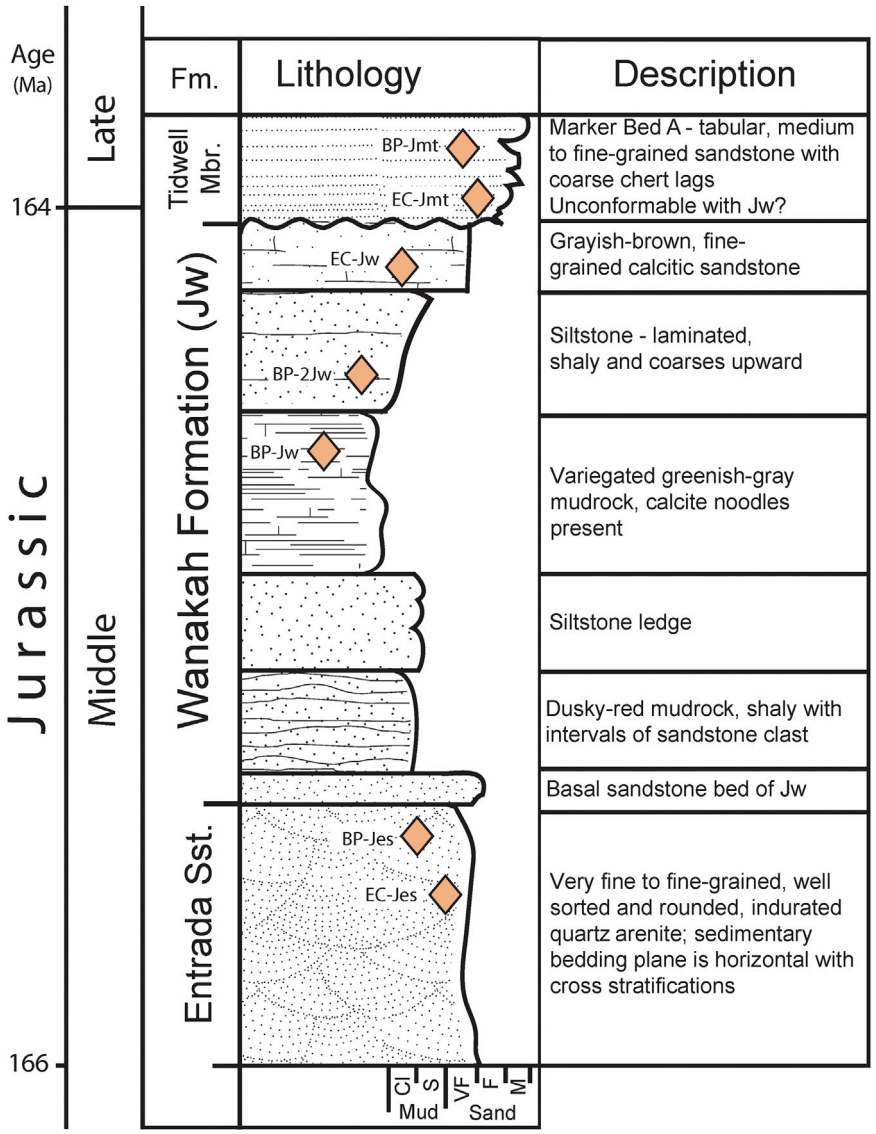

FIGURE 3 | Generalized stratigraphy of the Middle to early Late Jurassic in the study areas. Diamond symbols denote sampling horizons. Abbreviation of lithologies in the figure is Mud (Cl, clayey; S, silty), Sand (VF, very fine-grained; F, fine-grained; and M, medium-grained).

fluvial drainages (**Figure 1**). The Paradox Basin shows a prominent fold-and-fault belt defined by NW-SE striking faults, anticlines, and synclines (**Figure 2**). Some of these structures are related to salt walls and grabens caused by diapirism of the Paradox Formation (Nuccio and Condon, 1996).

The tectonic layer-parallel shortening (LPS) axis in the Paradox Basin is oriented NE-SW, parallel to the maximum principal stress (**Figure 2**). Kluth and Coney (1981) interpreted the orientation of this axis and the Ancestral Rocky Mountains as part of a complex intraplate response in the western United States due to the Ouachita-Marathon orogeny, a collision of the North American craton with South America and Africa during the Pennsylvanian. These authors also suggested that the suturing at the southern margin of the North American craton combined with northward directed thrusting from the Marathon region led to a progressive migration of stresses onto the continental interior. Other studies have suggested that 1) the origin of the Paradox Basin structures might be related to compressive stresses from either the Ancestral Rockies or Laramide orogenic events (Marshak et al., 2000) or 2) these structures predates these events but were reactivated along pre-existing faults in the basement (Davis, 1978; Baars and Stevenson, 1981).

The Uncompahgre Uplift was originally interpreted as a Pennsylvanian structure associated with the formation of the Ancestral Rocky Mountains (e.g., Kluth and Coney, 1981). However, recent thermochronological constraints document a

far more recent uplift history beginning in the Late Cretaceous (Laramide orogeny) and continuing with deep incision up to the Miocene-Pliocene (Rønnevik et al., 2017).

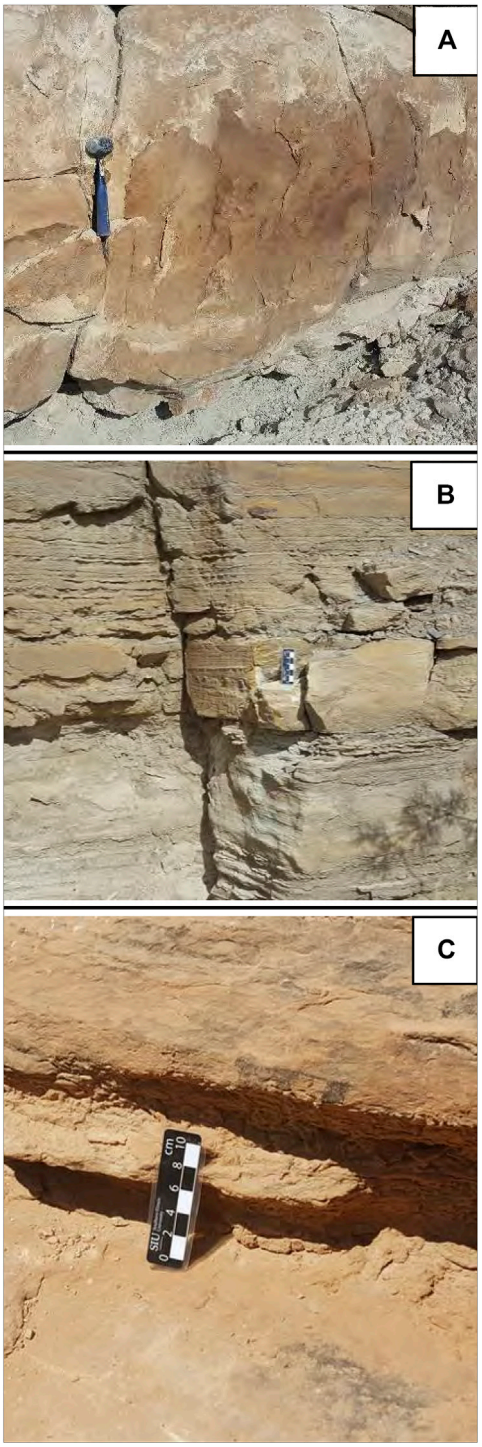

FIGURE 4 | Field photographs showing sedimentary bedding and sandstone lithologies of **(A)**. Marker Bed A - the basal sandstone of the Tidwell Mbr. of Morrison Fm. Marker Bed A is the sandstone bed that separates the Middle and Late Jurassic rocks. **(B)** Wanakah Fm. and **(C)** Entrada Sandstone. Hammer and scale bars are for scale.

ANALYTICAL METHODS

Sampling and Petrography

From oldest to youngest, we collected hand samples (with an average dimension of 15 × 12 × 8 cm) from the Entrada Sandstone, the Wanakah Formation, and the Tidwell Member of the Morrison Formation (**Figure 3**). Hand samples were georeferenced using hand-held Global Positioning System units (GPS). The geographic orientation of the samples was determined using a magnetic compass, after correction of the magnetic declination (11°E). Hand samples were extracted using a rock hammer to obtain fresh surfaces and to avoid supergene alteration overprints. The sandstones exhibit light brown to pale tan colors in the Tidwell Member of the Morrison Formation (**Figures 4A**), brown, pink or tan colors in the Wanakah Formation (**Figures 4B**) and relatively bright red to orange colors in the Entrada Sandstone (**Figures 4C**). These colors attest to the presence of iron oxides and hydroxides cement in the bulk sample. Polished petrographic thin-sections were prepared for selected, representative specimens to assess the mineralogy, morphology and grain size of the constituent mineral phases. The thin-sections were examined using a Hitachi S-3400N scanning electron microscope (SEM) in backscatter (BSE) mode at Montana State University Billings. Additional analyses with an energy dispersive spectroscopy (EDS) Ametek EDAX system provided semi-quantitative spot chemical analyses. Before imaging, thin-sections were coated with a 45 Å-thick layer of gold/palladium to prevent charging. The operation conditions of 15–20 kV accelerating voltage and a working distance of 10.0 μm yielded the best results.

Anisotropy of Magnetic Susceptibility Measurements

We cut several serial 2 cm-thick slabs from the hand samples to produce 2 cm sample cubes. The 2 cm AMS cubes were cut, side-by-side, from these slabs to yield about 15 cubic specimen per one hand sample. These oriented cubes were measured using the AGICO KLY-4S Kappabridge susceptibility meter at Southern Illinois University Carbondale. Measurements were performed at room temperature with an applied magnetic field of 300 A/m and frequency of 875 Hz. The AMS measurements were processed using the AGICO SUFAR program while the acquired data were plotted using the AGICO Anisoft 4.2 program. Directional data obtained from the projection of the three principal magnetic susceptibility axes on equal-area lower hemisphere stereonets, including their 95% confidence ellipses, were calculated using the Jelinek statistics (Jelínek, 1978; **Supplementary Material**).

The AMS is defined by a symmetric, second-rank tensor consisting of six independent elements represented by an ellipsoid with three mutually perpendicular axes. The three axes represent the three principal magnetic susceptibilities namely: K_1 (maximum), K_2 (intermediate), and K_3 (minimum). The AMS parameters used in this study include the mean magnetic susceptibility $K_m = \left(\frac{K_1 + K_2 + K_3}{3}\right)$, indicative

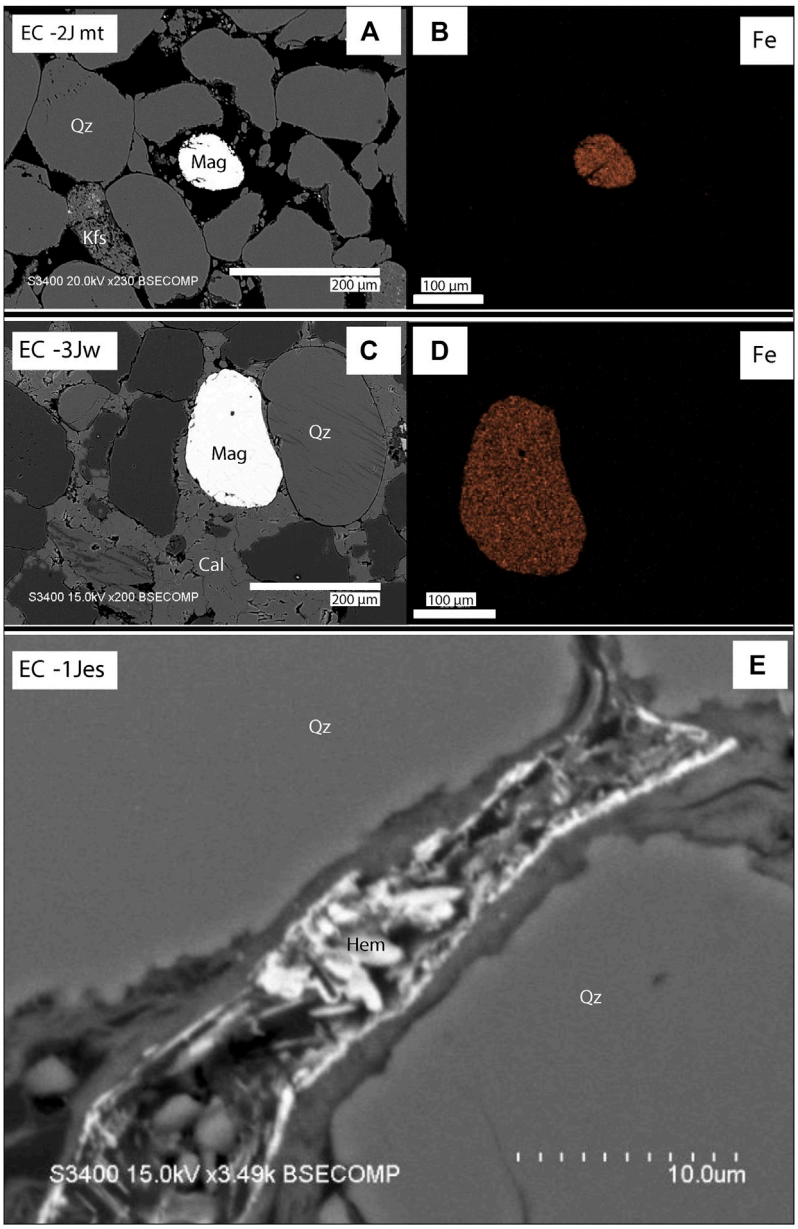

FIGURE 5 | Backscattered electron microscopy images of polished thin section from three represntative samples from Escalante Canyon **(A,C and E)** and elemental maps from x-ray EDC analysis **(B,D)** of the matrix and some framework grains. White grains in the EC-2Jmt and the EC-3Jw images are magnetite and and/or titanomagnetite grains. Hematite grain coatings are found in the EC-1Jes sample along quartz grain boundaries. Jes, Entrada Sandone; Jw, Wanakah Formation; Jmt, Tidwell Member; Fe, Iron; Qz, quartz; Hem, hematite; Mag, magnetite; Kfs, potassium feldspar; cal, calcite.

of the concentration of magnetic minerals present in the hand sample; the degree of magnetic anisotropy P' where $a_1 = ln\left(\frac{K_1}{K_m}\right)$, $a_2 = ln\left(\frac{K_2}{K_m}\right)$, and $a_3 = ln\left(\frac{K_3}{K_m}\right)$, which describes the strength of the magnetic fabric, and in general is a proxy for the type of magnetic fabric in the rocks; and the shape factor $T = 2((\ln K_2 - \ln K_3)/(\ln K_1 - \ln K_3)) - 1$, which represents the shape of the ellipsoid of the magnetic fabric (oblate or prolate), with T ranging from −1 to +1, prolate (with $T \leq 0$) and oblate (with $T \geq 0$).

Magnetic Hysteresis and Isothermal Remanent Magnetization Measurements

We performed both magnetic hysteresis experiments and Isothermal Remanent Magnetization (IRM) experiments at room temperature, on rock fragments to identify the nature of the AMS carriers. Magnetic hysteresis was measured on 11 specimens using the MicroMag 3900-04 vibrating sample magnetometer (VSM; Princeton Measurements Corporation) at Southern Illinois University Carbondale. IRM experiments were performed on two representative specimens with

TABLE 1 | Magnetic hysteresis properties of Middle-Late Jurassic sandstones from the Paradox Basin, western Colorado.

	Sample	Ms μAm^2	Mr μAm^2	Hc mT	Hcr mT	Mr/ Ms	Hcr/ Hc	HF Slope $\mu Am^2/T$	Hysteresis Loop
Dominguez	BP-2Jmt	1.33	0.32	20.63	66.24	0.24	3.21	+6.13	A
Canyon	BP-1Jmt	1.98	0.48	20.41	69.89	0.24	3.42	+11.04	A
	BP-2Jw	1.48	0.31	19.74	90.46	0.21	4.58	+17.60	A
	BP-1Jw	1.67	0.38	22.35	141.60	0.23	6.34	0.00	A
	BP-2Jes	1.79	0.54	40.98	188.30	0.30	4.59	+1.21	B
	BP-1Jes	2.25	0.81	54.70	202.10	0.36	3.69	+1.02	B
Escalante Canyon	EC-2Jmt	1.28	0.24	16.98	63.23	0.19	3.72	+14.21	A
	EC-1Jmt	1.51	0.27	12.55	49.46	0.18	3.94	+19.39	A
	EC-1Jw	1.13	0.14	10.80	41.03	0.12	3.80	+6.77	A
	EC-2Jes	6.94	2.18	39.82	158.80	0.31	3.99	+10.66	B
	EC-1Jes	4.24	1.48	42.35	175.70	0.35	4.15	−7.37	B

contrasting colors (one specimen from each locality). A field strength of up to 1.5 T was applied to saturate the specimens magnetically. For comparison, the induced magnetization in both specimens was normalized after correcting for high-field slope, in this case, 70% of the maximum applied field.

Paleomagnetic Measurements

Due to the assumed presence of hematite in the hand samples, we chose thermal demagnetization of the NRM to constrain the different magnetic phases present in each specimen. Thermal demagnetization of the NRM was performed at the CIMaN-ALP laboratory of paleomagnetism (Peveragno, Italy) using a Superconducting Rock Magnetometer 2G Enterprise 755 hosted in a shielded room. Forty-eight representative AMS cubes (16 per formation) were selected for thermal demagnetization of the NRM. The specimens were subjected to a stepwise thermal demagnetization in 15 steps from room temperature to 600°C, with additional four steps up to 700°C for specimens showing higher unblocking temperatures.

RESULTS

Petrographic Analysis

Previous work reports on the petrographic characteristics of the Entrada Sandstone, Wanakah Formation and Tidwell Member of the Morrison Formation (Ejembi et al., in review). Based on Folk (1980) sandstone classification, the Entrada Sandstone consists dominantly of sublitharenites, while the Wanakah Formation and Tidwell Member range from feldspathic litharenite to litharenite. The Entrada Sandstone in the two localities is predominantly pinkish to reddish brown, cross-bedded, and is composed of fine to very fine-grained, sub-rounded to rounded framework grains. The Wanakah Formation consists of distinct, thin beds (<0.15 m) of fine-grained sandstone with interbedded mudrocks that have a characteristic red and green color. The Tidwell Member consists of a regionally extensive, dark gray to tan, marker sandstone bed with overlying beds that are tabular, coarse-grained, and are interbedded with mudrocks. These sandstone beds vary in thicknesses (0.7–1.5 m), with a maximum measured thickness of ~1.5 m at Escalante Canyon.

The quartz and feldspar grains in these units are strikingly free of any transgranular or intergranular deformation fractures and inherited or cognate plastic deformation microstructures such as undulose extinction. Both optical microscopy and scanning electron microscopy reveal very pristine detrital grains assembled in undeformed, fabric-less assemblages. Cross-bedding structures, when present, result from grain size variation. **Figure 5**, for example, shows representative SEM-BSE images of polished thin sections along with corresponding maps of major elements from the sandstone specimens using x-ray energy-dispersive systems (EDS) analysis. The maps of iron distribution in the matrix reveal no specific coating along grain margins. The EDS chemical analyses help identify quartz, alkali feldspar, calcium carbonates, and iron oxides/hydroxides. However, magnetite and titanomagnetite detrital grains were observed in some of the specimen (based on the Fe, O and Ti elemental maps, e.g., EC-2Jmt and EC-3Jw (**Figure 5**). This lack of ferromagnetic grains is not unusual in terrestrial sandstones where these minerals are quickly degraded and precipitated as early hematite grain coatings (e.g., Chan et al., 2007).

Magnetic Hysteresis Properties and Isothermal Remanent Magnetization Behavior

The hysteresis behaviors show negligible contributions of diamagnetic minerals, minor contributions of paramagnetic minerals, and the dominance of ferromagnetic phases (**Table 1** and **Figure 6**). The magnetic hysteresis parameters, saturation magnetization (M_s), saturation remanent magnetization (M_r), and magnetic coercivity (H_c) are calculated after correction of the high field slope, which arises primarily from the sum of diamagnetic (quartz and carbonates) and paramagnetic (clay and other detrital grains) and antiferromagnetic contributions. The coercivity of remanence (H_{cr}) was determined through back-

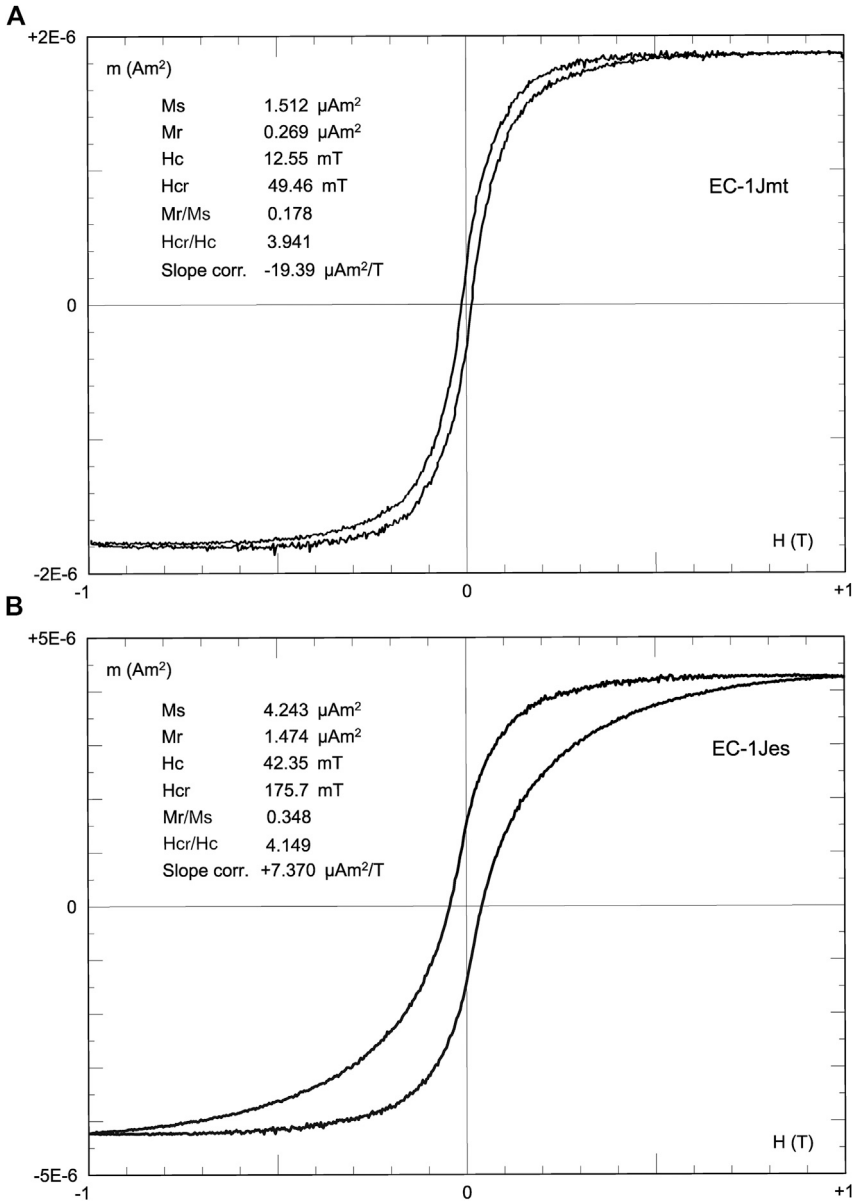

FIGURE 6 | Representative magnetic hysteresis curves (magnetic moment, m versus applied field, H) observed in all the sandstone samples. Both samples exhibit low paramagnetic susceptibility behaviour,with EC-1Jmt showing a single component magnetic hysteresis behavior **(A)** and EC-1Jes showing at least two components magnetic hystersis behaviour **(B)**.

field experiments. Two fundamental behaviors are observed: a single phase with a low to moderate remanent coercivity phase (e.g., EC-1Jmt, $H_{cr} \approx 49.5$ mT; **Figures 6A**); and a two-phase mixture with high- and moderate-coercivity phases resulting in a wasp-waisted shaped hysteresis loop (e.g., EC-1Jes, $H_{cr} \approx 176$ mT; **Figures 6B**). Most specimens reach magnetic saturation at fields above 0.6 T. A few specimens show a negative high-field slope (e.g., EC-1Jes) indicative of a very small diamagnetic contribution. As the contribution of the high-coercivity phase is highly variable, the M_r/M_s and H_{cr}/H_c ratios result from a mixture of several single-phase properties and therefore cannot be used as indicators of magnetic granulometry. The relatively low values of the high field slope (**Table 2**) indicate that paramagnetic phases cannot account for the observed AMS.

Two types of IRM acquisition behavior for specimens with contrasting lithofacies (i.e., color, texture, and porosity) are shown in **Figure 7**. The IRM plots show distinct approaches to magnetic saturation up to 1.5 T. These differences correlate with the color of the specimen: red sandstones are more magnetically coercitive than tan sandstones.

TABLE 2 | Average scalar and tensorial AMS data of Middle-Upper Jurassic sandstones from the Paradox Basin, western United States.

		Km × 10-6 [SI]		*P'*			*T*		
Field Location /	**No of AMS data**	**Scalar mean**	**Stand. dev**	**Tensorial mean**	**Scalar mean**	**Stand. dev**	**Tensorial mean**	**Scalar mean**	**Stand. dev**
Dominguez Canyon, CO									
BP-2Jmt	25	14.80	1.52	1.077	1.088	0.028	0.460	0.346	0.381
BP-1Jmt	18	19.50	1.69	1.027	1.029	0.005	0.306	0.241	0.283
BP-2Jw	15	20.20	1.95	1.050	1.052	0.015	0.570	0.322	0.292
BP-1Jw	18	26.20	1.42	1.020	1.020	0.003	0.110	0.060	0.266
BP-2Jes	16	13.29	1.92	1.072	1.082	0.014	0.042	0.045	0.342
BP-1Jes	20	9.70	1.50	1.154	1.181	0.044	0.215	0.081	0.272
Escalante Canyon, CO									
EC-2Jmt	20	23.60	1.84	1.017	1.021	0.007	0.408	0.281	0.332
EC-1Jmt	20	26.91	1.78	1.053	1.063	0.011	0.438	0.189	0.213
EC-1Jw	6	8.14	0.86	1.108	1.123	0.023	0.154	0.168	0.431
EC-2Jes	12	25.10	3.89	1.025	1.036	0.011	0.086	0.195	0.318
EC-1Jes	13	30.50	2.01	1.020	1.029	0.006	0.297	0.203	0.451

Km, magnetic susceptibility; P', degree of anisotropy; T, shape factor; K1, K2, and K3 are the maximum, intermediate, and minimum magnetic susceptibility axes, respectively. The mean direction and confidence ellipses of the susceptibility axes are calculated using the Jelinek statistics in Anisoft 4.2 software.

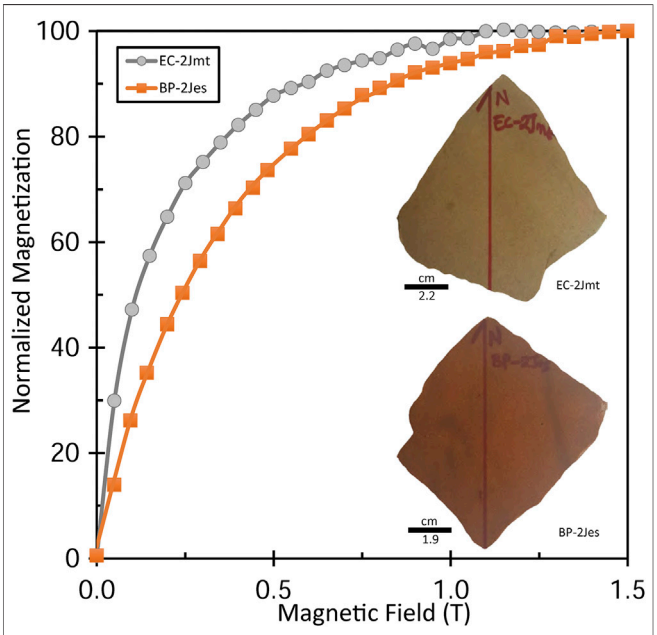

FIGURE 7 | Isothermal Remanent Magnetization (IRM) acquisition plot of two samples (BP-2Jes and EC-2Jmt) from the Middle and Late Jurassic, respectively. The two samples are remarkably different lithologically. Insets are photographs of a freshly cut slab of both samples taken during the AMS sample preparation stage. The marker on the sample surface shows the in situ geographic orientation.

Anisotropy of Magnetic Susceptibility

The AMS scalar parameters (K_m, T, and P') are plotted in binary diagrams in **Figure 8** and provided in **Table 2**. The specimens display consistent magnetic properties. P' shows a negative correlation with K_m, both at the scale of the specimen and across specimens. K_m ranges from ~8.14 to 31.0 × 10^{-6} SI (**Figures 8A**). There is no correlation between the rock color and AMS parameters. P' ranges from 1.02 to 1.27, clearly outside the range of values attributed to paramagnetic only assemblages, but most specimens have P' < 1.05 (**Figures 8B**). T varies substantially within each specimen but overall shows mainly oblate symmetry (**Figures 8C**). Although the degree of anisotropy in the specimens is strongly influenced by the weak magnetic susceptibility, it does not provide a reliable estimate of the strain at magnetic susceptibilities close to zero.

The stereonets of the three principal magnetic susceptibility axes (K_1, K_2, and K_3) obtained from the sandstone specimens from the two study sites are shown in **Figure 9**. The 95% confidence ellipses around averages per specimen are derived from the Jelinek statistics (Jelínek, 1978). The AMS directional parameters are rather consistent at the hand sample scale and between specimens. The specimens display a strong and consistent—but varying degree of steepness of the—magnetic foliation (planar fabric) defined by the K_1–K_2 plane (**Figure 9**), which dips to the SE. The double arrow shows the dip angle of the magnetic foliation. The magnetic lineation (K_1) is moderately well-defined and show discrete clusters. The AMS planar fabric of these rocks is clearly oblique with respect to the sub-horizontal bedding plane observed on the outcrop where each hand sample was collected from.

Thermal Demagnetization of the NRM

Stepwise thermal demagnetization of the NRM is shown for six out of forty-eight representative specimens in **Figure 10**. The NRM intensities range from 3.69 × 10^{-5} to 9.91 × 10^{-3} A/m, with an average of 1.86 × 10^{-3} A/m. Characteristic remanent magnetizations (ChRMs) were successfully isolated in 39 (over 48) specimens, both with normal (16 specimens) and reversed polarities (23 specimens). In most cases, the experiments show a stable single-component behavior, with a relatively straight ChRM toward the origin. Few specimens show evidence of a second directional components, isolated at lower temperatures (e.g., BP-1Jmt), including some with normal and reverse components. The ChRMs are scattered, and do not pass the

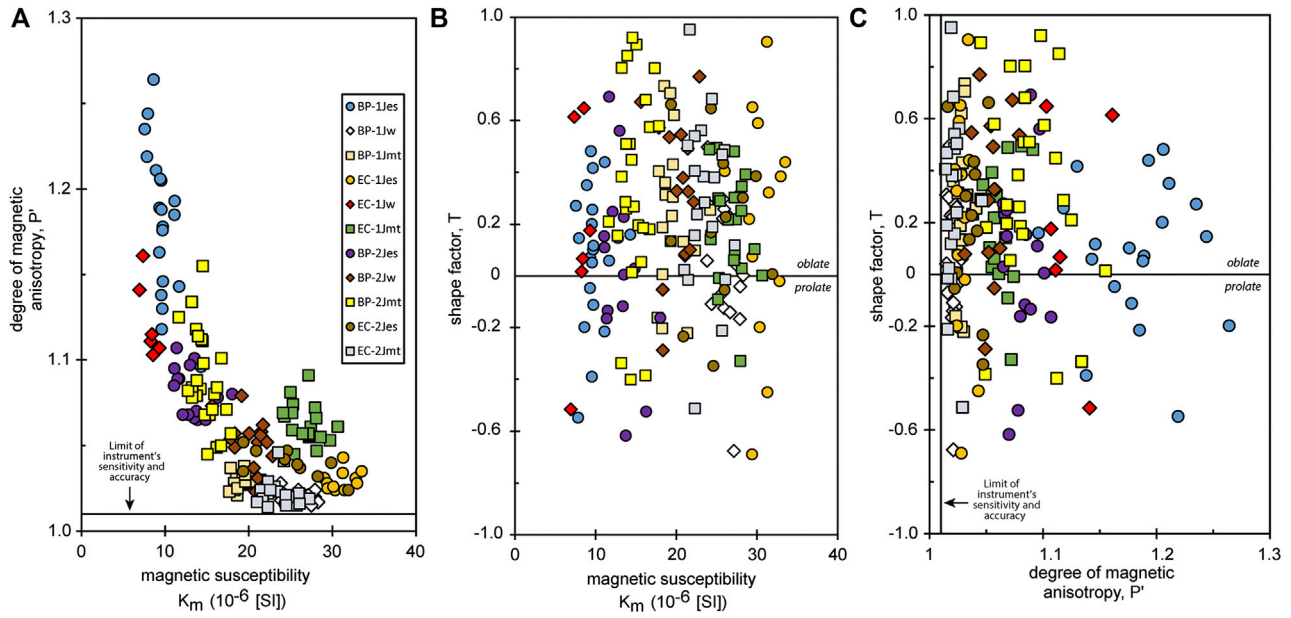

FIGURE 8 | Composite plots of AMS parameters of all the samples in both localities. **(A)** Mean magnetic susceptibility vs. the degree of magnetic anisotropy. **(B)** Mean magnetic susceptibility vs. the shape factor and **(C)**. The degree of magnetic anisotropy vs. the shape factor.

reversal test (McFadden and McElhinny, 1990). The weakly magnetized specimens (which were independent of the formation or lithology) that lack stable demagnetization behaviors could not be interpreted. In most specimens from the Tidwell Member and the Wanakah Formation, the main demagnetization occurs below 150°C while the remainder is generally removed below 300°C (e.g., **Figures 10A–D**). Most specimens from the Entrada Sandstone also display demagnetization below 150°C, but some retain part of their magnetization up to 500°C–680°C (e.g., **Figures 10F**). The stable demagnetization directions vary substantially in inclination (**Figure 10**) with an average ~55° for the <150°C stable component, while the variations in magnetic declination are also high.

DISCUSSION

Origin and Development of Anisotropy of Magnetic Susceptibility Fabrics in Sedimentary Rocks

Previous studies have shown that the origin of magnetic fabrics in sedimentary rocks is controlled by sedimentary vs. tectonic processes (e.g., Tarling and Hrouda, 1993; Li et al., 2014). The sedimentary origin of AMS lies in the depositional process by which particles settling in a slurry acquire a shape preferred orientation parallel to the depositional plane, which is close to horizontal in most cases. The compaction of sediments generally strengthens the planar component of the syn-depositional fabric because it results from the application of a vertical stress (gravity).

When bedding is horizontal, there is either no lineation of the maximum susceptibility, or a very weak lineation. Regardless of the magnetic carriers, the resulting AMS tends to be strongly planar and weakly linear, i.e., oblate fabrics (e.g., Schieber and Ellwood, 1993; Tarling and Hrouda, 1993; Saint-Bezar et al., 2002; Aubourg et al., 2004; Aubourg et al., 2010; Parés et al., 2007; Robion et al., 2007; Dall'Olio et al., 2013). Sedimentary magnetic fabrics in sedimentary rocks are characterized by a tight clustering of the K_3 axis along the bedding pole, with the K_1 and K_2 axes dispersed within the bedding plane (**Figures 11A**). In rare cases, eolian sedimentary rocks may acquire a linear fabric parallel to the wind direction (e.g., Lagroix and Banerjee, 2002). For materials deposited under a strong current, a linear fabric parallel to the current may be imparted, although such fabrics are typically reported in shales and rarely in sandstones (e.g., Ellwood and Howard, 1981; Schieber and Ellwood, 1993; Tarling and Hrouda, 1993), and the amplitude of the imbrication angle of deposited sediments is very small compared to the strongly oblique magnetic fabric observed in our specimens (**Figures 11B**).

Tectonic overprints of a sedimentary fabric can be detected with AMS even for anisotropies as low as 1% (1.01), e.g., Burmeister et al. (2009). In clay-bearing rocks, such overprints result in a reorientation of platy minerals perpendicular to the instantaneous shortening axis (i.e., the LPS) due to tectonic strain. In sandstones, tectonic overprints are typically identified through specific microstructures including transgranular or intra-granular fractures, recrystallization rims, lobate grain boundaries and outcrop-scale structures such as stylolites or deformation bands (e.g., Saint-Bezar et al., 2002).

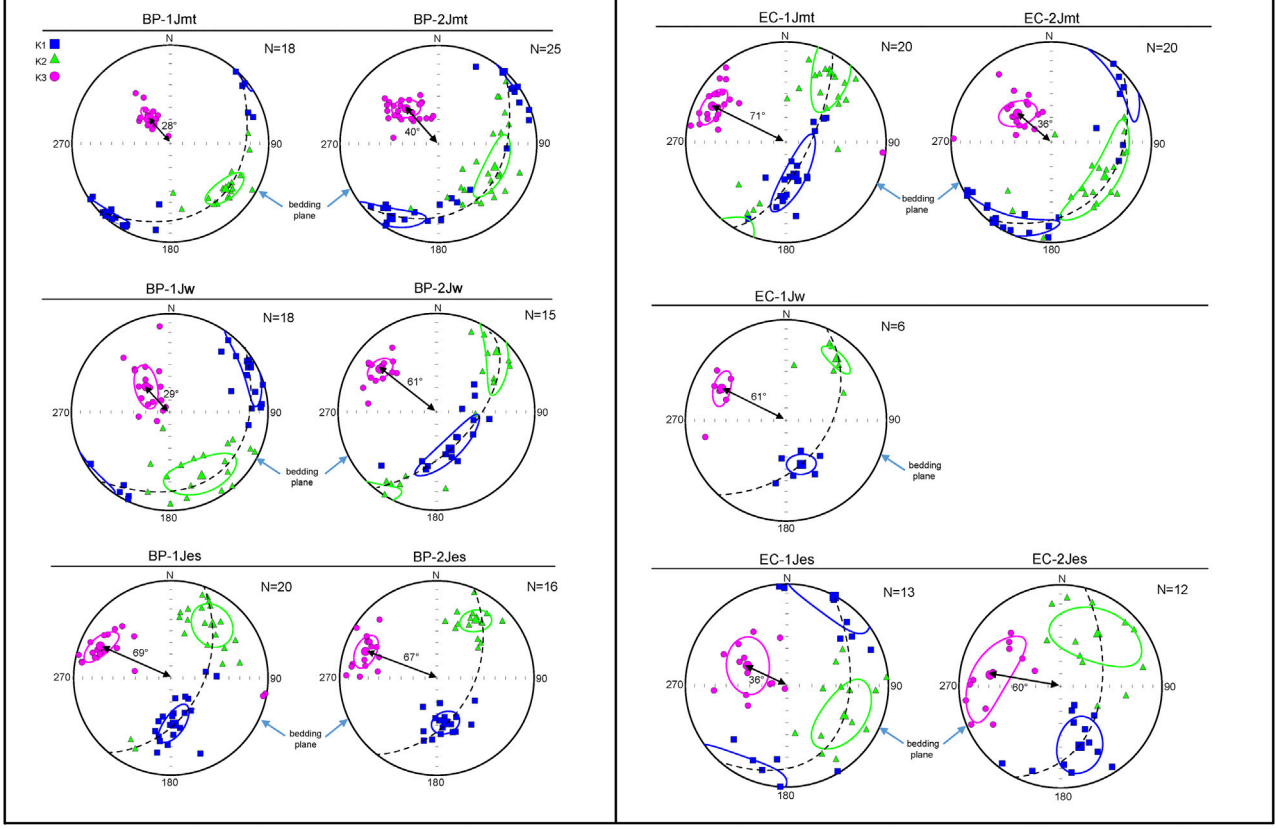

FIGURE 9 | Equal-area lower hemisphere stereographic projections of the three principal magnetic susceptibility axes, including their 95% confidence ellipses around weighted averages derived using Jelinek statistics (1981). Samples in A are from Bridgeport in Dominguez Canyon and B Escalante Canyon (**Figure 1**). Samples are in stratigraphic order from oldest- youngest: Jes, Entrade sandstone; Jw, Wanakah Fm. and Jmt, Tidwell Mbr of the Morrison Fm. K1 in squares, K2 in traingles and K3 in circles. Dotted arc is the K1-K2 plane which defines the magnetic foliation. K1 defines the magnetic lineation. The tilt of magnetic lineation. The tilt of the magnetic fabric, i.e., the deviation of the K3 axis from 90° (the sedimentary bedding pole), is represented by the double-headed arrow on the stereonet for each sample.

In the case of the Uncompahgre Uplift rocks investigated in this study, detailed petrographic observations indicate a lack of plastic deformation, beyond rare detrital quartz grain that exhibits pre-existing undulose extinction. The tectonic uplift that occurred in this region resulted in broad-scale tilting of beds, in places up to 10°. But at our sampling localities, the bedding is close to horizontal (<3 dip). Based on lack of deformation at the scale of the outcrop, the specimen and that of the thin-section, a tectonic origin for the observed AMS fabric can be ruled out. Further, the generally steep attitude (i.e., dip) of the magnetic foliation (~50°), if it were of tectonic origin, would require an attitude of the shortening axis inconsistent with regional tectonics.

The AMS fabrics of all the specimens are systematically strongly oblique (28–71 dip) with respect to the subhorizontal bedding. Considering this pronounced paradoxical obliquity and the remarkably consistent dip direction to the South East between hand samples from the same site and across the two sampling sites, a sedimentary origin for the AMS can be ruled out.

To better understand the origin of these magnetic fabrics we need to consider the magnetic minerals present in these rocks. At the outcrop scale, the Entrada Sandstone hand samples commonly show a red color (**Figures 4C**) indicative of the presence of relatively fine hematite. Most specimen also contain relatively large, multi-domain (up to 200 μm) magnetite grains that we interpret as detrital grains based on their rounded and smooth morphology as well as their location in between quartz clasts (**Figure 5**). The hysteresis behavior of most specimens shows a strong contribution from a high magnetic coercivity phase that cannot be magnetite because this mineral typically saturates at the field of 0.2 T or less (e.g., Dunlop and Özdemir, 1997). Hematite and goethite are, in a diagenetic environment, by far the most likely phases responsible for this behavior. The IRM acquisition curves (**Figure 7**) confirm the

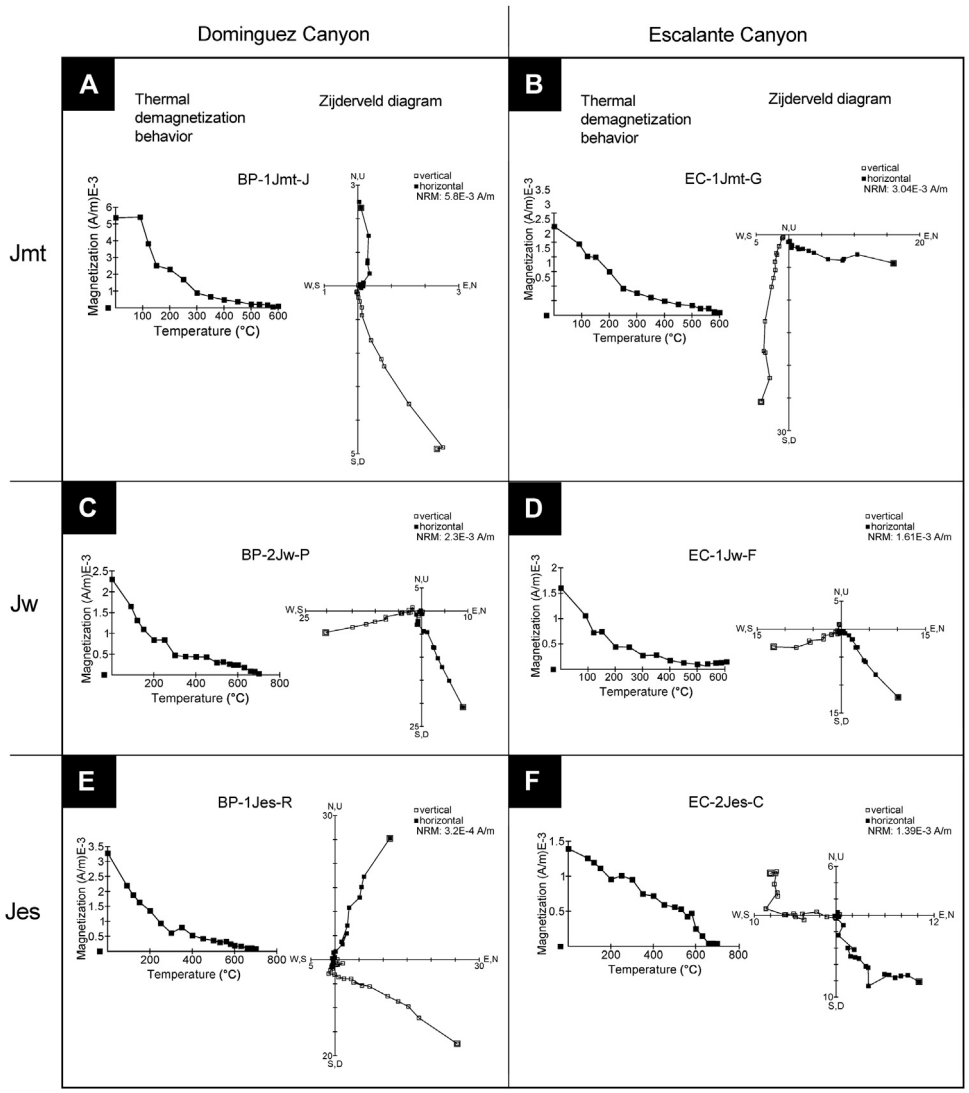

FIGURE 10 | Stepwise thermal demagnetization of the natural remanent magnetization (NRM) behaviour and corresponding Zijderveld diagram of representative samples from the two study localities. Demagnetization steps are in °C. Full (open) symbols in the Zijderveld diagram represent orthogonal projection on to the horizontal (vertical) plane. Refer to **Figure 9** caption for sample abbreviations.

presence of at least one high coercivity phase. Finally, the thermal demagnetization behavior of these rocks shows that in most cases, goethite dominates the NRM, except in the Entrada Formation where hematite contributes more. In general, the magnetic phase carrying the NRM can be—but is not necessarily the same as—the phase carrying the AMS. In summary, most specimens contain a mixture of detrital magnetite (Fe_3O_4), and its typical alteration products; hematite (Fe_2O_3) and goethite FeO(OH). While the absolute percentage of magnetite may be relatively small, this phase contributes substantially to AMS due to its high intrinsic magnetic susceptibility.

While the respective contributions of these three minerals to the AMS of our specimens remain quantitatively unconstrained, their intrinsic magnetic anisotropy may shed light on the origin of the AMS. Magnetite primarily has a magnetostatic anisotropy (i.e., shape anisotropy) that tends to dominate magnetic fabrics because it has a high magnetic susceptibility (Dunlop and Özdemir, 1997). Hematite, in low fields, has mainly a magnetocrystalline anisotropy that mimics its planar hexagonal shape (Rochette et al., 1992). Goethite grains are elongated along their crystallographic c-axis, which is also the K_3 axis and gives goethite an inverse AMS fabric (e.g., Rochette et al., 1992).

Considering the magnetic assemblage observed in our specimens, two alternative explanations can be proposed:

(1) The competition of goethite, with an inverse AMS fabric fabric (e.g., Martin-Hernandez and García-Hernández, 2010), and hematite + magnetite, with a normal fabric,

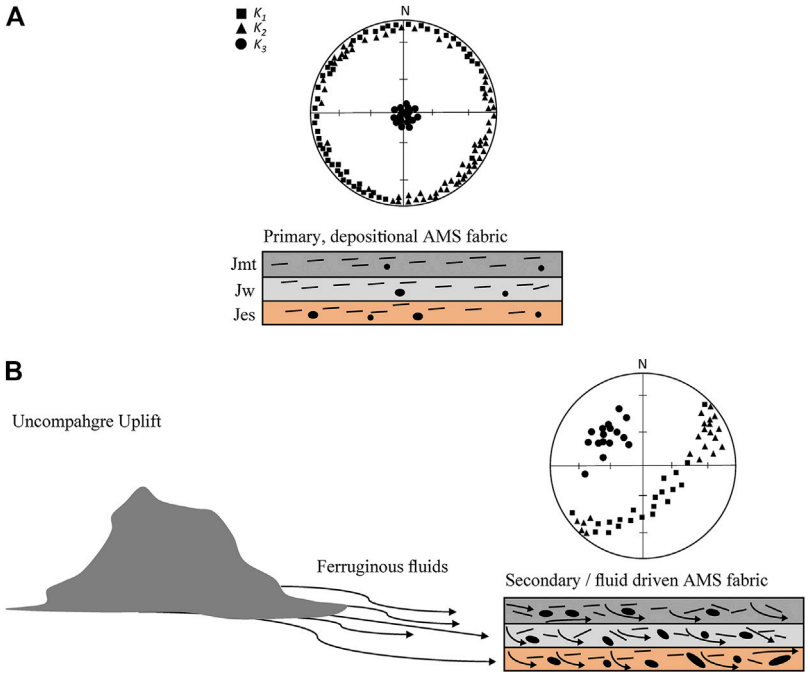

FIGURE 11 | Model for the acquisition of **(A)**. primary, depositional AMS fabrics in sedimentary rocks in this study, and **(B)**. modified AMS fabrics, caused by the alteration of primary detrital grains and/or presipitation of new magnetic minerals, in pore spaces due to the percolation of ferruginous fluids, driven by the Late Cretaceous Uncompahgre Uplift in western United States.

may result in inverse or intermediate AMS fabrics depending on the goethite proportion (e.g., Ferré, 2002; Robion et al., 2007).

(2) The percolation of ferruginous fluids through porous sandstones followed by mineral precipitation (**Figure 11B**) may explain the origin of the AMS (e.g., Sizaret et al., 2003; Essalhi et al., 2011).

In these studies, hot fluids precipitate iron oxides and hydroxides in pore spaces of a porous rock and the resulting AMS effectively reflects pore space shape anisotropy.

The first hypothesis cannot explain oblique AMS fabrics because mixtures of normal and inverse AMS fabrics systematically result in perpendicular AMS fabrics (Ferré, 2002). It also seems unlikely because the thermal demagnetization behaviors and magnetic properties of the specimens indicate that the proportion of magnetite, hematite, and goethite varies between hand samples (**Figure 10** and **Tables 1**, **2**).

The second hypothesis is consistent with most observations including the variations in magnetic mineralogy across formation depending on the availability of iron in the environment and possible variations in rock permeability. The fundamental mechanism driving fluids through these formations could be the tectonic uplift of the Uncompahgre mountains which would have caused a regionally consistent hydraulic head to the West of the sampling localities (**Figures 11B**). Although rock fractures are visible at outcrop scale (**Figure 4**), we did not identify any linkage to presence of systematic fracture or pore networks at the microscopic scale (**Figure 5**) and assessing the potential role of fracture networks in contributing to the regional fluid flow through these formation is beyond the scope of this work. Today, the paleomagnetic data showing a reverse period of magnetization at least in the Entrada Formation (e.g., EC-1Jes) supports a Cretaceous precipitation event associated with the Uncompahgre Uplift, although this process is highly unlikely because iron is a very mobile element and subsequent erosion created by the uplift and Quaternary downcutting of the Gunnison River almost certainly created a late-stage fluid flow event to the west.

Magnetic fabrics have previously been used both to characterize fluid flow through porous rocks (e.g., Sizaret et al., 2003; Just et al., 2004; Essalhi et al., 2011) and to quantify pore anisotropy (e.g., Pfleiderer and Halls, 1990; Pfleiderer and Halls, 1993; Benson et al., 2003). Crystallographic analyses of magnetite grains and whether its preferred grain orientation align with pore spaces in the bulk rock (if it exists) are outside the scope of this work. Here in this study of the Uncompahgre Uplift, contrarily to many similar studies of sedimentary rocks using magnetic fabrics, we show that the AMS does not inform on depositional processes, compaction or paleocurrents. Instead, the AMS reflects a regionally consistent post-depositional, tectonically-driven fluid flow owing to cycling via redox reactions of a highly mobile element (Fe) over geologic history in porous and permeable media.

CONCLUSION

The magnetic mineralogy of the Jurassic rocks on the Eastern flank of the Uncompahgre Uplift rocks attests to a primary, detrital magnetite subsequently altered into hematite and goethite. Further dedicated paleomagnetic studies might provide insights into the timing of the uplift and the origin of the oblique foliation symmetry, which we infer might be unrelated to the competition between different phases of ferromagnetic minerals carrying the AMS. This study shows that the AMS fabrics of the Middle-Late Jurassic sandstones of the Uncompahgre Uplift are not primary sedimentary magnetic fabrics. Instead, these fabrics are secondary in origin and most likely developed through unidirectional percolation of Fe-rich fluids that migrated due to the hydraulic head caused by the uplift. Future AMS studies on sedimentary rocks will have to consider that regional hydraulic systems may ultimately affect results and that caution should be exerted in the interpretation of magnetic fabrics.

DATA AVAILABILITY STATEMENT

The original contributions presented in the study are included in the article/**Supplementary Material**, further inquiries can be directed to the corresponding author.

AUTHOR CONTRIBUTIONS

JE did the fieldwork, collected and prepared the samples, performed the AMS, magnetic hysteresis, and IRM experiments, and wrote the first draft of the manuscript. EF advised, provided the lab equipment, directed the research, and edited the successive versions of the manuscript. EF, SS, and JE designed and arranged samples for the thermal demagnetization of the NRM experiment. SS performed the thermal demagnetization of the NRM experiment, took the measurements, and analyzed the data. EF, JE, and SF designed and arranged thin-section samples for SEM. SF performed the SEM experiment, analyzed, and collected the EDS data. JE and EF jointly analyzed all the data. All authors read, edited, and contributed to the final draft of the manuscript.

FUNDING

This research was partly funded by the American Chemical Society-Petroleum Research Fund (ACS-PRF) Grant No. 55161 (to Sally Potter-McIntyre) and the Department of Geology at Southern Illinois University. Sally Potter McIntyre also provided samples, thin-sections, unpublished field and petrographic data and input into this manuscript. The Classen Family Named, American Association of Petroleum Geologists (AAPG) Grants-in-Aid, the Geological Society of America (GSA) Graduate Research Grant and the National Association of Black Geoscientists (NABG) Scholarship Award to JE benefitted this research as well. Joe Krienert helped to digitize and compile the geologic map of the study area. Elham Hosseinzadehsabeti graciously assisted with some of the VSM measurements.

SUPPLEMENTARY MATERIAL

The Supplementary Material for this article can be found online at: https://www.frontiersin.org/articles/10.3389/feart.2020.601415/full#supplementary-material.

REFERENCES

Aubourg, C., Klootwijk, C., and Korsch, R. J. (2004). Magnetic fabric constraints on oroclinal bending of the Texas and Coffs Harbour blocks: new England Orogen, eastern Australia. *Geol. Soc. Spec. Publ.* 238 (1), 421. doi:10.1144/GSL.SP.2004.238.01.22

Aubourg, C., Smith, B., Eshraghi, A., Lacombe, O., Authemayou, C., Amrouch, K., et al. (2010). New magnetic fabric data and their comparison with palaeostress markers in the Western Fars Arc (Zagros, Iran): tectonic implications. *Geol. Soc. Spec. Publ.* 330 (1), 97. doi:10.1144/SP330.6

Baars, D. and Stevenson, G. (1981). "Tectonic evolution of western Colorado and eastern Utah," in *Western slope (western Colorado) - New Mexico geological society 32nd annual fall field conference guidebook*. Editors R. C. Epis and J. F. Callender (Socorro, NM: New Mexico Geological Society), 337.

Barbeau, D. L. (2003). A flexural model for the Paradox Basin: implications for the tectonics of the ancestral Rocky mountains. *Basin Res.* 15, 97–115. doi:10.1046/j.1365-2117.2003.00194.x

Beitler, B., Parry, W. T., and Chan, M. A. (2005). Fingerprints of Fluid Flow: Chemical Diagenetic History of the Jurassic Navajo Sandstone, Southern Utah, U.S.A, *J. Sediment. Res.* 75, 547–561. doi:10.2110/jsr.2005.045

Benson, P. M., Meredith, P. G., and Platzman, E. S. (2003). Relating pore fabric geometry to acoustic and permeability anisotropy in Crab Orchard Sandstone: A laboratory study using magnetic ferrofluid. *Geophys. Res. Lett.* 30 (19). doi:10.1029/2003gl017929

Burmeister, K. C., Harrison, M. J., Marshak, S., Ferré, E. C., Bannister, R. A., and Kodama, K. P. (2009). Comparison of Fry strain ellipse and AMS ellipsoid trends to tectonic fabric trends in very low-strain sandstone of the Appalachian fold–thrust belt. *J. Struct. Geol.* 31, 1028–1038. doi:10.1016/j.jsg.2009.03.010

Chan, M. A., Ormö, J., Park, A. J., Stich, M., Souza-Egipsy, V., and Komatsu, G. (2007). Models of iron oxide concretion formation: field, numerical, and laboratory comparisons. *Geofluids* 7 (3), 356–368. doi:10.1111/j.1468-8123.2007.00187.x

Chan, M. A., Parry, W. T., and Bowman, J. R. (2000). Diagenetic hematite and manganese oxides and fault-related fluid flow in Jurassic sandstones, Southeastern Utah. *AAPG (Am. Assoc. Pet. Geol.) Bull.* 84, 1281–1310. doi:10.1306/A9673E82-1738-11D7-8645000102C1865D

Cook, K. L., Whipple, K. X., Heimsath, A. M., and Hanks, T. C. (2009). Rapid incision of the Colorado River in Glen Canyon – insights from channel profiles, local incision rates, and modeling of lithologic controls, *Earth Surf. Process. Landforms* 34, 994–1010. doi:10.1002/esp.1790

Dall'Olio, E., Felletti, F., and Muttoni, G. (2013). Magnetic-fabric analysis as a tool to constrain mechanisms of deep-water mudstone deposition in the Marnoso Arenacea Formation (Miocene, Italy). *J. Sediment. Res.* 83, 170–182. doi:10.2110/jsr.2013.12

Davis, G. H. (1978). "Monocline fold pattern of the Colorado Plateau," in *Laramide folding associated with basement block faulting in the western United States*. Editors V. Matthews (Boulder, CO: Geological Society of America), 215–233.

Dunlop, D. J., and Özdemir, Ö. (1997). *Rock magnetism: fundamentals and Frontiers*. Cambridge, UK: Cambridge University Press.

Ejembi, J. I., Potter-McIntyre, S. L., Sharman, G. R., Smith, T. M., Saylor, J. E., Hatfield, K., et al. (in revision). Detrital zircon geochronology and provenance of the Middle to Upper Jurassic Paradox Basin, western Colorado: paleogeographic implications for southwestern Laurentia. Geosphere.

Ellwood, B. B., and Howard, J. H. (1981). Magnetic fabric development in an experimentally produced barchan dune, *J. Sediment. Res.* 51, 97–100. doi:10.1306/212F7C16-2B24-11D7-8648000102C1865D

Essalhi, M., Sizaret, S., Barbanson, L., Chen, Y., Branquet, Y., Panis, D., et al. (2009). Track of fluid paleocirculation in dolomite host rock at regional scale by the Anisotropy of Magnetic Susceptibility (AMS): An example from Aptian carbonates of La Florida, Northern Spain. *Earth Planet Sci. Lett.* 277, 501–513. doi:10.1016/j.epsl.2008.11.011

Essalhi, M., Sizaret, S., Barbanson, L., Chen, Y., Lagroix, F., Demory, F., et al. (2011). A case study of the internal structures of gossans and weathering processes in the Iberian Pyrite Belt using magnetic fabrics and paleomagnetic dating. *Miner. Deposita* 46, 981–999. doi:10.1007/s00126-011-0361-8

Ferré, E. C., Bordarier, C., and Marsh, J. S. (2002). Magma flow inferred from AMS fabrics in a layered mafic sill, Insizwa, South Africa. *Tectonophysics* 354, 1–23. doi:10.1016/s0040-1951(02)00273-1

Ferré, E. C. (2002). Theoretical models of intermediate and inverse AMS fabrics. *Geophys. Res. Lett.* 29, 31-1–31-4. doi:10.1029/2001gl014367

Folk, R. L. (1980). *Petrology of sedimentary rocks*. Austin, TX: Hemphill Publishing Company, 182.

Hunt, C. B. (1969). *Geological history of the Colorado river* in *the Colorado river region and John Wesley Powell. U.S. Geological Survey Professional Paper 669-C*. Reston, VA: United States Geological Survey, 59–130.

Hunt, J. M. (1990). Generation and migration of petroleum from abnormally pressured fluid compartments (1). *AAPG (Am. Assoc. Pet. Geol.) Bull.* 74, 1–12.

Ising, G. (1942). On the magnetic properties of varved clay, *Ark. Mat. Astron. Phys.* 29a (5), 1–37.

Jelínek, V. (1978). Statistical processing of anisotropy of magnetic susceptibility measured on groups of specimens. *Studia Geophys. Geod.* 22 (1), 50–62. doi:10.1007/BF01613632

Just, J., Kontny, A., De Wall, H., Hirt, A. M., and Martín-Hernández, F., 2004. Development of magnetic fabrics during hydrothermal alteration in the Soultz-sous-Forets granite from the EPS-1 borehole, Upper Rhine Graben, *Geolo. Soc., London, Special Publications* 238, 509–526. doi:10.1144/gsl.sp.2004.238.01.26

Kelley, V. C. (1958). "Tectonics of the region of the Paradox Basin," in *Guidebook to the Geology of the Paradox Basin: intermountain association of Petroleum Geologists*. Editors A. F. Sanborn (Salt Lake City, UT: Intermountain Association of Petroleum Geologists (U.S.)), 31–38.

Kluth, C. F., and Coney, P. J. (1981). Plate tectonics of the ancestral Rocky Mountains. *Geol.* 9, 10–15. doi:10.1130/0091-7613(1981)9<10:ptotar>2.0.co;2

Lagroix, F., and Banerjee, S. K. (2002). Paleowind directions from the magnetic fabric of loess profiles in central Alaska. *Earth Planet Sci. Lett.* 195, 99–112. doi:10.1016/s0012-821x(01)00564-7

Li, S., Deng, C., Paterson, G. A., Yao, H., Huang, S., Liu, C., et al. (2014). Tectonic and sedimentary evolution of the late Miocene–Pleistocene Dali Basin in the southeast margin of the Tibetan Plateau: Evidences from anisotropy of magnetic susceptibility and rock magnetic data. *Tectonophysics* 629, 362–377. doi:10.1016/j.tecto.2014.05.035

Marshak, S., Karlstrom, K., and Timmons, J. M. (2000). Inversion of Proterozoic extensional faults: An explanation for the pattern of Laramide and Ancestral Rockies intracratonic deformation. *United States, Geolo.* 28, 735–738. doi:10.1130/0091-7613(2000)28<735:iopefa>2.0.co;2

Martin-Hernandez, F., and García-Hernández, M. M. (2010). Magnetic properties and anisotropy constant of goethite single crystals at saturating high fields. *Geophys. J. Int.* 181 (2), 756–761. doi:10.1111/j.1365-246X.2010.04566.x

Massei, N., Lacroix, M., Wang, H. Q., and Dupont, J.-P. (2002). Transport of particulate material and dissolved tracer in a highly permeable porous medium: comparison of the transfer parameters. *J. Contam. Hydrol.* 57, 21–39. doi:10.1016/s0169-7722(01)00216-9

McFadden, P. L., and McElhinny, M. W. (1990). Classification of the reversal test in palaeomagnetism. *Geophys. J. Int.* 103, 725–729. doi:10.1111/j.1365-246x.1990.tb05683.x

Musgrove, M., and Banner, J. L. (1993). Regional ground-water mixing and the origin of saline fluids: midcontinent, United States. *Science* 259, 1877–1882. doi:10.1126/science.259.5103.1877

Nuccio, V. F., and Condon, S. M. (1996). *Burial and thermal history of the Paradox Basin, Utah and Colorado, and petroleum potential of the Middle Pennsylvanian Paradox Basin, U.S. Geol. Survey Bulletin 2000-O*. Boston, MA: U.S. Government Printing Office, 57–76.

Oliver, J. (1986). Fluids expelled tectonically from orogenic belts: Their role in hydrocarbon migration and other geologic phenomena. *Geol.* 14, 99–102. doi:10.1130/0091-7613(1986)14<99:fetfob>2.0.co;2

Parés, J. M., Hassold, N. J. C., Rea, D. K., and van der Pluijm, B. A. (2007). Paleocurrent directions from paleomagnetic reorientation of magnetic fabrics in deep-sea sediments at the Antarctic Peninsula Pacific margin (ODP Sites 1095, 1101). *Mar. Geol.* 242, 261–269. doi:10.1016/j.margeo.2007.04.002

Parés, J. M., Miguens, L., and Saiz, C. (2016). Characterizing pore fabric in sandstones with magnetic anisotropy methods: Initial results. *J. Petrol. Sci. Eng.* 143, 113–120. doi:10.1016/j.petrol.2016.02.028

Parry, W. T., Chan, M. A., and Beitler, B. (2004). Chemical bleaching indicates episodes of fluid flow in deformation bands in sandstone. *AAPG Bulletin* 88, 175–191. doi:10.1306/09090303034

Pederson, J. L., Mackley, R. D., and Eddleman, J. L. (2002). Colorado Plateau uplift and erosion evaluated using GIS. *GSA Today (Geol. Soc. Am.)* 12, 4–10. doi:10.1130/1052-5173(2002)012<0004:cpuaee>2.0.co;2

Pfleiderer, S., and Halls, H. C. (1993). Magnetic pore fabric analysis: Verification through image autocorrelation. *J. Geophys. Res.* 98, 4311–4316. doi:10.1029/92jb01851

Pfleiderer, S., and Halls, H. C. (1990). Magnetic susceptibility anisotropy of rocks saturated with ferrofluid: a new method to study pore fabric? *Phys. Earth Planet. In.* 65, 158–164. doi:10.1016/0031-9201(90)90083-a

Potter, S. L., and Chan, M. A. (2011). Joint controlled fluid flow patterns and iron mass transfer in Jurassic Navajo Sandstone. *Geofluids* 11, 184–198. doi:10.1111/j.1468-8123.2011.00329.x

Potter-McIntyre, S. L., Chan, M. A., and McPherson, B. J. (2014). Concretion formation in volcaniclastic host rocks: evaluating the role of organics, mineralogy, and geochemistry on early diagenesis. *J. Sediment. Res.* 84, 875–892. doi:10.2110/jsr.2014.58

Rønnevik, C., Ksienzyk, A. K., Fossen, H., and Jacobs, J. (2017). Thermal evolution and exhumation history of the Uncompahgre Plateau (northeastern Colorado Plateau), based on apatite fission track and (U-Th)-He thermochronology and zircon U-Pb dating *Geosphere* 13, 518–537. doi:10.1130/GES01415.1.

Robion, P., David, C., Dautriat, J., Colombier, J.-C., Zinsmeister, L., and Collin, P.-Y. (2014). Pore fabric geometry inferred from magnetic and acoustic anisotropies in rocks with various mineralogy, permeability and porosity. *Tectonophysics* 629, 109–122. doi:10.1016/j.tecto.2014.03.029

Robion, P., Grelaud, S., and Frizon de Lamotte, D. (2007). Pre-folding magnetic fabrics in fold-and-thrust belts: Why the apparent internal deformation of the sedimentary rocks from the Minervois basin (NE-Pyrenees, France) is so high compared to the Potwar basin (SW-Himalaya, Pakistan)? *Sediment. Geol.* 196, 181–200. doi:10.1016/j.sedgeo.2006.08.007

Rochette, P., Jackson, M., and Aubourg, C. (1992). Rock magnetism and the interpretation of anisotropy of magnetic susceptibility. *Rev. Geophys.* 30, 209–226. doi:10.1029/92rg00733

Saint-Bezar, B., Hebert, R. L., Aubourg, C., Robion, P., Swennen, R., and de Lamotte, D. F. (2002). Magnetic fabric and petrographic investigation of hematite-bearing sandstones within ramp-related folds: examples from the South Atlas Front (Morocco). *J. Struct. Geol.* 24, 1507–1520. doi:10.1016/s0191-8141(01)00140-7

Schieber, J. and Ellwood, B. B. (1993). Determination of basinwide paleocurrent patterns in a shale succession from anisotropy of magnetic susceptibility (AMS); a case study of the mid-Proterozoic Newland Formation, Montana. *J. Sediment. Res.* 63, 874–880.

Sizaret, S., Chen, Y., Barbanson, L., Henry, B., Camps, P., and Marcoux, E. (2006). Crystallization in flow–I. Palaeocirculation track by texture analysis and magnetic fabrics. *Geophys. J. Int.* 167, 605–612. doi:10.1111/j.1365-246x.2006.03106.x

Sizaret, S., Chen, Y., Chauvet, A., Marcoux, E., and Touray, J. C. (2003). Magnetic fabrics and fluid flow directions in hydrothermal systems. A case study in the Chaillac Ba–F–Fe deposits (France). *Earth Planet Sci. Lett.* 206, 555–570. doi:10.1016/s0012-821x(02)01112-3

Tarling, D. H., and Hrouda, F. (1993). *The Magnetic anisotropy of rocks*. Berlin, Germany: Springer, 218.

Tweto, O., and Schoenfeld, R. (1979). *Geologic map of Colorado*. Reston, VA: U.S. Geological Survey.

Ungerer, P., Burrus, J., Doligez, B., Chenet, P., and Bessis, F. (1990). Basin evaluation by integrated two-dimensional modeling of heat transfer, fluid flow, hydrocarbon generation, and migration (1). *AAPG (Am. Assoc. Pet. Geol.) Bull.* 74, 309–335.

Wilkinson, J. J. (2001). Fluid inclusions in hydrothermal ore deposits. *Lithos* 55, 229–272. doi:10.1016/s0024-4937(00)00047-5

Wing, B. A., and Ferry, J. M. (2007). Magnitude and geometry of reactive fluid flow from direct inversion of spatial patterns of geochemical alteration. *Am. J. Sci.* 307, 793–832. doi:10.2475/05.2007.02

Conflict of Interest: The authors declare that the research was conducted in the absence of any commercial or financial relationships that could be construed as a potential conflict of interest.

The handling editor declared a past co-authorship with one of the authors (SS).

frontiers in Earth Science

ORIGINAL RESEARCH
published: 22 December 2020
doi: 10.3389/feart.2020.609058

Classification of a Complexly Mixed Magnetic Mineral Assemblage in Pacific Ocean Surface Sediment by Electron Microscopy and Supervised Magnetic Unmixing

Jinhua Li[1,2,3,4]*, *Yan Liu*[1,2,3,4], *Shuangchi Liu*[1,4], *Andrew Philip Roberts*[5], *Hongmiao Pan*[3,6], *Tian Xiao*[3,6] and *Yongxin Pan*[1,2,3,4]

[1]Key Laboratory of Earth and Planetary Physics, Institute of Geology and Geophysics, Innovation Academy for Earth Sciences, Chinese Academy of Sciences, Beijing, China, [2]Laboratory for Marine Geology, Qingdao National Laboratory for Marine Science and Technology, Qingdao, China, [3]International Associated Laboratory of Evolution and Development of Magnetotactic Multicellular Organisms (LIA-MagMC), CNRS-CAS, Beijing, China, [4]College of Earth and Planetary Sciences, University of Chinese Academy of Sciences, Beijing, China, [5]Research School of Earth Sciences, Australian National University, Canberra, ACT, Australia, [6]Key Laboratory of Marine Ecology and Environmental Sciences, Institute of Oceanology, Chinese Academy of Sciences, Qingdao, China

OPEN ACCESS

Edited by:
Ricardo IF Trindade, University of São Paulo, Brazil

Reviewed by:
Gary Dean Acton, Texas A&M University, United States
Luis Manuel Alva Valdivia, National Autonomous University of Mexico, Mexico

***Correspondence:**
Jinhua Li
lijinhua@mail.iggcas.ac.cn

Specialty section:
This article was submitted to Geomagnetism and Paleomagnetism, a section of the journal Frontiers in Earth Science

Received: *22 September 2020*
Accepted: *23 November 2020*
Published: *22 December 2020*

Citation:
Li J, Liu Y, Liu S, Roberts AP, Pan H, Xiao T and Pan Y (2020) Classification of a Complexly Mixed Magnetic Mineral Assemblage in Pacific Ocean Surface Sediment by Electron Microscopy and Supervised Magnetic Unmixing. Front. Earth Sci. 8:609058. doi: 10.3389/feart.2020.609058

Unambiguous magnetic mineral identification in sediments is a prerequisite for reconstructing paleomagnetic and paleoenvironmental information from environmental magnetic parameters. We studied a deep-sea surface sediment sample from the Clarion Fracture Zone region, central Pacific Ocean, by combining magnetic measurements and scanning and transmission electron microscopic analyses. Eight titanomagnetite and magnetite particle types are recognized based on comprehensive documentation of crystal morphology, size, spatial arrangements, and compositions, which are indicative of their corresponding origins. Type-1 particles are detrital titanomagnetites with micron- and submicron sizes and irregular and angular shapes. Type-2 and -3 particles are well-defined octahedral titanomagnetites with submicron and nanometer sizes, respectively, which are likely related to local hydrothermal and volcanic activity. Type-4 particles are nanometer-sized titanomagnetites hosted within silicates, while type-5 particles are typical dendrite-like titanomagnetites that likely resulted from exsolution within host silicates. Type-6 particles are single domain magnetite magnetofossils related to local magnetotactic bacterial activity. Type-7 particles are superparamagnetic magnetite aggregates, while Type-8 particles are defect-rich single crystals composed of many small regions. Electron microscopy and supervised magnetic unmixing reveal that type-1 to -5 titanomagnetite and magnetite particles are the dominant magnetic minerals. In contrast, the magnetic contribution of magnetite magnetofossils appears to be small. Our work demonstrates that incorporating electron microscopic data removes much of the ambiguity associated with magnetic mineralogical interpretations in traditional rock magnetic measurements.

Keywords: marine sediments, magnetic minerals, environmental magnetism, magnetic techniques, transmission electron microscopy, magnetofossils, titanomagnetite

INTRODUCTION

Sedimentary sequences provide important geological records for understanding long-term variations of Earth's magnetic field and paleoclimate (e.g., Valet and Meynadier, 1993; Guyodo and Valet, 1999; Kissel et al., 1999; Evans and Heller, 2001; Evans and Heller, 2003; Yamazaki, 2009; Hao et al., 2012; Liu et al., 2012; Roberts et al., 2013; Kissel et al., 2020; Valet et al., 2020). Magnetic mineral identification in sediments is fundamentally important for both paleomagnetic and environmental magnetic studies because the type, concentration, size and shape of magnetic minerals control their magnetic properties, including magnetic recording quality (e.g., Dunlop and Özdemir, 1997; Dekkers, 2003; Liu et al., 2012; Chang et al., 2014a; Larrasoaña et al., 2014; Roberts et al., 2019). However, quantitative identification of individual magnetic mineral components is challenging because each component can have different origins, grain size, shape, mineralogy and stoichiometry. For example, four or five distinct magnetic mineral components are identified commonly in pelagic carbonate sediments, which might otherwise be considered to be among the simplest of magnetic mineral assemblages (e.g., Roberts et al., 2013). Quantitative identification of each magnetic mineral component and its magnetic contribution can be important in environmental and paleomagnetic studies (e.g., Ouyang et al., 2014; Chen et al., 2017).

Numerous magnetic techniques have been developed to measure the bulk magnetic properties of sediments to provide information about the concentration, domain state (a measure of magnetic grain size), and mineralogy of magnetic particles in a sample (e.g., Verosub and Roberts, 1995; Evans and Heller, 2003; Lascu et al., 2010; Liu et al., 2012; Roberts et al., 2014; Zhao et al., 2017; Roberts et al., 2019). Mathematical unmixing methods have also been developed to identify these magnetic mineral components quantitatively based on their bulk magnetic properties (e.g., Heslop, 2015). They generally involve fitting of functions to derivatives of isothermal remanent magnetization (IRM) acquisition or direct current demagnetization (DCD) curves (e.g., Robertson and France, 1994; Kruiver et al., 2001; Heslop et al., 2002; Egli, 2003, Egli, 2004a; Egli, 2004c; Heslop and Dillon, 2007; Maxbauer et al., 2016), alternating field demagnetization curves of an anhysteretic remanent magnetization or IRM (Egli and Lowrie, 2002; Egli, 2004a, Egli, 2004b, Egli, 2004c), or analysis of hysteresis loops (e.g., Roberts et al., 1995; Dunlop, 2002a, Dunlop, 2002b; Tauxe et al., 2002; Heslop and Roberts, 2012a; Heslop and Roberts, 2012b), ferromagnetic resonance (FMR) spectra (e.g., Weiss et al., 2004; Kopp et al., 2006a; Kopp et al., 2006b; Gehring et al., 2011; Kind et al., 2011; Gehring et al., 2013; Chang et al., 2014b), or first-order reversal curve (FORC) diagrams (e.g., Roberts et al., 2014; Lascu et al., 2015; Channell et al., 2016; Harrison et al., 2018; Roberts et al., 2018).

Nonuniqueness is a fundamental issue for bulk magnetic property analysis because 1) mathematical unmixing can produce an infinite number of solutions, and 2) magnetic minerals have variable magnetic properties that can overlap with those of other minerals (e.g., Liu et al., 2012). The combined presence of multiple magnetic mineral components produces a complicated relationship between the magnetic properties of magnetic minerals and their domain states, concentration, sizes, shapes and stoichiometry, which often frustrates component-specific magnetic diagnosis (e.g., Yamazaki and Ioka, 1997; Heslop, 2009; Roberts et al., 2011a; Li et al., 2012; Liu et al., 2012; Li et al., 2013a; Roberts et al., 2019). To minimize ambiguity for environmental and paleomagnetic interpretations, integration of multiple magnetic parameters and non-magnetic techniques is recommended to identify and quantify magnetic minerals in sediments (e.g., Kopp and Kirschvink, 2008; Liu et al., 2012; Chang et al., 2014b; Heslop, 2015; Roberts et al., 2019).

Transmission electron microscope (TEM) observations are among the most useful microscopic approaches because they can be used to characterize simultaneously mineralogy, stoichiometry, magnetism and crystallography of magnetic minerals at the micron and nanometer scales, even to the atomic level (e.g., Harrison et al., 2002; Galindo-Gonzalez et al., 2009; Pósfai et al., 2013; Li and Pan, 2015; Li et al., 2020). TEM and scanning electron microscope (SEM) observations have been used in environmental magnetism and paleomagnetism for many years (e.g., Evans and Wayman, 1970; Kirschvink and Chang, 1984; Harrison et al., 2002; Roberts and Weaver, 2005; Kopp and Kirschvink, 2008; Harrison and Feinberg, 2009). Most recent studies emphasize the use of TEM in testing for the presence of biogenic magnetite particles produced by magnetotactic bacteria (MTB) (magnetofossils) from sediments (e.g., Petersen et al., 1986; Stolz et al., 1986; Chang and Kirschvink, 1989; Vali and Kirschvink, 1989; Akai et al., 1991; Hesse, 1994; Snowball, 1994; Tarduno et al., 1998; Yamazaki and Kawahata, 1998; Pan et al., 2005; Housen and Moskowitz, 2006; Kopp et al., 2007; Maloof et al., 2007; Kopp and Kirschvink, 2008; Schumann et al., 2008; Kopp et al., 2009; Roberts et al., 2011b; Chang et al., 2012; Larrasoaña et al., 2012; Yamazaki and Shimono, 2013; Chang et al., 2014a; Chang et al., 2014b; Liu et al., 2015; Chang et al., 2016a; Dong et al., 2016; Chang et al., 2018; Usui et al., 2019; He and Pan, 2020; Jiang et al., 2020; Qian et al., 2020; Yamazaki et al., 2020; Yuan et al., 2020). In contrast, relatively few studies have used TEM observations to study the mineralogy and chemistry of other magnetic mineral types in sediments (e.g., Gibbs-Eggar et al., 1999; Franke et al., 2007; Chang et al., 2016b; Zhang et al., 2018; Li et al., 2019). While magnetofossils are relatively easy to recognize in TEM observations due to their distinctive crystal morphologies and chain structures compared to other magnetic mineral types (e.g., Kopp and Kirschvink, 2008; Jimenez-Lopez et al., 2010; Li et al., 2013b), this can lead to bias in overestimating their magnetic contributions, and/or to ignoring contributions from, for example, weakly interacting or noninteracting single domain (SD) magnetite particles hosted by silicates (e.g., Wang et al., 2015; Chang et al., 2016b).

We combine rock magnetic measurements with SEM and TEM observations to characterize the magnetic mineralogy of a surface sediment from the central Pacific Ocean. We show that by incorporating detailed SEM and TEM characterizations, much of the ambiguity that is inherent to magnetic mineralogy

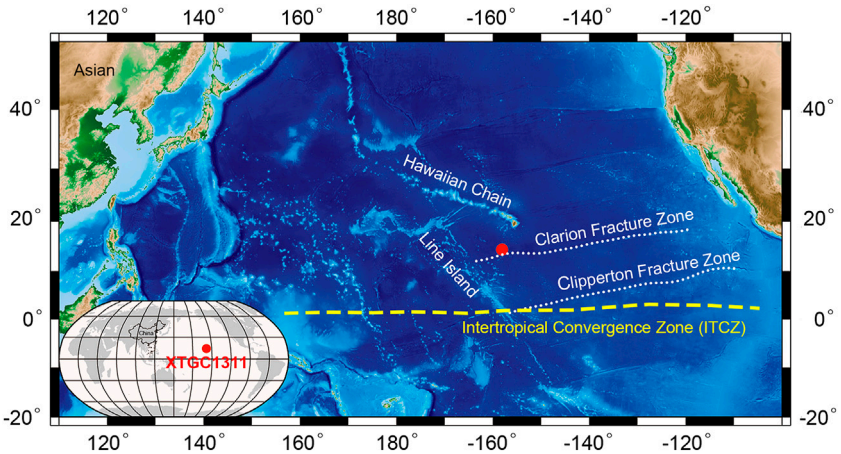

FIGURE 1 | Location map with the position of sample station.

interpretations when using only rock magnetic measurements is eliminated. This approach allows evaluation of the contribution of magnetic mineral components to paleomagnetic and rock magnetic signals and/or their environmental significance.

MATERIALS AND METHODS

Sample and Preparation

Surface sediment was retrieved at station XTGC1311 (158.0485,917 W, 14.44244 N; 5,260 m water depth; **Figure 1**) during cruise DY29–02 of R/V *Haiyang Liuhao* in 2013 to the Pacific Ocean (Dong et al., 2016). The station is adjacent to the Clarion Fracture Zone to the south, the Hawaiian Island Chain to the North, and Kiribati (Line Islands) to the West. The surrounding islands were formed by upper Jurassic to lower Cretaceous volcanic activity (Clouard and Bonneville, 2005). The seafloor between the Clarion Fracture Zone and the Clipperton Fracture Zone is characterized by long, north-south-trending hills, ridges, intervening valleys, and furrows (Vithana et al., 2019; Maciąg and Harff, 2020). Sediments in the area are characterized by organic carbon-starved siliceous clay (Mewes et al., 2016). Modern sedimentation at the sampled station consists of both Asian eolian dust transported by zonal westerlies and northeast trade winds and local hydrothermal and volcanic inputs (Hyeong et al., 2005; Hyeong et al., 2006; Maciąg and Harff, 2020). It is also possibly influenced by Antarctic Bottom Water (AABW), which is oxygen rich and migrates eastward and northward into this area (Deng et al., 2016; Mewes et al., 2016).

Sediment samples were collected using a gravity corer. Surface sediments were subsampled immediately on the ship from the upper 1 cm of the core (hereafter referred to as EPMNP-31) and were then stored at −20°C prior to analysis to minimize oxidation. Samples were vacuum dried at 30°C for 12 h and were then loaded into non-magnetic gelatin capsules for magnetic measurements.

For nanometer scale characterization, magnetic minerals were separated from the bulk sediment. Magnetic separation was carried out with the following procedure. First, about ~10 mg of sediment was suspended into ~50 ml of Milli-Q water in a ~100 ml beaker and was then mixed by ultrasonication assisted by agitation with a glass stirring rod. Second, a 5 × 5 mm cylindrical neodymium magnet (surface field strength > 100 mT) was attached to the outside of the beaker ~2 mm above the water-sediment surface. After ~4 h of magnetic absorption, magnetic minerals that were concentrated adjacent to the magnet were transferred to a 10 ml glass tube. To extract as much of the magnetic mineral content from the sediment as possible, the first and second steps were repeated several times until no obvious magnetic aggregates adjacent to the magnet were found. Third, extracted magnetic minerals were resuspended in ~5 ml of Milli-Q water in a 10 ml glass tube, mixed by ultrasonication, and then extracted magnetically again following a similar procedure as the second step above. To remove non-magnetic minerals from the extracts, the third step was repeated several times until non-magnetic particles were not observed at the bottom of the tube. The final three repeats were performed in 99.5% ethanol. Finally, extracted magnetic minerals were suspended in 50 μl of 99.5% ethanol and were stored at −20°C prior to TEM or SEM observations.

Magnetic Measurements

Low-temperature magnetic measurements were made with a Quantum Design Magnetic Property Measurement System (MPMS XP-5, 5.0×10^{-10} Am^2 sensitivity). Zero-field-cooled (ZFC) and field-cooled (FC) curves were obtained by cooling the sample from 300 to 10 K in a zero field and in a 2.5-T field, respectively, followed by imparting a saturation IRM (SIRM) to the sample in a 2.5-T field at 10 K (hereafter $SIRM_{10\ K\_2.5\ T}$), and then by measuring $SIRM_{10\ K\_2.5\ T}$ during warming back to 300 K in zero field (Moskowitz et al., 1993). For low-temperature cycling (LTC) of a room temperature SIRM obtained in a 2.5-T field at 300 K (hereafter $SIRM_{300\ K\_2.5\ T}$), remanence was measured in zero field during a cooling-warming cycle (300 → 10 → 300 K).

Room-temperature magnetic experiments were made using a Micromag Model 3,900 vibrating sample magnetometer (VSM) (Princeton Measurement Corporation; 5.0×10^{-11} Am^2 sensitivity).

A hysteresis loop was measured in a 1 T maximum field with 500 ms averaging time. The saturation magnetization (M_s), saturation remanence (M_{rs}), and coercivity (B_c), were determined after applying a high-field (0.7–1 T) slope correction. Static IRM acquisition and DCD curves were measured on an initially demagnetized and 1 T-re-magnetized sample, respectively. The coercivity of remanence (B_{cr}) was determined from the DCD curve. IRM acquisition and DCD curves were measured to 1 T using a logarithmic sweep mode with 1 mT initial field and 120 measurement points. To simplify comparison of remanence results and to calculate the *R*-value of the Wohlfarth-Cisowski test (Cisowski, 1981), the IRM acquisition curve was normalized to the SIRM, and the DCD curve was rescaled as ½ [1 + IRM(−H)/SIRM]. To quantify contributions from different coercivity families to the total IRM, the IRM curve was decomposed into cumulative log Gaussian (CLG) curves (Robertson and France, 1994) using the software of Heslop et al. (2002). The different coercivity families are defined by their half saturation IRM (SIRM) field ($B_{1/2}$) and the percentage of their contribution to the total IRM.

FORCs (Pike et al., 1999; Roberts et al., 2000) were also measured with the VSM using the protocol described by Egli et al. (2010). A total of 300 FORCs were measured with a positive saturation field of 1 T, increasing field steps of 0.976 mT, and a 600 ms averaging time. A FORC diagram was calculated using the FORCinel v3.06 software (Harrison and Feinberg, 2008) and smoothed using the VARIFORC algorithm (Egli, 2013). The horizontal (B_c) and vertical (B_i) axes on a FORC diagram indicate the microcoercivity and interaction field distribution for SD particles, respectively (Pike et al., 1999; Roberts et al., 2000).

Scanning Electron Microscope and Transmission Electron Microscope Analyses

Extracted magnetic minerals were deposited onto carbon-based, double sided adhesive tape that was mounted onto the surface of an aluminum stub for SEM observations. The sample was carbon coated prior to imaging to create a conductive layer. Extracted magnetic minerals were deposited onto carbon-coated copper grids for TEM experiments. SEM and TEM experiments were carried out with a Nova NanoSEM 450 field-emission SEM (15 kV accelerating voltage) and a JEM2100 TEM (200 kV accelerating voltage), respectively, at the Institute of Geology and Geophysics, Chinese Academy of Sciences (IGGCAS, Beijing, China). Microchemical analyses were made by Energy-dispersive X-ray spectrometry (EDXS) elemental mapping in the SEM and point analysis in the TEM.

RESULTS

Room- and Low-Temperature Magnetic Properties

A hysteresis loop for the sample is closed at values well below ~400 mT (**Figure 2A**). Stepwise SIRM acquisition and demagnetization indicate that the sample is saturated and demagnetized largely below ~300 mT, and completely at ~600 mT (**Figure 2B**). Hysteresis parameters after high-field slope correction are B_c = 20.6 mT, B_{cr} = 44.9 mT, B_{cr}/B_c = 2.18, and M_{rs}/M_s = 0.28. Normalized IRM acquisition and DCD curves are roughly symmetric with a calculated *R*-value of 0.45 for the Wohlfarth-Cisowski test (Cisowski, 1981).

Both ZFC and FC $SIRM_{10\ K\_2.5\ T}$ curves decrease gradually during warming from 10 to 300 K (**Figure 2C**). The LTC curve is humped. The $SIRM_{300\ K\_2.5\ T}$ cooling curve increases gradually from 300 to ~176 K and then decreases gradually to 10 K. The warming curve overlaps with the cooling curve below ~50 K, and then increases slowly to 153 K, and finally decreases gradually to 300 K. The $SIRM_{300\ K\_2.5\ T}$ cooling-warming curves are roughly reversible with a ~6% remanence loss after cycling (**Figure 2D**). The Verwey transition, which is characterized by an obvious remanence drop at ~100–120 K, is not clearly present in the ZFC/FC warming and LTC curves. This indicates that magnetite particles in this sample are nonstoichiometric, either due to surface oxidation or cation substitution (e.g., Muxworthy and McClelland, 2000; Özdemir and Dunlop, 2010).

First-Order Reversal Curve Results

FORC measurements provide information about all magnetic particles in a sample in terms of their magnetization (magnitude), microcoercivity (horizontal distribution) and magnetic interaction field for SD particles (vertical distribution) (Pike et al., 1999; Roberts et al., 2000; Roberts et al., 2014). The FORC diagram in **Figure 3** indicates the presence of non-interacting SD (Newell, 2005; Egli et al., 2010; Roberts et al., 2014), vortex state (Pike and Fernandez, 1999; Muxworthy and Dunlop, 2002; Roberts et al., 2017) and viscous particles near the superparamagnetic (SP)/SD threshold size (Pike et al., 2001). The non-interacting SD contribution produces a central ridge signal that can be extracted (**Figure 3B**) following Egli et al. (2010) and separated into three components along a horizontal profile at B_i = 0 mT (**Figure 3D**). The three SD components have peak coercivities of ~20.4, ~76.8, and 126.1 mT. The remaining FORC distribution after central ridge extraction has a tri-lobate shape (**Figure 3C**) associated with the vortex state (Lascu et al., 2018). The upper lobe intersects the vertical axis at higher values (B_i = ~50 mT) than the lower lobe, which intersects the vertical axis closer to the origin. The middle lobe is narrower and extends along the horizontal axis to B_c = ~140 mT (**Figure 3C**). A narrow FORC distribution along the lower vertical axis is related to viscous magnetic particles near the SP/SD threshold size (**Figures 3A,C**) (Pike et al., 2001; Roberts et al., 2014).

Scanning Electron Microscope Analyses of Magnetic Minerals

SEM observations combined with EDXS elemental mapping reveal the overall microscale morphology and composition of sedimentary magnetic minerals. Minerals can be distinguished readily by combining analysis of particle morphologies and corresponding backscattered electron contrast and chemical composition (**Figure 4**; **Supplementary Material S1**). Most particles with dark contrast generally consist of Si, O and Fe (and/or Mn), which indicates that they are Fe/Mn silicates. In

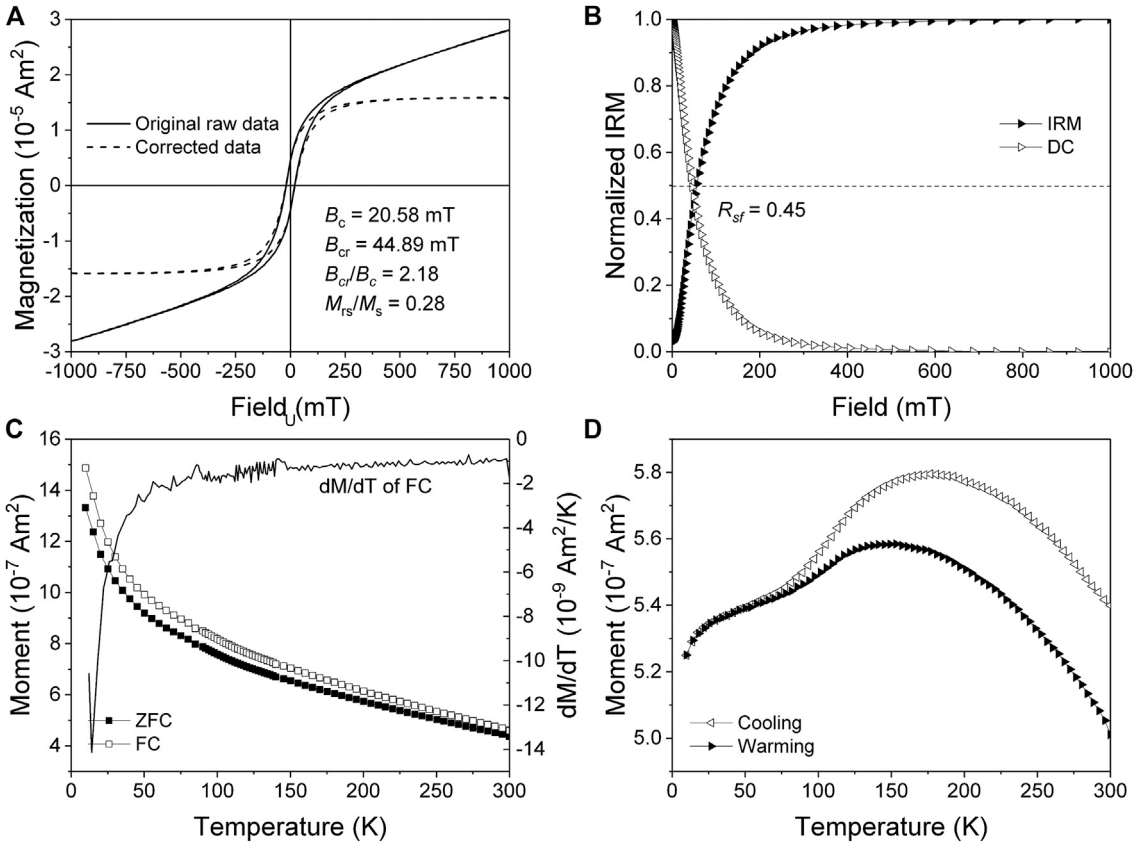

FIGURE 2 | (A) Room-temperature hysteresis loop (solid and dashed lines are the original raw and high-field slope-corrected data, respectively. **(B)** Normalized IRM acquisition and DCD curves. **(C)** FC-SIRM$_{10\ K_2.5\ T}$ and ZFC-SIRM$_{10\ K_2.5\ T}$ warming curves. **(D)** SIRM$_{300\ K_2.5\ T}$ cooling-warming cycle curves.

contrast, particles with bright contrast are often composed of Fe and O, some of which also contain Ti. They are titanomagnetite (with variable Ti contents) or magnetite, as confirmed by TEM analyses (see below). The particles are morphologically diverse with sizes ranging from tens of nm to tens of μm.

SEM observations reveal well-defined and uncorroded octahedral (**Figures 4G,I**), truncated octahedral (**Figure 4H**) and irregular and angular shapes for micron- and submicron magnetite particles (**Figures 4A–I**). Most nanometric magnetite particles are hosted within silicates (**Figures 4J–O**); a few are isolated or attached onto other particles (**Figures 4A–4F**). Two silicate-hosted titanomagnetite inclusion types are identified: randomly oriented, dispersed particles (**Figure 4J–L**) and dendritic particles (**Figures 4M–O**). Compared to the micron-sized titanomagnetite particles, the morphology and stoichiometry of these nanometric magnetite particles are difficult to characterize with SEM imaging and SEM-EDXS elemental mapping because of the ~1 nm spatial resolution limit.

Transmission Electron Microscope Analyses of Magnetic Minerals

Systematic TEM and high-resolution TEM (HRTEM) observations were made on different magnetic particle types to identify their mineralogy and stoichiometry. Representative particles were further studied by selected area electron diffraction (SAED) and TEM-EDXS point analyses. Eight magnetic particle types were identified based on crystal morphology, size, composition and spatial arrangement (**Figures 5–9**).

Type-1 and type-2 particles are micron-or submicron-sized and generally occur as loose aggregates (**Figures 5A,D**) or isolated particles (**Figure 5B**). They are too thick to image lattice fringes directly by HRTEM. We generally tilted the sample stage to allow the incident electron beam to pass through large particles along a certain zone axis, and then selected thinner edge areas for HRTEM, SAED and TEM-EDXS point analyses. As shown in **Figures 5A–F**, TEM observations from one zone axis combined with SAED analyses on individual Type-1 particles reveal that they consist mainly of micron or submicron angular titanomagnetite (**Figures 5A,B,D**), with Type-2 particles consisting of well-defined octahedral magnetite (**Figures 5G,H**). Type-3 aggregates tend to consist of randomly organized nanometric titanomagnetite particles. HRTEM observations combined with corresponding Fast Fourier Transform (FFT) analyses reveal that these particles are elongated octahedral magnetite with average length of 52.9 ± 10.9 nm, width of 43.9 ± 9.2 nm and aspect ratio (length/width) of 1.22 ± 0.18 (n = 30). TEM-EDXS point analyses reveal

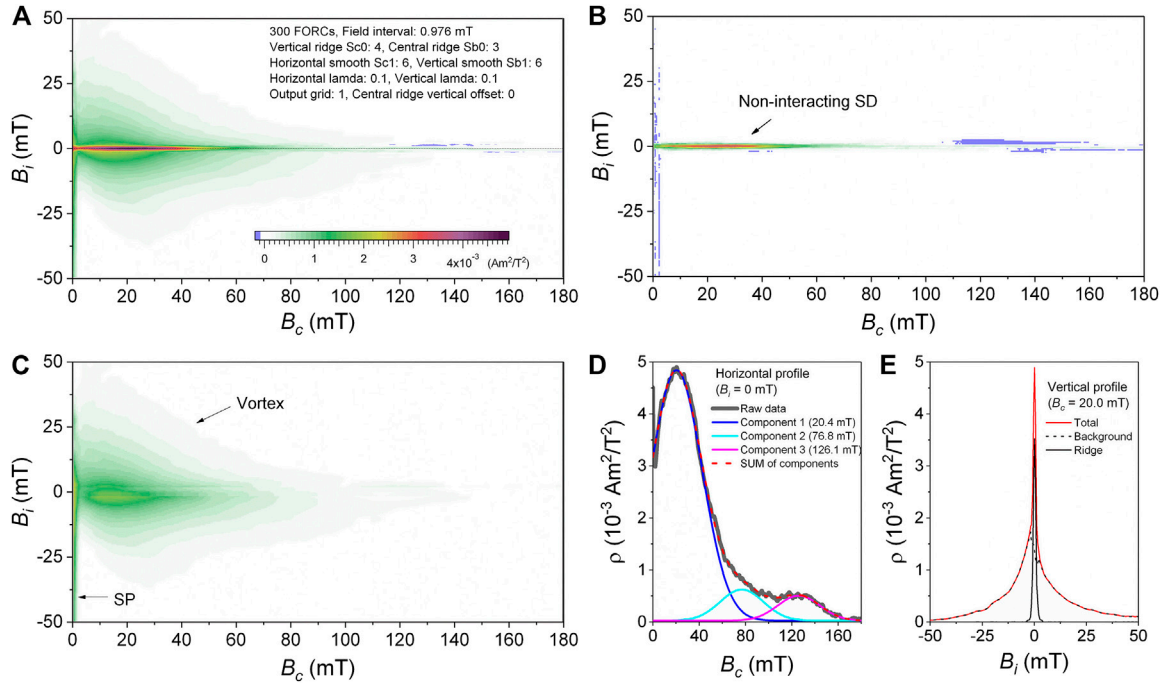

FIGURE 3 | First-order reversal curve (FORC) results. **(A)** FORC diagram. **(B)** Central ridge component extracted from the FORC diagram. **(C)** Background FORC component after removal of the central ridge. **(D)** Horizontal profile $\rho(B_c)$ of the FORC function (coercivity distribution at $B_i = 0$ mT). The black line indicates raw data, while blue, cyan and purple lines indicate three components decomposed from the raw data. The dashed red line indicates a sum of all three Gaussian components. **(E)** Vertical profiles $\rho(B_i)$ of the FORC function (magnetostatic-interaction field distribution) at 20 mT: the central ridge component (black), the background component with vertical spread (dashed black line), and the total of the two components (red line) are shown.

that Type-1 to Type-3 particles are titanomagnetite with variable Ti contents.

In contrast to Type-1 to Type-3 titanomagnetite, Type-4 and Type-5 magnetic particles are hosted within silicates (**Figures 6** and **7**). No preferred particle orientations are observed for the morphologically diverse Type-4 particles, which have sizes ranging from a few to several hundred nanometers. Some particles appear to have rounded or irregular 2D-projections in which crystal faces are difficult to define even from HRTEM lattice images (**Figures 6A–D**). In contrast, other particles likely have euhedral octahedral or cubo-octahedral shapes (**Figures 6E–N**). Type-5 particles are typical dendrite-like self-assembled magnetic nanoparticles (**Figure 7**). Combined HRTEM, SAED and TEM-EDXS point analyses reveal that these silicate-hosted nanometer-sized particles are titanomagnetite with variable Ti contents (**Figures 6** and **7**).

Consistent with SEM results, Type-1 to Type-5 particles dominate the magnetic mineral assemblage in TEM observations. With careful and extensive searching, we also found Type-6 particles, which clearly represent magnetite magnetofossils based on their well-defined crystal morphologies, nanometer sizes and chain organization (e.g., Kopp and Kirschvink, 2008; Li et al., 2013a). Three magnetofossil crystal morphologies are found in this sediment sample (**Figure 8**): octahedral magnetofossils have an average length of 53.0 ± 5.7 nm, width of 50.6 ± 5.9 nm and aspect ratio of 1.05 ± 0.05 (n = 19), prismatic magnetofossils have an average length of 103.3 ± 21.2 nm, width of 81.9 ± 15.8 nm and aspect ratio of 1.26 ± 0.13 (n = 13) and bullet-shaped magnetofossils have an average length of 116.5 ± 13.7 nm, width of 41.1 ± 1.3 nm and aspect ratio of 2.83 ± 0.3 (n = 3). HRTEM observations confirm that they are single crystals without obvious twinning defects.

Type-7 and Type-8 particles have similar morphology in low-magnification TEM observations. Both appear to be tight aggregates of nanometer-sized magnetite (**Figures 9A,D**). However, HRTEM observations and SAED analyses demonstrate that they are different. Type-7 magnetite aggregates are composed of many randomly oriented single crystals with sizes of about 10 nm. As a result, SAED analysis of Type-7 magnetite aggregates have a typical ring-like diffraction pattern for polycrystalline samples (**Figures 9B,C**). In contrast, Type-8 magnetite aggregates are single crystals with significant defects. Despite obvious boundaries that divide particles into different small regions, HRTEM observations reveal clearly that the same lattice fringes run intact through the particle, resulting in a typical spot-like single crystal diffraction pattern (**Figures 9E,F**).

DISCUSSION

Magnetic Mineral Assemblage in Surface Sediment Sample EPMNP-31

The generally low magnetic mineral concentration and mixture with non-magnetic minerals in sediments makes it necessary to

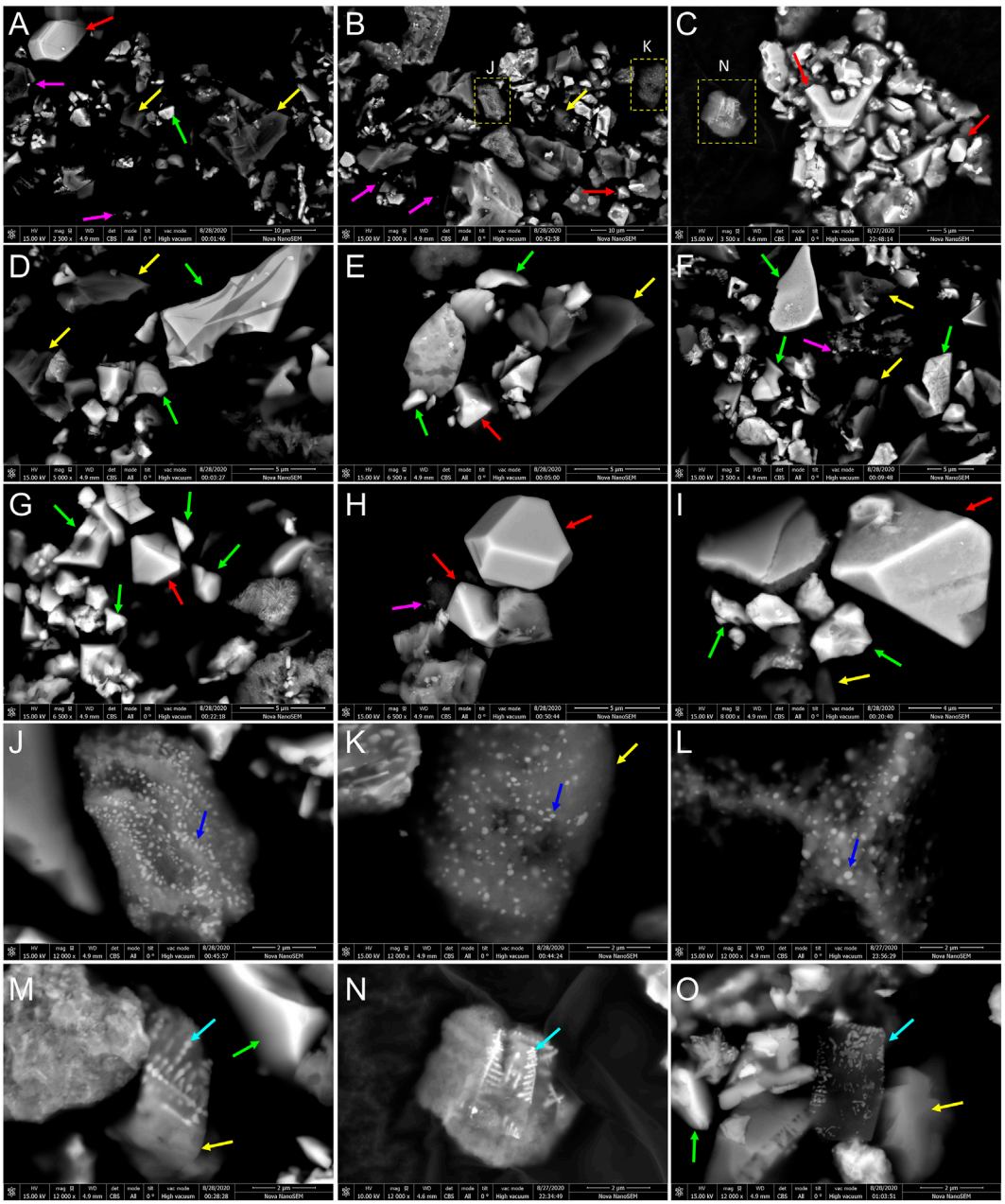

FIGURE 4 | Backscattered SEM images of magnetic mineral extracts. Fe-Mn silicate particles (yellow arrows), angular titanomagnetite particles (green arrows), octahedral or truncated octahedral titanomagnetite particles (red arrows), silicate-hosted magnetite particles (blue arrows), silicate-hosted dendritic magnetite particles (cyan arrows), and individual nanometer-sized magnetite particles (purple arrows) are recognized from SEM morphological observations and SEM-EDXS elemental mapping (**Supplementary Material S1**).

pre-treat samples effectively to extract and enrich magnetic minerals for SEM and TEM analyses. Any magnetic mineral extraction process has inevitable biases, i.e., strongly magnetic minerals are relatively easy to extract from sediments (e.g., Hounslow and Maher, 1996; Han et al., 2016). The extraction process used here did not involve chemical treatment (e.g., dissolution by acid-ammonium oxalate) or mechanical treatment apart from ultrasonication to disperse the sediment slurry. It is, therefore, a relatively straightforward process. Our experimental results indicate that this extraction procedure has removed most non-magnetic minerals and that it has concentrated magnetic minerals, which is necessary for SEM and TEM analyses, although the procedure might miss weakly magnetic minerals (e.g., hematite, goethite). Five dominant (Type-1 to -5) and three minor (Type-6 to-8) titanomagnetite and magnetite particle types were identified from sample EPMNP-31 by combined use of SEM, SEM-

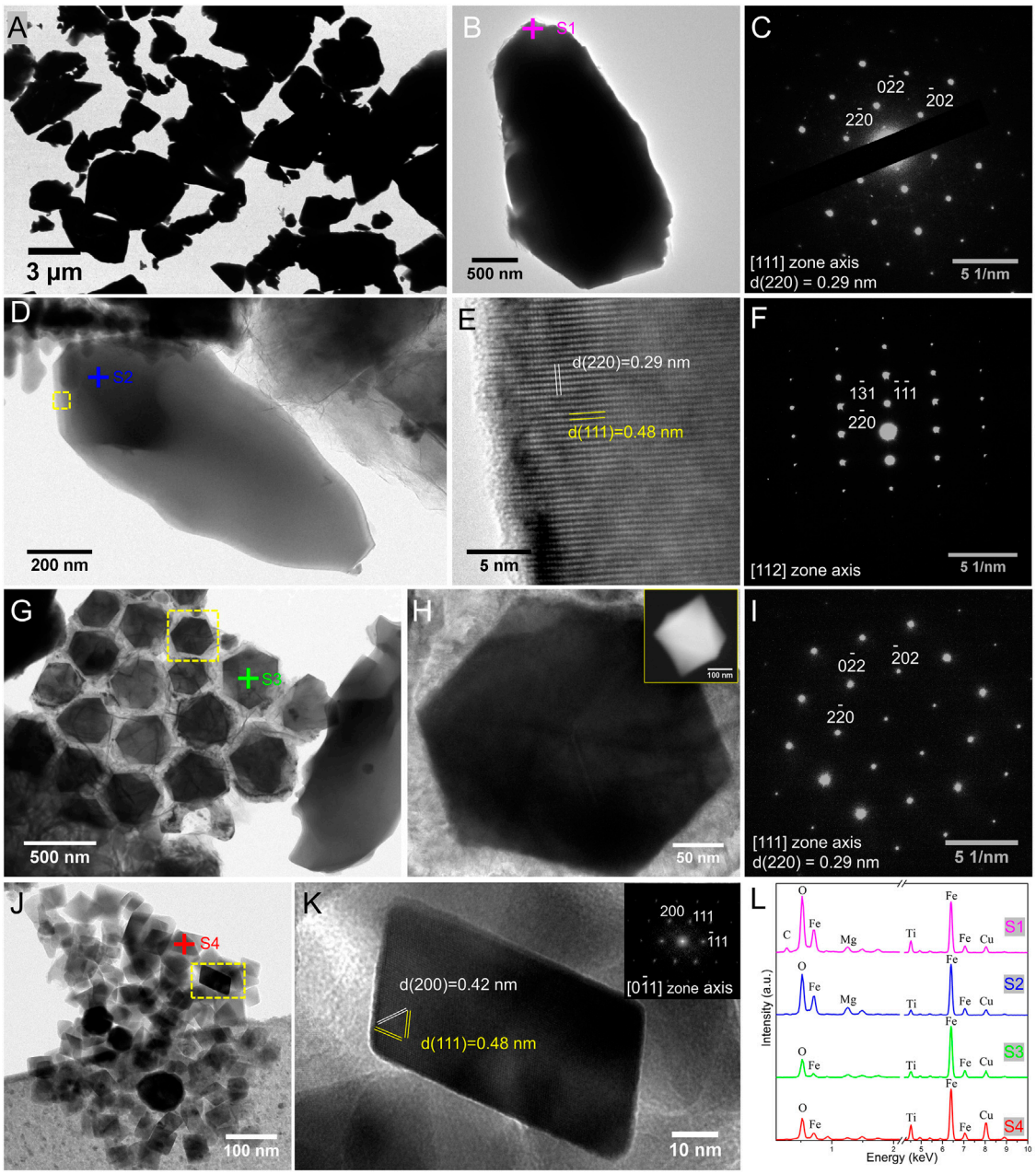

FIGURE 5 | TEM analyses of **(A–F)** Type-1, **(G–I)** Type-2, and **(J–K)** Type-3 magnetite particles. **(A)** Low-magnification TEM image of many micron-sized titanomagnetite particles. **(B)** TEM image of an individual titanomagnetite particle. **(C)** SAED pattern recorded from the [111] zone axis of the particle in **(B)**. **(D)** TEM image of an individual magnetite particle. **(E)** HRTEM image of a thin edge region of the particle in **(D)** (yellow dashed box). **(F)** SAED pattern recorded from the [112] zone axis of the particle in **(D)**. **(G)** TEM image of many octahedral magnetite particles [367.8 ± 44.9 nm average size (n = 18)]. **(H)** TEM image of a single octahedral magnetite particle recorded from the [111] zone axis [yellow dashed box in **(G)**]. The inset SEM image demonstrates an octahedral morphology. **(I)** SAED pattern of the particle in **(H)** recorded from the [111] zone axis of magnetite. **(J)** TEM image of many nanometer titanomagnetite particles. **(K)** HRTEM image of a single magnetite particle [yellow dashed box in **(J)**] recorded from the [0$\bar{1}$1] zone axis (the inset is the corresponding pattern). **(L)** EDXS spectra for individual particles (indicated by colored crosses and names in **(B)**, **(D)**, **(G)**, and **(J)**). The d-spacing values from HRTEM observations and indirectly calculated from SAED analyses, combined with corresponding TEM-EDXS point analyses, SAED and FFT patterns, match the crystal structure (Fd3m space group) of magnetite or titanomagnetite.

EDXS elemental mapping, TEM, HRTEM, SAED and TEM-EDXS point analyses from micron to atomic scales. These microscopic observations provide direct evidence to help understand bulk sediment magnetic properties.

IRM decomposition indicates that the remanent magnetization in this sample is carried by four main coercivity components (**Figure 10**). Component 1 has a 7% contribution and might represent the magnetic response from coarse vortex state grains

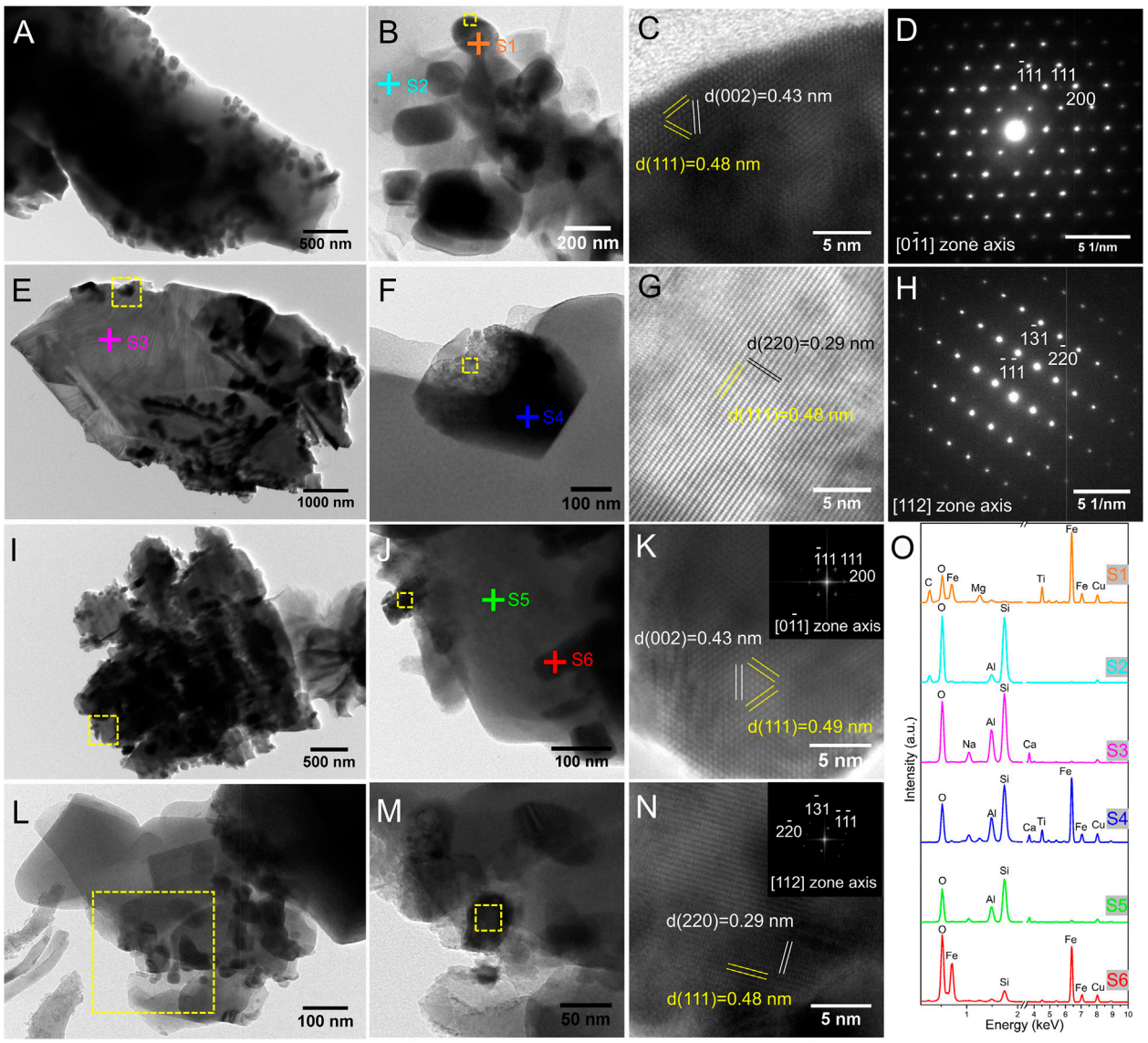

FIGURE 6 | TEM analyses of Type-4 magnetite inclusions hosted within silicates. **(A)** TEM image of a silicate particle hosting many dispersed titanomagnetite or magnetite inclusions. **(B–D)** Titanomagnetite or magnetite particles likely attached to silicates: **(B)** low-magnification TEM image, **(C)** HRTEM image of part of the particle in the yellow dashed box in **(B)** and **(D)** the corresponding SAED pattern recorded from the [0$\bar{1}$1] zone axis. **(E–H)** Silicate particle hosting many titanomagnetite or magnetite inclusions: **(E)** low-magnification TEM image, **(F)** TEM image of a single particle indicated by the yellow dashed box in **(E)**, **(G)** HRTEM image of a small region of the particle in **(F)** and **(H)** SAED pattern recorded from the [112] zone axis of the particle in **(F)**. **(I–K)** TEM images of **(I)** a silicate particle hosting many titanomagnetite or magnetite inclusions and **(J)** of a small region indicated by the yellow dashed box in **(I)**, **(K)** HRTEM image (inset is the corresponding FFT pattern) of a particle indicated by the yellow dashed box in **(J)**. **(L–N)** TEM images of **(L)** several titanomagnetite or magnetite inclusions that are likely embedded in, and attached to, silicates, and **(M)** a small region indicated by the yellow dashed box in **(L)**, and **(N)** HRTEM image (inset is the corresponding FFT pattern) of a particle indicated by the yellow dashed box in **(M)**. **(O)** EDXS spectra for different particles or regions of interest (indicated by colored crosses and names in **(B)**, **(E)**, **(F)** and **(J)**). The *d*-spacing values from HRTEM observations and indirectly calculated from SAED analyses, combined with corresponding TEM-EDXS point analyses, SAED and FFT patterns, match the crystal structure (*Fd3m* space group) of magnetite or titanomagnetite.

(e.g., Type-1,-2 and some submicron Type-4 and-5 particles). Component 2 has a 56% contribution and may originate mainly from SD magnetite particles with low Ti contents (e.g., Type-4 and -5), and SD magnetite magnetofossils (i.e., Type-6). Component 3 has a 28% contribution, which may originate from SD titanomagnetite particles with relatively high Ti contents, good crystallinity and elongated Type-3 particles. Component 4 has a 9% contribution and may represent the magnetic response of weakly magnetic minerals that were missed by the magnetic extraction procedure. The Type-7 and -8 magnetite aggregates were missed by IRM decomposition possibly because they are likely to have SP properties. It should be noted that magnetic unmixing with CLG functions does not enable fitting of skewed distributions, which can result in solutions with more components (e.g., from three to five

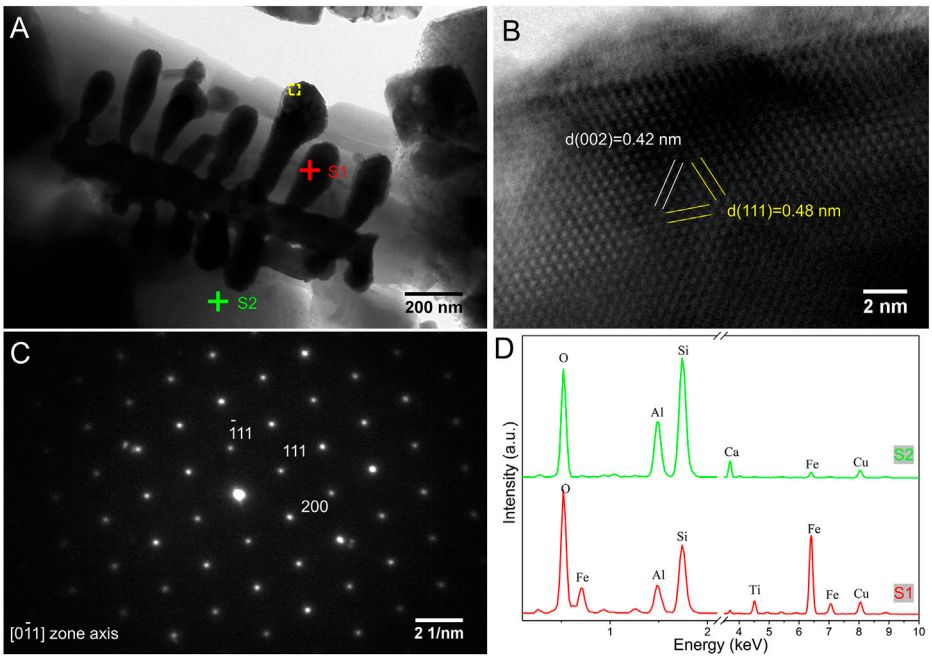

FIGURE 7 | TEM analyses of Type-5 magnetite dendrites hosted within silicates. **(A)** TEM image of a magnetite dendrite aggregate hosted within a silicate. **(B)** HRTEM image of a small region of the particle indicated by the yellow dashed box in **(A)**. **(C)** SAED pattern recorded from the [0$\bar{1}$1] zone axis of the particle in **(B)**. **(D)** EDXS spectra for dendrite magnetite and the host silicate [indicated by colored crosses in **(A)**].

components) (**Figures 11A,B**). When using skewed generalized Gaussian (SGG) functions (Egli, 2003), as few as two components can also give a good match (**Figures 11C,D**). Therefore, we argue that precise magnetic mineral assemblage identification based on systematic electron microscopic observations is a prerequisite for supervised unmixing.

Magnetic mineral types and their corresponding domain states were further identified by linking IRM, FORC and electron microscope analyses. Coarse-grained titanomagnetite or magnetite particles (e.g., IRM component 1) occur in the vortex state, as indicated by a tri-lobate FORC distribution after central ridge extraction (**Figure 3C**). A strong central ridge FORC signal can be divided into three components with distinctive peak coercivities, which correspond to the other three IRM components. The lowest coercivity SD FORC component is dominant and corresponds to IRM component 2 and likely corresponds to Type-4 and -5 fine magnetite and low-Ti titanomagnetite particles. The intermediate coercivity SD FORC component corresponds to IRM component 3 and may be carried by Type-3 high-Ti titanomagnetite particles. The highest coercivity SD FORC component corresponds to IRM component 4 and likely represents weakly magnetic minerals that were missed by the magnetic extraction procedure. The magnetic minerals responsible for IRM component 2 are non-interacting (e.g., Type-4 and -5). For IRM component 3, individual titanomagnetite particles may be separated by non-magnetic sediment matrix, and therefore behave as non-interacting SD particles (e.g., Type-3; particles aggregate relatively easily during magnetic extraction). IRM measurements cannot detect SP particles because they do not carry a remanence at room temperature. However, as shown in **Figures 3** and **9**, small particles (Type-7, -8 and some Type-4 particles) near the SP/SD threshold size (~25–30 nm for equidimensional magnetite; Muxworthy and Williams (2009)) produce a clear FORC signal, which is confirmed by TEM observations.

Magnetite magnetofossils (Type-6 particles) should also contribute to the central ridge FORC signal and IRM component 2. However, the magnetofossil contribution within the studied sample appears to be small. First, both SEM and TEM analyses reveal that Type-1 to -5 titanomagnetite or magnetite particles are the dominant magnetic minerals within the magnetic extract. Magnetofossil chain structures should be observed readily by SEM if they are as abundant in the magnetic mineral assemblage as they are in silicate-hosted nanometric magnetite particles. They were found only occasionally after much searching under TEM. Second, although magnetite magnetofossils may have comparable coercivities to IRM component 2, they generally produce two typical IRM components between ~30 and ~80 mT with DP values <0.2 due to their narrow grain size distributions (e.g., Kruiver et al., 2001; Egli, 2004b; Heslop, 2015). IRM component 2 has DP = 0.3, which matches well with the silicate-hosted magnetite particles with diverse grain sizes ranging from a few to several hundred nanometers. Third, the chain structure of magnetite particles produced by modern MTB or preserved within sediments as magnetofossils generally produces significant shape anisotropy, which can be enhanced by elongation of prismatic and bullet-shaped magnetite particles (e.g., Moskowitz et al., 1993; Pan et al., 2005; Housen and Moskowitz, 2006; Li et al., 2010; Li et al., 2012; Li et al., 2013a; Chang et al., 2016b). Such shape anisotropy results in

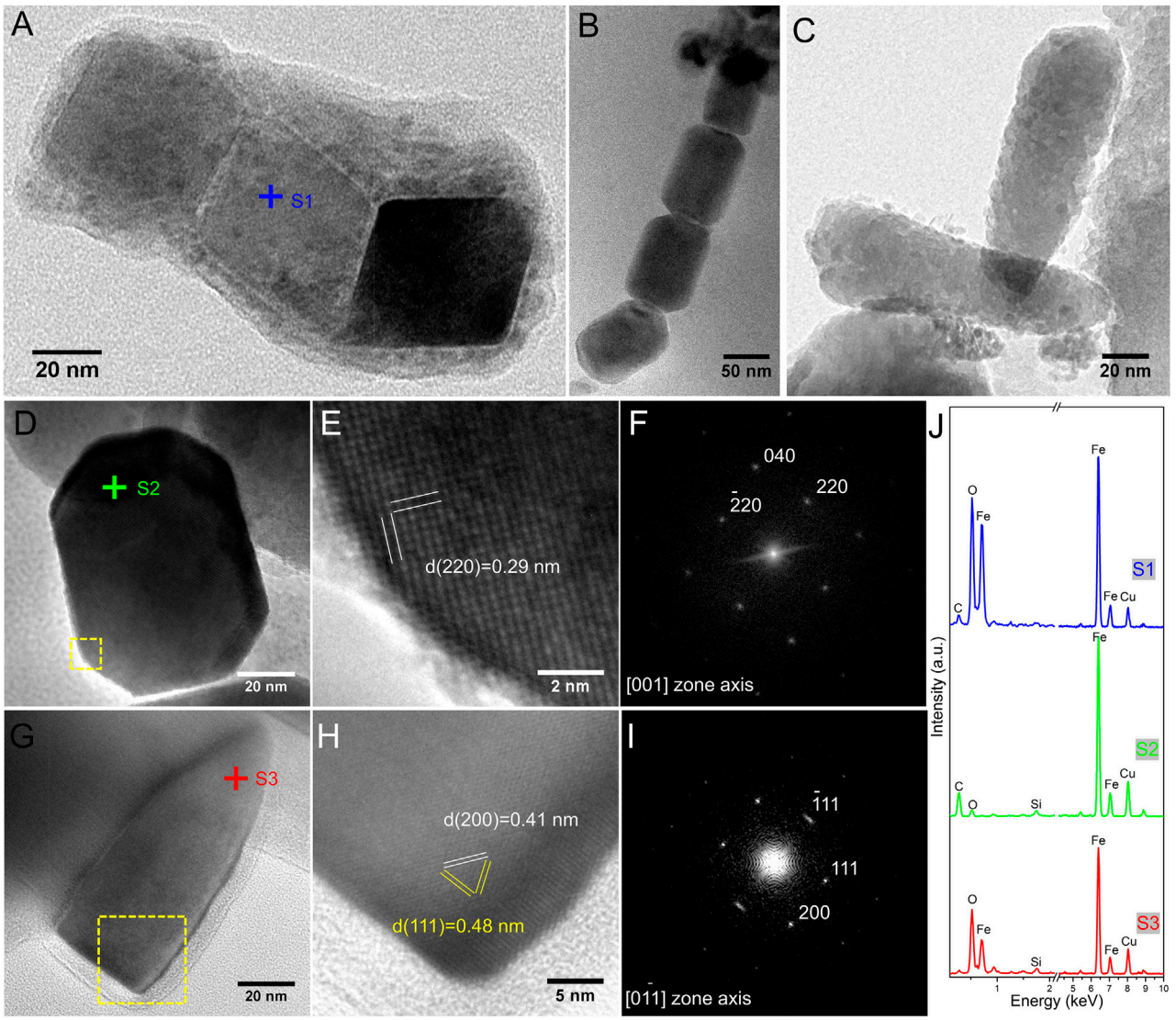

FIGURE 8 | TEM analyses of Type-6 magnetite magnetofossils. **(A)** Three octahedral magnetite particles with chain structure. **(B)** Four elongated prismatic magnetite particles with chain structure. **(C)** Two bullet-shaped magnetite particles. **(D)** HRTEM image of an individual elongated prismatic particle recorded from the [001] zone axis. **(E)** Close-up image of the lower left-hand part of the particle in **(D)** (indicated by the yellow dashed box). **(F)** FFT pattern from the HRTEM image of the particle in **(E)**. **(G)** HRTEM image of a bullet-shaped magnetite particle recorded from the [0$\bar{1}$1] zone axis **(H)** Close-up image of the lower right-hand part of the particle in **(G)** (indicated by the yellow dashed box) **(I)** FFT pattern from the HRTEM image of the particle in **(H)**. **(J)** EDXS spectra for different individual particles (for positions of colored crosses in **(A)**, **(D)** and **(G)**). The *d*-spacing values from HRTEM observations and indirectly calculated from SAED analyses, combined with corresponding TEM-EDXS point analyses, SAED and FFT patterns, match the crystal structure (*Fd3m* space group) of magnetite.

an apparent bifurcation of FC and ZFC warming curves below the Verwey transition temperature (i.e., ~90–110 K) (e.g., Moskowitz et al., 1993; Li et al., 2013b). Despite detection of chain structures for octahedral and prismatic magnetofossils and elongated bullet-shaped magnetofossils in TEM observations, FC and ZFC warming curves do not bifurcate; the former is slightly higher than the latter throughout warming, possibly due to the presence of particles that undergo thermal activation and remanence gain/loss during cooling/warming. Despite magnetite magnetofossils being found in the studied sediment, both bulk magnetic measurements and electron microscope observations reveal that they are much less abundant than other SD particle types, and that their magnetic contributions are small.

Combined Use of Magnetic and Microscopic Analyses: Importance and Necessity

Precise sedimentary magnetic mineral identification is a prerequisite for many paleomagnetic and environmental magnetic studies. In practice, bulk sediment samples are generally screened using bulk magnetic measurements to provide indications of the possible

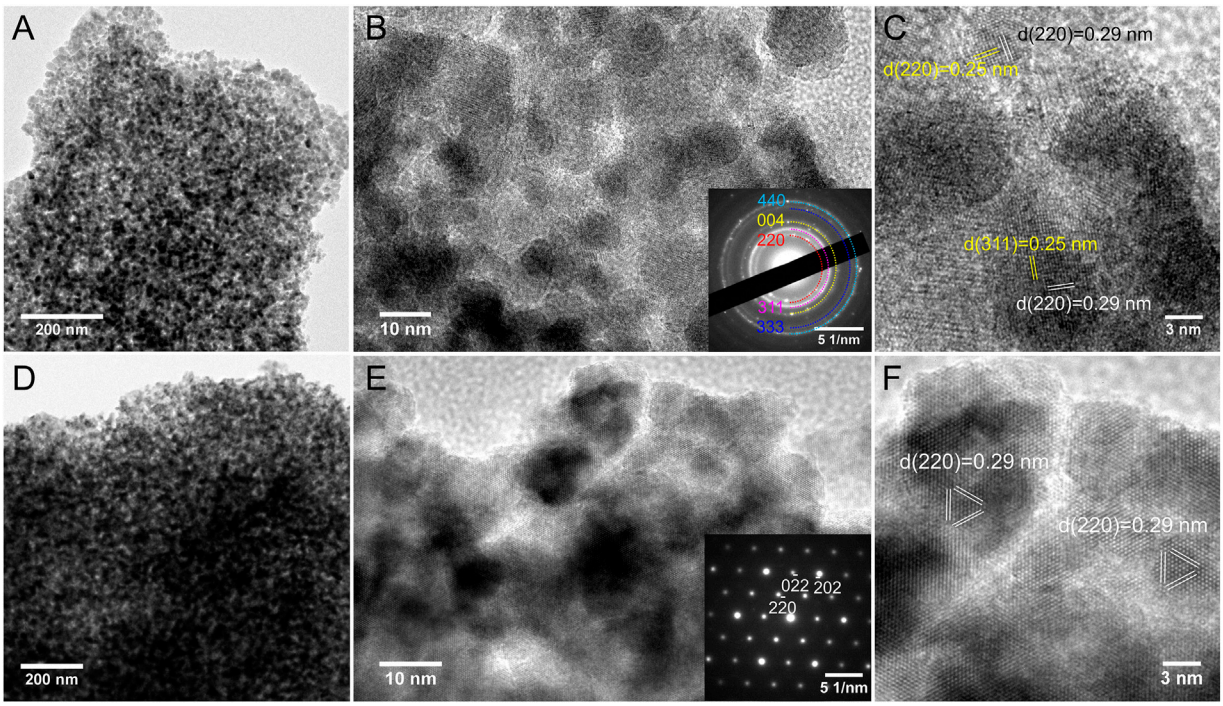

FIGURE 9 | TEM analyses of Type-7 **(A–C)** and Type-8 **(D–F)** nanometer-sized magnetite aggregates. **(A–C)** Randomly oriented magnetite crystal aggregates: **(A)** low-magnification TEM image, **(B)** HRTEM image of many particles with the corresponding SAED pattern (inset), and **(C)** HRTEM image of several particles with Miller indices. **(D–F)** Uniformly oriented magnetite crystal aggregates: **(D)** low-magnification TEM image, **(E)** HRTEM image of many particles with the corresponding SAED pattern (inset) and **(F)** HRTEM image of several particles with Miller indices.

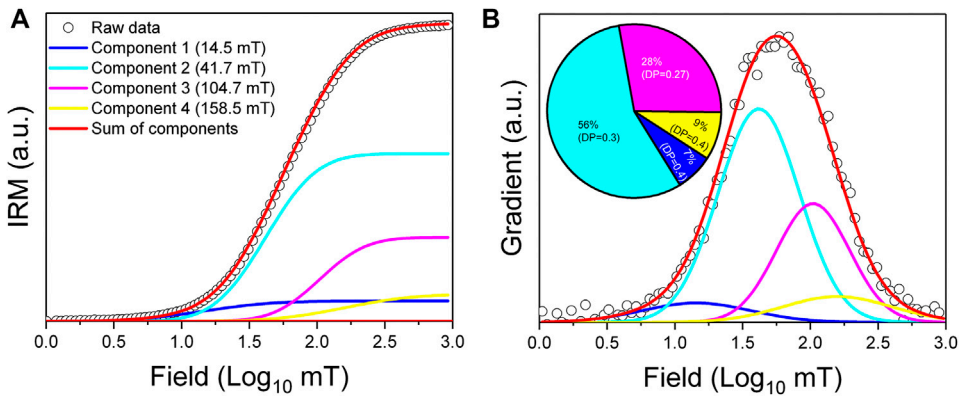

FIGURE 10 | IRM component analysis based on supervised unmixing with information from magnetic mineral assemblages identified from SEM and TEM analyses. **(A)** Linear acquisition plot. **(B)** Gradient of acquisition plot. Four CLG components are required to fit the IRM acquisition curve: raw data (black circles), component 1 (blue), component 2 (cyan), component 3 (purple), component 4 (yellow), and the sum of the four components (red). $B_{c,1/2}$ values (the acquisition field at which 50% of the IRM is reached) for each coercivity fraction are indicated in parentheses in **(A)**. The dispersion parameter (DP, i.e., IRM coercivity distribution width) and remanence contribution for each coercivity fraction are indicated in the pie chart in **(B)**.

presence of certain magnetic minerals, which are then confirmed by direct SEM or TEM observations. Such a strategy enables efficient identification of targeted magnetic minerals, which has been used widely to identify magnetofossils in marine and lake sediments (e.g., Kopp and Kirschvink, 2008; Roberts et al., 2012; Chang et al., 2014a). Of the available magnetic measurements, combined use of FORC diagrams and FMR analyses is powerful for detecting magnetofossil chain structures because these methods are sensitive to the SD properties and strong shape anisotropy of magnetofossil chains and less sensitive to surface magnetite oxidation, which can compromise low-temperature remanence warming tests (e.g., Kind et al., 2011; Chang et al., 2013). However, like all other magnetic

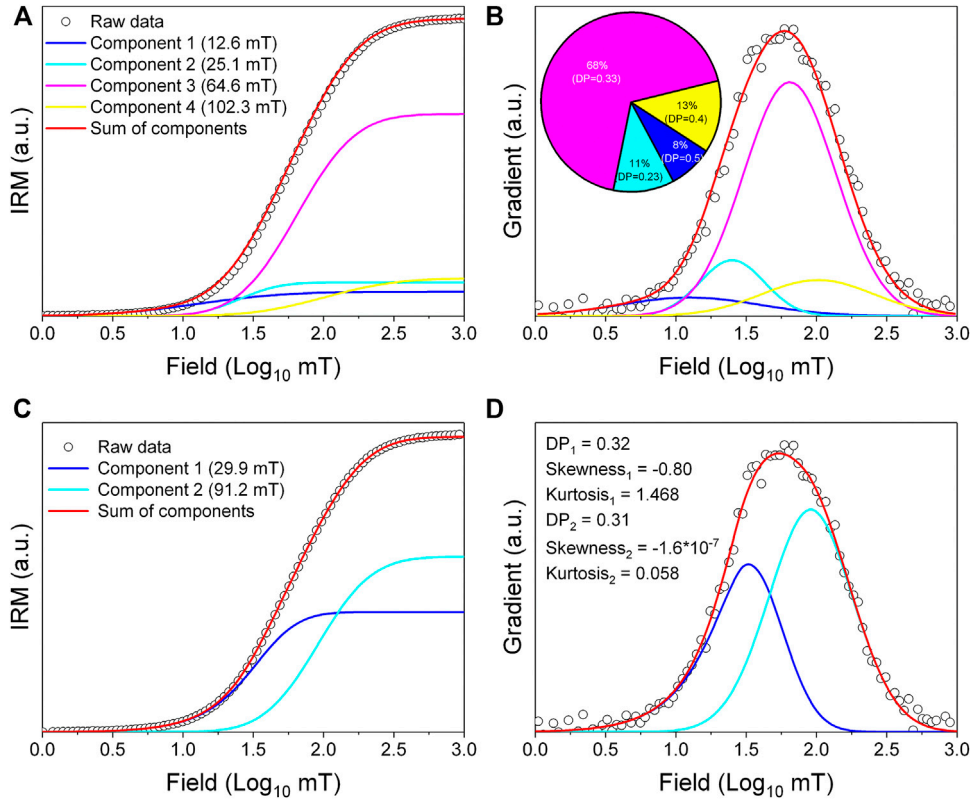

FIGURE 11 | Alternative IRM component analysis based on unsupervized fitting of coercivity distributions with **(A,B)** CLG functions (e.g., Kruiver et al., 2001) and **(C,D)** SGG functions (Egli, 2003). Left-hand column: linear acquisition plots; right-hand column: gradient of acquisition plots.

magnetofossil identification methods, FORC and FMR analyses also have limitations because neither method gives unique indications of a single magnetic mineral (e.g., Liu et al., 2012) and sediments tend to contain mixed magnetic mineral assemblages. Each component may have different origins and magnetic responses that can carry useful paleomagnetic and paleoenvironmental information. This is why so much effort has been expended in recent decades to identify magnetic minerals precisely and quantitatively in sediments by developing magnetic, mathematical, microscopic and non-magnetic methods (e.g., Liu et al., 2012; Heslop, 2015; Roberts et al., 2019).

Based on systematic analysis of a marine surface sediment sample, we emphasize the importance and necessity of combined use of bulk magnetic and electron microscopic approaches to precisely and comprehensively identify sedimentary magnetic minerals. First, direct SEM and TEM observations provide important constraints on supervising IRM curve unmixing, which allows quantification of four major remanence-bearing components. FORC analysis then enables association of each magnetic component with its respective domain state. FORC diagrams also indicate the presence of particles near the SP/SD threshold size, which cannot be detected by IRM measurements. IRM and FORC analyses also indicate that the sediment contains weakly magnetic high-coercivity minerals (e.g., hematite, goethite) that were not extracted or detected by SEM and TEM observations. Second, metagenomic analyses have shown that this sample contains 16S rRNA genes affiliated with MTB (Dong et al., 2016). A strong central ridge FORC component might be interpreted to indicate the presence of magnetofossils. However, careful comparative SEM and TEM analyses, along with IRM decomposition, demonstrate that magnetite magnetofossils are not abundant in this sample and that their contribution to remanence may be small or even negligible compared to abiotic SD magnetite and titanomagnetite. Third, systematic analyses of magnetic mineral morphology, mineralogy and composition by combined SEM and TEM approaches allow identification of at least eight magnetite and titanomagnetite particle types from central Pacific Ocean surface sediment. Each magnetic particle type may have its own origin that reflects local or remote environmental processes. Irregular angular shapes for Type-1 titanomagnetite or magnetite particles indicate that they have a detrital origin related to erosion of magnetite-bearing igneous rocks from elevated submarine volcanic sources, of which there are nearby sources (Clouard and Bonneville, 2005). Submicron (Type-2) and nanometer-sized (Type-3) octahedral titanomagnetite particles may have formed from local hydrothermal and volcanic activity in the Clarion Fracture Zone region (e.g., Mewes et al., 2016; Gartman and Hein, 2019). Dendritic titanomagnetite particles (Type-5) are generally self-assembled and embedded within silicates, which indicates that they are exsolved microstructures that formed by phase separation in an originally homogenous solid solution during igneous rock cooling. In contrast, nanometer-sized titanomagnetite and magnetite particles occur as randomly oriented inclusions within silicates. They may have formed prior to the host silicate minerals and were incorporated into the

TABLE 1 | Magnetic mineral types identified in sample EPMNP-31.

Type	Morphology	Size	Spatial arrangement	Chemistry	Domain state	Origin
Type 1	Irregular, angular	Several hundred nm to a few microns	Loose aggregates, isolated	Titanomagnetite, magnetite	Vortex state	Detrital
Type 2	Well-defined octahedral	367.8 ± 44.9 nm	Loose aggregates, isolated	Titanomagnetite	Vortex state	Hydrothermal or igneous
Type 3	Elongated octahedral	52.9 ± 10.9 nm (length); 43.9 ± 9.2 nm (width)	Random aggregates	Titanomagnetite, magnetite	Single domain	Hydrothermal or igneous
Type 4	Irregular, octahedral, cubo-octahedral	Tens to hundreds of nanometers	Hosted within silicates	Titanomagnetite, magnetite	Single domain, vortex state, superparamagnetic	Exsolved microstructures from precursor minerals
Type 5	Dendrite-like	Tens to hundreds of nanometers	Hosted within silicates	Titanomagnetite	Vortex state, single domain	Formed early and incorporated into host silicates
Type 6	Octahedral magnetofossils	53.0 ± 5.7 nm (length); 50.6 ± 5.9 nm (width)	Short chain	Magnetite	Single domain	Local magnetotactic bacteria
	Prismatic magnetofossils	103.3 ± 21.2 nm (length); 81.9 ± 15.8 nm (width)	Short chain	Magnetite	Single domain	Local magnetotactic bacteria
	Bullet-shaped magnetofossils	116.5 ± 13.7 nm (length); 41.1 ± 1.3 nm (width)	Loose aggregates, isolated	Magnetite	Single domain	Local magnetotactic bacteria
Type 7	Irregular	A few nanometers	Random aggregates of many single crystals	Magnetite	Superparamagnetic	Unknown
Type 8	Irregular	A few nanometers	Aggregates of single crystals with defects	Magnetite	Superparamagnetic	Unknown

silicate during its subsequent crystallization (e.g., Tarduno et al., 2006; Chang et al., 2016a). Magnetite magnetofossils (Type-6) represent local MTB activity (e.g., Dong et al., 2016). Weakly magnetic high-coercivity minerals likely result from remote westerly-transported input from the Asian interior (e.g., Hyeong et al., 2005; Hyeong et al., 2006). Despite their unknown origin, two types of SP magnetite particles were found, which indicates that reductive dissolution of fine-grained magnetite is limited in this area. Two oxygen sources, i.e., diffusive oxygen transfer from underlying seamount basaltic basement and oxygen rich AABW (e.g., Deng et al., 2016; Mewes et al., 2016), produce a fully oxic sediment column at the study site. Such an oxic environment will produce surficial titanomagnetite and magnetite oxidation, while limiting reductive diagenetic modification of fine-grained titanomagnetite and magnetite (e.g., Roberts, 2015).

CONCLUSIONS

We have studied systematically a deep-sea surface sediment from the Clarion Fracture Zone region in the central Pacific Ocean by combining bulk magnetic analyses and electron microscope observations. Eight titanomagnetite and magnetite particle types with different magnetic properties were identified, and their corresponding origins are discussed (**Table 1**). Type-1 particles are micron- and submicron-sized titanomagnetite with irregular and angular shapes, which are likely to be detrital particles that originated from erosion of magnetite-bearing igneous rocks in surrounding submarine volcanic highlands. Type-2 and-3 particles are well-defined octahedral titanomagnetite with submicron and nanometer sizes, respectively, which indicates that their formation may have been related to local hydrothermal and volcanic activity along the Clarion Fracture Zone region. Type-4 and-5 particles are silicate-hosted nanometer-sized titanomagnetite inclusions with diverse crystal morphologies and sizes that range from a few to a hundred nanometers. Type-4 particles are randomly assembled, while Type-5 particles are typical dendritic titanomagnetite. The inclusions would have resulted from exsolution within host silicates.

The above five magnetic particle types dominate the magnetization of the studied sediment. In contrast, Type-6 to-8 magnetic particles are much less abundant. Type-6 particles are magnetite magnetofossils, which are related to local MTB activity. Type-7 comprises SP magnetite aggregates that consist of many randomly oriented single crystals. Type-8 consists of single crystals with significant defects in which obvious boundaries divide particles into many small (SP-like) regions. The well-preserved nature of the fine-grained magnetite indicates that surface sediments in this area are fully oxic.

Electron microscope results are consistent with bulk magnetic properties. They also provide a basis to constrain supervised IRM unmixing to identify quantitatively each magnetic component in the sediment. Coarse-grained titanomagnetite (e.g., Type-1, -2, and some submicron Type-4 and-5 titanomagnetite particles) are in the vortex state and contribute 7% of the remanence. Noninteracting SD titanomagnetite particles of Type-4 and -5 contribute 56% of the remanence. Noninteracting SD titanomagnetite particles of Type-3 contribute 28% of the remanence. A fourth IRM component due to weakly magnetic high-coercivity minerals was not extracted successfully by our extraction method and was not documented in TEM observations; it contributes 9% of the remanence.

Our work demonstrates that diagenetically unmodified natural surface sediments host diverse detrital magnetic mineral assemblages. Magnetic methods are used widely to identify magnetic minerals within such assemblages, although unsupervized interpretation is unlikely to accurately represent the complexity of natural magnetic mineral assemblages. Electron

microscopic observations of the type presented here are time-consuming but essential for ground truthing of supervised magnetic unmixing. Nevertheless, the diversity of observed magnetic mineral types means that we aggregated different particle types to explain identified magnetic components. This demonstrates the complexity of producing consistent supervised magnetic data interpretations.

DATA AVAILABILITY STATEMENT

The original contributions presented in the study are included in the article/**Supplementary Material**, further inquiries can be directed to the corresponding author.

AUTHOR CONTRIBUTIONS

JL designed and initiated the study, interpreted the measurements, and prepared the manuscript. JL and YL performed electron microscopic experiments and data analyses. JL, YL, and SL performed magnetic experiments and data analyses. AR and YP participated in data interpretation and manuscript refinement. HP and TX helped with sampling.

FUNDING

This study was supported financially by the National Natural Science Foundation of China (Grant Nos. 41920104009, 41890843, and 41621004), The Senior User Project of RVKEXUE2019GZ06 (Center for Ocean Mega-Science, Chinese Academy of Sciences), and the Australian Research Council (Grant Nos. DP160100805 and DP200100765).

ACKNOWLEDGMENTS

We thank Dr Qingsong Liu and two reviewers for constructive comments that helped to improve the manuscript significantly. We thank Mr. Tang Xu for assistance with TEM experiments and the people from cruise DY29–02 on R/V *Haiyang Liuhao* in 2013 for assistance with sampling.

SUPPLEMENTARY MATERIAL

The Supplementary Material for this article can be found online at: https://www.frontiersin.org/articles/10.3389/feart.2020.609058/full#supplementary-material.

REFERENCES

Akai, J., Sato, T., and Okusa, S. (1991). TEM study on biogenic magnetite in deep-sea sediments from the Japan sea and the Western Pacific Ocean. *J. Electron. Microsc.* 40, 110–117. doi:10.1093/oxfordjournals.jmicro.a050878

Chang, S. B. R., and Kirschvink, J. L. (1989). Magnetofossils, the magnetization of sediments, and the evolution of magnetite biomineralization. *Annu. Rev. Earth Planet Sci.* 17, 169–195. doi:10.1146/annurev.ea.17.050189.001125

Chang, L., Roberts, A. P., Williams, W., Fitz Gerald, J. D., Larrasoaña, J. C., Jovane, L., et al. (2012). Giant magnetofossils and hyperthermal events. *Earth Planet Sci. Lett.* 351, 258–269. doi:10.1016/j.epsl.2012.07.031

Chang, L., Winklhofer, M., Roberts, A. P., Heslop, D., Florindo, F., Dekkers, M. J., et al. (2013). Low-temperature magnetic properties of pelagic carbonates: oxidation of biogenic magnetite and identification of magnetosome chains. *J. Geophys. Res. Solid Earth* 118, 6049–6065. doi:10.1002/2013JB010381

Chang, L., Roberts, A P., Winklhofer, M., Heslop, D., Dekkers, M. J., Krijgsman, W., et al. (2014a). Magnetic detection and characterization of biogenic magnetic minerals: a comparison of ferromagnetic resonance and first-order reversal curve diagrams. *J. Geophys. Res. Solid Earth* 119, 6136–6158. doi:10.1002/2014JB011213

Chang, L, Vasiliev, I., Baak, C. G. V., Krijgsman, W., Dekkers, M., Roberts, A. P., et al. (2014b). Identification and environmental interpretation of diagenetic and biogenic greigite in sediments: a lesson from the Messinian Black Sea. *Geochem. Geophys. Geosyst.* 15, 3612–3627. doi:10.1002/2014GC005411

Chang, L., Heslop, D., Roberts, A. P., Rey, D., and Mohamed, K. J. (2016a). Discrimination of biogenic and detrital magnetite through a double Verwey transition temperature. *J. Geophys. Res. Solid Earth* 121, 3–14. doi:10.1002/2015JB012485

Chang, L., Roberts, A P., Heslop, D., Hayashida, A., Li, J., Zhao, X., et al. (2016b). Widespread occurrence of silicate-hosted magnetic mineral inclusions in marine sediments and their contribution to paleomagnetic recording. *J. Geophys. Res. Solid Earth* 121, 8415–8431. doi:10.1002/2016JB013109

Chang, L., Harrison, R. J., Zeng, F., Berndt, T. A., Roberts, A. P., Heslop, D., et al. (2018). Coupled microbial bloom and oxygenation decline recorded by magnetofossils during the Palaeocene-Eocene Thermal Maximum. *Nat. Commun.* 9, 4007. doi:10.1038/s41467-018-06472-y

Channell, J. E. T., Harrison, R. J., Lascu, I., McCave, I. N., Hibbert, F. D., and Austin, W. E. N. (2016). Magnetic record of deglaciation using FORC-PCA, sortable-silt grain size, and magnetic excursion at 26 ka, from the Rockall Trough (NE Atlantic). *Geochem. Geophys. Geosyst.* 17, 1823–1841. doi:10.1002/2016GC006300

Chen, L., Heslop, D., Roberts, A. P., Chang, L., Zhao, X., McGregor, H. V., et al. (2017). Remanence acquisition efficiency in biogenic and detrital magnetite and recording of geomagnetic paleointensity. *Geochem. Geophys. Geosyst.* 18, 1435–1450. doi:10.1002/2016GC006753

Cisowski, S. (1981). Interacting vs. non-interacting single domain behavior in natural and synthetic samples. *Phys. Earth Planet. In.* 26, 56–62. doi:10.1016/0031-9201(81)90097-2

Clouard, V., and Bonneville, A. (2005). "Ages of seamounts, islands, and plateaus on the Pacific plate," in *Plates, plumes and paradigms*. Editors G.R. Foulger, J. H. Natland, D. C Presnall, and D. L. Anderson, Vol. 388, 71–90. doi:10.1130/0-8137-2388-4.71

Dekkers, M. J. (2003). "Magnetic properties of sediments," in *Encyclopedia of sediments and sedimentary rocks*. Editors G. V Middleton, M. J Church, M. Coniglio, L. A. Hardie, and F. J. Longstaffe (Dordrecht: Springer Netherlands), 418–424. doi:10.1007/978-1-4020-3609-5_130

Deng, X., Yi, L., Paterson, G. A., Qin, H., Wang, H., Yao, H., et al. (2016). Magnetostratigraphic evidence for deep-sea erosion on the Pacific Plate, south of Mariana Trench, since the middle Pleistocene: potential constraints for Antarctic bottom water circulation. *Int. Geol. Rev.* 58, 49–57. doi:10.1080/00206814.2015.1055597

Dong, Y., Li, J, Zhang, W, Zhang, W, Zhao, Y, Xiao, T, Wu, L-F, and Pan, H (2016). The detection of magnetotactic bacteria in deep sea sediments from the east Pacific Manganese Nodule Province. *Environ. Microbiol. Rep.* 8, 239–249. doi:10.1111/1758-2229.12374

Dunlop, D. J., and Özdemir, Ö. (1997). *Rock magnetism: fundamentals and frontiers*. London: Cambridge University Press. doi:10.1017/CBO9780511612794

Pan, D. J. (2002a). Theory and application of the Day plot (M_{rs}/M_s versus H_{cr}/H_c) 1. theoretical curves and tests using titanomagnetite data. *J. Geophys. Res.* 107 (B3). doi:10.1029/2001JB000486

Dunlop, D. J. (2002b). Theory and application of the Day plot (M_{rs}/M_s versus H_{cr}/H_c) 2. application to data for rocks, sediments, and soils. *J. Geophys. Res.* 107 (B3). doi:10.1029/2001JB000487

Egli, R., and Lowrie, W. (2002). Anhysteretic remanent magnetization of fine magnetic particles. *J. Geophys. Res.* 107 (B3), 2209. doi:10.1029/2001JB000671

Egli, R., Chen, A. P., Winklhofer, M., Kodama, K. P., and Horng, C. S. (2010). Detection of noninteracting single domain particles using first-order reversal curve diagrams. *Geochem. Geophys. Geosyst.* 11, Q01Z11. doi:10.1029/2009GC002916

Egli, R. (2003). Analysis of the field dependence of remanent magnetization curves. *J. Geophys. Res.* 108, 2081. doi:10.1029/2002JB002023

Egli, R. (2004a). Characterization of individual rock magnetic components by analysis of remanence curves, 1. Unmixing natural sediments. *Studia Geophys. Geod.* 48, 391–446. doi:10.1023/B:SGEG.0000020839.45304.6d

Egli, R. (2004b). Characterization of individual rock magnetic components by analysis of remanence curves. 2. Fundamental properties of coercivity distributions. *Phys. Chem. Earth* 29, 851–867. doi:10.1016/j.pce.2004.04.001

Egli, R. (2004c). Characterization of individual rock magnetic components by analysis of remanence curves. 3. Bacterial magnetite and natural processes in lakes. *Phys. Chem. Earth* 29, 869–884. doi:10.1016/j.pce.2004.03.010

Egli, R. (2013). VARIFORC: an optimized protocol for calculating non-regular first-order reversal curve (FORC) diagrams. *Global Planet. Change* 110, 302–320. doi:10.1016/j.gloplacha.2013.08.003

Evans, M. E., and Heller, F. (2001). Magnetism of loess/palaeosol sequence: recent developments. *Earth Sci. Rev.* 54, 129–144. doi:10.1016/S0012-8252(01)00044-7

Evans, M., and Heller, F. (2003). *Environmental magnetism: principles and applications of enviromagnetics*. San Diego, CA: Academic Press, Vol. 19. doi:10.1002/jqs.858

Evans, M. E., and Wayman, M. L. (1970). An investigation of small magnetic particles by electron microscopy. *Earth Planet Sci. Lett.* 9, 365–370. doi:10.1016/0012-821X(70)90137-8

Franke, C., von Dobeneck, T., Drury, M. R., Meeldijk, J. D., and Dekkers, M. J. (2007). Magnetic petrology of equatorial Atlantic sediments: electron microscopy results and their implications for environmental magnetic interpretation. *Paleoceanography* 22, PA4207. doi:10.1029/2007PA001442

Galindo-Gonzalez, C., Feinberg, J. M., Kasama, T., Gontard, L. C., Posfai, M., Kosa, I., et al. (2009). Magnetic and microscopic characterization of magnetite nanoparticles adhered to clay surfaces. *Am. Mineral.* 94, 1120–1129. doi:10.2138/am.2009.3167

Gartman, A., and Hein, J. R. (2019). "Mineralization at oceanic Transform faults and fracture zones," in *Transform plate boundaries and fracture zones*. Editor J.C Duarte (Amsterdam: Elsevier), 105–118. doi:10.1016/B978-0-12-812064-4.00005-0

Gehring, A. U., Kind, J., Charilaou, M., and García-Rubio, I. (2011). The detection of magnetotactic bacteria and magnetofossils by means of magnetic anisotropy. *Earth Planet Sci. Lett.* 309, 113–117. doi:10.1016/j.epsl.2011.06.024

Gehring, A. U., Kind, J., Charilaou, M., and García-Rubio, I. (2013). S-band ferromagnetic resonance spectroscopy and the detection of magnetofossils. *J. R. Soc. Interface* 10, 20120790. doi:10.1098/rsif.2012.0790

Gibbs-Eggar, Z., Jude, B., Dominik, J., Loizeau, J. L., and Oldfield, F. (1999). Possible evidence for dissimilatory bacterial magnetite dominating the magnetic properties of recent lake sediments. *Earth Planet Sci. Lett.* 168, 1–6. doi:10.1016/S0012-821X(99)00054-0

Guyodo, Y., and Valet, J-P. (1999). Global changes in intensity of the Earth's magnetic field during the past 800-kyr. *Nature* 399, 249–252. doi:10.1038/20420

Han, F., Wang, F. X., Li, J. H., Qin, H. F., Deng, C. L., and Pan, Y. X. (2016). Identification of magnetic minerals in surface sediments of Miyun Lake, Beijing. *Chin. J. Geophys.* 59, 2937–2948. doi:10.6038/cjg20160818

Hao, Q., Wang, L., Oldfield, F., Peng, S., Qin, L., Song, Y., et al. (2012). Delayed build-up of Arctic ice sheets during 400,000-year minima in insolation variability. *Nature* 490, 393–396. doi:10.1038/nature11493

Harrison, R. J., and Feinberg, J. M. (2008). FORCinel: an improved algorithm for calculating first-order reversal curve distributions using locally weighted regression smoothing. *Geochem. Geophys. Geosyst.* 9, Q05016. doi:10.1029/2008GC001987

Harrison, R. J., and Feinberg, J. M. (2009). Mineral magnetism: providing new insights into geoscience processes. *Elements* 5, 209–215. doi:10.2113/gselements.5.4.209

Guo, R. J., Dunin-Borkowski, R. E., and Putnis, A. (2002). Direct imaging of nanoscale magnetic interactions in minerals. *Proc. Natl. Acad. Sci. U.S.A.* 99 (16), 16556–16561. doi:10.1073/pnas.262514499

Harrison, R. J., Muraszko, J., Heslop, D., Lascu, I., Muxworthy, A. R., and Roberts, A. P. (2018). An improved algorithm for unmixing first-order reversal curve diagrams using principal component analysis. *Geochem. Geophys. Geosyst.* 19, 1595–1610. doi:10.1029/2018GC007511

He, K., and Pan, Y. X. (2020). Magnetofossil abundance and diversity as palaeoenvironmental proxies: a case study from Southwest Iberian margin sediments. *Geophys. Res. Lett.* 47, e2020GL087165. doi:10.1029/2020GL087165

Heslop, D., and Dillon, M. (2007). Unmixing magnetic remanence curves without a priori knowledge. *Geophys. J. Int.* 170, 556–566. doi:10.1111/j.1365-246X.2007.03432.x

Heslop, D., and Roberts, A. P. (2012a). Estimating best fit binary mixing lines in the Day plot. *J. Geophys. Res. Solid Earth* 117, B01101. doi:10.1029/2011JB008787

Heslop, D., and Roberts, A. P. (2012b). Estimation of significance levels and confidence intervals for first-order reversal curve distributions. *Geochem. Geophys. Geosyst.* 13, Q12Z40. doi:10.1029/2012GC004115

Heslop, D., Dekkers, M. J., Kruiver, P. P., and van Oorschot, I. H. M. (2002). Analysis of isothermal remanent magnetization acquisition curves using the expectation-maximization algorithm. *Geophys. J. Int.* 148, 58–64. doi:10.1046/j.0956-540x.2001.01558.x

Heslop, D. (2009). On the statistical analysis of the rock magnetic S-ratio. *Geophys. J. Int.* 178, 159–161. doi:10.1111/j.1365-246X.2009.04175.x

Heslop, D. (2015). Numerical strategies for magnetic mineral unmixing. *Earth Sci. Rev.* 150, 256–284. doi:10.1016/j.earscirev.2015.07.007

Hesse, P. P. (1994). Evidence for bacterial paleoecological origin of mineral magnetic cycles in oxic and sub-oxic Tasman Sea sediments. *Mar. Geol.* 117, 1–17. doi:10.1016/0025-3227(94)90003-5

Hounslow, M. W., and Maher, B. A. (1996). Quantitative extraction and analysis of carriers of magnetization in sediments. *Geophys. J. Int.* 124, 57–74. doi:10.1111/j.1365-246X.1996.tb06352.x

Housen, B. A., and Moskowitz, B. M. (2006). Depth distribution of magnetofossils in near-surface sediments from the Blake/Bahama Outer Ridge, western North Atlantic Ocean, determined by low-temperature magnetism. *J. Geophys. Res.* 111, G01005. doi:10.1029/2005JG000068

Hyeong, K., Park, S-H., Yoo, C. M., and Kim, K-H. (2005). Mineralogical and geochemical compositions of the eolian dust from the northeast equatorial Pacific and their implications on paleolocation of the Intertropical Convergence Zone. *Paleoceanography* 20, PA1010. doi:10.1029/2004PA001053

Hyeong, K., Yoo, C. M., Kim, J., Chi, S-B., and Kim, K-H. (2006). Flux and grain size variation of eolian dust as a proxy tool for the paleo-position of the Intertropical Convergence Zone in the northeast Pacific. *Palaeogeogr. Palaeoclimatol. Palaeoecol.* 241, 214–223. doi:10.1016/j.palaeo.2006.03.011

Jiang, X. D., Zhao, X., Chou, Y. M., Liu, Q. S., Roberts, A. P., Ren, J. B., et al. (2020). Characterization and quantification of magnetofossils within abyssal manganese nodules from the Western Pacific Ocean and implications for nodule formation. *Geochem. Geophys. Geosyst.* 21, e2019GC008811. doi:10.1029/2019GC008811

Jimenez-Lopez, C., Romanek, C. S., and Bazylinski, D. A. (2010). Magnetite as a prokaryotic biomarker: a review. *J. Geophys. Res.* 115, G00G03. doi:10.1029/2009JG001152

Kind, J., Gehring, A. U., Winklhofer, M., and Hirt, A. M. (2011). Combined use of magnetometry and spectroscopy for identifying magnetofossils in sediments. *Geochem. Geophys. Geosyst.* 12, Q08008. doi:10.1029/2011GC003633

Kirschvink, J. L., and Chang, S. B. R. (1984). Ultrafine-grained magnetite in deep-sea sediments: possible bacterial magnetofossils. *Geology* 12, 559–562. doi:10.1130/0091-7613(1984)12<559:UMIDSP>2.0.CO;2

Kissel, C., Laj, C., Labeyrie, L., Dokken, T., Voelker, A., and Blamart, D. (1999). Rapid climatic variations during marine isotopic stage 3: magnetic analysis of sediments from Nordic Seas and North Atlantic. *Earth Planet Sci. Lett.* 171, 489–502. doi:10.1016/S0012-821X(99)00162-4

Kissel, C., Laj, C., Jian, Z., Wang, P., Wandres, C., and Rebolledo-Vieyra, M. (2020). Past environmental and circulation changes in the South China Sea: input from the magnetic properties of deep-sea sediments. *Quat. Sci. Rev.* 236, 106263. doi:10.1016/j.quascirev.2020.106263

Kopp, R. E., and Kirschvink, J. L. (2008). The identification and biogeochemical interpretation of fossil magnetotactic bacteria. *Earth Sci. Rev.* 86, 42–61. doi:10.1016/j.earscirev.2007.08.001

Kopp, R. E., Nash, C. Z., Kobayashi, A., Weiss, B. P., Bazylinski, D. A., and Kirschvink, J. L. (2006a). Ferromagnetic resonance spectroscopy for assessment of magnetic anisotropy and magnetostatic interactions: a case study of mutant magnetotactic bacteria. *J. Geophys. Res.* 111, B12S25. doi:10.1029/2006JB004529

Kopp, R. E., Weiss, B. P., Maloof, A. C., Vali, H., Nash, C. Z., and Kirschvink, J. L. (2006b). Chains, clumps, and strings: magnetofossil taphonomy with ferromagnetic resonance spectroscopy. *Earth Planet Sci. Lett.* 247, 10–25. doi:10.1016/j.epsl.2006.05.001

Kopp, R. E., Raub, T. D., Schumann, D., Vali, H., Smirnov, A. V., and Kirschvink, J. L. (2007). Magnetofossil spike during the Paleocene-Eocene thermal maximum: ferromagnetic resonance, rock magnetic, and electron microscopy evidence from Ancora, New Jersey, United States. *Paleoceanography* 22, PA4103. doi:10.1029/2007PA001473

Kopp, R. E., Schumann, D., Raub, T D., Powars, D S., Godfrey, L V., Hysell, N. L. S., et al. (2009). An Appalachian Amazon? Magnetofossil evidence for the development of a tropical river-like system in the mid-Atlantic United States during the Paleocene-Eocene thermal maximum. *Paleoceanography* 24, PA4211. doi:10.1029/2009PA001783

Kruiver, P. P., Dekkers, M. J., and Heslop, D. (2001). Quantification of magnetic coercivity components by the analysis of acquisition curves of isothermal remanent magnetisation. *Earth Planet Sci. Lett.* 189, 269–276. doi:10.1016/S0012-821X(01)00367-3

Larrasoaña, J. C., Roberts, A. P., Chang, L., Schellenberg, S. A., Fitz Gerald, J. D., Norris, R. D., et al. (2012). Magnetotactic bacterial response to Antarctic dust supply during the Palaeocene–Eocene thermal maximum. *Earth Planet Sci. Lett.* 333–334, 122–133. doi:10.1016/j.epsl.2012.04.003

Larrasoaña, J. C., Liu, Q., Hu, P., Roberts, A. P., Mata, P., Civis, J., et al. (2014). Paleomagnetic and palaeoenvironmental implications of magnetofossil occurrences in late Miocene marine sediments from the Guadalquivir Basin, SW Spain. *Front. Microbiol.* 5, 71. doi:10.3389/fmicb.2014.00071

Lascu, I., Banerjee, S. K., and Berquo, T. S. (2010). Quantifying the concentration of ferrimagnetic particles in sediments using rock magnetic methods. *Geochem. Geophys. Geosyst.* 11, Q08Z19. doi:10.1029/2010GC003182

Lascu, I., Harrison, R. J., Li, Y. T., Muraszko, J. R., Channell, J. E. T., Piotrowski, A. M., et al. (2015). Magnetic unmixing of first-order reversal curve diagrams using principal component analysis. *Geochem. Geophys. Geosyst.* 16, 2900–2915. doi:10.1002/2015GC005909

Lascu, I., Einsle, J. F., Ball, M. R., and Harrison, R. J. (2018). The vortex state in geologic materials: a micromagnetic perspective. *J. Geophys. Res. Solid Earth* 123, 7285–7304. doi:10.1029/2018JB015909

Li, J. H., and Pan, Y. X. (2015). Applications of transmission electron microscopy in the earth sciences [C]. *Sci. Sinica Terrae* 45, 1359–1382. doi:10.1360/zd2015-45-9-1359

Li, J. H., Pan, Y., Liu, Q., Yu-Zhang, K., Menguy, N., Che, R., et al. (2010). Biomineralization, crystallography and magnetic properties of bullet-shaped magnetite magnetosomes in giant rod magnetotactic bacteria. *Earth Planet Sci. Lett.* 293, 368–376. doi:10.1016/j.epsl.2010.03.007

Li, J. H., Wu, W. F., Liu, Q. S., and Pan, Y. X. (2012). Magnetic anisotropy, magnetostatic interactions and identification of magnetofossils. *Geochem. Geophys. Geosyst.* 13, Q10Z51. doi:10.1029/2012GC004384

Li, J. H., Benzerara, K., Bernard, S., and Beyssac, O. (2013a). The link between biomineralization and fossilization of bacteria: insights from field and experimental studies. *Chem. Geol.* 359, 49–69. doi:10.1016/j.chemgeo.2013.09.013

Li, J. H., Ge, K. P., Pan, Y. X., Williams, W., Liu, Q. S., and Qin, H. F. (2013b). A strong angular dependence of magnetic properties of magnetosome chains: implications for rock magnetism and paleomagnetism. *Geochem. Geophys. Geosyst.* 14, 3887–3907. doi:10.1002/ggge.20228

Li, Q., Zhang, Q., Li, G. X., Liu, Q. S., Chen, M-T., Xu, J. S., et al. (2019). A new perspective for the sediment provenance evolution of the middle Okinawa trough since the last deglaciation based on integrated methods. *Earth Planet Sci. Lett.* 528, 115839. doi:10.1016/j.epsl.2019.115839

Li, J. H., Menguy, N., Roberts, A. P., Gu, L., Leroy, E., Bourgon, J., et al. (2020). Bullet-shaped magnetite biomineralization within a magnetotactic Deltaproteobacterium: implications for magnetofossil identification. *J. Geophys. Res. Biogeoscie.* 125, e2020JG005680. doi:10.1029/2020JG005680

Liu, Q. S., Roberts, A. P., Larrasoaña, J. C., Banerjee, S. K., Guyodo, Y., Tauxe, L., et al. (2012). Environmental magnetism: principles and applications. *Rev. Geophys.* 50, RG4002. doi:10.1029/2012RG000393

Liu, S. (2015). Insolation driven biomagnetic response to the Holocene warm period in semi-arid east Asia. *Sci. Rep.* 5, 8001. doi:10.1038/srep08001

Maciąg, Ł., and Harff, J. (2020). Application of multivariate geostatistics for local-scale lithological mapping – case study of pelagic surface sediments from the Clarion-Clipperton Fracture Zone, north-eastern equatorial Pacific (Interoceanmetal claim area). *Comput. Geosci.* 139, 104474. doi:10.1016/j.cageo.2020.104474

Maloof, A. C., Kopp, R. E., Grotzinger, J. P., Fike, D. A., Bosak, T., Vali, H., et al. (2007). Sedimentary iron cycling and the origin and preservation of magnetization in platform carbonate muds, Andros Island, Bahamas. *Earth Planet Sci. Lett.* 259, 581–598. doi:10.1016/j.epsl.2007.05.021

Maxbauer, D. P., Feinberg, J. M., and Fox, D. L. (2016). MAX UnMix: a web application for unmixing magnetic coercivity distributions. *Comput. Geosci.* 95, 140–145. doi:10.1016/j.cageo.2016.07.009

Mewes, K., Mogollón, J. M., Picard, A., Rühlemann, C., Eisenhauer, A., Kuhn, T., et al. (2016). Diffusive transfer of oxygen from seamount basaltic crust into overlying sediments: an example from the Clarion–Clipperton Fracture Zone. *Earth Planet Sci. Lett.* 433, 215–225. doi:10.1016/j.epsl.2015.10.028

Moskowitz, B. M., Frankel, R. B., and Bazylinski, D. A. (1993). Rock magnetic criteria for the detection of biogenic magnetite. *Earth Planet Sci. Lett.* 120, 283–300. doi:10.1016/0012-821X(93)90245-5

Muxworthy, A. R., and Dunlop, D. J. (2002). First-order reversal curve (FORC) diagrams for pseudo-single-domain magnetites at high temperature. *Earth Planet Sci. Lett.* 203, 369–382. doi:10.1016/S0012-821X(02)00880-4

Muxworthy, A. R., and McClelland, E. (2000). Review of the low-temperature magnetic properties of magnetite from a rock magnetic perspective. *Geophys. J. Int.* 140, 101–114. doi:10.1046/j.1365-246x.2000.00999.x

Muxworthy, A. R., and Williams, W. (2009). Critical superparamagnetic/single-domain grain sizes in interacting magnetite particles: implications for magnetosome crystals. *J. R. Soc. Interface* 6, 1207–1212. doi:10.1098/rsif.2008.0462

Newell, A. J. (2005). A high-precision model of first-order reversal curve (FORC) functions for single-domain ferromagnets with uniaxial anisotropy. *Geochem. Geophys. Geosyst.* 6, Q05010. doi:10.1029/2004GC000877

Ouyang, T. P., Heslop, D., Roberts, A. P., Tian, C. J., Zhu, Z. Y., Qiu, Y., et al. (2014). Variable remanence acquisition efficiency in sediments containing biogenic and detrital magnetites: implications for relative paleointensity signal recording. *Geochem. Geophys. Geosyst.* 15, 2780–2796. doi:10.1002/2014GC005301

Özdemir, Ö., and Dunlop, D. J. (2010). Hallmarks of maghemitization in low-temperature remanence cycling of partially oxidized magnetite nanoparticles. *J. Geophys. Res.* 115, B02101. doi:10.1029/2009JB006756

Pan, Y. X., Petersen, N., Davila, A. F., Zhang, L., Winklhofer, M., Liu, Q., et al. (2005). The detection of bacterial magnetite in recent sediments of Lake Chiemsee (Southern Germany). *Earth Planet Sci. Lett.* 232, 109–123. doi:10.1016/j.epsl.2005.01.006

Petersen, N., Von Dobeneck, T., and Vali, H. (1986). Fossil bacterial magnetite in deep-sea sediments from the South Atlantic Ocean. *Nature* 320, 611–615. doi:10.1038/320611a0

Pike, C., and Fernandez, A. (1999). An investigation of magnetic reversal in submicron-scale Co dots using first order reversal curve diagrams. *J. Appl. Phys.* 85, 6668–6676. doi:10.1063/1.370177

Pike, C. R., Roberts, A. P., and Verosub, K. L. (1999). Characterizing interactions in fine magnetic particle systems using first order reversal curves. *J. Appl. Phys.* 85, 6660–6667. doi:10.1063/1.370176

Pike, C. R., Roberts, A. P., and Verosub, K. L. (2001). First-order reversal curve diagrams and thermal relaxation effects in magnetic particles. *Geophys. J. Int.* 145, 721–730. doi:10.1046/j.0956-540x.2001.01419.x

Pósfai, M., Kasama, T., and Dunin-Borkowski, R. E. (2013). Biominerals at the nanoscale: transmission electron microscopy methods for studying the special properties of biominerals. *Eur. Mineral Union Notes Mineral* 14, 377–435. doi:10.1180/EMU-notes.14.11

Qian, Y., Roberts, A. P., Liu, Y., Hu, P., Zhao, X., Heslop, D., et al. (2020). Assessment and integration of bulk and component-specific methods for identifying mineral magnetic assemblages in environmental magnetism. *J. Geophys. Res. Solid Earth* 125, B019024. doi:10.1029/2019JB019024

Roberts, A. P., and Weaver, R. (2005). Multiple mechanisms of remagnetization involving sedimentary greigite (Fe_3S_4). *Earth Planet Sci. Lett.* 231, 263–277. doi:10.1016/j.epsl.2004.11.024

Roberts, A. P., Cui, Y., and Verosub, K. L. (1995). Wasp-waisted hysteresis loops: mineral magnetic characteristics and discrimination of components in mixed magnetic systems. *J. Geophys. Res.* 100, 909–917.

Roberts, A. P., Pike, C. R., and Verosub, K. L. (2000). First-order reversal curve diagrams: a new tool for characterizing the magnetic properties of natural samples. *J. Geophys. Res.* 105 (B12), 461–528 doi:10.1029/2000JB900326

Roberts, A. P., Chang, L., Rowan, C. J., Horng, C.-S., and Florindo, F. (2011a). Magnetic properties of sedimentary greigite (Fe_3S_4): an update. *Rev. Geophys.* 49, RG1002. doi:10.1029/2010RG000336

Roberts, A. P., Florindo, F., Villa, G., Chang, L., Jovane, L., Bohaty, S. M., et al. (2011b). Magnetotactic bacterial abundance in pelagic marine environments is limited by organic carbon flux and availability of dissolved iron. *Earth Planet Sci. Lett.* 310, 441–452. doi:10.1016/j.epsl.2011.08.011

Roberts, A. P., Chang, L., Heslop, D., Florindo, F., and Larrasoaña, J. C. (2012). Searching for single domain magnetite in the "pseudo-single-domain" sedimentary haystack: implications of biogenic magnetite preservation for sediment magnetism and relative paleointensity determinations. *J. Geophys. Res.* 117, B08104. doi:10.1029/2012JB009412

Roberts, A. P., Florindo, F., Chang, L., Heslop, D., Jovane, L., and Larrasoaña, J. C. (2013). Magnetic properties of pelagic marine carbonates. *Earth Sci. Rev.* 127, 111–139. doi:10.1016/j.earscirev.2013.09.009

Roberts, A. P., Heslop, D., Zhao, X., and Pike, C. R. (2014). Understanding fine magnetic particle systems through use of first-order reversal curve diagrams. *Rev. Geophys.* 52, 557–602. doi:10.1002/2014RG000462

Roberts, A. P., Almeida, T. P., Church, N. S., Harrison, R. J., Heslop, D., Li, Y., et al. (2017). Resolving the origin of pseudo-single domain magnetic behavior. *J. Geophys. Res. Solid Earth* 122, 9534–9558. doi:10.1002/2017JB014860

Roberts, A. P., Zhao, X., Harrison, R. J., Heslop, D., Muxworthy, A. R., Rowan, C. J., et al. (2018). Signatures of reductive magnetic mineral diagenesis from unmixing of first-order reversal curves. *J. Geophys. Res. Solid Earth* 123, 4500–4522. doi:10.1029/2018JB015706

Roberts, A. P., Hu, P, Harrison, R J, Heslop, D., Muxworthy, A R., et al. (2019). Domain state diagnosis in rock magnetism: evaluation of potential alternatives to the Day diagram. *J. Geophys. Res. Solid Earth* 124, 5286–5314. doi:10.1029/2018JB017049

Roberts, A. P. (2015). Magnetic mineral diagenesis. *Earth Sci. Rev.* 151, 1–47. doi:10.1016/j.earscirev.2015.09.010

Robertson, D. J., and France, D. E. (1994). Discrimination of remanence-carrying minerals in mixtures, using isothermal remanent magnetisation acquisition curves. *Phys. Earth Planet. In.* 82, 223–234. doi:10.1016/0031-9201(94)90074-4

Schumann, D. (2008). Gigantism in unique biogenic magnetite at the paleocene-eocene thermal maximum. *Proc. Natl. Acad. Sci. U.S.A.* 105 (17), 17648–17653. doi:10.1073/pnas.0803634105

Snowball, I. F. (1994). Bacterial magnetite and the magnetic properties of sediments in a Swedish lake. *Earth Planet Sci. Lett.* 126, 129–142. doi:10.1016/0012-821X(94)90246-1

Stolz, J. F., Chang, S. B. R., and Kirschvink, J. L. (1986). Magnetotactic bacteria and single-domain magnetite in hemipelagic sediments. *Nature* 321, 849–851. doi:10.1038/321849a0

Tarduno, J. A., Tian, W. L., and Wilkison, S. (1998). Biogeochemical remanent magnetization in pelagic sediments of the western equatorial Pacific Ocean. *Geophys. Res. Lett.* 25, 3987–3990. doi:10.1029/1998GL900079

Tarduno, J. A., Cottrell, R. D., and Smirnov, A. V. (2006). The paleomagnetism of single silicate crystals: recording geomagnetic field strength during mixed polarity intervals, superchrons, and inner core growth. *Rev. Geophys.* 44, RG1002. doi:10.1029/2005RG000189

Tauxe, L., Bertram, H. N., and Seberino, C. (2002). Physical interpretation of hysteresis loops: micromagnetic modeling of fine particle magnetite. *Geochem. Geophys. Geosyst.* 3, 1055. doi:10.1029/2001GC000241

Usui, Y., Yamazaki, T., Oka, T., and Kumagai, Y. (2019). Inverse magnetic susceptibility fabrics in pelagic sediment: implications for magnetofossil abundance and alignment. *J. Geophys. Res. Solid Earth* 124 (10), 672–710. doi:10.1029/2019JB018128

Valet, J.-P., and Meynadier, L. (1993). Geomagnetic field intensity and reversals during the past four million years. *Nature* 366, 234–238. doi:10.1038/366234a0

Valet, J.-P., Thevarasan, A., Bassinot, F., Savranskaia, T., and Haddam, N. (2020). Two records of relative paleointensity for the past 4 Myr. *Front. Earth Sci.* 8, 148. doi:10.3389/feart.2020.00148

Vali, H., and Kirschvink, J. L. (1989). Magnetofossil dissolution in a paleomagnetically unstable deep-sea sediment. *Nature* 339, 203–206. doi:10.1038/339203a0

Verosub, K. L., and Roberts, A. P. (1995). Environmental magnetism: past, present, and future. *J. Geophys. Res.* 100, 2175–2192. doi:10.1029/94JB02713

Vithana, M. V. P., Xu, M., Zhao, X., Zhang, M. C., and Luo, Y. M. (2019). Geological and geophysical signatures of the east pacific rise 8°–10°N. *Solid Earth Sci.* 4, 66–83. doi:10.1016/j.sesci.2019.04.001

Wang, H., Wang, J., Chen-Wiegart, Y. C., and Kent, D. V. (2015). Quantified abundance of magnetofossils at the Paleocene-Eocene boundary from synchrotron-based transmission X-ray microscopy. *Proc. Natl. Acad. Sci. U.S.A.* 112 (12), 12598–12603 doi:10.1073/pnas.1517475112

Weiss, B. P., Kim, S. S., Kirschvink, J. L., Kopp, R. E., Sankaran, M., Kobayashi, A., et al. (2004). Ferromagnetic resonance and low-temperature magnetic tests for biogenic magnetite. *Earth Planet Sci. Lett.* 224, 73–89. doi:10.1016/j.epsl.2004.04.024

Yamazaki, T., and Ioka, N. (1997). Cautionary note on magnetic grain-size estimation using the ratio of ARM to magnetic susceptibility. *Geophys. Res. Lett.* 24, 751–754. doi:10.1029/97GL00602

Yamazaki, T., and Kawahata, H. (1998). Organic carbon flux controls the morphology of magnetofossils in marine sediments. *Geology* 26, 1064–1066. doi:10.1130/0091-7613(1998)026<1064:OCFCTM>2.3.CO;2

Yamazaki, T., and Shimono, T. (2013). Abundant bacterial magnetite occurrence in oxic red clay. *Geology* 41, 1191–1194. doi:10.1130/G34782.1

Yamazaki, T., Fu, W., Shimono, T., and Usui, Y. (2020). Unmixing biogenic and terrigenous magnetic mineral components in red clay of the Pacific Ocean using principal component analyses of first-order reversal curve diagrams and palaeoenvironmental implications. *Earth Planets Space* 72, 120. doi:10.1186/s40623-020-01248-5

Yamazaki, T. (2009). Environmental magnetism of Pleistocene sediments in the North Pacific and Ontong-Java Plateau: temporal variations of detrital and biogenic components. *Geochem. Geophys. Geosyst.* 10, Q07Z04. doi:10.1029/2009GC002413

Yuan, W., Zhou, H. Y., Yang, Z. Y., Hein, J. R., and Yang, Q. H. (2020). Magnetite magnetofossils record biogeochemical remanent magnetization in hydrogenetic ferromanganese crusts. *Geology* 48, 298–302. doi:10.1130/G46881.1

Zhang, Q., Liu, Q. S., Li, J. H., and Sun, Y. B. (2018). An integrated study of the eolian dust in pelagic sediments from the North Pacific ocean based on environmental magnetism, transmission electron microscopy, and diffuse reflectance spectroscopy. *J. Geophys. Res. Solid Earth* 123, 3358–3376. doi:10.1002/2017JB014951

Zhao, X., Roberts, A. P., Heslop, D., Paterson, G. A., Li, Y. L., and Li, J. H. (2017). Magnetic domain state diagnosis using hysteresis reversal curves. *J. Geophys. Res. Solid Earth* 122, 4767–4789. doi:10.1002/2016JB013683

Conflict of Interest: The authors declare that the research was conducted in the absence of any commercial or financial relationships that could be construed as a potential conflict of interest.

frontiers in Earth Science

ORIGINAL RESEARCH
published: 23 December 2020
doi: 10.3389/feart.2020.592277

Testing the Reliability of Sedimentary Paleomagnetic Datasets for Paleogeographic Reconstructions

Edoardo Dallanave[1]* *and Uwe Kirscher*[2]

[1]Faculty of Geosciences, University of Bremen, Bremen, Germany, [2]Department of Geosciences, University of Tuebingen, Tuebingen, Germany

Paleogeographic reconstructions largely rely on paleomagnetic data, mostly in the form of paleomagnetic poles. Compilations of poles are used to determine so called apparent polar wander paths (APWPs), which capture the motion through time of a particular location with respect to an absolute reference frame such as the Earth's spin axis. Paleomagnetic datasets from sedimentary rocks are particularly relevant, because of their spatial distribution and temporal continuity. Several criteria have been proposed through the years to assess the reliability of paleomagnetic datasets. Among these, the latitudinal-dependent elongation of a given paleomagnetic directions distribution, predicted by a widely accepted paleosecular variations model, has been applied so far only to investigate inclination flattening commonly observed in sedimentary rocks. We show in this work that this concept can be generalized to detect "contamination" of paleomagnetic data derived from tectonic strain, which is not always detected by field observation only. After generating different sets of simulated geomagnetic directions at different latitudes, we monitored the variations in the shape of the distributions after applying deformation tensors that replicate the effect of increasing tectonic strain. We show that, in most cases, the "deformation" of the dataset can be detected by elongation vs. inclination ratios not conforming to the values predicted by the paleosecular variations model. Recently acquired paleomagnetic directions and anisotropy of magnetic susceptibility (AMS; a parameter very sensitive to tectonic strain) data from New Caledonia verifies the results of these simulations and highlights the importance of measuring AMS when using sedimentary paleomagnetic data for paleogeographic reconstruction. We suggest to include always AMS measurement and analysis of the distribution shape to assess sedimentary paleomagnetic data used for paleogeographic reconstructions.

Keywords: paleomagnetic directions, TK03.GAD, finite strain, paleogeographic reconstruction, anisotropy of magnetic susceptability (AMS)

OPEN ACCESS

Edited by:
Sara Satolli,
G. d'Annunzio University of Chieti and Pescara, Italy

Reviewed by:
Dennis Kent,
Lamont Doherty Earth Observatory (LDEO), United States
Baochun Huang,
Peking University, China

***Correspondence:**
Edoardo Dallanave
edoardo@uni-bremen.de

Specialty section:
This article was submitted to Geomagnetism and Paleomagnetism, a section of the journal Frontiers in Earth Science

Received: *06 August 2020*
Accepted: *16 November 2020*
Published: *23 December 2020*

Citation:
Dallanave E and Kirscher U (2020) Testing the Reliability of Sedimentary Paleomagnetic Datasets for Paleogeographic Reconstructions. Front. Earth Sci. 8:592277. doi: 10.3389/feart.2020.592277

INTRODUCTION

Paleomagnetism and Paleogeographic Reconstruction

Plate tectonics is a unifying theory that provides a solid background for understanding fundamental processes occurring on Earth. In this model, the outer shell of the Earth consists of moving lithospheric plates and their past movement can be traced using geological data (Torsvik et al., 2008). The relative and absolute motion of the tectonic plates is reconstructed using combinations of ocean floor magnetic anomalies, hot-spot tracks, and paleomagnetic data. The oldest hotspot track in the

South Atlantic is ~130 Ma, and the ocean floor magnetic anomalies allow estimating the relative finite rotation of plates back to ~180 Ma (Steinberger and Torsvik, 2008; Torsvik et al., 2008; DeMets et al., 2010; Wang et al., 2019). Paleomagnetic data are thus fundamental for paleogeographic reconstructions, particularly for pre-Jurassic times.

The basic element for all paleomagnetic-based paleogeographic reconstructions is the paleomagnetic direction. Paleomagnetic directions, measured at a given locality in rocks of any age, are expressed in the form of declination and inclination (D, I). Each direction, can be converted into a virtual geomagnetic pole (VGP), which is the point on the Earth's surface where the imaginary pole that would results in the measured D and I is located. To account for paleosecular variation of the geomagnetic field, an adequate number of VGPs should be averaged to determine a paleomagnetic pole. Subsequently, compilations of consecutive poles can be combined to establish pole paths, so-called apparent polar wander paths (APWPs). APWPs are normally plotted as a series of points "wandering" away from the geographic pole with increasing age, where paleopoles based on rocks with very young ages plot close to the geographic pole. The adjective "apparent" comes from the fact that the geographic pole does not move but APWPs rather reflect the changing orientation and distance of a plate with respect to the (fixed) geographic pole (Creer et al., 1954; Van der Voo, 1993; Besse and Courtillot, 2002; Torsvik et al., 2008). At the base of this approach lies the assumption that the geomagnetic field averaged over a few thousand years can be approximated by the one generated by a geocentric axial dipole (GAD), with the characteristic that the paleomagnetic pole, obtained by averaging the available VGPs, and the geographic poles coincide (e.g., Butler, 1992; Tauxe, 2010).

Geomagnetic Paleosecular Variation

Analyses of paleomagnetic data compilations for the last 5 Myr (McElhinny and McFadden, 1997; MM97) revealed that the recent geomagnetic field is largely dominated by the GAD component (Tauxe and Kent, 2004; Tauxe, 2005). However, a snapshot of the geomagnetic field in a particular moment at a given location on the globe would result in a VGP that is deviated from the one predicted from the GAD model up to ~10°. This is the result of the secular variation (Fleming, 1946; Lund, 2018). Starting from the work of Constable and Parker (1988), Tauxe and Kent (2004) developed a model for the paleosecular variation (TK03.GAD) designed to fit the latitudinal-dependent scatter of the VGPs observed in the paleomagnetic poles of the MM97 dataset. The TK03.GAD model results in predicted paleomagnetic direction distributions that are markedly North-South elongated, with a maximum elongation at the equator gradually diminishing toward the poles (Tauxe and Kent, 2004; Tauxe, 2005). Following this model, a collection of paleomagnetic directions from a locality, spanning a time interval long enough to average out secular variations, is expected to possess a distribution with a certain degree of elongation developed parallel to the mean declination.

Paleomagnetic Earth Filters

Sedimentary rocks constitutes about 66% of the rocks exposed on the Earth's surface (Blatt and Jones, 1975). Therefore, sedimentary paleomagnetic datasets are of extreme value for paleogeographic reconstructions. However, the record of the Earth's paleomagnetic field in sedimentary rocks is often "distorted" by different natural processes including tectonic deformation, remagnetization, or compaction-induced inclination flattening. These phenomena have been defined as "Earth filters" (Tauxe, 2005). In particular, sedimentary inclination shallowing of paleomagnetic directions is a long known problem, and it is described by the tangent function introduced by King (1955):

$$\tan I_o = f \bullet \tan I_f \quad (1)$$

where I_o is the observed remanence inclination, I_f is the inclination of the inducing field, and f is the flattening factor ranging from 0 (completely flattened directions) to 1 (absence of flattening). Directional sets affected by significant inclination shallowing typically possess an elongation developed perpendicular to the average declination (Tauxe and Kent, 1984). **Eq. 1** is at the base of the E/I (Elongation/Inclination) method for correcting shallow biased paleomagnetic directions (Tauxe and Kent, 2004). A given set of flattened paleomagnetic directions is corrected by applying gradually decreasing f values to each direction. The "unflattened" average inclination is reached when the elongation of the whole distribution matches the value predicted by the TK03.GAD model. This statistical technique has been successfully applied to a wide range of sedimentary rocks (Kent and Tauxe, 2005; Krijgsman and Tauxe, 2006; Tauxe et al., 2008; Dallanave et al., 2009, Dallanave et al., 2012, Dallanave et al., 2015, Dallanave et al., 2018a; Kirscher et al., 2014). A reliable APWP of Adria (the African promontory) since the Permian was recently compiled systematically applying the E/I correction to new and published datasets (Muttoni et al., 2013; Muttoni and Kent, 2019).

Paleomagnetic inclination flattening is not the only "Earth filter". Many sedimentary rocks are affected by tectonic strain, which is not always detectable by simple field observations, and that can deflect the characteristic remanent magnetization (ChRM) directions (Cogné and Perroud, 1985; Lowrie et al., 1986; Jackson et al., 1993; Borradaile, 1997). The finite strain state of a sedimentary rock can be qualitatively evaluated by using the anisotropy of magnetic susceptibility (AMS). By monitoring the AMS of Eocene mudstones of the Southern Pyrenean Foreland Basin, Parés et al. (1999) found that during incipient deformation, the fabric evolves through a series of stages that can be essentially synthetized in three types (**Figure 1**). In the absence of deformation, only compaction acts on the sediments resulting in an oblate AMS ellipsoid with a vertical minor axis (**Figure 1A**). As the deformation evolves to the *weak cleavage* state, the fabric changes toward a prolate shape with the major axis perpendicular to the shortening direction (**Figure 1B**). At the *strong cleavage* state, the fabric will assume a triaxial $k_1 > k_2 > k_3$ form (where k_1,

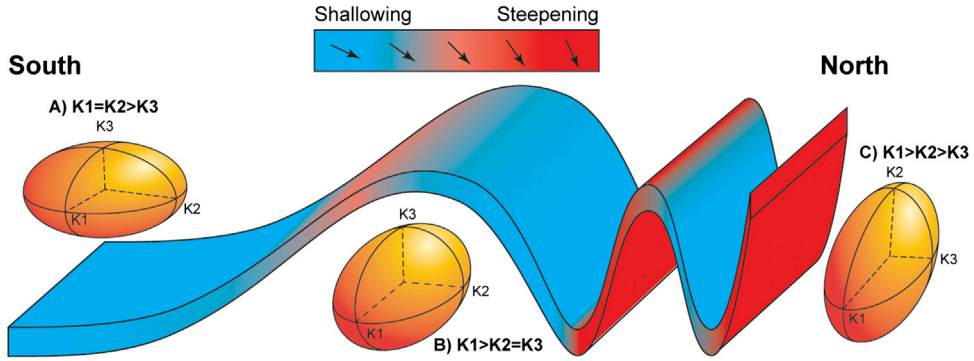

FIGURE 1 | Theoretical evolution of magnetic fabric in sedimentary rocks during incipient deformation. **(A)** Absence of finite strain results in the solely effect of compaction-derived oblate fabric. **(B)** During a *weak cleavage* stage the fabric assumes a prolate shape, with the major axis perpendicular to the shortening direction. **(C)** In a *strong cleavage* state the fabric is triaxial, with the minor and major axes respectively parallel and perpendicular to the shortening direction. The effect of the fabric evolution on the paleomagnetic inclintaion is shown on top of the figure; figure drawn adapting concepts from Parés et al., 1999 and Borradaile, 1997.

k_2, and k_3 are respectively the major, intermediate, and minor axes of the AMS tensor) with the minimum axis parallel and the maximum perpendicular to the shortening direction (**Figure 1C**).

In some pioneering work, ChRM directions in sedimentary rocks have been restored with an "unstrain" strategy (Cogné and Perroud, 1985, Cogné and Perround, 1987; Cogné, 1987). In this approach the paleomagnetic directions are considered as behaving like a passive line within the rock matrix, even though in some cases, due to the nature of the rock forming particles, this approach may be an oversimplification (Kligfield et al., 1983; Borradaile, 1997). The quality and reliability of the "unstrained" dataset was assessed using basic Fisher (1953) statistical criteria, whereby increasing of the precision parameter *k* reflects improved clustering of the directions. It is now clear that the remanence magnetization of sedimentary rocks reflects a more complex behavior of the geomagnetic field, and using just the standard Fisher (1953) statistics to evaluate the reliability of paleomagnetic datasets is an oversimplification. Monitoring the E/I of a paleomagnetic dataset in order to detect inclination flattening has become already a standard approach. Analogously, other earth filters can lead to E/I couples of values that are "unrealistic" (i.e., departing from the values expected from the TK03.GAD field model). In this paper we show that the shape of given ChRM directions set can be used to check if finite strain has undermined the reliability of the data. Using simulated paleomagnetic data, we show that strain related deflection of ChRM directions promptly modify the distribution elongation expected from the TK03.GAD model at a given latitude. We apply this concept to assess the reliability of a recently published dataset from Eocene sedimentary rocks exposed in New Caledonia (Dallanave et al., 2020).

METHODS

Data Generation

To clearly visualize the effect of inclination flattening and finite strain simulation on a theoretical distribution of directions, we first generated a purely circular distribution of 30° radius around a mean direction of D = 0° and I = 50° (**Figure 2A**). A circular distribution can be considered as a simplification of a Fisher (1953) distribution, which is defined as 1) uniformly distributed around the mean direction and 2) with a occurring frequency of directions decaying exponentially with the distance form the mean (see also Fisher et al., 1987).

To evaluate the effect of finite strain on more "realistic" directions, which reflect the secular variations of the geomagnetic field, we generated six sets of paleomagnetic directions using the tk03.py Python script compiled by Tauxe et al. (2016). The sets consist of declination-inclination-intensity triplets drawn accordingly to the TK03.GAD geomagnetic field model at specified latitudes. The six sets were generated applying latitudes of 10, 15, 20, 30, 40, and 50°N, imposing a normal polarity field. For all sets we selected a number (N) of 120 directions (**Supplementary Table S1**). Tauxe et al. (2008) indicated that an adequate number of directions to evaluate reliably the distribution shape is > 100. Since it is uncommon to find published direction sets that exceed this number by far, we consider N = 120 realistic. We excluded all directions with geomagnetic intensity lower than 10μT from the generated datasets. This is based on the assumption that the highest harmonics of the field (i.e., with the lowest intensity) are often not recorded by sediments, and if they are, they result in transitional directions that are normally excluded by directional cutoff (analogously to what done by McElhinny and McFadden (1997), for the MM97 compilation). The obtained distributions possess *k* values ranging from 20 to 35 (**Figure 3**; **Table 1**), which is in agreement with published high-quality sedimentary datasets (see e.g., compilation of Muttoni et al., 2013).

Strain Simulation and Elongation Monitoring

Paleomagnetic directions are commonly defined by D and I with unit length, so the intensity of the TK03.GAD directions was not considered further after filtering. For each generated set we

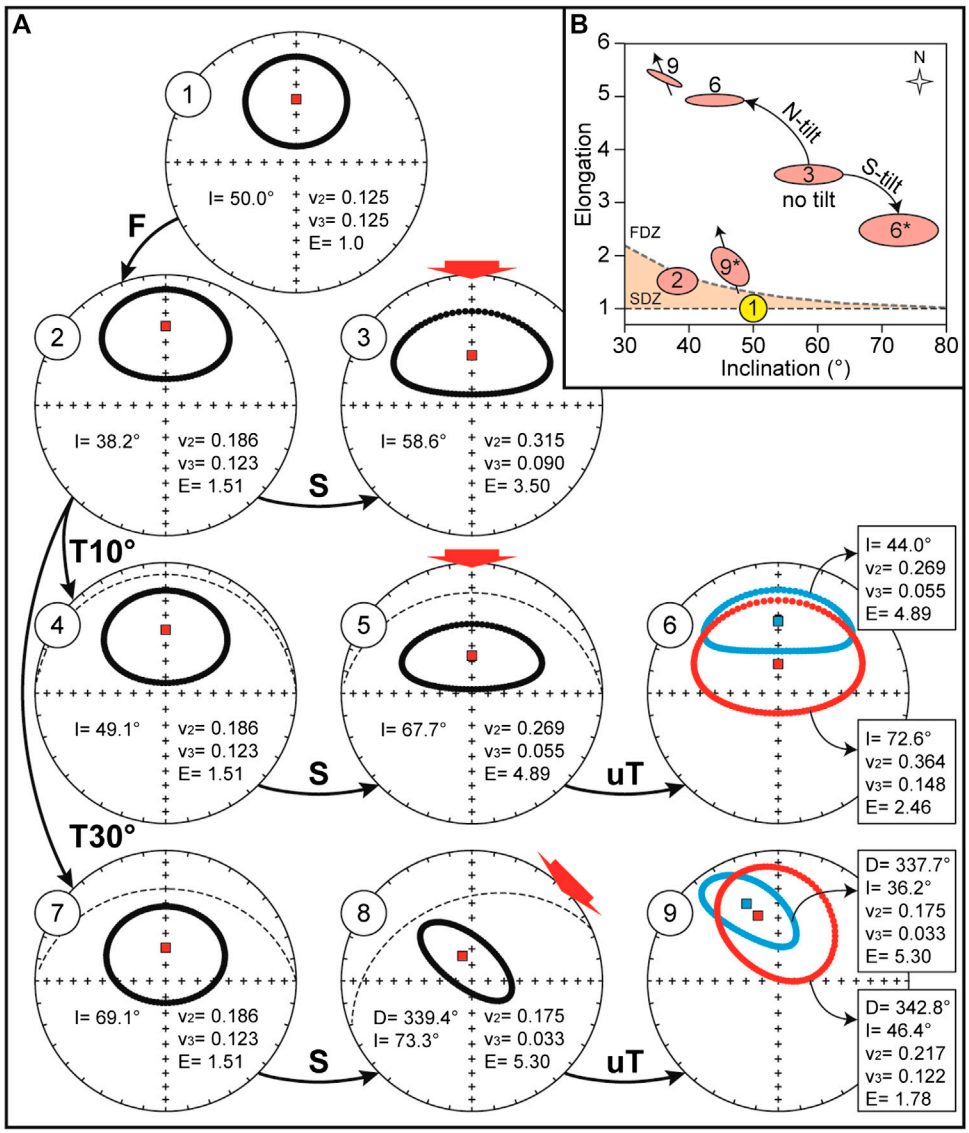

FIGURE 2 | Effect of strain simulation on a purely circular distribution. **(A)** 1 = original distribution; 2 = simulated inclination flattening; 3 = effect of a pure compressional shear, with shortening indicated by the red arrow; 4–6 = effect of combination of pre-compressional strata tilting followed by shortening; while only northward tilting is shown in equal area projections 4 and 5, projection 6 shows the effect, after correcting for the bedding tilt, of both northward (blue) and southward (red) tilting on the same distribution; 7–9 = same as 4–6 but with an initial tilting of 30° and simulated shortening directed NE–SW; F = flattening simulation; S = shortening; T10° and T30° = 10° and 30° tilting; uT = correction for strained tilt. In all insets: D = declination (°); I = inclination (°); v_2 and v_3 = medium and minimum axes of the distribution matrix (Scheidegger, 1965); E = elongation (v_2/v_3). **(B)** Diagram of elongation (E) *vs.* inclination (I) of the original circular distribution (1), after inclination flattening (2), and after all the listed strain simulations; 6 and 9 are the E/I couples for the blue data plotted in the corresponding projections of panel A, while 6* and 9* refer to the red data; the shape, size, and orientation of the ellipses reflects the variations of the directions distributions as determined by the distribution matrix, while the arrows behind the ellipses are the mean declination of the directions; SDZ and FDZ = shallowed and flawed distribution zone, respectively.

calculated the elongation E, which is defined as the v_2/v_3 ratio, where v_2 and v_3 are the intermediate and minimum eigenvalues of the directions distribution matrix (Scheidegger, 1965; **Table 1**). The directions of each set are first converted to Cartesian coordinates x_i with i = 1, 2, 3. We simulated the effect of the deformation by applying the strain matrix S, which is a symmetric matrix of elements $s_{i,j}$ (where i, j = 1, 2, 3, and $s_{i,j} = s_{j,i}$). The new coordinates d_i of each "strained" direction are obtained by:

$$\begin{pmatrix} d_1 \\ d_2 \\ d_3 \end{pmatrix} = \begin{pmatrix} s_{11} & s_{12} & s_{13} \\ s_{21} & s_{22} & s_{23} \\ s_{31} & s_{32} & s_{33} \end{pmatrix} \begin{pmatrix} x_1 \\ x_2 \\ x_3 \end{pmatrix} \quad (2)$$

This can also be used to simulate the effect of inclination shallowing by applying a diagonal matrix S of the form $s_{11} = s_{22} > s_{33}$ (flattening matrix F). Note that under this condition this operation is equivalent to apply **Eq. 1** with $f = s_{33}/s_{11}$.

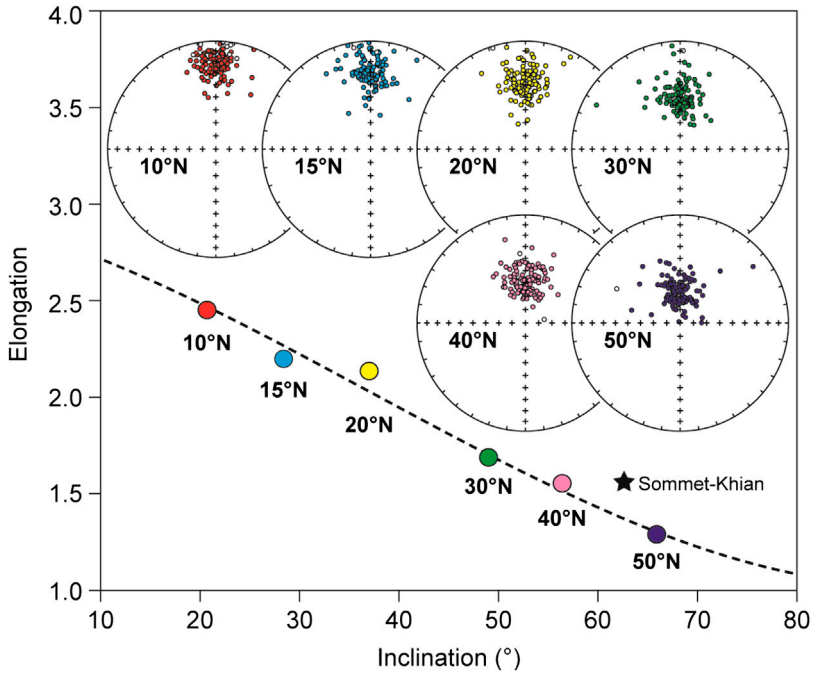

FIGURE 3 | Simulated sets of paleomagnetic directions predicted by the TK03.GAD paleosecular variation model. Each stereographic projection is shown with the associated latitude. The elongation/inclination (E/I) values predicted by the TK03.GAD model are shown by the dashed line, together with the E/I pair of each distribution (the color corresponds to the associated stereographic projection). The star is the E/I pair of the paleomagnetic directions set from Sommet-Khian discussed in the text.

TABLE 1 | List of the simulated paleomagnetic direction sets.

Set	Dec (°)	Inc (°)	k	α95(°)	E
10°N	0.4	20.7	35.2	2.2	2.451
15°N	359.7	28.4	28.7	2.4	2.199
20°N	360	37	30.2	2.4	2.136
30°N	359.6	49	27.2	2.5	1.688
40°N	0.8	56.4	20.6	2.9	1.554
50°N	357.1	65.9	24.3	2.7	1.290

*The sets are defined by their (approximated) latitude, as illustrated in **Figure 3**. Dec., Inc. = average declination and inclination; k, α_{95} = precision parameter and 95% confidence angle (Fisher, 1953); E = elongation of the distribution, defined as the ratio of the intermediate and minimum eigenvalues of the directions distribution matrix (Scheidegger, 1965). All simulated sets are listed in supporting **Supplementary Table S1** available online.*

TABLE 2 | List of the strain simulation matrices applied to the circular distribution and to the TK03.GAD distributions in presence of bedding tilt.

Matrix	s11	s22	s33	s12, s21	s13, s31
F	1.15385	1.15385	0.69230	0.00000	0.00000
C	0.50000	1.25000	1.25000	0.00000	0.00000
C (45°E)	0.87500	0.87500	1.25000	–0.37500	0.00000
Sw	0.69333	1.21333	1.15557	0.00000	0.00000
Sw (45°E)	0.95333	0.95333	1.15557	–0.26000	0.00000
St	0.43333	1.12666	1.73335	0.00000	0.00000
St (45°E)	0.78000	0.78000	1.73335	–0.34667	0.00000

*S_{ij} = elements of the matrix of **Eq. 2**; F = flattening matrix; C and C (45°E) = shortening matrices applied to the pure circular distributions, directed respectively N-S and NE-SW; S_w and S_t = matrices of **Eqs 3**, **4** simulating respectively the* weak cleavage *and the* strong cleavage *state; S_w (45°E) and S_t (45°E) = same as before but simulating shortening oriented NE-SW.*

We monitored the effect of the strain simulation on the directions distributions following the steps described as follows.

Circular Distribution

The workflow is shown in **Figure 2**. We first apply an inclination flattening with f = ~0.6 (detailed values of $s_{i,j}$ are listed in **Table 2**) to the circular distribution, which can be considered a reasonable assumption for sedimentary rocks (**Figures 2A**, diagram 1 and 2). In nature, the flattening factor is case sensitive and can easily range from 0.4 to 0.9 (see e.g. compilation of Muttoni et al., 2013). We simulated at first the simplest scenario, by applying shortening parallel to the average declination (**Table 2**) as indicated by the red arrow (**Figures 2A**, diagram 3). This situation, however, is not entirely realistic, because it implies no tilting of the strata, and in nature compressional strain is typically associated with folding. For this reason, in the next step we followed the case illustrated by Borradailee (1997). At the very initial stage of the deformation, low amplitude buckles, which result in tilted strata but not pervasive deformation, are subsequently passively strained, and the strain is affecting both the paleomagnetic directions and the strata attitude. The initial tilting of the strata is unknown, so we applied two different example scenarios, with initial tilting of 10°N (and 10°S), followed by N-S shortening (**Figure 2A**, diagrams 4–6), and initial tilting of 30°N (and 30°S) with shortening oriented NE-SW (**Figure 2A**, diagrams 7–9). We plot the strained directions, with associated

TABLE 3 | List of strain tensors applied to the TK03.GAD distribution in the case of shortening without tilting.

Tensor	s1	s2	s3
1	1.05	1.05	0.9
2	1.075	1.075	0.85
3	1.1	1.1	0.8
4	1.125	1.125	0.75
5	1.15	1.15	0.7
6	1.175	1.175	0.65
7	1.2	1.2	0.6
8	1.225	1.225	0.55
9	1.25	1.25	0.5
10	1.275	1.275	0.45
11	1.3	1.3	0.4
12	1.325	1.325	0.35
13	1.35	1.35	0.3
14	1.375	1.375	0.25
15	1.4	1.4	0.2

S_1, s_2, and s_3 are the maximum, intermediate, and minimum eigenvalues; eigenvector S_1 is assumed vertical in all simulations, while S_3 has a declination of 0°, 5°, 10°, 15°, and 20° as described in the main text.

means, in tilt corrected coordinates, and the variations of E/I ratios are monitored in **Figures 2B**.

TK03.GAD Distributions

Similar to what has been done for the circular distribution, we applied different straining scenarios, while monitoring the variations of E/I ratios in all cases. At first, to explore the effect on the original TK03.GAD distribution shape of pure compressional strain, we applied a series of oblate deformation tensors in the form (expressed as eigenvalues) of $s_1 = s_2 > s_3$, with s_1 vertical. The value of the (normalized) eigenvalue of s_3 ranges from 0.9 to 0.2 (**Table 3**). We then varied the orientation of the eigenvector s_3 with respect to the average declination of the distributions, ranging from 0° to 20°. Geometrically, this replicates different tectonic stresses oriented parallel to the strata but with a different azimuth (**Figures 4**, **5**). After each simulated deformation we calculate the average inclination and the elongation of the distribution for comparison with the E/I value expected from the TK03.GAD model.

A more complex but more realistic scenario has been applied to the direction sets simulated for low (10°N) and mid (40°N) latitudes, with the aim of recreating the fabrics shown in **Figure 1**. The directions have been first flattened with f = ~0.6 (**Figures 1A**). The *weak cleavage* and the *strong cleavage* fabrics are assumed to be the result of the sum of the flattening fabric and a successive strain. As the *weak cleavage* state is characterized by a prolate fabric with k1 > *k*2 = *k*3 (**Figures 1B**), while the *strong cleavage* by a triaxial fabric with k1 > *k*2 > *k*3 (**Figures 1C**), we applied to the flattened directions a deformation matrix calculated by either:

$$Sw = P_w \bullet F^{-1} \quad (3)$$

or

$$St = P_t \bullet F^{-1} \quad (4)$$

where S_w and S_t are the deformation matrix that simulate respectively the *weak* and the *strong cleavage* final stage, P_w (*weak cleavage*) and P_t (*strong cleavage*) are the (case sensitive) fabric that characterize the rocks, and F^{-1} is the inverse of the diagonal matrix F used to simulate the inclination shallowing (**Table 2**).

RESULTS

Circular Distribution

The effect of inclination shallowing followed by simulated shortening is shown in **Figure 2**. As expected, the solely flattening results in a variation of the elongation from circular to E-W elongated (**Figures 2B**). This condition can be easily restored by the site-level E/I correction (Tauxe and Kent, 2004), which gradually increase the directions inclination using **Eq. 1** until they are Fisher (1953) distributed (i.e., circular around the mean direction). The simple scenario of N-S shortening without rotation (i.e., bedding tilt) results in an increase of both elongation and inclination (**Figures 2A**,**B**, distribution 3). It is interesting to observe the influence of pre-existing tilting on the parameter variation, especially the inclination. The equal area projection 6 of **Figures 2A** shows the result of a N-S shortening simulation of distribution initially tilted by 10°N (blue ellipsis) and 10°S (red ellipsis). The final inclination is respectively ~15° shallower and ~14° steeper than the one obtained by the pure shear shortening (**Figures 2B**). This is also in agreement with the behavior in natural sedimentary rocks predicted by Borradaile (1997) and schematized in **Figure 1**. If tilting and paleomagnetic inclination are plunging toward the shortening direction, the final inclination with respect to the bedding will be flattened, while if the bedding and directions are antipodal, the final inclination will be steepened. Changing the orientation of the S matrix, will also affect the elongation direction, as shown in diagrams 7–9 of **Figure 2**. The inclination is less affected than during shortening parallel to the paleomagnetic declination, but the final elongation is not perpendicular to the declination, as expected if the inclination shallowing was the only filter acting on the data (**Figures 2B**, ellipses 9 and 9*). This concept is important also to help identifying the possible effect of finite strain in natural sedimentary rocks, as discussed below.

TK03.GAD Distributions

Effect of Strain Without Tilting

Figure 3 shows the simulated undeformed distributions. The calculated E/I lies in proximity to the expected values from the TK03.GAD model. We first apply the simplified model of strain that involves no pre-deformation rigid body rotation, with initial shortening parallel to the paleomagnetic declination (**Figure 4**, Group 1). The bold number within each equal area projection of **Figure 4** corresponds to the applied tensor listed in **Table 3**. The effect on the expected E/I couplets is shown in **Figure 5**. The most extreme applied simulated deformations are probably very unlikely to be found in nature, especially without the folding and tilting affecting the rocks, and possibly other remagnetization effects that would modify or even replace the original directions (i.e., piezoremanent magnetization; PRM; Till et al., 2010). As expected, when s_3 is parallel with the average declination there is a

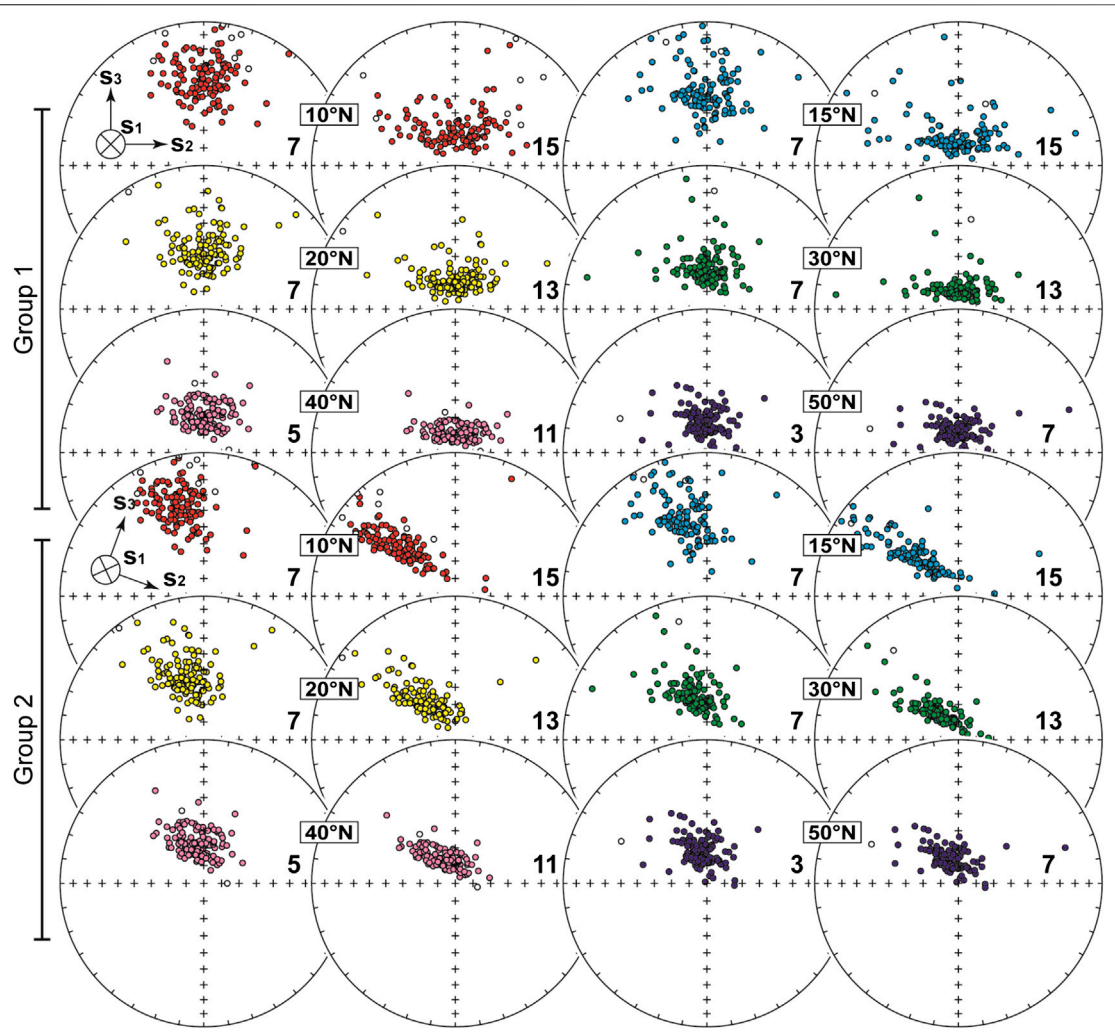

FIGURE 4 | Effect of simulated deformations, without strata tilting, on the TK03.GAD directions datasets. The latitude of the generated dataset is also indicated, and the colors of the data are as in **Figure 3**. Group 1 and 2 correspond respectively to a N-S and a 20°E oriented shortening, as represented by the eigenvectors of the strain matrix (S) shown in the insets. The bold numbers inside the projections indicate the S matrix applied to the set, listed in **Table 3**.

progressive increase of the inclination. The minimum of the curves in **Figure 5** coincides with the point where the elongation direction changes from parallel to perpendicular with respect to the declination. Before that point they are systematically below the reference TK03.GAD values. Soon after the elongation direction shifts from parallel to perpendicular with respect to the declination, the elongation increases to values higher than the reference TK03.GAD curve (**Figure 5**).

When increasing the angular distance between the declination and the eigenvector s_3, there is progressively less effect on the inclination. This occurs along with a stronger effect on the elongation (**Figure 5**). An angle of 20° between s_3 and the distribution declination is enough to drive the E/I to unrealistic values at low levels of strain. Direction distributions at high latitude, which are predicted to be quasi-circular by the TK03.GAD model, acquire an unrealistic elongation at very low strain (**Figures 5F**).

Effect of Strain With Tilting

We followed a chain of events closer to reality by combining the effects on the 10°N and 40°N TK03.GAD distributions of an initial compaction flattening, followed by finite strain simulations that replicate the *weak cleavage* and the *strong cleavage* fabric observed in natural rocks. Both strains are applied to directions belonging to two limbs of a fold (**Figures 6A**). We first assumed a shortening parallel to the paleomagnetic declination (**Figures 6B**,**C**). After applying the compaction flattening matrix F (**Table 2**), both the 10°N and the 40°N distributions acquire a nearly circular shape (**Figures 6C**). Because the initial bedding tilt before deformation is unknown, in the case of the *weak cleavage* we applied an initial strata inclination of 10°, plunging both to the north (front limb) and to the south (back limb). The effect of the S_w matrix of **Eq. 3** on the 10°N directions set is not significant in terms of inclination, but the distributions of both limbs acquire an elongation oriented E-W and falling below the reference TK03.GAD line (**Figures 6B,C**,

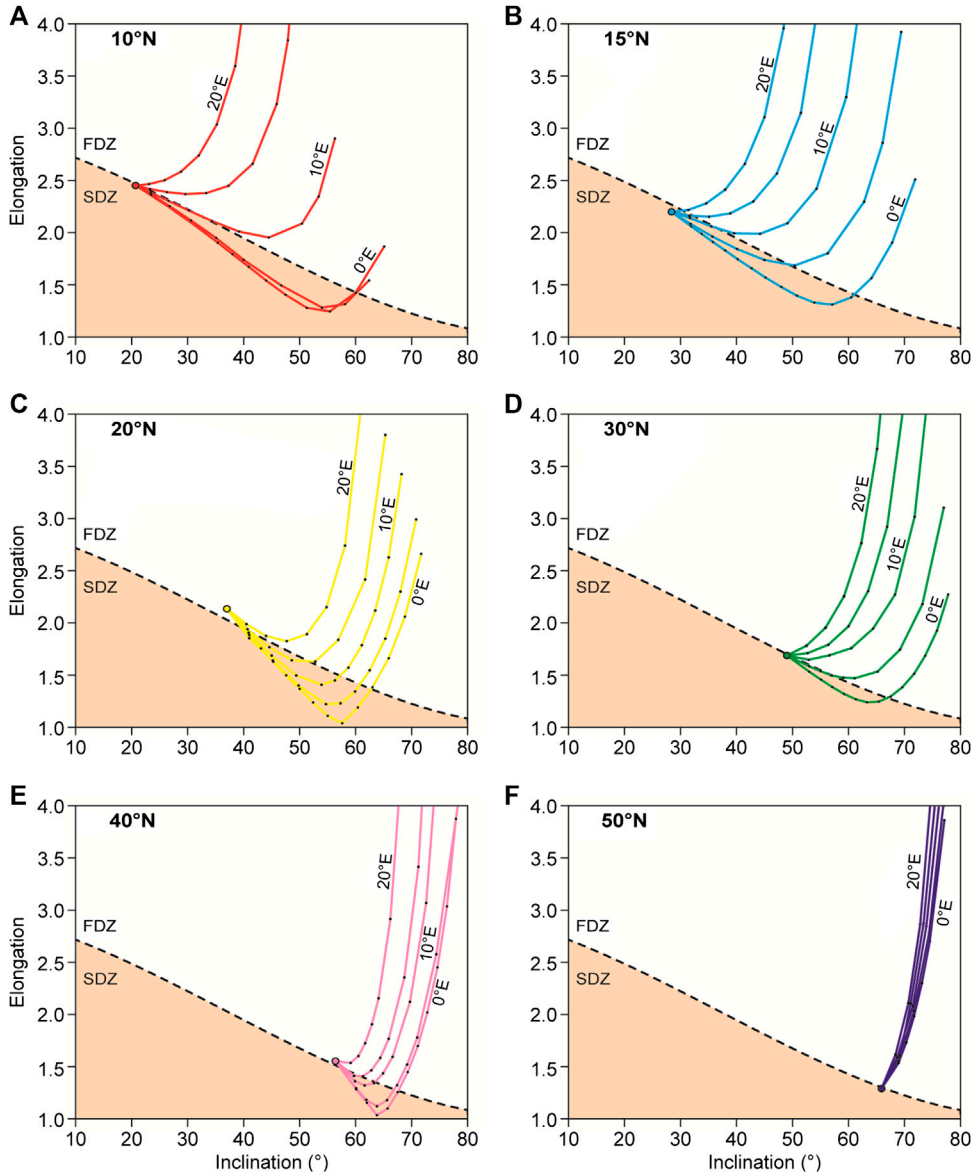

FIGURE 5 | Effect on the elongation/inclination (E/I) pairs of the TK03.GAD directions sets distribution varying the angle between the average declination and the eigenvector s_3 (i.e., shortening direction) of the strain (S) matrix (angles = 0°, 5°E, 10°E, 15°E, 20°E). Colors are as in **Figures 3**, **4**, and the latitude of the set is indicated for clarity (bold).

distr. 1 and 2). The same strain simulation appears to have a more severe impact on the 40°N set, because both fold limbs are characterized by distribution shapes jumping above the TK03. GAD line (**Fig. 6B**,**C**, distr. 3 and 4). When applying the S_t matrix (**Eq. 4**), which replicates the *strong cleavage* scenario, we assumed an initial bedding tilt of 30° for both limbs. The combined effects of stronger strain and higher initial bedding are immediately visible on the E/I ratios of both the 10°N and the 40°N sets. The inclinations of the 10°N set do not show a dramatic variation, but in the front limb case the strained distribution (which gets sensibly smaller) is strongly E-W elongated, while the back limb is still well below the TK03.GAD line (**Figures 6B**,**C**, distr. 5 and 6).

As for the *weak cleavage* simulation, the 40°N distribution appears to be more affected by the S_t matrix, with the front and the back limbs distributions showing respectively a marked shallowing and steepening of the inclination, parallel to a significant variation in elongation (**Figures 6B**,**C**, distr. 7 and 8).

Applying a shortening oriented 45° clockwise, has in general a more severe impact on all distributions (**Figures 6D**,**E**). The effect is particularly evident on the elongations; in all cases the *strong cleavage* scenario causes the E/I couples to assume unrealistic values. The *weak cleavage* simulations generate E/I values that are closer to the expected TK03.GAD reference line, nevertheless the direction of the elongation is significantly deviated (**Figures 6D**,**E**).

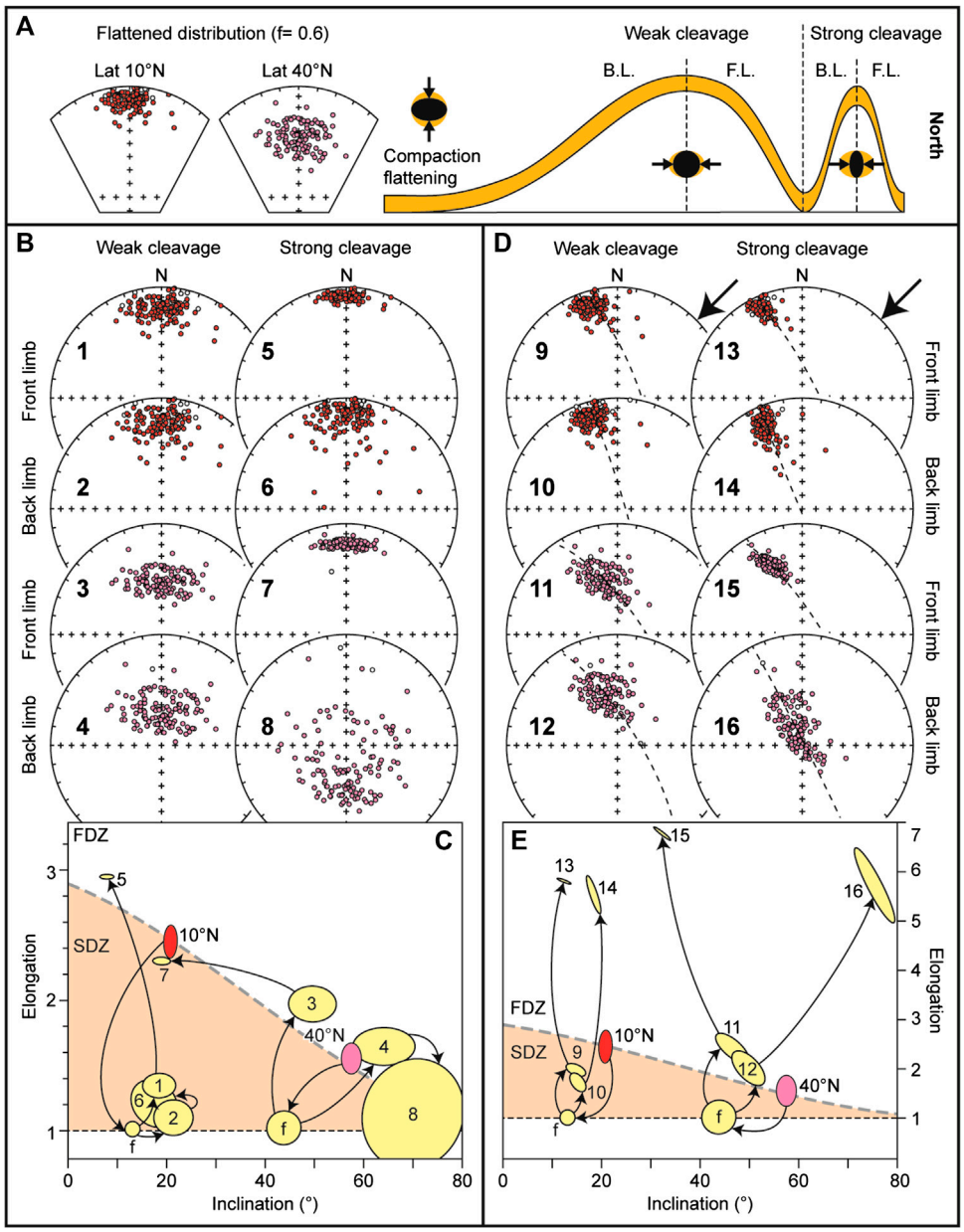

FIGURE 6 | Effect of the strain simulation with strata tilting. **(A)** Two reference TK03.GAD distributions generated for a 10 and 40°N latitude are first subjected to inclination shallowing as described in the text; to the right hand side the conceptual model of the theoretical *weak cleavage* and *strong cleavage* conditions is shown on both the back limb (B.L.) and front limb (F.L.) of a fold system. **(B)** Effect of the different strain simulation on the two distributions as described in the main text; the bold numbers correspond to the ellipses shown in panel C. **(C)** Elongation *vs*. inclination of the data shown in panel B; data are shown together with the reference curve expected by the TK03.GAD model (dashed line), on which the original 10°N latitude (red) and the 40°N latitude (pink) sets lie; the dotted line is the minimum possible value of E (1 = circle); SDZ and FDZ = shallowed and flawed distribution zone, respectively. **(D)** and **(E)** are as B and C, but with a simulated shortening direction (minimum axis of the S matrix) oriented NE-SW.

DISCUSSION

Strain and Distributions Shape

In the case of the circular distributions, the effect of either inclination shallowing or finite strain (or the combination of both) is readily visible, because the distribution departs from the original circular shape (E = 1). With the assumed circle (30° of radius) all the simulations, except for the pure compaction shallowing, fall above what we name the "shallowed distribution zone" (SDZ). This is the area where we would find all E-W elongated ellipses affected only by compaction shallowing, and they could be restored through the "site mean" E/I correction (Tauxe and Kent, 2004). All other E/I values of this diagram (for a circle of initial 30° radius)

indicate distributions that are flawed and affected by reorientation mechanisms like strain, which make them unreliable. We call this area of the diagram the "flawed distribution zone" (FDZ) (**Figures 2B**). From the analysis of the circle distribution it is also evident that the angle between the maximum axis of the elongation and the mean direction declination can be used as a reliability index. In fact, inclination flattening only produces elongations that are perpendicular with respect to the declination, and thus an angle that is not perpendicular is indicating a flawed distribution.

Similar concepts can be applied to the analyses of the TK03.GAD distributions. Applying the S matrix on the original TK03.GAD distributions, without imposing a pre-strain rotation (i.e., tilting), has an effect that depends mostly on the angle between the shortening direction (s_3 eigenvector of the strain matrix) and the average direction declination. When they are parallel (**Figure 4**, Group 1) many of the E/I values of the deformed datasets, fall below the expected TK03.GAD function line, in the SDZ section of the diagram (**Figures 5A–F**). Analogously to what has been described for the circular distributions, this is the area of the diagram where normally the E/I pair of sets that are affected by sedimentary inclination flattening are found. Applying the E/I unflattening method of Tauxe and Kent (2004) to such a distribution would result in a final inclination even further steepened. As the degree of the simulated strain increases, the distributions acquire unrealistic E/I pairs, falling in the FDZ. Since high latitude simulations are originally quasi circular, they are promptly deformed to unrealistic E/I values by the simulated strain (**Figures 5F**). A similar effect is obtained by increasing the angle between the shortening direction and the declination (**Figure 4**, Group 2, **Figure 5**). This is the case because it affects more the distribution shape rather than the inclination. A shortening direction oriented E-W would in fact act only on the shape, which would peak straight to unrealistic values.

The effect of pre-strain tilting is affecting the final directions inclination (calculated with respect to the bedding plane) in a more complex way. With the applied boundary conditions (flattening and initial bedding tilt), especially in the *strong cleavage* scenario, the direction belonging to the front limb of the modeled fold tends to be flattened, while the ones belonging to the back limbs are steepened. This is in agreement with the behavior predicted by Borradaile (1997). Strain simulations with a shortening azimuth deviated from the mean declination affect more the elongation, also in terms of orientation. Any paleomagnetic set that is elongated neither parallel (as predicted by the TK03.GAD model) nor perpendicular (i.e., affected by compaction shallowing) with respect to the average declination should thus be considered potentially flawed. These analyses also show how sensitive the initial conditions like flattening and bedding tilt, which are *a priori* unknown, influence the final result.

This is why paleomagnetic analyses for paleogeographic reconstructions should always be carried out in combination with AMS analyses, as a proxy of the presence of finite strain. Only when the AMS fabric is sedimentary, a standard E/I correction can be safely applied.

THE NEW CALEDONIA CASE

Paleomagnetic Directions and Anisotropy of Magnetic Susceptibility

Dallanave et al. (2020) recently published paleomagnetic data from carbonate rocks exposed in the Koumac region of northern New Caledonia. New Caledonia is the emergent part of the northernmost Norfolk Ridge, which is in turn part of a large continental mass that is submerged for more than 90%, referred to as Zealandia (Mortimer et al., 2017; Sutherland et al., 2019). The sampled section (Sommet-Khian, 260 stratigraphic meters) consists of a massive basal pelagic micrite (0–83 m) overlain upsection by terrigenous–rich calciturbidites (83–260 m). For this work we exclude the dataset from the terrigenous-rich calciturbidite because of the general lower quality of the ChRM directions and a negative reversal test (see Dallanave et al., 2020 for details). The dataset from the massive micrite consists of 88 ChRM directions that allow a correlation of the section with Chrons C23n.2n to C21n (51–46 Ma, corresponding to the early-middle Eocene; Ogg, 2012). Of these 88 directions, 77 have been isolated using the interpolation proposed by Kirschvink (1980) and, to maximize the reliability, each direction was anchored (or not) to the origin of the demagnetization axes following the Bayesian criteria proposed by Heslop and Roberts (2016). Eight directions were determined by means of fisher mean on the vector end points, while three through great circles analyses (McFadden and McElhinny, 1988); (**Supplementary Table S2**). The dataset is statistically antipodal, with a positive bootstrap-based reversal test (Tauxe et al., 1991). Despite the high quality of the dataset, there is a mismatch between the average inclination from Sommet-Khian and the reference directions expected for this time (Veevers and Li, 1991; Torsvik et al., 2012). The average direction from New Caledonia is steeper (i.e., higher inclination) compared to the reference directions from the literature. When compared with the inclination derived from the synthetic global APWP of Torsvik et al. (2012), the resulted steepening is ~10°. However, this reference compilation consists of a limited number of entries that has to go through multiple rotations to be plotted into Zealandia coordinates, and there is only one entry from the Australian plate (53 Ma; Torsvik et al., 2012) (**Figures 7A–C**; **Supplementary Table S3**). The steepening decreases to 5.4° if the inclination is compared with the APWP of Veevers and Li (1991), which is based on entries from Australia and India, but using old datasets with poorly defined quality criteria and age control (**Figures 8A**).

AMS data of 89 samples from Sommet-Khian yield an oblate tensor with a low degree of anisotropy (Jelínek, 1981) (Pj = 1.05). The foliation plane (defined by k_1 and k_2 axes of the AMS) does not coincide with the bedding, indicating a tectonic-induced magnetic fabric in contrast to a sedimentary fabric typically observed in absence of finite strain (**Figures 8B**). The orientation of this fabric is in agreement with the general tectonic style of New Caledonia, which is the result of a

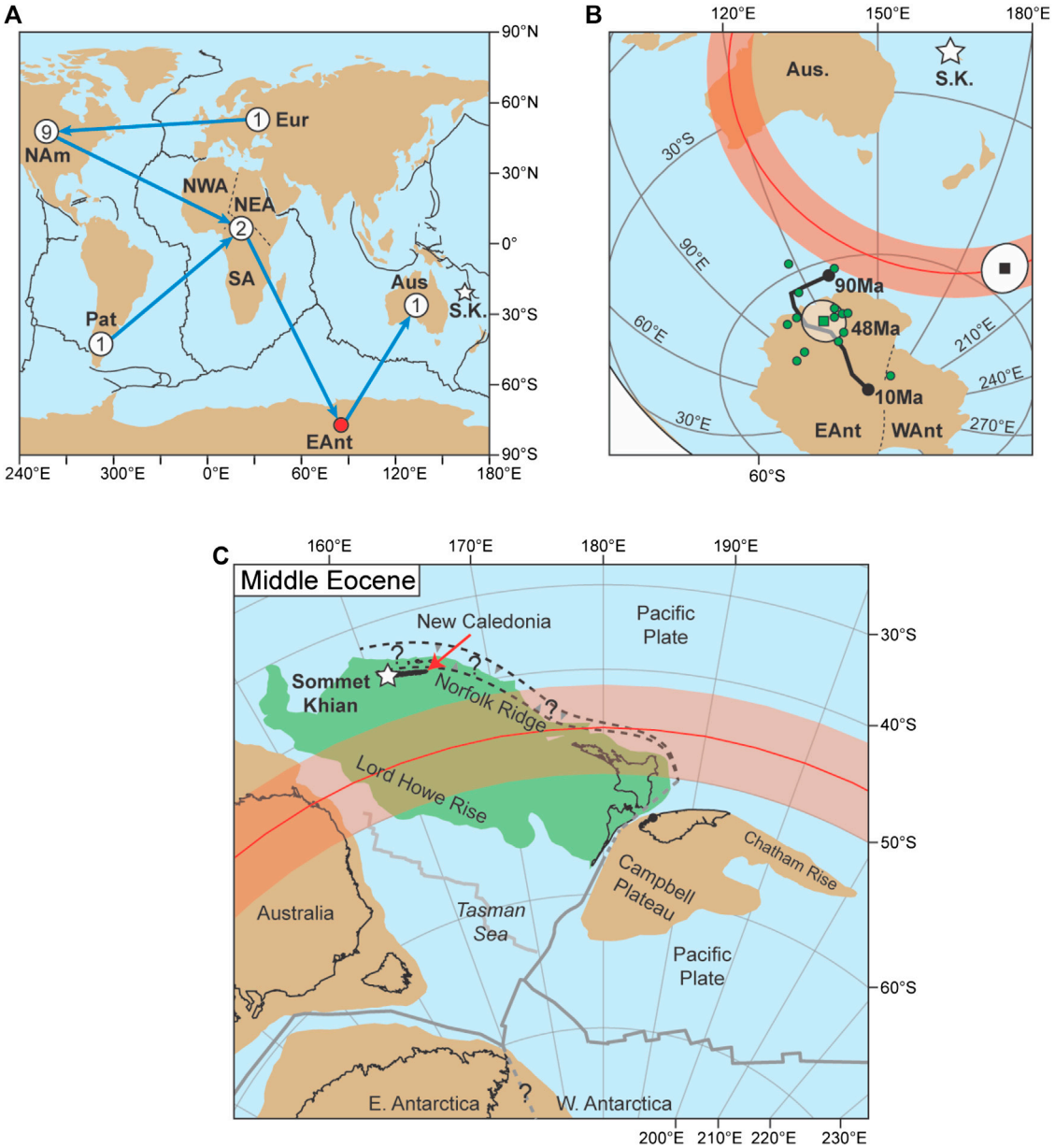

FIGURE 7 | Geological and paleomagnetic-paleogeographic framework of the Sommet-Khian record from northern New Caledonia; in all panels: Aus = Australia; Eur = stable Europe; EAnt and WAnt = east and west Antarctica; NAm = north America; NWA, NEA, and SA = northwest, northeast, and south Africa; Pat = Patagonia; S.K. = Sommet-Khian. **(A)** Global plate configuration and circuits (blue arrows) connecting the Australian plate with the source of the paleomagnetic data for the 53–43 Ma interval included in the reference compilation of Torsvik et al. (2012); (**Supplementary Table S3**); white circle indicate the source plate of the data and the number of entries. **(B)** The average paleomagnetic pole from Sommet-Khian (black square with white 95% confidence cone) is compared with the reference paleomagnetic pole (green square) calculated averaging 14 entries (green dots) from the compilation of Torsvik et al. (2012) that fall within the 53–43 Ma window (**Supplementary Table S3**); the 90–10 Ma global synthetic apparent polar wander path from the same compilation, plotted in Australian coordinates, is also shown as thick black line; the red line with the shaded area shows that, even rotating the S.K. pole to toward reference 48 Ma one, they remain statistically distinguishable. **(C)** Paleogeographic reconstruction of the Southwest Pacific area in the middle Eocene (~45 Ma); continental areas are filled in light brown except for northern Zealandia (light green); the light gray line is the Tasman Ocean spreading ridge, which activity ended during Chron 24n (~53 Ma), and the dark gray lines are active spreading ridges; dotted black lines are the approximate position of the proto-Tonga-Kermadec subduction zone and the north-east dipping early Eocene east-dipping subduction zone inferred by the geology of New Caledonia (see text); the white star is the location of Sommet-Khian. While the reconstruction is based on the published reference data, the red line with the red shaded area is the paleolatitude and associated confidence boundaries obtained from the paleomagnetic directions from Sommet-Khian.

convergence broadly oriented NE-SW, perpendicular to the length of the island (e.g., Lillie and Brothers, 1969; Cluzel et al., 2012). Tectonic strain largely influences the AMS fabric (e.g., Parés et al., 1999) but using the absolute value of the AMS to quantify the internal strain of the rock is difficult because of the number of variables that can influence it (Evans et al., 2003).

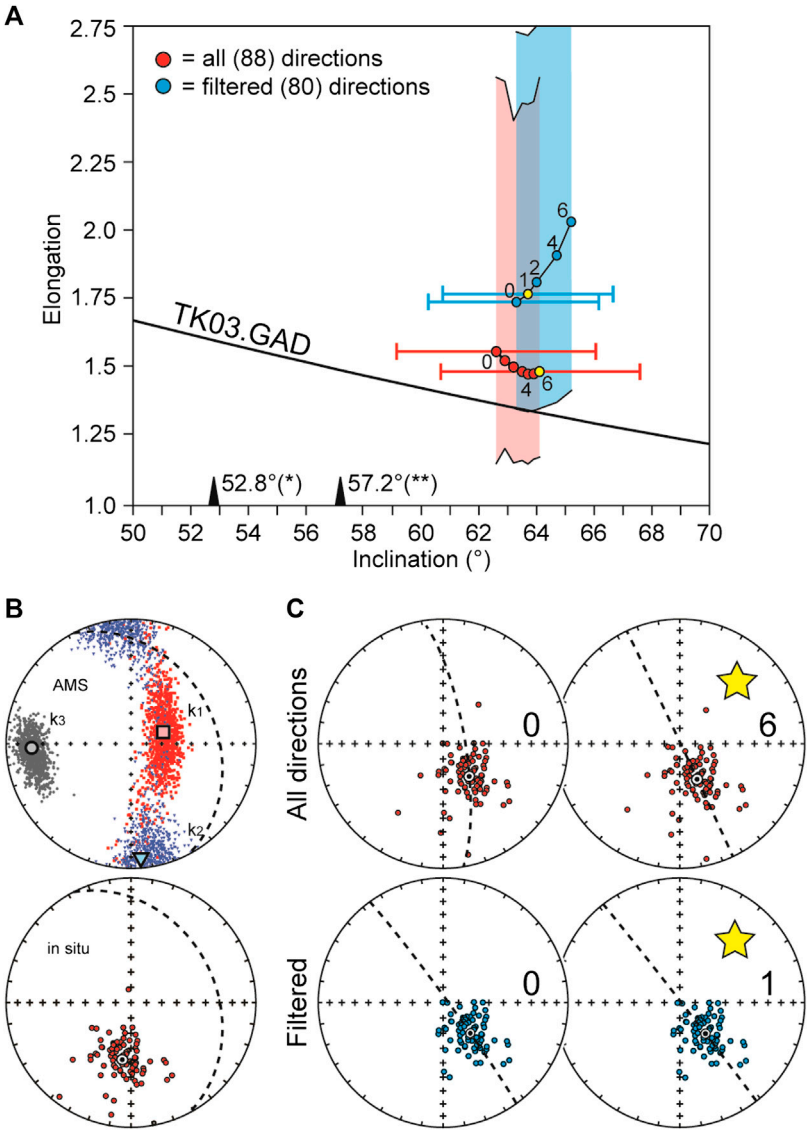

FIGURE 8 | Paleomagnetic directions, anisotropy of magnetic susceptibility (AMS), and distribution shape analysis of Sommet-Khian. **(A)** Elongation *vs.* inclination (E/I) of the paleomagnetic distribution for the whole (red) and the filtered (blue) dataset, compared with the value expected by the TK03.GAD model; the yellow dots represent the "unstrained" condition where the elongation direction is parallel to the average declination, shown with the inclination 95% confidence angle determined by applying standard Fisher (1953) statistics; the elongation values of the original and "unstrained" steps are shown with the 90% confidence zone determined by means of 1,000 bootstrapped pseudo-dataset expected inclination calculated from the compilations of Torsvik et al. (2012*) and Veevers and Li (1991**) are shown. **(B)** Upper projection: AMS from Sommet-Khian; k1 (red symbols), k2 (blue symbols), and k3 (gray symbols) are respectively the major, intermediate, and minor axes of the AMS, with average direction of the eigenvectors; lower projection: characteristic remanent magnetization (ChRM) directions from Sommet-Khian in *insitu* coordinates, together with the Fisher (1953) mean; in both projections the dashed circle is the bedding plane; data from Dallanave et al. (2020). **(B)** Effect of the "unstraining" on the whole (red) and filtered (blue) dataset from Sommet-Khian; the yellow star indicates the condition where the elongation direction (dotted line) is parallel to the declination; the number within the diagrams indicate the matrix used (**Table 4**) and the associated E/I couple in panel A.

Analysis of the Directions Distribution From Sommet-Khian

The first step is comparing the E/I ratio of the dataset from Sommet-Khian with the one predicted by the TK03.GAD model. The original ChRM directions have an elongation that falls above the value predicted by the TK03.GAD model. Repeated calculations on 1,000 bootstrapped pseudo-distributions (Tauxe et al., 1991) estimate a (fairly large) 90% confidence boundary for the elongation that overlaps with the expected value (**Figures 8A**), implying that the E/I ratio itself is, at a 90% confidence, realistic. The wide extension of the 90% confidence margins is likely due to the limited number (<100) of directions. This outlines the importance of having an adequate number of paleomagnetic directions for a fully reliable analysis. We repeated the same calculation using the dataset filtered from the three directions determined by great circle analyses and also

eliminating five directions which VGP is > 45° apart from the mean paleomagnetic pole, similarly to the cutoff applied to the MM97 dataset of McElhinny and McFadden (1997). The obtained inclination is very similar, with a slightly higher elongation (**Figures 8A**). Despite the confidence margins, the fact that both datasets have an elongation higher than expected is an indication of potential contamination of the dataset, possibly steepened by the effect of strain.

We tried to restore the original inclination by progressively "unstrain" the paleomagnetic directions until they match the elongation predicted by the TK03.GAD model. In order to do this we considered the bedding also as a physical entity affected by the total strain. We therefore apply the "unstrain" matrix in the form of $s_1 > s_2 = s_3$ with progressively higher degrees of elongation, with s_1 parallel to the k_3 AMS axis (**Figure 8**). We applied the "unstrain" matrix to all the ChRM directions in *situ* (IS) coordinates as well as to the bedding plane using the eigenvalues listed in **Table 4**, and we monitor the E/I couplets after correcting the dataset for ("unstrained") bedding tilt (**Table 5**). We applied the same process to both the whole and the filtered dataset, so that we can evaluate the effect of outlier directions within the (not-filtered) dataset. In both cases the progressive "unstrain" led to a minor increase of the inclination, which however always falls within the confidence bounds of the original distribution (**Figures 8A**). The value of E changes in different fashion in the two cases: for the whole dataset it progressively decreases, but without crossing the model line. Despite that, the bootstrap-based 90% confidence interval indicates that the elongation is statistically acceptable throughout the whole "unstrain" process, and it reaches a minimum after applying matrix 4 of **Table 4** (**Figures 8A**). The filtered dataset on the contrary is characterized by a steep rise of the elongation, which becomes statistically unacceptable (at a 90% confidence) after a very mild unstrain (S matrix 2 of **Table 4**; **Figures 8A**).

A close inspection of the equal area projections, plotted together with the elongation direction (**Figures 8C**) reveals that the elongation assumes an orientation parallel to the declination after applying unstrain matrix 6 (in the case of the whole dataset) and 1 (in the case of the filtered dataset). Having the elongation parallel to the mean declination is, together with the latitude dependent specific value of E, a condition predicted by the TK03.GAD model. The inclinations obtained are 64.1 ± 3.5° and 63.5 ± 2.9° respectively for the whole and the filtered dataset (**Figures 8A**). In both cases the elongation is still statistically acceptable at a 90% of confidence. In synthesis, both datasets give similar corrected results, even if the limited number of directions results in wide elongation confidence bounds.

TABLE 4 | List of the "unstraining" tensors applied to the paleomagnetic directions from Sommet-Khian.

Tensor	v3	V3_dec	V3_inc	v2	V2_dec	V2_inc	v1	V1_dec	V1_inc
1	0.99	70.1	67.6	0.99	175.2	6.1	1.02	267.6	21.4
2	0.98	70.1	67.6	0.98	175.2	6.1	1.04	267.6	21.4
3	0.97	70.1	67.6	0.97	175.2	6.1	1.06	267.6	21.4
4	0.96	70.1	67.6	0.96	175.2	6.1	1.08	267.6	21.4
5	0.95	70.1	67.6	0.95	175.2	6.1	1.1	267.6	21.4
6	0.94	70.1	67.6	0.94	175.2	6.1	1.12	267.6	21.4

*The eigenvector are oriented as the average eigenvector of the anisotropy of magnetic susceptibility (AMS), shown in **Figure 8B**. The eigenvalues used for the "unstraining" process are indicated as v_1, v_2, and v_3, with the orientation (V_i_dec, V_i_inc. = declination and inclination) of the associated eigenvector.*

Paleogeographic Implications

The southwest Pacific area went through a complex tectonic and paleogeographic evolution during the Eocene, related to the inception of the Tonga-Kermadec subduction system (recent reviews can be found in Cluzel et al., 2012; Collot et al., 2020; Dallanave et al., 2018b, Dallanave et al., 2020; Maurizot et al., 2020a, Maurizot et al., 2020b; Sutherland et al., 2020). The Tonga-Kermadec subduction initiated in the middle Eocene immediately to the east of the Norfolk Ridge, the northernmost part of which is

TABLE 5 | Effect of the "unstraining" tensors on the paleomagnetic directions and bedding of Sommet-Khian.

	In situ coordinates				Bedding		Tilt corrected coordinates				
Set	Dec (°)	Inc (°)	k	α95 (°)	Dec (°)	Inc (°)	Dec (°)	Inc (°)	E	E (-)	E (+)
All_0	188.70	51.80	20.70	3.40	56.40	30.50	141.40	62.60	1.562	1.155	2.563
All_1	189.60	51.80	20.40	3.40	56.89	29.86	143.40	62.90	1.529	1.209	2.548
All_2	190.50	51.80	20.20	3.40	57.36	29.24	145.50	63.20	1.506	1.157	2.405
All_3	191.50	51.90	20.00	3.50	57.84	28.61	147.60	63.50	1.489	1.166	2.469
All_4	192.50	51.90	19.70	3.50	58.30	27.97	149.70	63.70	1.480	1.153	2.465
All_5	193.50	51.90	19.50	3.50	58.77	27.34	151.90	63.90	1.481	1.171	2.475
All_6	194.40	51.90	19.30	3.50	59.23	26.70	154.20	64.10	1.489	1.178	2.562
Filtr_0	188.20	53.20	30.70	2.90	56.40	30.50	138.40	63.20	1.743	1.351	2.728
Filtr_1	189.20	53.20	30.10	2.90	56.89	29.86	140.50	63.50	1.772	1.342	2.716
Filtr_2	190.20	53.30	29.50	3.00	57.36	29.24	142.60	63.90	1.815	1.350	2.886
Filtr_4	192.20	53.30	28.50	3.00	58.30	27.97	146.90	64.50	1.913	1.376	3.113
Filtr_6	194.20	53.30	27.50	3.10	59.23	26.70	151.50	65.00	2.036	1.419	3.237

*All_0 to 6 refer to the completed directional dataset (88 direction) without filtering, while Filtr_0 to 6 refer to the filtered dataset (80 directions) as specified in the text; Dec, Inc. = declination and inclination; k and α_{95} = precision parameter and 95% of Fisher, 1953. The bedding, expressed as declination and inclination of the plunge, is also "unstrained" before applying the bedding correction to the paleomagnetic directions. The derived tilt corrected directions are given with the associated elongation (E) of the distribution and the 90% confidence boundaries determined by repeating the analysis on 1,000 bootstrapped sets of directions; (-) and (+) are respectively the lower and the higher confidence margins. The complete sets of directions are given in supporting **Supplementary Table S2** available online.*

emerging to form the New Caledonia archipelagos (**Figures 7C**). The history of the eastern margin of northern Zealandia before the Tonga-Kermadec subduction is still debated, because the geology of New Caledonia suggests the presence of a pre-Tonga east-dipping subduction zone (Cluzel et al., 2012; Collot et al., 2020; Maurizot, 2011; Maurizot et al., 2020a, Maurizot et al., 2020b), which is, however, difficult to reconcile with the geologic history derived from seismic profiles acquired in the Tasman area (Sutherland et al., 2017). Zealandia is separated from continental Australia by the oceanic crust of the Tasman Ocean basin, which ended its spreading activity during magnetic anomaly 24 in the early Eocene (~53 Ma; Gaina et al., 1998; **Figures 7C**). Therefore, middle Eocene paleomagnetic data from Australia should be applicable also to northern Zealandia. The most widely used APWP was compiled by Torsvik et al. (2012), but a closer look at the dataset reveals that there is only one early Eocene (53 Ma) entry from Australia for the entire Paleogene based on a study on the Barrington Volcano in New South Wales (Wellman et al., 1969, later confirmed by; Hill et al., 2002). Recent authochtonous data have been published only for the Oligocene (Hansma and Tohver, 2019). The reference Australian APWP for the Paleogene (and the entire time back to the Permian) is constructed mainly using data rotated from other plates. For this reason, the paleomagnetic record of Sommet-Khian is extremely valuable, because it is the first early-middle Eocene autochthonous directional dataset from northern Zealandia (and Australia).

The Eocene sedimentary record of the Koumac area lies on top of the Mesozoic basement, but New Caledonia as a whole is constituted by sedimentary, metamorphic, and igneous terranes that are overlain by allochthons of sedimentary, mafic, and ultramafic nappes obducted from the late Eocene with the opening of the North Loyalty Basin (Cluzel et al., 2001, Cluzel et al., 2005, Cluzel et al., 2006, Cluzel et al., 2012; Maurizot, 2011; Maurizot et al., 2020a). The paleomagnetic declination obtained by Dallanave et al. (2020) is in general agreement with the tectonic constraints, indicating a post-middle Eocene rotation of New Caledonia of about 60° CCW. The ChRM directions inclination is primary and should be usable (at a first inspection) as paleogeographic constraint.

The "unstrained" mean paleomagnetic inclination is ~64° (**Figures 8A**). Using the dataset with the widest uncertainties (i.e., the unfiltered directions; 64.1 ± 3.5°) we obtained an average paleolatitude of deposition of 45.8°S (confidence boundaries: 50.5°S, 41.6°S; **Figures 7C**). We estimated precisely the expected paleolatitude of Sommet-Khian by using 14 paleomagnetic poles falling within the 53 and 43 Ma age window from the global selection of Torsvik et al. (2012), who also provide the parameters for rotating the poles into Australian coordinates (**Figures 7–C**; **Supplementary Table S3**). We selected this specific 10 Myr time-window because it is approximately centered on the age of the Sommet-Khian section (~51–46 Ma). The resulting paleolatitude (33.4°S) is significantly lower than the 45.8°S calculated using the dataset from Sommet-Khian. The same applies for the paleolatitude of ~38°S predicted by the dataset of Veevers and Li (1991). This implies that either the tectonic strain affecting the Sommet-Khian sediments pervasively affected the dataset (even if it seems acceptable within the statistically determined bounds) or the lack of autochthonous (*i.e.,* Australian) data for the Eocene results in an erroneous paleolatitude estimation for the area. We are more inclined to consider that the problem resides in the Sommet-Khian directions, because the AMS data clearly indicate a non-sedimentary fabric. We stress the fact that without AMS analysis, the dataset could have been considered reliable, because of the presence of several reversals and a positive reversal test. A collection of autochthonous Eocene data from either continental Zealandia or Australia might add new constraints to resolve the paleogeography of the southwest Pacific area. Our approach highlights that AMS measurement should be always presented to help assessing the quality of the data.

CONCLUSION

Finite strain in sedimentary rocks induced by tectonism can deviate primary paleomagnetic directions. Using different simulated deformations on distributions drawn according to the TK03. GAD paleosecular variation model, we show how finite strain affects the shape of the directions distribution, which can be used as an indicator of the reliability of paleomagnetic directions. Only if the shape agrees with the expected one based on the TK03.GAD model, a direction distribution can be regarded as of high quality. Otherwise, a "flawed" distribution shape is indicative of post depositional changes requiring further investigation. We apply this concept to a recently published early-middle Eocene paleomagnetic and AMS dataset from New Caledonia. Despite the high quality of the directions and a positive reversal test, the paleomagnetic inclination from New Caledonia is considerably steeper than the one expected from published reference datasets, which are however limited in number and mostly rotated into Australian coordinate from other plates. Paleomagnetic directions from New Caledonia are likely affected by some amount of finite strain, as revealed by a weak prolate AMS fabric of tectonic origin. The distribution shape appears to be in agreement with the TK03.GAD model within a (large) 90%-bootstrap-determined confidence boundaries. Nevertheless, the presence of an AMS tectonic fabric is enough to undermine the reliability of the data. New Eocene data from continental Australia and/or Zealandia should solve the conflict between the autochthonous paleomagnetic dataset and the reference data, which, as is, results in a considerable paleolatitude discrepancy. More importantly, we suggest that AMS measurements should be always measured and presented together with directional datasets when performing paleogeographic reconstructions based on paleomagnetic data from sedimentary rocks.

DATA AVAILABILITY STATEMENT

The original contributions presented in the study are included in the article/**Supplementary Material**, further inquiries can be directed to the corresponding author.

AUTHOR CONTRIBUTIONS

All authors listed have made a substantial, direct, and intellectual contribution to the work and approved it for publication.

FUNDING

ED is supported by the Deutsche Forschungsgemeinschaft (DFG) through grants DA1757/1-1 and DA1757/2-1.

ACKNOWLEDGMENTS

We thank SS (Editor) and the Reviewers for the comments that greatly improve the quality of the manuscript.

SUPPLEMENTARY MATERIAL

The Supplementary Material for this article can be found online at: https://www.frontiersin.org/articles/10.3389/feart.2020.592277/full#supplementary-material.

REFERENCES

Besse, J., and Courtillot, V. (2002). Apparent and true polar wander and the geometry of the geomagnetic field over the last 200 Myr. *J. Geophys. Res.* 107, 2300. doi:10.1029/2000JB000050

Blatt, H., and Jones, R. L. (1975). Proportions of exposed igneous, metamorphic, and sedimentary rocks. *Bull. Geol. Soc. Am.* 86, 1085–1088. doi:10.1130/0016-7606(1975)86<1085:POEIMA>2.0.CO 2

Borradaile, G. J. (1997). Deformation and paleomagnetism. *Surv. Geophys.* 18, 405–435. doi:10.1023/A:1006555906559

Butler, R. F. (1992). *Paleomagnetism*. Boston, Iran: Blackwell Scientific Publication, 238.

Cluzel, D., Aitchison, J. C., and Picard, C. (2001). Tectonic accretion and underplating of mafic terranes in the Late Eocene intraoceanic fore-arc of New Caledonia (Southwest Pacific): geodynamic implications. *Tectonophysics* 340, 23–59. doi:10.1016/S0040-1951(01)00148-2

Cluzel, D., Bosch, D., Paquette, J.-L., Lemennicier, Y., Montjoie, P., and Ménot, R.-P. (2005). Late Oligocene post-obduction granitoids of New Caledonia: a case for reactivated subduction and slab break-off. *Isl. Arc.* 14, 254–271. doi:10.1111/j.1440-1738.2005.00470.x

Cluzel, D., Maurizot, P., Collot, J., and Sevin, B. (2012). An outline of the geology of New Caledonia; from Permian–Mesozoic Southeast Gondwanaland active margin to Cenozoic obduction and supergene evolution. *Episodes* 35, 72–86. doi:10.18814/epiiugs/2012/v35i1/007

Cluzel, D., Meffre, S., Maurizot, P., and Crawford, A. J. (2006). Earliest Eocene (53 Ma) convergence in the southwest pacific: evidence from pre-obduction dikes in the ophiolite of New Caledonia. *Terra. Nova.* 18, 395–402. doi:10.1111/j.1365-3121.2006.00704.x

Cogné, J. P. (1987). Paleomagnetic direction obtained by strain removal in the Pyrenean Permian redbeds at the "Col du Somport" (France). *Earth Planet Sci. Lett.* 85, 162–172. doi:10.1016/0012-821X(87)90029-X

Cogné, J. P., and Perroud, H. (1985). Strain removal applied to paleomagnetic directions in an orogenic belt: the Permian red slates of the Alpes Maritimes, France. *Earth Planet Sci. Lett.* 72, 125–140. doi:10.1016/0012-821X(85)90122-0

Cogné, J. P., and Perroud, H. (1987). Unstraining paleomagnetic vectors: the current state of debate. *Eos, Trans. Am. Geophys. Union.* 68, 705–712. doi:10.1029/EO068i034p00705-01

Collot, J., Patriat, M., Sutherland, R., Williams, S., Cluzel, D., Seton, M., et al. (2020). "Geodynamics of the southwest Pacific: a brief review and relations to New Caledonian geology,"in. *New Caledonia–geology, geodynamic evolution, and mineral resources*. Editors P. Maurizot and N. Mortimer (London, United Kingdom: Geological Society of London MemoirsGeological Society of London), 51, 1–14.

Constable, C., and Parker, R. L. (1988). Statistics of the geomagnetic secular variation for the past 5 m. *Y. J. Geophys. Res.* 93, 11569–11581. doi:10.1029/jb093ib10p11569

Creer, K. M., Irving, E., and Runcorn, S. K. (1954). The direction of the geomagnetic in great field in remote epochs britain. *J. Geomagn. Geoelectr.* 6, 163–168. doi:10.5636/jgg.6.163

Dallanave, E., Agnini, C., Bachtadse, V., Muttoni, G., Crampton, J. S., Strong, C. P., et al. (2015). Early to middle Eocene magneto-biochronology of the southwest Pacific Ocean and climate influence on sedimentation: insights from the Mead Stream section, New Zealand. *Geol. Soc. Am. Bull.* 127, 643–660. doi:10.1130/B31147.1

Dallanave, E., Agnini, C., Muttoni, G., and Rio, D. (2009). Magneto-biostratigraphy of the Cicogna section (Italy): implications for the late Paleocene–early Eocene time scale. *Earth Planet Sci. Lett.* 285, 39–51. doi:10.1016/j.epsl.2009.05.033

Dallanave, E., Agnini, C., Muttoni, G., and Rio, D. (2012). Paleocene magneto-biostratigraphy and climate-controlled rock magnetism from the belluno basin, tethys ocean. *Italy. Palaeogeogr. Palaeoclimatol. Palaeoecol.* 337–338, 130–142. doi:10.1016/j.palaeo.2012.04.007

Dallanave, E., Agnini, C., Pascher, K. M., Maurizot, P., Bachtadse, V., Hollis, C. J., et al. (2018b). Magneto-biostratigraphic constraints of the Eocene micrite–calciturbidite transition in New Caledonia: tectonic implications. *N. Z. J. Geol. Geophys.* 61, 145–163. doi:10.1080/00288306.2018.1443946

Dallanave, E., Kirscher, U., Hesse, R., Bachtadse, V., and Wortmann, U. G. (2018a). Palaeomagnetic time and space constraints of the early cretaceous rhenodanubian flysch zone (eastern alps). *Geophys. J. Int.* 213, 1804–1817. doi:10.1093/gji/ggy077

Dallanave, E., Maurizot, P., Agnini, C., Sutherland, R., Hollis, C. J., Collot, J., et al. (2020). Eocene (46-44 Ma) onset of Australia-Pacific plate motion in the southwest Pacific inferred from stratigraphy in New Caledonia and New Zealand. *Geochem. Geophys. Geosys.* 21, e2019GC008699. doi:10.1029/2019GC008699

DeMets, C., Gordon, R. G., and Argus, D. F. (2010). Geologically current plate motions. *Geophys. J. Int.* 181, 1–80. doi:10.1111/j.1365-246X.2009.04491.x

Evans, M. A., Lewchuk, M. T., and Elmore, R. D. (2003). Strain partitioning of deformation mechanisms in limestones: examining the relationship of strain and anisotropy of magnetic susceptibility (AMS). *J. Struct. Geol.* 25, 1525–1549. doi:10.1016/S0191-8141(02)00186-4

Fisher, N. I., Lewis, T., and Embleton, B. J. J. (1987). *Statistical analysis of spherical data*. Cambridge, United Kingdom: Cambridge University Press, 329.

Fisher, R. (1953). Dispersion on a sphere. *Proc. Roy. Soc. Lond.* A217, 295–305. doi:10.1098/rspa.1953.0064

Fleming, J. A. (1946). Geomagnetic secular variations and surveys. *Proc. Phys. Soc.* 58, 213–247. doi:10.1088/0959-5309/58/3/301

Gaina, C., Müller, R. D., Royer, J. Y., Stock, J., Hardebeck, J., and Symonds, P. (1998). The tectonic history of the Tasman Sea: a puzzle with 13 pieces. *J. Geophys. Res.* 103, 12413–12433. doi:10.1029/98JB00386

Hansma, J., and Tohver, E. (2019). Paleomagnetism of Oligocene hot spot volcanics in central queensland, Australia. *J. Geophys. Res. Solid Earth.* 124, 6280–6296. doi:10.1029/2019JB017639

Heslop, D., and Roberts, A. P. (2016). Analyzing paleomagnetic data: to anchor or not to anchor?. *J. Geophys. Res. Solid Earth.* 121, 7742–7753. doi:10.1002/2016JB013387

Hill, M. J., Gratton, M. N., and Shaw, J. (2002). Palaeomagnetic investigation of Tertiary lava from Barrington Tops, NSW, Australia, using thermal and microwave techniques. *Earth Planet Sci. Lett.* 198, 245–256. doi:10.1016/S0012-821X(02)00534-4

Jackson, M. J., Borradaile, G. J., Hudleston, P., and Banerjee, S. K. (1993). Experimental deformation of synthetic magnetite-bearing calcite sandstones: effects on remanence, bulk magnetic properties, and magnetic anisotropy. *J. Geophys. Res.* 98, 383–401. doi:10.1029/92JB01028

Jelínek, V. (1981). Characterization of the magnetic fabric of rocks. *Tectonophysics* 79, T63–T67. doi:10.1016/0040-1951(81)90110-4

Kent, D. V., and Tauxe, L. (2005). Corrected late triassic latitudes for continents adjacent to the north atlantic. *Science* 307, 240–244. doi:10.1126/science.1105826

King, R. F. (1955). The remanent magnetism of artificially deposited sediments. *Monogr. Nat. R. Astron. Soc. Geophys. Suppl.* 7, 115–134. doi:10.1111/j.1365-246X.1955.tb06558.x

Kirscher, U., Bilardello, D., Mikolaichuk, A., and Bachtadse, V. (2014). Correcting for inclination shallowing of early Carboniferous sedimentary rocks from Kyrgyzstan--indication of stable subtropical position of the North Tianshan Zone in the mid-late Palaeozoic. *Geophys. J. Int.* 198, 1000–1015. doi:10.1093/gji/ggu177

Kirschvink, J. L. (1980). The least-squares line and plane and the analysis of palaeomagnetic data. *Geophys. J. Roy. Astron. Soc.* 62, 699–718. doi:10.1111/j.1365-246X.1980.tb02601.x

Kligfield, R., Lowrie, W., Hirt, A. M., and Siddans, A. W. B. (1983). Effect of progressive deformation on remanent magnetization of permian redbeds from the alpes maritimes (France). *Tectonophysics* 97, 59–85.

Krijgsman, W., and Tauxe, L. (2006). E/I corrected paleolatitudes for the sedimentary rocks of the Baja British Columbia hypothesis. *Earth Planet Sci. Lett.* 242, 205–216. doi:10.1016/j.epsl.2005.11.052

Lillie, A. R., and Brothers, R. N. (1969). Geology of New Caledonia. *N. Z. J. Geol. Geophys.* 13, 145–183.

Lowrie, W., Hirt, A. M., and Kligfield, R. (1986). Effects of tectonic deformation on the remanent magnetization of rocks. *Tectonics* 5, 713–722. doi:10.1029/TC005i005p00713

Lund, S. P. (2018). A new view of long-term geomagnetic field secular variation. *Front. Earth Sci.* 6, 1–13. doi:10.3389/feart.2018.00040

Maurizot, P., Bordenave, A., Cluzel, D., Collot, J., and Etienne, S. J. G. (2020a). "Late Cretaceous to Eocene cover: from rifting to convergence," in *New Caledonia–geology, geodynamic evolution, and mineral resources, memoirs of the geological society, 51*. Editor N. Mortimer (London, United Kingdom: Geological Society of London), 285.

Maurizot, P. (2011). First sedimentary record of the pre-obduction convergence in New Caledonia: formation of an Early Eocene accretionary complex in the north of Grande Terre and emplacement of the 'Montagnes Blanches' nappe. *Bull. la Soc. Geol. Fr.* 182, 479–491. doi:10.2113/gssgfbull.182.6.479

Maurizot, P., Robineau, B., Vendé-Leclerc, M., and Cluzel, D. (2020b). Chapter 1 Introduction to New Caledonia: geology, geodynamic evolution and mineral resources. *Geol. Soc. London, Mem.* 51, 1–12. doi:10.1144/m51-2019-33

McElhinny, M. W., and McFadden, P. L. (1997). Palaeosecular variation over the past 5 Myr based on a new generalized database. *Geophys. J. Int.* 131, 240–252. doi:10.1111/j.1365-246X.1997.tb01219.x

McFadden, P. L., and McElhinny, M. W. (1988). The combined analysis of remagnetization circles and direct observations in palaeomagnetism. *Earth Planet Sci. Lett.* 87, 161–172. https://doi.org/10.1016/0012-821X(88)90072-6.

Mortimer, N., Campbell, H. J., Tulloch, A. J., King, P. R., Stagpoole, V. M., Wood, R. A., et al. (2017). Zealandia: earth's hidden continent. *GSA Today.* 27, 1–8. doi:10.1130/GSATG321A.1

Muttoni, G., Dallanave, E., and Channell, J. E. T. (2013). The drift history of Adria and Africa from 280 Ma to Present, Jurassic true polar wander, and zonal climate control on Tethyan sedimentary facies. *Palaeogeogr. Palaeoclimatol. Palaeoecol.* 386, 415–435. doi:10.1016/j.palaeo.2013.06.011

Muttoni, G., and Kent, D. V. (2019). Jurassic monster polar shift confirmed by sequential paleopoles from Adria, promontory of Africa. *J. Geophys. Res. Solid Earth.* 124, 1–19. doi:10.1029/2018JB017199

Ogg, J. G. (2012). "The geomagnetic polarity time scale," in *The geologic time scale 2012*. Editors F. M. Gradstein, J. G. Ogg, M. D. Schmitz, and G. M. Ogg (Amsterdam, Netherlands: Elsevier), 85–113

Parés, J. M., van der Pluijm, B. A., and Dinarès-Turell, J. (1999). Evolution of magnetic fabrics during incipient deformation of mudrocks (Pyrenees, northern Spain). *Tectonophysics* 307, 1–14. doi:10.1016/S0040-1951(99)00115-8

Scheidegger, A. E. (1965). On the statistics of the orientation of bedding planes, grain axes, and similar sedimentological data. *U. S. Geol. Surv. Prof. Pap.* 525, 164–167.

Steinberger, B., and Torsvik, T. H. (2008). Absolute plate motions and true polar wander in the absence of hotspot tracks. *Nature* 452, 620–623. doi:10.1038/nature06824

Sutherland, R., Collot, J., Bache, F., Henrys, S., Barker, D., Browne, G. H., et al. (2017). Widespread compression associated with Eocene Tonga- Kermadec subduction initiation. *Geology* 45, 355–358. doi:10.1130/G38617.1

Sutherland, R., Dickens, G. R., Blum, P., Agnini, C., Alegret, L., Asatryan, G., et al. (2020). Continental scale of geographic change across Zealandia during Paleogene subduction zone initiation. *Geology* 48, 419–424. doi:10.1130/G47008.1

Sutherland, R., Dickens, G. R., Blum, P., Agnini, C., Alegret, L., Asatryan, G., et al. (2019). Tasman frontier subduction initiation and Paleogene climate. *Proc. Int. Ocean Discov. Progr.* 371, doi:10.14379/iodp.proc.371.101.2019

Tauxe, L. (2005). Inclination flattening and the geocentric axial dipole hypothesis. *Earth Planet Sci. Lett.* 233, 247–261. doi:10.1016/j.epsl.2005.01.027

Tauxe, L., and Kent, D. V. (2004). "A simplified statistical model for the geomagnetic field and the detection of shallow bias in paleomagnetic inclinations: was the ancient magnetic field dipolar?," in *Timescales of the paleomagnetic field, geophys. Monogr*. Editors J. E. T. Channell, D. V. Kent, W. Lowrie, and J. G. Meert (Washington, DC: American Geophysical Union), 101–115.

Tauxe, L., and Kent, D. V. (1984). Properties of a detrital remanence carried by haematite from study of modern river deposits and laboratory redeposition experiments. *Geophys. J. Roy. Astron. Soc.* 77, 543–561.

Tauxe, L., Kodama, K. P., and Kent, D. V. (2008). Testing corrections for paleomagnetic inclination error in sedimentary rocks: a comparative approach. *Phys. Earth Planet. In.* 169, 152–165. doi:10.1016/j.pepi.2008.05.006

Tauxe, L., Kylstra, N., and Constable, C. (1991). Bootstrap statistics for paleomagnetic data. *J. Geophys. Res.* 96, 11723–117490. doi:10.1029/91jb00572

Tauxe, L. (2010). *Paleomagnetic principle and practice*. New York, NY: Kluwer academic publishers, 301.

Tauxe, L., Shaar, R., Jonestrask, L., Swanson-Hysell, N. L., Minnett, R., Koppers, A. A. P., et al. (2016). PmagPy: software package for paleomagnetic data analysis and a bridge to the magnetics information consortium (MagIC) database. *Geochemi. Geophys. Geosys.* 17, 2450–2463. doi:10.1002/2015GC006307

Till, J. L., Jackson, M. J., and Moskowitz, B. M. (2010). Remanence stability and magnetic fabric development in synthetic shear zones deformed at 500°C. *Geochemistry, Geophys. Geosystems.* 11, Q12Z21. doi:10.1029/2010GC003320

Torsvik, T. H., Müller, R. D., Van der Voo, R., Steinberger, B., and Gaina, C. (2008). Global plate motion frames: toward a unified model. *Rev. Geophys.* 46, 1–54. doi:10.1029/2007RG000227.1

Torsvik, T. H., Van der Voo, R., Preeden, U., Mac Niocaill, C., Steinberger, B., Doubrovine, P. V., et al. (2012). Phanerozoic polar wander, palaeogeography and dynamics. *Earth Sci. Rev.* 114, 325–368. doi:10.1016/j.earscirev.2012.06.007

Van der Voo, R. (1993). *Paleomagnetism of the atlantic, tethys and iapetus oceans*. Cambridge, United Kingdom: Cambridge University Press, 411.

Veevers, J. J., and Li, Z. X. (1991). Review of seafloor spreading around Australia. II. Marine magnetic anomaly modelling. *Aust. J. Earth Sci.* 38, 391–408. doi:10.1080/08120099108727980

Wang, C., Gordon, R. G., Zhang, T., and Zheng, L. (2019). Observational test of the global moving hot spot reference frame. *Geophys. Res. Lett.* 46, 8031–8038. doi:10.1029/2019GL083663

Wellman, P., McElhinny, M. W., and McDougall, I. (1969). On the polar-wander path for Australia during the cenozoic. *Geophys. J. Roy. Astron. Soc.* 18, 371–395. doi:10.1111/j.1365-246X.1969.tb03575.x

Conflict of Interest: The authors declare that the research was conducted in the absence of any commercial or financial relationships that could be construed as a potential conflict of interest.

The reviewer (DK) declared a past co-authorship with one of the authors (UK) to the handling editor.

frontiers in Earth Science

ORIGINAL RESEARCH
published: 12 January 2021
doi: 10.3389/feart.2020.592659

Magnetic Properties of Plant Ashes and Their Influence on Magnetic Signatures of Fire in Soils

Jessica L. Till[1,2]*, *Bruce Moskowitz*[2] *and Simon W. Poulton*[3]

[1]Institute of Earth Sciences and Institute of Life and Environmental Sciences, University of Iceland, Reykjavik, Iceland, [2]Institute for Rock Magnetism, University of Minnesota, Minneapolis, MN, United States, [3]School of Earth and Environment, University of Leeds, Leeds, United Kingdom

Fires are an integral part of many terrestrial ecosystems and have a strong impact on soil properties. While reports of topsoil magnetic enhancement after fires vary widely, recent evidence suggests that plant ashes provide the most significant source of magnetic enhancement after burning. To investigate the magnetic properties of burnt plant material, samples of individual plant species from Iceland and Germany were cleaned and combusted at various temperatures prior to rock magnetic and geochemical characterization. Mass-normalized saturation magnetization values for burnt plant residues increase with the extent of burning in nearly all samples. However, when normalized to the loss on ignition, fewer than half of ash and charcoal samples display magnetic enhancement relative to intact plant material. Thus, while magnetic mineral concentrations generally increase, changes in the total amount of magnetic material are much more variable. Elemental analyses of Icelandic samples reveal that both total plant Fe and saturation magnetization are strongly correlated with Ti and Al, indicating that most of the Fe-bearing magnetic phases originate from inorganic material such as soil and atmospheric dust. Electron microscopy confirmed that inorganic particulate matter remains on most plant surfaces after cleaning. Plants with more textured leaf surfaces retain more dust, and ash from these samples tend to exhibit higher saturation magnetization and metal concentrations. Magnetic properties of plant ash therefore result from the thermal transformation of Fe in both organic compounds and inorganic particulate matter, which become concentrated on a mass basis when organic matter is combusted. These results indicate that the soil magnetic response to burning will vary among sites and regions as a function of 1) fire intensity, 2) the local composition of dust and soil particles on leaf surfaces, and 3) vegetation type and consequent differences in leaf morphologies.

Keywords: soils, rock magnetism, vegetation, soil magnetism, fire

OPEN ACCESS

Edited by:
Sara Satolli, G.d'Annunzio University of Chieti and Pescara, Italy

Reviewed by:
Aldo Winkler, Istituto Nazionale di Geofisica e Vulcanologia (INGV), Italy
Neli Jordanova, National Institute of Geophysics, Geodesy and Geography (BAS), Bulgaria
Eduard Petrovsky, Institute of Geophysics (ASCR), Czechia

***Correspondence:**
Jessica L. Till
jtill@hi.is

Specialty section:
This article was submitted to Geomagnetism and Paleomagnetism, a section of the journal Frontiers in Earth Science

Received: *07 August 2020*
Accepted: *04 November 2020*
Published: *12 January 2021*

Citation:
Till JL, Moskowitz B and Poulton SW (2021) Magnetic Properties of Plant Ashes and Their Influence on Magnetic Signatures of Fire in Soils. Front. Earth Sci. 8:592659. doi: 10.3389/feart.2020.592659

1 INTRODUCTION

Wildfires and anthropogenic burning affect many aspects of soils, including their magnetic properties. Wildfires have long been suggested as a possible source of topsoil magnetic enhancement (e.g., Le Borgne, 1960; Kletetschka and Banerjee, 1995) and many examples of increased magnetic susceptibility following fires have been observed (Clement et al., 2011;

Jordanova et al., 2019a). Because magnetic enhancement in soils relative to unweathered parent material often correlates closely with various environmental factors (Maher et al., 2003), understanding the impact of fires on soil magnetism is important for accurate interpretation of magnetic paleoenvironmental proxies.

Fire-induced magnetic enhancement may occur through thermal transformation of weakly magnetic ferric oxide and oxyhydroxide soil minerals such as ferrihydrite, lepidocrocite, goethite, and hematite (Hanesch et al., 2006; Till et al., 2014; Jiang et al., 2018; Till and Nowaczyk, 2018) to strongly magnetic phases such as magnetite or maghemite. Such reactions likely contribute to the enhanced magnetic susceptibility observed in some burnt soils compared with unburnt soils (Gedye et al., 2000; Blake et al., 2006), particularly in forest fires and similar high-intensity burning events. By contrast, a study by Roman et al. (2013) on grassland fire temperatures concluded that fire is an unlikely source of significant magnetic enhancement in prairie soils based on the relatively low temperatures experienced by the soil compared with temperatures necessary to produce mineralogical changes during laboratory heating.

Another potential source of pyrogenic magnetic minerals is the plant ash itself. Several archeological studies have noted that ashes from wood and other plant-based fuel sources often contain high concentrations of magnetic minerals relative to soils (Peters et al., 2001; Peters and Batt, 2002; Church et al., 2007), a feature that is sometimes exploited for archaeological surveying (McClean and Kean, 1993). One of the few investigations of plant ash magnetic properties was conducted by Lu et al. (2000), who determined that the magnetic susceptibility of plant ash exceeds that of many well-developed soils. They further concluded that only about half of the soil magnetic enhancement in natural burn sites could be attributed to mineralogical changes due to heating of the soil. Petrovský et al. (2018) studied magnetic susceptibility of forest soils that had been fertilized by wood ash, noting that the ash contained significant concentrations of superparamagnetic ferromagnetic particles that persisted in the soil following wood ash addition. Similarly, Jordanova et al. (2018) argued that plant ashes were the source of enhanced topsoil magnetic susceptibility following forest fires, which was typically observed in the uppermost few cm.

However, the source of magnetism in plant ash has never been investigated in detail and only limited magnetic data has been reported for ash material. This study presents a detailed analysis of changes in magnetic properties that accompany burning of plant materials. Using burnt residues from known species, we synthesize rock magnetic properties with geochemical data and microscopy observations to identify the likely origin of magnetic material in plant-derived ash and char deposits to better understand how soil and sediment magnetic properties reflect vegetation burning.

2 METHODS

2.1 Sample Collection and Preparation

Recently fallen litter and senescent plant material was collected from over 20 plant genera (see **Table 1**) in the Reykjavik Botanical Garden in autumn of 2017 and 2018. Depending on the plant type, materials collected included dead leaves or needles, shoots, cones, stems and woody litter, flowers, and seeds. Green leaves were also collected from selected plant types to investigate potential seasonal effects on the composition of plant ash. *Lupinus nootkatensis* plants (leaves, flowers, seeds, stems) were sampled in summer and autumn of 2017 from the Borgarfjordir region in western Iceland. Additional cleaned and milled plant samples were prepared and provided by the Leibniz Centre for Agricultural Landscape Research (ZALF), Germany. Specimen details and sampling locations are given in **Table 1**.

Most Icelandic plant samples were cleaned shortly after collection by agitating vigorously in a solution of 0.1 (v/v) Triton X-100 biological detergent followed by thoroughly rinsing in water. Cleaned samples were then oven-dried at 70°C for 24–48 h and gently crushed. Subsets from several selected samples were dried directly after collection without cleaning to determine the effect of washing on magnetic properties. 2–4 g of dried plant material were combusted in ceramic crucibles in a muffle furnace at 200 and 300°C for 6 h to produce char and at 550°C for 4 h to produce ash. Sample and crucible masses were measured immediately before and after heating to determine loss-on-ignition values. Multiple batches of ash were produced for most plant samples, which were pooled. For these samples, the LOI represents an average across ash specimens. The percent of mass remaining after combustion is given for each sample in **Supplementary Table S1**.

Small amounts (30–100 mg) of ash, char, or intact plant material were ground to powder and firmly packed into gelatin capsules with quartz wool for hysteresis and low-temperature magnetic measurements.

2.2 Magnetic Measurements and Sample Characterization

Thermomagnetic measurements were made on selected ash and char samples to identify characteristic Curie temperatures (T_C) of the main magnetic phases. Susceptibility was measured from room temperature up to either 650 or 700°C and again on cooling to 50°C on a low-field AC susceptometer (Kappabridge KLY-3) in flowing Ar gas. A small number of thermomagnetic curves were run in air, and these generally exhibited more irreversible behavior than measurements in Ar, indicating that the burnt samples contain phases sensitive to oxygen. Curie temperatures were determined by plotting the derivative of each susceptibility curve on heating, where the temperature at the minimum in the derivative curve was taken as T_C, as discussed in Petrovský and Kapička (2006); Fabian et al. (2013).

Low temperature magnetization and AC susceptibility (χ) were obtained with a superconducting quantum interference device (SQUID) magnetometer (Quantum Design, San Diego, CA, United states – MPMS). Low-temperature remanence properties can reveal diagnostic phase transitions in certain magnetic minerals as well as providing information about magnetic domain states, and hence, grain size. Magnetization measurements follow the FC-ZFC-LTSIRM-RTSIRM LTD

TABLE 1 | List of plant species and sampling details.

Scientific name	Sampling location	Plant parts collected
Alchemilla alpina	Reykavik Botanical Garden, Iceland	Dead leaves and flowers
Athyrium felix-femina	Reykavik Botanical Garden, Iceland	Green and dead leaves and stems
Avenula pubescens	Reykavik Botanical Garden, Iceland	Dead leaves and seeds
Betula pubescens	Reykavik Botanical Garden, Iceland	Leaf litter
Carex nigra	Reykavik Botanical Garden, Iceland	Dead leaves
Deschampsia cespitosa	Reykavik Botanical Garden, Iceland	Dead leaves and seeds
Equisetum sylvaticum	Reykavik Botanical Garden, Iceland	Dead leaves and stems
Juniperis communis	Reykavik Botanical Garden, Iceland	Needles and woody litter
Leymus arenarius	Reykavik Botanical Garden, Iceland	Green and dead leaves and seeds
Picea sitchensis	Reykavik Botanical Garden, Iceland	Needles, cones, and woody litter
Pinus contorta	Reykavik Botanical Garden, Iceland	Needles, cones, and woody litter
Populus trichocarpa	Reykavik Botanical Garden, Iceland	Green leaves and leaf and woody litter
Ranunculus repens	Reykavik Botanical Garden, Iceland	Green and dead leaves
Rumex longifolius	Reykavik Botanical Garden, Iceland	Seeds and stems
Salix caprea	Reykavik Botanical Garden, Iceland	Leaf litter
Sorbus decora	Reykavik Botanical Garden, Iceland	Leaf litter
Trifolium pratense	Reykavik Botanical Garden, Iceland	Green and dead leaves, stems and flowers
Lupinus nootkatensis	Fossatún valley, western Iceland	Fresh and dead leaves, flowers, seeds, and stems
Calamagrostis epigejos	Russendamm, Lower Odra Valley, Germany	Green leaves
Zea mays	Dedelow, Germany	Stover
Fagus sylvatica	Beerenbusch, Germany	Leaf litter
Festuca arundinacea	Paulinenaue, Germany	Green leaves
Cirsium arvense	Paulinenaue, Germany	Green leaves and flowers
Phalaris arundinacea	Criewen, Lower Odra Valley, Germany	Green leaves

measurement protocol from Bilardello and Jackson (2013). Low-temperature saturation isothermal remanent magnetization (LTSIRM) was acquired as a field-cooled (FC) and zero-field-cooled (ZFC) magnetization by cooling to 10 K in either a 2.5 T field or in zero-field. At 10 K, a 2.5 T field was applied and then reduced to zero (<1 μT) and magnetization was measured during warming to 300 K in 5 K steps. Following the FC-ZFC measurements, a 2.5 T field was applied and then reduced to zero at 300 K imparting a remanent magnetization (RTSIRM). The RTSIRM curve was measured during cooling to 10 K and subsequent warming back to 300 K at 5 K increments. In-phase (χ') and quadrature (χ'') magnetic susceptibility was measured in an AC field with a peak amplitude of 0.3 mT at 1, 10, and 100 Hz on warming from 10 to 300 K. To estimate the presence of ultrafine-grained superparamagnetic particles, frequency dependence was calculated from the room-temperature susceptibility values as: $X_{fd} = 100(X_{lf}–X_{hf})/X_{lf}$, where X_{lf} and X_{hf} are the susceptibilities at low and high frequencies (1 and 100 Hz), respectively.

Hysteresis loops at room temperature were measured up to a maximum field of 1 T on a Princeton Corporation Measurements vibrating sample magnetometer at the Institute of Rock Magnetism at the University of Minnesota (United States) to constrain the domain state and grain size distributions of magnetic remanence carriers in the specimens. Averaging times ranged from 100 ms for ash to 500 ms for unburnt plant samples. Backfield remanence (DC demagnetization) curves were also measured for most samples up to −500 mT after saturation in a 1 T field. Saturation magnetization (M_S), saturation remanent magnetization (M_R), coercivity (H_c), and high-field susceptibility (X_{HF}) values were determined from hysteresis loops after subtracting the high-field slope over the interval of 0.7–1.0 T using the nonlinear approach-to-saturation fitting method of Jackson and Solheid (2010). All hysteresis parameters in figures and tables represent slope-corrected data. The M_S values in **Supplementary Table S1** are normalized by the specimen mass, which is a good indicator of ferromagnetic mineral concentrations in the sample. However, it is also useful to view M_S values when normalized by the initial plant mass before burning because the mass of the system is not constant during combustion. This allows us to see how the total amount of ferromagnetic material in the system changes during burning.

Selected plant samples were mounted on carbon adhesive discs and carbon-coated for scanning electron microscopy characterization using a Hitachi tabletop SEM with a LaB^6 filament equipped with an energy dispersive X-ray detector. Magnetic extracts from representative Icelandic ash samples were also prepared and imaged in the same way.

Total element compositions of Icelandic plant ash samples were analyzed via ICP-OES after extraction with HNO^3-HF-$HClO^4$-H^3BO^3, following the procedure outlined in Xiong et al. (2019). In brief, samples were ashed at 550°C and then dissolved in HNO^3-HF-$HClO^4$. After evaporation to dryness, H^3BO^3 was added to the samples and evaporated to dryness to ensure re-dissolution of aluminum salts. Finally, samples were re-dissolved in warm 6N HCl. No residue remained after this procedure. We used an international sediment standard (PACS-2) to test the procedure to ensure full extraction of mineral phases. Replicate extractions of this standard gave recoveries of >95% for all elements of interest, with RSDs of <2%.

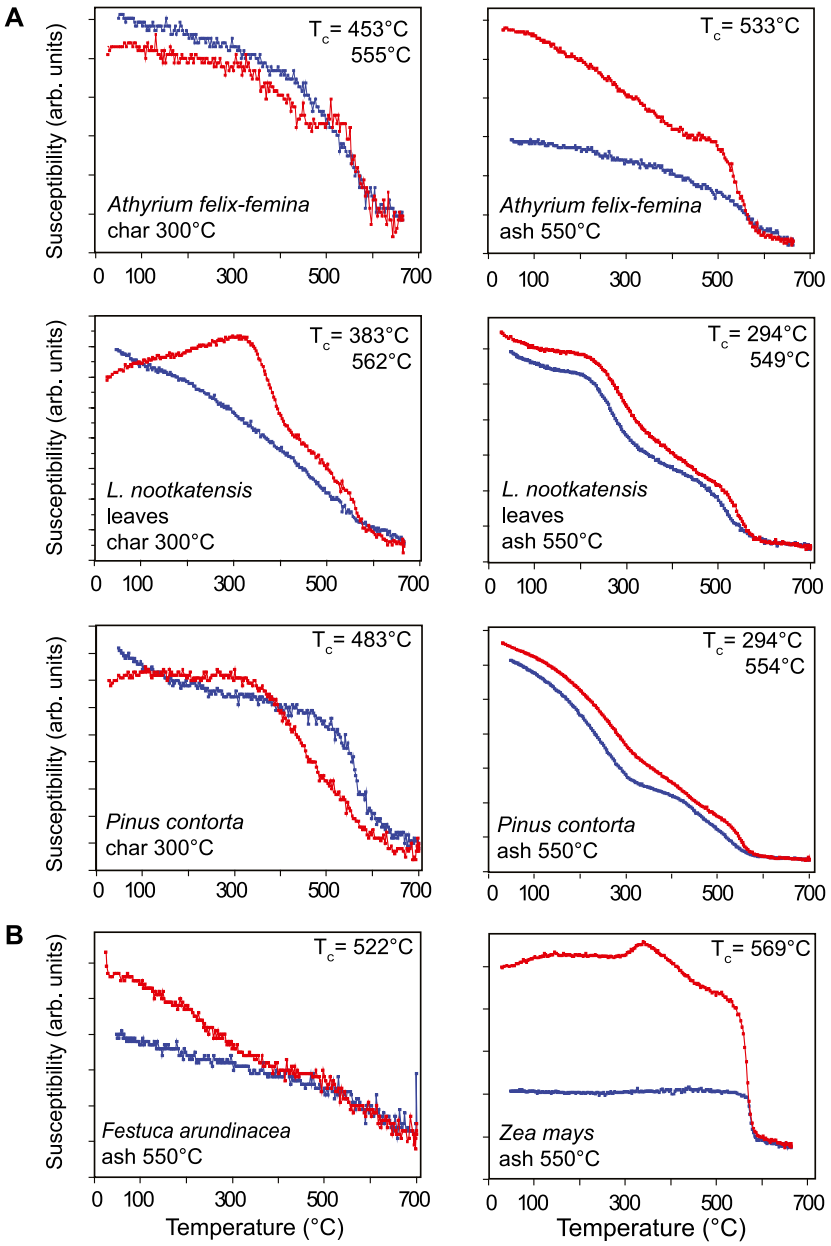

FIGURE 1 | Example thermomagnetic curves of susceptibility measured on warming (red) and cooling (blue) for selected ash and char from **(A)** Icelandic plant litter and **(B)** German plant samples.

3 RESULTS

3.1 Thermomagnetic Behavior

Thermomagnetic curves for plant char and ash from Icelandic samples nearly all exhibit a drop in bulk susceptibility between 560 and 580°C, consistent with the Curie temperature (T_C) of magnetite (**Figure 1A**). Several Icelandic samples also indicate the presence of a phase with a T_C around 300°C. In general, the shape of the χ vs. T curves are different for char and ash produced from the same plant sample, suggesting that heating to the higher temperatures used for ashing produces magnetic phases with somewhat different compositions than those resulting from lower temperature treatments. By contrast, ash from the German plant samples display continuous decreases in susceptibility with heating and do not exhibit distinct disordering temperatures, except for *Zea mays*, which has a pronounced Curie temperature around 580°C (**Figure 1B**). No clear evidence of hematite or maghemite was observed in either high- or low-temperature magnetic data.

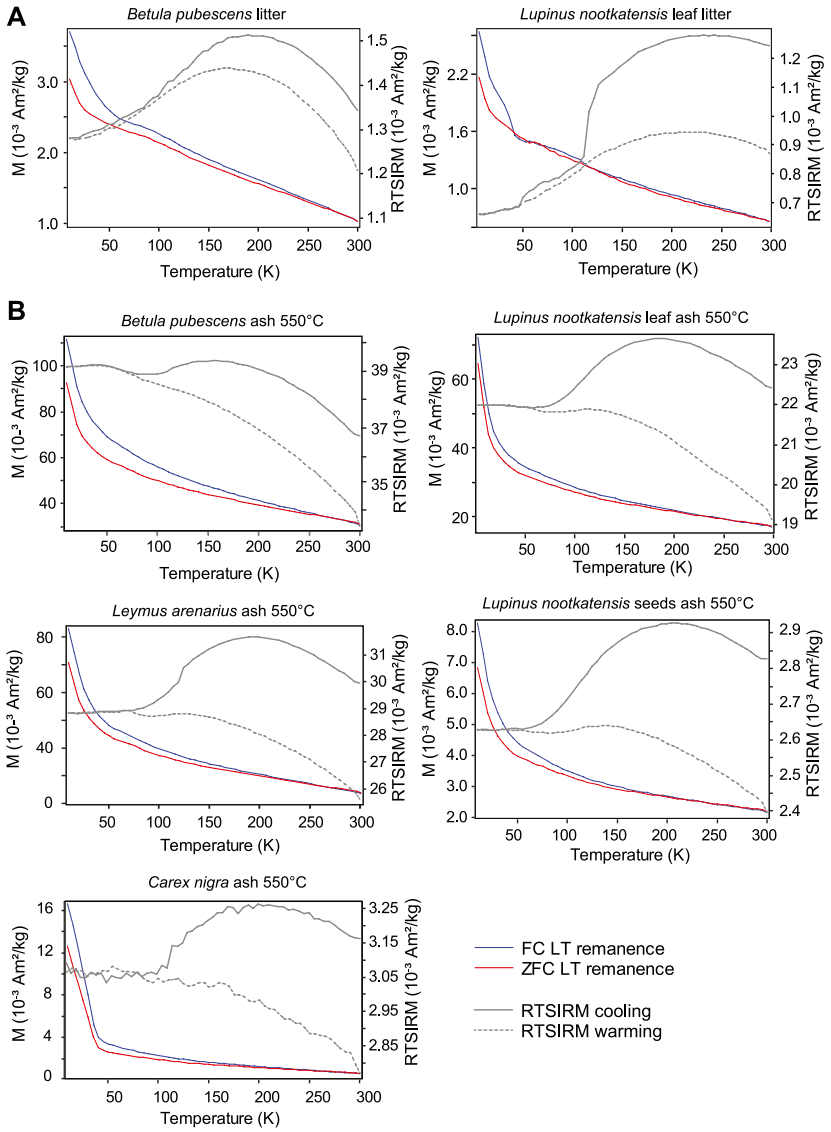

FIGURE 2 | Low-temperature remanence measurements after field-cooling (FC) and zero-field cooling (ZFC) along with cooling and warming curves of room-temperature remanence (right-hand scales) for **(A)** unheated Icelandic plant litter and **(B)** ashed Icelandic litter samples.

3.2 Low-Temperature Magnetic Properties

Low temperature magnetization curves (FC, ZFC, and RTSIRM) were measured for several sets of unburned, char and ash samples. In general, the FC and ZFC curves for Icelandic and German samples showed a steady decay of remanence on warming from 15 to 300 K, indicative of progressive unblocking of superparamagnetic nanoparticles. There were weak indications of the Verwey transition (T ~ 100–120 K) for magnetite (**Figure 2A**) for the unburnt forms but no indication after combustion at 550°C. The exception was *Zea mays* (Germany) after charring at 300°C which had a noticeable expression of the Verwey transition on warming (**Figure 3A**). For two other samples from Iceland (*Betula pubsescens* and *Lupinus nootkatensis*), the unburned samples also indicated a magnetic transition near 40–50 K, but this disappeared once the samples were reduced to ash. However, the presence of magnetite in all samples (unburned, char, and ash) was confirmed from RTSIRM measurements on cooling from 300 K, which showed the characteristic magnetic signature for the Verwey transition (**Figure 2B**). In addition, hump-shaped remanence curves observed on cooling suggested that some of the magnetite was likely partially oxidized (Özdemir and Dunlop, 2010). For all samples measured there was no indication of the Morin transition (T ~ 260 K) associated with hematite in any the FC, ZFC, or RTSIRM curves. Several of the measurements made on cooling after imparting a RTSIRM exhibit sharp drops around 150 K. These are considered to be artifacts that occurred due to shifting of the capsule in the sample holder. Data in **Figure 2** have been adjusted to correct for this artifact, while the raw measurements are included in the **Supplementary Table S3**.

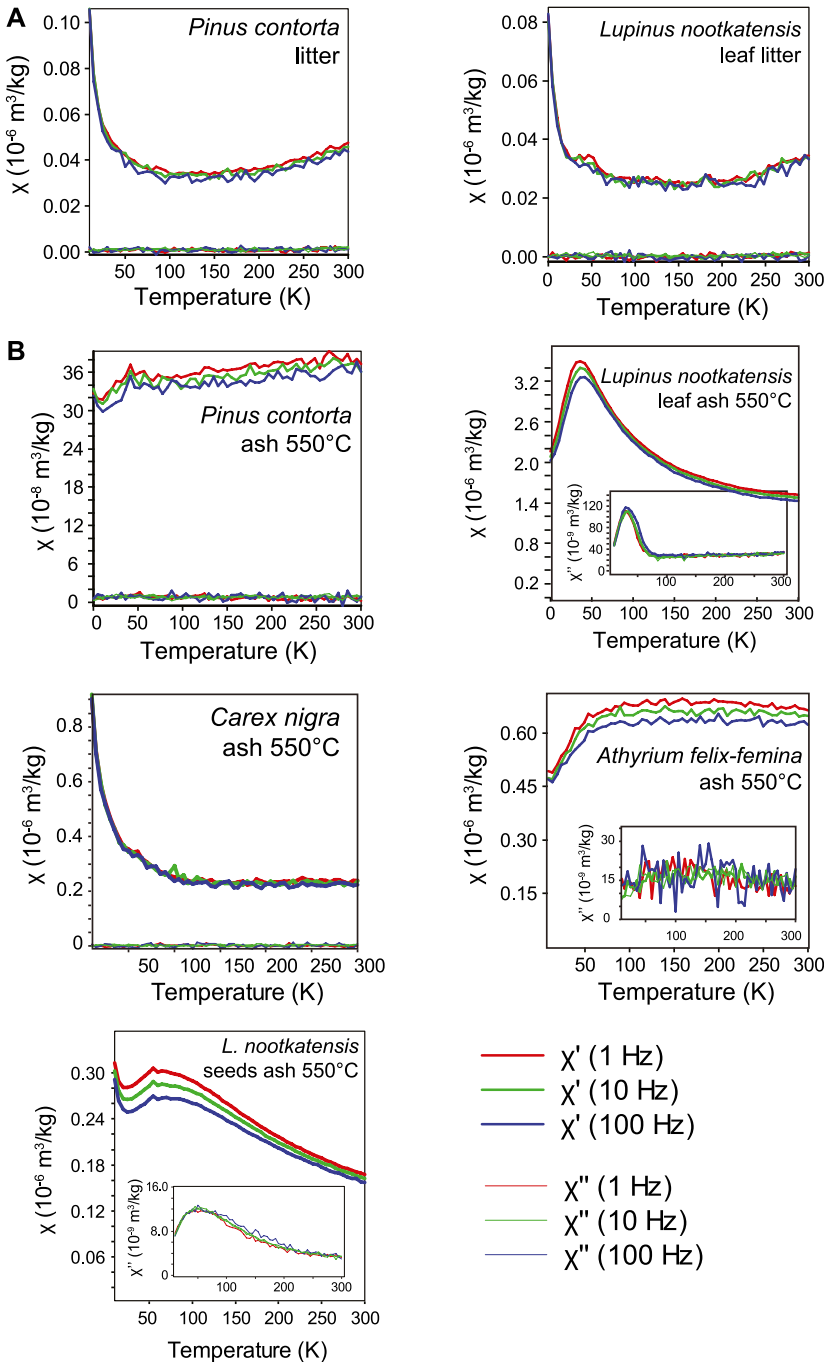

FIGURE 3 | Low-temperature measurements of **(A)** FC-ZFC and RTSIRM remanence and **(B)** frequency-dependent susceptibility for German char and ash samples.

The temperature and frequency dependence of AC susceptibility (χ', χ'') for selected samples show a combination of paramagnetic and ferrimagnetic behavior (**Figures 3** and **4**). Unburnt samples displayed paramagnetic behavior ($\chi' \propto 1/T$) at the lowest measurement temperatures with a rapid decrease in χ' with increasing temperature until around 150–200 K, when susceptibility begins to level off or increase slightly due to the ferrimagnetic contribution from magnetite. In this temperature range, some frequency dependence of susceptibility was observed, but the out-of-phase susceptibility was near zero with no temperature-dependent behavior. There was no clear indication in the χ-T curves of magnetite.

After combustion and transformation to char or ash, significant changes in susceptibility behavior occurred, with

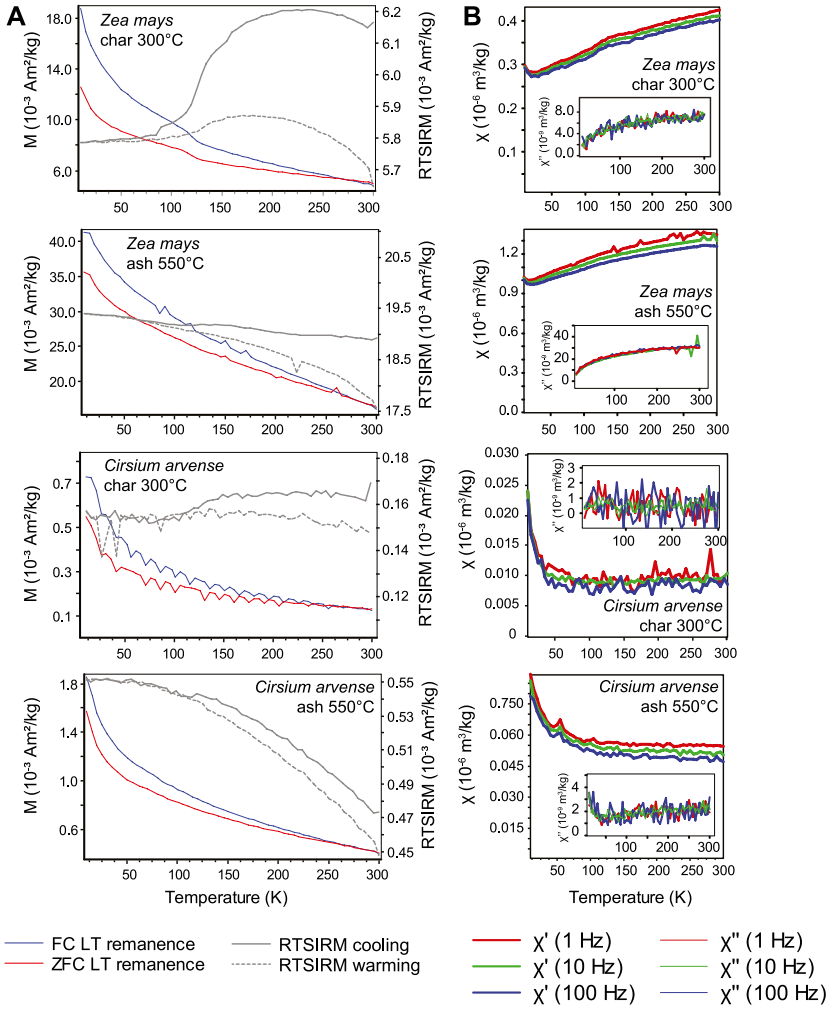

FIGURE 4 | Low-temperature frequency-dependent susceptibility measurements for **(A)** Icelandic litter and **(B)** Icelandic ash samples. Out-of-phase susceptibility measurements are shown in inset plots.

the exception being the ash from *Carex nigra* which displayed pure paramagnetic behavior. The most noticeable changes occurred for ash from *Lupinus nootkatensis* and *Betula pubsescens*, where paramagnetic behavior is replaced by frequency dependent susceptibility and thermal relaxation peaks at T ~40–50 K in both χ' and χ'', characteristic of superparamagnetism in nanoparticles. In contrast to relaxation peaks, ash samples from *Pinus contorta* and *Athyrium felix-femina* displayed an increase in susceptibility from 15 to 50 K followed by gradual increase in χ'(T) to 300 K. For both *Pinus contorta* and *Athyrium felix-femina*, χ'' was near zero and showed no temperature-dependent behavior.

The char and ash samples of *Zea mays* show similar χ-T behavior with a small paramagnetic tail below 20 K followed by steady increase in susceptibility to 300 K. The Verwey transition is seen in the sample charred at 300°C but is absent in the ash sample, similar to the FC-ZFC results. There is also both frequency dependence and a monotonically increasing temperature dependent χ''(T) over the entire temperature range. Unlike *Zea mays*, χ-T curves for char and ash samples of *Cirsium arvense* displayed stronger paramagnetic behavior. Frequency-dependent behavior and temperature-dependent χ'' was seen only for the ash sample.

Low-field room-temperature susceptibility values obtained from the MPMS measurements indicate that bulk susceptibilities for fresh litter and 200°C char are in the range 7.0×10^{-8}–1.3×10^{-7} m^3/kg, while the 300°C char in the range 2.3×10^{-8}–2.3×10^{-6} m^3/kg, and values for ash are in the range 7.9×10^{-8}–2.8×10^{-6} m^3/kg. Frequency dependence of susceptibility is generally higher than than in char or unburnt litter samples, reaching 7.1% in ash from Icelandic plants and as much as nearly 12% in the German sample *Cirsium arvense*. The bulk susceptibilities for our ash samples are very similar to the range values reported for wood ash and cigarette ashes by Jordanova et al. (2006). They also reported X_{fd} values ranging from 5.0 to 8.5%, which is consistent with the range of values observed in this study. The highest susceptibilities in our Icelandic samples are lower than the average value of

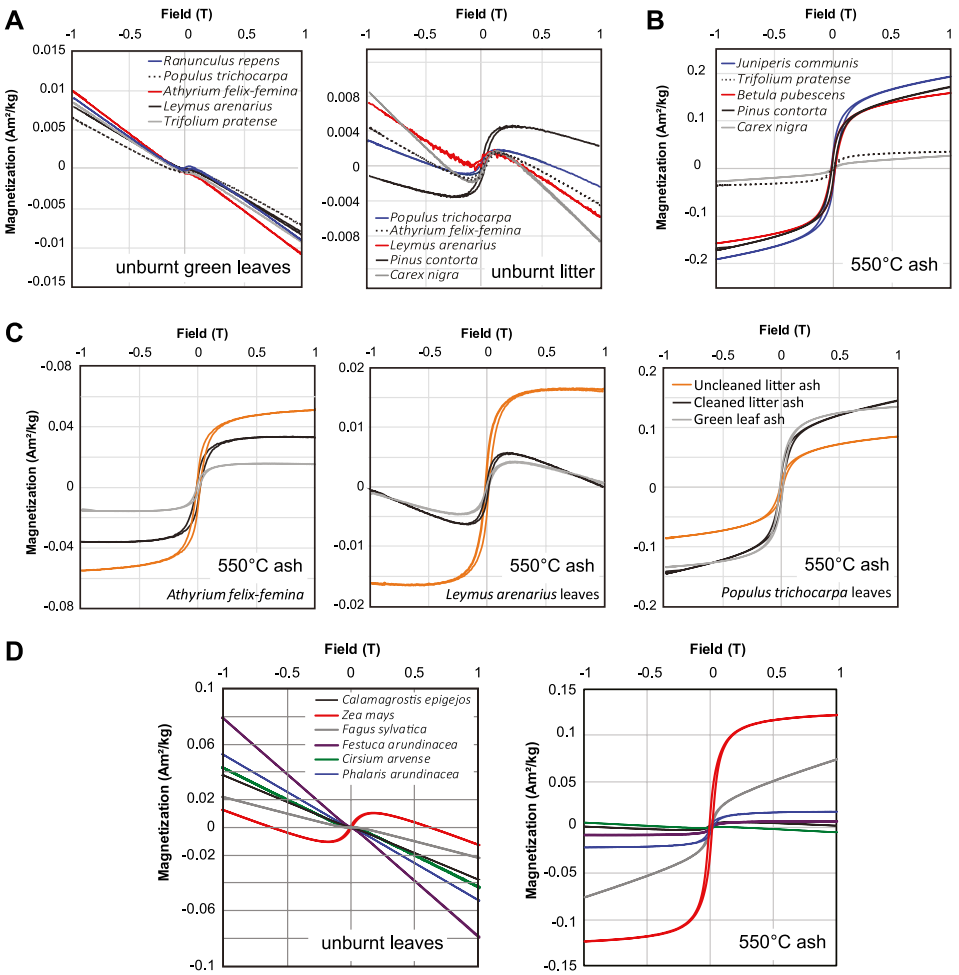

FIGURE 5 | Example hysteresis loops for **(A)** unburnt Icelandic plant samples, **(B,C)** ashed Icelandic plants, and **(D)** unburnt and ashed German plant samples.

5.3×10^{-6} m^3/kg reported for ash from C4 plants from China by Lu et al. (2000). It is also worth noting that the average susceptibility of ash from C3 plants studied by Lu et al. (2000) was significantly lower at 1.2×10^{-6} m^3/kg.

3.3 Hysteresis Properties

Hysteresis loops of unburned plant samples from both Iceland and Germany are dominantly characterized by diamagnetic high-field slopes with a superimposed ferromagnetic signal of variable strength (**Figures 5A,D**). Green leaves have notably smaller ferromagnetic components compared with dead leaves and plant litter samples. The diamagnetic background becomes reduced after burning at 300 and 550°C, with most ash samples having a dominantly ferromagnetic character and a small paramagnetic high-field slope. Several samples charred at 200°C had no discernible ferromagnetic component or the signal-to-noize ratios were not sufficient to confidently resolve hysteresis parameters, even in plants for which unburnt litter samples exhibited measurable hysteresis.

Ash from litter samples that were not cleaned before burning have consistently higher M_s compared to ash from cleaned litter (**Figure 5C**), however, the hysteresis loop shapes are nearly identical. Hysteresis parameters of ash and char from cleaned samples cannot be distinguished from uncleaned plant samples in plots of squareness (M_R/M_s) vs. H_C (**Figure 6A**). However, char and ash from green Icelandic plants and German plant samples have overall lower coercivities and M_R/M_s ratios. The majority of measured plant samples fall in between the compositional trends proposed by Wang and Van der Voo (2004) for Ti-free magnetite (TM0) and TM60 titanomagnetite (**Figure 6A**), although several samples plot close to the magnetite trend. Icelandic samples charred at 300°C exhibit somewhat lower coercivities than unburnt samples or ash and char from other temperatures (**Supplementary Table S1**), but otherwise M_R/M_s and H_C do not exhibit a clear dependence on burning temperature suggestive of a systematic change in domain state.

Saturation magnetization values of ash and char vary significantly among plant types for all burning temperatures. A comparison of mass-normalized M_s (based on the mass of the burnt samples) as a function of combustion temperature is shown in **Figure 7** for both Icelandic and German samples relative to the unburnt plants. After charring at 200°C, M_s either decreases or

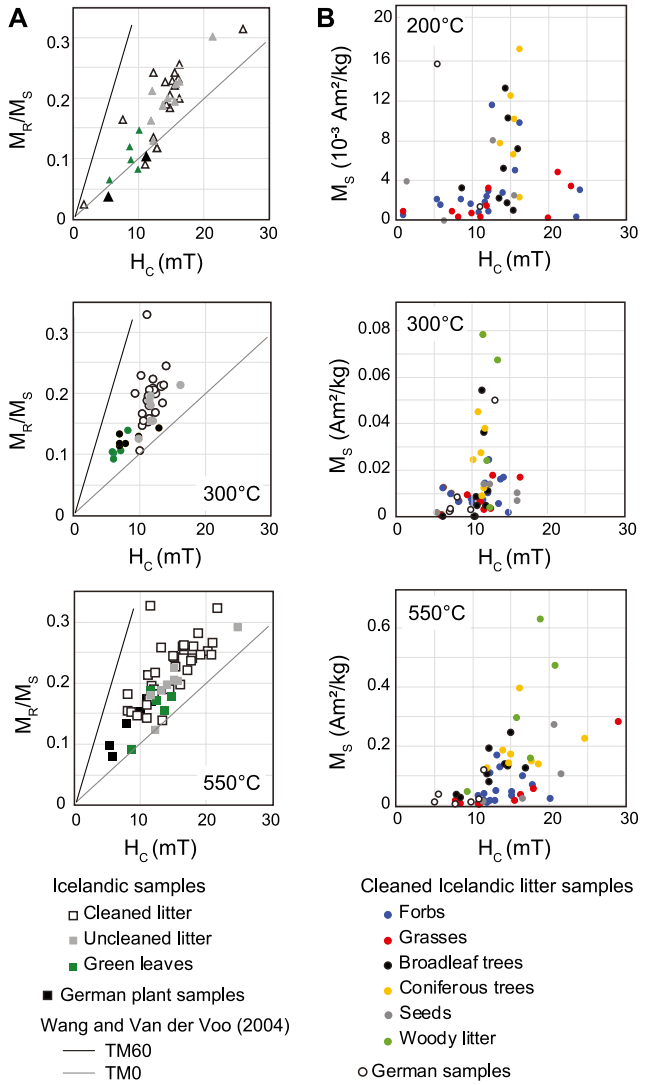

FIGURE 6 | (A) Hysteresis squareness (M_R/M_s vs. H_c plots for ash and char from different subsets of plant samples along with compositional trends proposed by Wang and Van der Voo (2004). **(B)** Variations in saturation magnetization vs. coercivity by plant type for ash and char from cleaned Icelandic litter samples.

remains relatively unchanged for most samples, while the majority of samples burnt at 300 and 550°C exhibit elevated M_s (**Figure 7A**). Ash from Icelandic litter samples exhibit M_s values that are higher than those of the unburnt litter by a factor ranging from approximately 2–35. By contrast, ash from green Icelandic samples are enhanced by as much as a factor of 160, while ash from German samples display more moderate enhancements, up to a factor of 16 (**Figure 7D**). The pattern of changes in M_s with burning temperature for uncleaned Iceland litter samples are generally very similar to those of the cleaned litter samples (**Figure 7C**).

Average loss-on-ignition values after burning at 200°, 300°, and 550°C were 26%, 78%, and 93%, respectively, for Icelandic litter and German samples. Green leaf samples from Iceland had LOI values of 39%, 68% and 91%, respectively (**Supplementary Table S1**). To examine the relationship between LOI and magnetic properties of ash and char, hysteresis parameters are plotted as a function of mass remaining after burning in **Figure 8**. To account for the effect of mass loss during burning on the mass-normalized M_s values, we also calculated saturation magnetization values using the initial mass of plant material prior to burning based on the measured LOI values for each sample. When these values are plotted relative to that of the unburnt plant material, the changes in M_s as a function of burning temperature are much more variable. Approximately half of the samples exhibit decreases in M_s after ashing at 550°C while M_s increases by up to a factor of 2.3 in the remaining samples. However, ash from certain green Icelandic plant samples exhibit sharply enhanced M_s even after accounting for the LOI (**Figure 7B**). M_s is similarly lower in char and ash for most German plant samples when normalized by the initial plant mass.

3.4 Composition and Surface Features of Plant Material

Total concentrations of Fe, Ti and Al determined from complete digestion of ash from cleaned Icelandic plant litter samples are shown in **Figure 9A** and listed in **Supplementary Table S2**, along with other selected metal concentrations. Among the plant species sampled, Fe and Ti contents vary by approximately 20-fold, with Fe concentrations in ash ranging from 3.9 to 71.5 mg/g. Total Fe is strongly correlated with both Ti and Al but is poorly correlated with micronutrients such as Mg, Mn, Cu, and Zn (see Supplemental Data). Saturation magnetization values in ash samples (burnt at 550°C) also exhibit a slightly weaker but clear positive correlation with Ti content (**Figure 9B**). Ti (and to a lesser extent Al) in plant tissues is commonly considered an indicator of soil and dust inclusion in plants, as Ti is not present at appreciable levels in most biological materials but is abundant in soils and atmospheric dust, as well as in particulate matter from pollution sources (Cherney and Robinson, 1983; Cary et al., 1986; Cook et al., 2009). The close correlations between Fe and both Ti and Al in the Icelandic ash samples suggest that a significant proportion of the Fe is from inorganic sources.

Jóhannesson et al. (2007) reported Fe concentrations in a range of 57–1,379 ppm in grasses and other forage plants from nearly 50 Icelandic farms. Similarly, Eiríksson et al. (2010) found an even wider variation of Fe contents in Iceland forage, from 100 to 5,000 ppm. These previous analyses are consistent with our determined elemental compositions in ash, which correspond to Fe contents in dry plant matter in the range 221–4,531 ppm. In an overview of chemical compositions of biomass, Vassilev et al. (2010) gives mean values of Fe, Ti, and Al contents in various forms of plant material that fall in the middle of the values observed for our Icelandic ash samples (**Figure 9A**), and with very similar elemental ratios to those reported here. Vassilev et al. (2010) further notes that strong correlations exist among Fe, Ti, Si, Na, and Al among various forms of biomass, and that significant Al concentrations are usually regarded as an indicator of soil inclusion.

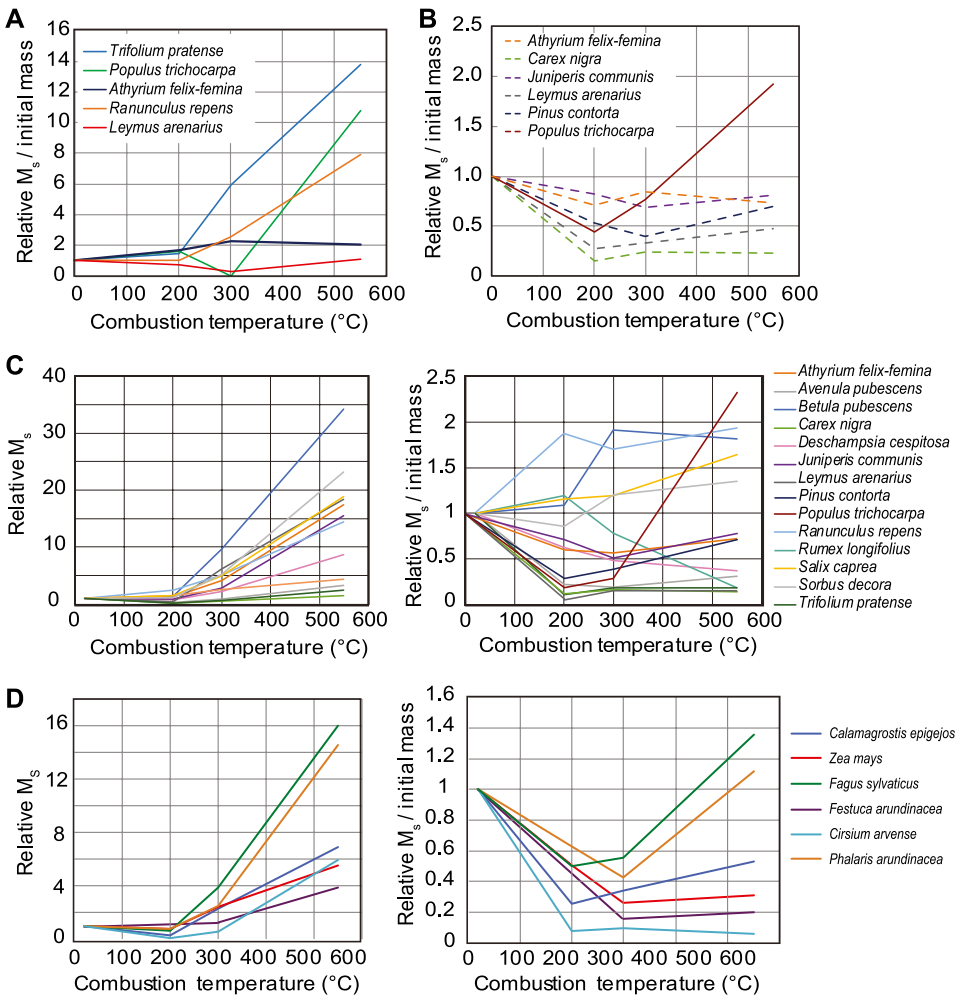

FIGURE 7 | Changes in saturation magnetization values in ash and char with burning relative to unburnt material for **(A)** green leaves from Icelandic plants, **(B)** uncleaned Icelandic plant litter, **(C)** cleaned Icelandic plant litter, and **(D)** German plant samples. Lefthand plots in C and D show M_s normalized by ash/char sample mass after burning while the righthand plots, as well as those in A and B, indicate relative M_s normalized by the initial plant mass prior to burning.

Examination of cleaned plant samples with SEM imaging prior to burning revealed variable quantities of particulate matter on plant surfaces (**Figure 10A**). These particles appear as bright phases in backscattered electron imaging mode, and are interpreted to be fine inorganic dust and soil material that remain entrained in the leaf surfaces after cleaning. Based on these images, we inferred a qualitative relationship between leaf texture and particulate matter content. For example, large amounts of particulate matter are embedded in the thick, waxy cuticle on needles of conifer species such as Sitka spruce (*Picea sitchensis*, **Figure 10A**). Similarly, the fine leaf hairs of downy birch (*Betula pubescens*) are also effective in trapping particles on the leaf surface. By contrast, black sedge (*Carex nigra*) has a relatively smooth leaf surface with little inorganic material. Particulate matter was also observed on the surface of German plant samples, especially *Zea mays*. Energy dispersive spectroscopy (EDS) maps of Fe and Ti in magnetic extracts from selected Icelandic ash samples are shown in **Figure 10B**. The majority of Fe-rich grains in these samples are associated with Ti, and these are assumed to be derived from lithogenic titanomagnetite in the basaltic soil and dust parent materials.

4 DISCUSSION

4.1 Possible Domain States of Magnetic Carriers in Ash

Most previous studies investigating magnetic properties of pyrogenic magnetic phases have found evidence for predominantly fine-grained magnetite of SD or SP-size. Kent et al. (2017) interpreted a unit enriched in isolated SD magnetite particles in continental shelf deposits as representing increased wildfire occurrence on land. In a simulated archeological burn, Carrancho and Villalaín (2011) observed the formation of SD magnetite across the heated surface of an experimental hearth. Similarly, Oldfield and Crowther (2007) found that pyrogenic

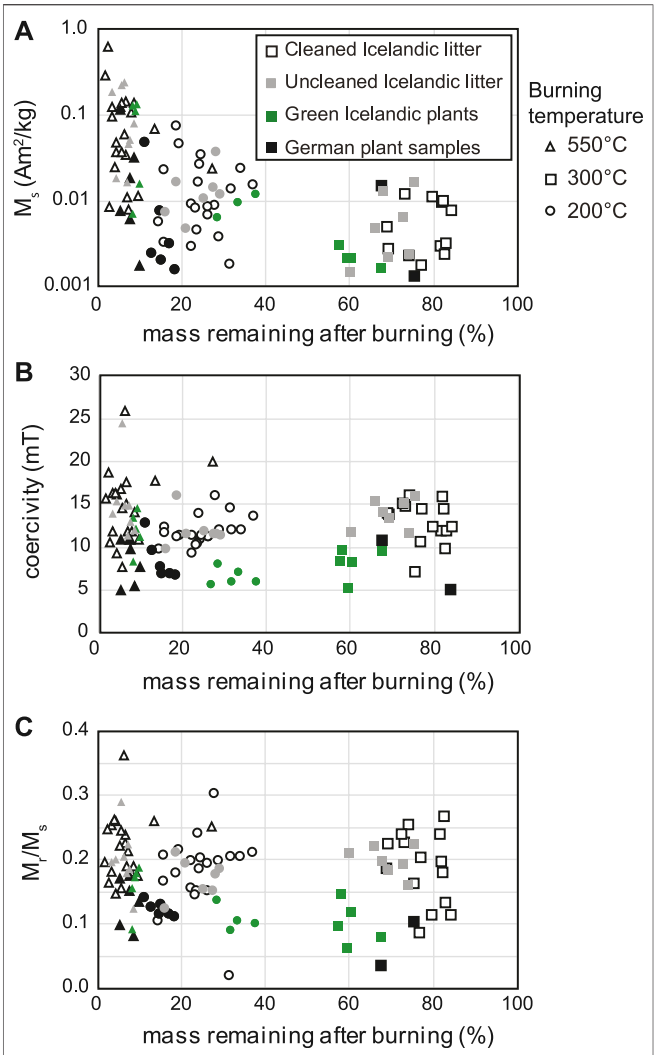

FIGURE 8 | Hysteresis parameters as a function of % mass remaining after burning. **(A)** Saturation magnetization, **(B)** coercivity, and **(C)** (M_R/M_s) of ash and char from different subsets of plant samples. Note that the vertical axis in A is plotted on a logarithmic scale.

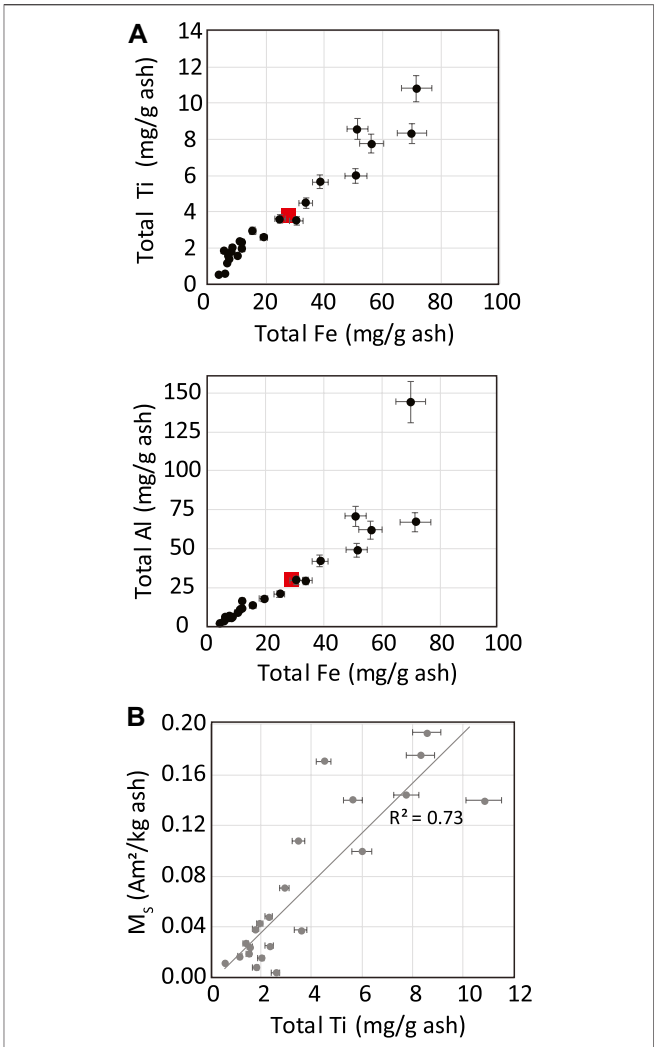

FIGURE 9 | (A) Concentrations of Fe plotted against Al and Ti in Icelandic plant ash samples determined by wet digestion. **(B)** Comparison of Ti content with saturation magnetization based on the ashed mass of Icelandic plants. Error bars are based on relative standard deviation among analytical replicates. Data shown are for samples combusted at 550°C for 4 h. Red symbols in A represent mean elemental concentrations in various forms of biomass reported by Vassilev et al. (2010).

ferrimagnetic phases are characteristically finer grained than typical pedogenic ferrimagnetic mineral assemblages. While we observed relatively large, MD-sized particles in SEM analysis of magnetic extracts from the ash, the elevated coercivities and moderately strong frequency dependence of susceptibility in many of the ash samples also suggests that there is likely a significant component of fine-grained SD and SP-sized magnetite as well.

In our low-temperature remanence measurements, the FC and ZFC curves for ash samples do not exactly correspond to the behavior expected for SD magnetite. For SD magnetite, FC and ZFC curves are typically bifurcated only below the Verwey transition (T_v), while merging together above T_v. In the data shown in **Figures 2** and **3**, the separation between FC and ZFC curves extends almost over the entire temperature range of measurement (20 –300 K) and, therefore, is not a clear indicator of pure SD magnetite. This type of behavior is observed in non-SD sized titanomagnetites and possibly maghemite (e.g., Smirnov and Tarduno, 2000; Carter-Stiglitz et al., 2006; Church et al., 2011), which are both likely present in the Icelandic samples. While RTSIRM curves indicate the presence of magnetite (based on T_v), the curves also display behavior typical of oxidized (maghemitized) magnetite (based on the humped shaped cooling curve) or titanomagnetite. The amount of remanence recovered after a cooling-warming cycle ranging from 85 to 95% is not a typical true MD magnetite response. Both the FC/ZFC and RTSIRM curves more likely

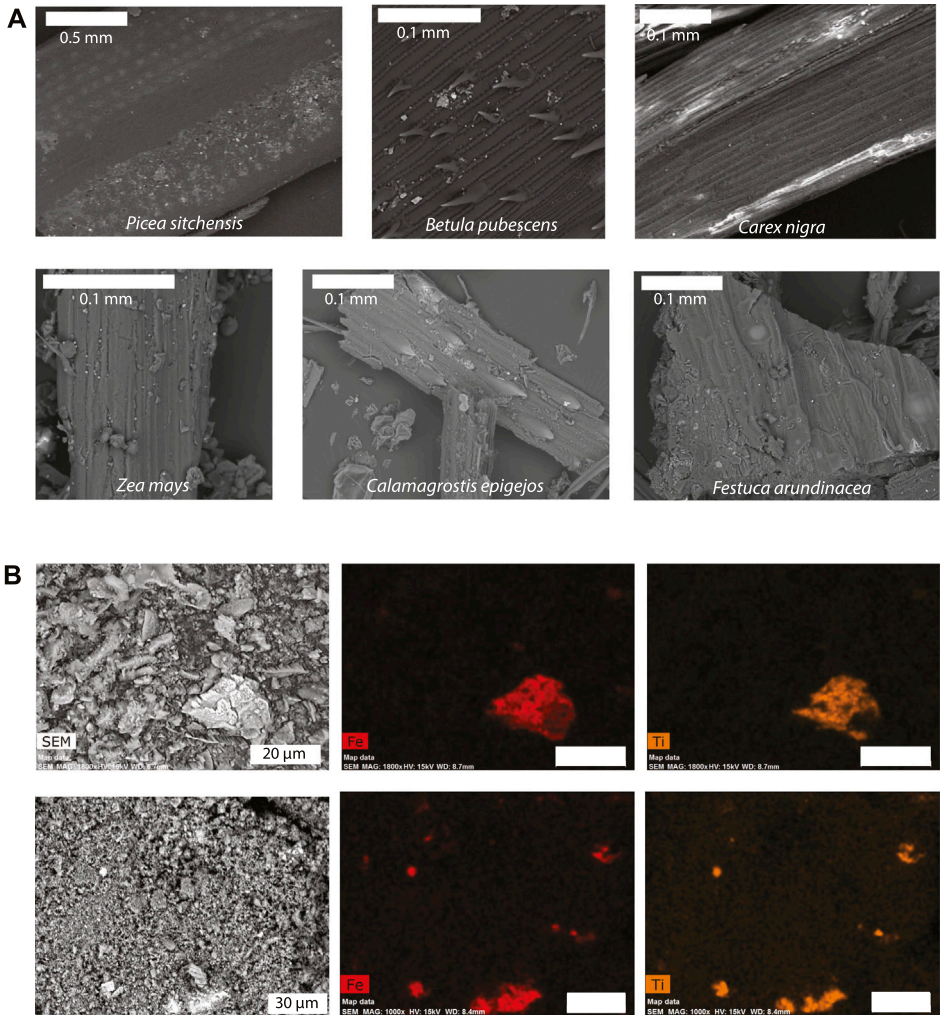

FIGURE 10 | SEM and EDS maps of plant and ash samples. **(A)** Backscattered electron images of Icelandic (top row) and German (bottom row) plant sample surfaces before burning. Small bright features are particulate matter. **(B)** EDS maps of Fe-bearing particles in Icelandic plant ash showing associations with Ti.

represent combinations of partially oxidized particles (magnetite and titanomagnetite) in the SD- to small PSD size range.

4.2 Origin of Magnetic Phases in Plant Ash

4.2.1 Inorganic Sources of Fe in Plant Ash

Plants surfaces accumulate dust through atmospheric deposition and redistribution of soil particles by wind and water, some of which may be taken up into the leaf tissue (De Nicola et al., 2008). Although cleaning treatments such as washing with water, biological detergents, weak acids, and ultrasonication are useful in reducing metal concentrations from soil and dust on the surface of plant materials (Ugolini et al., 2013), no cleaning procedure has been found to successfully remove all surface contamination (Jones and Wallace, 1992; Cook et al., 2009). This is especially true for plants with a thick waxy cuticle, in which dust and soil particles may become embedded. Residual dust and soil can produce significant overestimates of the metal content in plant tissues, especially for Fe (Jones and Wallace, 1992; Cary et al., 1994). However, the extent of soil inclusion may be estimated by determining elemental concentrations of Ti and Al, which are not present at appreciable levels in most biological materials but are abundant in soils and atmospheric dust, as well as in particulate matter from pollution sources (Cherney and Robinson, 1983; Cook et al., 2009).

An increasing number of recent studies have demonstrated that magnetic measurements of leaves, especially tree leaves in urban environments, provides a good estimate of atmospheric particulate matter (Mitchell and Maher, 2009; Hofman et al., 2014). Previous analysis of Icelandic dust by X-ray diffraction and SEM found that it is largely composed of volcanic glass, with approximately 0.7 wt% magnetite and ulvospinel (Dagsson-Waldhauserova et al., 2014). The dust and soil in Iceland are derived from basaltic parent materials and are higher in Fe, Al, and Ti than dust and soils in typical continental settings. The

strong correlation between total Fe content and M_S with Ti and Al in plant ash is likely more pronounced in Iceland than it would be in other regions. The low T_C values observed for some Icelandic samples are probably associated with titanomagnetite. Differences in soil and dust parent material composition probably account for the greater apparent enhancement in M_S after burning (without accounting for LOI) for the Icelandic plant ash compared with German plant ash.

The remaining changes in M_S with burning temperature after correcting for the loss of plant mass is attributed to thermal alteration of inorganic particulate matter. The nature of this alteration seems to vary among plant types, with significant increases in LOI-normalized M_S indicating net production of strongly magnetic minerals. This phase is presumed to be magnetite, some of which is superparamagnetic and nanosized, which is the dominant phase observed in thermomagnetic curves for ash samples (**Figure 1**). However, it is not possible to distinguish possible pyrogenic magnetite from relict lithogenic magnetite based on the available data. Decreases in saturation magnetization after burning may reflect oxidation of lithogenic Fe-oxides, as the samples were heated in air inside a muffle furnace with a large volume. However, conditions appear to have been insufficiently oxidizing during ashing to produce hematite, which was not detected in any low-temperature or thermomagnetic (in air or argon) measurements.

4.2.2 Fe in Plant Tissues

In this study we observe a clear association between saturation magnetization and Ti content (**Figure 9B**), indicating that much of the magnetic material and Fe associated with the plant material is inorganic in origin. Plant tissues contain trace amounts of Fe as a micronutrient, with typical leaf concentrations for plants grown in growth chambers in the range 10–200 ppm (Himelblau and Amasino, 2001; Garnett and Graham, 2005). In contrast, the Fe concentrations measured in our ash samples correspond to leaf concentrations ranging from 220 to over 4,000 ppm. Among various organic Fe compounds, the protein phytoferritin stores iron as a ferric hydroxide similar to ferrihydrite (Briat et al., 2015), which some studies have hypothesized may contribute to pedogenic Fe mineral assemblages in soils (Gajdardziska-Josifovska et al., 2001; McClean et al., 2001). Fe stored in ferritin and other organic compounds could potentially also transform to ferromagnetic phases during burning of live plant material. Such transformations may be partially responsible for the larger increases in M_S observed in green leaves compared to leaf litter from the same species (**Figure 7A**). However, phytoferritin and other plant proteins typically become degraded and mobilized during senescence, so ferritin is unlikely to remain intact in plant litter, which forms the bulk of the O horizon of soils. While Fe in plant tissues probably does contribute to the formation of Fe-oxide phases in plant ash, in most settings the organic component will be far outweighed by the contribution of inorganic particulate matter given the low concentrations of Fe in biological tissues compared to those in dust or soil.

4.3 Factors Influencing Magnetic Signatures of Plant Ash

Our experimental burning results indicate that the concentration of strongly magnetic phases in plant ash depends strongly on combustion temperature. The observed differences between saturation magnetization values normalized by the burnt sample mass vs. the initial plant mass demonstrate that while the concentration of magnetic material typically increases after burning at temperatures above 300°C, this increase may not necessarily reflect the formation of new magnetic phases. In many samples, most or all of the apparent increase in mass-normalized M_S can be accounted for by the loss of mass during burning.

It follows that other mass-specific magnetic properties, such as susceptibility, that appear to increase in soils following wildfire events may also dominantly reflect a reduction in organic matter mass instead of pyrogenic mineral formation or transformation. Magnetic enhancement in fire-affected soils may therefore be a reasonable proxy for organic matter loss due to burning, which supports the suggestion of Jordanova et al. (2019a) that fire intensity is directly correlated with the resulting degree of magnetic enhancement. Our results further indicate that elevated mass-specific magnetic parameters following high-intensity burning, such as forest fires, primarily occur because mass loss associated with organic matter combustion serves to increase the concentrations of inorganic magnetic particles incorporated into plant material and secondarily occur due to thermal transformation of weakly magnetic inorganic phases to strongly magnetic phases (see **Section 4.3** below).

While M_S values are consistently elevated in char and ash produced at 300 and 550°C, the extent of this increase varies substantially among plant types. This variation is likely influenced by the amount of soil and dust inclusion in plant samples surfaces, as indicated by the strong correlation of M_S with Ti content. In turn, our SEM observations indicate that Ti and particulate matter content qualitatively depend on plant type through differences in leaf texture and morphology. A study by Kardel et al. (2011) also found a species effect on leaf SIRM and the amount of retained particulate matter on urban tree leaves, where hairy or rough-textured leaves tend to accumulate more dust, while smoother, more hydrophobic leaves are more likely to shed dust. Kardel et al. (2011) additionally observed a strong seasonal affect, with particulate matter concentrations increasing throughout the growing season. Our findings also suggest that seasonality may play a role in the magnetic properties of plant ash, based on the contrasting burning-induced enhancement in green leaves compared to plant litter.

4.4 Implications for Magnetic Enhancement of Soils by Fire

Our results help to resolve seemingly conflicting results from earlier studies documenting changes in magnetic susceptibility in soils affected by fire, with some finding evidence for strong enhancement after burning (Blake et al., 2006; Clement et al., 2011, e.g.), while others find weak or no magnetic signatures of burning (Roman et al., 2013). We demonstrate that low-temperature burning even for several hours tends to decrease the magnetization of plant material, while higher burning temperatures produce significant increases in magnetization. Our finding that M_S is reduced or relatively unchanged by burning at 200°C is consistent with the observations of Roman et al. (2013), who saw no significant changes in soil magnetic properties following short-duration, moderate-intensity grass fires.

Ferric (hydr)oxides such as goethite, lepidocrocite, and ferrihydrite are common phases in dust and soil. If present on plant surfaces, these phases will easily alter on heating and can transform rapidly to magnetite and maghemite, especially in the reducing environment created by combusting organic matter (Till et al., 2017; Till and Nowaczyk, 2018). For weakly magnetic ferric phases such as goethite and hematite in soils affected by low-intensity fires, the modest rise in temperature, which is restricted to the uppermost few cm, is likely insufficient to produce thermal alteration of these minerals (Roman et al., 2013; Jordanova et al., 2019a). However, high-intensity fires can heat soil down to depths of at least 10 cm to temperatures high enough to trigger reductive alteration of goethite and hematite to magnetite or maghemite Clement et al. (2011); Nørnberg et al. (2009); Ketterings et al. (2000). Soil in Iceland, like in other volcanic regions, typically contain high concentrations of poorly crystalline phases such as ferrihydrite and allophane (up to 15 and 30%, respectively, according to Arnalds (2004)). Ferrihydrite easily alters to magnetite when heated in the presence of organic matter (Hanesch et al., 2006; Till and Nowaczyk, 2018) and is a likely source of the ferromagnetic phase detected in Icelandic plant ash samples. Pyrogenic magnetite derived from ferric (oxy)hydroxides are typically fined-grained mixtures of superparamagnetic and single-domain particles (Gendler et al., 2005; Jeleńska et al., 2010; Till et al., 2015).

Another pathway for the formation of pyrogenic magnetite is through alteration of Fe-bearing clay minerals during heating, particularly smectites. Although structural Fe in smectites is stable up to temperature of 700°C (Moskowitz and Hargraves, 1982), Hirt et al. (1993) documented the formation of magnetite from weakly adsorbed Fe on smectite surfaces after heating to more moderate temperatures above 250°C. Certain clay minerals also have the potential to partially reduce hematite to magnetite on heating above 600°C, especially in less crystalline Al-hematites (Jiang et al., 2015). The magnetic properties of fire-affected topsoils will reflect mineralogical changes created by the combustion of organic matter and incorporated surface dust, including the possible formation of pyrogenic Fe-oxides, as well as heating-induced conversion of soil minerals if soil temperatures are sufficiently high.

Ash from wildfires is often both highly mobile (Whicker et al., 2002; Pereira et al., 2015) and reactive. While magnetic enhancement of fire events may be preserved over longer timescales in sedimentary archives such as lakes and continental shelf deposits Oldfield and Crowther (2007); Kent et al. (2017), it is unclear how long fire-related magnetic enhancement may persist in soils. For example, Jordanova et al. (2019b) found that the initial enhanced magnetic signal in soils containing wildfire ash decreased over a period of 3 years, presumably due to oxidation of magnetite by weathering and biogenic processes.

Finally, in comparing our experimentally produced char and ashes with burnt plant residues created by wildfires, it is important to note that natural burning conditions are far less controlled and constant than laboratory conditions Bodí et al. (2014) and that factors such as oxygen and fuel supply as well as temperature and heat transfer Pingree and Kobziar (2019) may be highly heterogeneous in field settings. Nevertheless, laboratory burning of individual plant species is a valuable approach for distinguishing the chemistry and magnetic properties of burnt plant material from that of soils.

5 CONCLUSION

We conducted a detailed rock magnetic characterization of burnt plant residues from individual species collected in Iceland and Germany. A close correlation between total Fe and Ti in the Icelandic plant samples indicates that a significant amount of the iron in plant ash is derived from inorganic particulate matter embedded in plant surfaces, which dominates the magnetic properties of the ash. Strong increases in saturation magnetization were observed after burning at temperatures of 300°C and above, indicating increasing concentrations of ferromagnetic particles. Most of this increase is attributed to the reduction in plant mass during burning, while thermal alteration of entrained dust and soil on plant surfaces plays a lesser role in determining the magnetic properties of plant char and ash. Ash from cleaned plant material exhibited hysteresis parameters very similar to that from uncleaned plant samples but with lower saturation magnetization values, suggesting that cleaning effectively reduced the concentration of surface dust, but the main magnetic phases are the same for cleaned and uncleaned plant material. Based on our study results, we do not expect plant ash to generate a unique magnetic plant-based fingerprint of burning events. Instead, magnetic properties of vegetation ash in soil and sediments will vary with the extent of burning, time of year, the local composition of dust and soil, and plant type due to differences in leaf morphology, which strongly influences the amount of retained inorganic material.

DATA AVAILABILITY STATEMENT

The original contributions presented in the study are included in the article/**Supplementary Material**, further inquiries can be directed to the corresponding author.

AUTHOR CONTRIBUTIONS

JT conceived the study, prepared the samples, and performed magnetic measurements. BM conducted and interpreted low-temperature magnetic measurements. SP facilitated geochemical analysis and contributed to the interpretation and discussion of compositional data. All authors contributed to and approved the final manuscript.

FUNDING

This project was funded by Rannís, the Iceland Centre for Research, through a postdoctoral fellowship grant (#173743-051) to JT from the Icelandic Research Fund. Part of this work was performed as a Visiting Fellow at the Institute for Rock Magnetism (IRM) at the University of Minnesota. The IRM is a United States National Multi-user Facility supported through the Instrumentation and Facilities program of the National Science Foundation, Earth Sciences Division, and by funding from the University of Minnesota.

ACKNOWLEDGMENTS

Mike Jackson, Maxwell Brown, and Peat Solheid are thanked for support with magnetic measurements. Zena Severin is thanked for assistance with sample collection and preparation. We are grateful to Andy Hobson for laboratory assistance and support with geochemical analysis. Axel Höhn at the Leibniz Center for Landscape Agriculture (ZALF) kindly provided the German plant samples used in this study. We thank our reviewers for providing constructive comments to help improve the manuscript. This is IRM contribution 2006.

SUPPLEMENTARY MATERIAL

The Supplementary Material for this article can be found online at: https://www.frontiersin.org/articles/10.3389/feart.2020.592659/full#supplementary-material.

REFERENCES

Arnalds, O. (2004). Volcanic soils of iceland. *Catena* 56, 3–20. doi:10.1016/j.catena.2003.10.002

Bilardello, D., and Jackson, M. (2013). What do the mumpsies do? *IRM Q.* 23, 11–15.

Blake, W., Wallbrink, P., Doerr, S., Shakesby, R., and Humphreys, G. (2006). Magnetic enhancement in wildfire-affected soil and its potential for sediment-source ascription. *Earth Surf. Process. Landforms* 31, 249–264. doi:10.1002/esp.1247

Bodí, M. B., Martin, D. A., Balfour, V. N., Santín, C., Doerr, S. H., Pereira, P., et al. (2014). Wildland fire ash: production, composition and eco-hydro-geomorphic effects. *Earth Sci. Rev.* 130, 103–127. doi:10.1016/j.earscirev.2013.12.007

Briat, J. F., Dubos, C., and Gaymard, F. (2015). Iron nutrition, biomass production, and plant product quality. *Trends Plant Sci.* 20, 33–40. doi:10.1016/j.tplants.2014.07.005

Carrancho, Á., and Villalaín, J. (2011). Different mechanisms of magnetisation recorded in experimental fires: archaeomagnetic implications. *Earth Planet Sci. Lett.* 312, 176–187. doi:10.1016/j.epsl.2011.10.006

Carter-Stiglitz, B., Moskowitz, B., Solheid, P., Berquó, T. S., Jackson, M., and Kosterov, A. (2006). Low-temperature magnetic behavior of multidomain titanomagnetites: Tm0, tm16, and tm35. *J. Geophys. Res.: Solid Earth* 111, B12S05. doi:10.1029/2006JB004561

Cary, E., Grunes, D., Bohman, V., and Sanchirico, C. (1986). Titanium determination for correction of plant sample contamination by soil. *Agron. J.* 78, 933–936. doi:10.2134/agronj1986.00021962007800050038x

Cary, E., Grunes, D., Dallyn, S., Pearson, G., Peck, N., and Hulme, R. (1994). Plant Fe, Al and Cr concentrations in vegetables as influenced by soil inclusion. *J. Food Qual.* 17, 467–476. doi:10.1111/j.1745-4557.1994.tb00167.x

Cherney, J., and Robinson, D. (1983). A comparison of plant digestion methods for identifying soil contamination of plant tissue by Ti analysis. *Agron. J.* 75, 145–147. doi:10.2134/agronj1983.00021962007500010037x

Church, M., Peters, C., and Batt, C. (2007). Sourcing fire ash on archaeological sites in the Western and Northern Isles of Scotland, using mineral magnetism. *Geoarchaeology* 22, 747–774. doi:10.1002/gea.20185

Church, N., Feinberg, J. M., and Harrison, R. (2011). Low-temperature domain wall pinning in titanomagnetite: quantitative modeling of multidomain first-order reversal curve diagrams and ac susceptibility. *G-cubed* 12. doi:10.1029/2011gc003538

Clement, B. M., Javier, J., Sah, J. P., and Ross, M. S. (2011). The effects of wildfires on the magnetic properties of soils in the Everglades. *Earth Surf. Process. Landforms* 36, 460–466. doi:10.1002/esp.2060

Cook, L. L., McGonigle, T. P., and Inouye, R. S. (2009). Titanium as an indicator of residual soil on arid-land plants. *J. Environ. Qual.* 38, 188–199. doi:10.2134/jeq2007.0034

Dagsson-Waldhauserova, P., Arnalds, O., Olafsson, H., Skrabalova, L., Sigurdardóttir, G. M., Branis, M., et al. (2014). Physical properties of suspended dust during moist and low wind conditions in Iceland. *Icel. Agric. Sci.* 27, 25–39.

De Nicola, F., Maisto, G., Prati, M., and Alfani, A. (2008). Leaf accumulation of trace elements and polycyclic aromatic hydrocarbons (PAHs) in Quercus ilex L. *Environ. Pollut.* 153, 376–383. doi:10.1016/j.envpol.2007.08.008

Eiríksson, T., Björnsson, H., Gudmundsdóttir, K. B., Kristinsson, J., and Jóhannesson, T. (2010). The distribution of four trace elements (Fe, Mn, Cu, Zn) in forage and the relation to scrapie in Iceland. *Acta Vet. Scand.* 52, 34. doi:10.1186/1751-0147-52-34

Fabian, K., Shcherbakov, V. P., and McEnroe, S. A. (2013). Measuring the curie temperature. *G-cubed* 14, 947–961. doi:10.1029/2012GC004440

Gajdardziska-Josifovska, M., McCLEAN, R. G., Schofield, M. A., Sommer, C. V., et al. (2001). Discovery of nanocrystalline botanical magnetite. *Eur. J. Mineral* 13, 863–870. doi:10.1127/0935-1221/2001/0013-0863

Garnett, T. P., and Graham, R. D. (2005). Distribution and remobilization of iron and copper in wheat. *Ann. Bot.* 95, 817–826. doi:10.1093/aob/mci085

Gedye, S., Jones, R., Tinner, W., Ammann, B., and Oldfield, F. (2000). The use of mineral magnetism in the reconstruction of fire history: a case study from Lago di Origlio, Swiss Alps. *Palaeogeogr. Palaeoclimatol. Palaeoecol.* 164, 101–110. doi:10.1016/S0031-0182(00)00178-4

Gendler, T., Shcherbakov, V., Dekkers, M., Gapeev, A., Gribov, S., and McClelland, E. (2005). The lepidocrocite–maghemite–haematite reaction chain—I. Acquisition of chemical remanent magnetization by maghemite, its magnetic properties and thermal stability. *Geophys. J. Int.* 160, 815–832. doi:10.1111/j.1365-246X.2005.02550.x

Hanesch, M., Stanjek, H., and Petersen, N. (2006). Thermomagnetic measurements of soil iron minerals: the role of organic carbon. *Geophys. J. Int.* 165, 53–61. doi:10.1111/j.1365-246X.2006.02933.x

Himelblau, E., and Amasino, R. M. (2001). Nutrients mobilized from leaves of arabidopsis thaliana during leaf senescence. *J. Plant Physiol.* 158, 1317–1323. doi:10.1078/0176-1617-00608

Hirt, A., Banin, A., and Gehring, A. (1993). Thermal generation of ferromagnetic minerals from iron-enriched smectites. *Geophys. J. Int.* 115, 1161–1168. doi:10.1111/j.1365-246X.1993.tb01518.x

Hofman, J., Wuyts, K., Van Wittenberghe, S., Brackx, M., and Samson, R. (2014). Reprint of on the link between biomagnetic monitoring and leaf-deposited dust load of urban trees: relationships and spatial variability of different particle size fractions. *Environ. Pollut.* 192, 285–372. doi:10.1016/j.envpol.2014.05.006

Jackson, M., and Solheid, P. (2010). On the quantitative analysis and evaluation of magnetic hysteresis data. *G-cubed* 11, Q04Z15. doi:10.1029/2009GC002932

Jeleńska, M., Hasso-Agopsowicz, A., and Kopcewicz, B. (2010). Thermally induced transformation of magnetic minerals in soil based on rock magnetic study and

mössbauer analysis. *Phys. Earth Planet. In.* 179, 164–177. doi:10.1016/j.pepi.2009.11.004

Jiang, Z., Liu, Q., Roberts, A. P., Barrón, V., Torrent, J., and Zhang, Q. (2018). A new model for transformation of ferrihydrite to hematite in soils and sediments. *Geology* 46, 987–990. doi:10.1130/G45386.1

Jiang, Z., Liu, Q., Zhao, X., Jin, C., Liu, C., and Li, S. (2015). Thermal magnetic behaviour of al-substituted haematite mixed with clay minerals and its geological significance. *Geophys. J. Int.* 200, 130–143. doi:10.1093/gji/ggu377

Jóhannesson, T., Eiríksson, T., Gudmundsdóttir, K. B., Sigurdarson, S., and Kristinsson, J. (2007). Overview: seven trace elements in Icelandic forage. Their value in animal health and with special relation to scrapie. *Icel. Agric. Sci.* 20, 3–24.

Jones, J. B., and Wallace, A. (1992). Sample preparation and determination of iron in plant tissue samples. *J. Plant Nutr.* 15, 2085–2108. doi:10.1080/01904169209364460

Jordanova, D., Jordanova, N., Barrón, V., and Petrov, P. (2018). The signs of past wildfires encoded in the magnetic properties of forest soils. *Catena* 171, 265–279. doi:10.1016/j.catena.2018.07.030

Jordanova, N., Jordanova, D., and Barrón, V. (2019a). Wildfire severity: environmental effects revealed by soil magnetic properties. *Land Degrad. Dev.* 30, 2226–2242. doi:10.1002/ldr.3411

Jordanova, N., Jordanova, D., Henry, B., Le Goff, M., Dimov, D., and Tsacheva, T. (2006). Magnetism of cigarette ashes. *J. Magn. Magn Mater.* 301, 50–66. doi:10.1016/j.jmmm.2005.06.008

Jordanova, N., Jordanova, D., Mokreva, A., Ishlyamski, D., and Georgieva, B. (2019b). Temporal changes in magnetic signal of burnt soils–a compelling three years pilot study. *Sci. Total Environ.* 669, 729–738. doi:10.1016/j.scitotenv.2019.03.173

Kardel, F., Wuyts, K., Maher, B., Hansard, R., and Samson, R. (2011). Leaf saturation isothermal remanent magnetization (sirm) as a proxy for particulate matter monitoring: inter-species differences and in-season variation. *Atmos. Environ.* 45, 5164–5171. doi:10.1016/j.scitotenv.2019.03.173

Kent, D. V., Lanci, L., Wang, H., and Wright, J. D. (2017). Enhanced magnetization of the marlboro clay as a product of soil pyrogenesis at the paleocene–eocene boundary? *Earth Planet Sci. Lett.* 473, 303–312. doi:10.1016/j.epsl.2017.06.014

Ketterings, Q. M., Bigham, J. M., and Laperche, V. (2000). Changes in soil mineralogy and texture caused by slash-and-burn fires in Sumatra, Indonesia. *Soil Sci. Soc. Am. J.* 64, 1108–1117. doi:10.2136/sssaj2000.6431108x

Kletetschka, G., and Banerjee, S. K. (1995). Magnetic stratigraphy of Chinese loess as a record of natural fires. *Geophys. Res. Lett.* 22, 1341–1343. doi:10.1029/95GL01324

Le Borgne, E. (1960). Influence du feu sur les propriétés magnétiques du sol et sur celles du schiste et du granite. *Ann. Geophys.* 16, 159.

Lu, H., Liu, T., Gu, Z., Liu, B., Zhou, L., Han, J., et al. (2000). Effect of burning C3 and C4 plants on the magnetic susceptibility signal in soils. *Geophys. Res. Lett.* 27, 2013–2016. doi:10.1029/2000GL011459

Maher, B. A., Alekseev, A., and Alekseeva, T. (2003). Magnetic mineralogy of soils across the Russian steppe: climatic dependence of pedogenic magnetite formation. *Palaeogeogr. Palaeoclimatol. Palaeoecol.* 201, 321–341. doi:10.1016/S0031-0182(03)00618-7

McClean, R. G., and Kean, W. (1993). Contributions of wood ash magnetism to archaeomagnetic properties of fire pits and hearths. *Earth Planet Sci. Lett.* 119, 387–394. doi:10.1016/0012-821X(93)90146-Z

McClean, R. G., Schofield, M. A., Sommer, C. V., Robertson, D. P., Dick, T., Gajdardziska-Josifovska, M., et al. (2001). Botanical iron minerals correlation between nanocrystal structure and modes of biological self-assembly. *Eur. J. Mineral.* 13, 1235–1242. doi:10.1127/0935-1221/2001/0013-1235

Mitchell, R., and Maher, B. A. (2009). Evaluation and application of biomagnetic monitoring of traffic-derived particulate pollution. *Atmos. Environ.* 43, 2095–2103. doi:10.1016/j.atmosenv.2009.01.042

Moskowitz, B. M., and Hargraves, R. B. (1982). Magnetic changes accompanying the thermal decomposition of nontronite (in air) and its relevance to martian mineralogy. *J. Geophys. Res.: Solid Earth.* 87, 10115–10128. doi:10.1029/JB087iB12p10115

Nørnberg, P., Vendelboe, A. L., Gunnlaugsson, H. P., Merrison, J. P., Finster, K., and Jensen, S. K. (2009). Comparison of the mineralogical effects of an experimental forest fire on a goethite/ferrihydrite soil with a topsoil that contains hematite, maghemite and goethite. *Clay Miner.* 44, 239–247. doi:10.1180/claymin.2009.044.2.239

Oldfield, F., and Crowther, J. (2007). Establishing fire incidence in temperate soils using magnetic measurements. *Palaeogeogr. Palaeoclimatol. Palaeoecol.* 249, 362–369. doi:10.1016/j.palaeo.2007.02.007

Özdemir, Ö., and Dunlop, D. J. (2010). Hallmarks of maghemitization in low-temperature remanence cycling of partially oxidized magnetite nanoparticles. *J. Geophys. Res.: Solid Earth.* 115, B02101. doi:10.1029/2009JB006756

Pereira, P., Cerdà, A., Úbeda, X., Mataix-Solera, J., Arcenegui, V., and Zavala, L. (2015). Modelling the impacts of wildfire on ash thickness in a short-term period. *Land Degrad. Dev.* 26, 180–192. doi:10.1002/ldr.2195

Peters, C., and Batt, C. (2002). Dating and sourcing fuel ash residues from Cladh Hallan, South Uist, Scotland, using magnetic techniques. *Phys. Chem. Earth, Parts A/B/C.* 27, 1349–1353. doi:10.1016/S1474-7065(02)00132-8

Peters, C., Church, M., and Mitchell, C. (2001). Investigation of fire ash residues using mineral magnetism. *Archaeol. Prospect.* 8, 227–237. doi:10.1002/arp.171

Petrovskỳ, E., and Kapička, A. (2006). On determination of the curie point from thermomagnetic curves. *J. Geophys. Res.: Solid Earth* 111, B12S27. doi:10.1029/2006JB004507

Petrovskỳ, E., Remeš, J., Kapička, A., Podrázskỳ, V., Grison, H., and Borůvka, L. (2018). Magnetic mapping of distribution of wood ash used for fertilization of forest soil. *Sci. Total Environ.* 626, 228–234. doi:10.1016/j.scitotenv.2018.01.095

Pingree, M. R., and Kobziar, L. N. (2019). The myth of the biological threshold: a review of biological responses to soil heating associated with wildland fire. *For. Ecol. Manag.* 432, 1022–1029. doi:10.1016/j.foreco.2018.10.032

Roman, S. A., Johnson, W. C., and Geiss, C. E. (2013). Grass fires—an unlikely process to explain the magnetic properties of prairie soils. *Geophys. J. Int.* 195, 1566–1575. doi:10.1093/gji/ggt349

Smirnov, A. V., and Tarduno, J. A. (2000). Low-temperature magnetic properties of pelagic sediments (ocean drilling program site 805c): tracers of maghemitization and magnetic mineral reduction. *J. Geophys. Res.: Solid Earth* 105, 16457–16471. doi:10.1029/2000JB900140

Till, J. L., and Nowaczyk, N. (2018). Authigenic magnetite formation from goethite and hematite and chemical remanent magnetization acquisition. *Geophys. J. Int.* 213, 1818–1831. doi:10.1093/gji/ggy083

Till, J., Guyodo, Y., Lagroix, F., Morin, G., and Ona-Nguema, G. (2015). Goethite as a potential source of magnetic nanoparticles in sediments. *Geology* 43, 75–78. doi:10.1130/G36186.1

Till, J., Guyodo, Y., Lagroix, F., Ona-Nguema, G., and Brest, J. (2014). Magnetic comparison of abiogenic and biogenic alteration products of lepidocrocite. *Earth Planet Sci. Lett.* 395, 149–158. doi:10.1016/j.epsl.2014.03.051

Till, J. L., Guyodo, Y., Lagroix, F., Morin, G., Menguy, N., and Ona-Nguema, G. (2017). Presumed magnetic biosignatures observed in magnetite derived from abiotic reductive alteration of nanogoethite. *Compt. Rendus Geosci.* 349, 63–70. doi:10.1016/j.crte.2017.02.001

Ugolini, F., Tognetti, R., Raschi, A., and Bacci, L. (2013). Quercus ilex L. as bioaccumulator for heavy metals in urban areas: effectiveness of leaf washing with distilled water and considerations on the trees distance from traffic. *Urban For. Urban Green.* 12, 576–584. doi:10.1016/j.ufug.2013.05.007

Vassilev, S. V., Baxter, D., Andersen, L. K., and Vassileva, C. G. (2010). An overview of the chemical composition of biomass. *Fuel* 89, 913–933. doi:10.1016/j.fuel.2009.10.022

Wang, D., and Van der Voo, R. (2004). The hysteresis properties of multidomain magnetite and titanomagnetite/titanomaghemite in mid-ocean ridge basalts. *Earth Planet Sci. Lett.* 220, 175–184. doi:10.1016/S0012-821X(04)00052-4

Whicker, J. J., Breshears, D. D., Wasiolek, P. T., Kirchner, T. B., Tavani, R. A., Schoep, D. A., et al. (2002). Temporal and spatial variation of episodic wind erosion in unburned and burned semiarid shrubland. *J. Environ. Qual.* 31, 599–612. doi:10.2134/jeq2002.5990

Xiong, Y., Guilbaud, R., Peacock, C. L., Cox, R. P., Canfield, D. E., Krom, M. D., et al. (2019). Phosphorus cycling in Lake Cadagno, Switzerland: a low sulfate euxinic ocean analogue. *Geochem. Cosmochim. Acta* 251, 116–135. doi:10.1016/j.gca.2019.02.011

Conflict of Interest: The authors declare that the research was conducted in the absence of any commercial or financial relationships that could be construed as a potential conflict of interest.

The reviewer NJ declared a past co-authorship with one of the authors JT to the handling editor.

frontiers in Earth Science

ORIGINAL RESEARCH
published: 14 January 2021
doi: 10.3389/feart.2020.604505

High-Resolution Environmental Magnetism Using the Quantum Diamond Microscope (QDM): Application to a Tropical Speleothem

Roger R. Fu[1], Kimberly Hess[1], Plinio Jaqueto[2,3], Valdir F. Novello[3], Tyler Kukla[4], Ricardo I. F. Trindade[3], Nicolás M. Stríkis[5], Francisco W. Cruz Jr.[3] and Oren Ben Dor[1,6]*

[1]*Department of Earth and Planetary Sciences, Harvard University, Cambridge, MA, United States,* [2]*Department of Earth and Environmental Sciences, University of Minnesota, Minneapolis, MN, United States,* [3]*Instituto de Astronomia, Geofísica e Ciências Atmosféricas, Universidade de São Paulo, São Paulo, Brazil,* [4]*Department of Geological Sciences, Stanford University, Stanford, CA, United States,* [5]*Universidade Federal Fluminense, Niterói, Brazil,* [6]*Department of Physics, Harvard University, Cambridge, MA, United States*

Quantum diamond microscope (QDM) magnetic field imaging is a recently developed technique capable of mapping magnetic field sources in geologic samples at 1 micrometer resolution. Applying QDM imaging to speleothems can provide high-resolution time series of detrital input into the cave environment, which, in turn, can yield useful paleoenvironmental information. Here we map the magnetic field over a speleothem from midwest Brazil over a 174 year timespan with annual to sub-annual resolution and perform backfield remanence acquisition experiments to quantify changes in the magnetic grain population through time. We find that magnetic particles occur in highly enriched layers of 10–100 μm thickness that sample the same detrital source population. Combined with petrographic observations and electron microprobe mapping of Mg and Ca, we conclude that detrital enrichment in our sample is caused by drier conditions leading to slow or halted speleothem growth. This interpretation is compatible with oxygen isotopic data and implies that speleothem magnetism can be used to infer the past occurrence of drought and potentially quantify their duration. Future high-resolution magnetic imaging of speleothems may provide additional insight into the mechanism of detrital enrichment and establish their role as a proxy for local moisture and infiltration.

Keywords: speleothem, environmental magnetism, paleoclimate, rock magnetism, drought

OPEN ACCESS

Edited by:
Junsheng Nie,
Lanzhou University, China

Reviewed by:
Qingsong Liu,
Chinese Academy of Sciences (CAS), China
Yu-Min Chou,
Southern University of Science and Technology, China

****Correspondence:***
Roger R. Fu
rogerfu@fas.harvard.edu

Specialty section:
This article was submitted to Geomagnetism and Paleomagnetism, a section of the journal Frontiers in Earth Science

Received: *09 September 2020*
Accepted: *04 December 2020*
Published: *14 January 2021*

Citation:
Fu RR, Hess K, Jaqueto P, Novello VF, Kukla T, Trindade RIF, Stríkis NM, Cruz FW and Ben Dor O (2021) High-Resolution Environmental Magnetism Using the Quantum Diamond Microscope (QDM): Application to a Tropical Speleothem. Front. Earth Sci. 8:604505. doi: 10.3389/feart.2020.604505

INTRODUCTION

Environmental magnetism studies seek to extract information about past Earth surface conditions using rock magnetic techniques, which can quantify properties of Fe-bearing mineral populations in sediments. Compared to geochemical and isotopic techniques, rock magnetism can characterize mineral populations at extremely low concentrations and is uniquely sensitive to some parameters such as grain size and Fe oxidation state. As such, environmental magnetism studies provide unique insight into past climates and environments. Although full applications of environmental magnetism are reviewed elsewhere (Verosub and Roberts, 1995; Liu et al., 2012), prominent examples include quantifying climatic and chemical conditions during deposition [e.g. (Maher et al., 1994; Liu et al.,

2007; Slotznick et al., 2018)], identifying the provenance of detrital particles [e.g. (Blundell et al., 2009; Maher et al., 2009)], and understanding the mechanisms of pedogenesis and diagenesis (Bloemendal et al., 1992; Roberts, 2015).

Most environmental magnetism studies are based on measurements of magnetic properties in millimeter to centimeter scale specimens, hereafter referred to as bulk specimens. In the case of sedimentary samples deposited over time, analyses of bulk specimens at a range of stratigraphic heights can be compiled to construct a time series of magnetic properties, which can in turn be interpreted to record paleoenvironmental change. The temporal resolution of such studies is limited by the minimum volume of sample that retains sufficient magnetic content to be detectable using available instrumentation.

By recovering maps of magnetic fields with sub-millimeter resolution, magnetic imaging is a complementary approach that can circumvent spatial resolution limitations inherent to bulk specimens analyses. In addition to providing high temporal resolution, spatially resolved maps of magnetic field sources can pinpoint the mineralogical source of magnetic field signal. Combined with microscopy over the same regions of interest, this information permits the definitive attribution of a given magnetic signal to specific grain populations.

Magnetic field imaging techniques are therefore well-suited for analyzing environmental magnetism records that display heterogeneity at fine spatial scales. Cave deposits, or speleothems, hold unique potential for generating high-resolution time series due to the availability of high-precision U-Th age dating. Intensive study over the past decades has demonstrated their potential to retain paleoenvironmental information through a range of chemical and isotopic systems [e.g., McDermott (2004)]. With respect to magnetic studies, bulk samples extracted from speleothems have been used to show that the concentration of ferromagnetic minerals covary with other paleoenvironmental proxies. In mid-latitudes, magnetization intensity has been found to correlate with oxygen isotopic variations (Bourne et al., 2015) as well as with organic proxies for moisture (Zhu et al., 2017). These correlations, observed at the centennial to millennial timescale, may be due to greater production and transport of detrital magnetite into cave environments during times of heavier rainfall, which drive shifts in other moisture proxies.

Other mid-latitude speleothem studies have shown no clear relationship between stable isotopic and magnetic variations, finding instead a correlation between magnetism and other proxies for local detrital input such as speleothem coloration (Font et al., 2014). Finally, one multi-proxy study of a tropical speleothem from midwest Brazil has suggested that, at a multidecadal scale, drier periods with sparse vegetation dominated by plants with C_4 photosynthesis lead to soil erosion and, therefore, enhanced flux of magnetic particles into the cave environment (Jaqueto et al., 2016).

All studies of speleothem magnetism described above used bulk specimens in their analyses, thus limiting temporal resolution to multi-decadal to millennial timescales. Although these records are suitable for understanding long-term climatic variations driven by insolation changes at these timescales, analysis with higher resolution time series, such as provided by magnetic field imaging, can potentially provide complementary insights. First, time series with annual or even finer resolution may reveal rapid paleoenvironmental changes occurring on these timescales such as effects of the El Niño Southern Oscillation or extreme climate events such as major floods. Second, high resolution records can help identify underlying forces that drive changes in the magnetic content of speleothems. For example, a seasonally resolved record would test the hypothesis that enhanced summer precipitation is responsible for enrichment of magnetic content in North American speleothems (Bourne et al., 2015). Finally, records with annual resolution over historical times would also allow comparison to instrumental or written records of environmental forcings such as precipitation, runoff, and soil pH. Relationships established through these direct comparisons may lead to more robust interpretations of speleothem magnetism records in deeper time.

Magnetic field imaging techniques used in speleothem analyses have thus far been limited to superconducting quantum interference device (SQUID) microscopy, which is capable of ~150 μm resolution. In an analysis of ferromagnetic particle distribution in a North American speleothem deposited over a 500 years interval, Feinberg et al. (2020) found that magnetized layers correspond to major floods, showing that, at least in some settings, detrital enrichment in speleothems is a tracer of extreme precipitation events. However, the resolution of the SQUID microscope was unable to clearly separate individual flooding events during intervals where multiple events occurred within the same decade. Furthermore, because major floods typically occur after elevated precipitation over multiple timescales spanning days to years (Seiler et al., 2002), depositional layers from major floods may be accompanied by minor events that cannot be resolved by the SQUID microscope in the studied speleothem.

Although Feinberg et al. (2020) established a flood origin for magnetic particle enrichment in their sample, the mechanism responsible for incorporating magnetic particles in other speleothems remains poorly understood. High-resolution magnetic imaging of speleothems from distinct climate settings may be useful for identifying the mechanism of magnetic particle enrichment and thereby establishing their paleoenvironmental interpretation. Acquiring such a process-based understanding of magnetic particle enrichment is critical for the broader application of speleothem magnetism as a paleoclimate proxy.

High-resolution mapping of different speleothems using the recently developed quantum diamond microscope (QDM), which has 30–100 times higher spatial resolution than the SQUID microscope, can potentially locate individual magnetic enrichment peaks with higher precision and provide fine details on the distribution of magnetic particles. Combined with other proxy data and petrography, such a high-resolution record can help identify the origin of detrital enrichment and reveal evidence for environmental change immediately before and after discrete depositional events.

In this study we use the QDM to map magnetic field sources in a Brazilian speleothem with annual resolution over a 174 year interval. Leveraging the annual to sub-annual temporal resolution of the analysis, we find that Fe-bearing detritus in the speleothem are highly concentrated in 10–100 μm scale bands that show no resolvable change in rock magnetic properties over the analyzed time interval. Combined with the fine-scale morphology, mineralogy, and composition of the magnetized layers, we conclude that the magnetized layers were deposited during slowdowns or hiatuses in speleothem deposition, possibly coupled with enhanced soil erosion during drier time intervals.

MATERIALS AND METHODS

We performed QDM imaging on the same speleothem sample from Mato Grosso State, Brazil analyzed for stable isotopes by Novello et al. (2016) and bulk specimens magnetic properties by Jaqueto et al. (2016) (**Figure 1**). The full candle-type stalagmite, known has ALHO6, was deposited in the Pau D'Alho cave (15°12′20″S, 56°48′41″W) over approximately 1,370 years between 490 CE and 1860 CE with an average deposition rate of 0.17 mm y^{-1} in the central column. Applying the QDM, which has a minimum pixel size of 1.2 μm and maximum field of view width of 2.25 mm, to the central column of the speleothem would therefore result in approximately 13 years per field of view with a nominal resolution of <1 week, which is too fine to compare to other proxy records. We therefore first binned pixels by a factor of 4 to achieve a spatial resolution of 4.7 μm per pixel, which is more closely matches the length scale of the magnetic signal and increases the signal to noise ratio. We also chose to image an approximately 5 × 10 mm sample with 0.5 mm thickness polished with 1 μm alumina grit extracted from the flank of the speleothem with finer laminae (**Figure 2**), thereby minimizing the measurement time required for a given timespan.

Isotopic studies have shown that kinetic fractionation effects may bias the signal in speleothem flank compared to the central column while paleomagnetic studies have found evidence of grain rotations on inclined speleothem surfaces (Dorale and Liu, 2009; Ponte et al., 2017). However, compiling the anhysteretic remanent magnetization (ARM) susceptibility of 47 speleothem samples with lamina inclination between 34° and 90° showed no correlation between this angle and magnetization intensity (Ponte et al., 2017). Further, all but one prominent dark, magnetized lamina measured in our QDM section can be traced continuously between the speleothem flank and center (**Figure 2**; see green arrows). The disappearance of this lamina near the central column may be due to a drip water washing effect. Analysis of a speleothem with coarser, flood-deposited detrital particles has shown even stronger effects of drip water washing with pervasive depletion of detrital layers near the central column (Feinberg et al., 2020). Together, these observations imply that the central column of speleothems may not retain the most complete record of detritus deposition and that speleothem flanks should be preferred for measurements of particulate enrichment. We therefore argue that our choice to analyze the speleothem flank does not imply a lower fidelity record of detrital

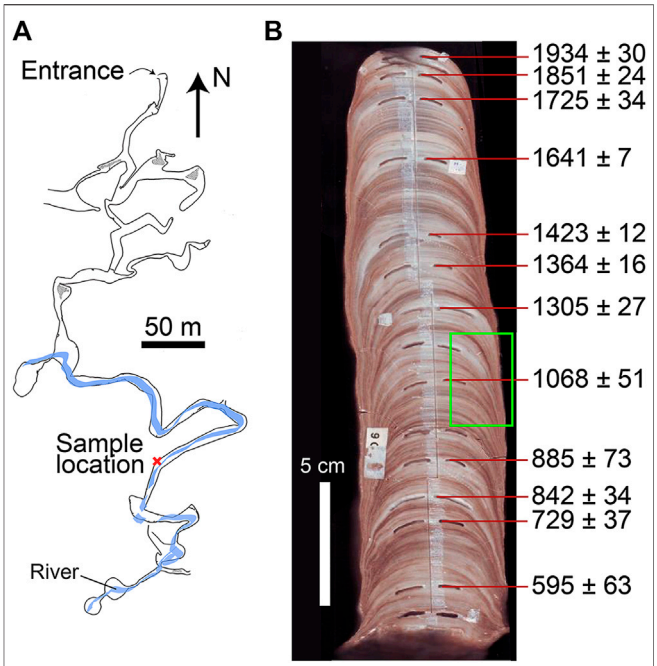

FIGURE 1 | (A) Map of the Pau D'Alho cave and **(B)** optical image of the ALHO6 stalagmite sample. Green region in panel **(B)** indicates the age range studied in this work. Hashed patches in panel **(A)** denote collapsed rock piles.

enrichment events compared to analysis of the central column and that changes in the deposition surface angle within our speleothem sample is unlikely to affect the relative intensities of measured peaks.

The compressed spatial scale of the speleothem flank section permitted our measurements, consisting of three tiled fields of view, to cover a 174 year interval between 957 CE and 1131 CE with temporal resolution ranging between 0.08 and 0.93 years per pixel. This period covers the Medieval Climate Anomaly (MCA) that occurred between 950 CE and 1250 CE. In tropical South America, this event was characterized a relatively dry climate caused by a weakened South American Summer Monsoon [SASM; (Vuille et al., 2012; Campos et al., 2019)]. This effect likely had widespread consequences for climate patterns across the South American continent as the SASM is responsible for ~70% of the rainfall over South America and is considered a key driver for climate variability over the continent.

Each QDM magnetic field map was acquired in an instantaneous bias magnetic field of 0.9 mT, which was reversed repeatedly during the course of measurement to provide a near-zero net bias field [**Figure 3**; (Glenn et al., 2017)]. As a result, each QDM experimental run produces two magnetic field maps simultaneously. The first map shows the fields resulting from remanent magnetization carried by ferromagnetic grains with coercivity greater than the 0.9 mT instantaneous bias field while the second map shows the induced magnetic field corresponding to the instantaneous bias field. For the measurements analyzed here, field reversals during measurement resulted in a residual bias field of ≤0.7 μT.

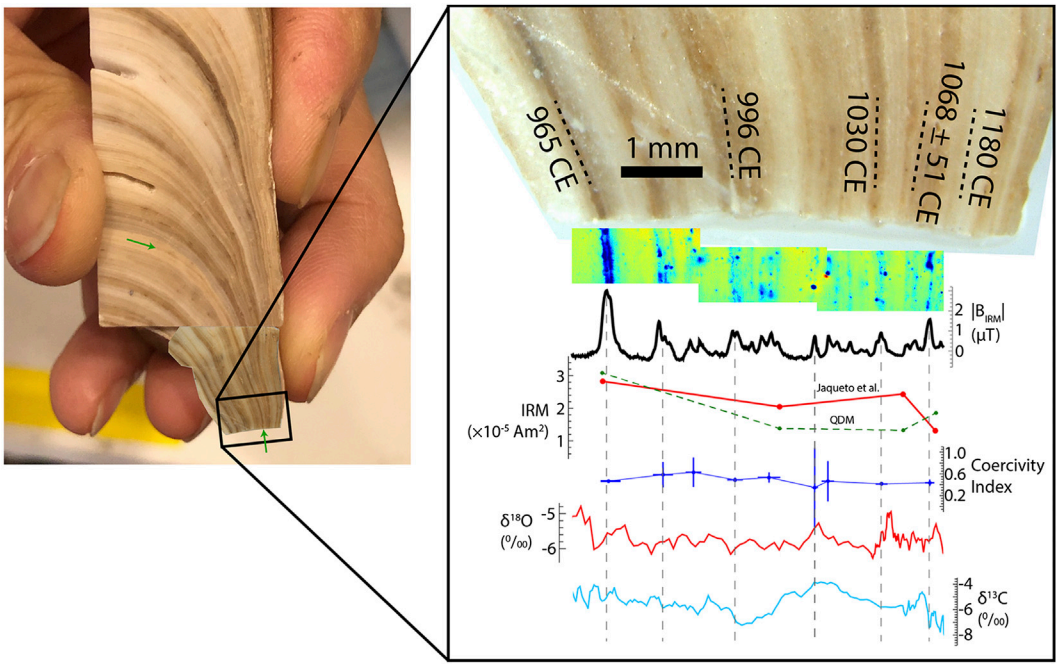

FIGURE 2 | Photographs of the measured sections of the ALHO6 speleothem with age dates, magnetic field time series, and $\delta^{18}O$ and $\delta^{13}C$ data. Age tie point of 1068 CE is based on U-Th dating of laminae while other tie points are interpolated from other U-Th ages based on distances in the speleothem central column. In right panel, first overlay shows the magnetic field map corresponding to a 1.5 T IRM oriented into the mapping plane. B_{IRM} curve is a time series of mean magnetic field intensity computed from the map above. Red and green IRM curves are the bulk samples of Jaqueto et al. (2016) and QDM magnetic field values binned to the same time intervals. Coercivity Index curve is computed for each magnetized band and approximates the fraction of total magnetization with coercivity between 17 and 70 mT. Vertical error bars are 2σ. Oxygen and carbon isotopic data are from Novello et al. (2016). In the left panel, green arrows highlight example of a lamina that shows much stronger coloration in the speleothem flank, although most laminae show greater continuity.

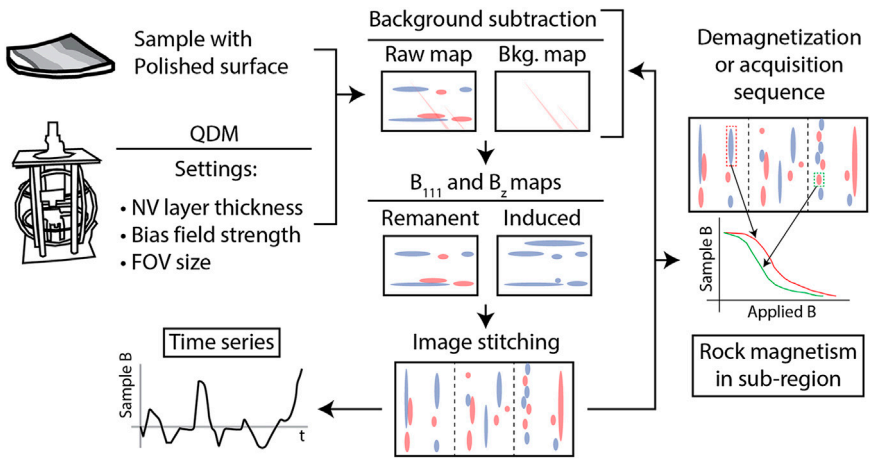

FIGURE 3 | Flowchart summary of experimental procedure. After we obtain a raw map of the magnetic field in the <111> crystallographic direction (B_{111}), we apply background subtraction where necessary, convert to B_z using a Fourier domain transform, and stitch adjacent fields of view using the optical image associated with each magnetic field map. A time series of magnetic field strength, which is a proxy for magnetization, can be obtained with an age model. Repeated imaging of the same field(s) of view combined with a demagnetization or remanence acquisition sequence can be used to construct demagnetization or acquisition curves for small sub-regions.

The resulting pair of maps therefore show the remanent magnetization in a ≤0.7 μT bias field and the induced magnetization in a 0.9 mT bias field.

We ran the QDM in projective magnetic microscopy (PMM) mode to maximize the signal-to-noize ratio (Glenn et al., 2017). The resulting raw maps therefore show the magnetic field

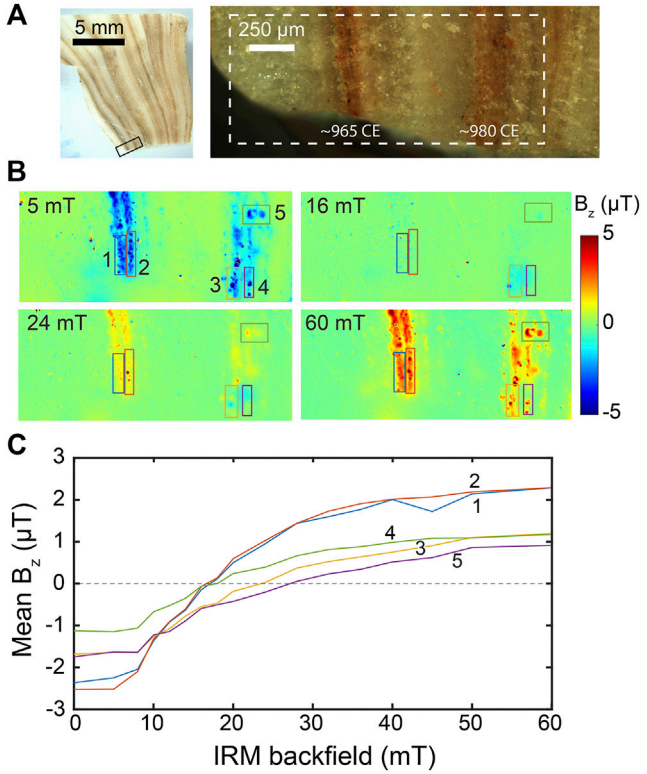

FIGURE 4 | Backfield IRM acquisition experiment from one field of field. **(A)** Reflected light, crossed polarizer images of the mapped region. **(B)** Vertical component of the magnetic field after the application of a 1.5 pulse IRM into the mapping plane and an IRM of the indicated strength out of the plane. Mapped region corresponds to white dashed box in panel **(A)**. **(C)** Backfield IRM acquisition curves of the five rectangular regions indicated in panel **(B)**.

strength in the <111> crystallographic direction, which is oriented toward 12 o'clock and 35.26° out of the mapping plane. For further analysis, we recomputed the maps to show the magnetic field component perpendicular to the surface (B_z) using a Fourier algorithm (Fu et al., 2020).

To recover rock magnetic information from speleothem samples, we first subjected the sample to a 1.5 T isothermal remanent magnetization (IRM) directed into the mapping plane. Previous rock magnetic characterization suggests that this treatment should result in a near-saturation magnetization carried by all but a small population of goethite or fine-grained hematite (Jaqueto et al., 2016). We then measured a backfield IRM acquisition sequence for a single field of view in steps of 2–10 mT up to 60 mT, at which point the magnetization in the QDM maps appeared to have fully reversed except for isolated regions (**Figure 4**). We further conducted a highly condensed backfield IRM acquisition experiment for all three ALHO6 fields of view by mapping the magnetic field after exposure to a downward 1.5 T IRM followed by upward 17 and 70 mT IRMs. Although speleothems typically have low concentrations of magnetic particles (Lascu and Feinberg, 2011), the applied IRMs resulted in generally strong magnetic field signals. We therefore used integration times of 30–60 min for our QDM magnetic field maps.

Due to artifacts arising from internal strain in the field-sensitive layer of the QDM diamond, we obtained blank magnetic field maps of an empty, polished quartz plate and subtracted it from the maps of speleothem magnetic fields (**Figure 5**). To construct time series extending beyond the coverage of a single QDM field of view, we imaged the magnetic fields in three tiled fields of view near the edge of the polished ALHO6 sample surface, using pixels located over empty space past the edge of the sample to calibrate the zero magnetic field value. We then stitched together the magnetic field maps by matching features in an optical image taken over the overlapping region. These optical images, which are taken using the QDM camera and optics, permit registration between the magnetic field maps and optical or electron microscope images with <5 µm accuracy.

Quantifying variations in the concentration of ferromagnetic minerals ultimately requires finding the per unit volume magnetization intensity. Although the magnetization intensity of unidirectionally magnetized sources such as the speleothem subjected to a saturation IRM can be determined uniquely (Feinberg et al., 2020), this technique cannot be used for backfield experiments that contain both positively and negatively oriented magnetizations. We therefore use the magnetic field strength observed at a fixed height above the sample as a proxy for the magnetization. This procedure requires repeatable positioning of the sample to the sensing diamond surface such that differences in sensor-to-sample distance do not bias the inferred intensity of magnetization. Using visible interference fringes between the polished sample surface and the diamond, we achieved reproducibility of 2 µm in the sensor-to-sample distance. Given the 10 µm thickness of the nitrogen-vacancy layer over which the magnetic field signal is averaged and the ~0.5 µm thickness of the speleothem sections, these variations result in negligible magnetic field changes due to sample positioning.

From the calibrated and stitched maps, we averaged the magnetic field value from pixels along lines parallel to visible laminae to produce a curve for the mean magnetic field intensity as a function of time (**Figure 3**). We assigned calendar year ages to each data point in the time series of magnetic field strength using linear interpolations between U-Th ages obtained from the same speleothem (Novello et al., 2016). The QDM-mapped time interval included a single U-Th age tie point at 1,068 ± 51 CE and is bracketed by two additional tie points at 885 ± 73 CE and 1,305 ± 27 CE. We note that these age uncertainties are not relevant to comparisons between our QDM-derived magnetic field time series and other datasets from ALHO6 such as bulk specimens magnetization and isotopic data as these time series are cross-referenced based on visible features on the speleothem itself.

To complement these magnetic field imaging data, we quantified the coloration of the speleothem section analyzed using the QDM by converting a diffusely illuminated optical image to grayscale and averaging the brightness value along each lamina. We then rescaled the brightness data such that the

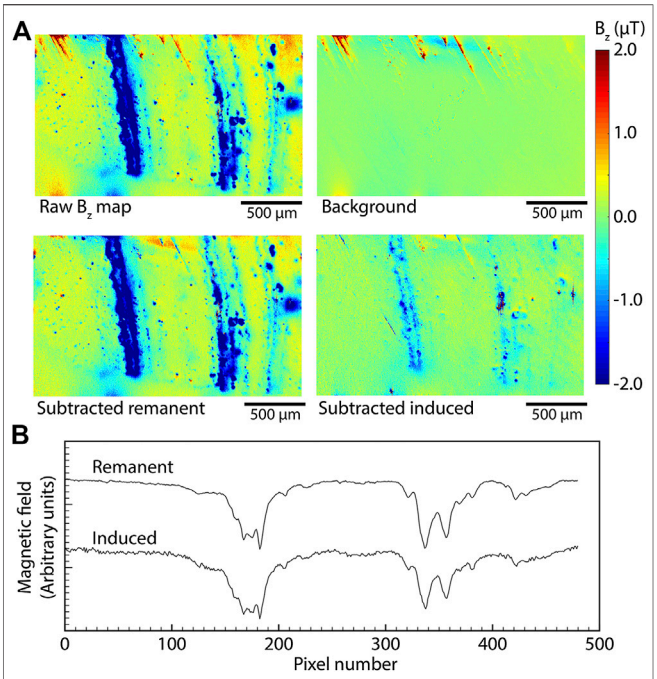

FIGURE 5 | Examples of high-resolution remanent and induced magnetization maps and demonstration of background subtraction. **(A)** Map of magnetic fields over the oldest of three mapped sections of the ALHO6 speleothem corresponding to approximately the 957–987 CE interval with time progressing toward the right. Sample has been imparted with a 1.5 T IRM in the into-the-plane (negative) direction. Positive and negative values denote the intensity of the magnetic field component out of and into to the mapping plane, respectively. **(B)** Field values in the remanent and induced field maps averaged across lines of equal deposition time.

maximum value is one and pure black is 0. To further support interpretation of the speleothem mineral assemblage, we obtained reflected light photomicrographs under crossed polar illumination on a Leica DM750 petrographic microscope and elemental maps of Si, Ca, and Mg using energy dispersive spectroscopy (EDS) on a JEOL 7900F electron microprobe at the Harvard Center for Nanoscale systems.

Finally, we performed spectral analysis to identify periodicities in the magnetic field time series using REDFIT (Schulz and Mudelsee, 2002) and wavelet analyses (Torrence and Compo, 1998) implemented in the software PAST (Hammer et al., 2001). All QDM remanence magnetic field maps and integrated magnetic field time series are available on the Harvard Dataverse (Fu, 2020).

RESULTS

Our time series of remanence-associated magnetic field over the ALHO6 speleothem extends over 174 years and shows strong concentrations of signal over narrow zones of high magnetic particle content (**Figure 5**). Compared to magnetization measured from bulk specimens (Jaqueto et al., 2016), the QDM-derived time series when binned at the same resolution appears to show a similar decrease in ferromagnetic content during the full analyzed interval between 957 CE and 1131 CE (**Figure 2**). The zones of high magnetization correlate clearly (Pearson correlation coefficient of $r^2 = 0.37$; P value of $P = 3.0 \times 10^{-9}$) with the speleothem color with darker laminae consistently showing stronger magnetic signal (**Figure 6**).

The laminae-scale resolution of the QDM time series can inform the interpretation of magnetization variations observed in the bulk specimens analysis. Specifically, the concentration of magnetic signal in a small subset of laminae suggests that the majority of magnetic particles are deposited during discrete events. Further, each strongly magnetic band is typically divided into between 2 and 6 identifiable and laterally continuous fine laminae with enhanced magnetic signal (**Figure 5**), revealing that the detrital events responsible for the magnetic particle enrichment interval were clustered in time. Although the major magnetized bands are generally associated with visually dark laminae, the fine-scale magnetized laminations are not identifiable in optical imagery and would not have been identifiable using lower resolution SQUID microscopy (**Figure 7**). Most prominently, the highly magnetic laminae corresponding to 965 CE may be responsible for the elevated ferromagnetic signal observed in the corresponding bulk specimens (**Figure 2**). As such, bulk specimen analyses of the ALHO6 and similar speleothems are effectively documenting the intensity and frequency of discrete events that lead to enhanced deposition of magnetic particles.

Comparing the full backfield acquisition curves over a mapped area can identify the spatial context of different grain populations. While a 70 mT backfield IRM is apparently sufficient to re-saturate most ferromagnetic grains, two sub-regions of the ~980 CE band show weaker magnetic signal after application of a 70 mT backfield IRM compared to after the original 1.5 T IRM (**Figure 4**, sub-regions 3 and 5). This behavior implies that these sub-regions contain a distinct, high-coercivity ferromagnetic mineral, which likely corresponds to the goethite or hematite phase detected in bulk sample analyses (Jaqueto et al., 2016). The coexistence of these mineral populations within the same laminae shows that both low-coercivity minerals, likely pedogenic magnetite (Jaqueto et al., 2016), and high-coercivity minerals, possibly weathered from overlying bedrock, are enriched simultaneously in the speleothem during the same depositional episode. Similarly, the spatially resolved backfield curves also indicate variations in the coercivity of remanence (H_{CR}), which corresponds to the x-axis cross value of the curve, within the same lamina (**Figure 4**, sub-regions 4 and 5). These observations suggest that the low and high-coercivity grain types sample the same source population of detrital material.

These contrasts among the coercivity spectra of specific locations within the same detritus-rich laminae demonstrate that localized regions within laminae may not be representative of the layer as a whole. We therefore

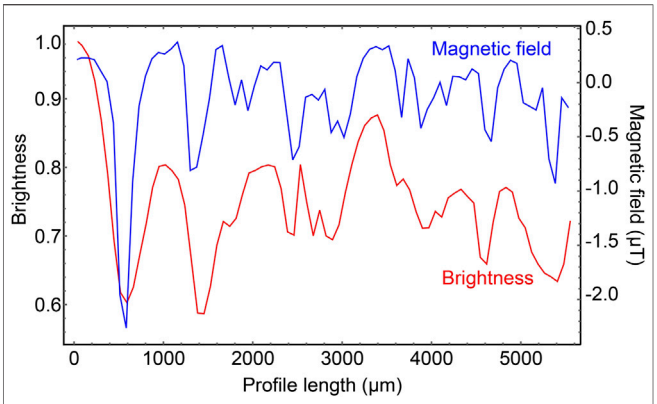

FIGURE 6 | Comparison between magnetic field intensity and grayscale brightness over the full QDM mapped profile with time progressing toward the right. The brightness levels have been normalized such that the maximum value is one and black is 0. Note that more negative values of magnetic field correspond to stronger magnetization due to the negative direction of the applied IRM. Both datasets have been binned in 48 μm intervals. Values on *x*-axis denote distance from the youngest end of the mapped profile.

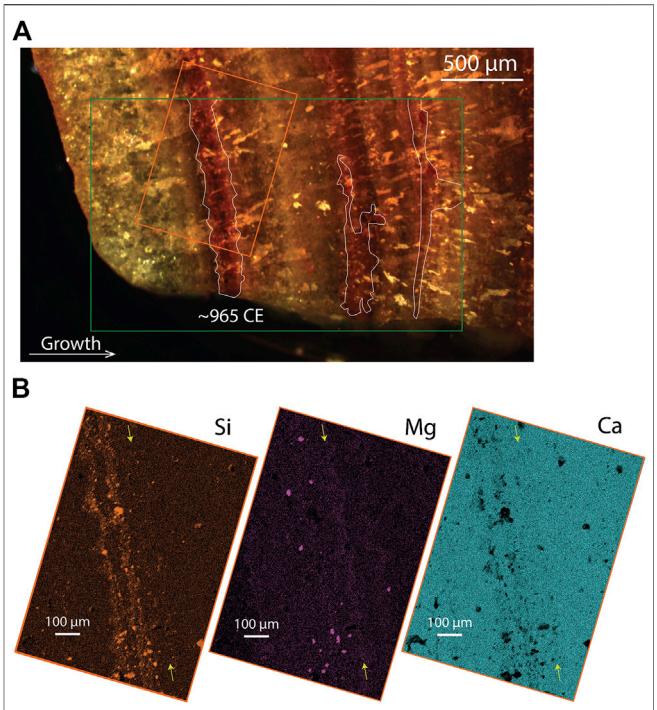

FIGURE 7 | Optical and electron microprobe analyses of a speleothem region covering the magnetically enriched 965 CE lamination. **(A)** Reflected light photomicrograph with crossed polarizers. Green box denotes the QDM field of view shown in **Figure 5**. Thin white outlines indicate the strongly magnetized regions. **(B)** EDS elemental composition maps of the orange boxed region in panel **(A)**. Yellow arrows indicate position of zone with enriched Mg in all three maps.

quantified both the mean and dispersion of coercivity for each magnetized band to construct our coercivity time series. We first conducted a highly condensed backfield IRM experiment, which consists of negative near-saturation IRM, a single intermediate IRM near the approximate H_{CR} value (17 mT), and a positive near-saturation IRM (**Figure 2**). We then defined a parameter called the coercivity index that can be computed for each lamina in all three fields of view. This coercivity index is equal to the difference in magnetic field intensity between the final and the intermediate IRMs normalized by the difference between the positive and negative near-saturation IRMs. As such, this parameter effectively quantifies the fraction of remanence with coercivity above 17 mT.

We computed the mean coercivity index in four, equally sized sub-sections of each magnetized lamina. The scatter in the coercivity index among the four sub-sections is then used to compute a standard deviation around the combined mean value. Accounting for this scatter within individual laminae, we find no significant change in the coercivity index of successive magnetized laminae (**Figure 2**).

Another potential source of rock magnetic information about the speleothem laminae is the comparison between maps of remanent and induced magnetic fields, which can be obtained simultaneously on each field of view. This analysis for the ALHO6 fields of view found close similarity between the magnetic field pattern generated by a saturation remanence and by the induced magnetization (**Figure 5**). From this observation we infer that the bulk of remanent magnetization and low-field induced magnetization are carried by the same grain population, which likely consists of fine-grained magnetite (Jaqueto et al., 2016). In agreement with the coercivity index analysis above, differences in the ratio of induced to remanent magnetization are not clearly resolved between successive laminae.

DISCUSSION

Our QDM-based analysis of the ALHO6 section has provided an annually resolved time series quantifying variations in both the concentration and coercivity of ferromagnetic detrital particles. We now use these observations to investigate the mechanisms driving variations in magnetization and their paleoenvironmental implications. The concentration of most magnetic field signal in discrete, strongly magnetized laminae is similar to the magnetization pattern observed in a North American speleothem taken from Spring Valley Caverns, Minnesota and analyzed using the SQUID microscope (Feinberg et al., 2020). Well-defined magnetized horizons in that speleothem correspond to major flooding events, some of which were known from the historical record.

By analogy, episodic flooding events are a candidate source of detrital grains in the ALHO6 sample. However, no independent record of flooding exists for the Pau D'Alho cave in the investigated time interval to provide a direct test of this hypothesis. As a potentially relevant proxy record, $\delta^{18}O$ values, which are most likely governed by the amount effect resulting in more negative values during times of stronger precipitation (Novello et al., 2016), do not show any consistent positive or negative excursions corresponding to the most magnetic laminae in our sample (**Figure 2**). This lack of

strong correlation between $\delta^{18}O$ and speleothem magnetism has been noted in previous observations (Font et al., 2014), although Jaqueto et al. (2016) found evidence for limited correspondence between high $\delta^{18}O$ values and high magnetization intensity at multi-decadal timescales in the ALHO6 sample. However, $\delta^{18}O$ is partially controlled by regional and global factors uncorrelated with local precipitation, while major flooding events are associated with high precipitation on multiple timescales and may not be well-predicted by short-term precipitation alone (Seiler et al., 2002; Lachniet, 2009). Therefore, the $\delta^{18}O$ record is unlikely to provide a high-fidelity record of past flooding in the Pau D'Alho cave, and its lack of correlation with the magnetic signal does not provide evidence in favor of or against a flood origin for the detritus-rich layers.

Our QDM magnetic field imaging of the ALHO6 speleothem may aid in testing a flood mechanism for the concentration of magnetic particles. Previous researchers have used the occurrence of dissolution features (Railsback et al., 2013; Frisia, 2015) and the presence of coarse detrital clay particles as evidence for a flood origin (Dasgupta et al., 2010). At the ≤100 μm scale, our maps show that the magnetized horizons are sub-divided into thin, continuous laminae with enhanced magnetic signal (**Figure 5**). Optical observations of dark laminae that correspond to the stronger magnetized horizons also show no evidence for dissolution such as microcavities (**Figures 1**, **7**). Although the strongly magnetized bands indeed show enrichment in coarse detrital silicates as expected for flood deposits (**Figure 7B**), they occur in much lower concentrations than in known flood deposits (Dasgupta et al., 2010).

In addition, because more severe flood events are able to loft and transport coarser grain sediments, the most prominent flood-related detrital layers are expected to contain coarser grains than minor layers (González-Lemos et al., 2015). The presence of a coarser grain population, which is more likely to exhibit multidomain behavior, in the most prominent flood layers would likely result in a shift toward softer coercivities (Dunlop and Ozdemir, 1997). Further, a shift in the grain size distribution is likely to change the relative abundance of magnetite and higher coercivity goethite and hematite particles, which are unlikely to have the same grain size distribution. Such a compositional shift would result in additional change in coercivity. Our QDM mapping, however, reveals no resolvable correlation between coercivity and the intensity of magnetization in magnetized laminae (**Figure 2**). Instead, the coercivity index time series suggests that the same population of ferromagnetic particles was incorporated throughout the analyzed time interval.

Finally, although the ALHO6 speleothem was sampled at a relative narrow corridor in Pau d'Alho cave close to a river stream that is subjected to episodic floods (**Figure 1**), the water from this river was observed to be predominantly limpid during a 13-months cave monitoring study (Novello et al., 2016). Therefore, it is unlikely for floods from this river to deposit allochthonous mineral grains on nearby stalagmites. Combining these observations, we find that flood events are an unlikely explanation for the formation of magnetized bands in the ALHO6 speleothem.

Aside from flood events, a hiatus or slowdown in speleothem deposition may also lead to concentration of detrital particles, leading to layers with high Fe content that are difficult to distinguish from flood-deposited horizons (Wassenburg et al., 2012; Denniston and Leutscher, 2017). As an additional factor, vegetation retreat during dry intervals may enhance soil erosion, further enhancing detrital particle delivery to the speleothem during periods of slow growth. Focusing first on the morphology of magnetized layers imaged in the QDM, most magnetized horizons are thin (<50 μm), continuous, and occur in groups that include one or more strongly magnetized layers. This morphology is most similar to L-type layer bounding surfaces deposited during intervals of reduced or halted speleothem growth. Such aridity-induced features are associated with fine-grained detritus and typically include groups of laminae that show smaller progressively separation [**Figure 5**; (Railsback et al., 2013)].

The observation of constant coercivity through time, which is inconsistent with a flood origin as discussed above, may be more consistent with a hiatus or slow deposition origin for the detritally enriched horizons. In this scenario, brief decreases or hiatuses in the speleothem growth rate would have led to the concentration of detrital particles, forming the thin, <20 μm detritus-enriched layers observed in the QDM maps (**Figures 1**, **4**). Meanwhile, prolonged slowdowns in growth would have caused the major magnetized bands. Given the location of the ALHO6 speleothem far from the cave entrance, the ultimate source of the accumulating particles was likely epikarstic soil washed down into the cave and carried by drip water instead of airborne dust (Herman et al., 2012). In either case, the source population of detrital grains is controlled by the composition of surrounding soils and not expected to covary with speleothem growth rate. This formation mechanism is therefore compatible with the observation of indistinguishable coercivities in major and minor magnetized bands.

Our analyses of crystal habit and elemental composition in the ALH6 speleothem may provide additional tests for the hypothesis that magnetized zones are associated with hiatuses or slow deposition. Reflected light imaging through crossed polarizers shows that strongly magnetic horizons are associated with fine grained (≤10 μm), unoriented calcite crystals intermixed with 10 μm scale silicate grains (**Figure 7**). These horizons immediately precede columnar calcite with 100–400 μm length grains. Although by itself not a conclusive indicator of past moisture environment, fine-grained calcite layers with fine detrital enrichment followed in time by coarse, pure columnar calcite growth have been associated with hiatuses in other studied speleothems (Frisia, 2015; González-Lemos et al., 2015; Vanghi et al., 2019). Further, one textural study at sub-annual resolution has suggested that cycles of fine-grained calcite followed by columnar habits correspond to higher and lower calcite saturation in the drip water, respectively (Mattey et al., 2008). If the textural changes in the ALHO6 sample are caused by a similar mechanism, it would provide support for an association between fine-grained, highly magnetic zones with low moisture.

Similarly, variations in calcite Mg/Ca ratios can indicate shifts in local hydroclimate. Specifically, higher Mg/Ca is frequently

attributed to prior calcite precipitation (PCP), which refers to the exsolution of calcite out of percolating water prior to deposition on the speleothem. Because increased PCP implies higher calcite saturation in the drip water, higher Mg/Ca is indicative of dryer conditions or low pCO_2 in the cave environment (Hellstrom and McCulloch, 2000; Huang and Fairchild, 2001; Cruz et al., 2007; Fairchild and Treble, 2009; Oster et al., 2012). Our electron microprobe imaging of the ~965 CE magnetized horizon revealed higher Mg counts in the interval corresponding to strong magnetizations while Ca counts remained constant throughout. Some Mg enrichment, especially as strong isolated sources, are correlated with Si enrichment. These Mg sources can be attributed to detrital particle enrichment and are unrelated to PCP-induced shifts in the Mg/Ca ratio. However, the Mg map also shows diffuse enrichment not clearly associated with Si signal (**Figure 7B**), which suggests a distinct, non-detrital enrichment mechanism. In addition, regions of diffuse Si enrichment do not correlate with high Mg, implying that fine silicate particles are not detectable in the Mg map and cannot explain the regions of diffuse Mg enrichment. These observations strongly suggest that the higher Mg/Ca ratios in ratios of diffusely enriched Mg are due to higher Mg/Ca in the host carbonate. If this shift is due to increased PCP, it most likely suggests the occurrence of drier conditions during the deposition of magnetic intervals because cave pCO_2, which is an alternative driver of Mg/Ca change, typically varies on much shorter, sub-annual timescales (Baldini et al., 2008; Oster et al., 2012).

As a further test for the dry interval hypothesis of magnetic enrichment, we examine the $\delta^{18}O$ record, which may document variations in ancient precipitation. Our high temporal resolution time series does not show a significant correlation between magnetization and $\delta^{18}O$ ($r^2 = -0.003$), in contrast with the work of Jaqueto et al. (2016) on the same speleothem at coarser resolution (**Figure 2**). As discussed in the Materials and Methods section, the fact that our samples derive from the flank of the speleothem while the $\delta^{18}O$ record was taken from the central column is unlikely to explain the lack of correlation.

The specific time interval chosen for the analysis, which corresponds to the MCA (Vuille et al., 2012), may contribute to the lack of correlations between magnetic and $\delta^{18}O$ records, as the strongest correlation between bulk specimens magnetization and $\delta^{18}O$ was observed prior to 900 CE and after 1450 CE. Further, the mechanisms controlling variations in magnetization and $\delta^{18}O$ may not respond to climate forcings on the same timescales, resulting in decoupling at the highest resolution. For example, local $\delta^{18}O$ may be influenced by the composition of upstream rainwater within a single watershed, leading to a spatial and temporal averaging effect while magnetization, according to our hypothesis, reflects the balance between local moisture and dust mobilization. Therefore, the lack of correlation between magnetization and $\delta^{18}O$ at annual to sub-annual timescales does not support or rule out a connection between speleothem magnetization and local precipitation intensity.

In contrast to our annual resolution study, Jaqueto et al. (2016) observed that strong bulk specimens magnetizations correlate with positive $\delta^{18}O$ excursions on multi-decadal to century timescales. Assuming the amount effect as the dominant driver of $\delta^{18}O$ variation on annual to decadal timescales, this observation implies that stronger magnetizations occurred during times of reduced precipitation. To explain this correspondence, the previous authors argued that sparser vegetation during drier intervals enhanced erosion in the overlying soil. Similar correspondence between less depleted $\delta^{13}C$ compositions and strong bulk specimens magnetizations provided further direct support for an ecosystem shift toward aridity-tolerant grassland plants during times of higher magnetic particle flux.

Although our high-resolution magnetization time series does not show direct correlation with either $\delta^{18}O$ or $\delta^{13}C$ variations (**Figure 2**), our aridity-driven hypothesis for the formation of magnetized laminae is compatible with the apparent correspondence between magnetization and these stable isotope proxies at longer timescales. Comparison of our binned data with bulk specimens results as presented above suggests that other periods of strong magnetization in the Jaqueto et al. (2016) analysis likely correspond to more frequent occurrence of magnetized bands. Less depleted $\delta^{18}O$ and $\delta^{13}C$ signals during these intervals point to a drier environment, which is fully consistent with our interpretation that decrease or hiatus in the rate of speleothem deposition leads to magnetic particle enrichment.

Finally, speleothem coloration, which in our sample is correlated with magnetic particle content (**Figure 6**), has been suggested as an indicator of past hydroclimate in other speleothems. Several studies have found darker coloration to be associated with enrichment in organics and wetter conditions (van Beynen et al., 2001; Martínez-Pillado et al., 2020), which, if applicable to the ALHO6 sample, would contradict our interpretation of aridity-driven magnetic particle enrichment. However, the presence of fine detrital particles, associated with flooding or hiatus, may also lead to darker coloration (Dasgupta et al., 2010; González-Lemos et al., 2015). This coloration mechanism is consistent with optical and electron microprobe observations of ALHO6 that reveal enrichment of silicate minerals and visible opaque phases corresponding to magnetized zones (**Figure 7**).

However, not all magnetic horizons can be associated with detrital horizons visible in optical or electron microscopy. This lack of corresponding visible grains may be because the remanence-carrying ferromagnetic grains are smaller than the resolution of these microscopy techniques, which is consistent with the pseudo-single domain behavior of the bulk rock magnetic samples (Jaqueto et al., 2016). At the same time, magnetic field measurements are sensitive to ferromagnetic particles buried beneath the polished surface and is indicative of the detrital particle concentration throughout a larger volume than optical or electron microscopy. We therefore argue that magnetization in the ALHO6 sample is a more sensitive indicator of detrital particle enrichment than coloration alone.

Our observation that the magnetic signal is concentrated in distinct 10–100 μm intervals demonstrates that enhancements in speleothem magnetization occurred in multiple discrete events. This behavior suggests that magnetic particle concentration was

driven by individual hiatuses instead of solely by generally enhanced soil erosion during dry intervals, which is caused by vegetation changes and likely to be elevated during the full duration of aridity (Jaqueto et al., 2016). Fine-scale magnetic imaging of the ALHO6 speleothem, therefore, shifts the emphasis from soil erosion to the speleothem growth rate as the primary driver of detrital enrichment (Jaqueto et al., 2016). We note, however, that slow speleothem growth and enhanced soil erosion are likely to occur simultaneously during arid intervals and may both contribute to the enhancement of detrital content in ALHO6.

Although no significant correlation exists between our magnetic field data and previously published $\delta^{18}O$ and $\delta^{13}C$ time series [see above; (Novello et al., 2016)], the two datasets may contain overlapping peaks in the frequency domain. To test this, we performed spectral analysis on the full magnetic field time series using the REDFIT routine, which revealed periodicities between 18 and 45 years with ≥99% significance level (**Figure 8A**). Our complementary wavelet analysis confirmed the existence of significant periodicity in this frequency range throughout the entire time interval of our data (**Figure 8B**). In comparison, the ALHO6 oxygen isotopic record from an approximately 1,600 year interval found a dominant periodicity of 208 years along with other significant periodicities of 83, 31, 18–16, 11, 9 and 7–3 years. Most of these periodicities were interpreted to be associated with solar cycles influencing the SASM. Comparison to the magnetic field data shows that both datasets contain significant power with ~30 and ~18 years periodicity, although the latter is only significant during the early part of the magnetically analyzed interval. The dominant periodicity in the $\delta^{18}O$ data could not be recovered from the magnetic field time series due the short, 174 years duration of the latter. This correspondence between the spectral content of the two time series despite a lack of time domain correlation may be due to an offset in their age calibrations over part of the time interval. Regardless, the similar spectral characteristics of the magnetic field and $\delta^{18}O$ data suggests that the two quantities may respond to similar drivers, including environmental moisture.

The occurrence of thin magnetically enriched horizons both before and after major magnetized bands suggests that, if detrital particle enrichment was due to dryness as argued above, these sets of magnetized layers during multi-year dry intervals during which speleothem growth rate gradually slowed to minimum, possibly null, rate and recovered over a similar interval. The preservation of an apparent transitional period prior to the main magnetized laminae indicates the lack of dissolution during the interval of peak aridity, which is supported by the lack of erosion and replacement features such as microcavities (Railsback et al., 2013). Future high-resolution U-Th dating of the speleothem combined with QDM analysis of magnetic particle concentration may allow quantification of the aridity onset timescale. Comparison between the present dataset, which reflects drier, weak monsoon conditions during the MCA, and the magnetization record outside of the MCA may help to determine to what degree the severity and the frequency of drought each contributed to the enhanced aridity during this anomalous period.

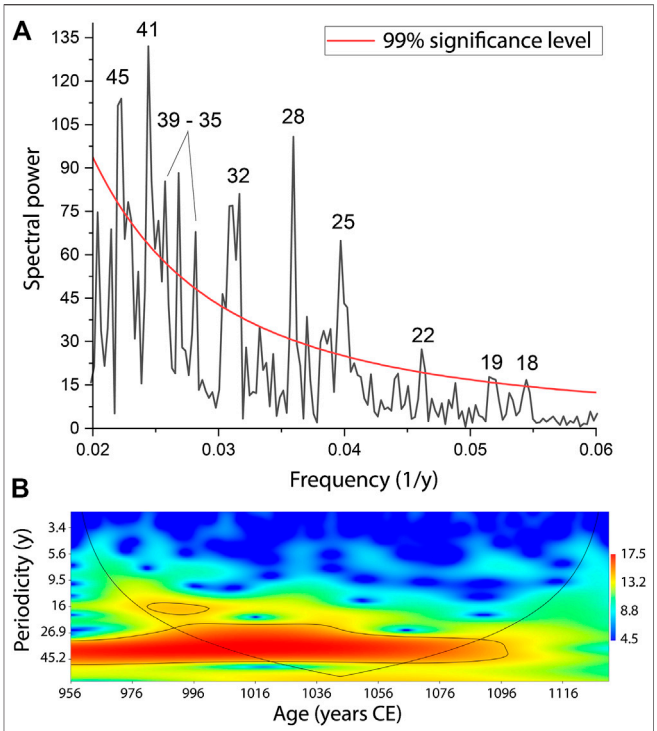

FIGURE 8 | Spectral analysis of the magnetic field time series. **(A)** Spectral analysis (REDFIT) performed on the magnetic time series (in units of μT and with equally spaced 0.25 years intervals) using the software PAST2 (Hammer et al., 2001). The parameters used were: *window*: rectangle; *oversample*: 2; *segment*: 5. The red line represents the 99% χ^2 confidence level. The number above the picks indicates the periodicity values in years. **(B)** Wavelet analysis performed on the magnetic field time series using the software PAST and the Morlet mother wavelet (Torrence and Compton, 1998). Black lines indicate the 95% significance level and the cone of influence, inside of which the record is of sufficient length to interpret results.

SUMMARY AND OUTLOOK

Our QDM magnetic field imaging of the ALHO6 speleothem has produced the first time series of multiple rock magnetic parameters with annual to sub-annual resolution. We find that the distribution of ferromagnetic content within the speleothem is highly non-uniform, with virtually all resolvable signal occurring in 10–100 μm scale horizons of high magnetic field intensity (**Figure 5**). The coercivity of magnetic particles as determined by backfield IRM acquisition experiments vary within individual laminae, indicating that magnetic hard and soft grain populations were deposited simultaneously and therefore likely sample the same detrital particle source.

The averaged coercivity of discrete magnetized regions does not show resolvable variation over the 174 years interval of measurements. This lack of covariance between the amplitude and detrital grain size of magnetized layers, coupled with the clustered nature of magnetized horizons and the lack of coarse detrital material, suggests that magnetized layers formed due to detritus accumulation during times of slow or halted speleothem growth instead of during flood events.

This aridity-driven origin of magnetization is also compatible with apparent correlations at longer timescales between the speleothem magnetization and positive $\delta^{18}O$ excursions assuming that the amount effect is the primary driver of $\delta^{18}O$ variability (Jaqueto et al., 2016). Finally the change in calcite crystal habit and higher Mg/Ca ratios in highly magnetized zone provide further support for dryness, which is likely accompanied by vegetation retreat and enhanced soil erosion, as the driver of magnetic particle enrichment. If the association between magnetization and aridity is correct, the presence of multiple thin (~20 μm) magnetized horizons pre- and post-dating the main magnetized laminae suggests that the arid intervals occurred with gradual onset and resolution.

Future QDM imaging of speleothems from Pau D'Alho and surrounding caves during other time intervals can test the consistency of the detrital particle enrichment mechanism. In particular, because our analyzed time period occurred during a generally drier interval in central Brazil corresponding to the MCA (Vuille et al., 2012), data from wetter intervals may show different controls on the occurrence and intensity of magnetic enhancement.

Other future QDM-based studies can be used to characterize the micrometer-scale morphology and rock magnetism of speleothem samples from other cave systems and climate regions. In particular, extra-tropical speleothems from North America and China have been described with positive correlations between speleothem magnetism and inferred paleoprecipitation (Bourne et al., 2015; Zhu et al., 2017), which is the opposite of the relationship found in the ALHO6 sample. QDM magnetic field imaging of these samples may provide insight into the mechanism of detrital enrichment. For example, inference of anomalously coarse mineral grains in major detrital horizons through coercivity analysis would provide support for paleofloods as the main delivery mechanism (González-Lemos et al., 2015). Meanwhile, magnetization due to dispersed magnetic grains sampling a single source population would suggest that bulk speleothem magnetization is modulated by the flux of fine particles carried into the cave via drip water. Such studies would provide a foundation toward understanding the diverse processes influencing the concentration of detrital material in speleothems and inform the paleoclimate interpretations of observed variations.

High-resolution time series provided by QDM analyses would also permit novel comparisons between magnetization and other measurements or proxies taken at annual to sub-annual resolutions. Importantly, QDM-produced time series can match or exceed the temporal resolution of $\delta^{18}O$ records, enabling testing of the mechanisms that drive stable isotope fractionation at short timescales. At the same time, direct comparison between QDM-generated time series and historical records such as rain gauge data may produce conclusive tests regarding the mechanism of magnetic particle enrichment, at least in specific cave settings. If such studies can establish a consistent relationship between past precipitation conditions and speleothem magnetization, QDM imaging may be able to provide annually resolved records of local moisture over thousand-year timespans.

DATA AVAILABILITY STATEMENT

The original contributions presented in the study are included in the article while all raw data are availble in the Harvard Dataverse (Fu, 2020).

AUTHOR CONTRIBUTIONS

RF: Managed project, performed most measurements and analysis, and wrote paper. KH: Performed measurements and analysis. Edited paper. PJ: Provided samples, helped with analysis, and edited paper. VN: Provided discussions and edited paper. TK: Provided key discussions and edited paper. RT: Provided samples, managed project, and edited paper. NS: Provided key discussions and edited paper. FC: Provided samples. OD: Provided technical support with magnetic field measurements.

FUNDING

Funding for RF and KH was provided by the Lemann Brazil Fund and NSF Grant PHY-1843727. This work was performed in part at the Harvard Center for Nanoscale Systems (CNS), which is supported by the National Science Foundation under NSF Award 1541959. Further support for this work was provided by the São Paulo Research Foundation Grants 2016/24870-2, 2019/0670-9 and by the Serrapilheira Institute (Serra-1812-27990). Two reviewers contributed their valuable insights to this work.

ACKNOWLEDGMENTS

We are grateful to Instituto Brasileiro do Meio Ambiente e dos Recursos Renováveis for permission to collect stalagmite samples. We thank T. Cavanaugh for help with electron microscopy.

REFERENCES

Baldini, J. U. L., McDermott, F., Hoffmann, D. L., Richards, D. A., and Clipson, N. (2008). Very high-frequency and seasonal cave atmosphere PCO_2 variability: implications for stalagmite growth and oxygen isotope-based paleoclimate records: Earth Planet. *Sci. Lett.* 272, 118–129. doi:10.1016/j.epsl.2008.04.031

Bloemendal, J., King, J. W., Hall, F. R., and Doh, S.-J. (1992). Rock magnetism of Late Neogene and Pleistocene deep-sea sediments: relationship to sediment source, diagenetic processes, and the sediment lithology. *J. Geophys. Res.* 97, 4361–4375. doi:10.1029/91JB03068

Blundell, A., Hannam, J. A., Dearing, J. A., and Boyle, J. F. (2009). Detecting atmospheric pollution in surface soils using magnetic measurements: a reappraisal using an England and Wales database. *Environ. Pollut.* 157, 2878–2890. doi:10.1016/j.envpol.2009.02.031

Bourne, M. D., Feinberg, J. M., Strauss, B. E., Hardt, B., Cheng, H., Rowe, H. D., et al. (2015). Long-term changes in precipitation recorded by magnetic minerals in speleothems. *Geology* 43, 595–598. doi:10.1130/G36695.1

Campos, J. L. P. S., Cruz, F. W., Ambrizzi, T., Deininger, M., Vuille, M., Novello, V. F., et al. (2019). Coherent South American Monsoon variability during the last millennium revealed through high-resolution proxy records: Geophys. *Res. Lett.* 46, 8261–8270. doi:10.1029/2019GL082513

Cruz, F. W., Burns, S. J., Jercinovic, M., Karmann, I., Sharp, W. D., and Vuille, M. (2007). Evidence of rainfall variations in Southern Brazil from trace element ratios (Mg/Ca and Sr/Ca) in a Late Pleistocene stalagmite. *Geochem. Cosmochim. Acta.* 71, 2250–2263. doi:10.1016/j.gca.2007.02.005

Dasgupta, S., Saar, M. O., Edwards, R. L., Shen, C.-C., Cheng, H., and Alexander, E. C. (2010). Three thousand years of extreme rainfall events recorded in stalagmites from Spring Valley Caverns, Minnesota. *Earth Planet Sci. Lett.* 300, 46–54. doi:10.1016/j.epsl.2010.09.032

Denniston, R. F., and Leutscher, M. (2017). Speleothems as high-resolution paleoflood archives. *Quat. Sci. Rev.* 170, 1–13. doi:10.1016/j.quascirev.2017.05.006

Dorale, J. A., and Liu, Z. (2009). Limitations of the Hendy test criteria in judging the paleoclimatic suitability of speleothems and the need for replication. *J. Cave Karst Stud.* 71, 73–80.

Dunlop, D. J., and Ozdemir, O. (1997). *Rock magnetism: fundamentals and Frontiers*. Cambridge, United Kingdom: Cambridge University Press, 573.

Fairchild, I. J., and Treble, P. C. (2009). Trace elements in speleothems as recorders of environmental change. *Quat. Sci. Rev.* 28, 449–468. doi:10.1016/j.quascirev.2008.11.007

Feinberg, J. M., Lascu, I., Lima, E. A., Weiss, B. P., Dorale, J. A., Alexander, E. C., et al. (2020). Magnetic detection of paleoflood layers in stalagmites and implications for historical land use changes: Earth Planet. *Sci. Lett.* 530, 115946. doi:10.1016/j.epsl.2019.115946

Font, E., Veiga-Pires, C., Pozo, M., Carvallo, C., de Siquiera Neto, A. C., Camps, P., et al. (2014). Magnetic fingerprint of southern Portuguese speleothems and implications for paleomagnetism and environmental magnetism. *J. Geophys. Res. Solid Earth* 119, 7993–8020. doi:10.1002/2014JB011381

Frisia, S. (2015). Microstratigraphic logging of calcite fabrics in speleothems as tool for palaeoclimate studies. *Int. J. Speleol.* 44, 1–16. doi:10.5038/1827-806X.44.1.1

Fu, R. R, Lima, E. A., Volk, M. W. R., and Trubko, R. (2020). High sensitivity moment magnetometry with the quantum diamond microscope. *Geochem. Geophys. Geosyst.* 21, e2020GC009147. doi:10.1029/2020GC009147

Fu, R. (2020). Replication data for: High-resolution environmental magnetism using the quantum diamond microscope (QDM): application to a tropical speleothem. Harvard Dataverse, V1. doi:10.7910/DVN/BQ1LCB

Glenn, D. R., Fu, R. R., Kehayias, P., Le Sage, D., Lima, E. A., Weiss, B. P., et al. (2017). Micrometer-scale magnetic imaging of geological samples using a quantum diamond microscope. *Geochemistry, Geophysics, Geosystems* 18, 2017GC006946. doi:10.1002/2017GC006946

González-Lemos, S., Müller, W., Pisonero, J., Cheng, H., Edwards, R. L., and Stoll, H. M. (2015). Holocene flood frequency reconstruction from speleothems in northern Spain. *Quat. Sci. Rev.* 127, 129–140. doi:10.1016/j.quascirev.2015.06.002

Hammer, O., Harper, D. A. T., and Ryan, P. D. (2001). Paleontological statistics software package for education and data analysis. *Palaeontol. Electron* 4, 1–9.

Hellstrom, J. C., and McCulloch, M. T. (2000). Multi-proxy constraints on the climatic significance of trace element records from a New Zealand speleothem. *Earth Planet Sci. Lett.* 179, 287–297. doi:10.1016/S0012-821X(00)00115-1

Herman, E. K., Toran, L., and White, W. B. (2012). Clastic sediment transport and storage in fluviokarst aquifers: an essential component of karst hydrogeology. *Carbonates Evaporites* 27, 211–241. doi:10.1007/s13146-012-0112-7

Huang, Y., and Fairchild, I. J. (2001). Partitioning of Sr^{2+} and Mg^{2+} into calcite under karst-analogue experimental conditions. *Geochem. Cosmochim. Acta.* 65, 47–62. doi:10.1016/S0016-7037(00)00513-5

Jaqueto, P., Trindade, R. I. F., Hartmann, G. A., Novello, V. F., Cruz, F. W., Karmann, I., et al. (2016). Linking speleothem and soil magnetism in the Pau d'Alho cave (central South America). *J. Geophys. Res. Solid Earth* 121, 7024–7039. doi:10.1002/2016jb013541

Lachniet, M. (2009). Climatic and environmental controls on speleothem oxygen-isotope values. *Quat. Sci. Rev.* 28, 412–432. doi:10.1016/j.quascirev.2008.10.021

Lascu, I., and Feinberg, J. M. (2011). Speleothem magnetism. *Quat. Sci. Rev.* 30, 3306–3320. doi:10.1016/j.quascirev.2011.08.004

Liu, Q., Deng, C., Torrent, J., and Zhu, R. (2007). Review of recent developments in mineral magnetism of the Chinese loess. *Quat. Sci. Rev.* 26, 368–385. doi:10.1016/j.quascirev.2006.08.004

Liu, Q., Roberts, A. P., Larrasoaña, J. C., Banerjee, S. K., Guyodo, Y., Tauxe, L., et al. (2012). Environmental magnetism: principles and applications. *Rev. Geophys.* 50, RG4002. doi:10.1029/2012RG000393

Maher, B. A., Mutch, T. J., and Cunningham, D. (2009). Magnetic and geochemical characteristics of gobi desert surface sediments: implications for provenance of the Chinese loess plateau. *Geology* 37, 279–282. doi:10.1130/G25293A.1

Maher, B. A., Thompson, R., and Zhou, L. P. (1994). Spatial and temporal reconstructions of changes in the Asian palaeomonsoon: a new mineral magnetic approach. *Earth Planet Sci. Lett.* 125, 461–471. doi:10.1016/0012-821X(94)90232-1

Martínez-Pillado, V., Yusta, I., Iriarte, E., Álvaro, A., Ortega, N., Aranburu, A., et al. (2020). The red coloration of Goikoetxe Cave's speleothems (Busturia, Spain): an indicator of paleoclimatic changes. *Quat. Int.* 566-567, 141–151. doi:10.1016/j.quaint.2020.04.006

Mattey, D., Lowry, D., Duffet, J., Fisher, R., Hodge, E., and Frisia, S. (2008). A 53 year seasonally resolved oxygen and carbon isotope record from a modern Gibraltar speleothem: reconstructed drip water and relationship to local precipitation: Earth Planet. *Sci. Lett.* 269, 80–95. doi:10.1016/j.epsl.2008.01.051

McDermott, F. (2004). Palaeo-climate reconstruction from stable isotope variations in speleothems: a review. *Quat. Sci. Rev.* 23, 901–918. doi:10.1016/j.quascirev.2003.06.021

Novello, V. F., Vuille, M., Cruz, F. W., Stríkis, N. M., de Paula, M. S., Edwards, R. L., et al. (2016). Centennial-scale solar forcing of the South American Monsoon System recorded in stalagmites. *Sci. Rep.* 6, 24762. doi:10.1038/srep24762

Oster, J. L., Montañez, I. P., and Kelley, N. P. (2012). Response of a modern cave system to large seasonal precipitation variability. *Geochem. Cosmochim. Acta.* 91, 92–108. doi:10.1016/j.gca.2012.05.027

Ponte, J. M., Font, E., Veiga-Pires, C., Hillaire-Marcel, C., and Ghaleb, B. (2017). The effect of speleothem surface slope on the remanent magnetic inclination. *J. Geoph. Res. Solid Earth* 122, 4143–4156. doi:10.1002/2016JB013789

Railsback, L. B., Akers, P. D., Wang, L., Holdridge, G. A., and Voarintsoa, N. R. (2013). Layer-bounding surfaces in stalagmites as keys to better paleoclimatological histories and chronologies. *Int. J. Speleol.* 42, 167–180. doi:10.5038/1827-806X.42.3.1

Roberts, A. P. (2015). Magnetic mineral diagenesis. *Earth Sci. Rev.* 151, 1–47. doi:10.1016/j.earscirev.2015.09.010

Schulz, M., and Mudelsee, M. (2002). REDFIT: estimating red-noise spectra directly from unevenly spaced paleoclimatic time series. *Comput. Geosci.* 28, 421–426. doi:10.1016/S0098-3004(01)00044-9

Seiler, R. A., Hayes, M., and Bressan, L. (2002). Using the standardized precipitation index for flood risk monitoring. *Int. J. Climatol.* 22, 1365–1376. doi:10.1002/joc.799

Slotznick, S. P., Swanson-Hysell, N. L., and Sperling, E. A. (2018). Oxygenated Mesoproterozoic lake revealed through magnetic mineralogy. *Proc. Natl. Acad. Sci. U. S. A* 115, 12938–12943. doi:10.1073/pnas.1813493115

Torrence, C., and Compo, G. P. (1998). A practical gruide to wavelet analysis. *Bull. Am. Meteorol. Soc.* 79, 61–78. doi:10.1175/1520-0477(1998)079<0061:APGTWA>2.0.CO;2

van Beynen, P., Bourbonniere, R., Ford, D., and Schwarcz, H. (2001). Causes of colour and fluorescence in speleothems. *Chem. Geol.* 175, 319–341. doi:10.1016/S0009-2541(00)00343-0

Vanghi, V., Borsato, A., Frisia, S., Howard, D. L., Gloy, G., Hellstrom, J., et al. (2019). High-resolution synchrotron X-ray fluorescence investigation of calcite coralloid speleothems: elemental incorporation and their potential as environmental archives. *Sedimentology* 66, 2661–2685. doi:10.1111/sed.12607

Verosub, K. L., and Roberts, A. P. (1995). Environmental magnetism: past, present, and future. *J. Geophys. Res.* 100, 2175–2192. doi:10.1029/94JB02713

Vuille, M., Burns, S. J., Taylor, B. L., Cruz, F. W., Bird, B. W., Abbott, M. B., et al. (2012). A review of the South American Monsoon history as recorded in stable isotopic proxies over the past two millennia: Clim. *Past Discuss.* 8, 637–668. doi:10.5194/cpd-8-637-2012

Wassenburg, J. A., Immenhauser, A., Richter, D. K., Jochum, K. P., Fietzke, J., Deininger, M., et al. (2012). Climate and cave control on Pleistocene/Holocene calcite-to-aragonite transitions in speleothems from Morocco: elemental and isotopic evidence. *Geochem. Cosmochim. Acta.* 92, 23–47. doi:10.1016/j.gca.2012.06.002

Zhu, Z., Feinberg, J. M., Xie, S., Bourne, M. D., Huang, C., Hu, C., et al. (2017). Holocene ENSO-related cyclic storms recorded by magnetic minerals in speleothems of central China. *Proc. Natl. Acad. Sci. U.S.A* 114, 852–857. doi:10.1073/pnas.1610930114

Conflict of Interest: The authors declare that the research was conducted in the absence of any commercial or financial relationships that could be construed as a potential conflict of interest.

frontiers in Earth Science

BRIEF RESEARCH REPORT
published: 15 January 2021
doi: 10.3389/feart.2020.592986

Ground Magnetic Surveying and Susceptibility Mapping Across Weathered Basalt Dikes Reveal Soil Creep and Pedoturbation

Tilo von Dobeneck, Maximilian Müller, Benjamin Bosbach and Andreas Klügel*

Faculty of Geosciences, University of Bremen, Bremen, Germany

Ground magnetic survey profiles across a soil-covered and weathered mafic dike in sedimentary host rock not only permit to delineate the strike, width and burial depth of the intrusive basalt sheet, but also reflect the subsurface deformation of its clayey weathering products. We illustrate this finding and its practical geomorphological applicability by an example from the mid-German Heldburg Dike Swarm, where blue- and olive-gray basalt-derived clays inherited not just the dike space previously occupied by the basalt, but also large parts of its magnetic iron minerals and their strong induced and remanent magnetization. Such ductile basaltic "marker soils" deform and move with the surrounding low-magnetic host soils, but remain distinguishable by their contrasting colors and high magnetic susceptibility. Ground magnetic surveys can therefore delineate soil creep distance at meter- and basalt weathering depth at decimeter-precision. Magnetic mapping of a weathered dike's cross-section from an exploration trench by *in-situ* susceptometry permits to analyze past soil deformation in great detail. Weathering and solifluction transforms the simple "vertical sheet" anomalies of dikes into complex, but still interpretable composite patterns, providing a new and promising exploratory approach for field studies concerned with soil creep and pedoturbation.

Keywords: soil creep marker, weathered basalt dikes, magnetic anomaly, ground magnetic survey, *in-situ* susceptometry, Heldburg Dike Swarm

OPEN ACCESS

Edited by:
Ricardo IF Trindade, University of São Paulo, Brazil

Reviewed by:
Melina Macouin, UMR5563 Géosciences Environnement Toulouse (GET), France
Antonio Casas, University of Zaragoza, Spain

****Correspondence:***
Tilo von Dobeneck
dobeneck@uni-bremen.de

Specialty section:
This article was submitted to Geomagnetism and Paleomagnetism, a section of the journal Frontiers in Earth Science

Received: *09 August 2020*
Accepted: *07 December 2020*
Published: *15 January 2021*

Citation:
von Dobeneck T, Müller M, Bosbach B and Klügel A (2021) Ground Magnetic Surveying and Susceptibility Mapping Across Weathered Basalt Dikes Reveal Soil Creep and Pedoturbation. Front. Earth Sci. 8:592986. doi: 10.3389/feart.2020.592986

INTRODUCTION

Soil creep and pedoturbation are fundamental issues of geomorphology and pedology (Pawlik and Šamonil, 2018). Patient observations, often over several years, are needed to assess and quantify the slow motion and deformation of soils properly. Biological creep markers such as tree tilting have been occasionally used (e.g., Alestalo, 1971; Gärtner and Heinrich, 2013), but their vertical, lateral and temporal resolution is fairly limited. Geological soil creep markers such as soil-embedded "stone lines" originating from weathering-resistant quartz veins in the underlying bed rock (Johnson, 2002) can potentially delineate the entire creep trajectory of a soil complex from pedogenesis to erosion. However, finding such durable marker rocks in a soil complex and following their spatial dispersal requires fortunate geological settings and massive, meticulous soil excavations. Here, we propose a more rapid and less invasive concept to deduce past soil creep from irregular magnetic anomalies of weathered basalt dikes using established ground magnetic survey and *in-situ* susceptometry methods.

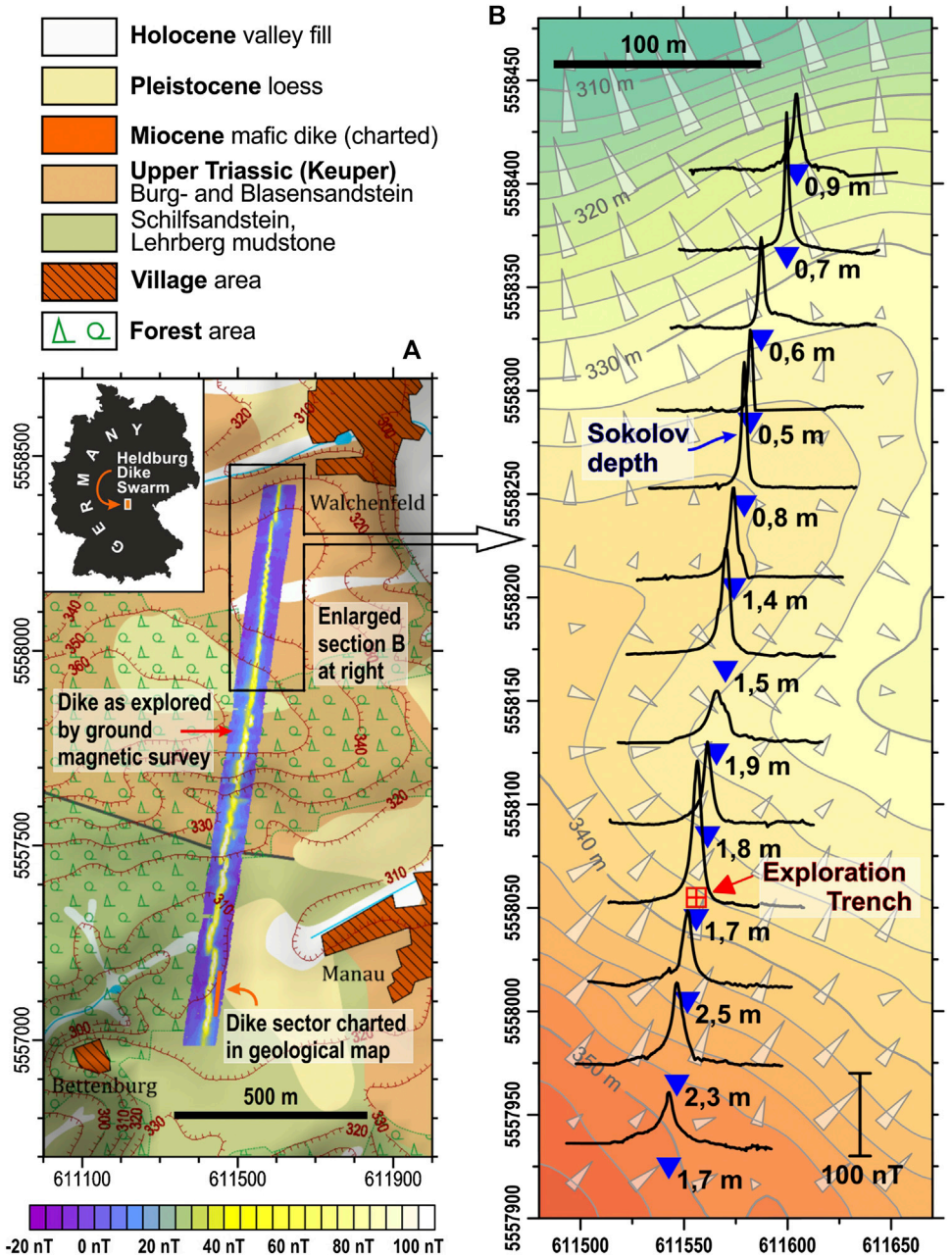

FIGURE 1 | (A) Inset: The Heldburg Dike Swarm (HDS) region is located in the mid-German Upper Triassic "Keuper" formations. Previously charted sector (orange line) and newly explored complete course (magnetic anomaly map in blue/yellow) of a weathered mid-Miocene basalt dike near the villages of Manau and Walchenfeld (Hassberge, Northern Bavaria). The shown geological map is redrawn from Schröder (1976) and georeferenced to UTM coordinates (WGS 84 sector 32N). **(B)** Northern dike section delineated by 13 precision ground magnetic W-E profiles. Note the varying amplitudes and shoulders of the anomaly. Blue triangles and numbers mark dike center positions and Sokolov depth estimates. The red square symbolizes the position of the exploration trench. Topographic contour lines are based on own GPS elevation data; gray arrows mark slope gradients.

GEOLOGICAL SETTINGS

Volcanic dike swarms in sedimentary host rock are typical features of extensional continental basins with underlying small-volume intraplate volcanic fields. We chose the "Heldburg Dike Swarm" (HDS) for our ground magnetic studies, a 70 × 20 km large mid-German intraplate volcanic field with numerous typically 0.1–10 km long, ~1 m wide, near-vertical basalt dikes, that are parallel with the "Rhenish" NNE-SSW strike of the European Cenozoic Rift System (Wilson and Downes, 2006). The silica-undersaturated basalts of the HDS intruded into the Upper Triassic "Keuper" formations of the

Hassberge cuesta range in Northern Bavaria during early Oligocene and in mid-Miocene (Abratis et al., 2015; Pfänder et al., 2018). Typical local host rocks of HDS dikes are partly dolomitized quartz and arkose sandstones, siltstones and claystones (Geyer and Schmidt-Kaler, 2006).

Owing to intense weathering and solifluction, in particular under past periglacial conditions, these dikes are now concealed under meter-thick soil cover and hard to detect with geological field methods. Their representation in official geological maps is largely incomplete and often oversimplified as **Figure 1A** exemplifies. Finding and tracking hidden mafic dikes is a classical task for ground magnetic surveying. During yearly applied magnetics field courses from 2013 to 2020, Bremen geoscience students have magnetically explored several Bavarian HDS dikes in full length and high resolution. As the basalt's strong magnetization highly contrasts with the low magnetizations of the sedimentary host rocks and soils, the magnetic anomalies of clay-weathered HDS dikes emerge prominently from the very quiet magnetic background of the Keuper formations. We present as our case study a so far largely unknown buried dike near the Franconian villages of Manau and Walchenfeld, whose course through hilly forest- and farmland is clearly delineated by its magnetic anomaly (**Figure 1A**).

METHODS

Ground Magnetic Surveying and Data Processing

During two four-days campaigns in 2015 and 2018, we surveyed the total magnetic field B (x, y) and its vertical gradient dB/dz (x, y) over a parallelogram-shaped area enclosing the Manau-Walchenfeld dike using three portable *GEM GSM-19GW* Overhauser gradiometers as "rovers" and a fourth *GEM GSM-19* as "base." The lower of the rover's two Overhauser sensors (whose data are shown here) was attached to a vertical aluminum pole such that it was always held or carried 0.7 m above ground. The upper (gradiometer) sensor was mounted in 1.7 m and the GPS antenna in 2.5 m height. Starting from a short previously known dike section (orange line in **Figure 1A**), the dike's course and full length (~1.5 km) was first determined by zigzagging GPS-guided exploratory search profiles. The entire dike was then surveyed in great detail along some 130 parallel ground magnetic W-E lines of 200 m (2015) or 100 m (2018) length, mutually offset by 20 m in the southern sector (lower part of **Figure 1A**) and by 8 m in the northern sector (**Figure 1B**).

Every fifth survey line was measured in the more precise "point mode," where the magnetometer was manually placed on an oriented surveyor's ribbon in 50 cm steps (exploration trench profile: 25 cm) and readings were averaged over 3 s sampling time. This more time-consuming method enabled us to obtain ±1 nT data repeatability and an estimated relative positioning error of $\Delta x \leq 10$ cm required for dependable numerical anomaly modeling. The other four out of five intermediary survey lines were surveyed in the faster "walking mode," where the operator carried the two sensors on a non-magnetic backpack along staked-out ranging rod lines. Walking at a speed of ~1 m/s, the chosen sampling time of 0.5 s is equivalent to ~0.5 m data spacing. On open farmland, walking mode data have a dynamic GPS positioning error of about ±1 m, which is acceptable for mapping purposes. In densely forested areas, an intolerable GPS error of up to ±5 m forced us to partly return to traditional, more laborious surveying methods based on ranging rods, surveyor's ribbon and compass for profile setup.

Data processing and numerical 2D forward modeling were conducted with *Geosoft Oasis montaj* software. All ground magnetic data were corrected for diurnal field variation using own base station recordings and levelled to remove heading error. Anthropogenic structures like roads, wire fences or signposts were charted and their assumed anomalies eliminated from profiles. An averaged regional geomagnetic background field was subtracted from all survey profiles; an additional linear regional trend correction was applied to the modeled profile.

Exploration Trench and *In-Situ* Susceptometry

In order to reveal the geometry and weathering state and to determine the paleo- and rock magnetic properties of the buried dike structure, an approximately 2.50 m long, 0.80 m wide and 1.80 m deep exploration trench was dug across the anomaly center in a hillslope location (marked in **Figure 1B**) and extended sideways by auger drill soil probing. The near-vertical northern trench wall was subdivided into 5 × 7 sectors of 50 × 25 cm size with pegs and strings, that were individually photographed (photo mosaic in **Figure 2A**), visually described (with finger probe), and magnetically mapped using a battery-powered *Bartington MS2F* susceptometer with point sensor, whose sampling time was set to 10 or 1 s depending on the required sensitivity range. A stencil with 50 holes on a 5 × 5 cm grid was attached to each trench wall sector to facilitate a quick and accurate sequential placement of the point sensor to all 50 × 37 = 1850 susceptibility grid positions on the trench wall (**Figure 2B**).

Paleo- and Rock Magnetic Sampling and Laboratory Measurements

To obtain calibrated volume susceptibility (κ) and Natural Remanent Magnetization (NRM) values for all observed materials, required for subsequent numerical anomaly modeling, 106 paleomagnetic sample cubes of 6.2 cm^3 volume were pressed into the trench wall along three vertical transects to collect host soils and different basalt weathering stages. Some soil-embedded basalt relicts of the local dike and from pristine nearby basalt outcrops were likewise fixated in sample cubes. Volume susceptibility measurements of all collected cube samples were taken with a *Kappabridge KLY-2* precision susceptometer. NRM intensity and orientation were determined with the automated *2G 755R* cryogenic DC SQUID magnetometer of our paleomagnetic laboratory (Mullender et al., 2016). The remanent (M_{rem}) and induced (M_{ind}) magnetizations of all samples s and their (dimensionless) Koenigsberger Q ratios (Koenigsberger, 1938) were determined based on the standard formula

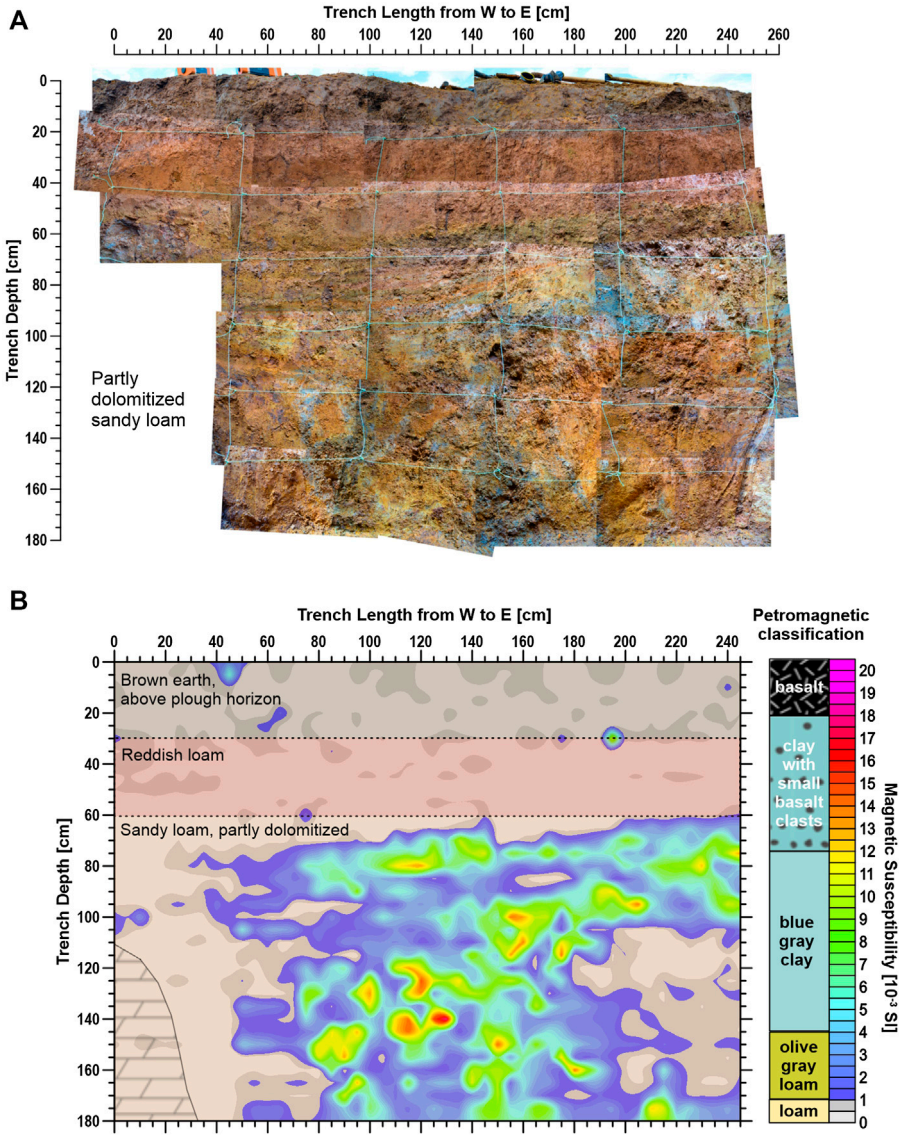

FIGURE 2 | (A) Photo mosaic of exploration trench wall with strings marking 25 × 50 cm sectors. The dolomitized sandstone in the lower left was later removed and measured, but not photographed. **(B)** Schematic host soil sections with overlain magnetic susceptibility contour plot based on *in-situ* susceptometry data collected on a 5 × 5 cm grid. Low-magnetic host rock soils (0–1 × 10^{-3} SI, gray) show pedoturbated fringes with the ochre and olive-gray medium-magnetic (1–4 × 10^{-3} SI, dark to light blue) and blue-gray high-magnetic (4–16 × 10^{-3} SI, green to yellow) basaltic weathering products. In 60 to 110 cm depth, basalt-derived clays are laterally protracted. The petromagnetic classification and color scheme at right associates basalt weathering stage with *in-situ* magnetic susceptibility.

$$Q(s) = \frac{M_{\mathrm{rem}}(s)}{M_{\mathrm{ind}}(s)} = \frac{\mathrm{NRM}(s)}{\kappa(s) \cdot B/\mu_0}$$

RESULTS

Magnetic Anomaly Patterns and Burial Depth Estimates

At first glance, most ground magnetic W-E profiles (**Figure 1B**) remind on textbook-style anomalies of thin vertical dikes with soil or sediment overburden (Telford et al., 1990; Hinze et al., 2013). Each of these profiles features a single central anomaly maximum of 60–160 nT amplitude dropping off to the local background without obvious side minima. These anomalies are perfectly aligned and trace the course of one single, straight, narrow, near-vertical volcanic dike with a length of ~1.5 km and a "Rhenish" strike of N8°E, intersected by two sinistral and one dextral *en échelon* offsets (**Figure 1A**).

However, at closer inspection, most of the observed anomalies display a greater range of shapes than theoretical "vertical sheet" anomaly formulas (Telford et al., 1990) can assume. Most peaks have single- or double-sided shoulders and/or tails of varying extent, some are crested with smaller spikes (<5 nT). These

irregular and diverse anomaly features within and beyond the dike section of **Figure 1B** imply, that additional magnetically enhanced material must exist at one or both sides of the dike. As these "abnormal" anomaly features are recorded with lower amplitudes at the upper magnetometer sensor and show a considerable short-range variability, they must relate to shallow (sub) soil structures.

Graphical depth estimation methods exploit the easily demonstrable circumstance, that overburden increases the half-width and straight slope length of a dike's magnetic anomaly (e.g., Skilbrei 1993; Hinze et al., 2013). Testing various established methods, the most consistent and conclusive burial depths were obtained from the so-called "Sokolov Length" (Sokolov 1956). Under the assumption of a ~1 m wide buried dike, our Sokolov depth estimates (**Figure 1B**) declined from 2.5–1.7 m just below a hilltop situation in the southern part down to 0.9–0.5 m along a steepening valley slope in the northern part, which may reflect local equilibria of soil formation and soil erosion.

Soil Profile and Magnetic Susceptibility Map of Exploration Trench Section

The exploration trench was deliberately dug at a position where the dike is oblique to the hillslope and seemed to be only moderately buried (**Figure 1B**). A brown, well-mixed ("ploughed") Ap topsoil reached down to a depth of ~30 cm (**Figure 2A**), which was still largely frozen during our early March campaign time, but could be easily identified by its crumbly texture and high content of shredded crop fibers. Below followed a ductile, clay-rich ("vertic") Bv subsoil layer of 30–40 cm thickness (**Figure 2A**). This reddish loam was thought to be a colluvial soil from a previously overlying reddish Keuper mudstone. The beige sandy loam encountered below at 60–70 cm depth forms the C horizon and appears to originate from the underlying Burgsandstein bedrock, a dolomitic arkose. Below ~110 cm depth, this material became too hard to be penetrated by spade, and a gasoline-powered breaker hammer had to be used to reach the final trench depth of 180 cm.

In the center of the trench and coinciding with the magnetic anomaly peak, relicts of a vertical dike appeared in ochre, olive-, and blue-gray hues underneath the overlying colluvial soil (**Figure 2A**). The original basalt was fully replaced by cohesive, easily penetrable clays. Enclosed, mm-sized basaltic fragments scattered in the blue-gray clay witnessed the parent rock. The basalt-derived soil showed signs of decimeter-scale pedoturbation and/or pseudo-gley dynamics. In 60–110 cm depth, i.e. below the ductile reddish loam and above the hard, dolomitized beige sandy loam, this confined clay body was laterally protracted in downhill direction (**Figure 2**). Its lateral extent, determined by auger probing, reached ~2.5 m away from the dike, equivalent to a creep distance of ~4 m in downslope direction.

Whereas these complex deformation structures were partly camouflaged by pedoturbation (**Figure 2A**), the susceptibility map resolved the exposed basaltic soils and their boundaries in impressive detail (**Figure 2B**). Topsoil and subsoil originating from the Upper Triassic Burgsandstein host rock were as low-magnetic (~0.5 × 10^{-3} SI) as to be expected, while the susceptibilities of the basalt-derived olive- (~1–4 × 10^{-3} SI) and blue-gray clays (4–12 × 10^{-3} SI) evidenced far higher magnetic mineral contents. Local susceptibility maxima of up to 18 × 10^{-3} SI marked patches of highly weathered basalt fragments. Consistent associations of soil color and magnetic susceptibility enabled us to establish a tentative, strictly local petromagnetic classification scheme (**Figure 2B**) dividing the observed dike materials in four progressive weathering stages: 1) pristine massive basalt, 2) partly weathered basalt with residual rock clasts, 3) fully weathered blue-gray basaltic clay with small rock fragments, and 4) oxidized olive-gray basaltic soil or loam. For simplicity, the arkose host rock and overlying host soils with their negligibly low background magnetizations were jointly classified as "Burgsandstein."

Analytical 2D Anomaly Model of Weathered and Deformed Dike

When comparing the observed burial depth of the weathered dike (0.6 m, **Figure 2B**) with our Sokolov depth estimate (1.7 m, **Figure 1B**), a large discrepancy not just of both values, but also of both methods becomes apparent. While the observed burial depth marks the contact between the colluvial host soil and the clay-weathered dike head, the Sokolov method primarily "sees" the deeper, better preserved and more strongly magnetized dike segments. To separate the specific expressions of soil overburden and basalt weathering for a dike's magnetic anomaly, we combined the structural information gained from the exploration trench with zonally averaged rock magnetic property values (**Figure 3B**), creating a case-specific 2D model dike (**Figure 3A**), whose magnetic anomaly can be numerically calculated (**Figure 3C**). To keep this numerical 2D model manageable required certain simplifications, but the dimensions, geometry and lateral zonation of the excavated dike section are rather well represented.

Our initial 2D model dike (not shown) produced a higher and broader anomaly than shown by our field data, which, as we assumed, was probably caused by over-estimating the pristine basalt volume at depth. As we had observed lateral weathering of a similar basalt dike down to 10–20 m depth at a river bank outcrop NE of Manau, we provided our model dike also with increasingly weathered outer flanks above 30 m depth (**Figure 3A**). Another modelling problem was linked to the inherent assumption of anomaly models that all bodies are homogeneously magnetized. Any deformation and dislocation of soil volumes and rock clasts should, however, result in a certain directional scatter and partial internal cancellation of their NRM vectors. We considered this cancellation effect suggested by our observed NRM inclinations and declinations by reducing measured NRM values by 30–50%, while keeping the induced magnetization unchanged (M_{ind} always follows the ambient geomagnetic field!). This lowers the Koenigsberger Q ratios of remanent vs. induced magnetization (**Figure 3B**), but Q values still agree well with value ranges reported in literature (Koenigsberger, 1938; Clark and Emerson, 1991). Our final

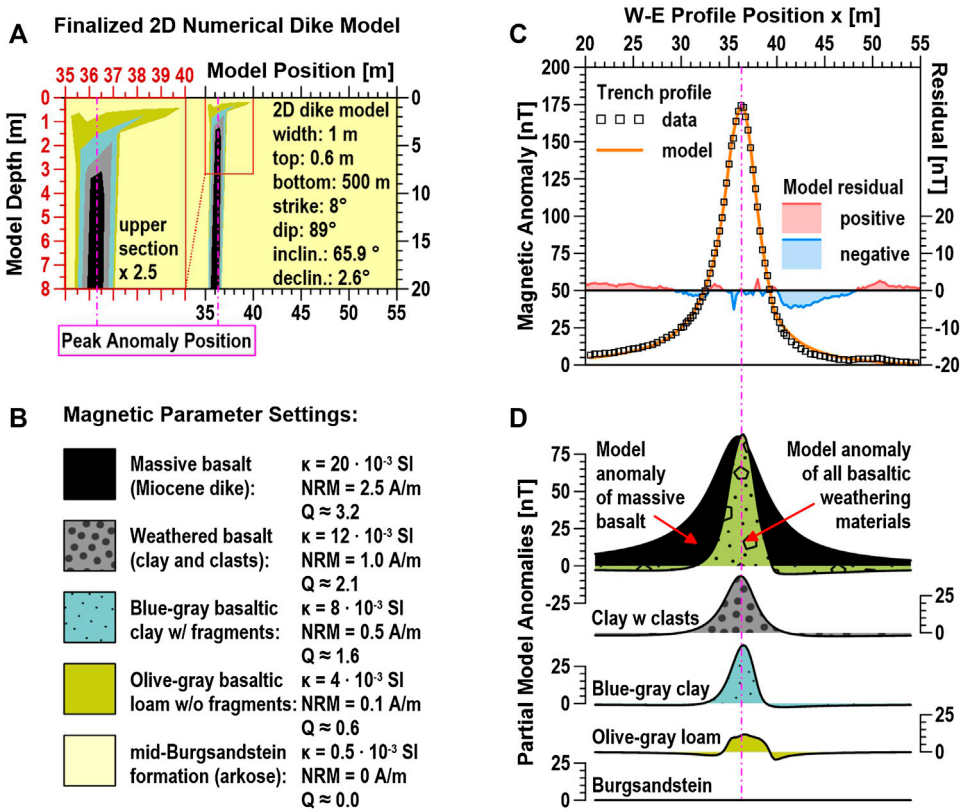

FIGURE 3 | (A) 2D model of weathered HDS dike based on the simplified and extrapolated exploration trench section of **Figure 2**. Shown at left (red axes) is a 2.5x enlarged view of the dike top; the smaller model at right (black axes) is scaled proportionally with **Figure 3C**. **(B)** Distinguished model materials, their color patterns and magnetic properties. **(C)** Total 2D dike model anomaly (orange line) and corrected ground magnetic survey anomaly data (squares) with model residuals (note vertical offset and expanded scaling of residual axis). **(D)** 2D model-based partial magnetic anomalies of pristine basalt (black), all weathering materials (olive green), and specific anomaly contributions by each material classified in **Figure 3B**. All anomaly axes are equivalently scaled in nT.

model has a Q of 3.2 for pristine basalt, which decreases to 2.1, 1.6, and 0.6 for the progressive weathering stages, reflecting a gradual loss of inherited thermoremanent and/or acquired chemical magnetization. A positive net magnetic anomaly at Q ratios >1 implies, that the basalt dike should have intruded and chilled during a period of a normally oriented geomagnetic field. Directional NRM data of the cube samples support this interpretation (see data in **Supplementary Material**).

With these justifiable geometry and parameter adjustments of the starting model, an excellent overall fit of modeled and observed magnetic anomalies was reached (note small model residuals in **Figure 3C**). The final model delivered not only a well-matching anomaly shape and amplitude, but also the formerly unknown contributions (i.e., "partial magnetic anomalies") of all involved rocks and soils (**Figure 3D**). The pristine, semi-infinite basalt dike at depth creates a broad "vertical sheet" anomaly of ~8 m half-width. With its lesser depth and finite vertical extent, the weathered dike top generates a narrow "thick bed" anomaly (Eppelbaum, 2015) of ~3 m half-width with small, slightly asymmetric double-sided minima (**Figure 3D**). At this specific profile, the pristine basalt at depth contributes nearly 50% (86 nT) of the calculated peak anomaly (173 nT), while all basaltic weathering products together yield the remaining 50% (87 nT). The W-E anomaly of this weathered dike model with N8°E strike and 88.9° dip features a slender central maximum with low, broad, slightly asymmetric, non-negative anomaly shoulders (**Figure 3C**) — a "composite" shape, that is typical for most HDS profiles (**Figure 1B**).

DISCUSSION AND CONCLUSION

Practical and Fundamental Insights From Our HDS Surveys

Ground magnetic surveying proved to be a reliable and efficient method to find and track weathered HDS dikes under meter-thick soil cover. Typical magnetic anomaly profiles across a buried HDS dike usually have a peak amplitude between 30 and 200 nT, but may occasionally reach 1,000 nT and more, when low-weathered basalt outcrops. We recognized that depth estimates from "Sokolov Length" and similar graphical methods provide just a relative guideline for the burial depth of clay-weathered dikes. Better depth estimates may be expected from specialized "weathered dike" models, whose control parameters include burial depth, weathering depth and dike top deformation. Creeping, slumping and blending of basaltic soil units within a

host soil complex can adds tails, side peaks and troughs to the main dike anomaly (**Figure 1B**). Such complex and irregular anomaly patterns probably overstrain the adaptability of any parametrized inverse modelling approach and will always require forward anomaly modelling based on representative soil probing and a realistic starting model.

While pedogenesis converts a basalt's magmatic silicate minerals to clays, primary (titano-)magnetite is initially just oxidized to the likewise ferrimagnetic Fe mineral (titano-) maghemite (Cui et al., 1994; Garcia de Oliveira et al., 2002; Chen et al., 2005; Zhang et al., 2020). Basalt-derived clays thereby inherit large parts of their parent rock's magnetic minerals along with their strong induced and remanent magnetization. This circumstance explains the surprisingly high magnetization and excellent magnetic detectability of weathered dikes. As basalt weathering continues, this (Ti-) maghemite plus the iron released from weathered silicate minerals transform into secondary hematite and goethite (Lu et al., 2008). These antiferromagnetic minerals have far lower magnetizations, but lend their characteristic red and yellow colors to the ochre/olive-gray limonitic loam. *In-situ* susceptometry of weathered dikes is therefore an efficient method to visualize and map basalt weathering stages and soil creep in great detail. The contrasting colors and susceptibilities of basalt-derived marker soils are easy to follow along their deformation trajectory. Along-track mixing of basaltic and ambient soils should be quantifiable by linear magnetic unmixing based on endmember material properties (Heslop, 2015; Leng et al., 2019). As digging trenches in greater numbers and dimensions may get impractical, low-invasive, small-bore soil susceptometers as described by Petrovsky et al. (2004) could simplify *in-situ* susceptometry of larger soil sections and avoid unnecessary land damage.

Benefit of Basalt-Derived Marker Soils for Geomorphological Investigations

The diversity of magnetic anomaly shapes observed in this and other similar HDS surveys suggests, that old creep and slump structures underneath a usually well-mixed topsoil are very common (**Figure 1B**). The chosen exploration trench site represents a clear, but still modest case of soil deformation and creep. We found the most deviant magnetic anomalies predominantly at locations, where slope gradients were steeper and at larger angles with dikes, particularly in soil failure or confluence zones (**Figure 1B**). Counter-intuitively, basalt exhumed in our exploration trenches was typically more deeply weathered than the adjacent sandstone host rock. Where anomalies were locally large and narrow, this was always indicative of surficial low-weathered basalt related to topographically enhanced denudation or past human impact such as historical landscape terracing. Anomaly-based depth estimates necessarily overestimate the overburden of the weathered dike top and underestimate the depth of the pristine basalt. The spatial distribution of these numbers is nevertheless very useful to determine systematic and frequently observable relative changes in soil cover, e.g., between hillcrest, hillslope and valley-floor, or between unworked (forests), pastured (meadows) and cultivated soils (cornfields).

Noticeably, our student surveys in the HDS region pursued geophysical and not geomorphological aims and provide just a pilot study for the proposed method. A dedicated soil creep study would e.g., include geotechnical soil properties and soil mechanics. Our findings can nevertheless illustrate the feasibility and validity of the depicted combined ground and rock magnetic dike mapping approach, that permits to find, map and diagnose the deformation of clay-weathered dike tops in continuity through changing terrain. Dike swarms like the HDS are globally abundant and transect different landscapes types parallel to crustal fracture systems. Their structural uniformity and good magnetic detectability make weathered dikes attractive as cross-temporary witnesses of soil deformation and delocalization under the joint influence of topography, bed-rock geology, pedogenesis, climate, vegetation and land use.

DATA AVAILABILITY STATEMENT

The original contributions presented in the study are included in the article/**Supplementary Material**, further inquiries can be directed to the corresponding author.

AUTHOR CONTRIBUTIONS

TD guided field courses, wrote the manuscript and designed or revised figures. MM and BB carried out the field work, performed laboratory measurements and processed and analyzed data for their MSc resp. BSc thesis. AK co-supervised the thesis projects as petrologist and regional expert. All coauthors actively contributed to the manuscript with ideas and comments.

ACKNOWLEDGMENTS

We greatly enjoyed the fabulous hospitality of Franconian country folks, who never bothered about our trespassing of their farmlands and readily shared their own observations on soil behavior with us. We wouldn't know the true course of any HDS dike without the highly committed field work of so far 120 field class participants. Two reviews and previous critical comments by Helge Stanjek helped us to substantially improve this manuscript and are gratefully acknowledged.

SUPPLEMENTARY MATERIAL

The Supplementary Material for this article can be found online at: https://www.frontiersin.org/articles/10.3389/feart.2020.592986/full#supplementary-material.

REFERENCES

Abratis, M., Viereck, L., Pfänder, J. A., and Hentschel, R. (2015). Geochemical composition, petrography and $^{40}Ar/^{39}Ar$ age of the Heldburg phonolite: implications on magma mixing and mingling. *Int. J. Earth Sci*. 104, 2033–2055. doi:10.1007/s00531-015-1207-x

Alestalo, J. (1971). Dendrochronological interpretation of geomorphic processes. *Fennia*. 105, 1–140.

Chen, T. H., Xu, H. F., Xie, Q. Q., Chen, J., Ji, J. F., and Lu, H. Y. (2005). Characteristics and genesis of maghemite in Chinese loess and paleosols: mechanism for magnetic susceptibility enhancement in paleosols. *Earth Planet Sci. Lett*. 240, 790–802. doi:10.1016/j.epsl.2005.09.026

Clark, D. A., and Emerson, D. W. (1991). Notes on rock magnetization characteristics in applied geophysical studies. *Explor. Geophys* 30, 547–555. doi:10.1071/EG991547

Cui, Y., Verosub, K. L., and Roberts, A. (1994). The effect of low-temperature oxidation on large multi-domain magnetite. *Geophys. Res. Lett*. 21, 757–760. doi:10.1029/94GL00639

Eppelbaum, L. V. (2015). Quantitative interpretation of magnetic anomalies from thick bed, horizontal plate and intermediate models under complex physical-geological environments in archaeological prospection. *Archaeol. Prospect*. 22, 255–268. doi:10.1002/arp.1511

Garcia de Oliveira, M. T., Formoso, M. L. L., Indio da Costa, M., and Meunier, A. (2002). The titanomagnetite to titanomaghemite conversion in a weathered basalt profile from southern Paraná Basin. Brazil: *Clay Clay Miner*. 50, 478–493. doi:10.1346/000986002320514208

Gärtner, H., and Heinrich, I. (2013). "Dendrogeomorphology," in *Encyclopedia of quaternary science*. Editor S. A. Elias (Amsterdam, Netherlands: Elsevier B.V.), Vol. 2, 91–103. doi:10.1016/B978-0-444-53643-3.00356-3

Geyer, G., and Schmidt-Kaler, H. (2006). *Die Haßberge und ihr Vorland: Wanderungen in die Erdgeschichte*. (Munich, Germany: Verlag Dr. Friedrich Pfeil), Vol. 20.

Heslop, D. (2015). Numerical strategies for magnetic mineral unmixing. *Earth Sci. Rev*. 150, 256–284. doi:10.1016/j.earscirev.2015.07.007

Hinze, W. J., von Frese, R. R. B., and Saad, A. H. (2013). *Gravity and magnetic exploration—principles, practices, and applications*. Cambridge, UK: Cambridge University Press.

Johnson, D. L. (2002). Darwin would be proud: bioturbation, dynamic denudation, and the power of theory in science. *Geoarchaeology* 17, 7–40. doi:10.1002/gea.10001

Koenigsberger, J. G. (1938). Natural residual magnetism of eruptive rocks. *Terr. Magnetism Atmos. Electr*. 43 (3), 299–320.

Leng, W., von Dobeneck, T., Just, J., Govin, A., St-Onge, G., and Piper, D. J. W. (2019). Compositional changes in deglacial red mud event beds off the Laurentian Channel reveal source mixing, grain-size partitioning and ice retreat. *Quat. Sci. Rev*. 215, 98–115. doi:10.1016/j.quascirev.2019.04.031

Lu, S.-G., Xue, Q.-F., Zhu, L., and Yu, J.-Y. (2008). Mineral magnetic properties of a weathering sequence of soils derived from basalt in Eastern China. *Catena*. 73, 23–33. doi:10.1016/j.catena.2007.08.004

Mullender, T., Frederichs, T., Hilgenfeldt, C., de Groot, L., Fabian, K., and Dekkers, M. (2016). Automated paleomagnetic and rock magnetic data acquisition with an in-line horizontal "2G" system. *G-cubed*. 17, 3546–3559. doi:10.1002/2016GC006436

Pawlik, Ł., and Šamonil, P. (2018). Soil creep: the driving factors, evidence and significance for biogeomorphic and pedogenic domains and systems—a critical literature review. *Earth Sci. Rev*. 178, 257–278. doi:10.1016/j.earscirev.2018.01.008

Petrovsky, E., Hulka, Z., and Kapicka, A. (2004). A new tool for *in situ* measurements of the vertical distribution of magnetic susceptibility in soils as basis for mapping deposited dust. *Environ. Technol*. 25, 1021–1029. doi:10.1080/09593332508618391

Pfänder, J. A., Jung, S., Klügel, A., Münker, C., Romer, R. L., Sperner, B., et al. (2018). Recurrent local melting of metasomatised lithospheric mantle in response to continental rifting: constraints from basanites and nephelinites/melilitites from SE Germany. *J. Petrol*. 59, 667–694. doi:10.1093/petrology/egy041

Schröder, B. (1976). *Geologische Karte von Bayern, Blattnummer 5829 Hofheim: Bayerisches Landesamt für Umwelt*. (München, Germany: Scale 1:25,000).

Skilbrei, J. R. (1993). The straight-slope method for basement depth determination revisited. *Geophysics* 58, 593–595. doi:10.1190/1.1443442

Sokolov, K. P. (1956). *Geological interpretation of magnetosurvey data*. Moscow, Russia: Gosgeoltechizdat, [in Russian].

Telford, W. M., Geldart, L. P., and Sheriff, R. E. (1990). *Applied geophysics*. Cambridge, UK: Cambridge University Press.

Wilson, M., and Downes, H. (2006). "Tertiary-Quaternary intraplate magmatism in Europe and its relationship to mantle dynamics," in *European lithosphere dynamics*. Editors D. G. Gee and R. A. Stephenson (London, UK: Geological Society Memoirs), Vol. 32, 147–166.

Zhang, Q., Appel, E., Stanjek, H., Byrne, J. M., Berthold, C., Sorwat, J., et al. (2020). Humidity related magnetite alteration in an experimental setup. *Geophys. J. Int*. 224, 69–85. doi:10.1093/gji/ggaa394

Conflict of Interest: The authors declare that the research was conducted in the absence of any commercial or financial relationships that could be construed as a potential conflict of interest.

frontiers in Earth Science

ORIGINAL RESEARCH
published: 05 March 2021
doi: 10.3389/feart.2021.603805

A Feasibility Study of Microbialites as Paleomagnetic Recorders

Ji-In Jung and Julie A. Bowles*

Department of Geosciences, University of Wisconsin-Milwaukee, Milwaukee, WI, United States

Microbialites–layered, organosedimentary deposits–exist in the geologic record and extend back in deep time, including all estimated times of inner core nucleation. Microbialites may preserve magnetic field variations at high-resolution based on their estimated growth rates. Previous studies have shown that microbialites can have a stable magnetization. However, the timing and origin of microbialite magnetization were not well determined, and no study has attempted to evaluate whether actively growing microbialites record the geomagnetic field. Here, we present centimeter-scale magnetization and magnetic property variations within the structure of modern microbialites from Great Salt Lake (GSL), United States, and Laguna Bacalar, Mexico, Pleistocene microbialites from GSL, and a Cambrian microbialite from Mongolia. All samples record field directions close to the expected value. The dominant magnetic carrier has a coercivity of 35–50 mT and unblocking temperatures are consistent with magnetite. A small proportion of additional high coercivity minerals such as hematite are also present, but do not appear to appreciably contribute to the natural remanent magnetization (NRM). Magnetization is broadly consistent along microbialite layers, and directional variations correlate with the internal slope of the layers. These observations suggest that the documented NRM may be primarily detrital in origin and that the timing of magnetization acquisition can be close to that of sediment deposition.

Keywords: microbialites, stromatolites, paleomagnetism, rock magnetism, paleosecular variation

OPEN ACCESS

Edited by:
Eric C. Ferre,
University of Louisiana at Lafayette,
United States

Reviewed by:
Andrew Philip Roberts,
Australian National University,
Australia
Nicholas L. Swanson-Hysell,
University of California, Berkeley,
United States

****Correspondence:***
Ji-In Jung
jiinjung@stanford.edu

Specialty section:
This article was submitted to Geomagnetism and Paleomagnetism, a section of the journal Frontiers in Earth Science

Received: *08 September 2020*
Accepted: *25 January 2021*
Published: *05 March 2021*

Citation:
Jung J-I and Bowles JA (2021) A Feasibility Study of Microbialites as Paleomagnetic Recorders. Front. Earth Sci. 9:603805. doi: 10.3389/feart.2021.603805

INTRODUCTION

Recent work demonstrates the potential of speleothems as paleomagnetic recorders. These laminated cave deposits form by precipitation of carbonate and include detrital or authigenic magnetic particles that appear to document paleosecular variation (PSV) at high temporal resolution (e.g., Lascu and Feinberg, 2011; Bourne et al., 2015; Chou et al., 2018; Trindade et al., 2018). Stromatolites are also finely laminated carbonate materials, thought to have often formed by a microbially-mediated balance between sedimentation and intermittent lithification (Reid et al., 2000). Compared to speleothems, stromatolites are well represented in the geologic record, and the oldest examples go back at least 3.5 billion years (e.g., Awramik, 1992; Riding, 2010; Baumgartner et al., 2019). This spans all estimated times of inner core nucleation, which range from the late Archean to early Proterozoic (2.4–2.5 Ga) (e.g., Tarduno et al., 2006; Valet et al., 2014), to Mesoproterozoic times (~1.2 Ga) (e.g., Biggin et al., 2015; Smirnov et al., 2016), to the Ediacaran period (~570 Ma) (e.g., Bono et al., 2019). These materials may, therefore, hold promise as paleomagnetic recorders with high temporal resolution, and this type of record in deep time could have potential for capturing geomagnetic field behavior when the core may have been in different states.

Modern stromatolites have widely varying estimated growth rates ranging from 0.05 mm/yr to about 50 mm/yr (Paull et al., 1992; Brady et al., 2009; Berelson et al., 2011; Petryshyn et al., 2012). Laminations (when present), represent hiatal periods in sediment accretion, are thought to form approximately every 4–10 years in some studied stromatolites (Paull et al., 1992; Petryshyn et al., 2012), with one study finding yearly laminations (Rasmussen et al., 1993). In modern stromatolites (Reid et al., 2000), microbial filaments trap and bind sand and carbonate grains during periods of rapid accretion. During hiatal periods, a continuous exopolymer surface film develops, and bacterial activity promotes formation of a thin micritic crust which may be further modified into a thicker, fused carbonate crust. These laminated crusts therefore represent a sequence of lithified and preserved microbial mat surfaces. Laminations in ancient (>1 billion year old) stromatolites have been interpreted to represent day-night growth cycles (e.g., Vanyo and Awramik, 1982), although these interpretations have been increasingly called into question in light of the work on modern stromatolites mentioned above.

In this work, we look more broadly at microbialites, an umbrella term that includes at least some stromatolites. Burne and Moore (1987) define microbialites as organosedimentary deposits accreted by a benthic microbial community via trapping and binding detrital sediment and/or precipitation of calcite (abiotic or biologically induced). Microbialites have a relatively wide environmental distribution, found at the sediment-water interface in marine, alkaline freshwater, hypersaline lakes, evaporitic, and hydrothermal environments. They can be classified by different internal structures as stromatolite (laminated structure), thrombolite (clotted structure lacking lamination), dendrolite (dendritic structure), leolite (structureless), or some intergradational combination (Riding, 2000; Riding, 2011). Stromatolite diversity abundance increased from the late Archean (~2.4 Ga), peaking around ~1.25 Ga (Awramik and Sprinkle, 1999). Diversity declined up to the Eradican (~550 Ma) (Walter and Heys, 1985; Awramik and Sprinkle, 1999), but resurged in the early Phanerozoic and late Cambrian when thrombolites and dendrolites became the predominant type of microbialite (Riding, 2000; Kiessling, 2002). Grazing and metazoan competition have been suggested as a major factor contributing to the decline of stromatolite diversity, but other factors such as seawater chemistry and atmospheric composition could also affect their diversity (Riding, 2006). There are some arguments that not all Archean stromatolites are biogenic in origin (Lowe, 1994; Brasier et al., 2004; McLoughlin et al., 2008) but this interpretation remains controversial (Awramik and Graey, 2005; Allwood et al., 2006; Awramik, 2006; Schopf et al., 2007).

A primary magnetization in microbialites may arise from a detrital remanent magnetization (DRM) or a biogenic magnetization, or some combination of the two. Microbialites may trap detrital ferromagnetic (*sensu lactu*) particles from nearby sources within the microbialite matrix and carry a DRM. Lund et al. (2010) examined coral reef cores and observed detrital titanomagnetite bound within microbialites that had filled the primary cavities of the coral framework. These grains were determined to carry the natural remanent magnetization (NRM) and appeared to accurately record geomagnetic field variability. A DRM may also be biomediated in that the sticky microbial mat may play a role in particle retention and immobilization. Petryshyn et al. (2016) used bulk magnetic susceptibility to differentiate between stromatolites that are biogenic or abiogenic in origin and demonstrated that a cyanobacterial mat traps and binds grains more readily than abiogenic carbonate precipitates.

The other potential source of magnetic particles is biogenic magnetite which can be produced by biologically controlled mineralization (BCM) and biologically induced mineralization (BIM). Magnetotactic bacteria can create single-domain magnetic particles in chains by a matrix mediated BCM process. The presence of biogenic magnetite has been inferred in ancient (Chang et al., 1989) and modern (Stolz et al., 1989) microbialite environments by using rock magnetic techniques and transmission electron microscopy (TEM) to identify single domain magnetite with the unique crystal structures typically associated with magnetotactic bacteria. However, it has since been demonstrated that similar crystal morphologies can also be produced abiotically through reductive alteration of nanogoethite (Till et al., 2017) or via thermal decomposition of siderite (Golden et al., 2004). Maher and Taylor (1988) also observed similar fine-grained magnetite in soils and suggested that it may have formed via oxidation of Fe^{2+} solutions (Taylor et al., 1987). Biogenic magnetite might also be produced extracellularly by iron-reducing bacteria through BIM processes (Lovley, 1991; Konhauser et al., 2011; Konhauser and Riding 2012). Maloof et al. (2007) used TEM and ferromagnetic resonance to infer the presence of superparamagnetic magnetite formed via extracellular processes. Although superparamagnetic material will not contribute to remanence, extracellular magnetite typically has a wide grain size distribution including grains that are large enough to have stable single domain behavior (e.g., Egli, 2004).

Relatively little paleomagnetic work has intentionally focused on microbialites. Vanyo and Awramik (1982) extracted a paleomagnetic direction via alternating field demagnetization from a single specimen of late Proterozoic stromatolite. Thermal demagnetization of Jurassic stromatolites from Poland have shown them to carry a stable magnetization, including a polarity reversal (Muraszko, 2014) also observed in middle-late Jurassic limestones, stromatolites, and radiolarites in Poland (Kądziałko-Hofmokl and Kruczyk, 1987). As noted above, microbialites found in a post Last-Glacial-Maximum and late Pleistocene coral reef framework appear to accurately record the field direction (Lund et al., 2010). Several studies have sampled in or near ancient carbonate beds containing microbialites. The Love's Creek Member of the Bitter Springs Formation contains stromatolite and microbialite facies and was interpreted to be remagnetized through magnetite authigenesis along with the remainder of the section (Swanson-Hysell et al., 2012). However, the lower Ordovician Oneota dolomite which is locally stromatolitic carries a direction interpreted to be potentially primary (Jackson and Van der Voo, 1985), and Neoproterozoic dolomites containing microbialite laminites are

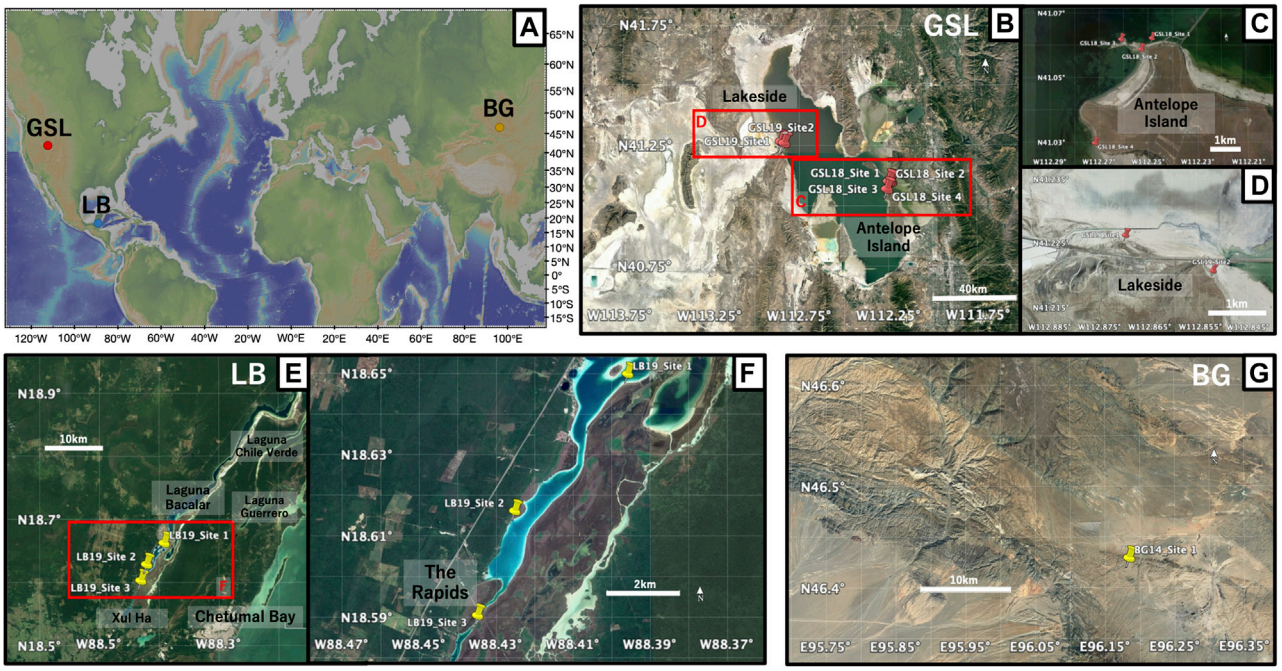

FIGURE 1 | (A) Global map of the locations of three microbialite samples: Great Salt Lake (GSL), Utah; Laguna Bacalar (LB), Quintana Roo, MX; Bayan Gol formation (BG), Southwestern Mongolia. The figure was made with GeoMapApp (www.geomapapp.org) (Ryan et al., 2009). **(B)** Satellite image of the sampling locations of microbialites at GSL **(C)** Close-up of GSL18 study localities at the Antelope Island and **(D)** GSL 19 sampling sites at Lakeside. **(E)** Satellite image of sampling locations of microbialites at LB. **(F)** Close-up of LB19 study localities and three sampling sites. **(G)** Satellite image of sampling locations at BG. Imagery from July 2019 for GSL, april 2018 for LB, and april 2019 for BG, ©2019 Google, Image Landsat/Copernicus.

interpreted to carry primary DRM (Trindade et al., 2003; Font et al., 2005). Maloof et al. (2007) sampled modern platform carbonate muds in the Bahamas and proposed that early cemented, laminated microbially-bound carbonates may preserve syn-depositional paleomagnetic directions. Few of these studies focus on the timing of magnetization with respect to microbialite formation, and no studies have attempted to evaluate whether actively growing microbialites accurately record the known field.

This study is designed to further assess the feasibility of microbialites as paleomagnetic recorders. We examined two actively growing or recently lithified microbialites, as well as one Cambrian microbialite. Variations in magnetization and magnetic mineralogy were evaluated at the centimeter scale. We also consider the timing of the magnetization with respect to deposition or microbialite growth.

METHODS

Sampling and Settings

This study focuses on microbialites from three localities/environments: 1) Great Salt Lake (GSL), Utah, United States (hypersaline lake environment); 2) Laguna Bacalar (LB), Quintana Roo, Mexico (freshwater alkaline environment); 3) the Cambrian Bayan Gol (BG) formation, southwestern Mongolia (marine environment) (**Figure 1**). Detailed information about locations, sample types, and descriptions are provided in **Table 1**.

At the Great Salt Lake, living and recently lithified modern microbialites were sampled from shallow water on the shores of Antelope Island in the southwestern part of the lake (GSL18). Samples were taken from living, low-profile ring-shaped structures and elongated, narrow ridge structures (Chidsey et al., 2015; Berg, 2019), but we were unable to maintain orientation, and the soft samples easily fell apart. These samples were preserved in lake water during transportation back to the laboratory. One oriented hand sample was collected from the steep side of a lithified, dome-style thrombolite structure that has been exposed by a lake level drop over the past few decades. Pleistocene microbialites are exposed along the western shoreline of the lake at Lakeside (Newell et al., 2017), and oriented hand samples were collected from two locations (GSL19).

Living deposits and lithified giant Holocene microbialites (Gischler et al., 2008; Castro-Contreras et al., 2014) were collected from shallow water at three sites at Laguna Bacalar. Microbialites from Site 1 are unlithified layered domal structure deposits with a stromatolitic structure at the bottom but transitioning to a more thrombolitic fabric toward the top (**Figure 2C**). The approximate thickness of the actively growing greenish microbial mat was ~2 cm from the surface. Site 2 microbialites were lithified but porous. The Site 3 giant microbialites had soft surfaces including living cyanobacteria

TABLE 1 | Microbialite sample locations and descriptions.

Location/ID	Latitude	Longitude	Features	Status/Age
GSL18/Site 1 (GSL18_01)	41.06054	−112.24909	Ring structure microbialite	Living and recently lithified
GSL18/Site 2 (GSL18_02)	41.05709	−112.25351	Ring structure microbialite	Living and recently lithified
GSL18/Site 3 (GSL18_03)	41.06014	−112.26168	Dome style thrombolite	Recently lithified
GSL18/Site 4 (GSL18_04)	41.02802	−112.27246	Ridge structure and ring structure microbialite	Living and recently lithified
GSL19/Site 1 (GSL19_01)	41.21402	−112.85211	Monk-head structure microbialite	Pleistocene
GSL19/Site 2 (GSL19_02)	41.15964	−112.86058	Cauliflower structure microbialite	Pleistocene
LB19/Site 1 (LB19_01)	18.64766	−88.39658	Thrombolitic stromatolites with cyanobacteria layer	Living and unlithified sediments
LB19/Site 2 (LB19_02)	18.61383	−88.42595	Poorly lithified porous microbialite	Holocene or recently lithified?
LB19/Site 3 (LB19_03)	18.55834	−88.43537	Poorly lithified porous microbialite with cyanobacteria layer	Living and recently lithified
BG14/Site 1 (BG14_01)	46.4213	96.18608	Dome style laminated stromatolite	Cambrian

layers (~2 cm) and lithified microbialites underneath. Living microbial mats on the surface at Site 1 (LB19_0101) and 3 (LB19_0304) were easily penetrated and collected by pushing standard 2 cm^3 plastic cubes) into the mats. One hand sample from Site 1 (LB19_0102) was subsampled with 2 cm^3 plastic cubes. Site 1 microbialites were additionally sampled with 5 cm diameter by 14 cm long (LB19_0103) and 7 cm diameter by 30 cm long (LB19_0104) plastic cores by push coring. Lithified samples were collected at Sites 2 and 3 using an electric drill with a 1 inch diamond coring bit. Soft samples collected by push core and directly in cubes were frozen after sampling.

A lower Cambrian stromatolite limestone head was taken from the middle of Unit 18 (Khomentovsky and Gibsher, 1996) of the Bayan Gol section within the Bayan Gol Formation. The sample was only oriented with respect to stratigraphic up, and with relatively high uncertainty as the sample was not originally collected for paleomagnetic study. The sample has parallel, but not horizontal, internal laminations (**Figure 2F**), consistent with convex-upward growth over a domal structure.

In the laboratory, lithified hand samples were sliced perpendicular to laminations or growth directions. Each slice was further subdivided along a grid forming samples of 1–1.5 cm^3. These specimens, as well as the unoriented living GSL specimens, were immobilized in 2 cm^3 plastic cubes using nonmagnetic paddings. Push cores from LB were split longitudinally while frozen and were then allowed to soften so they could be subsampled vertically every 3.5 cm using 2 cm^3 cubes. Four specimens from each vertical horizon were collected. Electric drilled samples were cut into 2 cm long specimens. Types of samples and the number of sub-sampled specimens are listed in **Table 2**.

Magnetic Methods

NRM and magnetic susceptibility (χ) were measured on all specimens with the exception of χ on LB drill core specimens. Most specimens were stepwise alternating field (AF) demagnetized to the point where a specimen lost 85–95% of the initial magnetization intensity. LB push core specimens from samples LB_0103, 0104 were not demagnetized because they dried and orientation was lost following NRM measurement. Frozen living LB samples LB_0101 and 0102 were demagnetized, but specimens thawed during measurement, leading to movement inside the cubes and noisy data that could not be interpreted. Specimen orientation during demagnetization was alternated between + X/+Y/+Z and -X/-Y/-Z directions to reduce the effects of possible unwanted bias field inside the AF demagnetizing device. Additional specimens (GSL19_0103 and BG14_0101) were subjected to stepwise thermal demagnetization to 700°C for comparison. A best-fit characteristic remanent magnetization (ChRM) was calculated using principal component analysis (Kirschvink, 1980) from the higher coercivity or temperature fraction. To calculate sample-average ChRM statistics (Fisher, 1953), we accepted AF-demagnetized specimens with anchored maximum angular deviation (MAD) < 10°. Data interpretation and sample-level Fisher mean calculations were performed using the PmagPy software (Tauxe et al., 2016).

Following AF demagnetization, a single-step anhysteretic remanent magnetization (ARM) was acquired in a 150 mT AF with 0.05 mT bias field. An isothermal remanent magnetization (IRM) was acquired in steps between 0 mT and 1,000 mT on fully demagnetized specimens. Some specimens had already been exposed to high fields, and in this case a stepwise IRM was acquired starting from a backfield of -1,000 mT IRM. These two methods are symbolized as IRM_{0mT} for the first case and $IRM_{-1000mT}$ for the second case. To calculate the S-ratio, fully AF-demagnetized (to 200 mT) specimens were given an IRM at 300 mT after an exposure to a saturation field at a 1,000 mT in the opposite direction. The S-ratio was calculated based on the formula of Thompson and Oldfield, 1986 as S-ratio = $-IRM_{300mT}/IRM_{1000mT}$.

The first derivatives of IRM acquisition curves were unmixed mathmatically to provide information on coercivity distributions and magnetic mineral populations (e.g., Robertson and France, 1994). This was carried out using MaxUnmix (Maxbauer et al., 2016) online software which fits a set of skew normal distributions to the data. For each distribution, the mean coercivity (MC), dispersion parameter (DP), relative proportion, skewness, and standard deviations were obtained.

Finally, to better constrain magnetic mineralogy, selected specimens were subjected to thermal demagnetization of a 3-axis IRM (Lowrie, 1990). IRMs of 1,000, 300, and 100 mT were applied in three orthogonal directions to separate the hard, medium, and soft coercivity fractions, and specimens were then thermally demagnetized to 700°C.

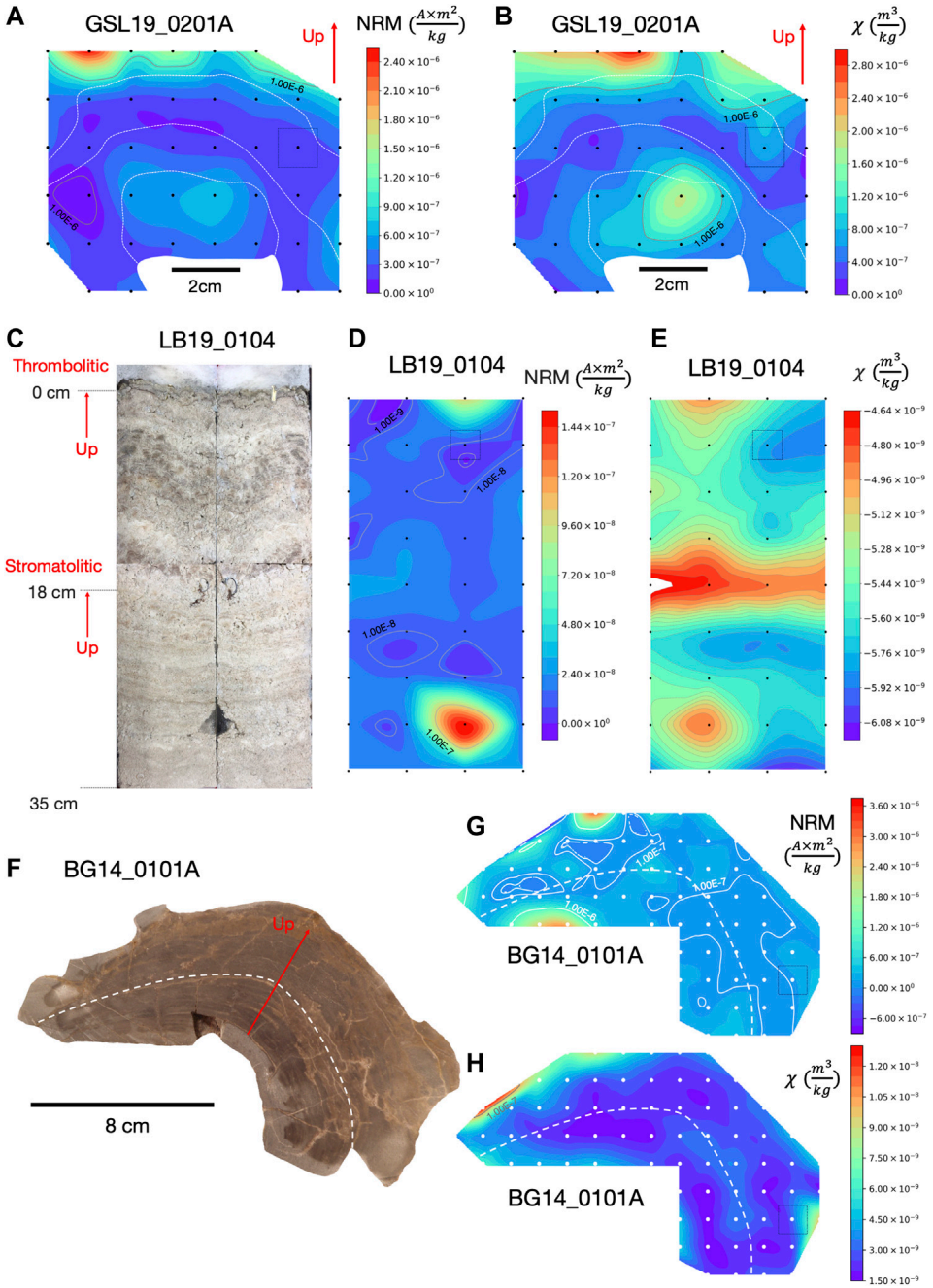

FIGURE 2 | NRM intensity and magnetic susceptibility maps of microbialites with cubic interpolation to produce contours. **(A)** NRM intensity map and **(B)** magnetic susceptibility map of GSL19_0201A with approximate 1.5 cm spatial resolution. **(C)** Photo of split large push core (LB19_0104) from unlithified living microbialite with stromatolitic structures laminations up to 18 cm and thrombolitic structures from 18 cm to the top. **(D)** NRM intensity map and **(E)** magnetic susceptibility map of LB19_0104 with approximate 3.5 cm spatial resolution. **(F)** Photograph of BG14_0101 sample slice prior to sub-sampling, and **(G)** its NRM intensity map and **(H)** magnetic susceptibility map with approximate 1 cm spatial resolution. Color contours are on a linear scale but labeled gray contour lines show order of magnitude variations. Black or white dots are sample positions and the color bars represent NRM intensity (Am^2/kg) and magnetic susceptibility (m^3/kg) values in the color range. Gray squares illustrate approximate specimen sizes on sample maps. Solid (up) red arrow indicates up in the field and is similar to the sample growth direction. White dashed lines roughly represent locations of distinct laminations. The red arrow represents the up direction in the field, which is close to the growth direction.

Remanence measurements were made using a 2G Enterprises 755SRMS Superconducting Rock Magnetometer inside a magnetically shielded room. Magnetic susceptibilities were acquired using an AGICO MFK1-FA Multifunction Kappabridge susceptibility bridge. AF demagnetization and ARM acquisition were undertaken with an ASC D-2000 AF

TABLE 2 | Sample types and magnetic properties.

Sample Id	Type	O	X (n)	X. σ	NRM (n)	NRM. σ	ARM (n)	ARM. σ	IRM (n)	IRM. σ	S-ratio (n)	S. σ
GSL18_0101	HS	U	2.05E-07 (2)	3.86E-07	4.79E-07 (2)	3.36E-07	9.42E-07 (2)	6.57E-07	6.01E-05 (2)	3.63E-06		
GSL18_0102	HS	U	1.67E-07 (1)		2.52E-07 (1)		4.38E-07 (1)					
GSL18_0104	HS	U	−7.63E-08 (1)		2.50E-07 (1)		2.42E-07 (1)					
GSL18_0201	HS	U	5.97E-07 (1)		4.84E-07 (1)		7.42E-07 (1)					
GSL18_0202	HS	U	9.63E-07 (4)	6.66E-07	3.34E-06 (4)	4.60E-06	8.15E-07 (4)	1.93E-07				
GSL18_0301	HS	F	9.90E-07 (55)	5.07E-07	4.42E-07 (55)	4.42E-07	6.58E-07 (55)	2.92E-07	9.05E-05 (19)	5.87E-05	0.96 (19)	0.03
GSL18_0401	HS	U	9.80E-08 (2)	1.34E-07	1.47E-06 (2)	7.10E-07	7.94E-07 (2)	8.35E-08				
GSL18_0402	HS	U	9.91E-07 (4)	3.81E-07	7.07E-07 (4)	5.98E-07	9.88E-07 (4)	3.72E-07				
GSL19_0103	HS	F	3.12E-07 (45)	1.03E-06	9.76E-07 (45)	8.96E-07					0.92 (35)	0.01
GSL19_0201	HS	F	8.26E-07 (42)	6.16E-07	5.08E-07 (42)	4.64E-07					0.92 (42)	0.02
GSL19_0202	HS	F	9.05E-07 (22)	4.57E-07	4.69E-07 (22)	3.41E-07	1.01E-06 (22)	3.46E-07	7.65E-05 (6)	2.72E-05	0.92 (16)	0.02
LB19_0101	BS	F	−5.99E-07 (8)	2.56E-08	2.08E-08 (8)	9.14E-09	8.92E-08 (8)	8.58E-09				
LB19_0102	BS	F	−5.66E-07 (9)	2.09E-08	4.49E-08 (9)	3.68E-08	1.02E-07 (2)	2.18E-08	5.17E-06 (1)			
LB19_0103	PS	P	−4.71E-09 (8)	4.76E-10	3.84E-08 (8)	2.61E-08						
LB19_0104	PS	P	−5.47E-09 (36)	7.53E-09	2.17E-08 (36)	2.69E-08						
LB19_0201	DC	P			4.87E-08 (3)	1.62E-08						
LB19_0301	DC	P			5.12E-08 (5)	7.24E-09	1.03E-07 (5)	3.80E-08	3.46E-06 (5)	3.01E-06	1.02 (5)	0.02
LB19_0302	DC	P			1.34E-07 (6)	1.16E-07						
LB19_0304	BS	F	−5.90E-07 (6)	6.48E-08	1.87E-07 (6)	4.13E-07	1.08E-07 (2)	8.07E-09	7.14E-06 (2)	3.34E-06		
BG14_0101	HS	P	3.49E-09 (71)	1.98E-09	3.33E-07 (71)	5.54E-07	9.53E-07 (28)	4.73E-07	2.79E-05 (35)	1.55E-05	0.76 (35)	0.14

O, orientation, n, number of measured specimens, χ, mean magnetic susceptibility (m^3/kg), χ. σ, standard deviation of magnetic susceptibility (m^3/kg), NRM, mean natural remanent magnetization intensity (Am^2/kg), NRM. σ, standard deviation of NRM (Am^2/kg), ARM, mean anhysteretic remanent magnetization (Am^2/kg), ARM. σ, standard deviation of ARM (Am^2/kg), IRM, mean 1000 mT isothermal remanent magnetization (Am^2/kg), IRM. σ, standard deviation of IRM (Am^2/kg), S-ratio, mean value of -IRM_{300mT}/IRM_{1000mT}, S. σ, standard deviation of S-ratio. HS, hand sample, BS, block sample directly collected from surface, PC, push piston core samples, DC, drilled core samples by portable electric drill, U, unoriented, F, fully oriented, P, partially oriented.

demagnetizer. Stepwise thermal demagnetization was undertaken by an ASC Thermal Demagnetizer, and IRM was imparted with an ASC Impulse Magnetizer. These measurements were all conducted at the Paleomagnetism Laboratory at the University of Wisconsin- Milwaukee. Additionally, magnetization vs. applied field (up to 1 T) measurements were conducted on a Princeton Measurements vibrating sample magnetometer at the Institute for Rock Magnetism, University of Minnesota. The samples were all weakly magnetic and had a high diamagnetic: ferrimagnetic or paramagnetic:ferrimagnetic ratio, and hysteresis parameters could not be accurately calculated. We instead report the high-field behavior of the samples.

RESULTS

Magnetization Intensity and Susceptibility Variations

With the exception of LB samples, all samples possess an average NRM intensity 1.00E-07 Am^2/kg. **Table 2** displays average magnetic susceptibility, NRM, ARM and IRM_{1000mT} with standard deviations of each sample. The NRM intensity measurements for all samples (>1.00E-11 Am^2) were not limited by the sensitivity of the cryogenic SQUID magnetometer (~1.00E-12 Am^2 moment sensitivity limit). However, specimens with NRM intensity less than 1.00E-10 Am^2 approach the magnetization of sample container (1.00E-13 to 1.00E-11 Am^2). χ measurements are limited by the sensitivity of the MFK1 Kappabridge susceptibility bridge (~2.00E-08 SI or ~2.00E-13 m^3).

To assess internal spatial variations in magnetization and distribution of magnetic minerals, mass-normalized magnetic susceptibility and NRM intensity of four GSL hand samples, two LB push core samples, and one BG hand sample were contoured by cubic interpolation (**Figure 2**). Spatial variations in magnetization within these microbialite structures were compared to their internal laminations with the aim of understanding magnetization processes and assessing NRM reliability.

Samples GSL19_0103, GSL19_0201, and GSL19_0202 have a spatial correlation between NRM intensity and magnetic susceptibility. GSL19 microbialite NRM and susceptibility vary along the growth directions and are consistent along internal laminations (**Figures 2A,B**, **Supplementary Figure S1**). With the exception of a high NRM intensity spot at the bottom right, LB19_0104 has roughly consistent NRM intensity distribution along internal structures (**Figure 2D**). The magnetic susceptibility mapping shows high values around 18 cm depth, the transition level where stromatolitic laminations changed to a thrombolytic structure (**Figure 2E**). BG14_0101 has roughly constant NRM intensity (**Figure 2G**) and magnetic susceptibilities (**Figure 2H**) along laminations, with a low value in middle layers compared to outer and bottom layers. Magnetic susceptibility and NRM of GSL18_0301 and LB19_0103 (not shown), which have a width less than 10 cm, have similar magnetic susceptibility and NRM intensity trends. However, no obvious correlations with laminations are observed within these small samples.

Magnetic Mineralogy

Results from all samples are consistent with magnetite as a dominant magnetic carrier. This component has a mean

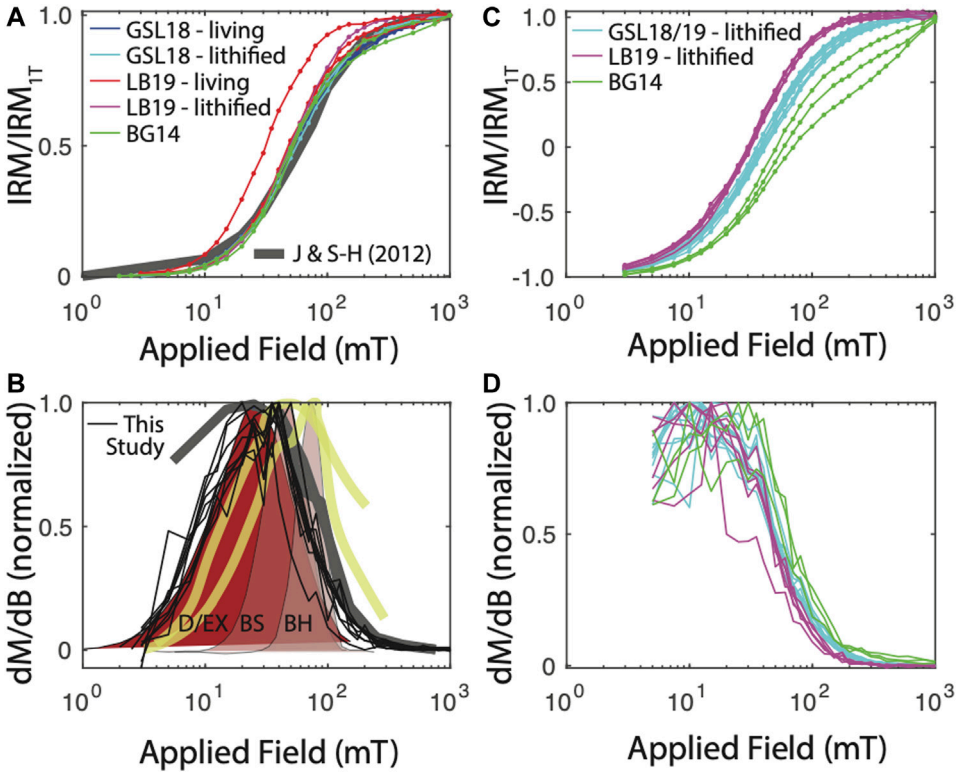

FIGURE 3 | IRM acquisition results. **(A)** IRM acquisition starting from the AF-demagnetized state. For comparison, IRM acquisition curves for two remagnetized carbonates are shown (Jackson and Swanson-Hysell, 2012). **(B)** Derivative of IRM acquisition, normalized to peak value to better compare spectra. Data from **(A)** shown in thin black lines. For comparison, data from Jackson and Swanson-Hysell (2012) in thick gray line. Surface carbonate platform muds in thick yellow lines (Maloof et al., 2007). Biogenic hard (BH), biogenic soft (BS), and detrital + extracellular (D/EX) shown in shaded brown from Egli (2004). Maloof et al. (2007) and Egli (2004) distributions derived from AF demagnetization of a 300–350 mT IRM and are therefore not strictly analagous to data from this study. **(C)** Backfield IRM acquisition and **(D)** derivative.

coercivity of ~29–57 mT (**Supplementary Table S1**), consistent with single domain (SD) to 'pseudo-single-domain' (PSD) minerals that have non-uniform spin behavior. Modern samples (e.g., GSL, LB) are dominated by this component and have large negative high-field diamagnetic slopes. The Cambrian BG sample, however, has a mixture of low- and high-coercivity minerals with positive high-field paramagnetic slopes (**Supplementary Figure S2**).

GSL18: The S-ratio range of 19 lithified GSL18_0301 specimens is 0.92–1.06, with an average of 0.96, indicating that low coercivity ferrimagnetic minerals such as magnetite are dominant. Based on IRM unmixing results, the dominant magnetic components of the GSL18 living and GSL18_0301 lithified specimens have a mean coercivity of ~56 mT for four IRM_{0mT} unmixing results and ~38 mT for four $IRM_{-1000mT}$ unmixing results, with similar DPs of 2.7 mT. Coercivity spectra derived from IRM acquisition data for all specimens are shown in **Figure 3**. There is little variability between living and lithified specimens from the same site. The three-component IRM demagnetization experiment shows a gradual decrease of the soft (71–78%) and medium (17–23%) coercivity fractions to 575°C and flattening after 620°C (**Figure 4A**). This gradual unblocking is consistent unblocking of domain walls, but may also represent some compositional variability. A high-coercivity fraction contributes <7% to the total IRM, and measurement noise made it difficult to evaluate a maximum unblocking temperature.

GSL19: The average S-ratio value of 93 GSL19 specimens is slightly lower than GSL18, with an average of 0.92 and a range of 0.87–0.96 (**Table 2**). All three GSL19 samples have a spatially correlated NRM intensity and S-ratio. High NRM correlates with high S-ratio (**Supplementary Figures S1**, **S3**). Only a single magnetic component can be confidently identified in six specimens of the Pleistocene GSL19_0202 based on $IRM_{-1000mT}$ unmixing. This dominant component has a mean coercivity of 38 mT with a DP of 3.1 mT, again consistent with SD to 'PSD'-like magnetite. The soft (68–73%) and medium (22–26%) coercivity fractions flatten out at ~580°C in the three-component IRM test (**Figure 4B**). Although a higher-coercivity component was not identified in the relatively noisy IRM unmixing data, hard minerals comprise a small fraction (5–8%) of the three-component IRM and gradually decrease to 675°C, consistent with hematite.

LB19: LB results are similar to those observed in GSL18 specimens. The S-ratio range of five LB19_0301 specimens is 0.99–1.05 with a mean value of 1.02, again consistent with low-

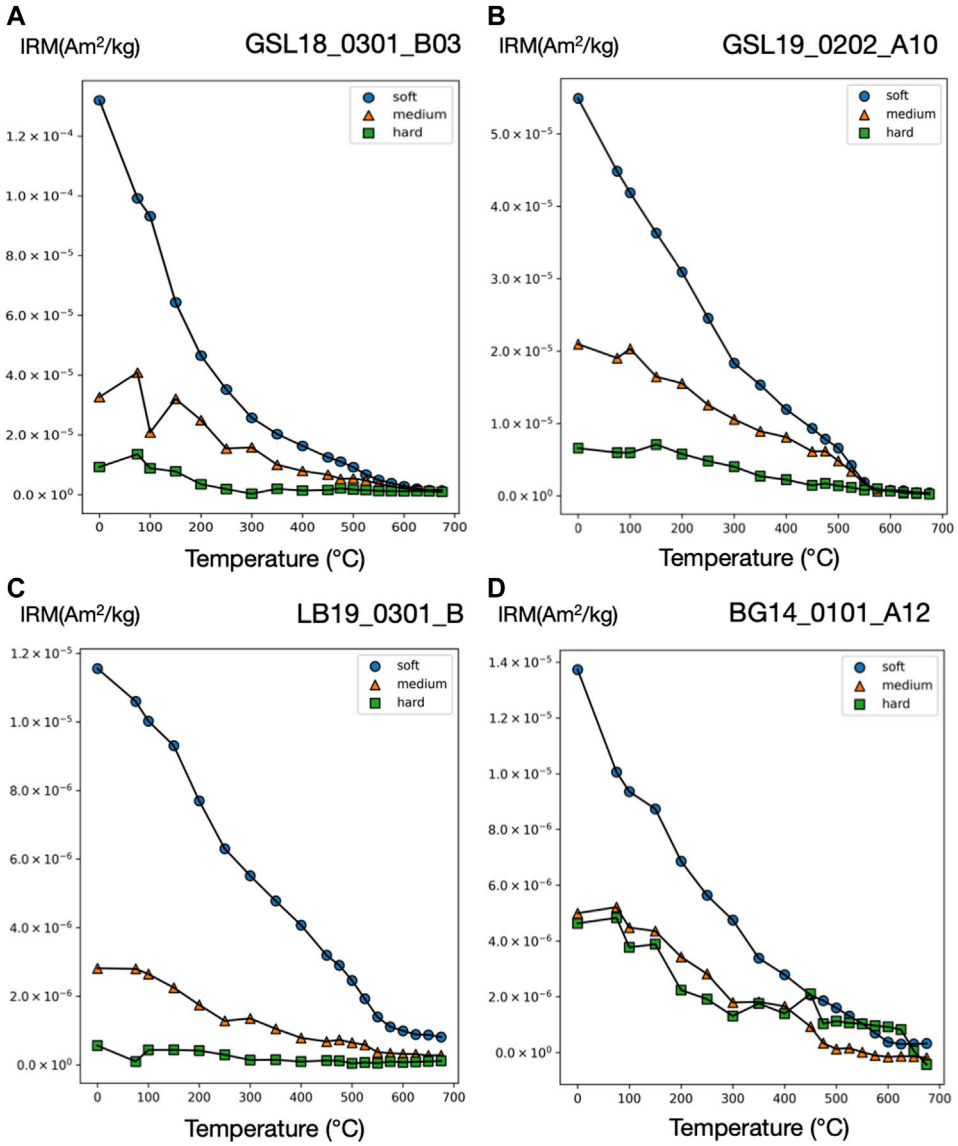

FIGURE 4 | Three-component IRM technique thermal demagnetization results for microbialite samples **(A)** GSL18 **(B)** GSL19 **(C)** LB19, and **(D)** BG14. Three-component IRM (Am^2/kg) produced with applied field of 100 mT (soft), 300 mT (intermediate), and 1,000 mT (hard). Soft, medium, and hard fractions are shown as blue circle, orange triangle, and green square, respectively. Additional plots are included in **Supplementary Figure S4**.

coercivity minerals like magnetite. LB19_0102, 0301, and 0304 were subjected to IRM unmixing experiments and all LB microbialites have a consistent dominant component with a mean coercivity of 28–50 mT with a DP of 2.2–2.9. No major differences are observed between living microbial sediments and lithified microbialite samples in terms of component numbers, major MC, or DP. In the three-component IRM experiment, the low-coercivity fraction accounted for the highest proportion (75–81%) of IRM for 4 specimens of LB19_0301. This component gradually decreased and flattened out after 575°C–600°C, indicating magnetite (**Figure 4C**). With the exception of LB19_0301_C, the medium coercivity (17–22%) components have maximum unblocking temperatures of 550°C, and there is no significant hard coercivity fraction (<5%) (**Supplementary Figure S4**).

BG14: Unlike the GSL and LB samples, the BG stromatolite has variable magnetic mineralogy with a large S-ratio range from 0.42 to 0.95 (**Figure 5**). Low coercivity minerals are present in higher concentrations in inner layers and high coercivity minerals occur in outermost layers except two points at the left top. This is also shown in IRM acquisition (**Figure 3C**) and unmixing curves (**Figures 3D**, **5**) where outer layers have a significant high coercivity component (purple lines in **Figure 5**). Based on the three-component IRM results (**Figure 4D**), the soft fraction is the largest (51–69%) and gradually unblocks up to ~575°C, again consistent with magnetite. The medium fraction (20–25%)

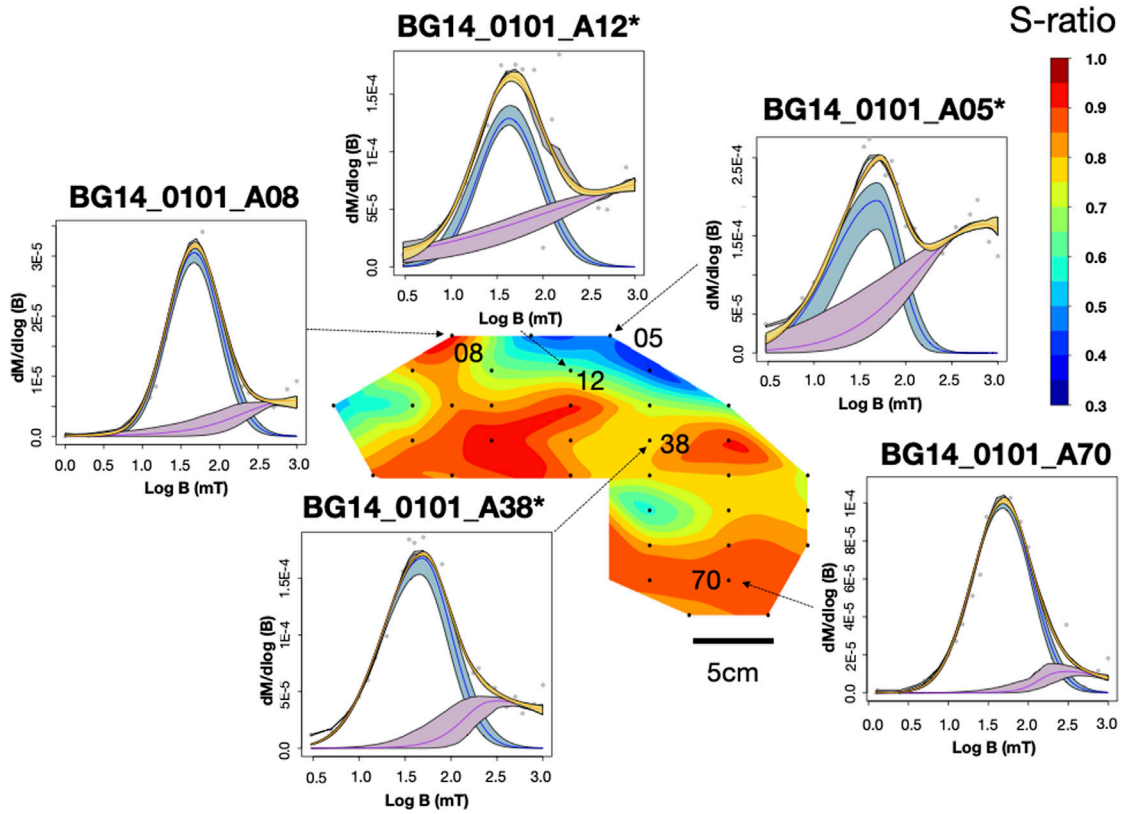

FIGURE 5 | IRM unmixing curve and S-ratio distribution for sample BG14_0101. IRM results were plotted through the MaxUnmix online software (Maxbauer et al., 2016) on a log scale. Gray dots represent actual data, and yellow lines represent total IRM best-fit based on real data. Colored lines (blue and purple) represent different coercivity components. The shadings represent 95% confidence intervals calculated using a resampling algorithm with $N = 300$. An asterisk next to a specimen name indicates that the specimen went through the -1000mT IRM process.

decreases to ~300–350°C for low S-ratio specimens (e.g., BG14_0101_A05 and 12), consistent with titanomagnetite and/or pyrrhotite. The medium fraction in high S-ratio specimens additionally decreases to ~650°C (e.g., BG14_0101_A12 and 70), consistent with (titano)hematite and/or thermally stable maghemite (**Supplementary Figure S4**). The hard fraction of low S-ratio and high S-ratio specimens accounts for 20–30% and <12% of the IRM, respectively. This fraction decreases to about 625°C–675°C, consistent with the presence of hematite.

Directional Analysis

GSL: Fifteen measured (unoriented) actively growing cyanobacteria layers are fully demagnetized by around 40–100 mT, and a stable paleomagnetic direction is isolated up to 60 mT (**Figure 6A**). A small overprint is typically removed by ~7.5 mT. Of the lithified (oriented) samples GSL18_0301, GSL19_0103, and GSL19_0202, 47% (26/55), 100% (10/10) and 35% (8/23) respectively have stable AF demagnetization behavior (**Figure 6C**), and 80% (8/10) of GSL19_0103 specimens have stable thermal demagnetization behavior (**Figure 6D**). Sample-level Fisher mean declinations (**Figure 7A**) of all samples are close to that predicted for a geocentric axial dipole (GAD) or to models of paleosecular variation for the past 10 kyr (CALS10k.2; Constable et al., 2016). However, GSL18_0301 (43.9°) and GSL19_0103 (36.7°) have anomalously shallow inclinations.

LB: Living sediments (e.g., LB19_0101, 0102, 0304) and lithified microbialites (e.g., LB19_0301) were fully demagnetized by 25–60 mT and 60–70 mT, respectively. Five specimens of lithified microbialite LB19_0301 have stable AF-demagnetization, and magnetic directions are isolated between 12.5 mT and 60 mT (**Figure 6B**). Most of the LB sites were located in moving water, which may complicate interpretation of DRM directions. LB19 Site 1 was in a stagnant environment, so only specimens from this site were used for directional analysis. These samples were not demagnetized (see *Magnetic Methods*), we report only NRM directions for this site. The Fisher (1953) mean direction (**Table 3**) of LB19_0101 (N = 8) and LB_0102 (N = 8) overlap the CALS10k.2 or GAD, although they have high α_{95} values. LB19_0104 (N = 36) has a large declination dispersion consistent with rotation of the core during sampling. The inclination-only (McFadden and Reid, 1982) Fisher mean of LB19_0104 is 36.8° ± 7.15, which overlaps the GAD value of 33.9° (**Figure 7B**; **Table 3**).

BG: BG14_0,101 was only oriented with respect to up, but specimens in the structure were mutually oriented. AF

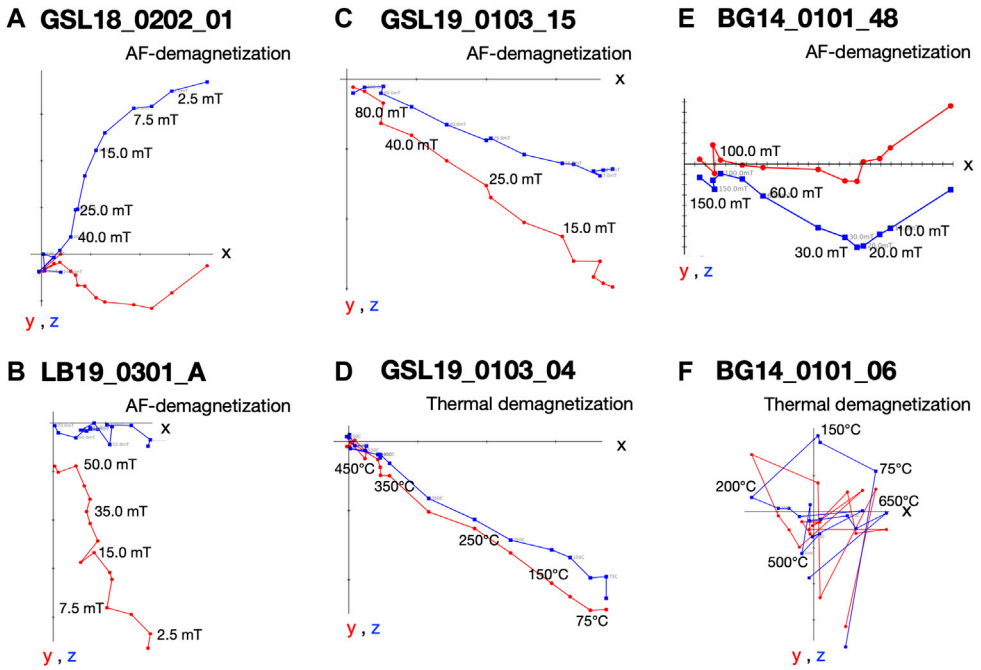

FIGURE 6 | Vector endpoint diagrams for representative microbialite specimens. **(A)** AF demagnetization pattern for living Antelope Island GSL microbialite specimen GSL18_0202_01 **(B)** AF demagnetization pattern for living lithified LB Site 3 microbialite specimen LB19_0301_A **(C)** AF demagnetization pattern for specimen Lakeside lithified GSL microbialite GSL19_0103_15 **(D)** thermal demagnetization of specimen GSL19_0103_04 **(E)** AF demagnetization for BG stromatolite specimen BG14_0101_48; and **(F)** thermal demagnetization for specimen BG14_0101_06.

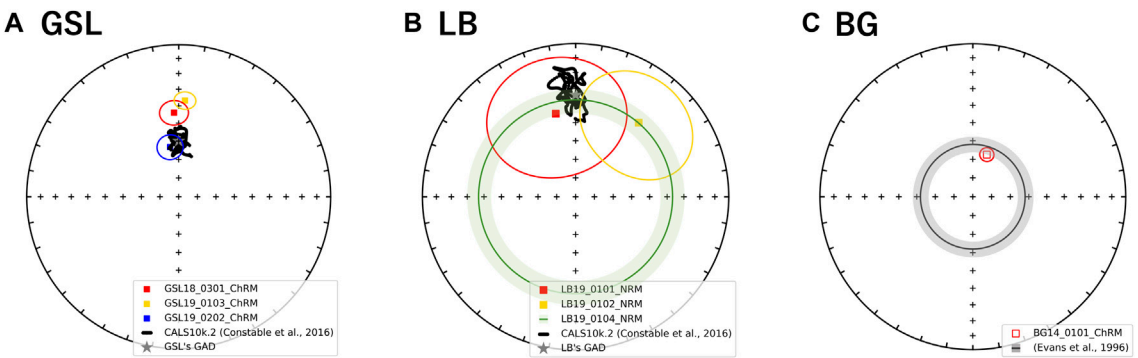

FIGURE 7 | Equal area stereographic projection of magnetization components observed from **(A)** GSL **(B)** LB, and **(C)** BG samples. The mean declination and inclination with α95 ellipses of NRM or ChRM. Where declination was not available (LB19_0104) mean inclination is shown as a circle around the center with α95. Open and closed symbols represent directions in the upper and lower hemisphere, respectively. A gray star in **(A)** GSL **(B)** LB panel represents GAD value of each site. The black line on GSL and LB stereographic projections represent the CALSk10.2 model based on the latitude and longitude of GSL sampling site from 10 ka to present (Constable et al., 2016). The gray shading annulus on the BG panel (inclination: −62 ± 4°) represents the expected directions derived from sedimentary beds in the same formation (Evans et al., 1996).

demagnetization was more effective in extracting stable magnetizations (59.4%), and an overprint is typically removed by ~30 mT. None of the thermally processed specimens ($N = 10$) had a coherent demagnetization pattern (**Figures 6E,F**). Pilot thermomagnetic data, c(T), show the production of magnetite at temperatures > ~400°C (**Supplementary Figure S5**), consistent with the thermal decomposition of siderite (e.g., Pan et al., 2000). ChRM Fisher mean inclinations for 22 out of 37 AF-demagnetized specimens (−66.3° ± 3.7°) overlap with the inclination (−62 ± 4°) obtained from siliclastic sediments with calcareous interbeds in the Bayan Gol formation (Evans et al., 1996) (**Figure 7C**). There are inclination variations, however, associated with bedding/lamination slopes of the microbialite. While inclinations from one side with respect to the vertical have inclinations of −75.0° to −65.0°, those from the other side are −65.0° to −55.0° (**Figure 8**).

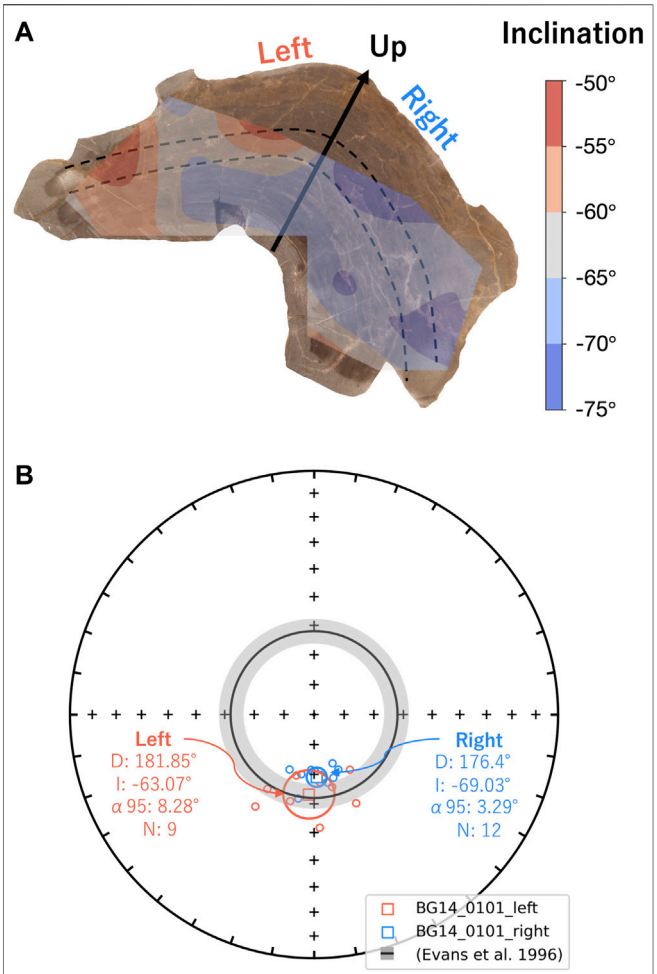

FIGURE 8 | (A) Inclination mapping of the BG14_0101 sample slice with contouring by cubic interpolation. The black arrow and dashed lines represent up directions and laminations. **(B)** Equal area stereographic projection of reoriented magnetization components of the sample BG14_0101 by rotating total mean declination to the magnetic north. Specimen declinations and inclinations from the left and right sides with respect to the stratigraphic up direction (black arrow) are symbolized as red and blue circles, respectively. The mean direction of each group is marked as a square symbol with α95 ellipses. The gray shading annulus on the BG panel (inclination: −62 ± 4°) represents the expected directions derived from sedimentary beds in the same formation (Evans et al., 1996).

DISCUSSION

Magnetic Minerology

While S-ratio values for all modern microbialites (i.e., GSL18, LB19) are high (i.e., magnetite), ancient samples (i.e., GSL19, BG14) have lower values that indicate the presence of additional high coercivity materials. IRM unmixing results and three-component IRM tests show that all modern samples are dominated by a component with a mean coercivity of 37 mT for $IRM_{-1000mT}$ and 48 mT for IRM_{0mT}, with the DP of 2.7, consistent with magnetite. The BG microbialite has a high relative proportion of high coercivity and high unblocking-temperature (up to 675°C) minerals consistent with hematite. A signature from high coercivity fractions is observed in IRM unmixing results for weakly magnetic living GSL18 and LB19 cyanobacteria layer samples. This might represent a small proportion of high coercivity material, but experimental noise means this component is poorly constrained. While three-component IRM results contain a hint of hard fractions (<7%), we infer that these signatures are experimental noise based on S-ratio results.

This difference in magnetic mineralogy between young and old microbialite samples may be attributed to different depositional material in the original environment. It is also possible that the high-coercivity minerals formed during diagenesis, leading to concerns of a partial or complete overprint in the ancient samples. However, these high-coercivity minerals do not appear to contribute to the NRM, which is fully AF-demagnetized at < 200 mT and is held entirely by low-coercivity minerals.

The coercivity distribution for nearly all GSL and LB specimens is remarkably similar, although GSL specimens have slightly higher coercivity (**Figure 3**). These distributions are similar to IRM acquisition for some remagnetized Devonian carbonates (Jackson and Swanson-Hysell, 2012). That study interpreted the magnetic signature to arise at least partially from authigenic formation of SD magnetite, an interpretation favored by many other studies of carbonate rocks (e.g., Jackson 1990; McCabe and Channell, 1994; Suk and Halgedahl, 1996; Swanson-Hysell et al., 2012). Diagenesis seems an unlikely explanation for the GSL and LB samples, where we see no difference between living and lithified specimens.

In **Figure 3B**, we also compare our coercivity spectra derived from the IRM_{0mT} with spectra derived from AF demagnetization of a 300 mT (Egli, 2004) or 350 mT (Maloof et al., 2007) IRM. Spectra are all normalized to their peak value for better comparison. While the methods are not strictly analogous, our spectra show a lower mean coercivity but similar dispersion (in log space) to two spectra measured on surface carbonate platform muds in the Bahamas (Maloof et al., 2007). Based on these and other data, Maloof et al. (2007) interpret the magnetic remanence in their samples to arise largely from magnetotactic bacteria. The component spectra from Egli (2004) are derived from IRM unmixing of lake sediment data. Two narrow spectra with peaks at ~45 mT ('biogenic soft') and ~75 mT ('biogenic hard') are interpreted to result from the presence of magnetotactic bacteria, while a much broader distribution with a peak at ~25 mT is thought to be a mixture of detrital magnetite and extracellular biogenic magnetite, which have overlapping distributions. Our spectra most closely resemble this detrital/extracellular component. We interpret the GSL and LB samples to be dominated by a similar component, although we cannot exclude some contribution from lower-coercivity magnetotactic bacteria.

The BG samples have a similar component consistent with detrital and/or extracellular magnetite, in addition to the high coercivity component. Due to the age of the sample, we cannot exclude the additional possibility of authigenic magnetite (e.g., Jackson and Swanson-Hysell, 2012), although there is some evidence the magnetization may be detrital in origin (*Origin*

and Timing of Magnetization). Authigenic magnetite is common in many carbonates (e.g., Jackson, 1990; McCabe and Channell, 1994; Suk and Halgedahl, 1996; Jackson and Swanson-Hysell, 2012; Swanson-Hysell et al., 2012). Early reductive diagenesis can dissolve primary magnetite and produce iron sulfides such as pyrite, which may then later oxidize to magnetite (e.g., Suk et al., 1990a; Suk et al., 1990b; Weil and Van der Voo, 2002; Kodama, 2012; Roberts, 2015). Nevertheless, it has been proposed that the early lithification and cementation associated with some microbialites may lead to an increased probability of preserving the primary magnetic mineralogy (Maloof et al., 2007).

Origin and Timing of Magnetization

Directional information from microbialites with moments <1.00E-10 Am^2 is apparently less reliable, likely due to a small but significant contribution from the chosen sample containers (1.00E-13 to 1.00E-11 Am^2). As these samples demagnetize, they also approach the stated sensitivity of the magnetometer (~1.00E-12 Am^2). These effects could be reduced in future studies in part by careful choice of sample holders.

Our results for microbialite ChRMs with sufficiently high magnetization appear to record directions close to the expected field direction, with some caveats. The Laguna Bacalar NRM directions are consistent with the expected field direction but have large uncertainties. We interpret these uncertainties to arise from the relatively small number of specimens measured and the lack of AF cleaning which would remove any overprints. While the inclination recorded by the Bayan Gol formation stromatolite is consistent with that reported by Evans et al. (1996) in sediments from the same formation, those authors could not preclude the possibility of a remagnetization. Even though the ChRM was determined to pre-date folding, the entire measured section was of a single polarity, leading the authors to question a primary remanence.

Despite these limitations, an attraction of using ancient microbialites is to potentially recover high temporal resolution variations of geomagnetic field, and it is therefore important to assess the timing and origin of the acquired magnetization. Is the magnetization detrital, locked in soon after deposition and incorporated into the microbialite matrix? Or is it a chemical remanence (biomediated or otherwise) acquired soon after deposition? Or is it related to later diagenesis?

The observed relatively homogenous magnetization along microbialite laminations and variations across laminations suggests a magnetic mineral concentration and magnetization distribution associated with deposition. All studied microbialites seem to preserve this magnetization pattern.

The observed deviation of paleomagnetic directions away from expected values (declination ±10°, inclination ±20°) may be caused by deposition on sloping beds. King (1955) and Kodama (2012) proposed that when a bed dips (shallowly) in the same direction as the magnetic field, the magnetization vector would be steeper by the degree of dip gradient. If the bedding slope is opposite to the Earth's magnetic field, the inclination can be shallower. Many microbialites have domal internal structures, hence, magnetic directions recorded by different parts of the structure might be disturbed by the effect of deposition on a sloping bed, although there are some obvious differences between normal sedimentary deposition and incorporation into a filamentous microbial matrix. Sample GSL18_0301 was from the (very) steep side of the columnar mound structure, with a slope opposite to the magnetic field. The sample Fisher mean inclination of 43.9° is 16.1° shallower than the geocentric axial dipole (GAD) inclination, and the magnetic vectors may have experienced a bedding-related shallowing. Data from partially oriented sample BG14_0101 were rotated (**Figure 8B**) so that the mean declination corresponds to geographic south (expected declination for reverse polarity). In this orientation, the left side of the stromatolite (**Figure 8A**) dips down toward geographic south, opposite to the field direction which is up (negative inclination) and has an inclination shallower than total mean of −66.3° (**Figure 8B**). By contrast, the right side on **Figure 8A** dips down to geographic north, roughly parallel to the field, and has a steeper inclination. Inclinations from right side of the structure are −75.0° to −65.0° (Fisher mean = −69.0° ± 3.3°), while the specimens from left side are −65.0° to −55.0° (Fisher mean = −63.1° ± 8.3°), which might support the bedding slope effect. However, Watson's F-test (Watson, 1956) and V_w-test (Watson, 1983) both show that these means are not statistically distinct at the 95% confidence level. In contrast to these two samples which show inclination deviations, all GSL 19 samples are small structures (<40 cm diameter), and specimens from throughout the structure were used and averaged out. The push core sample LB19_0104 was from the middle of the structure with nearly horizontal layering, and here the Fisher mean inclination of 36.8° ± 7.2° is close to the expected GAD inclination of 33.94°. While not conclusive, these inclination variations associated with the slope of the microbialite layering are intriguing and point to preservation of a primary DRM.

DRM is a relatively inefficient magnetization process, so the DRM/ARM ratio should be relatively low. While not definitive, a ratio of NRM/ARM <1 is consistent with a DRM. Clastic sediments have a wide NRM/ARM range from ~0.1 to 0.8 (e.g., Levi and Banerjee, 1976; King et al., 1983; Constable, 1985). The NRM/ARM of biogenic magnetite is comparatively low (<0.05) in marine sediments (Roberts et al., 2012; Rodelli et al., 2019), but much higher values (0.4–1.4) have been documented in varved lake sediments dominated by biogenic magnetite (Snowball and Sandgrena, 2002). The low values in marine sediments are attributed to the SD state of the biogenic material which results in very efficient ARM acquisition (Egli and Lowrie, 2002) compared to larger particles. The elevated values in the varved sediments may be partially due to more efficient DRM acquisition in fresh water (Katari and Tauxe, 2000; Mitra and Tauxe, 2009); a higher concentration of particles leading to magnetic interaction effects on ARM acquisition (Egli and Lowrie, 2002); and/or reduced bioturbation (Egli and Zhao, 2015; Zhao et al., 2016). Chemical remanent magnetization (CRM) acquired by magnetite growth through the blocking volume has a CRM/ARM ratio of ~0.5 (Pick and Tauxe, 1991), which may be similar to extracellular magnetite produced *in situ* by bacteria within the microbialite matrix. It may or may not be similar to a CRM acquired during oxidation of

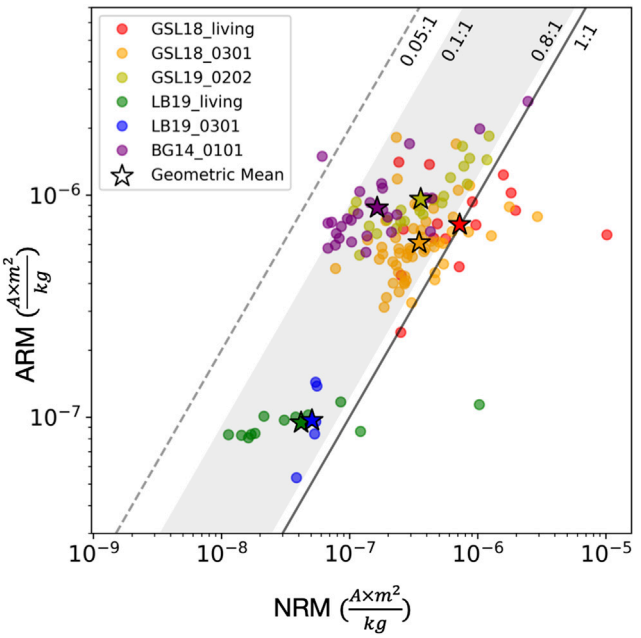

FIGURE 9 | NRM intensity (*x*-axis) vs. ARM intensity (*y*-axis) of microbialites on log scales. The sample group of GSL18_living (GSL18 living microbialites with cyanobacteria layer collected from Antelope Island Site 1, 2 and 4), GSL18_0301 (lithified microbialite from Antelope Island Site 3), GSL19_0202 (lithified modern microbialite from Lakeside Site 2), LB19_living (surface living microbialite samples collected from LB19 Site 1 and 3), LB19_0301 (lithified porous microbialite sample from LB19 Site 3), BG14_0101 (Cambrian Bayan Gol formation stromatolite) are shown with red, orange, yellow, green, blue, and purple circles, and their geometric means are symbolized with stars. The black solid line represents NRM to ARM ratio of 1 (x = *y*), and measurements plotted on the left side of this line (ARM >> NRM) is consistent with a DRM origin. The gray shading shows the NRM/ARM range of clastic sediments (0.1–0.8) (e.g., Levi and Banerjee, 1976; Constable, 1985), and the gray dashed line represents the maximum constraint for biogenic magnetite (0.05) (e.g., Roberts et al., 2012; Rodelli et al., 2019).

pyrite to magnetite, the processes possibly responsible for magnetite in remagnetized carbonates.

Figure 9 shows NRM vs ARM intensity data for this study, along with NRM/ARM bounds for clastic sediments (0.1–0.8) and marine biogenic magnetite (<0.05). The geometric mean of the NRM/ARM of GSL18 living microbialites, GSL18_0301, and GSL19_0202, are 0.98, 0.57, and 0.37, respectively. LB19 living microbialites and LB19_0301 have a geometric mean of 0.41 and 0.52, respectively. BG14_0101 has a geometric mean NRM/ARM ratio of 0.19, the lowest value among all microbialites. Most specimens are within the clastic detrital range with only one BG14_0101 specimen less than 0.05. These data are fully consistent with a predominantly clastic detrital origin, but some uncertainty in ratio for a biogenic contribution(s) and/or a CRM leaves room for other interpretations. While more work needs to be done to examine the magnetization process and the possible effects of diagenesis, the internal distribution of magnetization with respect to microbialite layering, NRM/ARM ratios, and the inclination variations correlated with bedding slopes suggest that the timing of sediment deposition and acquisition of magnetization samples are close and may be consistent with a primary DRM.

TABLE 3 | Sample-average Fisher statistics.

	D	I	N*	N	R	k	α95
GSL18_0301 (ChRM)	356.8	43.9	26	55	24.5	16.9	7.1
GSL19_0103 (ChRM)	3.76	36.7	18	20	17.6	44.8	5.2
GSL19_0202 (ChRM)	350.2	62.9	8	23	7.9	67.0	6.8
LB19_0101 (NRM)	346.6	43.6		8	6	3.5	34.9
LB19_0102 (NRM)	40.4	36.6		8	6.5	4.5	29.3
LB19_0104 (NRM)		36.8		36	31.5	7.8	7.15
BG14_0101 (ChRM)	18.5	−66.3	22	37	21.7	70.2	3.7

D, mean declination; I, mean inclination; N, number of MAD <10 specimens; N, number of total specimens; R, the length of the resultant vector; k, the precision parameter; α95; the circle of 95% confidence angle about the mean.*

CONCLUSION

We investigated the potential of modern and ancient microbialites as paleomagnetic recorders. Microbialites with NRM >1.00E-10 Am^2 record recoverable, stable magnetic directions. All microbialites appear to record average directions close to the expected field direction. The dominant NRM carrier in all samples is 35–50 mT SD to 'PSD' magnetite. The Cambrian BG sample also has a contribution from high coercivity minerals, which do not contribute to the NRM.

We interpret the NRM to be at least partially detrital in origin. This interpretation is based on the magnetization distribution in the structure, the NRM/ARM ratios consistent with detrital sediments, and inclination variations that correlate with changes in bedding slopes. In some cases, the NRM to ARM ratio is higher, suggesting another magnetization process. This may be due to biomineralization of magnetic minerals and/or diagenesis soon after deposition.

To reduce inclination variations resulting from sloping beds, samples from large domal structures should be collected avoiding steep sides or by sampling all sides. For smaller scale hand samples (<50 cm), the sample slice should be cut parallel to the expected direction of the magnetic declination. Then, specimens from different lamination angles should be collected to average out the deviations generated by sloping beds.

DATA AVAILABILITY STATEMENT

Raw data supporting the conclusions of this article are available in the Magnetics Information Consortium (MagIC) database at earthref.org/MagIC/17087.

AUTHOR CONTRIBUTIONS

J-IJ participated in GSL and LB field work, and collected and analyzed the data. JB designed the study and participated in GSL field work. Both authors contributed to the writing and editing of the manuscript.

FUNDING

This work was supported by a Research and Creative Activities Support (RACAS) award from the University of Wisconsin–Milwaukee (project AAD3431).

ACKNOWLEDGMENTS

We thank Bonnie Baxter and Jaimi Butler of Westminster College who provided assistance and education in sampling microbialites on Antelope Island. These samples were collected under permit provided to Westminster College by the Division of Parks and Recreation/Antelope Island State Park. We thank Tim Grundl for help with sampling at Laguna Bacalar, Steve Dornbos who provided the BG sample, and Joshua Marquardt for preliminary measurements on the BG sample. Many thanks to Andrew Roberts and Nick Swanson-Hysell whose comments helped improve this manuscript.

SUPPLEMENTARY MATERIAL

The Supplementary Material for this article can be found online at: https://www.frontiersin.org/articles/10.3389/feart.2021.603805/full#supplementary-material.

REFERENCES

Allwood, A. C., Walter, M. R., Kamber, B. S., Marshall, C. P., and Burch, I. W. (2006). Stromatolite reef from the early archaean era of Australia. *Nature* 441, 714–718. doi:10.1038/nature04764

Awramik, S. M. (2006). Palaeontology: respect for stromatolites. *Nature* 441, 700–701. doi:10.1038/44170010.1038/441700a

Awramik, S. M., and Grey, K. (2005). Stromatolites: biogenicity, biosignatures, and bioconfusion. *Proc. SPIE* 3906, 5906P1–5906P9. doi:10.1117/12.625556

Awramik, S. M., and Sprinkle, J. (1999). Proterozoic stromatolites: the first marine evolutionary biota. *Hist. Biol.* 13, 241–253. doi:10.1080/08912969909386584

Awramik, S. M. (1992). The oldest records of photosynthesis. *Photosyn Res.* 33, 75–89. doi:10.1007/bf00039172

Baumgartner, R. J., Kranendonk, M. J., Wacey, D., Fiorentini, M. L., Saunders, M., Caruso, S., et al. (2019). Nano–porous pyrite and organic matter in 3.5-billion-year-old stromatolites record primordial life. *Geology* 47, 1039–1043. doi:10.1130/g46365.1

Berelson, W. M., Corsetti, F. A., Pepe-Ranney, C., Hammond, D. E., Beaumont, W., and Spear, J. R. (2011). Hot spring siliceous stromatolites from Yellowstone National Park: assessing growth rate and laminae formation. *Geobiology* 9, 411–424. doi:10.1111/j.1472-4669.2011.00288.x

Berg, M. D. (2019). Domes, rings, ridges, and polygons: characteristics of microbialites from Utah's Great Salt Lake. *Sediment. Rec.* 17, 4–10. doi:10.2110/sedred.2019.1.4

Biggin, A. J., Piispa, E. J., Pesonen, L. J., Holme, R., Paterson, G. A., Veikkolainen, T., et al. (2015). Paleomagnetic field intensity variations suggest Mesoproterozoic inner-core nucleation. *Nature* 526, 245–248. doi:10.1038/nature15523

Bono, R. K., Tarduno, J. A., Nimmo, F., and Cottrell, R. D. (2019). Young inner core inferred from Ediacaran ultra-low geomagnetic field intensity. *Nat. Geosci.* 12, 143–147. doi:10.1038/s41561-018-0288-0

Bourne, M. D., Feinberg, J. M., Strauss, B. E., Hardt, B., Cheng, H., Rowe, H. D., et al. (2015). Long-term changes in precipitation recorded by magnetic minerals in speleothems. *Geology* 43, 595–598. doi:10.1130/g36695.1

Brady, A. L., Slater, G., Laval, B., and Lim, D. S. (2009). Constraining carbon sources and growth rates of freshwater microbialites in Pavilion Lake using (14) C analysis. *Geobiology* 7, 544–555. doi:10.1111/j.1472-4669.2009.0021510.1111/j.1472-4669.2009.00215.x

Brasier, M., Green, O., Lindsay, J., and Steele, A. (2004). "Earth's oldest (approximately 3.5 Ga) fossils and the "Early Eden hypothesis" questioning the evidence" in *Origins of Life and Evolution of the Biosphere*. Editor P. L. Luisi (Dordrecht: Kluwer), 257–269. doi:10.1023/B:ORIG.0000009845.62244.d3

Burne, R. V., and Moore, L. S. (1987). Microbialites: organosedimentary deposits of benthic microbial communities. *Palaios* 2, 241. doi:10.2307/3514674

Castro-Contreras, S. I., Gingras, M. K., Pecoits, E., Aubet, N. R., Petrash, D., Castro-Contreras, S. M., et al. (2014). Textural and geochemical features of freshwater microbialites from Laguna bacalar, Quintana Roo, Mexico. *Palaios* 29, 192–209. doi:10.2110/palo.2013.063

Chang, S. R., Stolz, J. F., Kirschvink, J. L., and Awramik, S. M. (1989). Biogenic magnetite in stromatolites. II. Occurrence in ancient sedimentary environments. *Precambrian Res.* 43, 305–315. doi:10.1016/0301-9268(89)90062-4

Chidsey, T. C., Berg, M. D., and Eby, D. E. (2015). *Petrography and characterization of microbial carbonates and associated facies from modern Great Salt Lake and Uinta Basin's Eocene Green River Formation in Utah, USA*. London: Geological Society, London, Special Publications, 418, 261-286. doi:10.1144/sp418.6

Chou, Y. M., Jiang, X., Liu, Q., Hu, H. M., Wu, C. C., Liu, J., et al. (2018). Multidecadally resolved polarity oscillations during a geomagnetic excursion. *Proc. Natl. Acad. Sci. U S A.* 115, 8913–8918. doi:10.1073/pnas.1720404115

Constable, C. G. (1985). Eastern Australian geomagnetic field intensity over the past 14000 yr. *Geophys. J. Int.* 81, 121–130. doi:10.1111/j.1365-246x.1985.tb01354.x

Constable, C., Korte, M., and Panovska, S. (2016). Persistent high paleosecular variation activity in southern hemisphere for at least 10 000 years. *Earth Planet. Sci. Lett.* 453, 78–86. doi:10.1016/j.epsl.2016.08.015

Egli, R. (2004). Characterization of individual rock magnetic components by analysis of remanence curves, 1. Unmixing Natural Sediments. *Studia Geophysica et Geodaetica* 48, 391–446. doi:10.1023/B:SGEG.0000020839.45304.6d

Egli, R., and Lowrie, W. (2002). Anhysteretic remanent magnetization of fine magnetic particles. *J. Geophys. Res.* 107, 2209. doi:10.1029/2001JB000671

Egli, R., and Zhao, X. (2015). Natural remanent magnetization acquisition in bioturbated sediment: general theory and implications for relative paleointensity reconstructions. *Geochem. Geophys. Geosystems* 16, 995–1016. doi:10.1002/2014GC005672

Evans, D. A., Zhuravlev, A. Y., Budney, C. J., and Kirschvink, J. L. (1996). Paleomagnetism of the bayan Gol formation, western Mongolia. *Geol. Mag.* 133, 487–496. doi:10.1017/s0016756800007615

Fisher, R. (1953). Dispersion on a sphere. *Proc. R. Soc. A: Math. Phys. Eng. Sci.* 217, 295–305. doi:10.1098/rspa.1953.0064

Font, E., Trindade, R. I., and Nédélec, A. (2005). Detrital remanent magnetization in haematite-bearing Neoproterozoic Puga cap dolostone, Amazon craton: a rock magnetic and SEM study. *Geophys. J. Int.* 163, 491–500. doi:10.1111/j.1365-246x.2005.02776.x

Gischler, E., Gibson, M. A., and Oschmann, W. (2008). Giant Holocene freshwater microbialites, Laguna bacalar, Quintana Roo, Mexico. *Sedimentology* 55, 1293–1309. doi:10.1111/j.1365-3091.2007.00946.x

Golden, D., Ming, D., Morris, R., Brearley, A., Lauer, H., Treiman, A., et al. (2004). Evidence for exclusively inorganic formation of magnetite in Martian meteorite ALH84001. *Am. Mineral.* 89, 681–695. doi:10.2138/am-2004-5-602

Jackson, M. (1990). Diagenetic sources of stable remanence in remagnetized paleozoic cratonic carbonates: a rock magnetic study. *J. Geophys. Res.* 95, 2753. doi:10.1029/jb095ib03p02753

Jackson, M., and Swanson-Hysell, N. L. (2012). Rock magnetism of remagnetized carbonate rocks: another look. *Geol. Soc. Lond. Spec. Publ* 371, 229–251. doi:10.1144/sp371.3

Jackson, M., and Van der Voo, R. (1985). A lower ordovician paleomagnetic pole from the Oneida dolomite, upper Mississippi river valley. *J. Geophys. Res.* 90, 10449. doi:10.1029/jb090ib12p10449

Katari, K., and Tauxe, L. (2000). Effects of pH and salinity on the intensity of magnetization in redeposited sediments. *Earth Planet. Sci. Lett.* 181, 489–496. doi:10.1016/S0012-821X(00)00226-0

Khomentovsky, V. V., and Gibsher, A. S. (1996). The Neoproterozoic–lower Cambrian in northern Govi-Altay, western Mongolia: Regional setting, lithostratigraphy and biostratigraphy. *Geolog. Mag.* 133, 371-390. doi:10.1017/s001675680000755x Society for Sedimentary Geology.

Kiessling, W. (2002). Secular variations in the phanerozoic reef ecosystem. *Soc. Sediment. Geology.* 72, 625–690. doi:10.2110/pec.02.72.0625

King, J. W., Banerjee, S. K., and Marvin, J. (1983). A new rock-magnetic approach to selecting sediments for geomagnetic paleointensity studies: application to paleointensity for the last 4000 years. *J. Geophys. Res. Solid Earth* 88, 5911–5921. doi:10.1029/jb088ib07p05911

King, R. F. (1955). The remanent magnetism of artificially deposited sediments. *Geophys. J. Int.* 7, 115–134. doi:10.1111/j.1365-246x.1955.tb06558.x

Kirschvink, J. L. (1980). The least-squares line and plane and the analysis of paleomagnetic data. *Geophys. J. Int.* 62, 699–718. doi:10.1111/j.1365-246x.1980.tb02601.x

Kodama, K. P. (2012). *Paleomagnetism of sedimentary rocks: process and interpretation*. Chichester: Wiley-Blackwell.

Konhauser, K. O., Kappler, A., and Roden, E. E. (2011). Iron in microbial metabolisms. *Elements* 7, 89–93. doi:10.2113/gselements.7.2.89

Konhauser, K., and Riding, R. (2012). "Bacterial biomineralization," in *Fundamentals of geobiology*. Editors A. H. Knoll, D. E. Canfield, and K. O. Konhauser (Chichester: Wiley-Blackwell)), 105–130. doi:10.1002/9781118280874.ch8

Kądziałko-Hofmokl, M., and Kruczyk, J. (1987). Paleomagnetism of Middle-Late Jurassic sediments from Poland and implications for the polarity of the geomagnetic field. *Tectonophysics* 139, 53–66. doi:10.1016/0040-1951(87)90197-1

Lascu, I., and Feinberg, J. M. (2011). Speleothem magnetism. *Quat. Sci. Rev.* 30, 3306–3320. doi:10.1016/j.quascirev.2011.08.004

Levi, S., and Banerjee, S. K. (1976). On the possibility of obtaining relative paleointensities from lake sediments. *Earth Planet. Sci. Lett.* 29, 219–226. doi:10.1016/0012-821x(76)90042-x

Lovley, D. R. (1991). "Magnetite formation during microbial dissimilatory iron reduction," in *Iron biominerals*. Editors R. B. Frankel and R. P. Blakemore (Boston, MA: Springer), 151–166. doi:10.1007/978-1-4615-3810-3_11

Lowe, D. R. (1994). Abiological origin of described stromatolites older than 3.2 Ga. *Geology* 22, 387. doi:10.1130/0091-7613(1994)0222.3.co;2

Lowrie, W. (1990). Identification of ferromagnetic minerals in a rock by coercivity and unblocking temperature properties. *Geophys. Res. Lett.* 17, 159–162. doi:10.1029/gl017i002p00159

Lund, S., Platzman, E., Thouveny, N., Camoin, G., Corsetti, F., and Berelson, W. (2010). Biological control of paleomagnetic remanence acquisition in carbonate framework rocks of the Tahiti coral reef. *Earth Planet. Sci. Lett.* 298, 14–22. doi:10.1016/j.epsl.2010.07.010

Maher, B., and Taylor, R. (1988). Formation of ultrafine-grained magnetite in soils. *Nature* 336, 368–370. doi:10.1038/336368a0

Maloof, A. C., Kopp, R. E., Grotzinger, J. P., Fike, D. A., Bosak, T., Vali, H., et al. (2007). Sedimentary iron cycling and the origin and preservation of magnetization in platform carbonate muds, Andros Island, Bahamas. *Earth Planet. Sci. Lett.* 259, 581–598. doi:10.1016/j.epsl.2007.05.021

Maxbauer, D. P., Feinberg, J. M., and Fox, D. L. (2016). MAX UnMix: a web application for unmixing magnetic coercivity distributions. *Comput. Geosciences* 95, 140–145. doi:10.1016/j.cageo.2016.07.009

McCabe, C., and Channell, J. E. (1994). Late Paleozoic remagnetization in limestones of the Craven Basin (northern England) and the rock magnetic fingerprint of remagnetized sedimentary carbonates. *J. Geophys. Res. Solid Earth* 99, 4603–4612. doi:10.1029/93jb02802

McFadden, P. L., and Reid, A. B. (1982). Analysis of paleomagnetic inclination data. *Geophys. J. Int.* 69, 307–319. doi:10.1111/j.1365-246X.1982.tb04950.x\

McLoughlin, N., Wilson, L. A., and Brasier, M. D. (2008). Growth of synthetic stromatolites and wrinkle structures in the absence of microbes - implications for the early fossil record. *Geobiology* 6, 95–105. doi:10.1111/j.1472-4669.2007.00141.x

Mitra, R., and Tauxe, L. (2009). Full vector model for magnetization in sediments. *Earth Planet. Sci. Lett.* 286, 535–545. doi:10.1016/j.epsl.2009.07.019

Muraszko, J. R. (2014). *Magnetic properties of Jurassic stromatolites from selected localities in Poland*. [master's thesis]. [Poland]: University of Warsaw.

Newell, D. L., Jensen, J. L., Frantz, C. M., and Berg, M. D. (2017). Great Salt Lake (Utah) Microbialite δ13C, δ18O, and δ15N record fluctuations in lake biogeochemistry since the late Pleistocene. *Geochem. Geophys. Geosystems* 18, 3631–3645. doi:10.1002/2017gc007078

Pan, Y., Zhu, R., Banerjee, S. K., Gill, J., and Williams, Q. (2000). Rock magnetic properties related to thermal treatment of siderite: behavior and interpretation. *J. Geophys. Res. Solid Earth* 105, 783–794. doi:10.1029/1999jb900358

Paull, C., Neumann, A., Bebout, B., Zabielski, V., and Showers, W. (1992). Growth rate and stable isotopic character of modern stromatolites from San Salvador, Bahamas. *Palaeogeogr. Palaeoclimatol. Palaeoecol.* 95, 335–344. doi:10.1016/0031-0182(92)90149-y

Petryshyn, V. A., Corsetti, F. A., Berelson, W. M., Beaumont, W., and Lund, S. P. (2012). Stromatolite lamination frequency, Walker Lake, Nevada: implications for stromatolites as biosignatures. *Geology* 40, 499–502. doi:10.1130/g32675.1

Petryshyn, V. A., Corsetti, F. A., Frantz, C. M., Lund, S. P., and Berelson, W. M. (2016). Magnetic susceptibility as a biosignature in stromatolites. *Earth Planet. Sci. Lett.* 437, 66–75. doi:10.1016/j.epsl.2015.12.016

Pick, T., and Tauxe, L. (1991). Chemical remanent magnetization in synthetic magnetite. *J. Geophys. Res.* 96, 9925–9936. doi:10.1029/91JB00706

Rasmussen, K. A., Macintyre, I. G., and Prufert, L. (1993). Modern stromatolite reefs fringing a brackish coastline, Chetumal Bay, Belize. *Geology* 21, 199. doi:10.1130/0091-7613(1993)0212.3.co;2

Reid, R. P., Visscher, P. T., Decho, A. W., Stolz, J. F., Bebout, B. M., Dupraz, C., et al. (2000). The role of microbes in accretion, lamination and early lithification of modern marine stromatolites. *Nature* 406, 989–992. doi:10.1038/35023158

Riding, R. (2006). Microbial carbonate abundance compared with fluctuations in metazoan diversity over geological time. *Sediment. Geology.* 185, 229–238. doi:10.1016/j.sedgeo.2005.12.01

Riding, R. (2000). Microbial carbonates: the geological record of calcified bacterial-algal mats and biofilms. *Sedimentology* 47, 179–214. doi:10.1046/j.1365-3091.2000.00003.x

Riding, R. (2011). "Microbialites, stromatolites, and thrombolites," in *Encyclopedia of geobiology encyclopedia of Earth sciences series*. Editors J. Reitner and V. Thiel (Dordrecht: Springer), 635–654. doi:10.1007/978-1-4020-9212-1_196

Riding, R. (2010). The nature of stromatolites: 3,500 million years of history and a century of research. *Adv. Stromatolite Geobiology Lecture Notes Earth Sci.* 131, 29–74. doi:10.1007/978-3-642-10415-2_3

Roberts, A. P., Chang, L., Heslop, D., Florindo, F., and Larrasoaña, J. C. (2012). Searching for single domain magnetite in the "pseudo-single-domain" sedimentary haystack: implications of biogenic magnetite preservation for sediment magnetism and relative paleointensity determinations. *J. Geophys. Res. Solid Earth* 117. doi:10.1029/2012jb009412

Roberts, A. P. (2015). Magnetic mineral diagenesis. *Earth-Science Rev.* 151, 1–47. doi:10.1016/j.earscirev.2015.09.010

Robertson, D., and France, D. (1994). Discrimination of remanence-carrying minerals in mixtures, using isothermal remanent magnetisation acquisition curves. *Phys. Earth Planet. Interiors* 82, 223–234. doi:10.1016/0031-9201(94)90074-4

Rodelli, D., Jovane, L., Giorgioni, M., Rego, E. S., Cornaggia, F., Benites, M., et al. (2019). Diagenetic fate of biogenic soft and hard magnetite in chemically stratified sedimentary environments of mamanguá ría, Brazil. *J. Geophys. Res. Solid Earth* 124, 2313–2330. doi:10.1029/2018jb016576

Ryan, W. B., Carbotte, S. M., Coplan, J. O., O'hara, S., Melkonian, A., Arko, R., et al. (2009). Global multi-resolution topography (GRMT) synthesis. *Geochem. Geophys. Geosystems* 10. doi:10.1029/2008gc002332

Schopf, J. W., Kudryavtsev, A. B., Czaja, A. D., and Tripathi, A. B. (2007). Evidence of archean life: stromatolites and microfossils. *Precambrian Res.* 158, 141–155. doi:10.1016/j.precamres.2007.04.009

Smirnov, A. V., Tarduno, J. A., Kulakov, E. V., Mcenroe, S. A., and Bono, R. K. (2016). Palaeointensity, core thermal conductivity and the unknown age of the inner core. *Geophys. J. Int.* 205, 1190–1195. doi:10.1093/gji/ggw080

Snowball, I., and Sandgrena, P. (2002). Geomagnetic field variations in northern Sweden during the Holocene quantified from varved lake sediments and their implications for cosmogenic nuclide production rates. *The Holocene* 12, 517–530. doi:10.1191/0959683602hl562rp

Stolz, J. F., Chang, S. R., and Kirschvink, J. L. (1989). Biogenic magnetite in stromatolites. I. Occurrence in modern sedimentary environments. *Precambrian Res.* 43, 295–304. doi:10.1016/0301-9268(89)90061-2

Suk, D., and Halgedahl, S. L. (1996). Hysteresis properties of magnetic spherules and whole rock specimens from some Paleozoic platform carbonate rocks. *J. Geophys. Res. Solid Earth* 101, 25053–25075. doi:10.1029/96jb02271

Suk, D., Peacor, D. R., and Voo, R. V. (1990a). Replacement of pyrite framboids by magnetite in limestone and implications for paleomagnetism. *Nature* 345, 611–613. doi:10.1038/345611a0

Suk, D., Voo, R. V., and Peacor, D. R. (1990b). Scanning and transmission electron microscope observations of magnetite and other iron phases in Ordovician carbonates from east Tennessee. *J. Geophys. Res. Solid Earth* 95, 12327–12336. doi:10.1029/JB095iB08p1232

Swanson-Hysell, N. L., Maloof, A. C., Kirschvink, J. L., Evans, D. A., Halverson, G. P., and Hurtgen, M. T. (2012). Constraints on neoproterozoic paleogeography and paleozoic orogenesis from paleomagnetic records of the bitter Springs Formation, amadeus basin, central Australia. *Am. J. Sci.* 312, 817–884. doi:10.2475/08.2012.01

Tarduno, J. A., Cottrell, R. D., and Smirnov, A. V. (2006). The paleomagnetism of single silicate crystals: recording geomagnetic field strength during mixed polarity intervals, superchrons, and inner core growth. *Rev. Geophys.* 44. doi:10.1029/2005rg000189

Tauxe, L., Shaar, R., Jonestrask, L., Swanson-Hysell, N. L., Minnett, R., Koppers, A. A., et al. (2016). PmagPy: software package for paleomagnetic data analysis and a bridge to the magnetics information Consortium (MagIC) database. *Geochem. Geophys. Geosystems* 17, 2450–2463. doi:10.1002/2016gc006307

Taylor, R. M., Maher, B. A., and Self, P. G. (1987). Magnetite in soils: 1. The synthesis of single-domain and superparamagnetic magnetite. *Clay Minerals* 22, 411–422. doi:10.1180/claymin.1987.022.4.05

Thompson, R., and Oldfieid, F. (1986). *Environmental magnetism*. Dordrecht: Springer. doi:10.1007/978-94-011-8036-8

Till, J. L., Guyodo, Y., Lagroix, F., Morin, G., Menguy, N., and Ona-Nguema, G. (2017). Presumed magnetic biosignatures observed in magnetite derived from abiotic reductive alteration of nanogoethite. *Comptes Rendus Geosci.* 349, 63–70. doi:10.1016/j.crte.2017.02.001

Trindade, R. I., Font, E., D'agrella-Filho, M. S., Nogueira, A. C., and Riccomini, C. (2003). Low-latitude and multiple geomagnetic reversals in the Neoproterozoic Puga cap carbonate, Amazon craton. *Terra Nova* 15, 441–446. doi:10.1046/j.1365-3121.2003.00510.x

Trindade, R. I., Jaqueto, P., Terra-Nova, F., Brandt, D., Hartmann, G. A., Feinberg, J. M., et al. (2018). Speleothem record of geomagnetic south atlantic anomaly recurrence. *Proc. Natl. Acad. Sci.* 115, 13198–13203. doi:10.1073/pnas.1809197115

Valet, J., Besse, J., Kumar, A., Vadakke-Chanat, S., and Philippe, E. (2014). The intensity of the geomagnetic field from 2.4 Ga old Indian dykes. *Geochem. Geophys. Geosystems* 15, 2426–2437. doi:10.1002/2014gc005296

Vanyo, J. P., and Awramik, S. M. (1982). Length of day and obliquity of the ecliptic 850 MA ago: preliminary results of a stromatolite growth model. *Geophys. Res. Lett.* 9, 1125–1128. doi:10.1029/gl009i010p01125

Walter, M. R., and Heys, G. R. (1985). Links between the rise of the metazoan and the decline of stromatolites. *Precambrian Res.* 29, 149–174. doi:10.1016/0301-9268(85)90066-X

Watson, G. S. (1956). Analysis of dispersion on a sphere. *Geophys. J. Int.* 7, 153–159. doi:10.1111/j.1365-246x.1956.tb05560.x

Watson, G. S. (1983). Large sample theory of the Langevin distribution. *J. Stat. Plann. Inference* 8, 245–256. doi:10.1016/0378-3758(83)90043-5

Weil, A. B., and Van der Voo, R. (2002). Insights into the mechanism for orogen-related carbonate remagnetization from growth of authigenic Fe-oxide: a scanning electron microscopy and rock magnetic study of Devonian carbonates from northern Spain. *J. Geophys. Res. Solid Earth* 107, 1–14. doi:10.1029/2001JB000200

Zhao, X., Egli, R., Gilder, S., and Müller, S. (2016). Microbial assisted recording of the Earth's magnetic field in sediment. *Nat. Commun.* 7, 10673. doi:10.1038/ncomms10673

Conflict of Interest: The authors declare that the research was conducted in the absence of any commercial or financial relationships that could be construed as a potential conflict of interest.

frontiers in Earth Science

ORIGINAL RESEARCH
published: 11 March 2021
doi: 10.3389/feart.2021.603363

Authigenic Greigite as an Indicator of Methane Diffusion in Gas Hydrate-Bearing Sediments of the Hikurangi Margin, New Zealand

Myriam Kars[1]*, *Annika Greve*[2] and *Lilly Zerbst*[3]

[1]Center for Advanced Marine Core Research, Kochi University, Nankoku, Japan, [2]Paleomagnetic Laboratory 'Fort Hoofddijk', Department of Earth Sciences, Utrecht University, Utrecht, Netherlands, [3]Geophysical Institute, Karlsruhe Institute of Technology, Karlsruhe, Germany

Authigenic ferrimagnetic iron sulfides, essentially greigite (Fe_3S_4), are commonly found in gas hydrate-bearing marine sediments of active accretionary prisms. Greigite is a by-product, either intracellular or extracellular, of microbial activity, and therefore provides good indication of microbial processes which are closely related to the occurrence of gas hydrate. A high-resolution rock magnetic study was conducted at Site U1518 of International Ocean Discovery Program Expedition 375, located in the frontal accretionary wedge of the Hikurangi Margin, offshore New Zealand. Samples were collected throughout the entire recovered stratigraphic sequence, from the surface to ~492 m below seafloor (mbsf) which includes the Pāpaku fault zone. This study aims to document the rock magnetic properties and the composition of the magnetic mineral assemblage at Site U1518. Based on downhole magnetic coercivity variations, the studied interval is divided into five consecutive zones. Most of the samples have high remanent coercivity (above 50 mT) and first-order reversal curves (FORC) diagrams typical of single-domain greigite. The top of the hanging wall has intervals that display a lower remanent coercivity, similar to lower coercivities measured on samples from the fault zone and footwall. The widespread distribution of greigite at Site U1518 is linked to methane diffusion and methane hydrate which is mainly disseminated within sediments. In three footwall gas hydrate-bearing intervals, investigated at higher resolution, an improved magnetic signal, especially a stronger FORC signature, is likely related to enhanced microbial activity which favors the formation and preservation of greigite. Our findings at the Hikurangi Margin show a close linkage between greigite, methane hydrate and microbial activity.

Keywords: Hikurangi Margin, Site U1518, greigite, methane hydrate, IODP Expedition 375

OPEN ACCESS

Edited by:
Anne-Christine Da Silva, University of Liège, Belgium

Reviewed by:
Saulwood Lin, National Taiwan University, Taiwan
Leonardo Sagnotti, Istituto Nazionale di Geofisica e Vulcanologia (INGV), Italy

***Correspondence:**
Myriam Kars
mkars@kochi-u.ac.jp

Specialty section:
This article was submitted to Sedimentology, Stratigraphy and Diagenesis, a section of the journal Frontiers in Earth Science

Received: *06 September 2020*
Accepted: *01 February 2021*
Published: *11 March 2021*

Citation:
Kars M, Greve A and Zerbst L (2021) Authigenic Greigite as an Indicator of Methane Diffusion in Gas Hydrate-Bearing Sediments of the Hikurangi Margin, New Zealand. Front. Earth Sci. 9:603363. doi: 10.3389/feart.2021.603363

INTRODUCTION

Gas hydrate is an ice-like crystalline structure containing hydrocarbon gas (mainly methane) trapped in a water lattice. In the last decades, gas hydrate has been intensively investigated for its energy resource potential (e.g., Kvenvolden, 1993; Buffet and Archer, 2004) and its possible impact on climate change (e.g., Ruppel and Kessler, 2017; Screaton et al., 2019). Moreover, gas

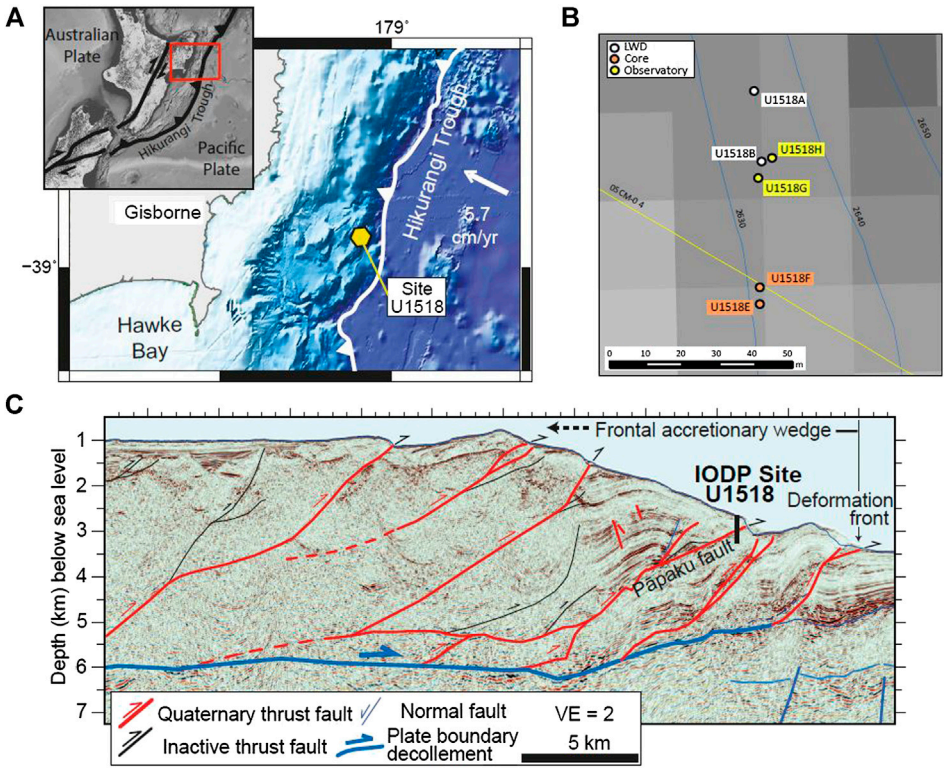

FIGURE 1 | (A) Location and geotectonic setting of the Hikurangi subduction margin and the New Zealand plate boundary (inset). Displayed in the bathymetric map of the northern Hikurangi subduction margin are also the main thrust faults, IODP Site U1518 and the relative plate convergence vector **(B)** Detailed location map of holes drilled at Site U1518 (from Saffer et al., 2019) **(C)** Seismic cross section of the frontal accretionary wedge near the drilling transect of IODP Expedition 375, including interpretation after Barker et al. (2018). The location of IODP Site U1518 and trace of the Pāpaku fault are indicated. Figures **(A)** and **(C)** are modified from Fagereng et al. (2019) and Greve et al. (2020).

hydrate can play a role on slope stability in continental margins. Gas hydrate dissociation can destabilize the seafloor and be at the origin of submarine landslides (e.g., Mountjoy et al., 2014). Gas hydrate is stable within a limited range of high pressure/low temperature with high methane/gas contents (e.g., You et al., 2019) and is, therefore, mainly found in permafrost and continental margins (for instance, Cascadia Margin, offshore Oregon; Nankai Trough, offshore Japan; Chile-Peru Margin). The presence of gas hydrate is generally inferred rather than proven because it dissociates very rapidly at ambient conditions in absence of pressure cores. Various analytical approaches on cores and during drilling are indicative of gas hydrate occurrences, including logging resistivity data (Collett, 2001), heat flow and thermal anomalies with lower core temperature (Kinoshita et al., 2015), isotopic and pore water anomalies (essentially chlorinity anomalies) (Hesse, 2003), and characteristic rock magnetic variations (e.g., Housen and Musgrave, 1996; Larrasoaña et al., 2007). Previous rock magnetic studies in the Cascadia Margin (e.g., Housen and Musgrave, 1996; Musgrave et al., 2006; Larrasoaña et al., 2007), in the Nankai Trough (Kars and Kodama, 2015a; Kars and Kodama, 2015b; Shi et al., 2017), in the Bay of Bengal (Badesab et al., 2019) and offshore Taiwan (e.g., Horng, 2018) report co-occurrence of authigenic iron sulfides and gas hydrate. Authigenic ferrimagnetic greigite (Fe_3S_4) is commonly observed in such environments. It is closely related to microbial activity as greigite can be formed either extracellularly or intracellularly (e.g., Mann et al., 1990; Roberts and Turner, 1993; Watson et al., 2000; Bazylinski and Williams, 2006).

Tectonically uplifted sediments of the Neogene marine sedimentary sequence from the Hikurangi Margin are known to contain authigenic greigite formed from magnetite dissolution during diagenesis after sediment deposition (Rowan and Roberts, 2005, 2006). In this study, we apply rock magnetic techniques in marine sediments of the Hikurangi Margin, offshore New Zealand, cored during recent International Ocean Discovery Program (IODP) expeditions (Pecher et al., 2019; Wallace et al., 2019) to investigate the occurrence of authigenic iron sulfides associated with gas hydrate. In this paper we present and discuss the distribution of greigite in marine sediments recovered during IODP Expedition 375 (Wallace et al., 2019). This study is the first systematic study in the Hikurangi Margin that establishes a close relationship between the occurrence of authigenic greigite, methane hydrate, and microbial activity. We also discuss how overthrusting along a subduction splay fault affected the diagenetic profile.

BACKGROUND

The northern part of the Hikurangi Margin is an erosional accretionary prism located offshore the North Island in New Zealand (**Figure 1A**). It is formed by the subduction of the Pacific Plate beneath the Australian Plate at a rate of 4.5–5.5 cm/year (Wallace et al., 2004).

International Ocean Discovery Program (IODP) Expeditions 372 and 375 were undertaken to understand the mechanisms and the *in situ* conditions near the suggested source region of aseismic slow slip in the Hikurangi Margin. IODP Expedition 372 was mainly dedicated to collecting real-time logging-while-drilling (LWD) data (Pecher et al., 2019) and Expedition 375 to coring (Wallace et al., 2019).

Site U1518 (38°51.57S, 178°53.76'E) is located on the lower continental slope near the trench and ~62 km from shore at ~2630 m water depth (Saffer et al., 2019) (**Figure 1C**). Several holes were drilled at Site U1518 (**Figure 1B**). In this study, samples are from Holes U1518E and U1518F (IODP Expedition 375), and LWD data were acquired in Hole U1518B (IODP Expedition 372). Coring at Site U1518 penetrated sediments down to ~495 m below sea floor (mbsf) and targeted the Pāpaku fault, a major frontal thrust, about 6.5 km west of the deformation front of the northern Hikurangi Margin (Saffer et al., 2019; Wallace et al., 2019). The Pāpaku fault zone was cored between 304.5 and 361.7 mbsf.

Three lithostratigraphic units were defined at Site U1518, all Quaternary in age. Sediment composition is mostly homogeneous, with silty clay(stone) as the dominant lithology alternating with thin beds of silt(stone) containing variable amounts of sand (Saffer et al., 2019). Mean sedimentation rate, based on calcareous nannofossil and planktonic foraminifer datums, has been estimated to 2.8 m/kyr in the Pleistocene. Some variability in sedimentation rate is likely related to the frequency and volume of gravity deposits (Saffer et al., 2019). Biostratigraphic observations identified an age inversion near the top of the fault zone suggesting that the majority of the fault zone interval is located within the younger footwall rock (<0.53 Ma; Saffer et al., 2019). Core observation and pore water downhole profiles indicate a well-preserved repetition of the early diagenetic sequence in the footwall, and diffusion modeling suggest recent overthrusting at ~10–30 kya (Morgan et al., 2020, personal communication)[1].

At Site U1518, an infra-red camera was used on the catwalk to image core temperature below 30 mbsf. A colder temperature indicated the dissociation of gas hydrate during depressurization in cores. Disseminated discrete gas hydrate in cores is inferred from ~33 to ~391 mbsf based on infra-red scanning and pore water chloride data (Holes U1518E and U1518F; Saffer et al., 2019). Small, centimeter-thick gas hydrate accumulations were identified at ~399.5–400, ~401.7–402.2 and ~419.5–419.8 mbsf in three sections. The low core recovery (43%) from ~198 to ~495 mbsf may explain scattered observations of hydrate in cores. LWD data were recorded continuously in Hole U1518B, thus, allowing a better characterization of hydrate occurrence at Site U1518. Peaks in borehole resistivity (LWD) data suggest that methane hydrate accumulations are not continuous and occur in thin layers of concentrated hydrate (of the order of cm to 10s of cm) from ~30 to the end of the hole at 585 mbsf. They seem to coincide mostly with coarse-grained sediments inferred from lower gamma ray counts (Cook et al., 2020). Methane hydrate is stable throughout Site U1518. The base of the gas hydrate stability zone, calculated from measured temperature, pore water salinity, and estimated pressure (Saffer et al., 2019), occurs at ~585 mbsf (Cook et al., 2020). From LWD resistivity data in Hole U1518B, Cook et al. (2020) describe lower hydrate saturation S_h (S_h < 0.1) in parts of the hanging wall between 235 and 263 mbsf, in the fault zone, and the footwall between 455–485 mbsf. Intervals in the hanging wall (above ~104 mbsf) were not logged for resistivity because of core gap and tool miscommunication (Wallace et al., 2019). Higher hydrate saturation (S_h > 0.2) is found in the immediate surrounding of the Pāpaku fault zone (~304–314 mbsf and 345–370 mbsf), in the hanging wall at ~230 mbsf and in the footwall at ~397–418 and ~488–498 mbsf (Cook et al., 2020). Cook et al. (2020) show that even though hydrate saturation varies with depth, it does not vary significantly between the hanging wall, fault zone and footwall.

MATERIALS AND METHODS

Materials

A total of 236 samples was analyzed from working half sections of IODP Expedition 375 Site U1518 (Saffer et al., 2019). Samples in 7cc plastic sampling boxes were extracted from fine-grained lithologies (i.e., claystone) of all Lithostratigraphic Units. Our sampling strategy did not include coarse-grained lithologies. One to two samples per 1.5 m-section were collected depending on the core recovery. In three footwall intervals containing gas hydrate, namely at ~399.5–400, ~401.7–402.2 and ~419.5–419.8 mbsf, samples were collected at a resolution of 5–10 cm to verify whether rock magnetic variations exist at a smaller scale where gas hydrate is present.

Methods

Paleomagnetic and rock magnetic measurements were performed at the paleomagnetic laboratory of the Center for Advanced Marine Core Research (Nankoku, Japan) and at Japan Agency for Marine Earth Science and Technology (Yokosuka, Japan). Low-field, low-frequency (0.465 kHz) magnetic susceptibility χ_{lf} was measured with a MS2B Bartington Instruments magnetic susceptibility meter (field = 250 μT). The natural remanent magnetization (NRM) and an anhysteretic remanent magnetization (ARM) were measured with a 2-G Enterprises 760R SQUID cryogenic magnetometer. ARM was imparted in a direct current (DC) bias field of 50 μT in the presence of an 80 mT peak alternating field (AF). A saturation isothermal remanent magnetization (SIRM) was subsequently imparted on the samples in the +z direction at 1.2 T by using a MMPM10 pulse magnetizer before being measured with a Natsuhara Giken spinner

[1]Morgan, J. K., Solomon, E. A., Fagereng, A., Savage, H., Wang, M., Meneghini, F., et al. (personal communication). Seafloor overthrusting at the Hikurangi margin: ductile fault deformation, fluid pressures, and implications for plate boundary processes. Abstracts, IODP expeditions 372 & 375 science meeting: creeping gas hydrate slides and Hikurangi subduction margin. Napier, New Zealand.

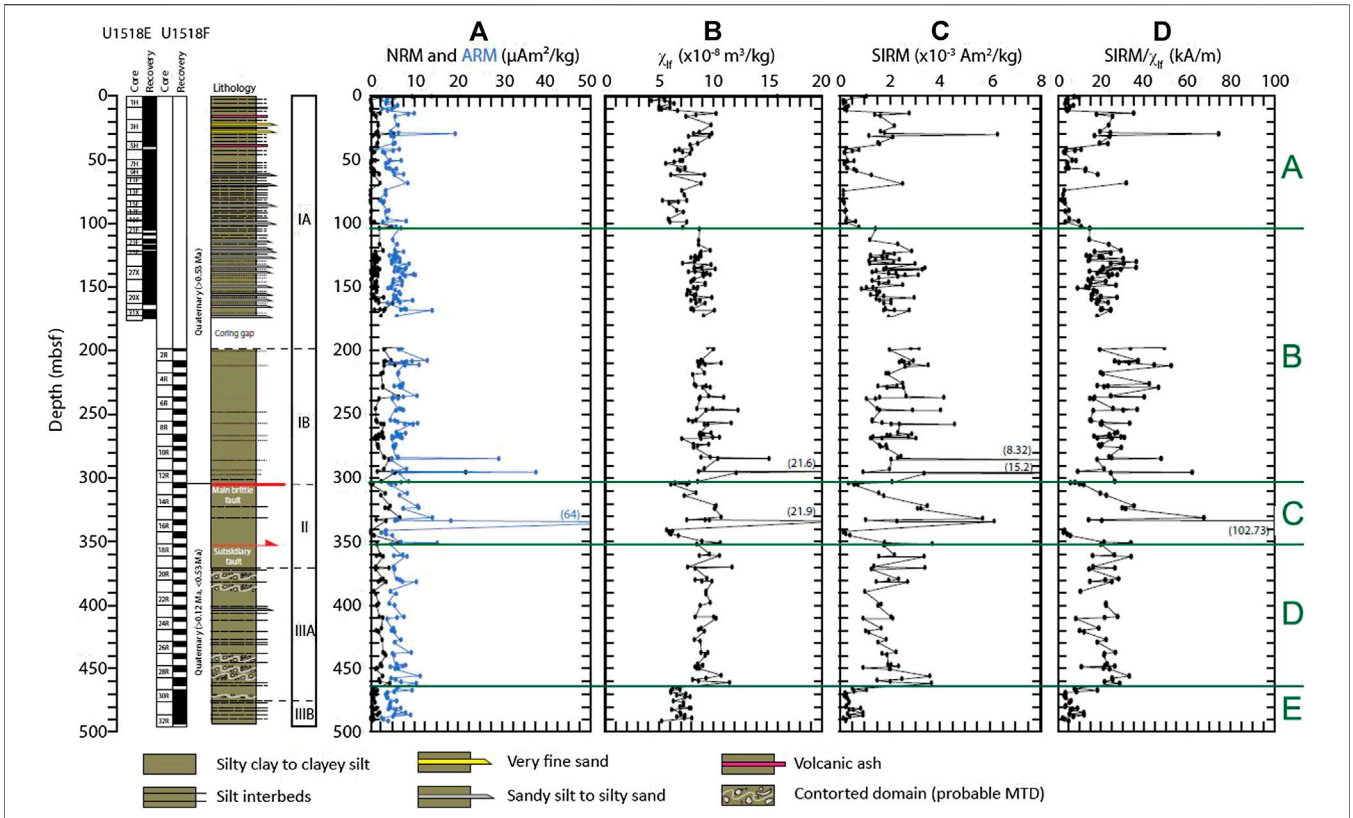

FIGURE 2 | Downhole rock magnetic parameters at Site U1518 **(A)** Natural Remanent Magnetization (NRM) and Anhysteretic Remanent Magnetization (ARM) **(B)** Magnetic susceptibility χ_{lf} **(C)** Saturation Isothermal Remanent Magnetization (SIRM) **(D)** SIRM/χ_{lf} ratio. Spikes in NRM, ARM, χ_{lf}, and SIRM are likely due to coarser lithology. Zones A to E, defined from coercivity variations (see **Figure 3**), are indicated. Core recovery, age and lithologic description are from Wallace et al. (2019).

magnetometer. The samples were subsequently remagnetized in the $-z$ direction with a DC field of 0.3 T and measured again to calculate the $S_{-0.3T}$ parameter (= [(−$IRM_{-0.3T}$)/SIRM) +1]/2; Bloemendal et al., 1992). The $S_{-0.3T}$ parameter provides an indication of the relative proportion of high coercivity minerals (e.g., hematite, goethite, ferrimagnetic iron sulfides) in a mixture with soft ferrimagnetic minerals (e.g., magnetite, maghemite).

Hysteresis loops with a maximum applied field of 1 T were measured on dry sediment powder at room temperature with a Princeton Measurements Corporation vibrating sample magnetometer (VSM). Saturation magnetization (M_s), saturation remanent magnetization (M_r), and coercivity (B_c) were extracted. Saturation is assumed above 70% of the maximum applied field, although this may underestimate M_r/M_s as discussed by Roberts et al. (2018) and references therein. Remanent coercivity (B_{cr}) was subsequently measured by backfield demagnetization of M_r. First-order reversal curves (FORCs; Pike et al., 1999; Roberts et al., 2000; Roberts et al., 2014) were measured for 60 samples selected at ~5–10 m stratigraphic intervals, with a 1 T saturating field (averaging time: 100 ms; field increment: 2 mT; number of FORCs: 150). FORC diagrams were processed using the FORCinel software (Harrison and Feinberg, 2008) with the VARIFORC protocol of Egli (2013). First point and lower branches were subtracted.

Low-temperature magnetic measurements were made with a Quantum Design SQUID magnetic properties measurements system (MPMS) for 29 selected samples. The samples each have ~50–120 mg mass and had been dried, ground lightly to a fine powder, and sealed in a gelatin capsule before being measured. A room temperature SIRM (RT-SIRM) was acquired at 2.5 T. A 300-10-300K cooling-warming cycle of the RT-SIRM was then measured in a zero magnetic field (trapped field inside the MPMS <20 μT). A low temperature SIRM (LT-SIRM) was imparted at 10K at 2.5 T. Samples were then warmed to room temperature in a zero magnetic field and measured (termed ZFC for zero-field-cooled). Samples were subsequently cooled to 10K in a 2.5 T magnetic field and the LT-SIRM was measured during warming to 300K (termed FC for field-cooled).

Thermomagnetic experiments in air were measured on 20 selected specimens with a Natsuhara Giken NMB-89 magnetic balance from room temperature to 700°C (with a heating rate of 10°C/min in a 0.3 T field).

RESULTS

Magnetic Mineral Concentration-dependent Parameters

NRM, ARM, magnetic susceptibility χ_{lf} and SIRM are proxies for magnetic mineral concentration. At Site U1518, NRM and ARM do not show significant variations with depth (**Figure 2A**). NRM

and ARM average around 2.04 ± 2.01 $\mu Am^2/kg$ and 6.90 ± 5.08 $\mu Am^2/kg$, respectively (**Supplementary Table S1**). ARM is sensitive to the amount of single domain (SD) magnetic particles, especially of magnetite. ARM is only three times higher than NRM, suggesting that grain size variations do not significantly affect the ARM/NRM ratio in the studied samples.

Magnetic susceptibility χ_{lf} and SIRM mimic each other with a similar trend to ARM (**Figures 2B,C**). χ_{lf} and SIRM average around $8.51 \pm 1.93 \times 10^{-8}$ m^3/kg and $1.71 \pm 1.46 \times 10^{-3}$ Am^2/kg, respectively (**Supplementary Table S1**). Even though care has been taken to sample homogenous fine-grained lithology (i.e., claystone), high peaks at ~285.5, ~296.3 and ~335.6 mbsf may be due to coarser-grained lithology (suggesting a higher detrital input in the samples). SIRM/χ_{lf}, which is an indicator of iron sulfide concentration, mimics the variations of both SIRM and χ_{lf} (**Figure 2D**). The ratio averages around 18.84 ± 12.87 kA/m (**Supplementary Table S1**).

As defined and discussed further below in *Magnetic coercivity*, the studied interval can be divided in five zones from top to bottom as follows: Zone A (top to ~104 mbsf), Zone B (from ~104 to ~304 mbsf), Zone C (from ~304 to ~352 mbsf), Zone D (from ~352 to ~463 mbsf), and Zone E (from ~466 to ~492 mbsf). In Zone A, NRM and ARM intensities alternate between higher and lower values of these parameters, while Zones B and D display higher than average values with no significant variations (**Supplementary Table S1**). Zone C, in between, which corresponds to the Pāpaku fault zone displays below average values in two narrow intervals (see also Greve et al., 2021). Zone E displays lower than average values (**Supplementary Table S1**). We propose that this zonation is caused by varying amount of ferrimagnetic minerals in the sediment. Higher (lower) values of the concentration-dependent parameters indicate higher (lower) concentration of ferrimagnetic minerals.

Magnetic Grain Size Proxies

The ARM/χ_{lf} and ARM/SIRM ratios are commonly used as proxies for magnetic grain size (especially of magnetite) with higher (lower) values commonly indicating finer (coarser) grain size (**Supplementary Figure S1**). Peaks of the ARM/χ_{lf} ratio coincide with peaks in ARM. In clay-rich lithologies such as those found at Site U1518, the magnetic susceptibility χ_{lf} is usually dominated by paramagnetic minerals (Greve et al., 2020). In such a setting with an overall low concentration of ferrimagnetic minerals and low magnetic susceptibility ($\chi_{lf} < 10 \times 10^{-8}$ m^3/kg) the ARM/χ_{lf} signal does not solely reflect the effect of ferrimagnetic minerals (e.g., Lu and Banerjee, 1994; Greve et al., 2020). While ARM/χ_{lf} does not show significant variations with depth, ARM/SIRM behaves differently with marked variations. Above ~110 mbsf, ARM/SIRM alternates between lower and higher values (Zone A). Between ~110 and ~460 mbsf, ARM/SIRM is low (generally below 4×10^{-3}) except for peaks in the fault zone. Finally, below ~460 mbsf (Zone E), the ratio is higher. The downhole ARM/SIRM variations are similar to coercivity variations as discussed below. We therefore conclude that neither ARM/χ_{lf} nor ARM/SIRM represent reliable magnetic grain size proxies at Site U1518 because of a high paramagnetic contribution and a magnetic remanence dominated by ferrimagnetic greigite as discussed further below (in *Composition of the Magnetic Mineral Assemblage*).

Magnetic Coercivity

$S_{-0.3T}$ indicates the relative contribution of higher coercivity (antiferromagnetic) magnetic minerals (e.g., hematite) with respect to generally lower coercivity (ferrimagnetic) magnetic minerals (e.g., magnetite). $S_{-0.3T}$ is close to 1, except for the very top part (below 20 mbsf), the fault zone (Zone C), and in between ~460 and 470 mbsf (**Supplementary Figure S1**). This suggests that antiferromagnetic minerals have a minor contribution to the global magnetic mineral assemblage.

More interestingly are the downhole variations of the hysteresis parameters (**Figure 3**). M_r/M_s, B_c, B_{cr} and D_{JH} ($D_{JH}=(M_r/M_s)/(B_{cr}/B_c)$; Housen and Musgrave, 1996) mimic each other. Zones A to E are defined from downhole coercivity variations. Their depths are based on sample depths.

1. Zone A (from top to ~104 mbsf): this zone has alternating low (generally $B_c < 25$ mT, $B_{cr} < 50$ mT) and high coercivity (generally $B_c > 40$ mT, $B_{cr} > 60$ mT) intervals;
2. Zone B (from ~104 to ~304 mbsf): this is a high coercivity zone with rather constant coercivity B_c and B_{cr} values averaging 51.9 ± 4.4 and 69.6 ± 3.3 mT, respectively;
3. Zone C (from ~304 to ~352 mbsf): this zone has alternating higher and lower coercivity values with the lower coercivity intervals in the main and subsidiary fault zones (see Greve et al., in press);
4. Zone D (from ~352 to ~463 mbsf): this is a zone of constant high coercivity values in the same range as in Zone B (B_c~51.6 ± 3.9 mT and B_{cr}~69.3 ± 2.5 mT);
5. Zone E (from ~466 to ~492 mbsf): this is an interval of low coercivity values with B_c and B_{cr} averaging 23.8 ± 6.4 and 51.2 ± 5.2 mT, respectively.

D_{JH} increases as the proportion of single domain (SD) ferrimagnetic minerals increases and is generally higher when greigite contributes a significant proportion of the ferrimagnetic population. In the lower coercivity intervals, D_{JH} is usually <0.2 and it is higher (>0.3) in the higher coercivity intervals (**Figure 3D**).

Composition of the Magnetic Mineral Assemblage

Saffer et al. (2019) noticed acquisition of gyroremanent magnetization (GRM) upon static alternating field (AF) demagnetization treatment of shipboard samples. GRM usually indicates the presence of greigite (e.g., Snowball, 1997). We conducted static AF demagnetization on the samples collected from the gas hydrate-bearing footwall sections (namely in the intervals ~399.5–400, ~401.7–402.2, and ~419.5–419.8 mbsf). Except for two samples, all studied samples grow a GRM during static AF demagnetization (**Supplementary Table S2**). The parameter ΔGRM/ΔNRM (= $[(NRM_{80mT}-NRM_{min})/(NRM_{initial}-NRM_{min})]$, where NRM_{min} is the minimum remanence measured (Fu et al., 2008) displays values above 0.5 (**Supplementary Table S2**). Such high values are generally encountered in greigite-rich layers (e.g., Fu et al., 2008). For all these samples, B_{cr} is higher than 55 mT and D_{JH} averages ~0.35

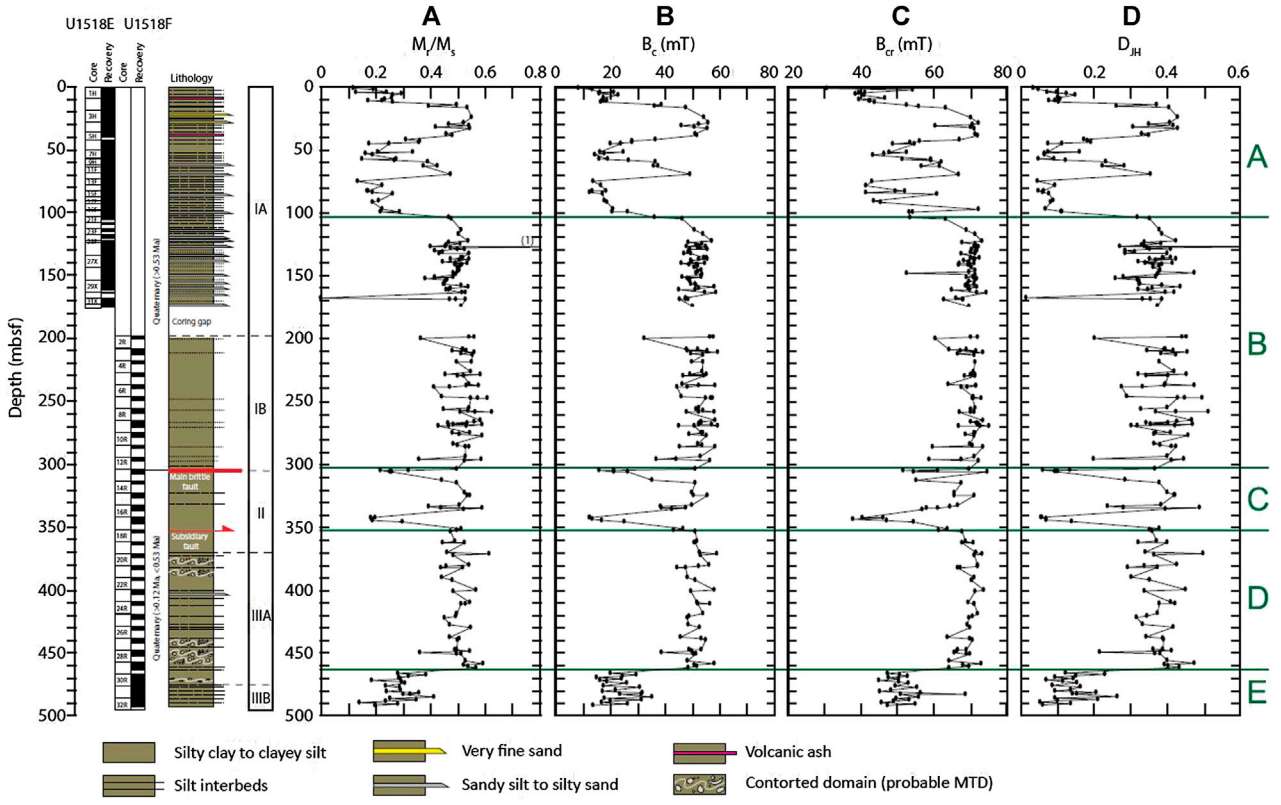

FIGURE 3 | Downhole magnetic hysteresis properties at Site U1518 **(A)** M_r/M_s ratio **(B)** coercivity B_c **(C)** remanent coercivity B_{cr} **(D)** D_{JH} index. Zones A to E are defined from coercivity variations. Core recovery, age and lithologic description are from Wallace et al. (2019).

(**Supplementary Figure S3**; **Supplementary Table S2**), which is similar to other samples from Zone D.

FORC diagrams (**Figure 4A**), thermomagnetic curves (**Figure 4B**) and low temperature magnetic measurements (**Figures 4C,D**) aim to characterize the magnetic mineral assemblages in low(er) and high(er) coercivity intervals, respectively. Rock magnetic measurements carried out on samples from the fault zone (i.e., Zone C) are presented and discussed in Greve et al. (2021) and are not further detailed in this manuscript.

Site U1518 samples can be divided into two groups based on their FORC diagrams. The first group represents most of the samples and the FORC diagrams display closed concentric contours with a mean coercivity B_c generally above 50 mT and interaction between grains (for instance, samples from Zones B and D, **Figure 4A**). The FORC diagrams for three gas hydrate-bearing footwall sections (**Supplementary Figure S3**) have smoother contours with a better defined shape than the FORC diagrams on **Figure 4**. This is due to a stronger magnetization and remanence of the samples. This FORC signature has been previously reported in Greve et al. (2020) and Greve et al. (2021) at Site U1518, and was attributed to SD greigite (e.g., Roberts et al., 2006). Although this FORC diagram signature is not unique to SD greigite, similar FORC diagrams were reported in other gas hydrate-bearing environments whose signature corresponds to greigite (e.g., Kars and Kodama, 2015a; Kars and Kodama, 2015b; Shi et al., 2017; Larrasoaña et al., 2007). The second group of samples shows a mixture of SD greigite with a lower coercivity magnetic phase (generally with a coercivity B_c below 20 mT). For this group, contours are open on the B_u axis indicating a coarser phase, likely in the vortex state (for instance, samples from Zones A (upper panel) and E, **Figure 4A**) (e.g., Roberts et al., 2000; Muxworthy and Dunlop, 2002). This additional phase is likely (titano)-magnetite, as indicated by thermomagnetic and low temperature magnetic measurements presented below.

Thermomagnetic curves on selected samples from the different magnetic zones are similar (**Figure 4B**). Magnetization upon warming decreases up to a peak temperature of ~420°C, from where it starts to increase until reaching a maximum at ~490°C and then decreases up to a temperature of 700°C. This magnetic behavior at temperatures higher than 400°C has been attributed to the oxidation of paramagnetic pyrite (FeS_2) into ferrimagnetic magnetite during heating (e.g., Passier et al., 2001). Some samples additionally display a change-in-slope at ~320°C, typically for the presence of greigite (see for example, samples from Zones B and C (lower panel), **Figure 4B**). Cooling and warming curves are not reversible, indicating modifications of the magnetic mineral assemblage during heating. This feature is common at Site U1518 (Greve et al., 2021).

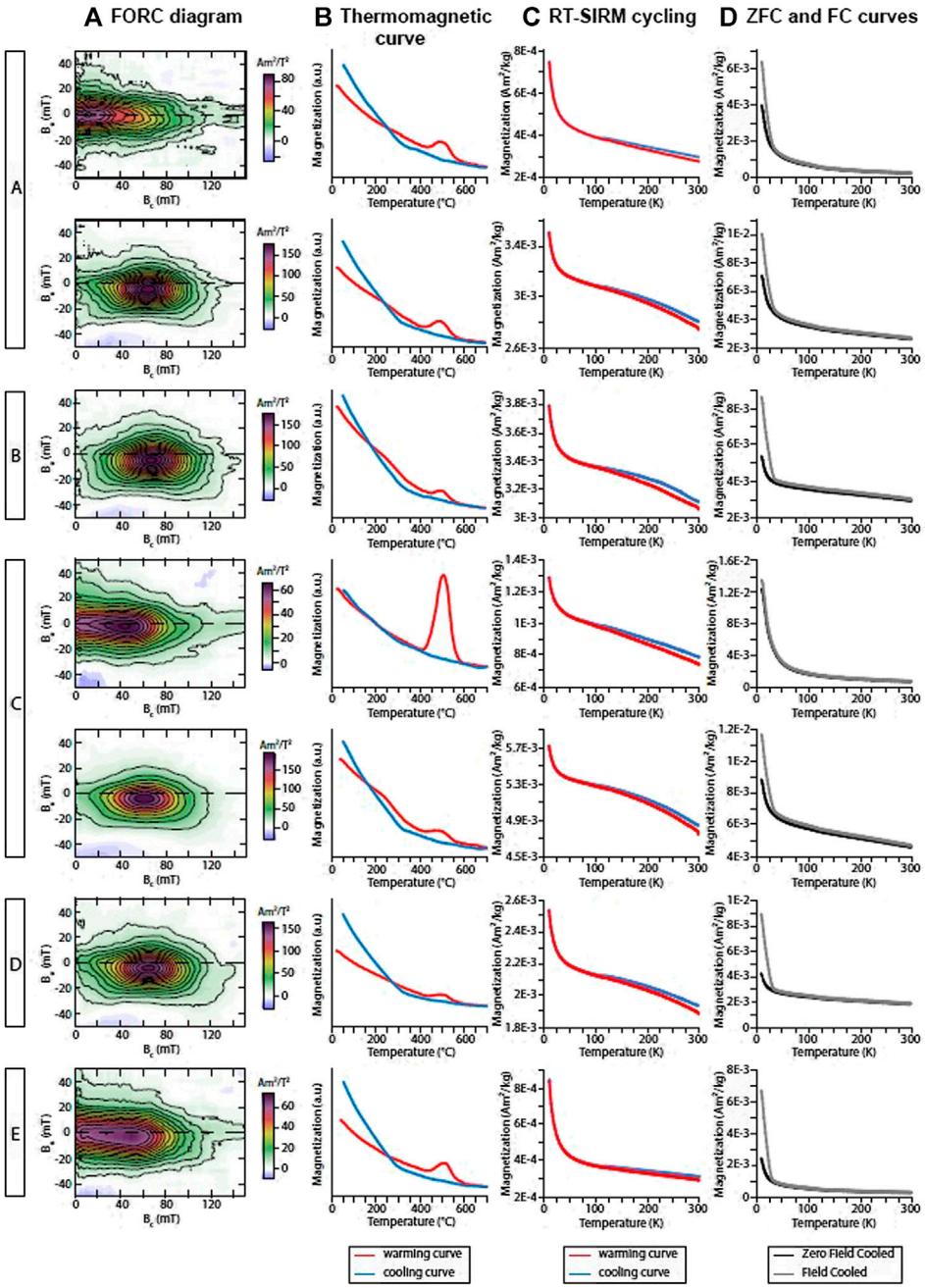

FIGURE 4 | Representative rock magnetic measurements for samples of the different coercivity zones (shown on the left) **(A)** FORC diagram **(B)** Thermomagnetic curve **(C)** RT-SIRM cycling and **(D)** Zero Field Cooled (ZFC) and Field Cooled (FC) curves. Selected samples are from top to bottom: U1518E-7H-5W, 13–15 cm (depth = 52.54 mbsf), U1518E-12F-2W, 22–24 cm (depth = 68.75 mbsf), U1518F-2R-1W, 44–46 cm (depth = 198.14 mbsf), U1518F-13R-2W, 99–101 cm (depth = 305.52 mbsf), U1518F-15R-2W, 67–69 cm (depth = 324.29 mbsf), U1518F-29R-3W, 6–8 cm (depth = 459.48 mbsf) and U1518F-32R-6W, 2–4 cm (depth = 490.57 mbsf). Samples from Coercivity Zone C are discussed in Greve et al. (2021).

Low temperature magnetic measurements do not significantly differ between samples from the different zones (**Figures 4C,D**). RT-SIRM curve on cooling (**Figure 4C**) shows a slight decrease of magnetization at ~110–120 K, which is comparable to the temperature T_V of the Verwey transition of magnetite (T_V~120 K) (e.g., Muxworthy and McClelland, 2000; Özdemir et al., 2002). Cooling and warming curves are not reversible through T_V, suggesting coarse-grained (Ti)-magnetite (e.g., Özdemir et al., 2002). The Verwey transition is barely seen on the ZFC and FC curves (**Figure 4D**). Their first derivatives do not display evidence for any additional magnetic phase. Greigite does not have any

low temperature magnetic transition (Chang et al., 2009; Roberts et al., 2011). Nevertheless, some key observations can be made. Samples from intervals for which the FORC signature indicates absence of greigite (i.e., Zones A and E, **Figure 4A**) display a significantly more marked decrease in SIRM intensity between 10 and 30 K than those from greigite-bearing intervals (**Figure 4D**). The decrease (**Supplementary Figure S2A**) is generally more than 50% for no greigite-bearing samples. Such a decrease suggests the presence of superparamagnetic (SP) grains (e.g., Passier and Dekkers, 2002) whose nature cannot be determined from the rock magnetic dataset presented in this manuscript.

The ratio of the remanence measured at 10 K between FC and ZFC, M_{FC}/M_{ZFC} (**Supplementary Figure S2B**), is generally higher than 1.4, suggesting the presence of SD-sized grains (Smirnov, 2009). High values of M_{FC}/M_{ZFC} generally occur in samples for which FORC diagrams indicate the presence of greigite. The loss in magnetization M for ZFC and FC curves during warming through the magnetite Verwey transition is calculated by using the parameter δ of Moskowitz et al. (1993) ($\delta = (M_{80K}\text{-}M_{150K})/M_{80K}$). The ratio δ_{FC}:δ_{ZFC} is close to 1:1 for samples from all zones (**Supplementary Figure S2C**). Higher δ_{FC} and δ_{ZFC} (>0.2) are found in Zones A, C and E, whereas lower δ_{FC} and δ_{ZFC} (<0.2) are found in Zones B and D, with a few exceptions. This distribution could reflect a difference in concentration and/or grain size distribution of (titano)-magnetite particles (Moskowitz et al., 1993) with higher values reflecting higher concentration and/or the presence of coarser (titano)-magnetite grains in Zones A, C, and E. Low values of δ_{FC} and δ_{ZFC} (<0.2) in samples containing ferrimagnetic iron sulfides have been previously reported in gas hydrate-bearing sediments of the Nankai Trough (Kars and Kodama, 2015a; Kars and Kodama, 2015b).

Site U1518 in the Hikurangi Margin is another example where low temperature magnetic measurement indirectly infer the presence of greigite. However, in this study, FORC diagrams are the best discriminatory technique to identify greigite in the samples.

DISCUSSION

The rock magnetic results presented above show a widespread occurrence of SD greigite in the studied sediments of Site U1518. This mineral is identified in the high coercivity intervals (B_{cr} > 50 mT) (**Figure 3**), whereas (titano)-magnetite is the main magnetic phase in the intervals with lower coercivity. Greigite forms via biogeochemical processes in the sedimentary column and is highly sensitive to changes in redox state. Especially, higher reactive iron contents and lower dissolved sulfide favor the formation and preservation of greigite (Kao et al., 2004). In the following sections we discuss how the distribution of greigite within the sequence of a young, active accretionary system provides insights into the interplay between fluid flow, gas hydrate accumulation and dissipation, and microbial activity.

Occurrence of Greigite and Methane Hydrate

A high value of SIRM/χ_{lf} has frequently been used as proxy for greigite-bearing intervals in marine sediments (e.g., Snowball, 1991). Larrasoaña et al. (2007) suggested that samples which contain iron sulfides typically display SIRM/χ_{lf} values higher than 15 kA/m. Based on SIRM/χ_{lf} (**Figure 2D**), B_{cr} (**Figure 3C**), and FORC diagrams (**Figure 4A** and **Supplementary Figure S3**), we define intervals that have concomitant rock magnetic properties characteristic of greigite-bearing sediment. **Figure 5** displays both greigite-bearing intervals and gas hydrate occurrence (Wallace et al., 2019; Cook et al., 2020). Greigite is quasi-ubiquitous at Site U1518 and present in sediments with discrete (disseminated) occurrence of gas hydrate. Similar findings were previously reported, for instance, in gas hydrate-bearing sediments of the Cascadia Margin (e.g., Housen and Musgrave, 1996; Larrasoaña et al., 2006) and of the Nankai Trough (Kars and Kodama, 2015a; Kars and Kodama, 2015b; Shi et al., 2017).

In Zone E and in some intervals of Zones A and C, lower values of SIRM (**Figure 2C**) and coercivity suggest lower contents or absence of greigite. We distinguish between "continuous" and "intermittent" occurrence of greigite. "Continuous" refers to depths with consecutive samples spanning a long interval where greigite is identified. "Intermittent" refers to intervals which contain some samples that do not have evidence for greigite. Continuous greigite occurrence is observed in Zones B and D, whereas intermittence is observed in Zones A and E. Zone C, corresponding to the Pāpaku fault zone, encompasses two narrow intervals in which greigite does not seem to be present (see Greve et al., 2021).

If we assume that SIRM is mostly carried by SD greigite, then this parameter reflects variations in the greigite concentration with depth. Higher values of SIRM suggest higher greigite contents. Quantification of greigite contents based on rock magnetic proxies is notoriously difficult because the remanence intensity is affected by magnetic grain size. Moreover, the saturation remanence (M_s) of greigite is still as of today undefined (Chang et al., 2008). Values range from as low as 3 Am^2/kg (Dekkers and Schoonen, 1996) to ~70 Am^2/kg (Li et al., 2014). Consequently, in the following discussion variations in greigite contents are expressed relatively to adjacent intervals and to the downhole trend.

Greve et al. (2021) conducted secondary and backscattered electron imaging on samples from low coercivity zones of the Pāpaku fault zone (Zone C). They identified an increase in the number of, size of framboids and signs of secondary pyritization. Different generations of pyrite (Greve et al., 2021) indicate that pyrite formation occurred during later diagenetic stages, perhaps related to further pyritization of authigenic greigite. By extrapolating this observation to other lower coercivity intervals, and by looking at similarities in rock magnetic parameters (for instance, D_{JH}, χ_{lf}, SIRM), we tentatively assume that pyrite is more abundant in the lower coercivity intervals in Zones A (in the hanging wall) and E (in the footwall) and that several generations of pyrite (with possible later reduction of greigite) exist. This assumption is supported by

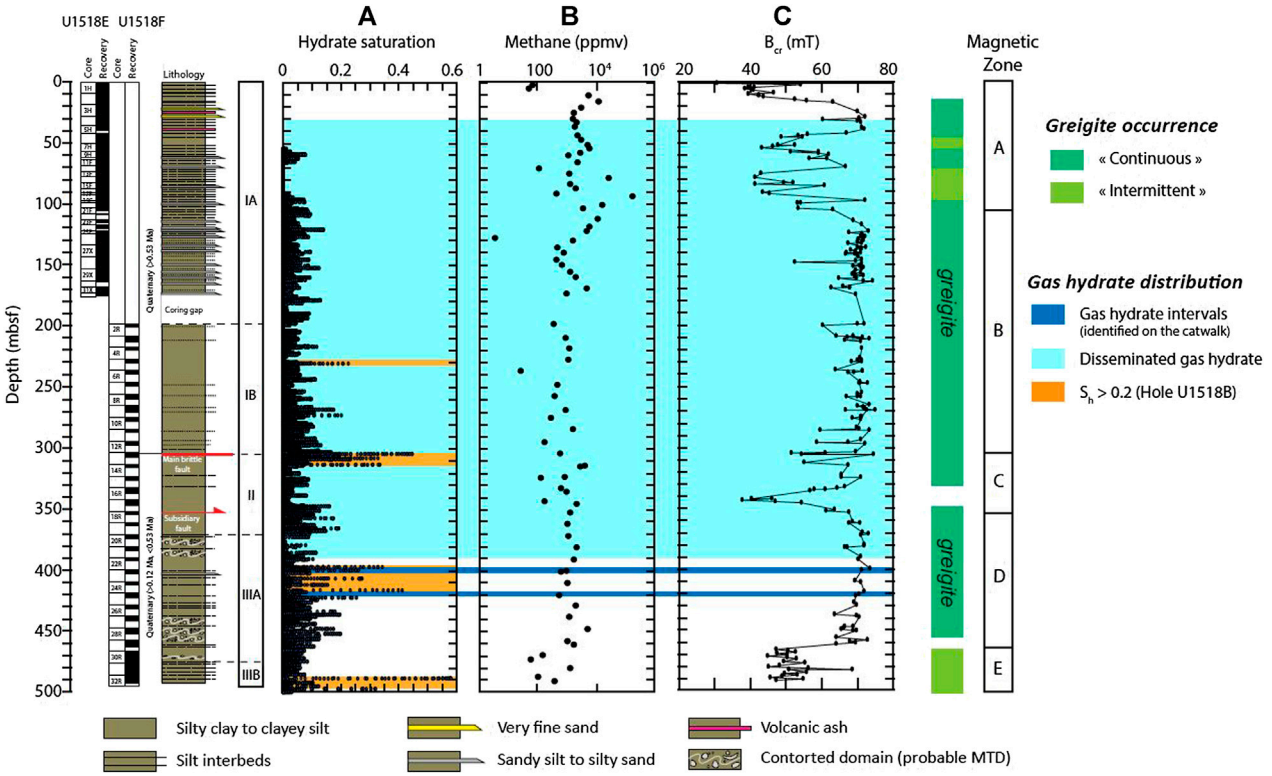

FIGURE 5 | Distribution of gas hydrate at Site U1518 based on shipboard observations (Wallace et al., 2019) **(A)** Hydrate saturation calculated from LWD resistivity data (Cook et al., 2020). Here a value of $n = 2.5$ for hydrate saturation calculation with Archie's equation has been used (Cook and Waite, 2018) **(B)** Shipboard methane contents **(C)** Remanent coercivity B_{cr}. Occurrence of greigite (dark green: continuous, light green: intermittent) from rock magnetic measurements is reported on the right with the coercivity zones defined in this study. The light blue shaded zone corresponds to disseminated gas hydrate and the dark blue shaded zones correspond to three gas hydrate-bearing sections identified aboard on the catwalk. The orange shaded zones correspond to intervals in Hole U1518B where hydrate saturation S_h calculated from LWD resistivity data exceeds 0.2 (Cook et al., 2020). Core recovery, age and lithologic description are from Wallace et al. (2019).

lower values of the remanence (e.g., SIRM) and χ_{lf} (**Figure 2**) that indicate lower contents of ferrimagnetic minerals (including iron oxides).

There are two major possible explanations for the absence of greigite: (i) it was never preserved because biogeochemical conditions favored complete pyritization at the sulfate-methane transition zone (SMTZ) during burial (e.g., Schoonen, 2004), or (ii) greigite was formed during early/syn-sedimentary diagenesis and later reduced to pyrite when environmental conditions changed. Secondary diagenesis to pyrite may for example be caused by advective or diffusive transport of fluids and methane through the sediment (e.g., Musgrave et al., 2019). The high sedimentation rate at this active margin probably resulted in a rapid burial beneath the SMTZ during initial deposition which would have prevented complete pyritization and enabled the preservation of greigite. This would invalidate the first explanation.

A striking observation is that greigite is intermittent or absent in sediment with lower resistivity and hydrate saturation, such as in the ~460–485 mbsf depth interval (Cook et al., 2020; **Figure 5**). Exceptional is the low hydrate saturation interval ($Sh < 0.1$) between 235 and 263 mbsf identified by Cook et al. (2020) which does not correspond to a depth interval with no greigite (**Figure 5**), instead it corresponds to a high coercivity interval with SD greigite in Hole U1518F. This discrepancy is likely explained by the fact that hydrate saturation calculated from LWD resistivity data is from Hole U1518B (Cook et al., 2020) located ~50 m to the north of Holes U1518E and U1518F (this study, **Figure 1B**). If we assume that greigite indicates presence of gas hydrate and methane diffusion, this discrepancy suggests discontinuous and patchy gas hydrate distribution in the frontal accretionary wedge of the Hikurangi Margin. In the following, we discuss how greigite is possibly linked to methane hydrate saturation.

Dissociation of methane hydrate may be one process responsible for later pyritization of authigenic greigite (e.g., Kars and Kodama, 2015a). When hydrate dissociates, released methane diffuses mostly upward. Subsequently, when conditions in pressure, temperature, methane concentration and solubility are met, it forms new hydrate. Methane diffusion is widespread at Site U1518 (Cook et al., 2020) and new hydrate formation is controlled by the hydraulic permeability, which is a function of sediment grain size and sorting. At Site U1518, methane hydrate is mostly found in coarse-grained lithology, i.e., sand and silt, in cm to 10s of cm-thick layers (Cook et al., 2020). While methane hydrate preferentially forms in coarse-grained lithology (silt- or

sandstone), the slow diffusion of methane through surrounding and clay-rich layers may be used by microorganisms for *in situ* formation of iron sulfides. When hydrates dissociate, the sudden release and accumulation of methane in porous intervals (below a less porous interval acting as a seal) would result in the secondary diagenesis of existing greigite to pyrite (e.g., Kars et al., 2018; Musgrave et al., 2019). The higher coercivity intervals in Zones A, B and D (**Figure 3**), which are also characterized by higher SIRM/χ_{lf} values (**Figure 2D**) indicate the preservation of diagenetic greigite, which formed at the SMTZ during sediment deposition and possibly at a later diagenetic stage due to enhanced microbial activity (see *Greigite as Indicator for Enhanced Microbial Activity*).

Repeating Hanging Wall and Footwall Diagenetic Pattern

Wallace et al. (2019) have identified an age inversion at ~304.5 mbsf that coincides with the top of the Pāpaku fault zone. The diagenetic sequence of the hanging wall (>0.53 Ma) based on lithostratigraphy, structural geology and pore water analysis is repeated below the Pāpaku fault zone in the footwall (<0.53 Ma). This has led Morgan et al. (personal communication) to suggest recent underthrusting and active displacement along the thrust fault.

In **Figures 2**,**3** concentration and composition of magnetic minerals above the Pāpaku fault zone in Zone B (~104–304 mbsf, i.e., lower half of Lithostratigraphic Unit IA, and Unit IB) are similar to those of below the fault zone in Zone D (~352–463 mbsf, i.e., Lithostratigraphic Unit IIA). Likewise, rock magnetic properties between ~466 and 492 mbsf (Zone E, i.e., very bottom of Lithostratigraphic Subunit IIIA, and Subunit IIIB), display lower values of the concentration-dependent parameters, and a lower coercivity. This signal resembles the weaker signal in the top part of the sediments in Zone A (i.e., upper half of Subunit IA). Comparable FORC diagram signature has been measured between Zones A and E, and B and D, respectively (**Figure 4**). These observations are in agreement with a repetition of the diagenetic sequence observed by Wallace et al. (2019) based on pore water analyses.

Low coercivity intervals in Zone A where greigite is not identified may be the result of completed pyritization at the SMTZ. By contrast, higher coercivity intervals would have been quickly buried below the SMTZ, favoring the preservation of greigite. At the drill site, sedimentation rate is varying through time with turbidite deposits increasing the sedimentation rate in a limited period (Wallace et al., 2019). A less prolonged time at, and a quick burial below the SMTZ would therefore favor the preservation of intermediary greigite. Consequently (early diagenetic) greigite formation predated any thrusting, because greigite occurs in the hanging wall (older) and the footwall (younger).

Zone D is a remaining interval currently in the footwall of shallower rocks (which are now eroded in the hanging wall). In Zone D, greigite, formed at much shallower depth at the SMTZ, has been preserved until present, likely at the favor of limited and transient fluid flow in the footwall (Cook et al., 2020; Fagereng et al., 2019; Greve et al., 2021). The magnetic mineral assemblage of Zone D which contains greigite would therefore correspond to the early diagenetic sequence, formerly present in the hanging wall, in the footwall. The absence of greigite in Zone E might be explained by either complete pyritization at the SMTZ or further reduction of greigite into pyrite, likely because of hydrate dissociation due to the proximity of this interval to the base of methane hydrate stability (at ~585 mbsf; Cook et al., 2020).

Greigite as Indicator for Enhanced Microbial Activity

Many formation pathways have been proposed for greigite. These pathways include early formation from pyrite precursors (e.g., Schoonen, 2004) and later diagenetic processes such as greigite growth on surface of pre-existing mineral phases (e.g., Roberts and Weaver, 2005). The reader is referred to Roberts (2015) for a review of these processes. In anoxic, sulfidic marine sediment, dissolved sulfide necessary for iron sulfide formation is produced by organo-clastic sulfate reduction (degradation of organic matter; Berner, 1981) and by anaerobic oxidation of methane (AOM) (e.g., Knittel and Boetius, 2009) performed by sulfate reducing bacteria (SRB) and a consortium of SRB and methanotrophic archaea (e.g., Knittel et al., 2003), respectively. This happens at the sulfate-methane transition zone (SMTZ). Dissolved sulfide further reacts with dissolved iron to form iron sulfides (e.g., Schoonen, 2004). Under specific anoxic and sulfidic conditions (e.g., Neretin et al., 2004), greigite can be preserved below the SMTZ. Changes in organic carbon input and sedimentation rate are amongst the most common factors controlling the formation of iron sulfides (e.g., Kasten et al., 1998).

At Site U1518, the SMTZ is located at ~8 mbsf where sulfate concentration drops to 0 mM and remains at this value to the bottom of the hole (Saffer et al., 2019). Elevated methane flux responsible for the shallow occurrence of methane hydrate and SMTZ infers low dissolved sulfide contents at the SMTZ (Wallace et al., 2019). Lower dissolved sulfide contents, thus, might arrest the pyritization process and favor the preservation of greigite (e.g., Kao et al., 2004).

Authigenic greigite is the main magnetic carrier in our samples, except for weakly magnetized intervals where pyrite and iron oxides are present in Zones A, C and E (**Figure 5**). As greigite is mainly formed as a by-product of microbial processes, it is assumed that microbial activity is playing an important role on greigite formation and preservation at Site U1518.

Microbiological studies, conducted in marine sediments of the Cascadia Margin (e.g., Cragg et al., 1996) and of the Nankai Trough (e.g., Reed et al., 2002; Inagaki et al., 2006), have shown that the total number of microorganisms increases in hydrate zones, compared to adjacent sediments. Moreover, Inagaki et al. (2006) have found that the microbial community composition is different in hydrate-bearing sediments relative to hydrate-free intervals. A strong interplay thus exists between hydrate and microbial activity (e.g., Cragg et al., 1996; Katayama et al., 2016). Microbial processes and community distributions, influenced by gas hydrate and gas and fluid venting, are thus key factors for understanding biogeochemical processes related to the

occurrence of biogenic gas hydrate. Microbial communities identified at cold seeps in the Hikurangi Margin are similar to those identified in cold seeps worldwide, with dominant anaerobic methanotrophic archaea (ANME) and proteobacteria (Ruff et al., 2013). ANME are the principal microorganisms involved in the AOM reaction (e.g., Knittel and Boetius, 2009) with production of dissolved sulfide in the pore water needed for iron sulfide formation.

Findings on the interplay between hydrate and microbial activity in the Cascadia Margin and the Nankai Trough suggest that a similar relationship exists in the Hikurangi Margin. Cook et al. (2020) posit that unconnected low to moderate hydrate saturation at Site U1518 implies that the source of methane in the hydrate is by local diffusion of microbially generated methane within the hydrate stability zone. At our knowledge, there is currently no microbiology study conducted at Site U1518 to characterize the microbial communities present in the sediment.

In intervals with higher D_{JH} (**Figure 3D**), SIRM/χ_{lf} (**Figure 2D**) and a stronger FORC signature indicating the prevalence of SD greigite (**Figure 4A**, **Supplementary Figure S3**), the production of greigite may be increased compared to other intervals with lower values where greigite is identified. Localized and limited dissolved sulfide, likely produced *in situ* by AOM, favors *in situ* formation and preservation of greigite by microbial activity. Higher values of concentration-dependent magnetic parameters (e.g., D_{JH}) might therefore indicate enhanced microbial activity (perhaps with an increased number of microorganisms) in gas hydrate intervals at Site U1518. The vertical distribution of authigenic greigite may be a good indicator of methane hydrate within sediment, and of microbial communities at the origin of biogenic hydrate formation.

Comparison With the Nankai Trough and the Cascadia Margin

Gas hydrate has been widely identified in accretionary prisms around the world (e.g., Kvenvolden, 1993). The Cascadia Margin, offshore Oregon, and the Nankai Trough, offshore Japan, have been widely studied for decades by ocean scientific drilling and several rock magnetic studies have been conducted to elucidate any relationship between gas hydrate and magnetic mineralogy.

Larrasoaña et al. (2007) proposed the use of a bivariate plot, χ_{lf} as a function of SIRM/χ_{lf}, to identify, at first approximation, the magnetic mineral assemblage composing marine sediments. Given ranges of SIRM/χ_{lf} values would indicate the relative dominance of ferrimagnetic iron sulfides in the mineral assemblage. **Supplementary Figure S4** is a comparison of our dataset with data from the Cascadia Margin (Housen and Musgrave, 1996; Larrasoaña et al., 2006) and Nankai Trough (Kars and Kodama, 2015a; Kars and Kodama, 2015b, unpublished). Site U1518 samples have relatively low magnetic susceptibility, similar to values obtained in the Nankai Trough. SIRM/χ_{lf} for Site U1518 varies between ~1.34 and 102.73 kA/m. Most samples have SIRM/χ_{lf} > 15 kA/m, which suggests, according to Larrasoaña et al. (2007), a magnetic mineral assemblage dominated by authigenic iron sulfides, as shown in our study.

The FORC diagrams measured in our study (**Figure 4A**; **Supplementary Figure S3**) are typical of FORC diagrams measured in the Cascadia Margin (Larrasoaña et al., 2007) and in the Nankai Trough (Kars and Kodama, 2015a; Kars and Kodama, 2015b; Shi et al., 2017), indicating occurrence of SD greigite in hydrate-bearing sediments. The Hikurangi Margin is, thus, an additional example of accretionary prism with co-occurrence of authigenic iron sulfides (mostly greigite) and gas hydrate. From this observation, one can expect that SD greigite would be more commonly identified in accretionary prisms and continental margins where gas hydrate occurs.

CONCLUSION

Marine sediments of Site U1518 can be divided into five consecutive intervals showing variations in magnetic properties, especially coercivity. Most of the samples have a high remanent coercivity B_{cr}, above 50 mT, and a FORC diagram signature typical of single domain greigite. Authigenic greigite is observed throughout the entire stratigraphic sequence, which was cored entirely in the gas hydrate stability zone. Lower coercivity zones are found at the top of the hanging wall and in the footwall below the Pāpaku fault zone, likely because of the repetition of the early diagenetic sequence in the footwall. Coercivity variations within the Pāpaku fault zone are discussed in Greve et al. (2021). This study is the first systematic study in the Hikurangi Margin establishing a close relationship between authigenic greigite and gas hydrate. Low hydrate saturation level seems to correspond to depth intervals where greigite is in lower concentration or absent. Greigite is found in sediments where hydrate saturation is higher. A higher greigite concentration may suggest an enhanced microbial activity in methane hydrate-bearing sediments. Further studies in gas hydrate environment combining rock magnetism and microbiology are necessary to elucidate greigite formation in this environment.

DATA AVAILABILITY STATEMENT

The original contributions presented in this study are available at https://www.pangaea.de. Shipboard data are available from the IODP database here: http://web.iodp.tamu.edu/LORE/.

AUTHOR CONTRIBUTIONS

MK conceived the study and performed rock magnetic measurements. AG collected the samples and performed paleomagnetic measurements. LZ assisted with early magnetic analyses during tenure of an undergraduate scholarship. MK and AG contributed to the interpretation and discussion of the data. All authors contributed to and approved the final manuscript.

FUNDING

AG acknowledges funding through NWO Deep NL grant 2018.040, the Korea Institute of Energy Technology Evaluation and Planning (KETEP) and the Ministry of Trade, Industry & Energy (MOTIE) of the Republic of Korea (No. 20168510030830). LZ assisted with early magnetic analyses during tenure of an undergraduate scholarship under the framework of the RISE worldwide program of the German Academic Exchange Service (DAAD).

ACKNOWLEDGMENTS

This study used samples and data provided by the International Ocean Discovery Program (IODP). We thank the science party and technical staff that assisted with the acquisition of samples, data and contributed to scientific discussions, and crew of IODP Expedition 375. Shipboard data are available from the IODP database (http://web.iodp.tamu.edu/LORE/) and the Expedition 375 Proceedings are available at http://publications.iodp.org/proceedings/372B_375/372B375title.html. We are grateful to Ann Cook for sharing with us her hydrate saturation calculation. Rock magnetic data presented in the paper are available at https://www.pangaea.de. AG acknowledges funding through NWO Deep NL grant 2018.040, the Korea Institute of Energy Technology Evaluation and Planning (KETEP) and the Ministry of Trade, Industry & Energy (MOTIE) of the Republic of Korea (No. 20168510030830). LZ assisted with early magnetic analyses during tenure of an undergraduate scholarship under the framework of the RISE worldwide program of the German Academic Exchange Service (DAAD).

SUPPLEMENTARY MATERIAL

The Supplementary Material for this article can be found online at: https://www.frontiersin.org/articles/10.3389/feart.2021.603363/full#supplementary-material.

REFERENCES

Badesab, F., Dewangan, P., Gaikwad, V., Kars, M., Kocherla, M., Krishna, K. S., et al. (2019). Magnetic mineralogical approach for the exploration of gas hydrates in the Bay of Bengal. *J. Geophys. Res. Solid Earth* 124, 4428–4451. doi:10.1029/2019JB017466

Barker, D. H. N., Henrys, S., Caratori Tontini, F., Barnes, P. M., Bassett, D., Todd, E., et al. (2018). Geophysical constraints on the relationship between seamount subduction, slow slip, and tremor at the North Hikurangi Subduction Zone, New Zealand. *Geophys. Res. Lett.* 45 (23), 12804–12813. doi:10.1029/2018gl080259

Bazylinski, D. A., and Williams, T. J. (2006). "Ecophysiology of magnetotactic bacteria," in *Magnetoreception and magnetosomes in bacteria*, Microbiology Monographs, Editor D. Schüler 3, 37–75. doi:10.1007/7171_038

Berner, R. A. (1981). A new geochemical classification of sedimentary environments. *J. Sediment. Petrology* 51, 359–365. 10.1306/212F7C7F-2B24-11D7-8648000102C1865D

Bloemendal, J., King, J. W., Hall, F. R., and Doh, S.-J. (1992). Rock magnetism of Late Neogene and Pleistocene deep-sea sediments: relationship to sediment sources, diagenetic processes and sediment lithology. *J. Geophys. Res.* 97 (B4), 4361–4375. doi:10.1029/91JB03068

Buffet, B., and Archer, D. (2004). Global inventory of methane clathrate: sensitivity to changes in the deep ocean. *Earth and Planet. Sci. Lett.* 227, 185–199. doi:10.1016/j.epsl.2004.09.005

Chang, L., Roberts, A. P., Rowan, C. J., Tang, Y., Pruner, P., Chen, Q., et al. (2009). Low-temperature magnetic properties of greigite (Fe_3S_4). *Geochem. Geophys. Geosystems* 10, Q01Y04. doi:10.1029/2008GC002276

Chang, L., Roberts, A. P., Tang, Y., Rainford, B. D., Muxworthy, A. R., and Chen, Q. (2008). Fundamental magnetic parameters from pure synthetic greigite (Fe_3S_4). *J. Geophys. Res.* 113, B06104. doi:10.1029/2007JB005502

Collett, T. S. (2001). "A review of well-log analysis techniques used to assess gas-hydrate bearing reservoirs," in *Natural gas hydrates: occurrence, distribution and detection*, Geophysical Monograph Series, Editors C. K. Paull and W. P. Dillon 124, 189–210. doi:10.1029/GM124p0189

Cook, A. E., Paganoni, M., Clennell, M. B., McNamara, D. D., Nole, M., Wang, X., et al. (2020). Physical properties and gas hydrate at a near-seafloor thrust fault, Hikurangi Margin, New Zealand. *Geophys. Res. Lett.* 47, e2020GL088474. doi:10.1029/2020GL088474

Cook, A. E., and Waite, W. F. (2018). Archie's saturation exponent for natural gas hydrate in coarse-grained reservoirs. *J. Geophys. Res. – Solid Earth* 123, 2069–2089. doi:10.1002/2017JB015138

Cragg, B. A., Parkes, R. J., Fry, J. C., Weightman, A. J., Rochelle, P. A., and Maxwell, J. R. (1996). Bacterial populations and processes in sediments containing gas hydrates (ODP leg 146: Cascadia Margin). *Earth and Planet. Sci. Lett.* 139, 497–507. doi:10.1016/0012-821X(95)00246-9

Dekkers, M. J., and Schoonen, M. A. A. (1996). Magnetic properties of hydrothermally synthesized greigite (Fe_3S_4) – I. Rock magnetic parameters at room temperature. *Geophys. J. Int.* 126, 360–368. doi:10.1111/j.1365-246X.1996.tb05296.x

Egli, R. (2013). VARIFORC: an optimized protocol for calculating non-regular first-order reversal curve (FORC) diagrams. *Glob. and Planet. Change* 110, 302–320. doi:10.1016/j.gloplacha.2013.08.003

Fagereng, Å., Savage, H. M., Morgan, J. K., Wang, M., Meneghini, F., Barnes, P. M., et al. (2019). Mixed deformation styles observed on a shallow subduction thrust, Hikurangi margin, New Zealand. *Geology* 47, 872–876. doi:10.1130/G46367.1

Fu, Y., von Dobeneck, T., Franke, C., Heslop, D., and Kasten, S. (2008). Rock magnetic identification and geochemical process models of greigite formation in Quaternary marine sediments from the Gulf of Mexico (IODP Hole U1319A). *Earth and Planet. Sci. Lett.* 275, 233–245. doi:10.1016/j.epsl.2008.07.034

Greve, A., Kars, M., and Dekkers, M. J. (2021). Fluid accumulation, migration and anaerobic oxidation of methane along a major splay fault at the Hikurangi subduction margin (New Zealand): A magnetic approach. *J. Geophy. Res. Solid Earth* 126, e2020JB020671. doi:10.1029/2020JB020671

Greve, A., Kars, M., Zerbst, L., Stipp, M., and Hashimoto, Y. (2020). Strain partitioning across a subduction thrust fault near the deformation front of the Hikurangi subduction margin, New Zealand: a magnetic fabric study on IODP Expedition 375 Site U1518. *Earth and Planet. Sci. Lett.* 542, 116322. doi:10.1016/j.epsl.2020.116322

Harrison, R. J., and Feinberg, J. (2008). FORCInel: an improved algorithm for calculating first order reversal curve distributions using locally weighted regression smoothing. *Geochem. Geophys. Geosystems* 9, Q05016. doi:10.1029/2008GC001987

Hesse, R. (2003). Pore water anomalies of submarine gas-hydrate zones as tool to assess hydrate abundance and distribution in the subsurface what have we learned in the past decade?. *Earth-Science Rev.* 61, 149–179. doi:10.1016/S0012-8252(02)00117-4

Horng, C.-S. (2018). Unusual magnetic properties of sedimentary pyrrhotite in methane seepage sediments: comparison with metamorphic pyrrhotite and sedimentary greigite. *J. Geophys. Res. Solid Earth* 123, 15262. doi:10.1002/2017JB015262

Housen, B. A., and Musgrave, R. J. (1996). Rock-magnetic signature of gas hydrates in accretionary prism sediments. *Earth and Planet. Sci. Lett.* 139 (3–4), 509–519. doi:10.1016/0012-821X(95)00245-8

Inagaki, F., Nunoura, T., Nakagawa, S., Teske, A., Lever, M., Lauer, A., et al. (2006). Biogeographical distribution and diversity of microbes in methane hydrate-bearing

deep marine sediments on the Pacific Ocean Margin. *Proc. Natl. Acad. Sci. USA* 103 (8), 2815–2820. doi:10.1073/pnas.0511033103

Kao, S.-J., Horng, C.-S., Roberts, A. P., and Liu, K.-K. (2004). Carbon-sulfur-iron relationships in sedimentary rocks from southwestern Taiwan: influence of geochemical environment on greigite and pyrrhotite formation. *Chem. Geology.* 203 (1–2), 153–168. doi:10.1016/j.chemgeo.2003.09.007

Kars, M., and Kodama, K. (2015a). Authigenesis of magnetic minerals in gas hydrate-bearing sediments in the Nankai Trough, offshore Japan. *Geochemisty, Geophys. Geosystems* 16, 947–961. doi:10.1002/2014GC005614

Kars, M., and Kodama, K. (2015b). Rock magnetic characterization of ferrimagnetic iron sulfides in gas hydrate-bearing marine sediments at Site C0008, Nankai Trough, Pacific Ocean, off-coast Japan. *Earth, Planets and Space* 67, 18. doi:10.1186/s40623-015-0287-y

Kars, M., Musgrave, R. J., Hoshino, T., Jonas, A-S., Bauersachs, T., Inagaki, F., et al. (2018). Magnetic mineral diagenesis in a high temperature and deep methanic zone in izu rear arc marine sediments, northwest pacific ocean. *J. Geophys. Res. Solid Earth*, 123 (10), 8331–8348. doi:10.1029/2018JB015861

Kasten, S., Freudenthal, T., Gingele, F. X., and Schulz, H. D. (1998). Simultaneous formation of iron-rich layers at different redox boundaries in sediments of the Amazon deep-sea fan. *Geochimica et Cosmochimica Acta* 62, 2253–2264. doi:10.1016/S0016-7037(98)00093-3

Katayama, T., Yoshioka, H., Takahashi, H. A., Amo, M., Fujii, T., and Sakata, S. (2016). Changes in microbial communities associated with gas hydrates in subseafloor sediments from the Nankai Trough. *FEMS Microbiol. Ecol.* 92, fiw093. doi:10.1093/femsec/fiw093

Kinoshita, M., Fukase, H., Goto, S., and Toki, T. (2015). *In situ* thermal excursions detected in the Nankai Trough forearc slope sediment at IODP NanTroSEIZE Site C0008. *Earth, Planets and Space* 67, 16. doi:10.1186/s40623-014-0171-1

Knittel, K., and Boetius, A. (2009). Anaerobic oxidation of methane: progress with an unknown process. *Annu. Rev. Microbiol.* 63 (1), 311–334. doi:10.1146/annurev.micro.61.080706.093130

Knittel, K., Boetius, A., Lemke, A., Eilers, H., Pfannkuche, O., and Linke, P. (2003). Activity, distribution, and diversity of sulfate reducers and other bacteria in sediments above gas hydrate (Cascadia Margin, Oregon). *Geomicrobiology J.* 20, 269–294. doi:10.1080/01490450390241008

Kvenvolden, K. A. (1993). Gas hydrates – geological perspective and global change. *Rev. Geophys.* 31 (2), 173–187. doi:10.1029/93RG00268

Larrasoaña, J. C., Gràcia, E., Garcés, M., Musgrave, R. J., Piñero, E., Martínez-Ruiz, F., et al. (2006). Rock magnetic identification of magnetic iron sulfides and its bearing on the occurrence of gas hydrates, ODP Leg 204 (Hydrate Ridge) in *Proceedings of the ocean drilling program, scientific results* Editors A. M. Tréhu, G. Bohrmann, M. E. Torres, and F. S. Colwell, 204. doi:10.2973/odp.proc.sr.204.111.2006

Larrasoaña, J. C., Roberts, A. P., Musgrave, R. J., Gràcia, E., Piñero, E., Vega, M., et al. (2007). Diagenetic formation of greigite and pyrrhotite in marine sedimentary systems containing gas hydrates. *Earth and Planet. Sci. Lett.* 261 (3–4), 350–366. doi:10.1016/j.epsl.2007.06.032

Li, G., Zhang, B., Yu, F., Novakova, A. A., Krivenkov, M. S., Kiseleva, T. Y., et al. (2014). High-purity Fe_3S_4 greigite microcrystals for magnetic and electrochemical performance. *Chem. Mater.* 26, 5821–5829. doi:10.1021/cm501493m

Lu, R., and Banerjee, S. K. (1994). Magnetite dissolution in deep sediments and its hydrologic implication: a detailed study of sediments from site 808, leg 131. *J. Geophys. Res.* 99 (B5), 9051–9059. doi:10.1029/93JB03204

Mann, S., Sparks, N. H. C., Frankel, R. B., Bazylinski, D. A., and Jannasch, H. W. (1990). Biomineralization of ferrimagnetic greigite (Fe_3S_4) and iron pyrite (FeS_2) in a magnetotactic bacterium. *Nature* 343, 258–261. doi:10.1038/343258a0

Moskowitz, B., Frenkel, R. B., and Bazylinski, D. A. (1993). Rock magnetic criteria for the detection of biogenic magnetite. *Earth and Planet. Sci. Lett.* 120, 283–300. doi:10.1016/0012-821X(93)90245-5

Mountjoy, J. J., Pecher, I., Henrys, S., Crutchley, G., Barnes, P. M., and Plaza-Faverola, A. (2014). Shallow methane hydrate system controls on going downslope sediment transport in a low-velocity active submarine landslide complex, Hikurangi Margin, New Zealand. *Geochem. Geophys. Geosystem* 15, 4137–4156. doi:10.1002/2014GC005379

Musgrave, R. J., Bangs, N. L., Larrasoaña, J. C., Gràcia, E., Hollamby, J. A., and Vega, M. E. (2006). Rise of the base of the gas hydrate zone since the last glacial recorded by rock magnetism. *Geology* 34 (2), 117–120. doi:10.1130/G22008.1

Musgrave, R. J., Kars, M., and Vega, M. E. (2019). Progressive and punctuated magnetic mineral diagenesis: the rock magnetic record of multiple fluid inputs and progressive pyritization in a volcano-bounded basin, IODP Site U1437, Izu Rear Arc. *J. Geophys. Res. Solid Earth* 124 (6), 5357–5378. doi:10.1029/2018jb017277

Muxworthy, A. R., and Dunlop, D. J. (2002). First-order reversal curve (FORC) diagrams for pseudosingle-domain magnetites at high temperature. *Earth and Planet. Sci. Lett.* 203, 369–382. doi:10.1016/S0012-821X(02)00880-4

Muxworthy, A. R., and McClelland, E. (2000). Review of the low-temperature magnetic properties of magnetite from a rock magnetic perspective. *Geophys. J. Int.* 140 (1), 101–114. doi:10.1046/j.1365-246x.2000.00999.x

Neretin, L. N., Böttcher, M. E., Jørgensen, B. B., Volkov, I. I., Lüschen, H., and Hilgenfeldt, K. (2004). Pyritization processes and greigite formation in the advancing sulfidization front in the Upper Pleistocene sediments of the Black Sea. *Geochimica et Cosmochimica Acta* 68, 2081–2093. doi:10.1016/S0016-7037(03)00450-2

Özdemir, Ö., Dunlop, D. J., and Moskowitz, B. M. (2002). Changes in remanence, coercivity and domain state at low temperature in magnetite. *Earth and Planet. Sci. Lett.* 194, 343–358. doi:10.1016/S0012-821X(01)00562-3

Passier, H. F., de Lange, G. J., and Dekkers, M. J. (2001). Magnetic properties and geochemistry of the active oxidation front and the youngest sapropel in the eastern Mediterranean Sea. *Geophys. J. Int.* 145 (3), 604–614. doi:10.1046/j.0956-540x.2001.01394.x

Passier, H. F., and Dekkers, M. J. (2002). Iron oxide formation in the active oxidation front above sapropel S1 in the eastern Mediterranean Sea as derived from low-temperature magnetism. *Geophys. J. Int.* 150, 230–240. doi:10.1046/j.1365-246X.2002.01704.x

Pecher, I. A., Barnes, P. M., LeVay, L. J. and the Expedition 372A Scientists, (2019). "Creeping gas hydrate slides," in Proceedings of the International Ocean Discovery Program, 372A: College Station, TX:. International Ocean Discovery Program. doi:10.14379/iodp.proc.372A.2019

Pike, C. R., Roberts, A. P., and Verosub, K. L. (1999). Characterizing interactions in fine magnetic particle systems using first order reversal curves. *J. Appl. Phys.* 85(9), 6660–6667. doi:10.1063/1.370176

Reed, D. W., Fujita, Y., Delwiche, M. E., Blackwelder, D. B., Sheridan, P. P., Uchida, T., et al. (2002). Microbial communities from methane hydrate-bearing deep marine sediments in a forearc basin. *Appl. Environ. Microbiol.* 68 (8), 3759–3770. doi:10.1128/AEM.68.8.3759–3770.2002

Roberts, A. P., Chang, L., Rowan, C. J., Horng, C.-S., and Florindo, F. (2011). Magnetic properties of sedimentary greigite (Fe_3S_4): an update. *Rev. Geophys.* 49, RG1002. doi:10.1029/2010rg000336.1

Roberts, A. P., Heslop, D., Zhao, X., and Pike, C. R. (2014). Understanding fine magnetic particle systems through use of first-order reversal curve diagrams. *Rev. Geophys.* 52, 557–602. doi:10.1002/2014RG000462

Roberts, A. P., Liu, Q., Rowan, C. J., Chang, L., Carvallo, C., Torrent, J., et al. (2006). Characterization of hematite (a-Fe_2O_3), goethite (a-FeOOH), greigite (Fe_3S_4), and pyrrhotite (Fe_7S_8) using first-order reversal curve diagrams. *J. Geophys. Res.* 111, B12S35, doi:10.1029/2006JB004715

Roberts, A. P. (2015). Magnetic mineral diagenesis. *Earth-Science Rev.* 151, 1–47. doi:10.1016/j.earscirev.2015.09.010

Roberts, A. P., Pike, C. R., and Verosub, K. L. (2000). First-order reversal curve diagrams: a new tool for characterizing the magnetic properties of natural samples. *J. Geophys. Res.*, 105 (B12), 28461–28475. doi:10.1029/2000JB900326

Roberts, A. P., Tauxe, L., Heslop, D., Zhao, X., and Jiang, Z. (2018). A critical appraisal of the "Day" diagram. *J. Geophys. Res. – Solid Earth*, 123, 2618–2644. doi:10.1002/2017JB015247

Roberts, A. P., and Turner, G. M. (1993). Diagenetic formation of ferrimagnetic iron sulphide minerals in rapidly deposited marine sediments, South Island, New Zealand. *Earth and Planet. Sci. Lett.* 115, 257–273. doi:10.1016/0012-821X(93)90226-Y

Roberts, A. P., and Weaver, R. (2005). Multiple mechanisms of remagnetization involving sedimentary greigite (Fe_3S_4). *Earth and Planet. Sci. Lett.* 231, 263–277. doi:10.1016/j.epsl.2004.11.024

Rowan, C. J., and Roberts, A. P. (2006). Magnetite dissolution, diachronous greigite formation, and secondary magnetizations from pyrite oxidation: unravelling complex magnetizations in Neogene marine sediments from New Zealand. *Earth and Planet. Sci. Lett.*, 241, 119–137. doi:10.1016/j.epsl.2005.10.017

Rowan, C. J., and Roberts, A. P. (2005). Tectonic and geochronological implications of variably timed magnetizations carried by authigenic greigite in marine sediments from New Zealand. *Geology* 33, 553–556. doi:10.1130/G21382.1

Ruff, S. E., Arnds, J., Knittel, K., Amann, R., Wegener, G., Ramette, A., et al. (2013). Microbial communities of deep-sea methane seeps at Hikurangi continental margin (New Zealand). *PLoS One* 8 (9), e72627. doi:10.1371/journal.pone.0072627

Ruppel, C. D., and Kessler, J. D. (2017). The interaction of climate change and methane hydrates, *Rev. Geophys.* 55, 126–168. doi:10.1002/2016RG000534

Saffer, D. M., Wallace, L. M., Barnes, P. M., Pecher, I. A., Petronotis, K. E., LeVay, L. J., et al. and the Expedition 372/375 Scientists. (2019). Site U1518. In Wallace, L.M., Saffer, D.M., Barnes, P.M., Pecher, I.A., Petronotis, K.E., LeVay, L.J., and the Expedition 372/375 Scientists, Hikurangi Subduction Margin Coring, Logging, and Observatories. Proceedings of the International Ocean Discovery Program, 372B/375: College Station, TX (International Ocean Discovery Program), https://doi.org/10.14379/iodp.proc.372B375.103.2019

Schoonen, M. A. A. (2004). Mechanisms of sedimentary pyrite formation, in *ulfur biogeochemistry—past and present*. Editors J. P. Amend, K. J. Edwards, and T. W. Lyons Boulder, Colorado: Geological Society of America Special Paper 379, 117–134. doi:10.1130/0-8137-2379-5.117

Screaton, E. J., Torres, M. E., Dugan, B., Heeschen, K. U., Mountjoy, J. J., Ayres, C., et al. (2019). Sedimentation controls on methane-hydrate dynamics across glacial/interglacial stages: an example from International Ocean Discovery Program Site U1517, Hikurangi Margin. *Geochem. Geophys. Geosystems* 20, 4906–4921. doi:10.1029/2019GC008603

Shi, M., Wu, H., Roberts, A. P., Zhang, S., Zhao, X., Li, H., et al. (2017). Tectonic, climatic, and diagenetic control of magnetic properties of sediments from Kumano Basin, Nankai margin, southwestern Japan. *Mar. Geology.* 391, 1–12. doi:10.1016/j.margeo.2017.07.006

Smirnov, A. V. (2009). Grain size dependence of low-temperature remanent magnetization in natural and synthetic magnetite: experimental study. *Earth Planets Space* 61, 119–124. doi:10.1186/BF03352891

Snowball, I. F. (1997). Gyroremanent magnetization and the magnetic properties of greigite-bearing clays in southern Sweden. *Geophys. J. Int.* 129, 624–636. doi:10.1111/j.1365-246X.1997.tb04498.x

Snowball, I. F. (1991). Magnetic hysteresis properties of greigite (Fe_3S_4) and a new occurrence in Holocene sediments from Swedish Lappland. *Phys. the Earth and Planet. Interiors*, 68 (1–2), 32–40. doi:10.1016/0031-9201(91)90004-2

Wallace, L. M., Beavan, J., McCaffrey, R., and Darby, D. (2004). Subduction zone coupling and tectonic block rotations in the North Island, New Zealand. *J. Geophys. Res. Solid Earth*, 109 (12), 3241. doi:10.1029/2004JB003241

Wallace, L. M., Saffer, D. M., Barnes, P. M., Pecher, I. A., Petronotis, K. E., LeVay, L. J., and the Expedition 372/375 Scientists. (2019). Hikurangi subduction margin coring, logging, and observatories. Proceedings of the International Ocean Discovery Program, College Station, TX, (International Ocean Discovery Program). 372B/375. doi:10.14379/iodp.proc.372B375.2019

Watson, J. H. P., Cressey, B. A., Roberts, A. P., Ellwood, D. C., Charnock, J. M., and Soper, A. K. (2000). Structural and magnetic studies on heavy-metal-adsorbing iron sulphide nanoparticles produced by sulphate-reducing bacteria. *J. Magnetism and Magn. Mater.* 214, 13–30. doi:10.1016/S0304-8853(00)00025-1

You, K., Flemings, P. B., Malinverno, A., Collett, T. S., and Darnell, K. (2019). Mechanisms of methane hydrate formation in geological systems. *Rev. Geophys.*, 57, 1146–1196. doi:10.1029/2018RG000638

Conflict of Interest: The authors declare that the research was conducted in the absence of any commercial or financial relationships that could be construed as a potential conflict of interest.

frontiers in Earth Science

ORIGINAL RESEARCH
published: 15 April 2021
doi: 10.3389/feart.2021.593332

Magnetic Properties of a Holocene Sediment Core from the Yeongsan Estuary, Southwest Korea: Implications for Diagenetic Effects and Availability as Paleoenvironmental Proxies

Hyeon–Seon Ahn[1]*, *Jaesoo Lim*[2]* and *Sung Won Kim*[2]

[1]Center for Advanced Marine Core Research (CMCR), Kochi University, Kochi, Japan, [2]Geology Division, Korea Institute of Geoscience and Mineral Resources (KIGAM), Daejeon, Republic of Korea

OPEN ACCESS

Edited by:
Sarah P Slotznick,
Dartmouth College, United States

Reviewed by:
Robert George Hatfield,
University of Florida, United States
Qingsong Liu,
Chinese Academy of Sciences (CAS), China

***Correspondence:**
Hyeon-Seon Ahn
mitsuki_ahs@hotmail.com
Jaesoo Lim
limjs@kigam.re.kr

Specialty section:
This article was submitted to Geomagnetism and Paleomagnetism, a section of the journal Frontiers in Earth Science

Received: 10 August 2020
Accepted: 01 February 2021
Published: 15 April 2021

Citation:
Ahn H–S, Lim J and Kim SW (2021) Magnetic Properties of a Holocene Sediment Core from the Yeongsan Estuary, Southwest Korea: Implications for Diagenetic Effects and Availability as Paleoenvironmental Proxies. Front. Earth Sci. 9:593332. doi: 10.3389/feart.2021.593332

The sensitivity of magnetic properties, which characterize the mineralogy, concentration, and grain size distribution of magnetic minerals, to environmental processes may provide useful information on paleoenvironmental changes in estuarine environments. Magnetic property studies of estuaries are less common than other environments and, due to the west coast of South Korea having an abundance of estuaries, it provides a good place to study these processes. In this study, we analyzed a variety of magnetic properties based on magnetic susceptibility, hysteresis parameters, progressive acquisition of isothermal remanent magnetization and first-order reversal curve data from a Holocene muddy sediment core recovered from the Yeongsan Estuary on the west coast of South Korea. We examined diagenetic effects on magnetic properties and tested their availability as proxies of paleoenvironmental change. The presence of generally low magnetic susceptibility, ubiquitous greigite-like authigenic magnetic component, and very fine magnetic particle occurrence suggested that the analyzed sediments had undergone considerable early diagenetic alteration. Electron microscopic observations of magnetic minerals support this suggestion. Our results confirm that the use of initial bulk susceptibility as a stand-alone environmental change proxy is not recommended unless it is supported by additional magnetic analyses. We recognized the existence of ferromagnetic-based variabilities related to something besides the adverse diagenetic effects, and have examined possible relationships with sea-level and major climate changes during the Holocene. The most remarkable finding of this study is the two distinct intervals with high values in magnetic coercivity (B_c), coercivity of remanence (B_{cr}), and ratio of remanent saturation moment to saturation moment (M_{rs}/M_s) that were well coincident with the respective abrupt decelerations in the rate of sea-level rise occurred at around 8.2 and 7 thousand years ago. It is then inferred that such condition with abrupt drop in sea-level rise rate would be favorable for the abrupt modification of grain size distribution toward more single-domain-like content. We modestly propose consideration of the B_c, B_{cr}, and M_{rs}/M_s variability as a potential indicator for the initiation/occurrence of

sea-level stillstand/slowstand or highstand during the Holocence, at least at estuarine environments in and around the studied area.

Keywords: diagenesis, Holocene sediments, magnetic properties, rate of sea-level rise, stillstand/slowstand, Yeongsan estuary

INTRODUCTION

Magnetic minerals are common constituents of a wide range of sediments and are sensitive to the physicochemical conditions of their surrounding environment (Thompson and Oldfield, 1986; Verosub and Roberts, 1995; Dekkers, 1997; Maher and Thompson, 1999; Evans and Heller, 2003; Torii, 2005; Liu et al., 2012). Magnetic measurements facilitate characterization of the mineralogy, concentration, and grain size distribution of magnetic minerals contained in sediments, providing information about sediment provenance, transportation, and deposition, as well as post-depositional diagenesis and input of urban and industrial sources into sediments (Karlin and Levi, 1983; Bloemendal et al., 1992; Robinson et al., 2000; Emiroğlu et al., 2004; Rey et al., 2005; Kim et al., 2009; Liu et al., 2010; Szuszkiewicz et al., 2015; Tauxe et al., 2015; Pan et al., 2017).

It is generally thought that sedimentation during Holocene at estuaries and coastal lines are sensitive to not only their catchment (terrestrial) environmental changes and extreme hydrologic events such as heavy rainfalls and storms, which are closely associated with regional and global climate changes, but also regional sea-level change (e.g., Lim et al., 2017, Lim et al., 2019). Hence, such estuarine–coastal sediments are of potential use for reconstructing records of paleoenvironmental changes during Holocene. Along the west coast of South Korea, facing the eastern Yellow Sea, estuaries of large rivers such as the Han, Geum, and Yeongsan Rivers are widely distributed from north to south; these are tide-dominated depositional environments (Chough et al., 2004) forming a variety of deposits during the Late Pleistocene and Holocene (Park et al., 1998; Choi et al., 2003; Lim and Park, 2003; Nahm et al., 2008; Nahm and Hong, 2014; Moon et al., 2018). During the Holocene, these western coastal areas would have experienced dramatic environmental changes due to e.g., sea-level changes such as the Holocene transgression (Stanley and Warne, 1994; Kim and Kennett, 1998), the El Niño Southern Oscillation (ENSO) activity (e.g., Lim et al., 2017; Lu et al., 2018; Lim et al., 2019), the eastern Asian Monsoon (EAM; e.g., Chang, 2004; Dykoski et al., 2005; Selvaraj et al., 2007), and the Holocene climate optimum (HCO; e.g., An et al., 2000; Zhou et al., 2016; Park et al., 2019).

Bulk low-field magnetic susceptibility has been widely applied to interpret such sediment environments in South Korea (Park et al., 1998; Moon et al., 2018; Lim et al., 2004; Lim et al., 2014; Lim et al., 2015), yet comprehensive studies using other magnetic properties have been rare. Further studies are needed to comprehensively explore magnetic minerals in terms of their supply into the accommodation space, dissolution or alteration or generation by early diagenesis, abundance, and response to environmental changes. Additionally, characterization of such magnetic properties among fine materials (muds) in the estuaries of the western Korean Peninsula may provide fundamental information on the provenance and hydrodynamic transport of mud deposits in the Yellow Sea and East China Sea, which remain poorly constrained (Yang et al., 2003; Liu et al., 2010; Wang et al., 2010; Koo et al., 2018).

The objective of this study was to characterize variations in magnetic properties from a sediment core retrieved from an estuarine system in the Yeongsan Estuary on the west coast of South Korea and to identify diagenetic effects that can cause down-core variation of magnetic properties. We then tested the availability of such magnetic properties as proxies of paleoenvironmental changes during the Holocene.

STUDY AREA, MATERIALS, AND RADIOCARBON AGES

The Yeongsan Estuary is located within the city of Mokpo (population, ~250,000) on the southwestern coast of South Korea; from land to sea, it is divided into Yeongsan Lake (fresh water lake), the inner and outer estuaries, and the coastal zone (**Figure 1**; Williams et al., 2014). The estuary is under a macrotidal regime, with primarily semidiurnal tides of about 4.5 m tidal range (Byun et al., 2004). Across the estuary, the Yeongsan River (total length, 115 km; drainage basin area, 3,371 km^2) flows into the Yellow Sea through the relatively shallow (mostly <50 m water depth) ria coastline. The average depth and width of the Yeongsan River ranges from ~10 to 19 m and from 0.6 to 1.3 km, respectively, in its lower reaches (Lee et al., 2009; Williams et al., 2014). The climate of the Korean Peninsula, including the study area, is dominated by seasonal monsoons: during winter, cold and dry north-northwesterly winds are accompanied by less precipitation; during summer, warmer and wetter south-southeasterly winds are accompanied by heavy precipitation and occasional typhoons (e.g., Chang, 2004). Due to the seasonality in precipitation, freshwater discharge of the Yeongsan River occurs mainly during summer (>80% of the annual mean; Ryu et al., 2004). The geology in and around the Yeongsan River basin is composed mainly of Precambrian gneiss, Paleozoic sedimentary rocks such as shale and mudstone, and Mesozoic granites, volcanic extrusive rocks, and tuffs (Choi et al., 2002).

The Yeongsan Estuary has experienced substantial coastal construction within the last 100 years, a dam construction (the Yeongsan Estuarine Dam, drawing boundary between the Inner Estuary and the Yeongsan Lake at present) by 1981, and land reclamation projects during the 1980s, which led to reduction of the estuarine area (e.g., Williams et al., 2014). Prior to the dam construction, tidally influenced environments spanned about 63 km upstream from the dam (Lee et al., 2009). During the

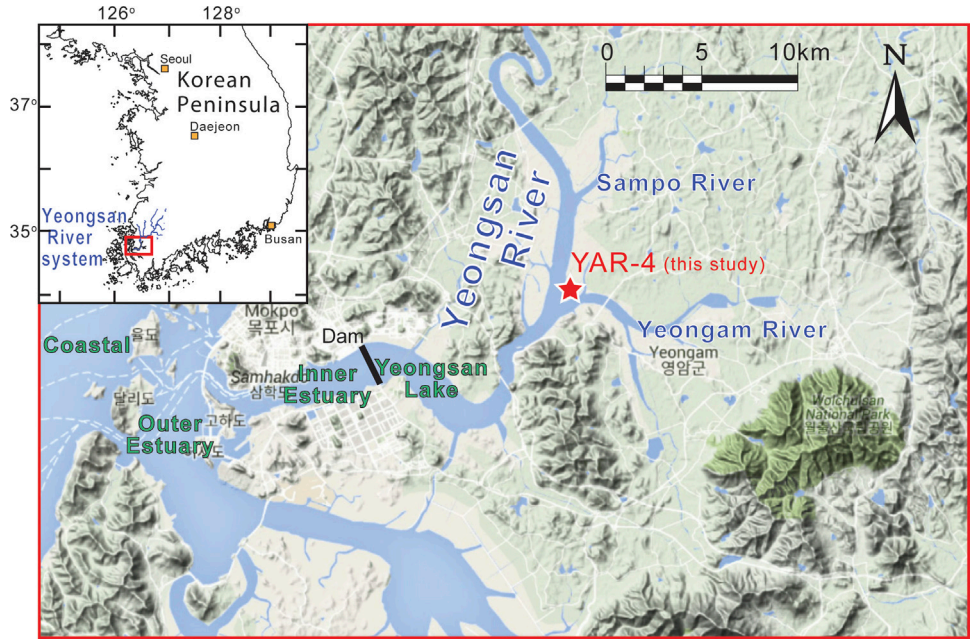

FIGURE 1 | Topographic map of the Yeongsan Estuary showing the location of the YAR-4 core site (red star). Inset: location of the Yeongsan River system (blue lines). Maps were obtained from Google Maps. The location of the Yeongsan Estuarine dam is also shown by black bar.

land reclamation projects, seawalls/embankments were constructed within the area.

YAR-4 (34.82167 °N, 126.55357 °E; 0.5 m below mean sea level at the top) is a 20-m-long sediment core (inner diameter, ~74 mm) that was recovered adjacent to the junction of the Yeongam River (also called the Yeongam tributary) and the main channel of the Yeongsan River (**Figure 1**). Prior to the dam construction the core site would have been below mean sea level and the dam construction actually exposed the core location. The YAR-4 core site has had no tidal influence since the dam construction. The average accumulation rate of sediments around the site is presently estimated at ~20 mm/yr (Williams et al., 2014). Weathered granite (basement rock) is apparent at the bottom 0.20 m of this core; from a core depth of 19.80 m to the top, various facies of sediments are visible (**Figure 2**). The sediment descriptions, interpretation of the sedimentary environments, and accelerator–mass spectrometer (AMS) radiocarbon (^{14}C) age data for this core have been previously documented (Nakanishi et al., 2013), and are briefly described as follows.

Nakanishi et al. (2013) divided the YAR-4 core sediment stratigraphy into six different sedimentary facies units (I, II, III, IV, V, and VI, in **Figure 2**) based on their analyses, including grain size, color, sedimentary features, and AMS ^{14}C age data. Units II and III are further subdivided into two subfacies units each, as IIa, IIb, IIIa, and IIIb. **Figure 2** presents a summary of the core's sedimentary characteristics and the interpretation of associated sedimentary environments. Nakanishi et al. (2013) also estimated a number of AMS ^{14}C ages (i.e., only conventional age estimates, without ^{14}C calibration) from materials of terrestrial (plants) and marine (shells) origins to evaluate the marine reservoir effects on the sediments. Their results revealed that the shell ^{14}C ages were older by 0–500 years (i.e., the marine reservoir effects) than the plant ^{14}C ages.

In the present study, we selected part of the plant ^{14}C age data from the published age dataset to represent appropriate sediment ages (**Table 1**; **Figure 3**) to build up an age–depth relationship for this core and to estimate the sedimentation rates. These ages ranged from 8,130 (±70, 1σ) to 3,760 (±50, 1σ) yr BP in conventional age for units II to V, being converted into calibrated ages from 9,088 (±310, 2σ) to 4,114 (±179, 2σ) cal. yr BP by using the OxCal (version 4.4) calibration program (https://c14.arch.ox.ac.uk/oxcal.html) with the IntCal20 (Reimer et al., 2020). Unit I had no ^{14}C age determination due to the absence of samples suitable for ^{14}C dating. Based on these selected data points, we constructed an age-depth model (**Figure 3**) by using the software "Undatable" (Lougheed and Obrochta, 2019), which ran 100,000 Monte Carlo iterations with setting parameters of xfactor = 0.1 and bootpc = 10 in treating uncertainty (for details about the xfactor, the bootpc, and the modeling, see Lougheed and Obrochta, 2019). This YAR-4 age–depth model indicated several drastic changes in the sedimentation rate, which ranged apparently between 0.4 and >25 mm/yr.

METHODS

All of the following subsample preparations and procedures for analyses of sediment particle size, total organic carbon (TOC), and a suite of magnetic properties were conducted at the laboratories of the Korea Institute of Geoscience and Mineral Resources (KIGAM, Republic of Korea). Only microscopic

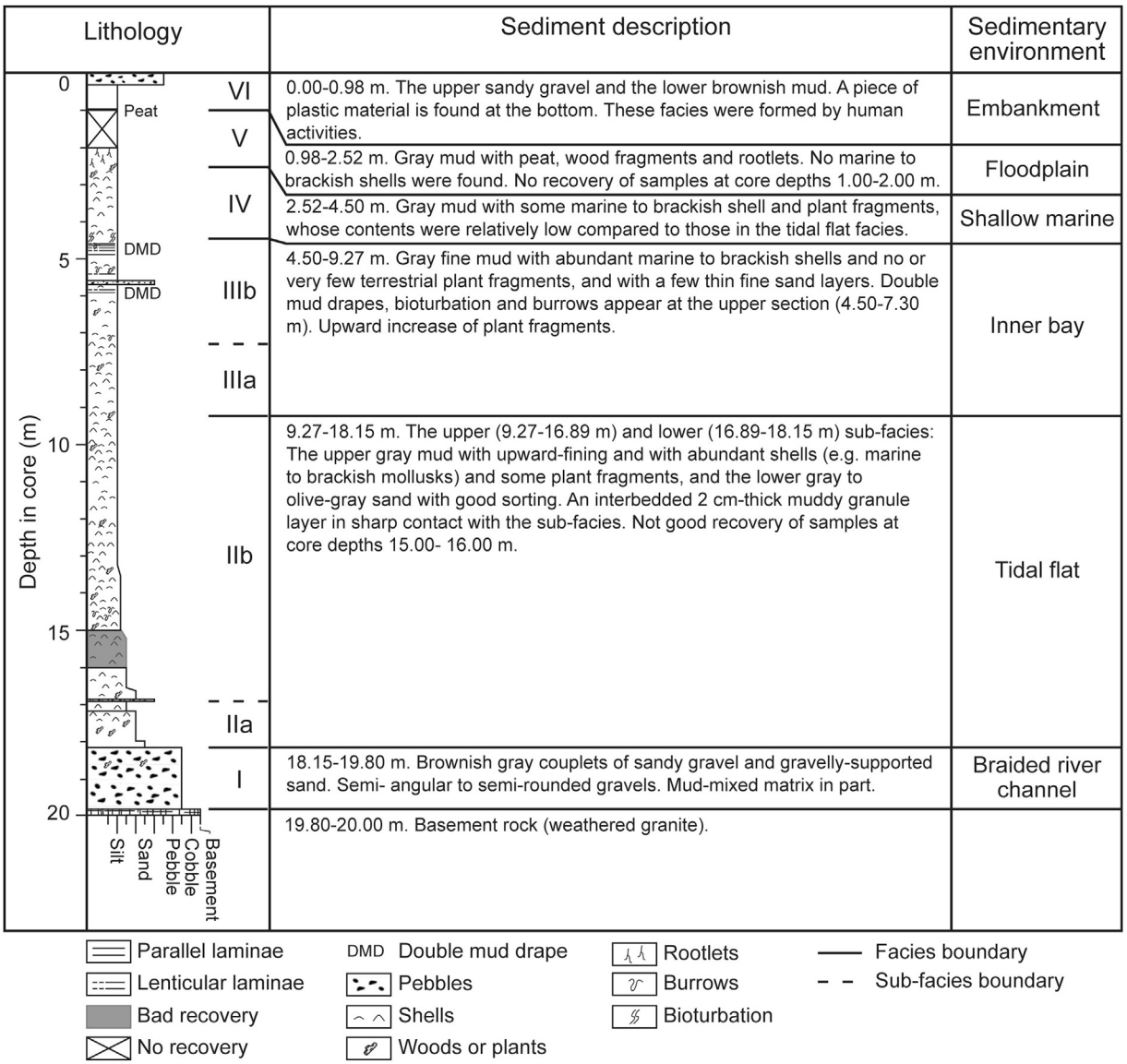

FIGURE 2 | Summary of sedimentary characteristics of the YAR04 core documented by Nakanishi et al. (2013), showing columnar lithology, sediment descriptions and inferred sedimentary environments.

observations were conducted at the Central Research Facilities of Gyeongsang National University (Republic of Korea).

For the split half-core, subsamples for analyses were collected using cylindrical plastic tubes generally at ~0.04-m intervals and a subsampling thickness of ~0.02 m from the core depth interval of 3.20–20.00 m. The subsamples were oven-dried at 40 °C for approximately 24 h prior to analyses.

Particle Size and Total Organic Carbon Measurements

The particle size distribution of bulk sediment was analyzed at ~0.5-m intervals using a Mastersizer 2000 laser analyzer (Malvern Instrument Ltd., United Kingdom) using approximately 300 mg of each dried subsample, after treatment with 35% H_2O_2 and 1 N HCl to dissolve organic matter and biogenic carbonates, respectively, and then with ultrasonic dispersion to facilitate complete disaggregation.

To measure the TOC content of bulk sediment, each subsample was treated with 1 N HCl at approximately 100°C for 1 h and then transferred to a tin combustion cup after rinsing with distilled water. The TOC content was analyzed at ~0.2-m intervals using a CNS elemental analyzer (vario Micro cube; Elementar, Germany).

Measurements of Magnetic Properties

Magnetic properties were measured using three types of dried subsamples: bulk sediment sealed in a non-magnetic plastic box

TABLE 1 | Accelerator mass spectrometry (AMS) ^{14}C age data for materials of terrestrial origin (plant fragments) of the YAR-4 core, selected from the dataset of Nakanishi et al. (2013). Age* denotes a conventional age estimate before ^{14}C calibration reported in Nakanishi et al. (2013). Age (±2σ) in cal. yr BP denotes the calibrated age estimate using the OxCal (version 4.4; https://c14.arch.ox.ac.uk/oxcal.html) and the IntCal20 (Reimer et al., 2020) by this study.

Depth in core (m)	Elevation (m)	Age* ±1σ (yr BP)	Age ±2σ (cal. yr BP)	Lab. code
2.510	−3.010	3760 ± 50	4114 ± 179	Twd110230
2.740	−3.240	4130 ± 50	4677 ± 153	Twd110281
4.275	−4.775	4460 ± 50	5091 ± 206	Twd110170
6.300	−6.800	4690 ± 60	5447 ± 134	Twd110172-1
7.270	−7.770	5510 ± 60	6318 ± 122	Twd110266
9.270	−9.770	6570 ± 60	7456 ± 120	Twd110174-1
11.525	−12.025	7170 ± 62	8016 ± 155	Twd110176-1
13.480	−13.980	7380 ± 60	8185 ± 151	Twd110178-1
14.890	−15.390	7400 ± 60	8193 ± 157	Twd110239
16.300	−16.800	7370 ± 60	8181 ± 150	Twd110240
16.600	−17.100	7350 ± 60	8175 ± 152	Twd110180
16.835	−17.335	7520 ± 60	8302 ± 109	Twd110241
17.305	−17.805	7600 ± 60	8381 ± 163	Twd110182-1
18.150	−18.650	8130 ± 70	9088 ± 310	Twd110267

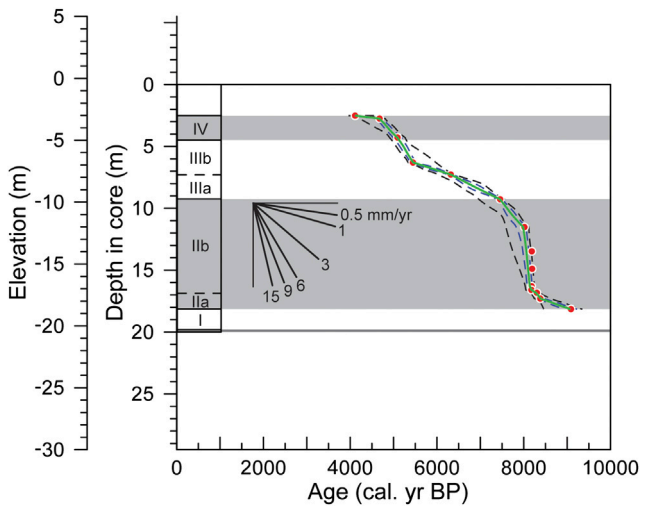

FIGURE 3 | Plot of the calibrated ^{14}C age data that are used for this study (also given in **Table 1**) with depth in core and elevation, and an age–depth model reconstructed by using the "Undatable" (Lougheed and Obrochta, 2019), with xfactor = 0.1, bootpc = 10, and 10^5 Monte Carlo iteration runs (see **Supplementary Table S6**). Each age data point is given by red-filled circle. The age-depth model median is denoted by green line. The 1σ and 2σ uncertainties of the age-depth model are denoted by dashed blues and black lines, respectively. The sedimentary unit divisions (I to VI) are supplementarily shown near the *y*-axis.

(volume, 7 cm^3), several tens of mg of bulk sediment sealed in a gelatin capsule and capped with glass wool, and several tens of mg of magnetic mineral extracts sealed in a gelatin capsule and capped with glass wool. Each extraction of magnetic minerals was obtained using a hand magnet. The numbers of each type of the subsample prepared were 153, 41, and 31, respectively. The "packed-in-plastic box" bulk subsamples were used in measurements with a MS2B magnetic susceptibility meter (Bartington Instruments Ltd., United Kingdom). Both of the bulk and extracts "packed-in-gelatin capsule" subsamples were used in measurements with a MicroMag Model 3,900 vibrating sample magnetometer (VSM; Princeton Measurements Corp., United States). By using the MS2B magnetic susceptibility meter, volume-specific magnetic susceptibilities with low-frequency (0.47 kHz) and high-frequency (4.7 kHz) (k_{LFQ} and k_{HFQ}, respectively) were obtained. By using the VSM, magnetic hysteresis loop measurement, progressive alternating field (AF) demagnetization of isothermal remanent magnetization (IRM), progressive IRM acquisition, and first-order reversal curves (FORCs) measurement were conducted. The MS2B measurements were applied on subsamples at about 0.04–0.10-m intervals, and the VSM measurements were applied on subsamples that were from a limited number of different horizons of the sediment core.

The k_{LFQ} and k_{HFQ} of subsample were established by the average of double measurements with the correction for diamagnetic contribution of the plastic box to magnetic susceptibility, which was made by subtracting the average value of measurements of five empty boxes. These allowed us to calculate frequency-dependent susceptibility (k_{FD} in %) using the following formula: $k_{FD} = (k_{LFQ} - k_{HFQ})/k_{LFQ} \times 100$.

Prior to the VSM measurements, the "packed-in-gelatin capsule" subsamples to be measured were weighed to permit calculation of mass-specific values. Each hysteresis loop was measured up to maximum fields of ±0.5 T, and then, after correction for paramagnetic contribution within the loop, saturation magnetization (M_s), saturation remanence (M_{rs}), and magnetic coercivity (B_c) were calculated. From each hysteresis loop, low-field magnetic susceptibility (χ_{lf}; total magnetic susceptibility) was calculated from the initial slope and high-field magnetic susceptibility (χ_{hf}), as a susceptibility estimate of paramagnetic (plus diamagnetic) minerals, was calculated from the high-field slope of the hysteresis loop. Note that for magnetic susceptibilities, *k* denotes volume-specific

TABLE 2 | Summary statistics of mean grain size (MZ), total organic carbon (TOC) content, and various bulk magnetic properties from the YAR04 core sediments (the Yeongsan Estuary). Note that calculations of k_{FD} statistics were made using only the k_{FD} values of no less than zero, for convenience with a consideration of the exclusion of unrealistic values presumably due to measurement errors.

Depth in core	Unit I	Unit IIa	Unit IIb	Unit IIb*	Unit IIIa	Unit IIIb	Unit IV
	18.15–19.80 m	16.89–18.15 m	9.27–16.89 m	9.27–14.00 m	7.30–9.27 m	4.50–7.30 m	2.52–4.50 m
MZ (μm)							
Min	15.4	21.2	8.9	8.9	8.7	9.5	10.0
Max	104.2	44.7	26.7	12.2	10.1	10.4	10.3
Mean	59.8	33.0	13.7	10.6	9.5	10.1	10.1
SD	–	–	5.6	1.0	0.6	0.4	0.2
n	2	2	14	8	4	6	3
TOC (%)							
Min	0.1	0.4	0.4	0.5	0.6	0.7	0.6
Max	0.7	0.7	1.3	1.3	0.8	0.9	0.8
Mean	0.4	0.5	0.6	0.7	0.7	0.7	0.7
SD	0.3	0.1	0.1	0.1	0.1	0.1	0.1
n	8	6	36	22	9	14	7
k_{LFQ} (μ SI)							
Min	172.5	80.5	18.5	18.5	24.5	42.5	75.0
Max	857.0	352.0	446.0	166.0	188.5	206.0	245.0
Mean	358.1	166.1	123.2	93.6	117.3	126.2	138.3
SD	165.5	79.0	70.2	42.3	45.8	36.3	37.7
n	14	13	60	34	18	27	20
IRM_{1T} (μ Am^2/kg)							
Min	227.9	23.3	–	–	22.3	391.1	565.5
Max	549.7	238.5	–	–	551.2	734.8	959.3
Mean	388.8	140.3	–	–	347.3	562.9	762.4
SD	–	108.8	–	–	284.5	–	–
n	2	3	0	0	3	2	2
χ_{hf}/χ_{lf}							
Min	0.60	0.82	–	–	0.60	0.65	0.64
Max	0.85	0.93	–	–	1.00	0.80	1.00
Mean	0.72	0.89	–	–	0.90	0.70	0.90
SD	–	0.06	–	–	0.19	–	0.20
n	2	3	0	0	4	2	3
k_{FD} (%)							
Min	0.1	0.2	0.0	0.0	0.0	2.1	1.0
Max	5.5	14.4	37.2	37.2	19.0	28.2	18.7
Mean	3.1	3.6	7.7	10.9	5.5	9.2	7.3
SD	1.6	4.0	9.1	10.8	5.8	6.7	6.1
n	14	12	52	28	15	21	19
B_c (mT)							
Min	5.4	6.1	5.9	6.1	5.4	11.2	10.0
Max	7.0	8.7	16.2	8.8	11.7	12.1	21.3
Mean	6.2	7.6	8.1	7.4	8.6	11.6	15.4
SD	–	1.3	2.1	0.8	2.4	0.5	4.6
n	2	3	22	10	5	3	4
B_{cr} (mT)							
Min	36.9	33.4	25.5	25.5	23.8	37.5	25.0
Max	37.0	37.6	47.6	35.3	36.7	44.9	44.0
Mean	37.0	35.2	33.5	31.3	29.0	41.8	36.8
SD	-	2.2	4.5	3.0	5.0	3.8	8.8
n	2	3	22	10	5	3	4
B_{cr}/B_c							
Min	5.2659	3.8587	2.9388	3.6797	2.4351	3.3578	1.1761
Max	6.8226	6.1407	5.4386	5.2003	4.7712	3.7130	3.5075
Mean	6.0442	4.7762	4.2493	4.2404	3.5069	3.5914	2.6052
SD	–	1.2048	0.6445	0.4748	0.8668	0.2024	1.0058
n	2	3	22	10	5	3	4
M_{rs}/M_s							
Min	0.0715	0.0754	0.0602	0.0644	0.0583	0.1536	0.0594
Max	0.0761	0.0924	0.1763	0.0993	0.1848	0.1629	0.2966
Mean	0.0738	0.0867	0.0889	0.0803	0.1263	0.1589	0.1593
SD	–	0.0098	0.0254	0.0124	0.0511	0.0047	0.1038
n	2	3	22	10	5	3	4

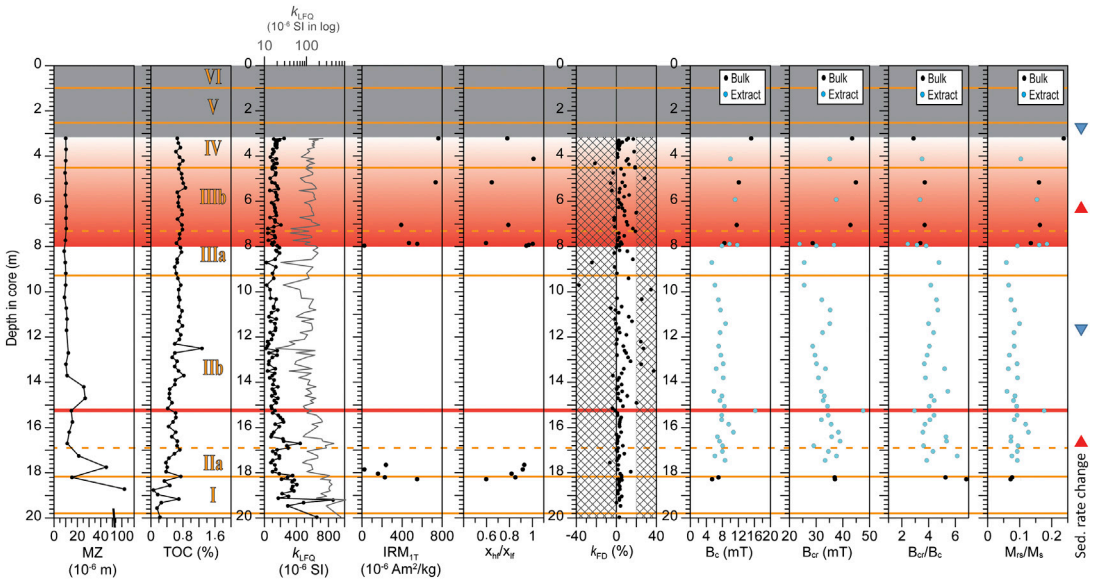

FIGURE 4 | Downcore variations in mean grain size (MZ), total organic carbon (TOC) content and various magnetic properties for bulk sediment samples of the YAR-4 core. The magnetic properties shown include bulk magnetic susceptibility (k_{LFQ}, in both linear and log scale), isothermal remanent magnetization (IRM) intensity imparted at 1 T (IRM$_{1T}$), high-field to low-field magnetic susceptibility ratio (χ_{hf}/χ_{lf}), frequency-dependent magnetic susceptibility (k_{FD}), coercive force (B$_c$), coercivity of remanence (B$_{cr}$), ratio of B$_{cr}$ to B$_c$ (B$_{cr}$/B$_c$), and ratio of saturation remanence to saturation magnetization (M$_{rs}$/M$_s$). In B$_c$, B$_{cr}$, B$_{cr}$/B$_c$, and M$_{rs}$/M$_s$ plots, exceptionally, the respective values for magnetic extracts were also shown (assuming their values for the extracts having no significant differences with those for bulk sediments). In the k_{FD}–depth diagram, the hatched area denotes lack of meaningful k_{FD} values due to weak signals. Sedimentary unit divisions (I to VI) are shown by orange lines. On the right edge of the figure, the depths at which significant change in sedimentation rate appeared based on the age-depth model (**Figure 3**) are shown: red triangle denotes increase in sedimentation rate at above the depth, and blue inverse triangle denotes its decrease at above the depth. Gray-shaded area denotes lack of analyzed data.

susceptibility in SI units (dimensionless), and χ denotes mass-specific susceptibility (m^3/kg in SI units). From each progressive AF demagnetization of IRM, the remanence coercivity (B$_{cr}$) was determined as the applied field at which the remanence becomes zero. Each progressive IRM acquisition was made until 1 T was reached. Among the IRM acquisition data, IRM obtained at 1 T (IRM$_{1T}$; roughly considered as SIRM) was used as a magnetic property in this study. To unmix the magnetic mineral components contributing to the total remanent magnetization, each progressive IRM acquisition dataset was processed using the Max Unmix software (Maxbauer et al., 2016), which obtains the best fit for the total IRM acquisition using the fewest possible components that are characterized by the SIRM, the median field (Bh) at which half of the SIRM is reached, and dispersion (Dp) of its corresponding cumulative lognormal distribution. For each FORC analysis, 232 or 266 FORCs were measured; these FORC data were processed to create a FORC diagram using the FORCinel software (Harrison and Feinberg, 2008) with a smoothing factor of 9 or 10.

Magnetic susceptibility and IRM$_{1T}$ generally reflect the abundance of the total of magnetic mineral types and ferromagnetic mineral types (refer to ferrimagnetic and antiferromagnetic, in this study), respectively. χ_{hf}/χ_{lf} reflects the contribution of paramagnetic components to the total susceptibility. k_{FD} indicates the contribution to total susceptibility made by viscous superparamagnetic (SP; < ~30 nm) grains. B$_c$ and B$_{cr}$ may be used as measures of the relative proportions between low- and high-coercivity ferromagnetic mineral components, with higher values corresponding to higher proportions of high-coercivity minerals. B$_{cr}$/B$_c$, M$_{rs}$/M$_s$ and FORC diagram provide information related to grain size distribution, mainly for ferromagnetic minerals.

Electron Microscope Observations

Electron microscopic observations were conducted selectively on bulk sediment subsamples from four horizons of 7.84, 8.70, 13.40, and 15.25 m depth in core, in order to identify existing magnetic minerals, especially low- and intermediate-coercivity minerals. Polished surfaces of the bulk sediment subsamples were observed using a JSM-7610 F field emission scanning electron microscope (FE-SEM, JEOL, Japan) equipped with an energy-dispersive X-ray spectroscopy (EDS). From the observations, back scattered electron images and EDS spectra of magnetic minerals were obtained.

RESULTS AND DISCUSSION

Particle Size and Total Organic Carbon for Bulk Sediments

Table 2 and **Figure 4** present the results of particle size and TOC analyses of bulk sediment subsamples, and statistics including minimum, maximum, mean and standard deviation values for sedimentary units, and their downcore variation. The mean

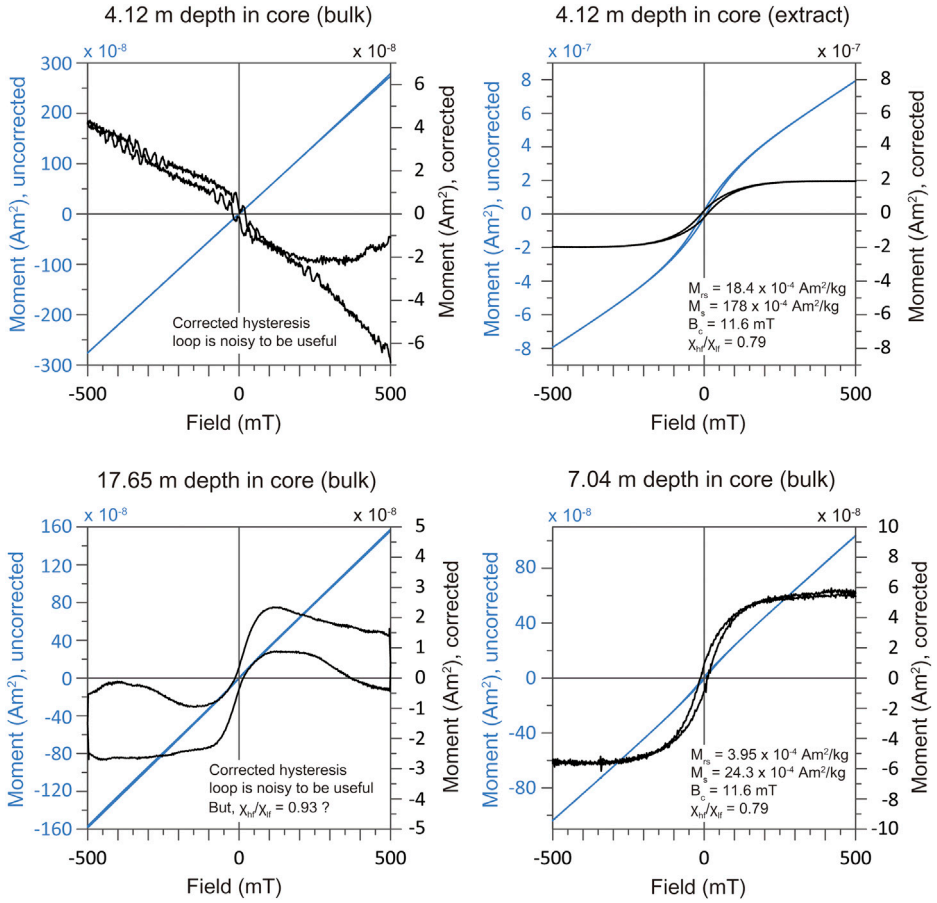

FIGURE 5 | Examples of measured (uncorrected) and high-field slope (i.e., paramagnetic contribution) corrected hysteresis loops. The differences between uncorrected and corrected loops indicate substantial non-ferromagnetic (i.e., paramagnetic) contribution in the studied sediments. Note that, for the extract subsample of 17.65 m depth (in core), the corrected loop seems to be less well-constrained so that the hysteresis parameters (M_{rs}, M_s, and B_c) could not be determinable, but the determined χ_{hf}/χ_{lf} seems meaningful.

particle sizes from depths of 3.2–~14 m was fairly constant at ~10 μm (fine silt); below a depth of 14 m, the mean size tended to increase with depth, with fluctuations reaching 104 μm (very fine sand) at a depth of 18.70 m. The TOC content was mainly very low (<0.9%); its variation was minor to a depth of ~14 m, except at 12.50 m, and appeared to be negatively correlated with the mean size variation throughout the entire sediment core.

Downcore Variation in Magnetic Properties

Table 2 and **Figure 4** summarize the results of major magnetic property analyses. **Table 2** provides summary statistics of the individual magnetic properties including k_{LFQ}, IRM_{1T}, χ_{hf}/χ_{lf}, k_{FD}, B_c, B_{cr}, B_{cr}/B_c and M_{rs}/M_s, for the sedimentary units. Examples of the measured and high-field slope corrected hysteresis loops are illustrated in **Figure 5**. VSM-derived magnetic properties for bulk subsamples were barely detectable due to the weak and quite noisy signals during measurements, such that most of these bulk samples did not produce meaningful values in IRM_{1T}, χ_{hf}/χ_{lf}, B_c, B_{cr}, B_{cr}/B_c and M_{rs}/M_s. Instead, B_c, B_{cr}, B_{cr}/B_c and M_{rs}/M_s were obtained mostly from magnetic extracts of subsamples. We assume that the extract subsamples are representative of the bulk materials for these B_c, B_{cr}, B_{cr}/B_c, and M_{rs}/M_s values. Although there was exactly no horizon where bulk and extract subsamples both were measured for these magnetic property values in this study, it may be supported in part by the fact that, in the interval of 7.90–8.00 m depth in core, their values on bulk and extract subsamples were apparently similar. Downcore variations in these magnetic properties are shown in **Figure 4**.

k_{LFQ}, which was obtained using the MS2B meter and was volume-corrected for its proper quantification, ranged between 18 and 857 × 10^{-6} SI for all analyzed samples, and the means of the respective sedimentary units were from 94 to 358 × 10^{-6} SI. Most of the individual values are much lower than 400 × 10^{-6} SI. Considerably high values with >400 × 10^{-6} SI are limited in the intervals corresponding to the gravel-rich (around 16.9 and 18.15–19.80 m depth) and the basement rock (19.80–20.00 m depth) lithology. In the downcore k_{LFQ} variation, there are a number of significant susceptibility minima representing lowering by at most 65–80% of the overall mean (for example, at depths of approximately 8.70, 9.70, and 12.20–12.50 m). There are some datasets of k values from Holocene sediment cores at

around the studied region, making available for comparison with our data: in the western coastal estuaries of South Korea, ~0.1–0.2 $\times 10^{-6}$ SI (Gyeonggi Bay, Moon et al., 2018), and ~2–12 $\times 10^{-6}$ SI (Namyang Bay, Lim et al., 2004); in the southern coast of South Korea, ~300–650 $\times 10^{-6}$ SI (Geoje Island, Lim et al., 2014), and ~50–400 $\times 10^{-6}$ SI (Yeoja Bay, Lim et al., 2015); in the inner shelf of the southwestern East China Sea, ~200–250 $\times 10^{-6}$ SI (Zheng et al., 2010), and ~100–220 $\times 10^{-6}$ SI (Zheng et al., 2011). The extremely low k values in the Gyeonggi Bay and the Namyang Bay may result from locally particular layers (e.g., organic-rich layer, siderite-rich layer). Besides this, the ranges of k values of the previous studies are comparable to that for the YAR-4 core. However, this comparison should be taken care because it is not straightforward to identify whether or not these previously reported k values were after applying volume corrections (including calibrations of the prepared sample volume and the sensor of instruments used).

Values of mass-specific susceptibility (χ) can be more proper in comparison with previously reported datasets. Unfortunately, our analyzed subsamples were not weighed, thereby not permitting to determine accurately χ values for the same subsamples. Nevertheless, the χ values could be approximated by converting the aforementioned volume-specific susceptibility (k) values, using a mean density of 1.17 g/cm^3 and a mean water content of 71.3 wt% for wet surface sediments in the Yeongsan Lake (An et al., 2019). Assuming the water density of 1.00 g/cm^3 and that the porosity of the studied sediments (silt-dominant, shallow depths) was little varied through the whole core (i.e., negligible porosity variation for shallow depths; e.g., Bahr et al., 2001), a mean value in dry density of the studied sediment samples could be approximated to 2.03 g/cm^3 (considered as a maximal value). Accordingly, the individual k_{LFQ} values could be converted to the mass-specific susceptibility (χ_{LFQ}) values in the range of ~0.9–~42 $\times 10^{-8}$ m^3/kg, and the χ_{LFQ} values were generally in the order of 5–10 $\times 10^{-8}$ m^3/kg. This range of mass magnetic susceptibility values is similar in the order of magnitude of or slightly lower than those of Holocene sediment cores of the Yangtze delta area (e.g., ~10–90 $\times 10^{-8}$ m^3/kg, Chen et al., 2015; ~35–130 $\times 10^{-8}$ m^3/kg, Pan et al., 2017), shallow shelf sediment cores with anoxic environments in the Korea Strait and off the west coast of the Korean Peninsula (~18 $\times 10^{-8}$ m^3/kg, Liu et al., 2004; ~14 $\times 10^{-8}$ m^3/kg, Liu et al., 2005).

Individual IRM_{1T} values for bulk sediments ranged between 22 and 959 $\times 10^{-6}$ Am^2/kg. These values are significantly lower than those observed in estuarine and shallow shelf sediments of the Korea Strait, the western Yellow Sea and the East China Sea, e.g., ~200–4,500 $\times 10^{-6}$ Am^2/kg (Liu et al., 2004); ~150–30,000 $\times 10^{-6}$ Am^2/kg (Chen et al., 2015); ~2,400–6,100 $\times 10^{-6}$ Am^2/kg (Pan et al., 2017). The individual IRM_{1T} values exhibited an apparent decreasing trend with depth to ~8 m, and we observed roughly similar values in the two intervals at depths of 7–8 and 17.5–18.5 m.

χ_{hf}/χ_{lf} values ranged between ~0.6 and 1.0, indicating significantly larger paramagnetic contributions than ferromagnetic contributions (see also **Figure 5**), presumably in most of the sampled sediments.

The k_{FD} values, with exception of negative values, ranged between 0.0 and 37.2%, of which values >20% may not be reliable due to weak susceptibility signals. The mean values for respective sedimentary units were approximately between 3 and 10%, indicative of, in general, somewhat or considerable SP contributions in the sediments. Due to concern from the mixing with untrustworthy data, we did not used the k_{FD} data in discussing on its detailed variability in association with the diagenetic, sea-level, and climate effects.

Individual B_c, B_{cr}, B_{cr}/B_c, and M_{rs}/M_s values ranged between 5 and 21 mT, between 24 and 45 mT, between 2.44 and 5.20, and between 0.06 and 0.30, respectively. Downcore variation in B_c and M_{rs}/M_s created an apparent division into two zones at a depth of ~8 m, with relatively constant low values in the lower zone and constant higher values in the upper zone. Interestingly, downcore variation in B_c, B_{cr}, and M_{rs}/M_s shared a distinct, drastic increase in the respective parameter at depths of 15.25 m and 7.84–7.96 m. At depths above 7.84 m, such high values were sustained after this abrupt increase, whereas low values appeared the same as the surrounding data points at depths immediately above and below 15.25 m (i.e., 15.05 and 15.45 m).

Figure 6 presents plots of k_{LFQ} vs. the other magnetic properties examined in this study, to assess possible relationships with k_{LFQ}. Generally, we observed no or very week correlation with k_{LFQ}, but B_{cr} had a moderate positive correlation with k_{LFQ}. This implies complexity of mineral magnetic factors controlling k_{LFQ} (e.g., content of paramagnetic minerals, content, composition ratio, and grain size of ferromagnetic minerals).

Magnetic Mineralogy and Granulometry from Magnetic Measurements and Scanning Electron Microscope Observations

SEM observations provided back scattered electron images and EDS spectra of magnetic minerals in the sediments (**Figures 7** and **Supplementary Figure S1**). From the observations, pyrite (FeS_2), greigite (Fe_3S_4), and (titano)magnetite are identified. It is found that pyrite is ubiquitous and has the most dominance in magnetic minerals in all analyzed bulk sediment samples (i.e., 7.84, 8.70, 13.40, and 15.25 m depth in core; **Figures 7A** and **Supplementary Figure S1**). The pyrite exists as framboidal aggregates and separated euhedral crystals with variable sizes in the sediment matrix, in the vicinity of silicates, and in the voids of the matrix (**Figures 7A,C**, and **Supplementary Figure S1**). The pyrite grains forming the framboids are much smaller (roughly <0.3 μm in maximal length) than the separated euhedral ones (roughly 0.5–<10 μm in maximal length). These pyrite grains all are considered to be of post-depositional authigenic origin. The (titano)magnetite grains occur in the matrix, their shape is angular, and their size is between several microns and more than 10 microns (**Figure 7B**). Such characteristics of the (titano) magnetite grains allows us to interpret it as detrital origin. The occurrence of (titano)magnetite grains is much less frequent than the pyrite grains. No sub-micron to nano-size (titano)magnetite grains are found. The greigite occurs in the shape of framboids or

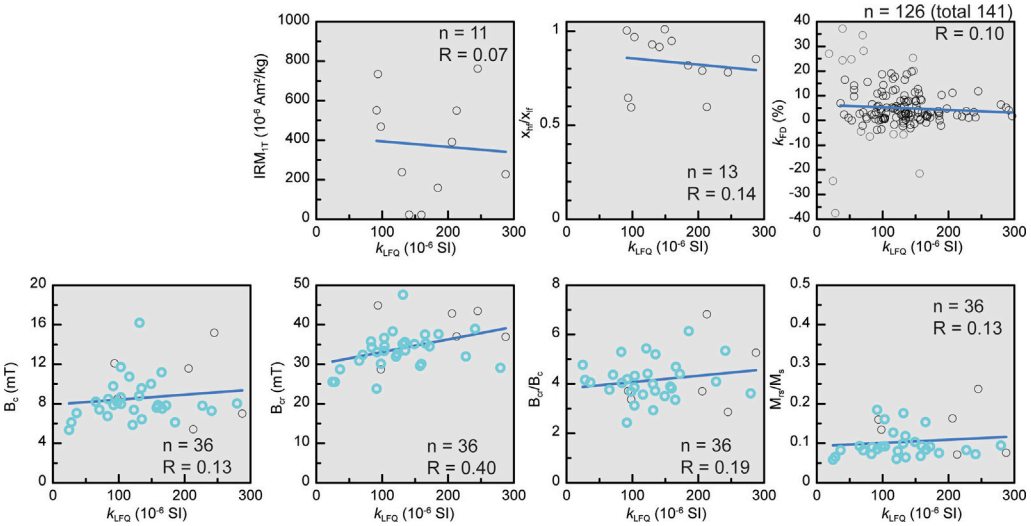

FIGURE 6 | Biplots of k_{LFQ} vs. each of several other magnetic properties (IRM_{1T}, χ_{hf}/χ_{lf}, k_{FD}, B_c, B_{cr}, B_{cr}/B_c and M_{rs}/M_s). k_{LFQ} all were from bulk sediment samples. For the respective biplots, a fit line and its corresponding correlation coefficient (R) is provided. Black (Cyan) circles denote the data where the magnetic property values were obtained from the bulk (extract) samples. For the k_{LFQ} vs. k_{FD} plot, the data that were in out of the range between −5 and 20 in k_{FD} (gray circles), being regarded less reliable, were excluded when consdiering the correlation degree between k_{LFQ} and k_{FD}.

irregular aggregates within and around aggregates of pyrite crystals, and their size is much smaller (nano-scale; presumably in the SP to stable SD size range) than the pyrite grains (**Figures 7C,D**). The gregite grains are interpreted as being of post-depositional origin.

As described in *Downcore Variation in Magnetic Properties* Section, paramagnetic minerals, rather than ferromagnetic minerals, appear to control the bulk magnetic properties (such as bulk magnetic susceptibility) of the studied sediments. Candidates for these major paramagnetic minerals are common iron-bearing clay minerals with detrital origin, pyrite, iron monosulfide (mackinawite, FeS), and siderite ($FeCO_3$) of diagenetic (authigenic) origin in estuarine sediments. The gray or olive-gray colors of most of the studied sediments may be associated with abundant pyrite, which is consistent with the SEM observations. Several studies of other Holocene tidal flat sediments on the west coast of South Korea have reported authigenic siderites that were formed by early diagenesis during the Holocene through interactions with freshwater (Khim et al., 2000; Choi et al., 2003; Lim et al., 2004). Lim et al. (2004) also documented the siderite-abundant sediment interval (the unit T1 in their study) that was characterized by reddish- or yellow-brown (10 YR 5/4) massive mud and 10–12 × 10^{-6} SI in bulk magnetic susceptibility.

Meanwhile, ferromagnetic minerals in the studied sediments also contribute to magnetic property variation, and leave meaningful signals. The IRM component unmixing analyses revealed occurrence of magnetic mineral components with different coercivity spectra from the total IRM. **Figure 8** presents the results of unmixed magnetic mineral components and their relative contributions in IRM unmixing analyses from selective stratigraphic levels in different sedimentary units (13 subsamples). These results indicate the presence of at least three components (in the upper part of the core, four) throughout the entire analyzed sediments: component 1, with low Bh (23–31 mT); component 2, with intermediate Bh (mainly 50–71 mT); component 3, with high Bh (129–399 mT); and occasionally component 4, with high Bh (>1,000 mT). The components 1, 3, and 4 were interpreted as pseudo-single-domain (PSD) and/or multi-domain (MD) magnetite (Fe_3O_4; ferrimagnetic), probably of detrital origin; hematite (α-Fe_2O_3; antiferromagnetic); and goethite (α-FeOOH; antiferromagnetic), respectively (e.g., Maxbauer et al., 2016). Note that the components 3 and 4 having high-coercivity spectra were not recognized in the SEM observations of this study. The component 2 possibly imply greigite (Fe_3S_4; ferrimagnetic) due to the similar remanence coercivity values for greigite-bearing sediments (mainly 60–95 mT, but 37–98 mT for a wider range; Roberts, 1995; Snowball, 1997; Peters and Dekkers, 2003). This can be supported by the occurrence of ultra-fine greigite grains in SEM observation. We find that the relative contributions of these components differ at different depths, but generally the contribution of the components 1 and 2 dominates throughout the sediments.

Peters and Thompson (1998) discriminated between different magnetic minerals by constraining the typical ranges for the respective minerals in a biplot of IRM_{1T}/χ_{lf} vs. B_{cr}. As shown in **Figure 9**, part of our YAR-4 data (n = 11) did not fall into the range of (titano-)magnetite or greigite, but instead were superimposed partly on the range of the A5 sediments of New Jersey Miocene clays reported in Nilsson et al. (2013) who interpreted them as mixtures of (titano-)magnetite and greigite. It might be also possible that the plotted range of our data was influenced partly by the presence of hematite (and occasionally goethite).

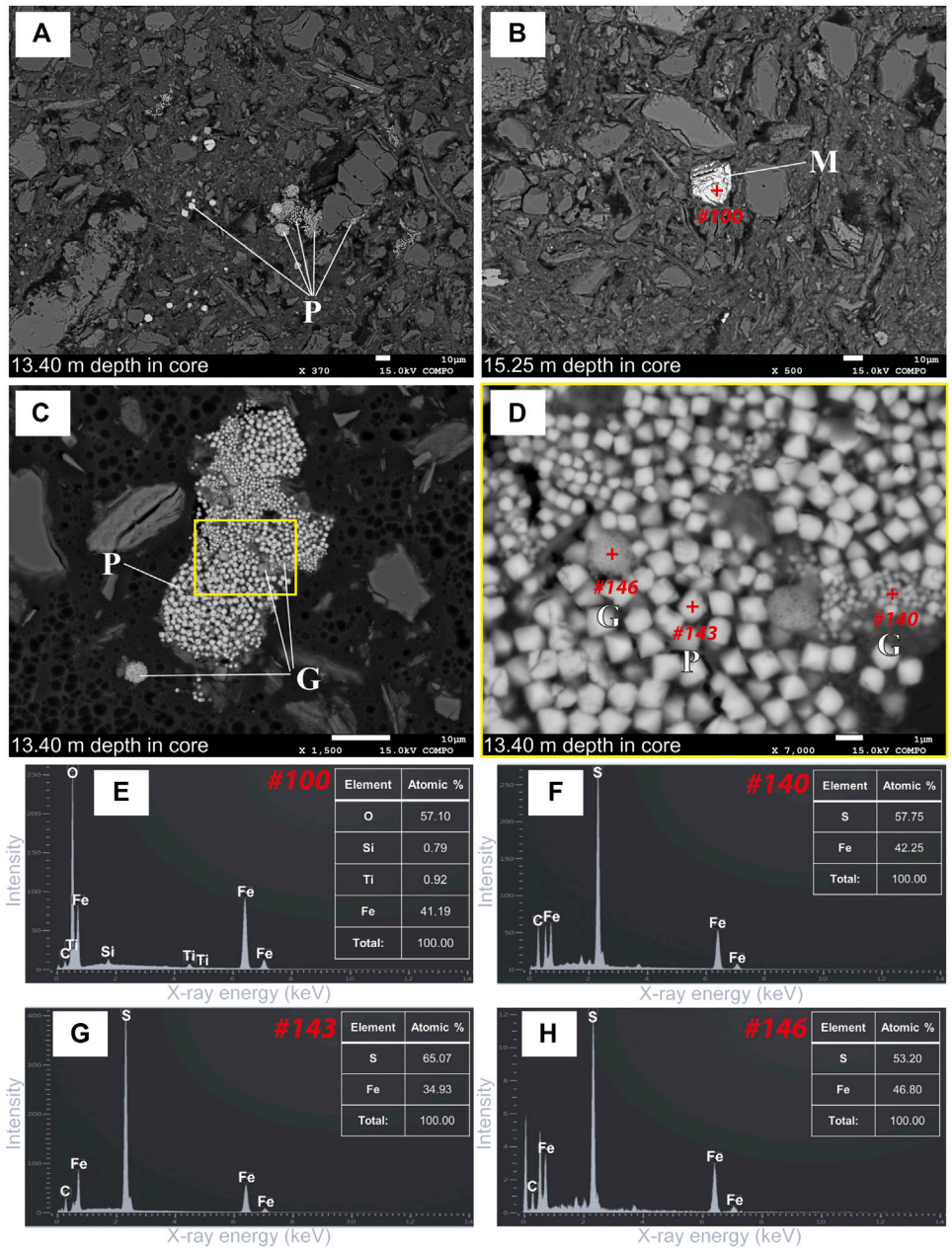

FIGURE 7 | BSE images and X-ray EDS spectra of magnetic minerals presented in bulk sediments from the YAR-4 core. **(A)** Euhedral pyrite grains, and framboidal and irregular pyrite aggregates (labeled P) in silicate/clay-dominated matrix from the 13.40 m depth sediment sample. **(B)** Titanomagnetite grain (labeled M) in silicate/clay-dominated matrix from the 15.25 m depth sediment sample, being probably of detrital origin. Red cross symbol indicates the target point where EDS analysis was conducted. **(C)** Polyframboidal aggregates of both pyrite (labeled P) and greigite (labeled G) grains from the 13.40 m depth sediment sample. **(D)** Zoom-in view of **(C)**. Ultra-fine-grained gregite aggregates (finer than the surrounding pyrite grains) within the aggregates of pyrite crystals of variable sizes. The greigite grains are roughly bimodal in size. Red cross symbols are the same as in **(B). (E–H)** EDS spectra of (Ti-poor) titanomagnetite ($Fe_{3-x}Ti_xO_4$; x = ~0.1) shown in **(B)** and pyrite and greigites shown in **(D)**, respectively, with element compositions in atomic %. Ideal atomic % is given approximately Fe = 33, and S = 67 for pyrite (FeS_2), and approximately Fe = 43, S = 57 for greigite (Fe_3S_4). The carbon **(C)** signal of EDS originates from the carbon coating of the sample thin section in preparation for the SEM observation.

Figure 10 presents FORC diagrams for four selective subsamples at different depths to provide additional information in terms of magnetic mineralogy and its domain state (also associated to grain size distribution of the magnetic mineral assemblage). Although the analyzed FORC diagrams are somewhat noisy, probably due to low concentrations of magnetic minerals, they still offer meaningful information. The FORC diagram for the 5.16-m-depth subsample had a B_c peak at ~10 mT and vertically suppressed divergence in contour distribution that was partly closed but the others intersected

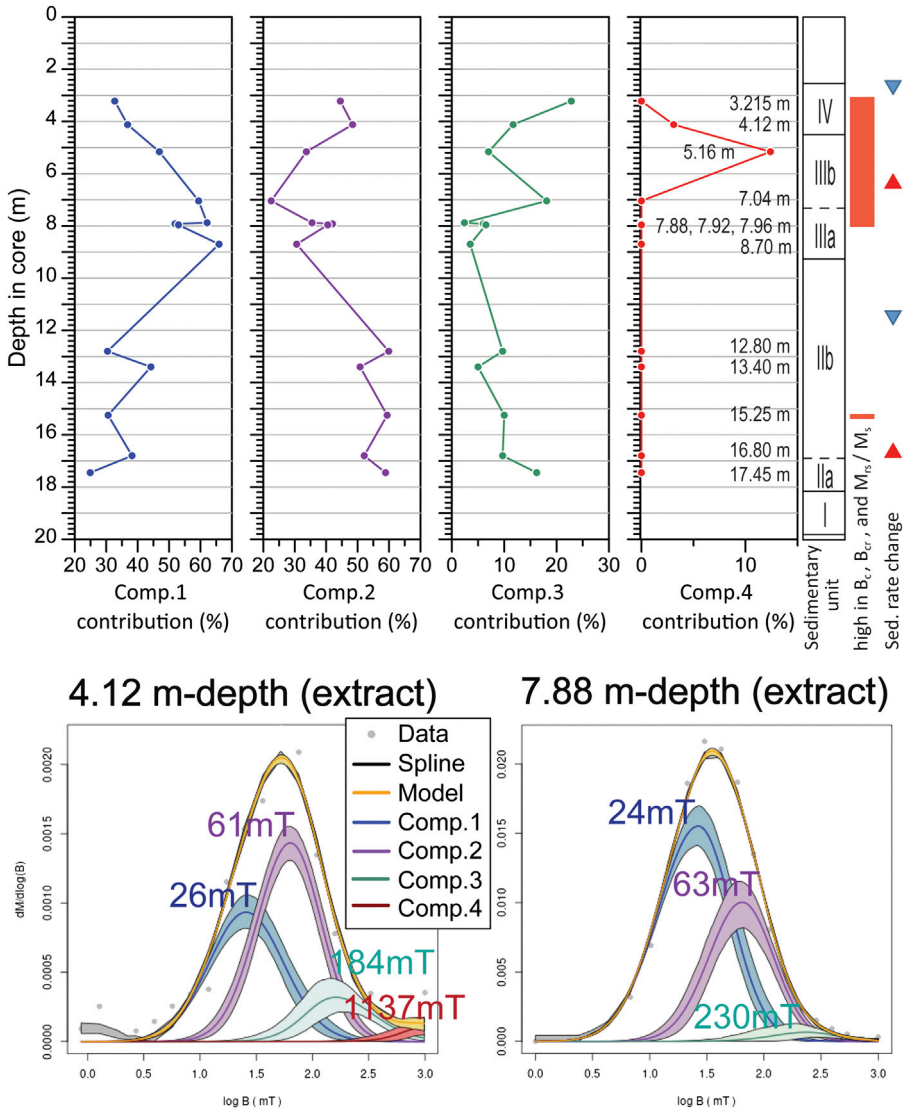

FIGURE 8 | Two examples of IRM component unmixing analyss results by using Maxbauer et al. (2016) **(lower)** and relative contributions of the unmixed magnetic mineral components for samples at different depths (**upper;** n = 13). In the figures of the lower panel, the mean coercivity (Bh) of each unmixed component (comp.) is labeled. On the right hand of the upper panel figure, the division of sedimentary units (the same as in **Figure 2**), the intervals with high values in B_c, B_{cr}, and M_{rs}/M_s (the same as in **Figure 4**), and the depths above which the sedimentation rate changes significantly (the same as identified in **Figure 3**; the triangles are the same as in **Figure 4**) are supplementarily shown.

the B_u axis. This pattern resembles the FORC diagrams of **Figures 6A,B** (Nankai Trough drilling sediments) in Kars and Kodama (2015) who interpreted them as the presence of single-domain (SD) to PSD magnetite. Dominant appearance of the magnetite-related signals for the subsample can be correlated to the most relative contribution of component 1 indicated by the IRM unmixing (**Figure 8**). The 7.84-m-depth FORC diagram had strong B_c (~10 mT) and weaker B_c (~27 mT) peaks, a closed but vertically spreading contour distribution that also elongated to higher coercivities along the B_c axis, and a negative region distributed along the lower half of the B_u axis. This pattern might be indicative of the presence of PSD greigite (e.g., Figure 5 in Roberts et al., 2011) in addition to SD-to-PSD magnetite. The 13.40-m-depth FORC diagram contained two B_c peaks at ~10 mT and near the origin. Its contours were spreading vertically wider at lower B_c values, and were not closed but intersected the B_u axis, being vertically stretched along the lower half of the B_u axis. At low B_c values, the contours were also distended diagonally downward. Such features possibly indicate the presence of PSD detrital magnetite (Roberts et al., 2018a) and SP magnetite or another magnetic mineral (Roberts et al., 2000). In this case, the SP-related feature could be interpreted to originate from ultra-fine greigite grains as indicated by the SEM observations. The 15.25-m-depth FORC contours had a B_c peak at ~18 mT, and larger elongation to higher coercivities along the B_c axis. The dense contour concentration up to at higher

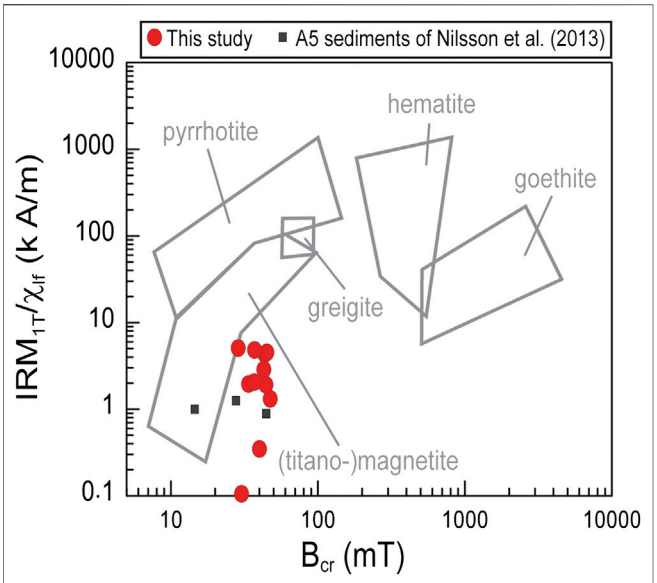

FIGURE 9 | Biplot of IRM_{1T}/χ_{lf} vs. B_{cr} for the YAR-4 core sediments (red circles; $n = 11$), with typical ranges (gray boxes) of the magnetic parameters for different minerals proposed by Peters and Thompson (1998) and data for the A5 sediments reported by Nilsson et al. (2013) (black squares).

B_c values relative to the other samples might be related to the higher component 2 content at the 15.25-m-depth indicated by the IRM unmixing result (**Figure 8**). The contours had a vertical spreading pattern that got wider gradually as B_c decreased toward the origin, and were partly closed but the others intersected the B_u axis. The contour pattern is interpreted to indicate the presence of SD and PSD grains (e.g., Roberts et al., 2000). Overall, the FORC contour patterns tell us that the 13.40-m-depth sample showed predominance of (relatively large) PSD and SP ferromagnetic grains, but the other three samples showed predominance of SD to (relatively small) PSD grains. The SP grains was interpreted as being of diagenetic greigite.

Also, none of the FORC diagrams shown had such a contour pattern of central ridge with mainly suppressed vertical spreading, which is indicative of the presence of biogenic magnetite of authigenic origin (Roberts et al., 2012). Thus, it is interpreted that biogenic magnetite cannot be a candidate for the middle-coercivity mineral component indicated by the IRM component unmixing (the component 2 in **Figure 8**).

Figure 11 presents our hysteresis parameter ratio data (M_{rs}/M_s and B_{cr}/B_c) on a Day diagram (Day et al., 1977). These data mostly fall in the PSD region of Dunlop (2002a), and almost all of them are distributed in the region between the SD + MD 3 and the SD + SP (10 nm) mixing lines of Dunlop (2002a) and Dunlop (2002b). As pointed out by Roberts et al. (2018b), such Day diagram result should be taken with care in diagnosing domain state (or grain size) particularly for mixed assemblage of multiple magnetic minerals as presented in this study. Nevertheless, it can be useful to recognize downcore relative variation in magnetic granulometric trend. The data at shallow depths down to 7.92 m fall within a relatively restricted region that is at the up left-hand side of the data distribution, whereas the others at deeper than 7.92 m, except the 15.25 m one, are distributed within the down right-hand region with low values in M_{rs}/M_s and B_{cr}/B_c. With a comprehensive view from the IRM unmixing and FORC results, such variation on Day diagram is interpreted to be caused mainly by difference in grain size distribution of ferromagnetic minerals, rather than by variation in mineralogical composition. Then it is interpreted that samples being plotted at more toward the up left-hand side on the Day diagram have more abundant ferromagnetic grains with close to stable SD to SD–PSD boundary in size but less SP grains, relative to the down right-hand plotted samples.

Diagenetic Effects on Downcore Variation in Magnetic Properties

In a wide range of sediments, but especially marine sediments from shallow continental shelf to deep-sea environments, early post-depositional diagenesis generally causes selective dissolution of relatively coarse micron-size detrital iron oxides (e.g., magnetite, hematite), and authigenic formation and growth of nano-to sub-micron-size magnetic minerals (e.g., pyrite, greigite, siderite), leading to systematic changes in the concentration and grain size of magnetic minerals with depth (e.g., Karlin and Levi, 1983; Liu et al., 2004; Rowan et al., 2009; Hatfield, 2014; Roberts, 2015). Due to the degradation of primary magnetic signals associated with paleoenvironmental changes, identifying and understanding the effects of such early diagenesis on magnetic minerals is crucial for interpreting environmental magnetic records (Snowball and Thompson, 1990; Verosub and Roberts, 1995; Liu et al., 2004; Demory et al., 2005).

Using our results from the depth interval of 3.2–13.9 m, at which sediment mean particle sizes and TOC contents vary little, we attempted to assess relatively straightforwardly early diagenetic effects on downcore variations in magnetic properties in the YAR-4 core.

In a general model for sediment cores influenced by early diagenesis, downcore variation exhibits significantly decreasing magnetic susceptibility with increasing depth in the suboxic zone (below the top shallow sediments (oxic zone) down to the suboxic–sulfidic (anoxic) boundary) and relatively constant low-susceptibility values at depths below the suboxic–sulfidic boundary, under anoxic zones. The magnetic susceptibility range in the 3.2–13.9 m depth interval of the core YAR-4 was similar in the order of magnitude of those observed in anoxic environments of coastal and shallow shelf sediment cores around South Korea and east China (Liu et al., 2004; Liu et al., 2005; Chen et al., 2015; Pan et al., 2017; see also *Downcore Variation in Magnetic Properties* Section). This result implies that the target interval of the YAR-4 sediments experienced considerable early reductive diagenesis under anoxic conditions, causing considerable dissolution of detrital magnetic minerals. It is apparently in agreement with the current anoxic conditions at depths below 0.03 m, where methane concentrations are higher, at a site in Yeongsan Lake (An et al., 2019). This suggestion is also consistent with the widespread presence of the middle-coercivity component (component 2 in **Figure 8**), i.e., greigite (see *Magnetic Mineralogy and Granulometry from Magnetic Measurements and*

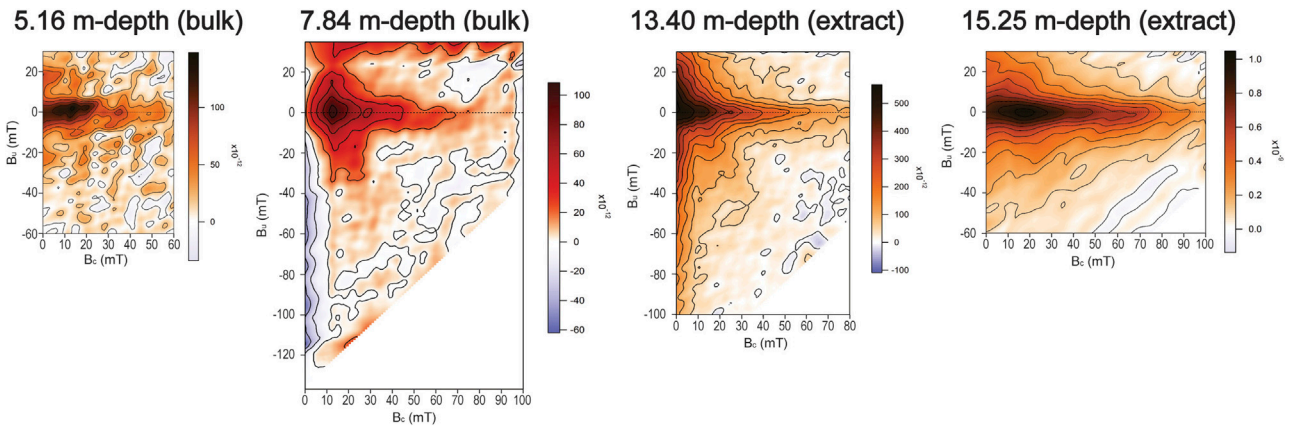

FIGURE 10 | First-order reversal curve (FORC) diagrams for four subsamples at different depths.

Scanning Electron Microscope Observations Section), which is a typical authigenic iron mineral, in addition to pyrite and iron monosulfide, which are generated in the sulfate–methane transition zone (SMTZ) (Roberts, 2015).

Rowan et al. (2009) identified downcore variations producing counterclockwise loop trends in Day diagram from marine sediment cores around the world (Figure 9 of Rowan et al., 2009). They ascribed the systematic trends to the superposition of spatio-temporally progressive diagenetic changes of magnetic minerals. This changes include progressive reductive dissolution where finer pre-existing ferromagnetic grains (mostly detrital magnetite) preferentially dissolve to leave a coarser assemblage, and progressive sulfidization resulting in SP greigite nucleation and its progressive growth into the SD size range. The trends occur as the result of magnetic property combinations between survived coarse detrital grains and SP to SD authigenic greigite grains. The looping trend and the YAR-4 downcore variation in Day diagram (**Figure 11**) apparently share a similar pattern in part, but visible difference between them exists. The whole analyzed interval of the YAR-4 core should be correlated to the "zone 3" of the downcore magnetic property profile shown in **Figures 2**, **3** of Rowan et al. (2009), based on being the low magnetic susceptibility values throughout the analyzed interval (**Figure 4**). However, the YAR-4 data in Day diagram lie within a wider B_{cr}/B_c range, being stretched toward the down right-hand region, than those of the "zone 3" (Rowan et al., 2009). Given this, the YAR-4 downcore variation is inferred to contain more complicated diagenetic effects than those indicated by Rowan et al. (2009) and/or possibly other effects caused by changes in depositional condition.

Magnetic mineral diagenesis is also generally thought to be controlled by depositional conditions, that is, mainly TOC and sedimentation rate (e.g., Hesse and Stolz, 1999). Changes in TOC and sedimentation rate often produce non-steady-state early diagenesis, where diagenetic reactions change with depth as the depositional conditions change (e.g., Thomson et al., 1984; Robinson et al., 2000; Emiroğlu et al., 2004; Fu et al., 2008; Roberts, 2015). If magnetic property variations of the 3.2–13.9 m depth interval of the YAR-4 core are further ascribed to such non-steady-state diagenesis, the YAR-4 downcore variations should be associated with changes in sedimentation rate because it is expected that the constant low TOC contents throughout the YAR-4 core would bring minimal or negligible effects. Riedinger et al. (2005) documented distinct minima in magnetic susceptibility within a distinct sediment interval, and interpreted them to result from a drastic change in sedimentation rate, which resulted in a fixation of the SMTZ at a specific depth causing substantial change of pre-existing abundant iron (oxyhydr)oxides to iron sulfides. Zheng et al. (2011) proposed that drastic changes in sedimentation rate resulted in vertical shifts of the SMTZ, of which each SMTZ eventually exhibited low magnetic susceptibility, high coercivity, and significant paramagnetic contribution as a result of dissolution of pre-existing detrital magnetite and hematite but strong resistance to the dissolution for hematite relative to magnetite, and their replacement mainly by paramagnetic pyrite. Abrajevitch and Kodama (2011) reported a relationship among mineral magnetic features, i.e., low magnetic susceptibility, coarsening of detrital magnetic grains (e.g., magnetite), increasing relative abundance of hematite, and decreasing relative abundance of goethite during periods with low sedimentation rate (i.e., sea-level highstand, in the case).

Indeed, the YAR-4 core appears to record at least four drastic changes in sedimentation rate and three distinct intervals with relatively low sedimentation rate, based on our age–depth model (**Figure 3**). However, none of the relations between magnetic properties such as those identified in the above-stated previous studies are identified in the YAR-4 core (see e.g., **Figures 4**, **8**). We thus infer that, in addition to the above-discussed possible diagenetic effects, additional effect(s) caused by another factor(s) should be contained in the downcore magnetic property variations for the YAR-4 core, and speculate the possible presence of certain paleoenvironmental change(s) or even less-known diagenetic processes linked to that (in similar manner as reported in e.g., Larrasoaña et al., 2003, Blanchet et al., 2009, and

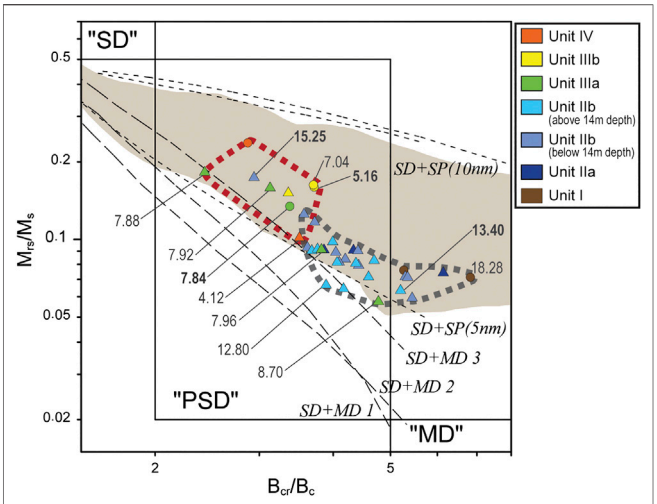

FIGURE 11 | Day plot of our YAR-4 core sediment data (n = 37) at different depths and sedimentary units. Circle and triangle symbols denotes the data measured from bulk and extract samples, respectively. Some data are labeled using the "depth in core" in meter, among which the data labeled in bold denote those where the associated FORC diagrams are provided in **Figure 10**. Single-domain (SD), pseudo-single-domain (PSD), and multi-domain (MD) boundaries, trend curves 1, 2, and 3 for SD + MD mixtures of magnetite and trend curves for SD + SP with 5-nm and SD + SP with 10-nm mixtures of magnetite were drawn by Dunlop (2002a), Dunlop (2002b). Color-shaded region represents a typical range for SD + SP mixtures of greigite indicated by Roberts et al. (2011). Division of the data into two groups by dashed enclosed lines was based on ranges of the B_c, B_{cr}, and M_{rs}/M_s values (see text for details).

the review of Roberts, 2015) for the YAR-4 site as the additional controlling factor(s).

Searching for Magnetic Property Features Associated With Paleoenvironmental Changes

Sedimentation in the studied YAR-4 site during the Holocene would have been considerably influenced by sea-level change and hydrologic events that are regarded as closely associated with regional climate changes such as the ENSO activity, the EAM, and the HCO. Accordingly, types, concentration, and grain size distribution of the contained magnetic minerals would change through time, at least partly in response to the sea-level change and/or regional climate changes. Based on our age-depth model (**Figure 3**), the YAR-4 record of magnetic property variabilities presented in this study covers a period of approximately 4,800–9,000 cal. yr BP (**Supplementary Figures S2, S3 and S4**). In order to search for magnetic property proxies for paleoenvironmental changes, we compare temporal variations between some of the obtained magnetic properties (we choose k_{LFQ}, B_c, B_{cr}, M_{rs}/M_s, and each of IRM-unmix components for this) and proxy indicating the change in sea-level (Lee and Chang, 2015; Song et al., 2018), the ENSO activity (Moy et al., 2002), the summer EAM (Dykoski et al., 2005), and the HCO with the 8.2 ka cooling event (Park et al., 2019) around the Korean Peninsula, respectively (**Figure 12**, **Supplementary Figures S2, S3 and S4**).

In advance of getting to the main discussion, we would like to mention that the use of only initial bulk magnetic susceptibility without detailed additional information about constituent magnetic minerals in interpreting a certain paleoenvironment change (as the same manner utilized in previous studies for Korea with similar purposes to this study) appears to be imprudent, given the k_{LFQ} values that were substantially influenced by complicated magnetic mineral diagenesis as in the studied case.

Comparisons With El Niño Southern Oscillation Activity, Summer Eastern Asian Monsoon, and Holocene Climate Optimum

Moy et al. (2002) presented a record of red color intensity variability through the Holocene as a proxy representing the ENSO activity variability from a sediment core of the lake Laguna Pallcacocha in the southern Ecuadorian Andes. There exist three extremely high peaks in ENSO activity during ~4,800–9,000 cal. yr BP (~4,750–5,000, ~5,900–6,000, and ~7,900–8,000 cal. yr BP; green shaded regions in **Supplementary Figure S2**), and such ENSO peaks are being considered to be related to high frequency and magnitude of flooding or freshwater input from inland at least in the southern part of the Korean Peninsula (Lim et al., 2017, Lim et al., 2019). However, we did not find any of our magnetic property variability data that could be well correlated to those ENSO peaks (**Supplementary Figure S2**). This implies no or, if any, meager regulation by extreme short-term hydrologic events (also associated with ENSO activity) on the magnetic property variabilities in the YAR-4 site.

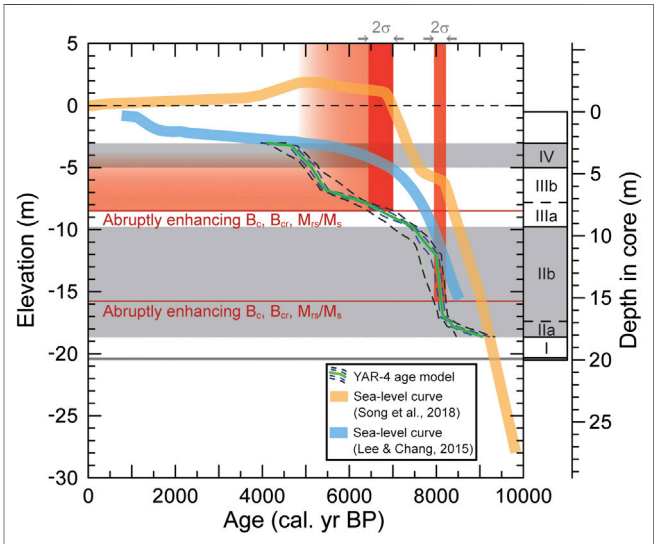

FIGURE 12 | Comparison of our age-depth model for the YAR-4 core with two different suggested sea-level curves for the western coast of South Korea (Lee and Chang, 2015; Song et al., 2018). HBBM intervals (characterized by subtantially high B_c, B_{cr}, and M_{rs}/M_s values) and their corresponding ages are indicated by red lines and red shaded boxes. The YAR-4 age-depth model curve with the uncertainties are the same as in **Figure 3**. Sedimentary unit divisions are also supplementarily shown.

The oxygen isotope ratio variability from the Dongge Cave in the South China by Dykoski et al. (2005), adopted worldwide as representative of the summer EAM variability, seems to have similarity partly in centennial (short-term excursion; blue shaded regions shown in **Supplementary Figure S3**) and millennial (long-term trend; intervals between blue shaded individuals in **Supplementary Figure S3**) scales to our B_c, B_{cr}, and M_{rs}/M_s variabilities (**Supplementary Figure S3**). It shows apparently a relationship of low B_c, B_{cr}, and M_{rs}/M_s values with strong summer EAM. Strong summer EAM generally accompany high accumulation of rainfall precipitation that leads to high terrestrial material input, which can be possibly accompanied with increasing concentration and grain size of detrital magnetic minerals (e.g., magnetite). If it can be assumed that the low B_c, B_{cr}, and M_{rs}/M_s values were carried mainly by increasing grain size of detrital magnetite for the YAR-4 sediments, these magnetic properties can be dealt as summer EAM proxies. According to this inference, strong summer EAM conditions should be favorable for coarsening of detrital magnetite, via controlling the local hydraulic condition around the studied area. On the other hand, if so, lowering B_c, B_{cr}, and M_{rs}/M_s values should occur at the periods with extremely high ENSO peak (~4,750–5,000, ~5,900–6,000, and ~7,900–8,000 cal. yr BP), through a similar process occurred in strong summer EAM periods with enhanced rainfall frequency and magnitude. However, such relationship appears not visible (**Supplementary Figure S2**). Therefore, we interpret that such potential hydraulic effect in relation to detrital magnetite grain size does not govern, but may control partly, the B_c, B_{cr}, and M_{rs}/M_s variabilities.

Additionally, the HCO period and the 8.2 ka (thousand years ago) abrupt cooling event are also the major phenomena of climate change during the Holocene. The HCO is a warm and humid period with relatively high precipitation, and occurred during ~4,800–7,600 cal. yr BP for the southern Korean Peninsula (Park et al., 2019; cf., ~5,100–8,200 cal. yr BP, a calibrated age range in this study with the OxCal and IntCal20 from ~4,500 to 7,400 years BP in uncalibrated age originally reported by Yang et al., 2008, or ~5,000–6,300 cal. yr BP by Nahm and Hong, 2014). The 8.2 ka event is a short-term climate excursion to cold and dry condition at ~8,200 cal. yr BP, and has been identified also in South Korea (Park et al., 2018; Park et al., 2019). It might be good to look at the high (detrital) magnetite relevant abundance (i.e., the IRM-unmixed component 1 contribution) with less greigite relevant abundance (i.e., the IRM-unmixed component 2 contribution) during the HCO period, and vice versa around the 8.2 ka event (**Supplementary Figure S4**). Blanchet et al. (2009) reported that large flood deposits and glacial deposits are favorable for preservation of diagenetic greigite, and interpreted it to be related to dominance of reactive iron over organic matter and/or HS^-, i.e., enrichment in terrigenous sediments. According to this, it might be possible that the 8.2 ka cooling triggered relatively enhanced greigite preservation through the early diagenetic process at the studied YAR-4 site. This potential relationship will be worth being tested further in future investigations with more high-resolution magnetic analyses and the use of multiple cores at different sites.

Possible Magnetic Response to Abrupt Drop in the Rate of Sea-Level Rise

Many sea-level change curves have been suggested for the western coast of South Korea during the Holocene (e.g., Bloom and Park, 1985; Hwang et al., 1997; Chough et al., 2004; Lee et al., 2008; Lee and Chang, 2015; Song et al., 2018); however, no consensus has been reached (cf. the review by Choi, 2018). A major discrepancy among them would be the sea level relative to the present mean sea level (MSL) and its change pattern since ~7,000 cal. yr BP: One group of the sea-level curves depicts that the sea level always was lower than the present MSL and continued a gradual rising toward the present MSL (e.g., Bloom and Park, 1985; Chough et al., 2004; Lee and Chang, 2015), whereas another group suggests a sea-level highstand (higher sea-level relative to the present MSL) during ~4,000–7,000 cal. yr BP followed by a sea-level drop toward the present MSL (e.g., Hwang et al., 1997; Song et al., 2018). Unfortunately, the sedimentary characteristics and our age-depth model of the YAR-4 core (**Figures 2**, **12**) independently do not allow to fully support one of the two different groups of suggested sea-level curves.

In any case, most suggested sea-level curves of these previous studies depict a drop in the rate of sea-level rise broadly at around 7,000 cal. yr BP. Besides this, the sea-level curve of Song et al. (2018) depicts an additional drastic drop in the sea-level rise rate at ~8,200 cal. yr BP, then shortly followed by an increase of this rate again, inferring formation of a concomitant short-term slowstand/stillstand (**Figure 12**). The existence of such "stepped" change in sea-level rise rate as indicated by Song et al. (2018) is being identified even in more recent studies (e.g., Tanabe, 2020). It also would be good to mention that attempts of the west coast sea-level reconstruction during the period back to prior to 8,000 cal. yr BP were rare in among the suggested sea-level curves (cf. **Figure 1A** in Choi, 2018). Lee and Chang (2015) generated the curve by fitting to the sea-level proxy data that were scarce but highly scattered in the sea-level value during prior to ~7,800 cal. yr BP (Figure 2 of Lee and Chang, 2015). This may be the reason why the ~8.2 ka potential drop in the rate of sea-level rise does not appear in the curve of Lee and Chang (2015) (and other previous studies depicting similar curves).

For the YAR-4 core, one remarkable, first-order magnetic feature is the abrupt increases in B_c, B_{cr} and M_{rs}/M_s (hereafter referred to as "HBBM feature") observed at depths of 15.25 and 7.84–7.96 m with their persistent high values at depths shallower than 7.84 m (**Figure 4**), corresponding to ~8,100 cal. yr BP and since ~6,700 cal. yr BP in inferred age (**Figure 3**; **Supplementary Table S6**). This observation seems not to be fully explained by solely the sulfidization-dominated diagenetic processes (even if sedimentation rate variability were considered) or correlated well with any of the ENSO activity variability (linked to the local hydrologic events), the summer EAM variability, and the HCO period, as interpreted above. Instead, the respective ages of the two abrupt B_c, B_{cr}, and M_{rs}/M_s increases are well coincident with those at which the rate of sea-level rise started to decrease suddenly according to the Song et al. (2018) sea-level curve, given the intrinsic uncertainty of the age-depth model construction (**Figures 3**,

12; **Supplementary Table S6**). These concordance allows us to infer that the HBBM feature is strongly related to change of the sea-level rise rate and possibly, sea-level stillstand/slowstand and highstand. The apparent absence of HBBM feature at the old stillstand/slowstand (**Figure 12**) possibly might be attributed to its short-lived period.

It is worthwhile to discuss and constrain concerning possible mechanism to explain the relation between the change of the sea-level rise rate and the HBBM magnetic feature. A possible major factor enhancing B_c and B_{cr} could be among increasing relative abundance of hematite and goethite, increasing relative abundance of greigite, and decreasing relative abundance of detrital magnetite, or a combination of them. However, no similar characteristic concerning relative abundance of ferromagnetic minerals between the HBBM intervals (**Figure 8**; see also *Magnetic Mineralogy and Granulometry from Magnetic Measurements and Scanning Electron Microscope Observations* Section) allows us to conclude its less probability of being major factor leading to enhancing B_c and B_{cr}. It, however, would like to be mentioned that, within the 3.21–7.04 m depth interval, there are decreasing magnetite with increasing more high-coercivity minerals in relative abundance, which may be attributable at least partly to the HBBM feature. On the other hand, the grain size distribution of ferromagnetic minerals between the HBBM-bearing intervals and the others could be clearly discriminated; the HBBM intervals showed more contents of stable SD to SD–PSD boundary grains but less SP contents (**Figures 10**, **11**; see also *Magnetic Mineralogy and Granulometry from Magnetic Measurements and Scanning Electron Microscope Observations* Section). Moreover, the occurrence of the HBBM features during the HCO and the 8.2 ka event that had different climate conditions (warm and humid vs. cold and dry; **Supplementary Figure S4**) indicates its independence of both surface temperature and humidity. The HBBM occurrence also does not appear to be associated with the sedimentation rate (**Figure 12**). Unfortunately, the exact mechanism driving the relation between the abrupt change in the grain size distribution and the abrupt drop in the sea-level rise rate is not identified by this study. However, we note that the varying sediment transport distance and pathway driven by the sea-level rise (e.g., Chen et al., 2017), leading to grain size change of detrital magnetic mineral sources, is not likely responsible for the observed abrupt change of B_c, B_{cr}, and M_{rs}/M_s values. We here modestly speculate one possibility that biochemical condition of the uppermost sediment involving the SMTZ and bottom water chemistry during the periods with low rate of sea-level rise might be favorable for rapid growth of greigite to the SD size range at the SMTZs (very close to the sediment top layer, in the studied site). Conversely, a certain condition during the periods with high rate of sea-level rise might permit forming SP greigite but inhibit its growth to the SD size range at the SMTZs that were shifted progressively upward. Consequently, the contrast between the grain size distributions driven by such sea-level change that controlled diagenetic modifications possibly might be the major cause of the occurrence of the HBBM features. This speculation will be verified in additional future works for firm establishment of a magnetic property proxy for the abrupt drop of the rate of sea-level rise or the initiation/occurrence of sea-level stillsatnd/slowstand.

CONCLUSION

In this study, we analyzed 3.2–to–19.8-m depth interval of a 20-m-long Holocene muddy sediment core recovered from the Yeongsan Estuary, South Korea, using mineral magnetic measurements with sediment particle size and TOC content to characterize downcore variations in a variety of magnetic properties. We then evaluated the diagenetic effects on magnetic signals and tested their availability as proxies of paleoenvironmental change. The magnetic measurements included magnetic susceptibilities, hysteresis parameters, progressive IRM acquisition, and FORC analysis for each of the selected subsamples. The major findings of this study are as follows:

(1) The analyzed sediments were generally characterized by relatively low bulk magnetic susceptibility values (~19–245 × 10^{-6} SI) and the predominance of paramagnetic (>60% of the total) rather than ferromagnetic contribution, but undoubtedly distinct downcore variations in ferromagnetic-related properties.
(2) The analyzed sediments would have undergone substantial early diagenetic alteration including dissolution and transformation of detrital magnetic minerals and authigenic magnetic mineral formation and growth, which eventually might led to the current complex variability in magnetic properties. For this reason, the raw bulk magnetic susceptibility values are not recommended as a stand-alone proxy of environmental change in (and around) the studied area.
(3) Abrupt increase in B_c, B_{cr}, and M_{rs}/M_s is coincide well with abrupt drop in the rate of sea-level rise, in other words, the initiation/occurrence of sea-level stillstand/slowstand or highstand, during the Holocene. It is worthwhile to clarify the exact mechanism causing their potential linkage and further consider the potential of these magnetic properties as a proxy, at least in and around the studied area (the western coast of South Korea), in future study.
(4) We also have preliminarily explored possible relationships of the magnetic property variabilities with the ENSO activity involving local hydrologic events, the summer EAM, the HCO and the 8.2 ka cooling event. Among which, the possible relationship between the magnetite and greigite relative abundance and the HCO or the abrupt short-term cooling appears to be worth being tested further in future study.

DATA AVAILABILITY STATEMENT

The original contributions presented in the study are included in the article/**Supplementary Material**, further inquiries can be directed to the corresponding authors.

AUTHOR CONTRIBUTIONS

HA contributed to the design of this study, performed subsample preparation, laboratory measurements and data analysis, and wrote the manuscript. JL contributed to core drilling fieldwork and the management of pre-treatments of the studied core, provided core samples, performed laboratory measurements, and contributed to the discussion. SK contributed to the discussion. All authors contributed to manuscript revision and approved the submitted version.

FUNDING

This study was supported in part by the Basic Research Project (GP 2020-003) of the KIGAM funded by the Ministry of Science and ICT, Republic of Korea.

ACKNOWLEDGMENTS

We are grateful to J.O. Jeong (Gyeongsang National University) for his help with FE-SEM observations. The first author wishes to thank Y. Yamamoto, C. Nishimori, and H. Tokuyama (CMCR, Kochi University) for welcoming me to the CMCR of Kochi University during the COVID-19 emergency, and letting me continue my research activities. We thank the editor Sarah P Slotznick and the specialty chief editor Kenneth Kodama for handling the reviews, and two reviewers for constructive comments, which greatly improved the manuscript.

SUPPLEMENTARY MATERIAL

The Supplementary Material for this article can be found online at: https://www.frontiersin.org/articles/10.3389/feart.2021.593332/full#supplementary-material.

REFERENCES

Abrajevitch, A., and Kodama, K. (2011). Diagenetic sensitivity of paleoenvironmental proxies: a rock magnetic study of Australian continental margin sediments. *Geochem. Geophys. Geosyst.* 12 (5), doi:10.1029/2010gc003481

An, S.-U., Mok, J.-S., Kim, S.-H., Choi, J.-H., and Hyun, J.-H. (2019). A large artificial dyke greatly alters partitioning of sulfate and iron reduction and resultant phosphorus dynamics in sediments of the Yeongsan River estuary, Yellow Sea. *Sci. Total Environ.* 665, 752–761. doi:10.1016/j.scitotenv.2019.02.058

An, Z., Porter, S. C., Kutzbach, J. E., Xihao, W., Suming, W., Xiaodong, L., et al. (2000). Asynchronous holocene optimum of the east asian monsoon. *Quat. Sci. Rev.* 19, 743–762. doi:10.1016/s0277-3791(99)00031-1

Bahr, D. B., Hutton, E. W. H., Syvitski, J. P. M., and Pratson, L. F. (2001). Exponential approximations to compacted sediment porosity profiles. *Comput. Geosciences.* 27 (6), 691–700. doi:10.1016/s0098-3004(00)00140-0

Blanchet, C. L., Thouveny, N., and Vidal, L. (2009). Formation and preservation of greigite (Fe3S4) in sediments from the Santa Barbara Basin: implications for paleoenvironmental changes during the past 35 ka. *Paleoceanography.* 24 (2), doi:10.1029/2008pa001719

Bloemendal, J., King, J. W., Hall, F. R., and Doh, S.-J. (1992). Rock magnetism of late neogene and pleistocene deep-sea sediments: relationship to sediment source, diagenetic processes, and sediment lithology. *J. Geophys. Res.* 97, 4361–4375. doi:10.1029/91jb03068

Bloom, A. L., and Park, Y. A. (1985). Holocene sea-level history and tectonic movements, republic of Korea. *Daiyonki-kenkyu.* 24, 77–84. doi:10.4116/jaqua.24.77

Byun, D. S., Wang, X. H., and Holloway, P. E. (2004). Tidal characteristic adjustment due to dyke and seawall construction in the Mokpo Coastal Zone, Korea. *Estuarine, Coastal Shelf Sci.* 59, 185–196. doi:10.1016/j.ecss.2003.08.007

Chang, C.-P. (2004). *East asian monsoon*. Singapore: World Scientific Publishing Co. Ptd. Ltd. doi:10.1142/5482

Chen, Q., Kissel, C., and Liu, Z. (2017). Late Quaternary climatic forcing on the terrigenous supply in the northern South China Sea: input from magnetic studies. *Earth Planet. Sci. Lett.* 471, 160–171. doi:10.1016/j.epsl.2017.04.047

Chen, T., Wang, Z., Wu, X., Gao, X., Li, L., and Zhan, Q. (2015). Magnetic properties of tidal flat sediments on the yangtze coast, China: early diagenetic alteration and implications. *The Holocene* 25, 832–843. doi:10.1177/0959683615571425

Choi, K. S., Khim, B. K., and Woo, K. S. (2003). Spherulitic siderites in the holocene coastal deposits of Korea (eastern Yellow Sea): elemental and isotopic composition and depositional environment. *Mar. Geology.* 202, 17–31. doi:10.1016/s0025-3227(03)00258-5

Choi, P., Choi, H., Hwang, J., Kee, W., Ko, H., Kim, Y., et al. (2002). *Explanatory note of the mokpo and yeosu sheets, 1: 250,000*. Daejeon: Korea Institute of Geoscience and Mineral Resources.

Choi, S.-J. (2018). Review on the relative sea-level changes in the Yellow Sea during the late holocene. *Econ. Environ. Geology.* 51, 463–471. (in Korean with English abstract).

Chough, S. K., Lee, H. J., Chun, S. S., and Shinn, Y. J. (2004). Depositional processes of late quaternary sediments in the Yellow Sea: a review. *Geosci. J.* 8, 211–264. doi:10.1007/bf02910197

Day, R., Fuller, M. D., and Schmidt, V. A. (1977). Magnetic hysteresis properties of synthetic titanomagnetites. *J. Geophys. Res.* 81, 873–880.

Dekkers, M. J. (1997). Environmental magnetism: an introduction. *Geologie en Mijnbouw.* 76, 163–182. doi:10.1023/a:1003122305503

Demory, F., Oberhänsli, H., Nowaczyk, N. R., Gottschalk, M., Wirth, R., and Naumann, R. (2005). Detrital input and early diagenesis in sediments from lake baikal revealed by rock magnetism. *Glob. Planet. Change.* 46, 145–166. doi:10.1016/j.gloplacha.2004.11.010

Dunlop, D. J. (2002a). Theory and application of the day plot (Mrs/Ms versus Hcr/Hc) 1. Theoretical curves and tests using titanomagnetite data. *J. Geophys. Res. Solid Earth.* 107. B3. doi:10.1029/2001JB000486

Dunlop, D. J. (2002b). Theory and application of the day plot (Mrs/Ms versus Hcr/Hc) 2. application to data for rocks, sediments, and soils. *J. Geophys. Res. Solid Earth.* 107. B3. doi:10.1029/2001JB000487

Dykoski, C., Edwards, R., Cheng, H., Yuan, D., Cai, Y., Zhang, M., et al. (2005). A high-resolution, absolute-dated holocene and deglacial Asian monsoon record from Dongge Cave, China. *Earth Planet. Sci. Lett.* 233, 71–86. doi:10.1016/j.epsl.2005.01.036

Emiroğlu, S., Rey, D., and Petersen, N. (2004). Magnetic properties of sediment in the Ría de Arousa (Spain): dissolution of iron oxides and formation of iron sulphides. *Phys. Chem. Earth, Parts A/B/C.* 29, 947–959.

Evans, M., and Heller, F. (2003). *Environmental magnetism: principles and applications of enviromagnetics*. Amsterdam: Elsevier.

Fu, Y., von Dobeneck, T., Franke, C., Heslop, D., and Kasten, S. (2008). Rock magnetic identification and geochemical process models of greigite formation in quaternary marine sediments from the Gulf of Mexico (IODP Hole U1319A). *Earth Planet. Sci. Lett.* 275 (3-4), 233–245. doi:10.1016/j.epsl.2008.07.034

Harrison, R. J., and Feinberg, J. M. (2008). FORCinel: an improved algorithm for calculating first-order reversal curve distributions using locally weighted regression smoothing. *Geochem. Geophys. Geosyst.* 9, doi:10.1029/2008gc001987

Hatfield, R. (2014). Particle size-specific magnetic measurements as a tool for enhancing our understanding of the bulk magnetic properties of sediments. *Minerals* 4, 758–787. doi:10.3390/min4040758

Hesse, P., and Stolz, J. (1999). Bacterial magnetite and the quaternary climate record. *Quat. climates, environments magnetism* 390, 161–198.

Hwang, S.-I., Yoon, S.-O., and Jo, W.-R. (1997). The change of the depositional environment on dodaecheon river basin during the middle holocene. *J. Korean Geographical Soc.* 32, 403–420.(in Korean with English abstract) doi:10.4097/kjae.1997.32.1.67

Karlin, R., and Levi, S. (1983). Diagenesis of magnetic minerals in recent haemipelagic sediments. *Nature* 303, 327–330. doi:10.1038/303327a0

Kars, M., and Kodama, K. (2015). Rock magnetic characterization of ferrimagnetic iron sulfides in gas hydrate-bearing marine sediments at Site C0008, nankai trough, Pacific Ocean, off-coast Japan. *Earth, Planets and Space* 67, 118. doi:10.1186/s40623-015-0287-y

Khim, B. K., Choi, K. S., and Park, Y. A. (2000). "Holocene deposits of youngjong Island (west coast of Korea), and its palaeoenvironmental implications," in *Elemental composition of siderite grains in early-. Proceedings in marine science*. Editors B. W. Flemming, M. T. Delafontaine, and G. Liebezeit (Amsterdam: Elsevier), 205–217. doi:10.1016/S1568-2692(00)80017-0

Kim, J.-M., and Kennett, J. P. (1998). Paleoenvironmental changes associated with the holocene marine transgression, yellow sea (hwanghae). *Mar. Micropaleontology* 34, 71–89. doi:10.1016/s0377-8398(98)00004-8

Kim, W., Doh, S.-J., and Yu, Y. (2009). Anthropogenic contribution of magnetic particulates in urban roadside dust. *Atmos. Environ.* 43, 3137–3144. doi:10.1016/j.atmosenv.2009.02.056

Koo, H., Lee, Y., Kim, S., and Cho, H. (2018). Clay mineral distribution and provenance in surface sediments of central yellow sea mud. *Geosci. J.* 22, 989–1000. doi:10.1007/s12303-018-0019-y

Larrasoaña, J. C., Roberts, A. P., Stoner, J. S., Richter, C., and Wehausen, R. (2003). A new proxy for bottom-water ventilation in the eastern mediterranean based on diagenetically controlled magnetic properties of sapropel-bearing sediments. *Palaeogeogr. Palaeoclimatol. Palaeoecol.* 190, 221–242. doi:10.1016/s0031-0182(02)00607-7

Lee, E., Chang, T. S., and Chang, T. S. 2015). Holocene sea level changes in the eastern Yellow Sea:A brief review using proxy records and measurement data. *J. Korean Earth Sci. Soc.* 36, 520–532. (in Korean with English abstract) doi:10.5467/jkess.2015.36.6.520

Lee, Y. G., An, K. G., Ha, P. T., Lee, K. Y., Kang, J. H., Cha, S. M., et al. (2009). Decadal and seasonal scale changes of an artificial lake environment after blocking tidal flows in the Yeongsan Estuary region, Korea. *Sci. Total Environ.* 407, 6063–6072. doi:10.1016/j.scitotenv.2009.08.031

Lee, Y. G., Choi, J. M., and Oertel, G. F. (2008). Postglacial sea-level change of the Korean southern sea shelf. *J. Coastal Res.* 4, 118–132. doi:10.2112/06-0737.1

Lim, D. I., Jung, H. S., Yang, S. Y., and Yoo, H. S. (2004). Sequential growth of early diagenetic freshwater siderites in the holocene coastal deposits, Korea. *Sediment. Geology.* 169, 107–120. doi:10.1016/j.sedgeo.2004.05.002

Lim, D. I., and Park, Y. A. (2003). Late quaternary stratigraphy and evolution of a Korean tidal flat, haenam bay, southeastern Yellow Sea, Korea. *Mar. Geology.* 193, 177–194. doi:10.1016/s0025-3227(02)00663-1

Lim, J., Lee, J.-Y., Hong, S.-S., Kim, J.-Y., Yi, S., and Nahm, W.-H. (2017). Holocene changes in flooding frequency in South Korea and their linkage to centennial-to-millennial-scale El Niño-Southern oscillation activity. *Quat. Res.* 87 (1), 37–48. doi:10.1017/qua.2016.8

Lim, J., Lee, J.-Y., Hong, S.-S., Park, S., Lee, E., and Yi, S. (2019). Holocene coastal environmental change and ENSO-driven hydroclimatic variability in East Asia. *Quat. Sci. Rev.* 220, 75–86. doi:10.1016/j.quascirev.2019.07.041

Lim, J., Lee, J.-Y., Kim, J.-C., Hong, S.-S., and Yang, D.-Y. (2015). Holocene environmental change at the southern coast of Korea based on organic carbon isotope (δ13C) and C/S ratios. *Quat. Int.* 384, 160–168. doi:10.1016/j.quaint.2015.05.017

Lim, J., Lee, J.-Y., Kim, J. C., Hong, S.-S., and Yang, D.-Y. (2014). Relationship between environmental change on Geoje Island, southern coast of Korea, and regional monsoon and temperature changes during the late Holocene. *Quat. Int.* 344, 11–16. doi:10.1016/j.quaint.2014.05.049

Liu, J., Zhu, R., Li, S., and Jeong-Hae, C. (2005). Magnetic mineral diagenesis in the post-glacial muddy sediments from the southeastern South Yellow Sea: Response to marine environmental changes. *Sci. China Ser. D* 48, 134–144. doi:10.1360/02yd0302

Liu, J., Zhu, R., Roberts, A. P., Li, S., and Chang, J.-H. (2004). High-resolution analysis of early diagenetic effects on magnetic minerals in post-middle-holocene continental shelf sediments from the Korea strait. *J. Geophys. Res.* 109, B03103. doi:10.1029/2003jb002813

Liu, Q., Roberts, A. P., Larrasoaña, J. C., Banerjee, S. K., Guyodo, Y., Tauxe, L., et al. (2012). Environmental magnetism: principles and applications. *Rev. Geophys.* 50, RG4002. doi:10.1029/2012rg000393

Liu, S., Zhang, W., He, Q., Li, D., Liu, H., and Yu, L. (2010). Magnetic properties of East China Sea shelf sediments off the Yangtze Estuary: influence of provenance and particle size. *Geomorphology* 119, 212–220. doi:10.1016/j.geomorph.2010.03.027

Lougheed, B. C., and Obrochta, S. P. (2019). A rapid, deterministic age-depth modeling routine for geological sequences with inherent depth uncertainty. *Paleoceanography and Paleoclimatology* 34, 122–133. doi:10.1029/2018PA003457

Lu, Z., Liu, Z., Zhu, J., and Cobb, K. M. (2018). A review of paleo El niño-southern oscillation. *Atmosphere* 9, 130. doi:10.3390/atmos9040130

Maher, B. A., and Thompson, R. (1999). *Quaternary climates, environments and magnetism*. Cambridge: Cambridge University Press. doi:10.1017/CBO9780511535635

Maxbauer, D. P., Feinberg, J. M., and Fox, D. L. (2016). MAX UnMix: a web application for unmixing magnetic coercivity distributions. *Comput. Geosciences* 95, 140–145. doi:10.1016/j.cageo.2016.07.009

Moon, J.-W., Song, Y., Moon, H. S., and Lee, G. H. (2018). Clay minerals from tidal flat sediments at Youngjong Island, Korea, as a potential indicator of sea-level change. *Clay miner.* 35, 841–855. doi:10.1180/000985500547278

Moy, C., Seltzer, G., Rodbell, D., and Anderson, D. M. (2002). Variability of El Niño/Southern Oscillation activity at millennial timescales during the Holocene epoch. *Nature* 420, 162–165. doi:10.1038/nature01194

Nahm, W.-H., and Hong, S.-S. (2014). Holocene environmental changes inferred from sedimentary records in the lower reach of the Yeongsan River, Korea. *The Holocene* 24, 1798–1809. doi:10.1177/0959683614551221

Nahm, W.-H., Kim, J. C., Bong, P.-Y., Kim, J.-Y., Yang, D.-Y., and Yu, K.-M. (2008). Late quaternary stratigraphy of the yeongsan estuary, southwestern Korea. *Quat. Int.* 176-177, 13–24. doi:10.1016/j.quaint.2007.03.024

Nakanishi, T., Hong, W., Sung, K. S., and Lim, J. (2013). Radiocarbon reservoir effect from shell and plant pairs in Holocene sediments around the Yeongsan River in Korea. *Nucl. Instr. Methods Phys. Res. Section B: Beam Interactions Mater. Atoms* 294, 444–451. doi:10.1016/j.nimb.2012.09.025

Nilsson, A., Lee, Y. S., Snowball, I., and Hill, M. (2013). Magnetostratigraphic importance of secondary chemical remanent magnetizations carried by greigite (Fe3S4) in Miocene sediments, New Jersey shelf (IODP Expedition 313). *Geosphere* 9, 510–520. doi:10.1130/ges00854.1

Pan, D., Chen, T., Zhan, Q., and Wang, Z. (2017). Mineral magnetic properties of holocene sediments in the subaqueous yangtze delta and the implications for human activity and early diagenesis. *Quat. Int.* 459, 133–143. doi:10.1016/j.quaint.2017.05.010

Park, J., Park, J., Yi, S., Cheul Kim, J., Lee, E., and Choi, J. (2019). Abrupt holocene climate shifts in coastal East Asia, including the 8.2 ka, 4.2 ka, and 2.8 ka BP events, and societal responses on the Korean peninsula. *Sci. Rep.* 9, 10806. doi:10.1038/s41598-019-47264-8

Park, J., Park, J., Yi, S., Kim, J. C., Lee, E., and Jin, Q. (2018). The 8.2 ka cooling event in coastal East Asia: high-resolution pollen evidence from southwestern Korea. *Sci. Rep.* 8, 12423. doi:10.1038/s41598-018-31002-7

Park, Y. A., Lim, D. I., Khim, B. K., Choi, J. Y., and Doh, S. J. (1998). Stratigraphy and subaerial exposure of late quaternary tidal deposits in haenam Bay, Korea (South-eastern Yellow Sea). *Estuarine, Coastal Shelf Sci.* 47, 523–533. doi:10.1006/ecss.1998.0381

Peters, C., and Dekkers, M. J. (2003). Selected room temperature magnetic parameters as a function of mineralogy, concentration and grain size. *Phys. Chem. Earth, Parts A/B/C.* 28, 659–667. doi:10.1016/s1474-7065(03)00120-7

Peters, C., and Thompson, R. (1998). Magnetic identification of selected natural iron oxides and sulphides. *J. Magnetism Magn. Mater.* 183, 365–374. doi:10.1016/s0304-8853(97)01097-4

Reimer, P. J., Austin, W. E. N., Bard, E., Bayliss, A., Blackwell, P. G., Bronk Ramsey, C., et al. (2020). The IntCal20 northern hemisphere radiocarbon age calibration curve (0-55 cal kBP). *Radiocarbon* 62, 725–757. doi:10.1017/RDC.2020.41

Rey, D., Mohamed, K. J., Bernabeu, A., Rubio, B., and Vilas, F. (2005). Early diagenesis of magnetic minerals in marine transitional environments: geochemical signatures of hydrodynamic forcing. *Mar. Geology.* 215, 215–236. doi:10.1016/j.margeo.2004.12.001

Riedinger, N., Pfeifer, K., Kasten, S., Garming, J. F. L., Vogt, C., and Hensen, C. (2005). Diagenetic alteration of magnetic signals by anaerobic oxidation of methane related to a change in sedimentation Rate. *Geochimica et Cosmochimica Acta* 69, 4117–4126. doi:10.1016/j.gca.2005.02.004

Roberts, A. P., Chang, L., Heslop, D., Florindo, F., and Larrasoaña, J. C. (2012). Searching for single domain magnetite in the "pseudo-single-domain" sedimentary haystack: implications of biogenic magnetite preservation for sediment magnetism and relative paleointensity determinations. *J. Geophys. Res.* 117, a. doi:10.1029/2012jb009412

Roberts, A. P., Chang, L., Rowan, C. J., Horng, C.-S., and Florindo, F. (2011). Magnetic properties of sedimentary greigite (Fe3S4): an update. *Rev. Geophys.* 49, RG1002. doi:10.1029/2010rg000336

Roberts, A. P. (2015). Magnetic mineral diagenesis. *Earth-Science Rev.* 151, 1–47. doi:10.1016/j.earscirev.2015.09.010

Roberts, A. P. (1995). Magnetic properties of sedimentary greigite (Fe3S4). *Earth Planet. Sci. Lett.* 134, 227–236. doi:10.1016/0012-821x(95)00131-u

Roberts, A. P., Pike, C. R., and Verosub, K. L. (2000). First-order reversal curve diagrams: a new tool for characterizing the magnetic properties of natural samples. *J. Geophys. Res.* 105, 28461–28475. doi:10.1029/2000jb900326

Roberts, A. P., Tauxe, L., Heslop, D., Zhao, X., and Jiang, Z. (2018a). A critical appraisal of the "Day" diagram. *J. Geophys. Res. Solid Earth.* 123 (4), 2618–2644. doi:10.1002/2017jb015247

Roberts, A. P., Zhao, X., Harrison, R. J., Heslop, D., Muxworthy, A. R., Rowan, C. J., et al. (2018b). Signatures of reductive magnetic mineral diagenesis from unmixing of first-order reversal curves. *J. Geophys. Res. Solid Earth.* 123, 4500–4522. doi:10.1029/2018jb015706

Robinson, S. G., Sahota, J. T. S., and Oldfield, F. (2000). Early diagenesis in North Atlantic abyssal plain sediments characterized by rock-magnetic and geochemical indices. *Mar. Geology.* 163, 77–107. doi:10.1016/s0025-3227(99)00108-5

Rowan, C. J., Roberts, A. P., and Broadbent, T. (2009). Reductive diagenesis, magnetite dissolution, greigite growth and paleomagnetic smoothing in marine sediments: a new view. *Earth Planet. Sci. Lett.* 277, 223–235. doi:10.1016/j.epsl.2008.10.016

Ryu, S. O., Lee, H. J., and Chang, J. H. (2004). Seasonal cycle of sedimentary process on mesotidal flats in the semienclosed muan bay, southern west coast of Korea: culminating summertime erosion. *Continental Shelf Res.* 24, 137–147. doi:10.1016/j.csr.2003.09.001

Selvaraj, K., Chen, C. T. A., and Lou, J.-Y. (2007). Holocene East Asian monsoon variability: links to solar and tropical pacific forcing. *Geophys. Res. Lett.* 34, L01703. doi:10.1029/2006gl028155

Snowball, I. F. (1997). The detection of single-domain greigite (Fe3S4) using rotational remanent magnetization (RRM) and the effective gyro field (Bg): mineral magnetic and palaeomagnetic applications. *Geophys. J. Int.* 130, 704–716. doi:10.1111/j.1365-246x.1997.tb01865.x

Snowball, I. F., and Thompson, R. (1990). A mineral magnetic study of holocene sedimentation in lough catherine, Northern Ireland. *Boreas* 19, 127–146. doi:10.1111/j.1502-3885.1990.tb00574.x

Song, B., Yi, S., Yu, S.-Y., Nahm, W.-H., Lee, J.-Y., Lim, J., et al. (2018). Holocene relative sea-level changes inferred from multiple proxies on the west coast of South Korea. *Palaeogeogr. Palaeoclimatol. Palaeoecol.* 496, 268–281. doi:10.1016/j.palaeo.2018.01.044

Stanley, D. J., and Warne, A. G. (1994). Worldwide initiation of holocene marine deltas by deceleration of sea-level rise. *Science* 265 (5169), 228–231. doi:10.1126/science.265.5169.228

Szuszkiewicz, M., Magiera, T., Kapička, A., Petrovský, E., Grison, H., and Gołuchowska, B. (2015). Magnetic characteristics of industrial dust from different sources of emission: a case study of Poland. *J. Appl. Geophys.* 116, 84–92. doi:10.1016/j.jappgeo.2015.02.027

Tanabe, S. (2020). Stepwise accelerations in the rate of sea-level rise in the area north of.Tokyo Bay during the Early Holocene. *Quat. Sci. Rev.* 248, 106575. doi:10.1016/j.quascirev.2020.106575

Tauxe, L., Sugisaki, S., Jiménez-Espejo, F., Escutia, C., Cook, C. P., Van De Flierdt, T., et al. (2015). Geology of the wilkes land sub-basin and stability of the east antarctic ice sheet: insights from rock magnetism at IODP site U1361. *Earth Planet. Sci. Lett.* 412, 61–69. doi:10.1016/j.epsl.2014.12.034

Thompson, R., and Oldfield, F. (1986). *Environmental magnetism*. London: Allen & Unwin. doi:10.1007/978-94-011-8036-8

Thomson, J., Wilson, T. R. S., Culkin, F., and Hydes, D. J. (1984). Non-steady state diagenetic record in eastern equatorial Atlantic sediments. *Earth Planet. Sci. Lett.* 71 (1), 23–30. doi:10.1016/0012-821x(84)90049-9

Torii, M. (2005). Environmental magnetism: a brief review. *J. Geogr. (Chigaku Zasshi).* 114, 284–295. (in Japanese with English abstract) doi:10.5026/jgeography.114.2_284

Verosub, K. L., and Roberts, A. P. (1995). Environmental magnetism: past, present, and future. *J. Geophys. Res.* 100, 2175–2192. doi:10.1029/94jb02713

Wang, Y., Dong, H., Li, G., Zhang, W., Oguchi, T., Bao, M., et al. (2010). Magnetic properties of muddy sediments on the northeastern continental shelves of China: implication for provenance and transportation. *Mar. Geology.* 274, 107–119. doi:10.1016/j.margeo.2010.03.009

Williams, J., Dellapenna, T., Lee, G.-H., and Louchouarn, P. (2014). Sedimentary impacts of anthropogenic alterations on the yeongsan estuary, South Korea. *Mar. Geology.* 357, 256–271. doi:10.1016/j.margeo.2014.08.004

Yang, D. Y., Kim, J.-Y., Nahm, W.-H., Ryu, E., Yi, S., Kim, J. C., et al. (2008). Holocene wetland environmental change based on major element concentrations and organic contents from the cheollipo coast, Korea. *Quat. Int.* 176-177, 143–155. doi:10.1016/j.quaint.2007.05.019

Yang, S. Y., Jung, H. S., Lim, D. I., and Li, C. X. (2003). A review on the provenance discrimination of sediments in the Yellow Sea. *Earth-Science Rev.* 63, 93–120. doi:10.1016/s0012-8252(03)00033-3

Zheng, Y., Kissel, C., Zheng, H. B., Laj, C., and Wang, K. (2010). Sedimentation on the inner shelf of the East China Sea: magnetic properties, diagenesis and paleoclimate implications. *Mar. Geology.* 268, 34–42. doi:10.1016/j.margeo.2009.10.009

Zheng, Y., Zheng, H., Kissel, C., and Laj, C. (2011). Sedimentation rate control on diagenesis, East China Sea sediments. *Phys. Earth Planet. Interiors* 187, 301–309. doi:10.1016/j.pepi.2011.05.005

Zhou, X., Sun, L., Zhan, T., Huang, W., Zhou, X., Hao, Q., et al. (2016). Time-transgressive onset of the holocene optimum in the east asian monsoon region. *Earth Planet. Sci. Lett.* 456, 39–46. doi:10.1016/j.epsl.2016.09.052

Conflict of Interest: The authors declare that the research was conducted in the absence of any commercial or financial relationships that could be construed as a potential conflict of interest.

frontiers in Earth Science

ORIGINAL RESEARCH
published: 17 June 2021
doi: 10.3389/feart.2021.601401

The Effect of Differential Weathering on The Magnetic Properties of Paleosols: A Case Study of Magnetic Enhancement vs. Magnetic Depletion in the Pleistocene Blackwater Draw Formation, Texas

J. Stine[1]*, *J.W. Geissman*[1,2], *D.E. Sweet*[3] *and H. Baird*[3]

[1]Department of Geosciences, University of Texas, Richardson, TX, United States, [2]Department of Earth and Planetary Sciences, University of New Mexico, Albuquerque, NM, United States, [3]Department of Geosciences, Texas Tech University, Lubbock, TX, United States

OPEN ACCESS

Edited by:
Sarah P Slotznick,
Dartmouth College, United States

Reviewed by:
Daniel Maxbauer,
Carleton College, United States
Jan Hošek,
Czech Geological Survey, Czechia
Junsheng Nie,
Lanzhou University, China

***Correspondence:**
J. Stine
Jonathan.stine@utdallas.edu

Specialty section:
This article was submitted to Geomagnetism and Paleomagnetism, a section of the journal Frontiers in Earth Science

Received: *31 August 2020*
Accepted: *10 May 2021*
Published: *17 June 2021*

Citation:
Stine J, Geissman JW, Sweet DE and Baird H (2021) The Effect of Differential Weathering on The Magnetic Properties of Paleosols: A Case Study of Magnetic Enhancement vs. Magnetic Depletion in the Pleistocene Blackwater Draw Formation, Texas. Front. Earth Sci. 9:601401. doi: 10.3389/feart.2021.601401

The type-section of the Blackwater Draw Formation (BDF) consists of a series of five paleosol horizons developed on eolian deposits and an overlying surficial soil. Previous work has shown that magnetic properties (e.g., χ, ARM, and IRM) as a function of depth in this type-section, display both magnetically enhanced and magnetically depleted signals for different paleosols. To better understand the magnetic mineralogy responsible for these varying responses, various rock-magnetic experiments, scanning electron microscopy, and Mössbauer spectroscopy were conducted on representative samples from the six soil units which constitute the BDF type-section. Our results show that sub-micron hematite [with a minor contribution from single-domain sized hematite (Hc = ~500 mT) dominates all the soils in terms of weight percent concentration. Whereas, low coercivity (Hc = ~35 mT or less) magnetite/maghemitized-magnetite grains, largely in the PSD state (Mr/Ms=~0.14 +/– 0.03588, Hcr/Hc=~2.68 +/– 0.298789), dominate the magnetic signal. Magnetically depleted soils show a relatively higher proportion of goethite, while magnetically enhanced soils show an increased contribution from SP/SSD magnetite/maghemite phases.By combining our data-set with geochemically-derived climofunctions, we have correlated the magnetically preserved, depleted, and enhanced sections of the type-section to three distinct environmental phases (I-III). The basal sediments of Phase I displays relatively homogenous (neither enhanced nor depleted) magnetic properties due to relatively arid conditions and minimal alteration of southerly derive eolian sands. Conversely, Phase II-III represents a change in weathering intensities and provenance, resulting in a mix of southerly derived sands and northerly derived silts. Phase II, experienced greater precipitation levels, resulting in the dissolution of Fe-oxide phases and thus magnetic depletion. The uppermost Phase III experienced intermediate precipitation intensities resulting in magnetic enhancement.Using previously published age models we tentatively interpret these changing environmental conditions to be influenced by the Middle-Pleistocene Transition (1.2-0.7 Ma), where the Earth's climatic cycles shifted

from a ~41 kyr to ~100 kyr cycles. However, ambiguities persist due to uncertainties in the currently published age model. Due to the complexity of the magnetic signal, we recommend future studies utilize a holistic approach, incorporating rock-magnetic, geochemical, and microscopy observations for more accurate reconstruction of regional paleoenvironments.

Keywords: blackwater draw formation, mid-pleistocene transition, rock magnetism, continental weathering, eolian strata, environmental magnetism, soil magnetism, magnetic mineralogy

INTRODUCTION

Iron is the fourth most common element forming the planet (Lepp, 1975; Thompson and Oldfield, 1986; Frey and Reed, 2012) therefore iron bearing minerals, including magnetic iron oxides (i.e. magnetite, maghemite, hematite, and others), are a common constituent in most rocks in the Earth's crust. Thompson and Oldfield (1986) recognized that environmentally influenced changes in iron oxide-bearing sediments correspond to changes in the magnetic properties of the bulk sediment material. Since then, numerous studies have shown that the magnetic properties of sediments, as well as sedimentary rocks, may serve as a valuable paleoclimate proxy (e.g., Evans and Heller (2003), and references therein), although ambiguities still exist concerning interpretations of the magnetic characteristics.

During pedogenesis, it is often the case that fine-grained magnetite/maghemite particles form from the alteration of parent material (Thompson and Oldfield, 1986; Maher et al., 2003a, 2003b; Jordanova, 2016). These pedogenic magnetite/maghemite particles include superparamagnetic (SP; grain size typically <30 nm) in addition to geologically stable, single domain (SSD; grain size 30–75 nm) grain populations (Zhou et al., 1990; Liu et al., 2003, 2004b; Liu, 2004; Nie et al., 2016). This is in contrast to detrital magnetic minerals which are often coarser multidomain (MD; grain size 100-300 nm and larger) or pseudo-single domain (PSD; grain size in between SSD and MD) grain sizes (Levi and Merrill, 1978; Newell and Merrill, 2000; Maxbauer et al., 2016a; Roberts et al., 2017).

Nevertheless the formation of new magnetic material during pedogenesis can result in a net increase in commonly measured rock magnetic parameters, such as bulk magnetic susceptibility (χ), anhysteretic remanent magnetization (ARM), and isothermal remanent magnetization (IRM) with respect to the parent material (a process often referred to as 'magnetic enhancement') (Maher, 1986; Thompson and Oldfield, 1986; Maher and Thompson, 1995; Evans and Heller, 2003; Torrent et al., 2006; Jordanova, 2016). A well-known example of this phenomenon, and its relation to climate cycles, is the intensely studied loess deposits on the Chinese Loess Plateau (Heller and Tungsheng, 1984; Zhou et al., 1990; Maher and Thompson, 1991; Liu et al., 1992, 2004a, 2007a; Verosub et al., 1993; Meng et al., 1997; Torrent et al., 2007; Song et al., 2010). There the variations in magnitude of χ in relation to depth corresponds not only with the alternating sequences of loess-paleosols but also with established glacial-interglacial cycles based on geochemical and geochronologic information as, first demonstrated by Heller and Tungsheng (1984) and Kukla et al. (1988).

However, pedogenesis does not always strictly result in magnetic enhancement of the parent material. Sequences that have been studied in Alaska, Siberia, and Argentina are well-cited examples where paleosols have lower magnetic values compared to underlying loess deposits (Chlachula et al., 1997, 1998; Maher, 1998; Chlachula, 2003; Chlachula and Little, 2011; Jordanova, 2016). For these sites the "Siberian/Alaskan" model was proposed, which states that glacial/interglacial time periods correlate to strong/weak winds resulting in the deposition of more/less magnetite/maghemite respectively (Chlachula et al., 1998; Matasova et al., 2001; Zhu et al., 2003; Matasova and Kazansky, 2005; Kravchinsky et al., 2008). However, high percent frequency dependence ($\%\chi_{FD}$) values for magnetically depleted palesols in Siberia suggest that pedogenesis is still a relevant factor (Matasova et al., 2001; Kravchinsky et al., 2008). Liu et al. (2008, 2013) offered an alternative model for magnetic depletion, where oversaturation of soils with water favors the conversion of detrital magnetite/maghemite into magnetically weaker mineral phases such as goethite or paramagnetic clays (Lu et al., 2012; Chen et al., 2015). Additionally, other researchers have identified that rises in temperature can also lead to magnetic depletion, through the conversion of magnetite into hematite (Schwertmann, 1958; Kämpf and Schwertmann, 1983; Scheinost and Schwertmann, 1999; Schwertmann et al., 1999; Liu et al., 2012; Wang et al., 2013; Jiang et al., 2018).

Understanding those specific circumstances where pedogenic processes may result in enhancing or depleting the magnetic signature of a soil is crucial to confidently interpreting rock magnetic data as a reliable climate proxy. In this paper, we contribute to ongoing research on the processes that might favor magnetic enhancement over depletion through studies of the magnetic mineralogy of the type section of the Blackwater Draw Formation (Reeves and Mahaney, 1976; Holliday, 1989). This formation consists of a series of Pleistocene eolian sediment-paleosol couplets preserved on the Southern High Plains (SHP) region of the United States (**Figure 1**), which display both magnetically depleted and magnetically enhanced eolian sediment-paleosol layers (Holliday, 1989; Gustavson and Holliday, 1999; Stine et al., 2020).

Through the use of a holistic data set which includes: rock-magnetic, geochemical, and scanning electron microscopy observations; our study reveals the complex environmental origins of the magnetic signal as a reflection of both changing provenance and weathering intensities. Moreover, through the use of geochemically-based climofunctions, three paleoenvironmental phases are identified. The earliest Phase (I) represents a period when increased aridity resulted in the relative preservation of the magnetic

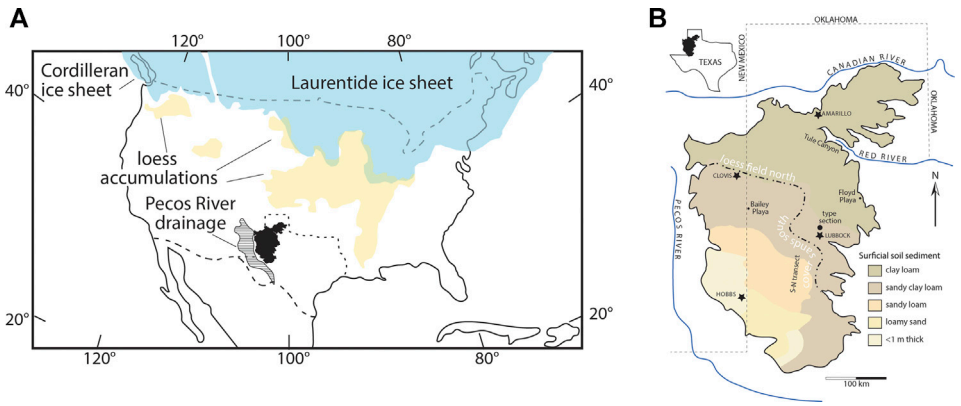

FIGURE 1 | (**A**) The North American continent during the Last Glacial Maximum (LGM), with emphasis placed on the location of major loess accumulations, the maximum extent of Northern Hemisphere ice sheets during the LGM, and the Pecos River drainage area. Distribution of loess is adapted from (Muhs, 2018), and sources therein). Extent of ice sheets is adapted from (Dyke et al., 2002). (**B**) Geographic extent of the Southern High Plains showing areas discussed in the text. Dashed line in center of the Southern High Plains defines the inferred boundary between loess and cover sands (after (Reeves and Mahaney, 1976)). Figure modified from (Stine et al., 2020).

signal, which is carried by southerly derived eolian coarse magnetic phases. This is followed by Phase II, characterized by a mix of southern sands and northern loess, where increased humidity results in magnetic depletion, through the destruction of magnetic phases. The soils of Phase III are similar to Phase II in that both are mixtures of southern sands and northern loess. However, Phase III represents an intermediate level of precipitation, i.e. great enough to result in magnetic enhancement but not so high as to destroy any newly made magnetic phases.

Using current age constraints, these environmental phases are tentatively correlated to Middle Pleistocene Transition (MPT), when interglacial-glacial cycles shifted from ~41-k.y. cycles to ~100-k.y. cycles. However, ambiguities in the age model makes it difficult to associate these environmental changes with larger scale climatic shifts.

BLACKWATER DRAW FORMATION

Geomorphic Evolution and Age

The Pleistocene Blackwater Draw Formation (BDF) is a series of eolian deposit-paleosol couplets that form a sheet like body across the Southern High Plains (SHP) in the south-central US. The SHP (often called the Llano Estacado) is a plateau covering ~ 130,000 km^2 across the Texas panhandle (**Figure 1**). The BDF varies in thickness across the SHP, commonly ranging from <1 to about 9 m thick, but locally is up to 27 m thick in the vicinity of Amarillo, Texas (Hovorka, 1995). Internally, the sediments are punctuated by distinct Bt and Bk pedogenic horizons, the number of which varies from 4 to 14 different units depending on location (Holliday, 1989; Hovorka, 1995; Stine et al., 2020). Notably, thicker intervals of the BDF tend to exhibit a greater number of paleosol profiles (Hovorka, 1995). The varying number of preserved paleosols likely reflects localized wind deflation or soil welding (Holliday, 1989). Nevertheless, each past soil-forming episode is considered a widespread phenomenon, and the (uppermost) soil , referred to as the "Surficial Soil", represents the most recent episode. Notably, the lack of exposures and a relatively low-resolution age model for the formation have made correlation of soil stratigraphy across the SHP problematic, especially in the oldest buried horizons (Holliday, 1989, 1997; Holliday et al., 1996a, 1996b, 2008; Gustavson and Holliday, 1999).

At some localities, the presence of the Guaje ash (ca. 1.4 Ma) in the lower sections of the BDF, where it is present above stage IV calcisols of the BDF, indicates that the base of the formation is likely older than ca. 1.4 Ma and potentially as old as ~1.9 Ma (Izett et al., 1972; Gustavson and Holliday, 1999). At the type-section, the focus of this study, the minimum age of the youngest paleosol is further constrained by an OSL date of ~0.12 Ma (Holliday, 1989). Although the Guaje ash is missing at the type-site, the identification of a magnetozone of reverse magnetic polarity implies that, at this specific locality, the lower part of the BDF must predate the Matuyama/Brunhes boundary and thus be older than ca. 0.773 Ma (Holliday, 1989; Patterson and Larson, 1990; Coe et al., 2004; Singer, 2014; Channell et al., 2020; Ogg, 2020).

Type Section

The type locality of the BDF is ~9 m in height and consists of five paleosols punctuated by a surficial soil horizon (Stine et al., 2020) (**Figure 2**). The topmost and youngest soil horizon is termed the "Surficial Soil"; the physical characteristics of which were all documented by Holliday (1989). This soil was classified as a Paleustalf that contains three distinguishable horizons: A, Bt, and Bk. The A horizon exhibits 5 YR 3/4 hues, is ~0.3 m thick, and is noted for having a sandy clay loam texture. The Bt horizon exhibits 5 YR 3/6 hues, is ~1 m thick, and has abundant clay films

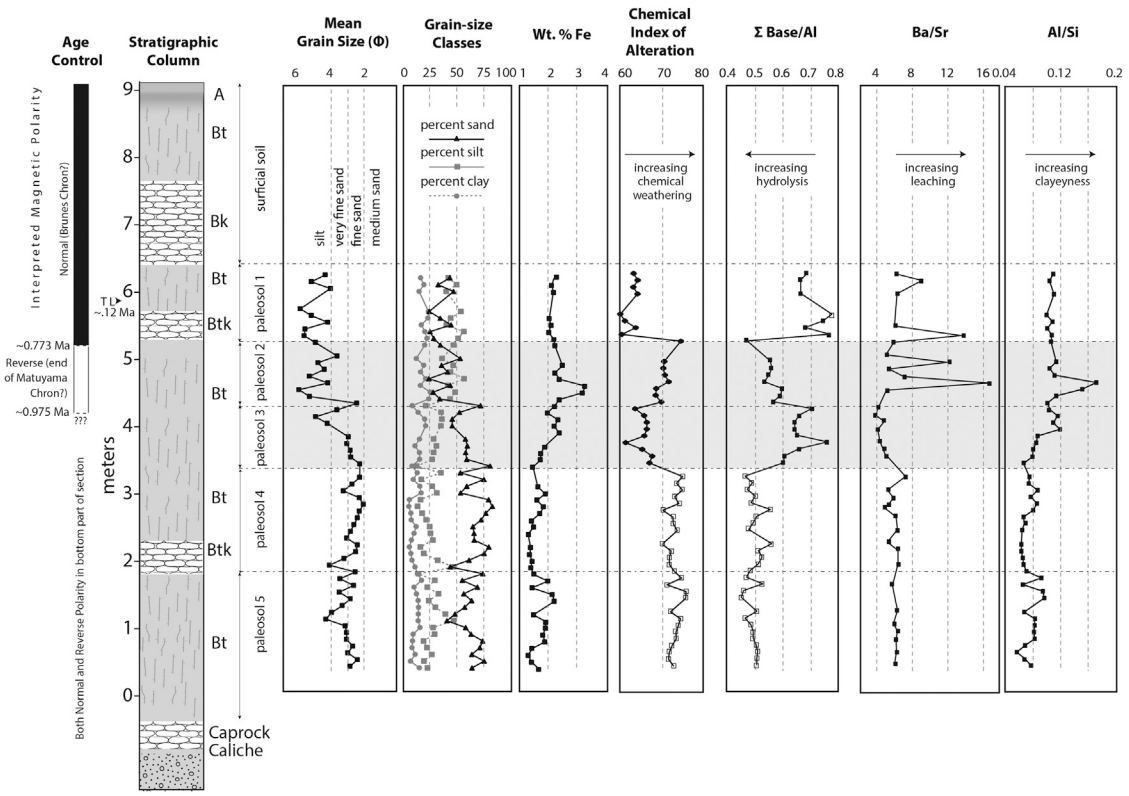

FIGURE 2 | Integration of sedimentologic, geochemical, and geochronologic data from the type section of the BDF. Horizontal lines represent soil boundaries. Grain-size data are reported in relative proportions of sand, silt, and clay. Geochemical samples were acid leached to remove calcium carbonate so that silicate weathering could be accurately assessed. Chemical index of alteration (CIA) is after (Nesbitt and Young, 1982). This figure also includes Wt % Fe vs depth, which was constructed using Table 1 from (Stine et al., 2020) note how Paleosol 2 has the highest percentage of Fe. (Stine et al., 2020) noted that the anonymously high CIA and ΣBase/Al values for Paleosol 4 and 5 were due to the high quartz content rather than high weathering and hence are represented with open squares. Nevertheless, CIA and ΣBase/Al values for the other paleosols are more representative of relative weathering intensity, and are represented with closed squares. Magnetic polarity is from (Patterson and Larson, 1990), and age calibration is from (Singer, 2014). Shaded gray background is the part of the section that closely aligns with the approximate duration (1250–700 ka) of the mid-Pleistocene transition from (Clark et al., 2006). TL—thermoluminescence-obtained date, from (Holliday, 1989). The stratigraphic position of the TL -date within Paleosol 1 is uncertain, hence it is currently interpreted to represent the minimum age of Paleosol 1. Soil horizon nomenclature follows standard (Soil Survey Staff, 1990) procedures. Figure modified from (Stine et al., 2020).

on ped facies. Similar to the A horizon, the Bt horizon of the Surficial Soil has a sandy clay loam texture (Holliday, 1989). The Bk horizon was described by Stine et al. (2020) as a Stage III calcic horizon that has 7.5 YR 5/8 hues, is ~1 m thick, and has a loamy texture.

Paleosol 1, classified as an argillic calcisol/calcic mollisol (Stine et al., 2020), is 1.3-meter thick and contains a Bt and Bk horizon, both of which exhibit 2.5YR 3/6 hues. The Bt horizon displays subangular blocky peds in clay-rich pockets, while the Bk horizon contains vertical columns of carbonate that grade laterally into zones of calcareous nodules that envelop quartz grains. Mean grain size (D^{50}) of the interval is coarse silt (5ϕ; 31 μm). Additionally, the average mode is displaced from the mean towards the coarser fraction, or finely skewed frequency distribution. Vertically, the interval records a slight coarsening-upward profile.

Paleosol 2, classified as a loamy argillisol/mollisol (Stine et al., 2020), is slightly more than a meter thick. This soil is characterized by a single Bt horizon composed of angular circumgranular peds with 2.5 YR 3/6 hues. Mean grain size varies from fine sand in the basal 20-cm to medium to coarse silt (6-4ϕ; 15-63 μm) throughout the rest of the interval. Paleosol 2 is similar to paleosol 1 in that the mean is coarse skewed; however, this horizon shows a slightly coarser signature. It should be noted that this horizon was identified via unique geochemical and rock-magnetic signatures (Stine et al., 2020), visually it can be difficult to distinguish paleosol 2 from vertically adjacent horizons in outcrop.

Paleosol 3, classified as an argillic protosol/mollisol (Stine et al., 2020), is about 70-cm thick. This paleosol is characterized by a single Bt horizon composed of prismatic peds exhibiting 2.5 YR 3/6 hues. Mean grain-size increases upward from fine sand (2.29ϕ; 31 μm) in the basal 30 cm to coarse silt (5ϕ; 31 μm) at the top of the interval. Pedogenic carbonate is observed only locally as matrix.

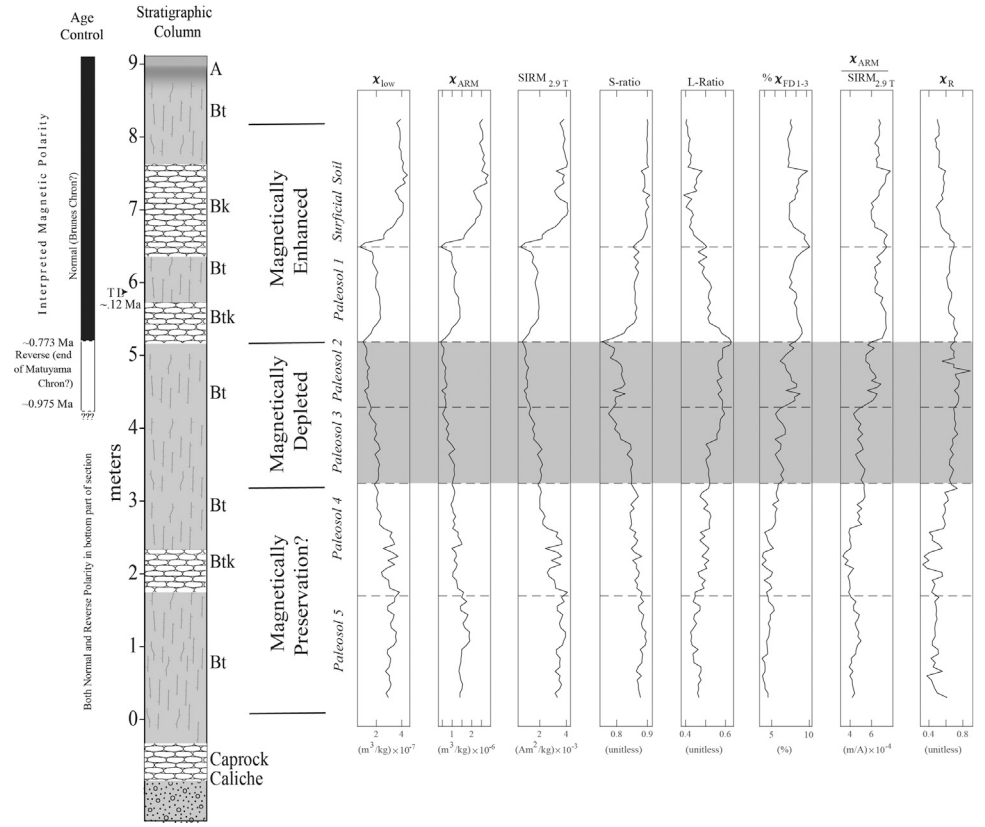

FIGURE 3 | Principal rock-magnetic parameters (χ_{low}, χ_{ARM}, and $SIRM_{2.9T}$) in addition to Environmental-magnetic ratios (S-ratio, L-ratio, $\%\chi_{FD1\text{-}3}$, $\chi_{ARM}/SIRM_{2.9T}$, and χ_R) all plotted as a function of depth in the type section. Note the similarity in behavior among all of the principal rock-magnetic parameters. The various rock-magnetic experiments in this paper show that the principal rock-magnetic parameters are primarily a reflection of the concentration of low-coercivity ferrimagnetic phases (magnetite and maghemite) (Thompson and Oldfield, 1986; Evans and Heller, 2003; Jordanova, 2016). This is supported by the high and low values of the S-ratio(Stine et al., 2020) and L-ratio (this study), respectively (Liu et al., 2007b). Low $\%\chi_{FD1\text{-}3}$, $\chi_{ARM}/SIRM_{2.9T}$, and χ_R values for Paleosols 5 and 4 imply that the magnetic signal is controlled primarily by a wide distribution of coarse magnetic phases, which were likely detrital in origin (Thompson and Oldfield, 1986; Evans and Heller, 2003; Hrouda, 2011; Jordanova, 2016; Stine et al., 2020). By contrast the relatively high $\%\chi_{FD1\text{-}3}$, $\chi_{ARM}/SIRM_{2.9T}$, and χ_R values for Paleosols 3- Surficial Soil implies that the magnetic signal is controlled by fine, potentially SP-SD magnetic phases (Hrouda, 2011; Maxbauer et al., 2016a), and thus the magnetically enhanced and depleted signals are likely a reflection of environmental processes.

Paleosol 4 represents a marked contrast from overlying horizons. This interval, classified as an argillic calcisol/aridisol (Stine et al., 2020), is about 1.5-m thick and contains a Bt and Bk horizons. The Bt horizon is characterized by a massive ped structure with 5 YR 9/1 hues, while the underlying Bk horizon is composed of columnar and nodular carbonate with 5 YR 9/1 hues. Mean grain size is demonstrably coarser than overlying layers and is predominantly fine sand (2.21ϕ; 216 μm).

Paleosol 5, classified as an argillic calcisol/aridisol (Stine et al., 2020), is about 2.2 m thick and rests directly above the Caprock Caliche. This interval is characterized by a single Btk horizon with 5 YR 4/8 hues, consisting of abundant pedogenic carbonate as isolated nodules or matrix. However, vertical columns of pedogenic carbonate are absent. This soil shows a relatively constant grain size that averages around fine sand (3.18ϕ; 110 μm).

Based on detailed geochemical (**Figure 2**), rock-magnetic parameter, and environmental magnetic ratio data sets (**Figure 3**), Stine et al. (2020) concluded that the lowermost paleosols (Paleosols 5 and 4) experienced relatively minor degrees of weathering, and therefore that the relatively high magnetic signal in them was in part due to the relative preservation of magnetic parent material. Anonymously high chemical index of alteration (CIA) values for Paleosols 5 and 4 were attributed to the high quartz content and thus were disregarded for those two layers (**Figure 2**). Moreover, given the existing age constraints, Paleosols 5 and 4 record conditions prior to the Matuyama/Brunhes boundary (Patterson and Larson, 1990), either prior to or during the onset of the Middle Pleistocene transition (Imbrie et al., 1993). In contrast, Paleosols 3 and 2, which directly overlie Paleosols 5 and 4, experienced a relatively high degree of weathering and hence the low magnetic values from these soils are characterized by as a magnetically depleted signal (Stine et al., 2020). Finally, the uppermost horizons, Paleosol 1 and the Surficial Soil, which displayed the highest magnetic values, experienced a moderate degree of weathering and are

defined as having a magnetically enhanced signal (Stine et al., 2020).

The Middle Pleistocene Transition

Between about 1.2 and 0.7 Ma, the climate cycles of the planet shifted from being primarily influenced by a ~41-ka obliquity cycle to one that was dominated by a ~100-ka eccentricity cycle (Imbrie et al., 1993). This shift in the temporal frequency of glacial and interglacial cycles is referred to as the Middle Pleistocene transition (MPT) and one of its most noticeable effects was the global increase in ice volume (Mudelsee and Schulz, 1997; Head and Gibbard, 2005; Clark et al., 2006; Clark, 2012). However, the 100-ka frequency is the weakest orbital parameter (Imbrie et al., 1993; Nie et al., 2008; Clark, 2012), therefore determining the forcings responsible for the MPT has been the subject of a large body of research, and various explanations have been proposed. Some workers suggest that longer-lived and larger northern hemisphere ice sheets that developed after the onset of the MPT are the direct result of an internal forcing (Nie et al., 2008; Lisiecki, 2010). The causes of which potentially include: long-term global cooling and CO_2 decline [e.g. (Raymo et al., 1988, 1997; Berger and Jansen, 1994b, 1994a; Raymo, 1994, 1997)], disruption or alteration of the thermo-haline, deep-water ocean current (Schmieder et al., 2000), increased volume of sea-ice (Tziperman and Gildor, 2003), or El Niño-Southern Oscillation patterns in the tropical Pacific ocean (McClymont and Rosell-Melé, 2005; Yu et al., 2018). However, in contrast to the previous hypotheses that focus on northern hemisphere ice buildup, Elderfield et al. (2012) proposed that the post-MPT 100-ka cycle was initiated by an abrupt increase in Antarctic ice volume at about 900 ka, implying that changes in northern hemisphere ice volume were the consequence of southern hemisphere ice buildup.

Nevertheless, most of these models rely heavily on sedimentologic and geochemical data from marine settings. In order to more fully understand the climatic effects of the MPT, additional data are needed from terrestrial settings. The challenge lies in the fact that many Quaternary loess deposits in North America are relatively thin (~20 m or less) and with few exceptions are no older than the penultimate glacial period (ca. 110 ka) (Muhs, 2018). This is in contrast to the thick and continuous loess-paleosol deposits in Central Asia that continuously span from the Holocene to at least the early Miocene and potentially even to the Oligocene (Head and Gibbard, 2005; Liu et al., 2007a; X. M. ; Liu, 2007; Muhs, 2013, 2018; Nie et al., 2016; Bird et al., 2020). A notable exception is the Quaternary BDF that mantles the Southern High Plains (SHP) in North America (Holliday, 1989; Holliday et al., 1996a, 1996b). Existing age control of the BDF indicates that these sediments span at least the last 1.4 Ma and potentially up to the last 2.0 Ma, therefore it is likely that the MPT is recorded within the BDF (Holliday, 1989; Patterson and Larson, 1990; Imbrie et al., 1993; Gustavson and Holliday, 1999). Implications that the MPT had on the specific environmental conditions that favor either magnetic enhancement or depletion within the type site of the formation are contemplated more extensively within the discussion section.

METHODS

The type locality of the BDF (Reeves and Mahaney, 1976) where we collected the suite of samples for this study lies 21 km north of Lubbock, Texas (33.766269°-101.874261°). Exposures of BDF deposits are rare on the SHP but here a gulley that first acted as an anthropogenic thoroughfare has incised down to the Caprock Caliche on top of the Ogallala Formation; this provides a complete section of the formation. A total of ~7 m of the BDF was able to be sampled for rock-magnetic measurements, from ~40 cm above the underlying Ogallala Formation to ~1.6 m into the Surficial Soil. The base of the formation was inaccessible due to cover and the top of the formation into the uppermost Surficial Soil was not sampled due to anthropogenic disturbance.

Samples for rock-magnetic analyses were obtained at ~5-cm intervals and were dug out of the exposure and collected into plastic bags after scraping away a few centimeters of surficial material with non-magnetic copper-beryllium tools. In the laboratory, samples were cleaned of any organic material, gently disaggregated with a mortar and pestle, and packed into standard (IODP, 7 cc internal volume) plastic boxes, while the remaining sediment were placed into marked plastic bags for future rock-magnetic tests. Once fully prepared these plastic boxes, served as the primary specimens for the rock-magnetic data vs depth measurements previously published in Stine et al. (2020), including: mass-normalized bulk magnetic susceptibility measured at 976 Hz (χ_{low}) and 15,616 Hz (χ_{high}); ARM measurements at AF fields of 100 mT with a DC bias field of 0.01 mT; IRM measurements measured at field intensities of 100 mT (IRM_{100mT}) , 300 mT (IRM_{300mT}), a saturating field of 2.9T (SIRM), and a back-field of -300 mT (IRM_{-300mT}). It should be noted that for this paper, the anhysteretic remanent susceptibility (χ_{ARM}) will be used in liu of the ARM reported by Stine et al. (2020). χ_{ARM} was calculated by normalizing the ARM data previously reported by Stine et al. (2020) to the DC bias field of 0.1 mT (79.77 A/m). Normalizing the ARM to χ_{ARM} does not change the signal behavior, nevertheless calculation of χ_{ARM} is recommended in order for future studies to compare the results here with data from other sites (Maher, 1998; Evans and Heller, 2003; Peters and Dekkers, 2003).

Environmental-magnetic ratios calculated from this complete set of rock-magnetic data included parameters previously reported in Stine et al. (2020): The S-ratio, $HIRM_{300mT}$, $\%\chi_{FD1-3}$, χ_{ARM}/χ_{low}, and χ_{ARM}/SIRM. Additionally, this paper will also compare two new environmental-magnetic ratios: χ_R and the L-Ratio. These environmental magnetic ratios were calculated by measuring mass-normalized bulk magnetic susceptibility measured at 3,904 Hz (χ_{med}) and a backfield IRM of -100 mT (IRM_{-100mT}). Bulk magnetic susceptibility was measured using a MFK 1-A Agico Kappabridge, while bulk

remanence measurements were made using an Agico JR6-A spinner magnetometer. All rock-magnetic parameters and environmental magnetic ratios are displayed in **Supplementary Datasheet S1**.

χ_R is a rock-magnetic parameter first proposed by Hrouda (2011) which is theoretically independent from dia-, para-, and MD ferromagnetic contributions in sediments. χ_R is useful for determining the difference between wide and narrow distributions of mean grain-size volume of SP-SSD particles in a sediment (Hrouda, 2011). It is calculated by the following equation:

$$X_R = \frac{X_{low} - X_{med}}{X_{med} - X_{high}}$$

The L-ratio first developed by Liu et al. (2007b) is interpreted to reflect coercivity variations in magnetically harder phases (i.e. hematite and/or goethite) where low/high values represent low/high coercivities respectively. It is calculated using the following equation:

$$L - RATIO = \frac{[0.5*(SIRM + IRM_{-300mT})]}{[0.5*(SIRM + IRM_{-100mT})]} = \frac{HIRM_{300mT}}{HIRM_{100mT}}$$

Select rock-magnetic data and environmental data from this study and from Stine et al. (2020) are plotted against depth in **Figure 3**. Calculations and common interpretations of all rock-magnetic parameters and environmental parameters presented in **Figure 3** are summarized in **Supplementary Datasheet S1, S2**, respectively. Moreover, all rock-magnetic parameters and environmental magnetic ratios from this study and from Stine et al. (2020) are displayed in **Supplementary Datasheet S1**.

In order to determine magnetic mineralogy several rock-magnetic experiments were conducted on representative specimens from each paleosol. These specimens were collected from the remaining sediment not packed into corresponding plastic boxes. Specimens were chosen based on how closely the χ measurements of a corresponding box specimen matched the median value for the paleosol as a whole. The corresponding depths are displayed on each figure in order to allow for easier correlation between the results published here and Stine et al. (2020).

Bulk magnetic susceptibility versus continuous heating/cooling experiments (χ vs temperature [T]) were conducted using ~0.7 g of material in an argon environment with a MFK 1-A AGICO Kappabridge interfaced with a CS4 thermal-heating attachment. First-order numerical derivatives of the bulk magnetic susceptibility with respect to temperature ($d\chi/dT$) were calculated in order to determine the Curie temperature. However, this process of differentiation did enhance noise, therefore a loess model with a 0.25°C-window was constructed, using the smooth.m function on Matlab R2019b. and compared to the raw $d\chi/dT$.

Step-wise acquisition of IRM, from 0 to ~2.9 T, was imparted on representative samples using an ASC impulse magnetizer, and measured using a JR-6A dual-spinner magnetometer. Following an applied field of 2.9 T, where saturation was essentially reached, the samples were then subjected to step-wise progressive DC demagnetization of IRM until the magnetization crossed the abscissa, defining the coercivity of remanence (H_{cr}). Magnetic-component unmixing analysis using the MAX UnMix protocol (Maxbauer et al., 2016b) was used in order to accurately determine the contribution of magnetic phases to the IRM signal.

In order to conduct the three-component test, ~1 g of material was taken from representative samples from all six soils. This material was then mixed with zircar cement after being placed into a 7 cc nonmagnetic ceramic box (Pluhar and Kirschvink, 1991; Prothero, 2011), these served as the primary specimens for the experiment. After drying, each specimen was imparted with a high-coercivity IRM (2.9 T), a medium-coercivity IRM (300 mT) and a low-coercivity IRM (50 mT), in that order, along three perpendicular axes. The magnetic remanence of each specimen was measured as it was progressively stepwise heated from room-temperature to ~685°C (Lowrie, 1990). All measurement were conducted using a 2G-Enterprises cryogenic magnetometer equipped with DC squids housed in a magnetically shielded room at the University of Texas at Dallas.

For measurements requiring smaller volume specimens, pressure pellets for each paleosol were prepared. This was done by mixing 0.03 g of sample with 0.1 g of Spectroblend binding material, once mixed the sample was then placed within a pellet die assembly and flattened with a hydraulic press for approximately 3 min. This process forms solid cylindrical specimens that are compact enough to prevent movement of the grains during various room temperature and low temperature measurements.

Room-temperature measurements conducted on the pressured pellets included hysteresis and First-Order Reversal Curves (FORCS). Both of which were measured on a PMC Vibrating Sample Magnetometer (VSM) 3900 series. Analysis of the first order reversal curves was conducted using FORCinel v. 3.0 originally designed by Harrison and Feinberg (2008).

Low-temperature remanence experiments were also conducted on the pressure pellets at the Institute for Rock Magnetism at the University of Minnesota, Minneapolis. All low-temperature remanence experiments were conducted using the Magnetic Properties Measurement System (MPMS-XL). Low-temperature remanence experiments included low-temperature demagnetization of room temperature Saturated-IRM (RTSIRM-LTD), the FC-ZFC procedure, and the low temperature hematite-goethite test (Lagroix and Guyodo, 2017).

The theoretical goethite contribution was removed from the RTSIRM-LTD by constructing a model similar to the parabolic behavior seen by synthetic goethite manufactured by the Alifa Aesar Co. (Lascu and Feinberg, 2011). For each Paleosol, this parabolic model was constructed using a loess smoothing model with a 100 K-window on the warming curves of the RTSIRM-LTD data. By subtracting this model from the raw-data, phase transitions (i.e the Morin and/or Verwey transition) become more evident.

The hematite-goethite test is a slight variation from that originally proposed by Guyodo et al. (2006), Lagroix et al. (2014), and Lagroix and Guyodo (2017), in that it involves

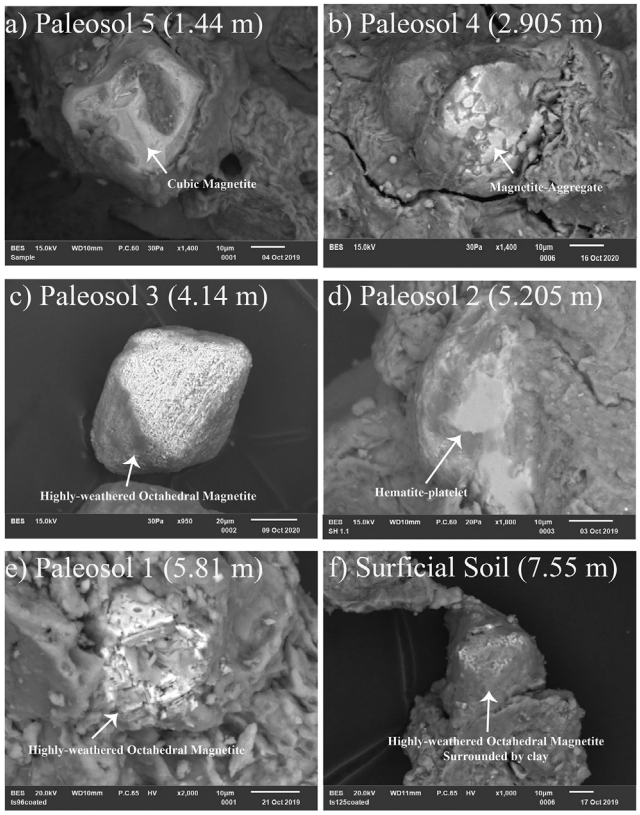

FIGURE 4 | Scanning electron microscopy (SEM) images of Blackwater Draw sediment images a-f respectively represent specimens from Paleosols 5-Surficial Soil. (**A**) Paleosol 5: Cubic shaped magnetite grain surrounded by clay, note the general absence of shrinkage cracks. (**B**) Paleosol 4: Aggregation, of magnetite particles, the triangular faces are interpreted to represent octahedral faces. (**C**,**E**,**F**) Paleosol 3,1, and Surficial Soil respectively: Heavily weathered magnetite grains, the shattered appearance of the grain is interpreted to represent an overabundance of shrinkage cracks, which in turn suggest low-temperature oxidation (Johnson and Merrill, 1973; Petersen and Vali, 1987; Cui et al., 1994; Zhou et al., 2001; Vahle et al., 2007; Gehring et al., 2009; Nowaczyk, 2011; Haltia and Nowaczyk, 2014). (**D**) Paleosol 2: Hematite platelet, in general the SEM was only able to detect a few examples of hematite in the specimens (Supplementary Files C_I–C_VI); this suggests that the majority of hematite content is likely submicron in scale.

subjecting the sample to a continuous magnetic field of 2.5 T while simultaneously heating the sample from room temperature (~300 K) to the Néel temperature of goethite (~400 K) (Mathé et al., 1999) and back to room temperature.

Afterwards the DC field is removed and the MPMS is set to oscillation mode which generates an oscillating DC current that begins at –300 mT and then decreases in amplitude until the sample is in a near-zero field, thus subjecting the sample to a rough equivalent of being AF demagnetized at 300 mT (Lagroix et al., 2014; Lagroix and Guyodo, 2017; B. Moskowitz and Dario Bilardello, personal communication, 2020). The purpose of this AF demagnetization procedure at ~300 mT is to eliminate any contribution from lower coercivity phases (i.e. magnetite/maghemite), although it should be noted that this AF procedure is considered to be not as effective as more traditional methods (Bruce Moskowitz and Dario Biladerllo, personal communication, 2020). After AF demagnetization, the remanence of the sample is measured while it is simultaneously cooled from 300 K to 15 K in a zero field. Then the remanence is measured while the sample is heated from 15 K to 400 K, which should thermally unblock any remanence residing in goethite. Finally, the remanence of the sample is measured while the sample is cooled from 400 K to 15 K and warmed back to room temperature. During this final step any remaining remanence can be attributed to those magnetic phases with a coercivity greater than 300 mT and a Néel temperature greater than 400 K (i.e. hematite).

In addition to low temperature remanence measurements, Mössbauer spectroscopy experiments were also conducted on representative specimens at the Institute of Rock Magnetism. Five representative specimens, as magnetic separates, were measured on a Ranger Scientific Mössbauer Spectrometer. All specimens were measured at room temperature, and three of the five specimens were also measured at 18 K in order to determine the presence of magnetic phases with low blocking temperatures. All Mössbauer spectra were fitted to known models using the mossferret software available at the Institute of Rock Magnetism.

Finally, scanning electron microscopy (SEM) inspection was carried out on six representative samples in order to determine the presence of micron scale (or larger) magnetic mineral phases. In order to maximized the likelihood of observing magnetic minerals, a neodymium magnet was used to magnetically separate magnetic phases from nonmagnetic phases of detrital or pedogenic origin (i.e., quartz, calcite, clay minerals). All SEM inspection was conducted on these magnetic separates.

RESULTS

Scanning Electron Microscopy

SEM inspection of the six magnetic separates from representative samples shows that the samples consist largely of clay minerals and quartz, although some Fe-oxide grains, interpreted to be either magnetite (**Figure 4A-C**, and e-f) or hematite (**Figure 4D**), are present. Moreover, monazite was also observed in specimens from Paleosol 1 and the Surficial Soil (**Supplementary Datasheet S5, S6**). Fe-oxide grains (e.g., hematite or magnetite/maghemite) are readily identified based on their higher atomic number and resulting brightness relative to surrounding clay minerals (Ul-Hamid, 2018) and by energy dispersive X-ray analysis (EDS) spectra (**Supplementary Datasheet S1-S6**). If apparent, crystallographic form and habit were used to further define an Fe-oxide as either magnetite (isometric forms such as cubes or octahedrons if, possibly, authigenic in origin or sub-rounded to rounded, anhedral, somewhat equant forms if detrital) or hematite (platy, micaceous, or tabular habit if authigenic) (Schwertmann and Cornell, 1991; Cornell and Schwertmann, 2006; Klein and Dutrow, 2007) (**Figure 4**). Some magnetite grains, inferred to be of detrital origin on the basis of their morphology, show shrinkage cracks (**Figure 4C,E,F**), which is evidence of low-temperature oxidation of magnetite into

maghemite (Johnson and Merrill, 1973; Petersen and Vali, 1987; Cui et al., 1994; Zhou et al., 2001; Vahle et al., 2007; Gehring et al., 2009; Nowaczyk, 2011; Haltia and Nowaczyk, 2014). Hematite particles are present (**Figure 4D**) yet scarce in all specimens observed (**Supplementary Datasheet S1-S6**). No grains unambiguously identified as goethite were identified in these specimens.

SEM observations show that the specimens from Paleosols 5-4 appear to have the highest concentration of what are inferred to be detrital Fe-oxide particles (**Figure 4A,B**), although some shrinkage cracks, indicative of maghemitization, were noted (**Supplementary Datasheet S1, S2**). Fe-oxide grains showing clear shrinkage cracks become much more prevalent, at the expense of fresher grains, in the specimen from Paleosol 3 (**Figure 4C**). Additionally, the intensity of grain cracking, potentially indicative of past weathering intensities, is more severe in Paleosol 3, with some magnetite grains appearing to be so damaged that they appear porous (**Figure 4C**). With the exception of a few tabular hematite crystals (**Figure 4D**) there are notably fewer observable Fe-oxides in the specimen from Paleosol 2, at least in the scale of resolution by the SEM. Nevertheless, it should be noted that some submicron Fe-oxides are evident in Paleosol 2, although their specific mineralogy is ambiguous (**Supplementary Datasheet S4**). Fe-oxide grains present in the specimens from Paleosol 1 and the Surficial Soil are largely characterized by shrinkage cracks (**Figure 4E,F**) resulting in a "shattered" appearance.

Rock-magnetic data and environmental proxies vs depth

Comparing rock-magnetic parameters from this study and Stine et al. (2020) allow for the calculation of two new environmental-magnetic ratios: χ_R and the L-ratio. Summaries of the calculation and common interpretation of the environmental-magnetic ratios obtained in this study and in Stine et al. (2020) are provided in **Supplementary Datasheet S1, S2**.

When compared to depth, the L-ratio at appears to be the inverse of the S-ratio, though subtle differences are apparent in Paleosols 2-Surficial Soil upon closer inspection (**Figure 3**). Paleosol 2 has a relatively narrower distribution of L-ratio compared to S-ratio values, which implies a smaller variation in the concentration of higher coercivity phases (i.e. hematite and goethite) compared to lower coercivity phases (i.e magnetite and maghemite) (Liu et al., 2007b). Moreover, the L-ratio appears to be more efficient than the S-ratio at demarcating the boundaries between the Bt and Bk horizons of Paleosol 1 and the Surficial Soil. These boundaries, correlate to subtle increases in L-ratio values, implying that each layer is separated by a slightly higher concentration of higher coercivity phases (Liu et al., 2007b).

The χ_R signal is distinct from the other environmental magnetic ratios, in that values begin to steadily increase in the top half of Paleosol 4, reaching peak values in Paleosol 2, and then begin to decrease in Paleosol 1. This behavior seemingly forms a concave arc which is facing lower values (**Figure 3**). High/low values for χ_R are interpreted to correlate to narrow/wide distributions of magnetic grain-sizes, respectively (Hrouda, 2011). Therefore, paleosol 2 which has the highest median χ_R values (0.7111) is interpreted to be characterized by a relatively more homogenous (in terms of grain-size) population of magnetic phases. By contrast, Paleosol 5, the bottom half of Paleosol 4, and the Surficial Soil are interpreted to more likely constitute a mix of varying grain sizes due to their low median χ_R values of 0.4729, 0.4353, and 0.5625, respectively.

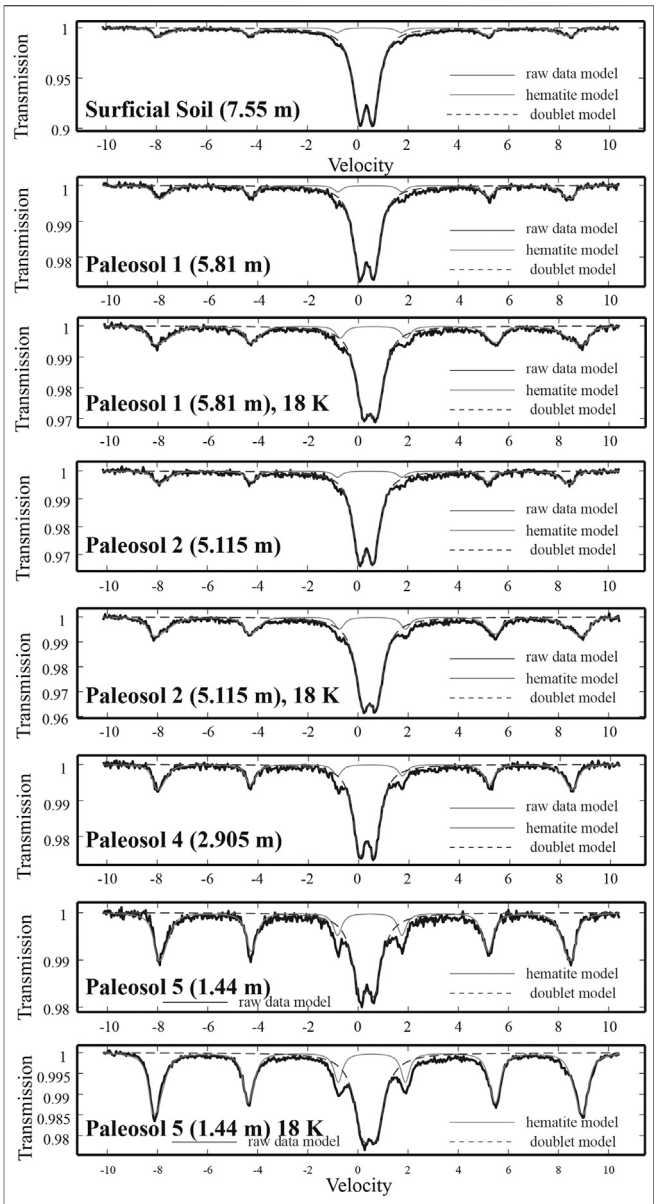

FIGURE 5 | Room temperature Mössbauer spectra of samples from the Surficial Soil, Paleosol 1, Paleosol 2, Paleosol 4, and Paleosol 5; in addition to low temperature spectra of Paleosols 1,2, and 5. Regardless of temperature of the experiments, all spectra can be fit to a hematite model and a doublet model, the latter indicating paramagnetic material (de Grave and Vandenberghe, 1990; Vandenberghe et al., 2000; Zhi et al., 2000; de Grave et al., 2002; Jeleńska et al., 2010; Necula et al., 2015).

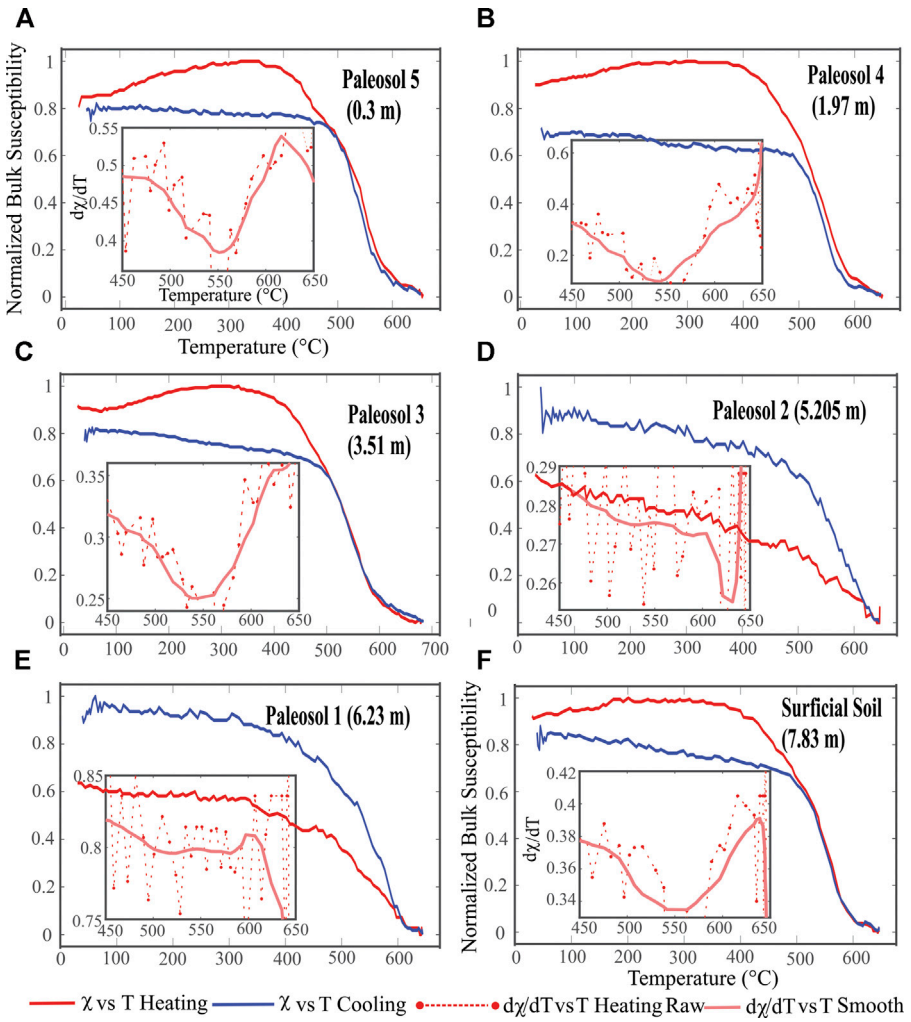

FIGURE 6 | Results of bulk magnetic susceptibility vs heating/cooling (red, blue respectively) experiments for representative samples from all soil horizons identified in the BDF for Paleosol 5 (6a), Paleosol 4 (6b), Paleosol 3 (6c), Paleosol 2 (6d), Paleosol 1 (6e), and the Surficial Soil (6f). The derivative of bulk magnetic susceptibility with respect to temperature (dχ/dT) is inset in the bottom left of each graph. The red-dashed lines represents the raw dχ/dT, while the light reddish-pink line represents the smoothed model, which was created in order to highlight the general trends. In general, the smoothed dχ/dT shows Curie temperatures of ~540°-560°C indicates the presence of low-Ti magnetite and or partially maghemitized magnetite (Tarling, 1983; Maher and Thompson, 1999; Hanesch et al., 2006). Loss of susceptibility after heating is interpreted to represent the inversion of maghemite into hematite (Dunlop and Özdemir, 1997).

Mössbauer Spectroscopy

Mössbauer spectroscopic experiments were conducted on magnetic separates from representative samples from five of the six paleosols in the type section. All Mössbauer spectra display a sextet with a doublet (**Figure 5**). Modelling of the sextet form suggests that all samples are dominated by hematite (de Grave and Vandenberghe, 1990; Vandenberghe et al., 2000; Zhi et al., 2000; de Grave et al., 2002). This implies that any magnetite identified in other rock magnetic experiments is extremely minor in terms of weight/modal percent, despite dominating the overall magnetic signal. The persistence of the doublet at low temperatures indicates that it is caused by Fe-bearing paramagnetic clay minerals, such as illite or Fe-bearing kaolinite (Jeleńska et al., 2010; Necula et al., 2015).

TEMPERATURE DEPENDENT BEHAVIOR OF SUSCEPTIBILITY AND REMANENCE

Bulk Susceptibility vs Temperature experiments

Most magnetic susceptibility vs. heating/cooling experiments yield a relatively low (~8 to 6 percent) reduction in susceptibility upon cooling, implying that during the heating process the original magnetic mineralogy is partially thermally altered to new phases with reduced magnetic susceptibility (**Figure 6**). This behavior suggests the transformation of either maghemite (which is thermally unstable) and/or magnetite into hematite, which results in a loss of magnetization (Tarling, 1983; Maher and

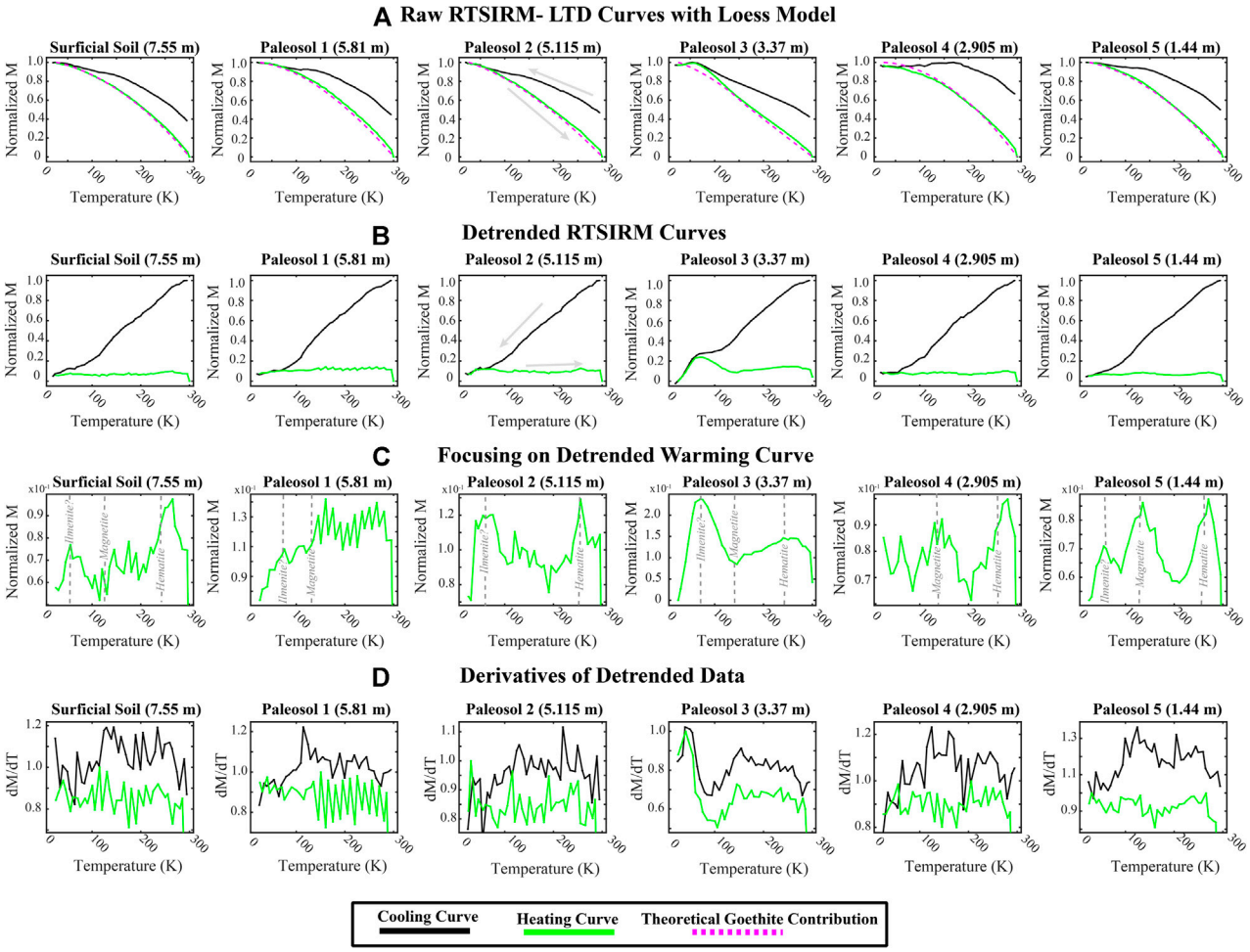

FIGURE 7 | RTSIRM-LTD data. 7a: Cooling (black) and warming (green) RTSIRM curves for all five paleosols and the Surficial Soil. Note the humps present on the cooling curve, this is indicative of maghemitization (Özdemir and Dunlop, 2010). The dashed purple line is a loess smooth of the warming curve, representing the potential contribution of goethite which often has a similar parabolic shape in RT-SIRM curves of synthetic samples (Lascu and Feinberg, 2011). 7b: Subtracting the loess-model from the raw RT-SIRM data, this theoretically removes the goethite contribution. 7c: Focusing on the detrended warming curve, note how the Morin (T_M) and Verwey (T_V) transitions are now visible (Verwey, 1939; Morin, 1950). 7d: Derivatives of the Smoothed RTSIRM curves with respect to temperature. Note the change in slope of the dM/dT cooling curves at ~120 K evident in all the soils, this is interpreted to be the Verwey transition that the detrending procedure enhances.

Thompson, 1999; Hanesch et al., 2006; Zan et al., 2017). Further evidence of experimentally induced thermal alteration is supported by the observation that the heating curves of Paleosols 5, 4, 3, and the Surficial Soil (**Figure 6A,B,C**) demonstrate a noticeable increase in magnetic susceptibility between ~200°C and ~400°C. This behavior is potentially caused by maghemite becoming superparamagnetic before reaching its Curie temperature (Gehring et al., 2009). However, considering that the specimens lose most magnetization between ~580 and 600°C and also the fact that most samples only display a slight decrease in magnetic susceptibility once cooled to room temperature, the likely magnetic mineral assemblage is dominated by magnetite with a relatively minor contribution from maghemite. Smoothing the derivatives of the heating curves shows that most samples have Curie temperatures ranging from ~540°C ~550°C, implying a titanomagnetite with low Ti concentration (**Figure 6**) (O'Reilly, 1976, 1984; Dunlop and Özdemir, 1997; Fabian et al., 2013). Above ~620°C all samples still display a weak magnetic signal, which is consistent with the presence of hematite, which becomes paramagnetic above ~675°C (Néel temperature) (Dunlop and Özdemir, 1997).

Paleosol 1 (**Figure 6E**) shows a substantial (up to ~60%) increase in susceptibility with cooling and this behavior suggests that the magnetic signal is due to magnetite alone with small contributions from hematite. The increase in magnetic susceptibility is likely due to some of the hematite fraction being converted to magnetite during heating (Tarling, 1983; Zan et al., 2017).

Low Temperature Behavior: RTSIRM LTD & ZFC-FC Curves

Low temperature behavior of remanence permits the identification of certain magnetic minerals without risking any

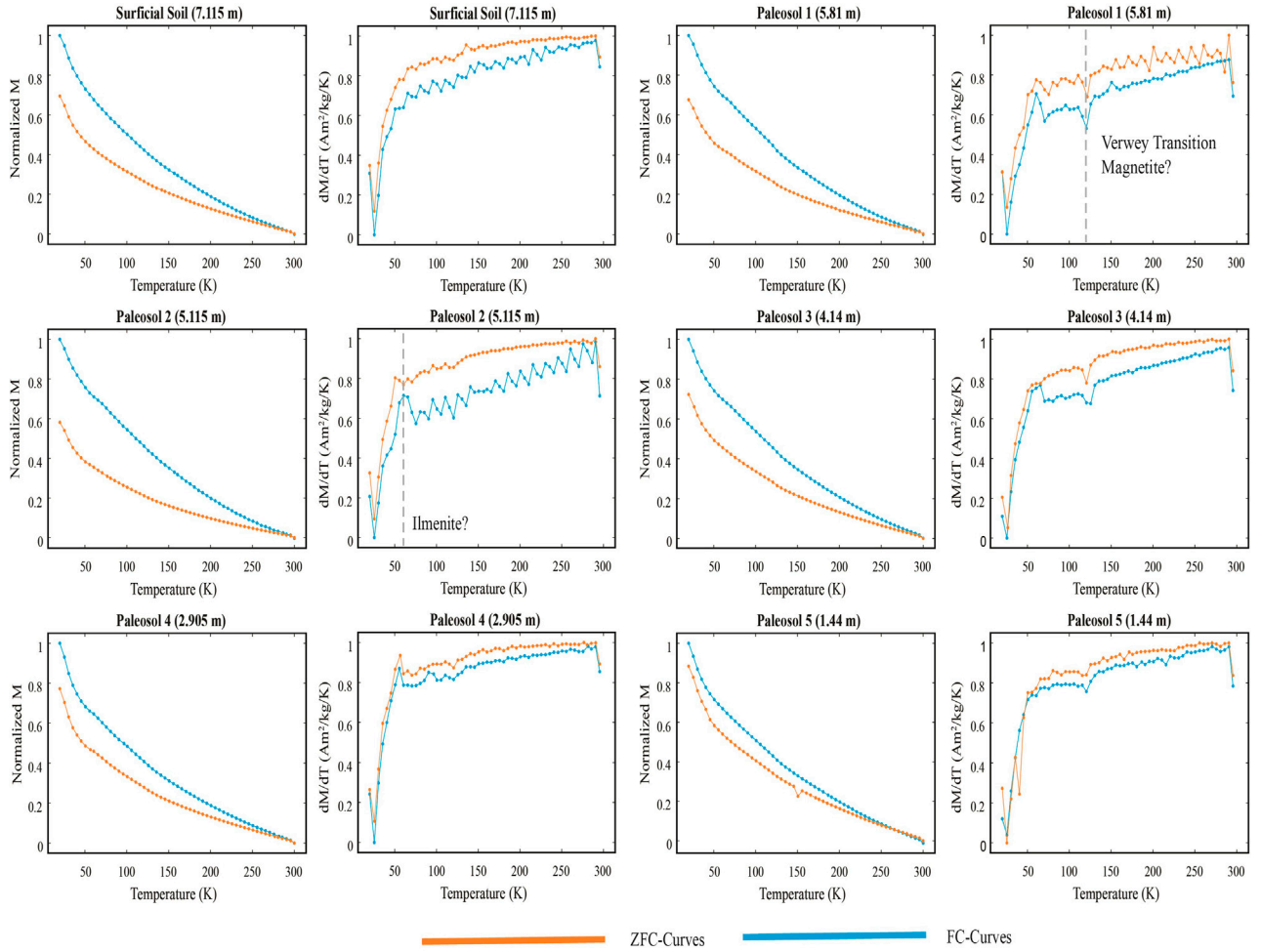

FIGURE 8 | ZFC (orange) and FC (blue) curves for all five paleosols and the Surficial Soil. Derivatives of the FC/ZFC curves with respect to temperature are displayed to the left of each paleosol. Note the subtle change in slope at ~120 K, most evident in Paleosols 1,3, and 5. This change (represented as a sharp drop in the derivatives) is interpreted to represent the Verwey transition of magnetite (Verwey, 1939).

form of chemical alteration commonly associated with experiments at elevated temperatures. Moreover, certain magnetic minerals display diagnostic behavior at depressed temperatures, including the "Verwey transition" (~120 K) and the "Morin transition" (~250-260 K), exhibited by magnetite and hematite, respectively (Verwey, 1939; Morin, 1950). When either of these minerals are cooled to and below those temperatures, a marked change in magnetization is identified, which is correlated to first order phase transitions of the minerals (Verwey, 1939; Morin, 1950; Stacey and Banerjee, 1974)

A slight change in slope, potentially caused by the Verwey transition, is shown by both the RTSIRM-LTD and ZFC-FC curves for all samples (**Figures 7**,**8**). The reason why the transition is so subtle could be potentially due to partial maghemitization of the magnetite grain surfaces, which has been shown to shift, subdue, or even mute the Verwey transition (Özdemir and Dunlop, 2010). Further evidence for maghemitization is revealed by the wide humps observed within all the RTSIRM-LTD data, which form wide arcs that begin at ~300 K and terminate at ~120 K that later of which corresponds to the Verwey transition (**Figure 7**). The specimen from Paleosol 3 serves as the exception, with a narrow hump around 100 K – 40 K, potentially representing the low-temperature shifting of the Verwey transition due to maghemitization, fine-grained hematite, or domain-wall pinning of magnetite (Strangway et al., 1967b; Özdemir et al., 2008; Özdemir and Dunlop, 2010; Jiang et al., 2014; Dunlop and Özdemir, 2018). Furthermore, the RTSIRM results for all samples display an increase in magnetization values with decreasing temperatures, a behavior that is attributed to the presence of goethite (Dekkers, 1989b). Subtracting a model of goethite from the RTSIRM-LTD curves results in a much more noticeable Morin transition and Verwey transition in the heating curves, though the Verwey transition is still muted or absent in specimens from Paleosols 3, 2, and the Surficial Soil (**Figure 7C**). It should also be noted that the detrended RTSIRM-LTD curves all display hump like features

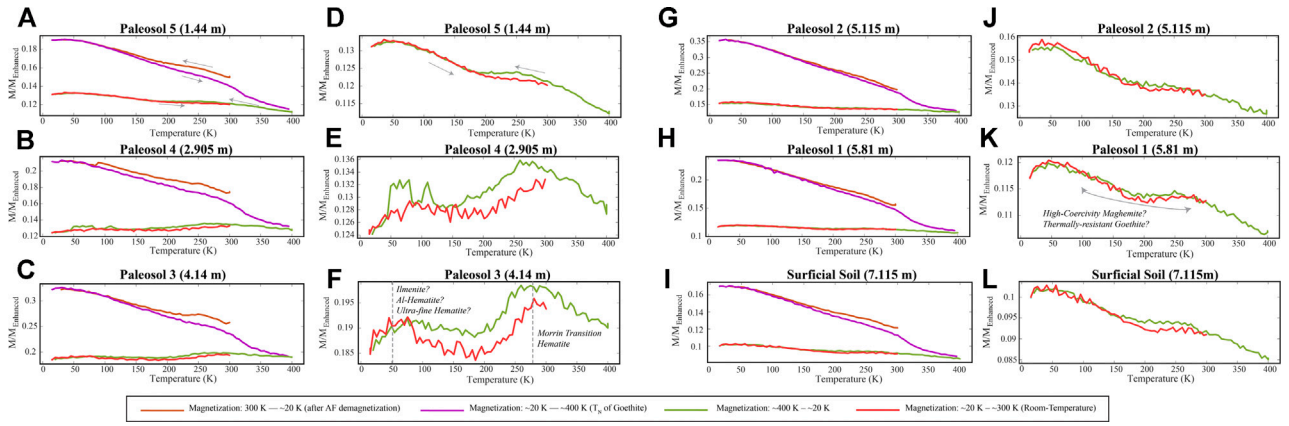

FIGURE 9 | Low-temperature hematite-goethite test for all six soils in the Blackwater draw type-site after AF demagnetizing the TRM acquired by field cooling each sample from 400 K to 300 K in a 2.5 T field. Brown curve represents cooling from 300 K to ~20 K after AF demagnetization at 300 mT. Magenta curve represents warming from ~20 K to 400 K in order to thermally demagnetize goethite. Green curve represents cooling from 400 K to ~20 K. Red curve represents final warming curve from ~20 K to 300 K. **Figure 8A-C** and **Figure 8G-I** includes all four curves for Paleosols 5-3 and Paleosols 2- Surficial Soil respectively. Note the difference in magnetization values between the first two curves (brown and magenta curves) and the final two curves in the sequence (green and red curves); the loss in magnetization in the final two curves is attributed to the thermal demagnetization of the goethite contribution at 400 K. **Figure 9D-E** and **Figure 9J-L** merely focus on the final two curves (green and red curves) of **Figure 9A-C** and **Figure 9G-I**, respectively so that they can be observed in more detail. Theoretically these curves should only represent the isolated hematite contribution for each soil specimen although the increase in magnetization with decreasing temperature (evident in Paleosols 5,2,1 and Surficial Soil) indicates that either high-coercivity maghemite was not completely AF-demagnetized or that a goethite contribution was not adequately thermally demagnetized. Nevertheless, all specimens display a Morin transition at ~220 K — ~200 K indicating the presence of hematite. Morin transitions shifted towards lower temperatures, in addition to the "humps" around ~100 K — ~25 K are interpreted to represent a distribution of very fine (potentially nano-sized) hematite grains (Özdemir et al., 2008; Jiang et al., 2014).

from ~90 K to ~40 K , which is first evident in the raw-data from Paleosol 3. This feature is tentatively interpreted to be caused by ilmenite, which can be magnetized by the surrounding magnetic phases after the former is cooled towards its ordering temperature of ~57 K (Fabian et al., 2008). Nevertheless, other possible causes such as finer-grained hematite or highly oxidized magnetite cannot be completely ruled out (Özdemir and Dunlop, 2010; Jiang et al., 2014; Dunlop and Özdemir, 2018).

For all paleosol samples, both the FC and ZFC curves display a monotonous increase in magnetization values, resulting in two similarly shaped curves that become closer in magnitude with increasing temperature (**Figure 8**). At lower temperatures, the FC curve always shows greater values than the ZFC curve, although the magnitude of the observed difference varies depending on the paleosol. This behavior is interpreted to reflect the presence of a combination of maghemite and goethite, as both minerals display a monotonous increase in LTSIRM values with decreasing temperature (Dekkers, 1989b; Rochette and Fillion, 1989; Özdemir and Dunlop, 2010). However, although pure maghemite has a completely reversible ZFC-FC curve (Özdemir and Dunlop, 2010), goethite is characterized by an FC curve that is double in value to the ZFC curve (Rochette and Fillion, 1989; Guyodo et al., 2003; Liu et al., 2006). Therefore, the greater the difference between the FC and ZFC curves, the greater the implied goethite contribution. On the basis of the data obtained, Paleosol 2 is interpreted to have the highest concentration of goethite.

Finally, at ~50 K all specimens show a noticeable change in slope, which is especially evident as a sharp peak in the derivatives (**Figure 8**). This is tentatively interpreted to indicate the presence of ilmenite which has a Néel temperature of ~ 57 K (Ishikawa and Akimoto, 1957).

The Low Temperature Behavior: Hematite-Goethite test

All representative samples lose about 80% of their remanence after the AF-demagnetization procedure (**Supplementary Datasheet S3**), implying a substantial contribution from low-coercivity phases (Tarling, 1983; Thompson and Oldfield, 1986; Evans and Heller, 2003; Tauxe, 2010; Lagroix and Guyodo, 2017). After AF- demagnetization all samples display a further loss in remanence when heated to 400 K, indicating the presence of goethite in all samples (**Figure.9A-C**; **Figure 9G-I**) (Strangway et al., 1967a, 1968). Nevertheless, all samples retain a remanence even after magnetite and goethite are both demagnetized, this surviving magnetization is attributed to the presence of hematite due to the identification of clear Morin transitions evident in the final cooling and warming curves for all the samples (**Figure 9D-F**; **Figure 9J-L**) (Morin, 1950; Lagroix and Guyodo, 2017). The presence of finer-grained (potentially nanometer-sized) hematite is attributed as the cause of samples that display Morin transitions shifted towards lower temperatures (~200 K) (Strangway et al., 1967b; Özdemir et al., 2008; Jiang et al., 2014). The general trend of increasing magnetization with decreasing temperature, as observed in Paleosols 5,2, 1, and the Surficial Soil, are attributed to goethite and or maghemite that

survived the thermal and AF demagnetization procedures respectively (Lagroix and Guyodo, 2017).

Similar to the detrended RT-SIRM LTD curves, each specimen displays ~150 K – ~40 K humps which are likewise interpreted to represent ilmenite (Fabian et al., 2008). Nevertheless, it should be noted that these features may also be reflective of high-oxidation or domain-wall of a higher-coercivity magnetite that was insufficiently demagnetized by the AF-procedure (Özdemir and Dunlop, 2010; Dunlop and Özdemir, 2018).

Three-Component Thermal Demagnetization of IRM

The response of the three IRMs acquired in different fields in relation to progressive thermal demagnetization for all five Paleosols in addition to the Surficial Soil (**Figure 10**) shows that the low-coercivity component in samples of Paleosols 1—5 was thermally unblocked by ~580° to 600°C indicating the presence of a low-Ti magnetite/maghemite (Dunlop and Özdemir, 1997; Lattard et al., 2006; Karumuri et al., 2009). Minor maghemitization of magnetite is interpreted to be responsible for laboratory unblocking temperatures slightly above the traditionally accepted maximum unblocking temperature for magnetite (580°C) (Gehring et al., 2009). In contrast, the low-coercivity component of the Surficial Soil is not thermally unblocked until about 640°C indicating the presence of fine-grained, thermally-stable maghemite (Özdemir and Banerjee, 1984; Liu et al., 2010).

Both the intermediate– and high–coercivity IRM components of Paleosols 4, 3 and 2, in addition to the intermediate–coercivity component of Paleosol 1, are thermally unblocked at ~640°C, indicating that these components are also dominated by fine-grained maghemite (Özdemir and Banerjee, 1984; Dunlop and Özdemir, 1997; Liu et al., 2010). The intermediate– and high–coercivity component of Paleosol 5 were both thermally unblocked at ~620°C indicating a thermally stable maghemitized-magnetite (Gehring et al., 2009). Finally, the intermediate– and high–coercivity IRM components of the Surficial Soil, in addition to the high–coercivity IRM component of Paleosol 1, lose a large percentage of remanence at ~640°C, but are not completely unblocked until ~675°C. This indicates the presence of both fine-grained thermally-stable maghemite and a sufficient concentration of hematite, the latter of which either originally existed within the sediment or potentially was formed by thermal inversion of maghemite (Özdemir and Banerjee, 1984; Dunlop and Özdemir, 1997; Liu et al., 2010). Nevertheless, the plethora of other

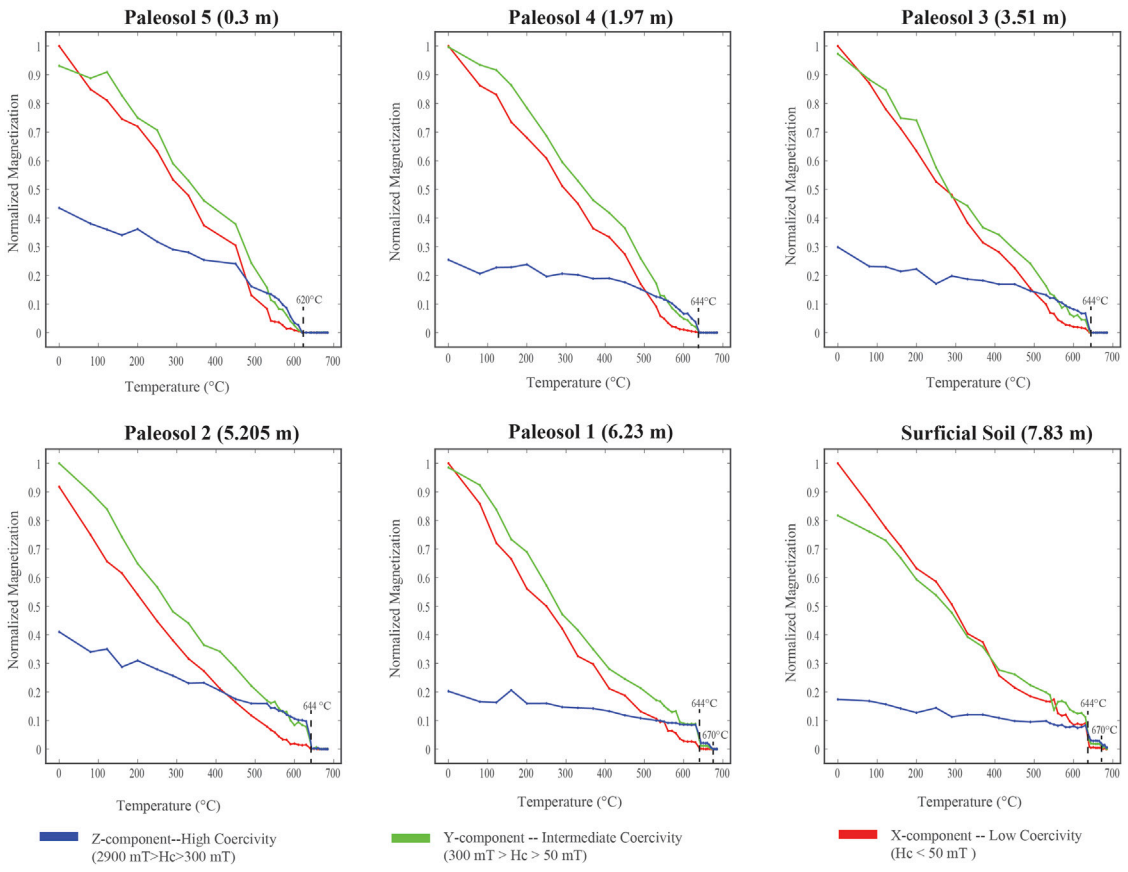

FIGURE 10 | Three component IRM progressive thermal demagnetization (Lowrie, 1990) of six representative specimens from each of the five palesols in addition to the Surficial Soil of the BDF. The z-direction (blue line) represent the hard-coercivity ($IRM_{2.9T}$) component, the y-direction (green line) represent the intermediate-coercivity component (IRM_{300mT}), and the x-direction (red line) represent the low-coercivity component (IRM_{50mT}).

positive hematite tests indicate that the hematite identified in Paleosol 1 and the Surficial Soil is natural, rather than laboratory induced.

ISOTHERMAL ROOM-TEMPERATURE BEHAVIOR

Hysteresis Data, and First-Order-Reversal-Curves

Hysteresis experiments (**Figure 11A**) conducted on six representative samples were carried out using a peak field of 500 mT. The paramagnetic contribution to the hysteresis curves varies throughout the section, with the maximum contribution associated with samples from Paleosol 2. After correcting for the paramagnetic contribution, all hysteresis loops are relatively narrow, with coercivity (Hc) values ranging from 5 to 10 mT. Moreover, all samples reach saturation between 300 and 400 mT. This behavior is consistent with other rock magnetic measurements, indicating that low to moderate coercivity ferrimagnetic minerals dominate the magnetic signal (Tarling, 1983; Thompson and Oldfield, 1986; Tauxe et al., 2002; Tauxe, 2010). Overall, the values of Hc, as determined by hysteresis measurements, appear to correlate with χ values in that samples with low χ values (e.g., Paleosol 2) typically have lower Hc values than those with higher susceptibility (e.g., Paleosols 4 and 5). This feature could potentially reflect differences in grain sizes and/or the increase in concentration of higher coercivity phases such as hematite (Tarling, 1983; Thompson and Oldfield, 1986; Evans and Heller, 2003; Tauxe, 2010; Özdemir and Dunlop, 2014).

In order to construct Day plots, the squareness ratio (Mrs/Ms) and the coercivity ratio (Hcr/Hc) were calculated using the parameters obtained from the hysteresis experiments for all the paleosols (**Supplementary Datasheet S2**) (Day et al., 1977; Dunlop, 2002a, 2002b). Overall, the ratios vary little regardless of paleosol with a squareness ratio average of 0.143208 ± 0.03588 (n=6 samples) and a coercivity ratio average of 2.68144 ± 0.298789 (n=6 samples), which correlate to a domination by PSD magnetite particles (Dunlop, 2002a, 2002b; Tauxe et al., 2002).

First-Order-Reversal-Curves (FORC(s)) were measured and analyzed for representative samples from all the soil units within the type section. All data display a central ridge that extends from the origin and descends past ~30-40 mT (**Figure 11B**). Generally, closed contour density focuses at ~10 mT, indicating the presence of low-coercivity-SD magnetite, although the slight spread along

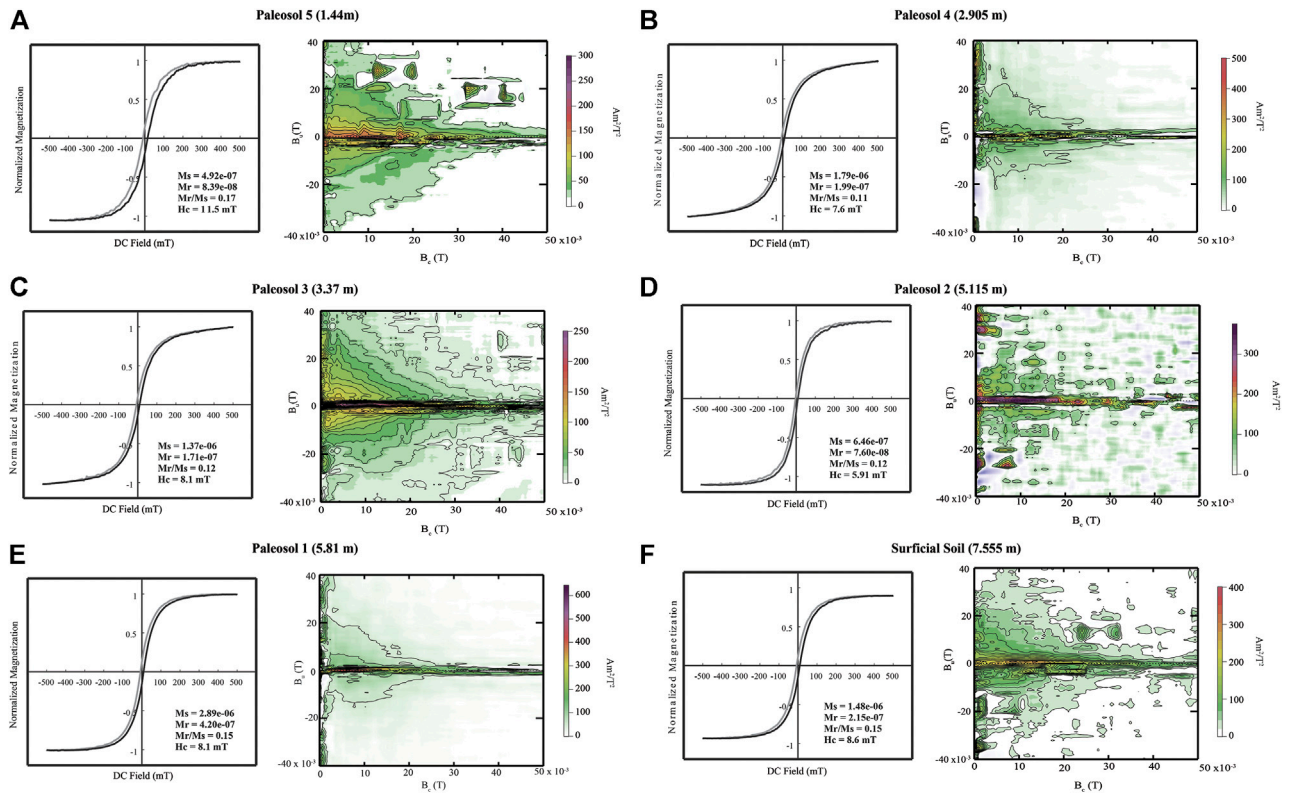

FIGURE 11 | Normalized hysteresis curves, after correction for any paramagnetic contribution, and First-Order-Reversal-Curves (FORC(s)) of representative samples from all five paleosols and the Surficial Soil. **Figure 10A-F** correlates respectively to Paleosols 5- Surficial Soil. For the hysteresis curves note the narrow loops and low coercivity values (5-10 mT), which indicate the dominance of low to moderate coercivity ferrimagnetic phases (Tarling, 1983; Thompson and Oldfield, 1986; Tauxe et al., 2002; Tauxe, 2010). For the FORCs, the weak magnetization of all 6 specimens resulted in (i.e., the vortex structures present over the central ridge in Paleosol 5 and the Surficial Soil). Nevertheless, all FORCs show a central ridge which indicates the presence of SD magnetic phases, while the spread of contours from the central ridge indicates the presence of PSD phases (Roberts et al., 2000, 2014; Muxworthy and Dunlop, 2002; Egli et al., 2010; Egli, 2013; Egli and Winklhofer, 2014; Ao et al., 2017).

the Bu axis does indicate some grain-interaction (Roberts et al., 2000, 2014; Egli et al., 2010; Egli, 2013; Ao et al., 2017). The presence of PSD magnetite (or maghemite) grains is indicated by the divergence of the outer contours along the Bu axis (Muxworthy and Dunlop, 2002; Egli and Winklhofer, 2014), however this behavior may also be reflective of a magnetic vortex state as demonstrated by Roberts et al. (2017).

Stepwise IRM Acquisition, Backfield Curves, and Component Unmixing Analysis:

Representative whole-rock samples were selected from the BDF for step-wise IRM acquisition curves (to a maximum field of 2.9 T) and step-wise backfield analysis (to a maximum required opposite field of 45 mT) (**Figure 12**). Most specimens attained a near-saturation IRM value within 90% and 95% of that acquired at $IRM_{2.9T}$ between DC field values of 30 mT and 180 mT, respectively. This behavior further implies that relatively low coercivity magnetic minerals are the primary magnetic phases in the BDF (Dunlop, 1986). The only exception to this is Paleosol 2 which attained an IRM within 90 percent and 95 percent of the $SIRM_{2.9T}$ between DC field values of 220 mT and 500 mT respectively. This indicates the presence of some higher coercivity material such as SSD magnetite and hematite (Merrill, 1968; Robertson and France, 1994; Dunlop and Özdemir, 1997; Özdemir and Dunlop, 2014). Moreover, the fact that all samples show a further steady increase in IRM to 2.9 T (and likely beyond) indicates a relatively minor amount of high coercivity material (e.g., hematite and/or goethite) (Strangway et al., 1968; Dekkers, 1989a; Dunlop and Özdemir, 1997; Tauxe, 2010; Özdemir and Dunlop, 2014).

After saturation or near-saturation at a DC field of 2.9 T, backfield demagnetization yields a steady decrease in intensity and Hcr values typically between about 35 and 45 mT. The Hcr values also indicate that relatively low coercivity magnetic minerals (magnetite or maghemite) are primarily responsible for the magnetic signal within the BDF, but that they are also influenced by the presence of higher coercivity phases (Dunlop, 1986; Dunlop and Özdemir, 1997; Tauxe, 2010).

In order to further utilize the IRM acquisition data as a means to understand the magnetic mineralogy of representative parts of the BDF, magnetic component unmixing analysis was utilized based on the MAX UnMix protocol (Maxbauer et al., 2016b) for the IRM acquisition data (**Figure 12**). Although possibly unrealistic, we assume that the data for all specimens are best represented by a set of five magnetic components. Unmixing analysis reveals a dominant component with Bh values of ~35 mT (magnetite/maghemite), and a secondary component with Bh values ~130-150 mT (high-coercivity maghemite/magnetite). Although these two components contribute the most to the remanence, three very minor components could also be identified, which included: a very low coercivity component (Bh values between ~5–~10 mT) (low-coercivity maghemite/magnetite), a high coercivity component (Bh values between ~600–~700 mT) (hematite), and a very high coercivity component (Bh values between ~3000–~6000 mT) (goethite). The dominant and secondary coercivity components, Bh = ~35 mT and Bh = ~130-150 mT respectively, are well-defined in that the range of coercivities is quite narrow (standard deviation of Bh (Bh.sd) is less than 0.145 log units). The two higher coercivity components are associated with a range of typically higher standard deviation values than the primary and secondary components, nevertheless standard deviation values are typically lower than 0.145 log units (**Figure 12**).

DISCUSSION

Effects of Provenance and Varying Weathering Intensity on Magnetic Enhancement vs Magnetic Depletion in the Blackwater Draw Formation

Overall, each of the paleosols in the Blackwater Draw Formation (BDF) contains roughly the same magnetic mineralogy, consisting of fine (potentially SP/SD-sized) hematite, goethite, and partially maghemitized magnetite in a range of domain states (SP, PSD, and SD) (**Figures 6**-**12**). Furthermore, Mössbauer analysis indicates that regardless of the varying weathering intensities reported by (Stine et al., 2020), each paleosol is dominated, in terms of volume percent, by hematite. This observation alone is not completely unexpected, for many researchers have noted that hematite and/or goethite are often the dominant Fe-oxides in terms of weight/volume percent within paleosols (e.g., Maher, 2011). However, this implies that the geochemically determined Fe concentrations of the BDF (Stine et al., 2020), is primarily a reflection of the hematite concentration rather than maghemite or magnetite.

Furthermore, the relative scarcity of hematite identified via SEM inspection indicates that the typical grain size of the hematite population is at the submicron (potential nanometer) scale. Nanoscale hematite, potentially pedogenic in origin, could possess domain states that range from SD to SP, which would affect the frequency dependence of this material as well as shifting or muting morin transitions (Strangway et al., 1967b; Cornell and Schwertmann, 2006; Özdemir et al., 2008; Özdemir and Dunlop, 2014; Jiang et al., 2018). However, we note that this suggestion is purely speculative, and thus future studies of the Blackwater Draw paleosols should utilize techniques capable of imaging at the nanometer scale (e.g., transmission electron microscopy or scanning TEM).

Despite the dominance of hematite throughout the profile, the rock magnetic experiments utilized in this study are interpreted to indicate that the magnetic signal, as typically evaluated using parameters such as bulk χ, χ_{ARM}, and IRM intensity as a function of depth, primarily reflects the variations in concentration of magnetite/maghemite throughout the BDF. This is of course a reflection of the high saturation magnetization of magnetite/maghemite. These phases have been noted to dominate the magnetic signal of other paleosols in eolian sequences, even if present as a very small volume/weight percent (Geiss and Zanner, 2006; Jordanova, 2016).

In spite of the general uniformity of the magnetic mineralogy, geochemical evidence, and granulometric evidence presented in Stine et al. (2020) indicates that the coarser-grained Paleosols 5

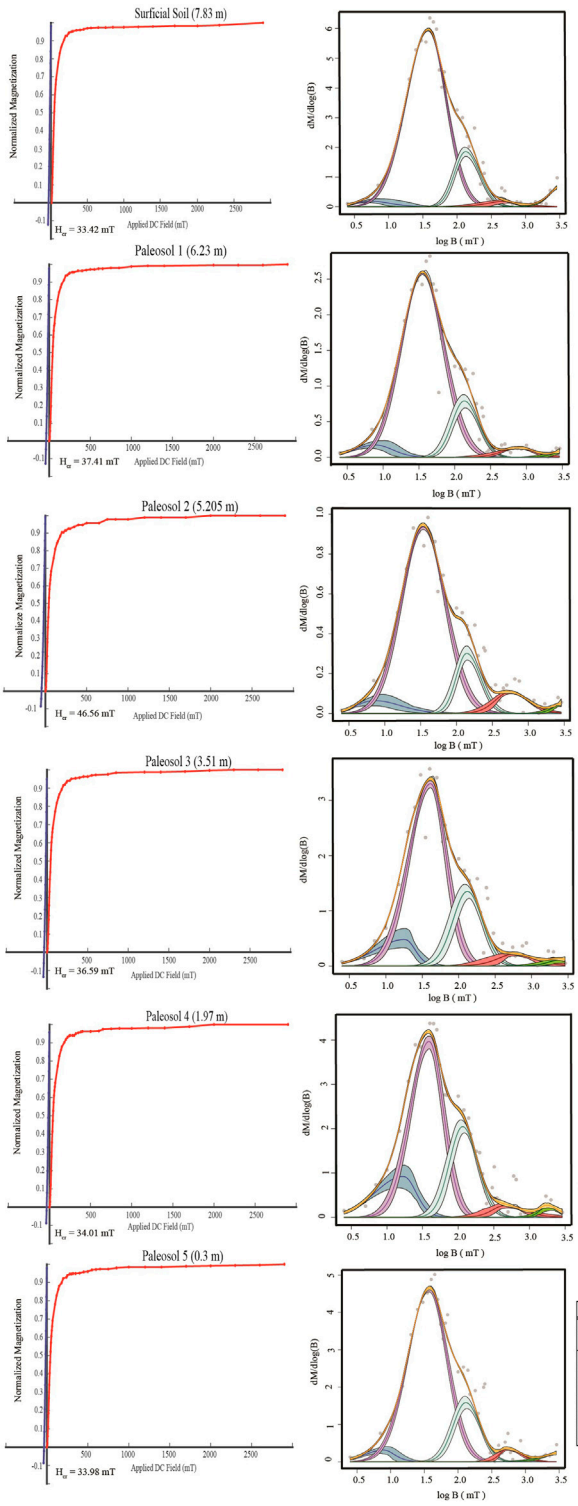

Surficial Soil (7.83 m)

Values	Component 1		Component 2		Component 3		Component 4		Component 5	
	Log Units	Linear Scale	Log Units	Linear Scale	Log Units	Linear Scale	Log Units	Linear Scale	Log Units	Linear Scale
Bh	0.763	5.795	1.530	33.893	2.158	143.824	2.649	445.158	3.523	3332.270
Bh.sd	0.074	1.186	0.007	1.016	0.010	1.023	0.057	1.141	0.050	1.121
DP	0.262	1.828	0.296	1.977	0.185	1.531	0.244	1.754	0.174	1.494
DP.sd	0.040	1.097	0.005	1.011	0.006	1.015	0.065	1.162	0.024	1.058
P	0.032	0.032	0.992	0.992	0.310	0.310	0.031	0.031	0.109	0.109
P.sd	0.007	0.007	0.003	0.003	0.015	0.015	0.004	0.004	0.005	0.005

Paleosol 1 (6.23 m)

Values	Component 1		Component 2		Component 3		Component 4		Component 5	
	Log Units	Linear Scale	Log Units	Linear Scale	Log Units	Linear Scale	Log Units	Linear Scale	Log Units	Linear Scale
Bh	0.836	6.858	1.548	35.346	2.154	142.410	2.872	744.891	3.623	4195.413
Bh.sd	0.047	1.114	0.010	1.023	0.012	1.028	0.028	1.067	0.094	1.242
DP	0.274	1.880	0.297	1.982	0.185	1.531	0.231	1.701	0.214	1.638
DP.sd	0.030	1.071	0.006	1.015	0.006	1.015	0.038	1.092	0.061	1.151
P	0.067	0.067	0.987	0.987	0.302	0.302	0.052	0.052	0.032	0.032
P.sd	0.011	0.011	0.004	0.004	0.018	0.018	0.003	0.003	0.008	0.008

Paleosol 2 (5.205 m)

Values	Component 1		Component 2		Component 3		Component 4		Component 5	
	Log Units	Linear Scale	Log Units	Linear Scale	Log Units	Linear Scale	Log Units	Linear Scale	Log Units	Linear Scale
Bh	0.946	8.828	1.539	34.568	2.179	150.857	2.786	610.784	3.509	3231.463
Bh.sd	0.045	1.110	0.012	1.027	0.012	1.027	0.025	1.058	0.057	1.140
DP	0.310	2.043	0.304	2.013	0.170	1.479	0.236	1.724	0.155	1.428
DP.sd	0.038	1.090	0.006	1.015	0.008	1.019	0.020	1.047	0.037	1.089
P	0.070	0.070	0.997	0.997	0.321	0.321	0.113	0.113	0.050	0.050
P.sd	0.015	0.015	0.007	0.007	0.019	0.019	0.004	0.004	0.010	0.010

Paleosol 3 (3.51 m)

Values	Component 1		Component 2		Component 3		Component 4		Component 5	
	Log Units	Linear Scale	Log Units	Linear Scale	Log Units	Linear Scale	Log Units	Linear Scale	Log Units	Linear Scale
Bh	1.049	11.205	1.551	35.535	2.125	133.345	2.799	630.084	3.505	3198.353
Bh.sd	0.027	1.063	0.012	1.028	0.019	1.044	0.038	1.091	0.071	1.178
DP	0.292	1.958	0.255	1.800	0.203	1.595	0.262	1.828	0.246	1.762
DP.sd	0.017	1.041	0.009	1.021	0.011	1.026	0.061	1.152	0.058	1.142
P	0.140	0.140	0.960	0.960	0.394	0.394	0.063	0.063	0.033	0.033
P.sd	0.026	0.026	0.011	0.011	0.019	0.019	0.004	0.004	0.008	0.008

Paleosol 4 (1.97 m)

Values	Component 1		Component 2		Component 3		Component 4		Component 5	
	Log Units	Linear Scale	Log Units	Linear Scale	Log Units	Linear Scale	Log Units	Linear Scale	Log Units	Linear Scale
Bh	1.056	11.373	1.542	34.806	2.080	120.307	2.729	535.812	3.302	2005.096
Bh.sd	0.021	1.049	0.012	1.029	0.018	1.042	0.037	1.088	0.037	1.089
DP	0.299	1.993	0.234	1.712	0.197	1.574	0.237	1.725	0.147	1.403
DP.sd	0.018	1.042	0.010	1.024	0.011	1.026	0.053	1.131	0.036	1.087
P	0.221	0.221	0.948	0.948	0.490	0.490	0.064	0.064	0.059	0.059
P.sd	0.027	0.027	0.018	0.018	0.021	0.021	0.006	0.006	0.008	0.008

Paleosol 5 (0.3 m)

Values	Component 1		Component 2		Component 3		Component 4		Component 5	
	Log Units	Linear Scale	Log Units	Linear Scale	Log Units	Linear Scale	Log Units	Linear Scale	Log Units	Linear Scale
Bh	0.799	6.297	1.532	34.069	2.132	135.610	2.798	628.752	3.613	4104.895
Bh.sd	0.045	1.108	0.009	1.022	0.013	1.030	0.019	1.044	0.132	1.354
DP	0.226	1.681	0.292	1.959	0.200	1.584	0.163	1.456	0.284	1.925
DP.sd	0.022	1.051	0.007	1.016	0.007	1.017	0.017	1.040	0.046	1.112
P	0.067	0.067	0.984	0.984	0.337	0.337	0.073	0.073	0.050	0.050
P.sd	0.011	0.011	0.006	0.006	0.018	0.018	0.004	0.004	0.006	0.006

FIGURE 12 | Coercivity analysis for specimens from representative samples of all five paleosols and the Surficial Soil in the BDF. Left side for each sample: Curves showing the acquisition of an isothermal remanent magnetization (IRM) and backfield direct field demagnetization of specimens. Right side for each sample: Corresponding magnetic component unmixing analysis results using the MAX UnMix protocol of (Maxbauer et al., 2016b) for IRM acquisition data. In terms of results of the unmixing analysis, Bh is the mean activating field (coercivity) of each component grain population and Bh.sd the standard deviation. Dp is the dispersion parameter, defined as one standard deviation in log space and Dp.sd the standard deviation. P is the optimum model parameter and P.sd the standard deviation. The IRM acquisition and backfield demagnetization data indicate the dominance of relatively low coercivity ferromagnetic phases in these intervals of the BDF and is

(*Continued*)

FIGURE 12 | supported by the results of the unmixing analysis that reveals two primary component: one dominant component with Bh values of about 35 mT (purple area –component 2) and a secondary component with Bh values ~130-150 mT (light blue area –component 3). The unmixing analysis also indicates very minor contribution of a low coercivity phase with Bh values of ~5–~10 mT (darker blue area –component 1) and two much higher coercivity phases with Bh values of about 600-700 mT (red area –component 4) and ~3000–~6000 mT (green area –component 5)

and 4, predominantly sand (**Figure 2**), are primarily sourced from the geographically closer Pecos River Valley area in the south. Moreover, the presence of titanomagnetite and ilmenite (**Figures 6–9**) indicates a potential influx of igneous material into the Pecos River Valley sediments. Likely sources for igneous material, include the volcanic areas in New Mexico (such as the Latir and Ocate volcanic fields) which are known to have provided sediment for the underlying Ogallala formation in the SHP (Eichler, 2020). Conversely, the finer-grained Paleosols 3, 2, and 1 constitute a mix of Pecos River sediments and wind-blown silt that may have had a northern derivation (**Figure 2**). When creating cross-plots of the various data sets, both Stine et al. (2020) and this study (**Figure 13** a, b, and d) show that two distinct populations can be identified which correlate to the single-sourced Pecos sands (i.e., Paleosols 5-4) and the mixed sediments (i.e. Paleosols 3-1). The geochemical classification diagram by (Herron, 1988) (**Figure 12A,B**), shows that the mixed-source cluster possesses less quartz, implying a granulometric control. However, spider-plots of select elements normalized to the North American Shale Composite (NASC) from (Condie, 1993), reveal that Paleosols 3-1 are also substantially enriched in Zr, Nb, Hf, and Ta (**Figure 13C**). This suggests that Paleosols 3-1 contain more heavy minerals such as zircon or columbite, implying that the silt comes from a more felsic source compared to the Pecos sands (Parker and Fleischer, 1968; Armstrong-Altrin et al., 2013; Nagarajan et al., 2016). Indeed, SEM inspection noted that, compared to other soils, the most Zircon grains were present in the specimens from Paleosols 2-1, and the Surficial Soil (**Supplementary Datasheet S5, S6**).

Ambiguity exists concerning the provenance of the Surficial Soil due to the lack of trace element data. However, SEM inspection of specimens from both Paleosol 1 and the Surficial Soil reveals the presence of monazite, a phase enriched in La and Ce, as well as zircon in both soils. This implies that the Surficial Soil has similarly high concentrations of rare earth elements and Zr as Paleosol 1, suggesting similar sources (**Figure 13C**) (McLennan, 1989; Stine et al., 2020). Therefore, the Surficial Soil is tentatively interpreted to consist of a mix of Pecos River sediments and wind-blown silt, similar to Paleosols 3-1.

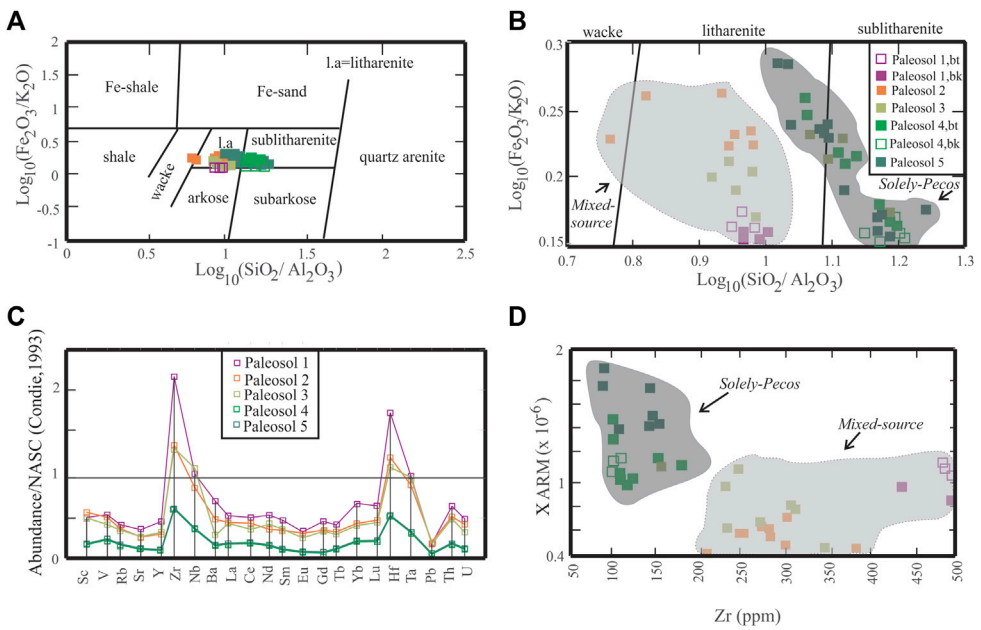

FIGURE 13 | Comparing the geochemical and rock-magnetic data set from (Stine et al., 2020) in order to determine change in provenance. **Figure 13A,B** are log10(Fe_2O_3/K_2O) vs log10(SiO_2/Al_2O_3) geochemical classifications based off of (Herron, 1988), with **Figure 13B** merely focusing in on the data-points. Note the clustering of the solely-pecos sediments (dark-grey circle: Paleosols 5-4) and the mixed-source sediments (light-grey circle: Paleosols 3-1), defined by (Stine et al., 2020). The few Paleosol 3 data-points that plot in the solely-Pecos region are from the basal-most section of the unit, and potentially represent a transitional zone from Paleosol 4 to 3. **Figure 13C** shows a spider-diagram of select trace element concentrations normalized to the North American Shale Composite (NASC) (Condie, 1993). Note how Paleosols 3-1 have substantially higher concentrations of Zr, Nb, Hf, and Ta, implying different provenance (Parker and Fleischer, 1968; Armstrong-Altrin et al., 2013; Nagarajan et al., 2016; Stine et al., 2020). **Figure 12D** is a cross-plot of χ_{ARM} vs the Zr concentration, note how the clustering of solely-Pecos and mixed-source sediments, similar to **Figure 13B**. This implies that the change in provenance is partly responsible for the change in magnetic properties.

Sand sourced from the southern Pecos river valley to the south of the study area likely contained coarser ferrimagnetic phases than the potentially northern derived silt. Indeed, relatively wider FORC distributions, low Hcr, and low χ_R values from this study (**Figures 3**, **11**-**12**) coupled with the lower magnetic granulometry ratio (χ_{ARM}/χ_{low}, χ_{ARM} /SIRM, and $\%\chi_{FD}$) values from Stine et al. (2020) (**Figure 3**) indicate that the sandier single-source Paleosols 5 and 4 are composed of a wider distribution of coarser magnetic phases than the finer mixed-source Paleosols 3, 2, and 1 (**Figures 2**,**3**,**11**) (Maher, 1988; Dunlop, 1995; Heider et al., 1996; Roberts, et al., 2000; Evans and Heller, 2003; Hrouda, 2011; Jordanova, 2016). The effects of changing provenance on the magnetic properties are also evident in cross-plots of rock-magnetic values vs immobile elements (e.g.: χ_{ARM} to Zr, (**Figure 13D**). Thus, the higher and relatively consistent χ, χ_{ARM}, and IRM intensity values for Paleosols 5 and 4 are tentatively interpreted to be due to a higher concentration of coarser ferrimagnetic phases singularly sourced from southern Pecos river valley sands as compared to the mixed-source Paleosols 3, 2, and 1.

Although shrinkage cracks are present in many detrital magnetite grains, the relatively low degree of alteration of magnetite grains in Paleosols 5-4 compared to other soils, as observed in the SEM (**Figure 4**), implies that weathering, and thus magnetic depletion, was minimal. Moreover, although the presence of maghemite, goethite and hematite (**Figures 5**, **7**-**10**) implies some degree of alteration, in general the minimal presence of SP-SSD phases, inferred from the lower magnetic granulometry ratio (χ_{ARM}/χ_{low}, χ_{ARM} /SIRM, and $\%\chi_{FD}$) (**Figure. 3**) (**Supplementary Datasheet S1**) (Stine et al., 2020), suggests little pedogenic neoformation of magnetite commonly attributed with increasing the magnetic signal of soils (Maher, 1988; Zhou et al., 1990; Dunlop, 1995; Heider et al., 1996; Soreghan et al., 1997; Liu et al., 1999, 2007b; Evans and Heller, 2003; Jordanova, 2016). Therefore, we interpret Paleosols 5-4 as being relatively magnetically preserved, i.e. experiencing minimal magnetic depletion and/or enhancement.

In contrast to Paleosols 5-4, pedogenic modification is interpreted to be far more consequential for the magnetically depleted Paleosols 3-2 and the magnetically enhanced Paleosol 1-Surficial Soil, all of which are inferred as mixed southern and northern sources (Stine et al., 2020). Indeed, **Figure 14**, shows that Paleosols 3-1, have a moderate negative correlation with CIA values, suggesting that the magnetically depleted soils are a result of weathering intensities higher than what the magnetically enhanced soils experienced. Paleosols 3 and 2 also contain a relatively higher percentage of goethite as indicated by the ZFC/FC experiment (**Figure 8**), the low-temperature hematite-goethite experiment (**Figure.10**) (**Supplementary Datasheet S3**), relatively high Hcr (**Figure 12**) and L-ratio values (reported here; **Figure 3**), as well as low S-ratio values (from Stine et al., 2020; **Figure 3**) (Stober and Thompson, 1977, 1979; Bloemendal et al., 1992; Maxbauer et al., 2016a).

Goethite is thermodynamically stable at surface conditions, therefore its presence is expected, even in minute quantities, for most soils on the planet (Schwertmann, 1971; Schwertmann and Taylor, 1972, 1989; Scheinost, 2004). Soils characterized by greater abundances of goethite are typically associated either with more humid climates (Thompson and Oldfield, 1986; Schwertmann, 1988) or those surface environments that experience less variation in precipitation seasonality (Balsam et al., 2004; Zhang and Nie, 2017). A truly humid climate is unlikely for the BDF due to the pervasive occurrence of pedogenic carbonate (Machette, 1985), and thus variation in precipitation seasonality is likely a factor.

Regardless, the relatively higher chemical index of alteration values (CIA) for Paleosols 3 and 2 coupled with increased presence of goethite indicates that these soils were subjected to more intense weathering conditions than the older paleosols, likely due to the increased presence of water (Chebykin et al., 2002; Sheldon et al., 2002; Wang et al., 2020). Magnetic depletion would have followed as both northern and southern-sourced aeolian magnetite/maghemite grains were converted into magnetically-weaker and/or non-magnetic phases (Santana et al., 2001; Jiang et al., 2018).

It should be noted that Paleosol 2 also displays higher $\%\chi_{FD}$ and $\chi_{ARM}/SIRM_{2.9T}$ values (**Figure 3**), and a relatively narrower FORC distribution (**Figure 11D**), suggesting the presence of finer magnetic SP and SD phases within this soil (Maher, 1988;

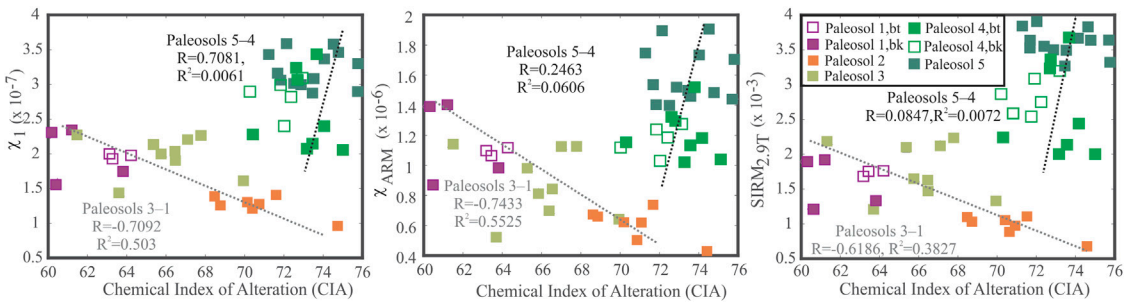

FIGURE 14 | Scatter-plots comparing χ1, χ_{ARM}, and $SIRM_{2.9T}$ to the Chemical Index of Alteration (CIA) calculated by (Stine et al., 2020). Note how each scatterplot results in two clusters. The cluster associated with the mixed sediments (Paleosols 3-1), shows a moderate negative correlation between rock-magnetic values and weathering intensities. This implies that the magnetically depleted values are related to the degree of weathering. The cluster associated with the Pecos-derived sediments (Paleosols 5-4), shows a low correlation between the high-magnetic values of those paleosols and the calculated weathering intensities. Nevertheless, it should be noted that the CIA values for Paleosols 5-4 are suspect due to high quartz content (Stine et al., 2020).

Dunlop, 1995, Heider et al., 1996; Roberts, et al., 2000; Evans and Heller, 2003; Hrouda, 2011; Jordanova, 2016). However, the low χ, χ_{ARM} , and IRM values suggest that these finer magnetic phases likely take the form of the magnetically weaker hematite or goethite rather than magnetite, as suggested by the high Fe-content, high L-ratio, and low S-Ratio values (Liu et al., 2007b; Chaparro et al., 2020; Stine et al., 2020) (**Figures 2**,**3**). The presence of SP phases within a magnetically depleted soil can be explained as an initial process of pedogenic formation of SP-magnetite grains, most of which are sequentially converted (oxidized) into a magnetically weaker phase with increasing weathering intensity, potentially due to relatively high soil temperature (Schwertmann, 1958; Liu et al., 2012; Wang et al., 2013; Jiang et al., 2018). Indeed, the detrended RTSIRM-LTD warming curves for these specimens show a notably muted Verwey transition indicating a high degree of oxidation (Paleosol 2 in **Figure 7C**) (Özdemir and Dunlop, 2010).

The magnetically enhanced Paleosol 1 is similar to the magnetically depleted Paleosols 3 and 2 in that all three are characterized by high environmental magnetic granulometry ratio values, indicating the presence of finer ferrimagnetic (sensu lato) phases (Evans and Heller, 2003; Jordanova, 2016). Furthermore, high χ_R values for Paleosols 3, 2, and 1 indicate that all three paleosols have similar distributions of fine ferrimagnetic phases (Hrouda, 2011), implying that Paleosol 1's higher χ, χ_{ARM}, and IRM intensity values are likely not the result of a higher proportion of southern- vs northern-sourced sediment. Instead, weathered magnetite grains, high frequency dependence, low H_{cr}, narrow FORC distributions, low L-ratio, and high S-ratio values (**Figures 3**,**4**,**11**,**12**) all imply that the magnetically enhanced values of Paleosol 1 are the result of the neoformation and preservation of SP/SD pedogenic maghemite/magnetite grains (Zhou et al., 1990; Soreghan et al., 1997; Liu et al., 1999, 2007b; Evans and Heller, 2003; Jordanova, 2016) (**Figures 3**,**12**). Lower CIA values for Paleosol 1 (Stine et al., 2020) (**Figure 2**) imply an intermediate degree of weathering intensity is the cause of magnetic enhancement. In other words, a moderate degree of weathering is required for pedogenesis to begin and ultrafine maghemite/magnetite grains to form, but weathering would not be so intense as to result in the complete conversion of this new material into hematite or goethite (such as what occurred in Paleosols 3 and 2).

The neoformation and preservation of SP/SD pedogenic maghemite/magnetite grains are also interpreted to be responsible for the high χ, χ_{ARM}, and IRM intensity values of the Surficial Soil (Eyre and Shaw, 1994; Evans and Heller, 2003; Liu et al., 2004a; Orgeira et al., 2011; Jordanova, 2016). Nevertheless, the lower χ_R values imply some contribution from coarser phases (Hrouda, 2011). This, in conjunction with the lack of geochemical data for this paleosol, means that an increased contribution from southern sources cannot be completely ruled out as a partial cause of the high magnetic values for the Surficial Soil.

Finally, it should be noted that both the magnetically depleted and enhanced soils seem to possess a slightly higher and narrower FORC distribution along the Hc axis than the magnetically preserved section (**Figure 11**). Coupling this observation, which implies the presence of pedogenic SD magnetites (Egli, 2004), with the dominance of hematite (**Figure 5**), suggests that magnetic enhancement and depletion are competing processes during soil development. However, as above, which process ultimately dominates appears to correlate to weathering intensity (**Figure 14**). The paleoenvironmental implications of this observation are discussed in more detail in the following section.

Combining Geochemically-based Climofunctions with Rock-Magnetic Data to Identify Changing Paleoenvironmental and Paleoclimatic Conditions

Through the use of geochemical data from modern soils under varying climate conditions, regression equations have been derived that estimate mean annual temperature (MAT) and mean annual precipitation (MAP) conditions that can be applied to paleosols (Sheldon et al., 2002). The calculations for determining these climofunctions are summarized in **Supplementary Datasheet S4**. The high SiO_2 (typically 88-90%) content of Paleosols 5 and 4 provide misleading calculations of MAT and MAP because there is not enough weathered product in the profile, and these paleosols were inferred to be predominantly quartz sand deposited as eolian sand sheets (Stine et al., 2020). Moreover, the Surficial Soil does not have any geochemical data. Thus, calculations of MAT are not possible for the Surficial Soil and Paleosols 5 and 4, whereas, MAP calculations are reserved only for the Surficial Soil and Paleosol 4, which contain a Bk horizon and through use to the depth to that horizon (Retallack, 2005) it is possible to provide rough estimates of MAP. This allows for the determination of relative MAT and MAP values for Paleosols 4-Surficial Soil (**Figure 15**). As above, Paleosol 5 consists solely of a well-developed Btk horizon, therefore no MAT or MAP values could be calculated.

Through the combined use of these proxies with the remainder of the data set, we tentatively model three paleoenvironmental phases which correspond to the magnetically preserved, depleted, and enhanced sections of the type-section respectively.

Phase I: Arid Environment leads to Magnetic Preservation of Pecos River-Valley Sands [Paleosols 5-4]

The first environmental phase, recorded by the basal two Paleosols 5 and 4, is characterized by a coarser set of eolian sediments, consisting of MD and PSD magnetite phases, primarily sourced from the Pecos River valley region in the south. Relatively warmer temperatures likely resulted in the development of maghemite rims around the eolian-sourced magnetite through oxidation in addition to the development of ultrafine hematite. Using the depth to Bk method, the MAP is calculated to be about 650 mm/yr for Paleosol 4, and no MAT was calculated. It should be noted that the error range of the calculated MAP coincides with what has been recorded for the SHP in modern times, measured at 310 to 560 mm/yr (Bomar, 1983). Therefore, Paleosol 4 is tentatively interpreted to have experienced

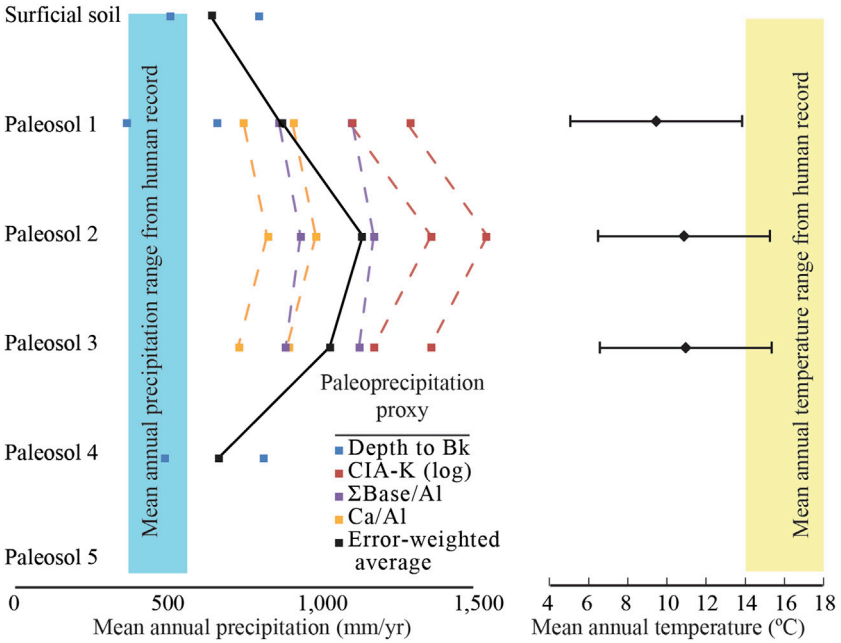

FIGURE 15 | Summarizing MAP (right) and MAT (left) for Paleosols 4-1 and the Surficial Soil. No MAT or MAP were determined for Paleosol 5 due to inadequate data, discussed in text. The modern record of MAP for the SHP, represented by the blue bar, ranges from 310-560 mm/yr (Bomar, 1983). In general, the paleosols appear to record an increasing in precipitation from Paleosols 4-2 and a decreasing trend in precipitation from Paleosols 2-1. The implications of these MAP calculations for paleoenvironmental reconstruction are discussed in the text. The modern record of MAT for the SHP, represented by the yellow bar, is 14°C and 18°C (Bomar, 1983), however the error bars are high, and thus more studies are recommended in order to confirm our initial findings.

precipitation at levels more similar to contemporary times than different. Although neither MAP or MAT values were calculated for Paleosol 5, the presence of well-developed carbonate horizons in both paleosols indicates that Paleosols 5-4 formed in similarly arid conditions (Machette, 1985; Holliday, 1989; Gustavson and Holliday, 1999; Stine et al., 2020). These observations, in conjunction with the general lack of frequency dependent SP phases and minimal goethite implies that the environment characteristic of Phase I was sufficiently arid such that neither magnetic enhancement nor magnetic depletion occurred (Balsam et al., 2011). Therefore, we define Phase I as being relatively magnetically preserved (**Figure 2**).

In order to better understand the paleoenvironmental causes, it is useful to use the contemporary SHP as an analog. Indeed, many remote sensing studies (Lee et al., 2009, 2012; Ginoux et al., 2012; Li et al., 2018; Achakulwisut et al., 2019; Kandakji et al., 2020) have noted that the Pecos River Valley region appears to be a significant source of dust for the numerous dust-storms that afflict the SHP. These dust storms are noted to occur most frequently during the late winter/early-spring which is typically when precipitation is lowest in the region, thus providing sediment that might otherwise be stabilized by vegetation cover (Chepil, 1957; Lee et al., 1994; Stout, 2001; Crabtree, 2005; Novlan et al., 2007). The similarities particularly in provenance imply that the Phase I paleosols were likely influenced by similar environmental conditions as the contemporary SHP, therefore this setting is best described as an arid to semiarid environment.

Phase II: Subhumid to Semiarid Environment leads to Magnetic Depletion of Pecos Sands and Northern Loess Mixture [Paleosols 2 and 3]

The magnetically depleted Paleosols 2 and 3, were deposited within the second environmental phase, which is differentiated from the previous phase by a mixed provenance and higher precipitation. Error weighed average of MAP is about 910 (mm/yr) for Paleosol 3 and about 1020 (mm/yr) for Paleosol 2. These values indicate that Phase II represents a distinctly wetter period than what has been recorded for the SHP in modern times (**Figure 15**), the latter of which ranges from 310 to 560 mm/yr (Bomar, 1983). The presence of goethite also implies relatively less seasonality than what may have occurred in the previous phase (Balsam et al., 2004; Zhang and Nie, 2017). Increasing both the frequency and total amount of annual precipitation would have resulted in the increased chemical weathering of the parent material, including the conversion of eolian magnetite into lesser magnetic phases. This general correlation of relatively high MAP and magnetic depletion agrees with Balsam et al. (2011) observation that modern surficial soils which experience higher rainfall have a corresponding decrease in magnetic susceptibility. Due to these factors, Phase II is tentatively interpreted to represent a subhumid-semiarid environment

A MAT of 10.9°C for Paleosol 3 and 10.7°C for Paleosol 2 was also calculated using the methods outlined in **Supplementary Datasheet S3**. This is notably cooler than the modern SHP MAT of 14°C to 18.6°C (Bomar, 1983), nevertheless the higher error bars does cast some doubts on the accuracy of our MAT calculations. A colder SHP

in conjunction with the addition of wind-blown silt to the sediment budget that was potentially northerly derived is consistent with glacial influence from the north as larger ice sheets developed during the mid-Pleistocene transition. However, this would require future studies to confirm our MAT measurements.

Phase III: Semiarid to Arid Environment leads to Magnetic Enhancement of Pecos Sands and Northern Loess Mixture [Paleosol 1 and Surficial Soil]

The third and final phase consists of the uppermost layers, Paleosol 1 and the Surficial Soil, the latter of which was paired with Paleosol 1 due to similar characteristics in the rock-magnetic data set and similarities in SEM observations. MAT and error weighted average MAP are 9.45°C and about 790 mm/yr respectively for Paleosol 1. MAP values of about 570 mm/yr are calculated for the Surficial Soil, initially implying that this soil was deposited during environmental conditions more similar to Phase I and the modern era (Bomar, 1983). However, similar rock-magnetic characteristics and SEM observations imply that Paleosol 1 and the Surficial Soil share similar provenance and weathering intensities. Therefore, we tentatively interpret Paleosol 1 and the Surficial Soil as having formed in similar environmental conditions. Moreover, the presence of SP-magnetic phases suggests a higher degree of pedogenesis, and in turn precipitation, than what occurred in Phase I (Evans and Heller, 2003; Maxbauer et al., 2016a; Jordanova, 2016). Incidentally, we interpret the soils of Phase III to represent environmental conditions which were distinct from the contemporary SHP and Phases I and II.

Overall, Phase III is interpreted to represent a semiarid to arid environment, relatively drier than Phase II, yet wetter than what was experienced in Phase I or the modern SHP. Moreover, it should be noted that Phase III is estimated to be a colder environment than Phase II and this, coupled with the continued presence of loess, indicates a possible relationship between larger northern hemisphere ice sheets and regional temperatures in the SHP. Although this later point is purely speculative until: (1) magnetic data from more sites are collected; (2) and future studies confirm our MAT results.

Phase III represents an intermediate position in terms of precipitation levels, and the correlation between intermediate MAP and magnetic enhancement implies that pedogenic ultrafine SP/SD magnetite require specific conditions in order to develop in the SHP. In short, precipitation levels need to be greater than what occurred in Phase I in order for pedogenesis to take place and nanomagnetites to form (Balsam et al., 2011), yet not so intense as to result in the dissolution of magnetic material (Balsam et al., 2011; Liu et al., 2013), as was the case for Phase II

Comparing magnetic data sets from modern surficial soils throughout the northern hemisphere and equatorial regions, Balsam et al. (2011) observed that magnetic enhancement generally only occurred in soils experiencing MAP from 200 mm/yr to 1000-1200 mm/yr. Any soil subjected to precipitation greater/less than 1200 / 200 mm/yr would experience magnetic depletion or no magnetic change, respectively (Balsam et al., 2011). Although our calculated MAP does not perfectly agree with Balsam et al. (2011) observations; the seeming correlation between low, intermediate, and high precipitation respectively with magnetic preservation, enhancement, and depletion is worth noting. This nonlinear relationship between magnetic properties and precipitation, complicates the use of magnetic parameters as a paleoprecipitation proxy, therefore it is highly recommended that future studies take a more holistic approach by incorporating both geochemical and rock-magnetic datasets to avoid ambiguity.

Correlation of Environmental Models to Previously Established Age Models: Effects of the Laurentide Ice Sheet and the Middle Pleistocene Transition?

Fundamental questions remain concerning the forcings responsible for: (1) changing provenance from southerly derived Pecos River Valley sands in Phase I to a mix of Pecos sands and wind-blown silt for Phases II and III; and (2) changing MAT and MAP values from Phase II to III. However, correlation of these results to established paleoclimatic shifts, i.e., the Middle-Pleistocene Transition (MPT), is problematic due to the lack of precise age control at the BDF type site.

Nevertheless, previous magnetic polarity stratigraphy work (Patterson and Larson, 1990), the presence of stage IV calcisols, in addition to age estimates derived at other sites, all imply that the BDF as a whole is likely no older than ca. 1.4 Ma (Izett et al., 1972; Gustavson and Holliday, 1999) and that the base of the type-section in particular is at least older than ca. 773 ka (Holliday, 1989; Patterson and Larson, 1990; Coe et al., 2004; Singer, 2014; Channell et al., 2020; Ogg, 2020). Within the context of these rough age constraints, it is highly likely that the MPT is recorded within the type-section of the BDF.

As above, the MPT is a time interval between ca. 1.2 and 0.7 Ma during which the frequency of glacial-interglacial cycles shifted from a ~41 ky cycle to a ~100 ky cycle (Imbrie et al., 1993). Within North America, the MPT coincided with the coalescence and expansion of the Laurentide Ice sheet as the longer ~100 ky cycles led to enhanced ice growth (Mudelsee and Schulz, 1997; Head and Gibbard, 2005; Clark et al., 2006; Batchelor et al., 2019). Moreover, magnetic polarity data (Balco et al., 2005; Balco and Rovey, 2010; Jennings et al., 2013) and numerical models (Batchelor et al., 2019) imply that the Laurentide ice sheet first reached a geographic extent comparable to the last glacial maximum (LGM) at ~0.9 Ma, when 100 ky cycles first become dominant in the Marine Isotope Stage (MIS) records (Hughes and Gibbard, 2018, and references therein).

MPT-influenced expansion of the Laurentide ice sheet in turn led to a change in river drainage patterns (Lemmen et al., 1994; Wickert et al., 2013; Wickert, 2016) weakening of the North American Monsoon (NAM) (Bhattacharya et al., 2017, 2018), and the deposition of vast amounts of loess on the continental interior (Muhs, 2018; Muhs et al., 2018; Li et al., 2020). Although the mechanisms are still debated, it has been hypothesized that the expansion of the Laurentide Ice sheet likely affected regional atmospheric circulation and subsequent weather of adjacent regions such as the SHP (Bromwich et al., 2004, 2005; Löfverström and Lora, 2017). If future studies confirm our MAT measurements for Phases II and III, then this could

potentially be explained as the migration of the polar jet stream to much lower latitudes which in turn could have brought colder air to the SHP (Munroe and Laabs, 2013). Moreover, it also likely that the presence of the Laurentide ice-sheet substantially affected wind direction (Broccoli and Manabe, 1987; Klink, 1999; Bromwich et al., 2004, 2005; Löfverström and Lora, 2017). In modeling surface-wind directions during the LGM (~20 ka to ~12 ka), Löfverström and Lora (2017) determined that a more expansive Laurentide ice sheet (at ~20 ka) and a diminished Laurentide ice sheet (at ~12 ka) corresponded to mean surface wind directions that primarily flow from north to south and west to east, respectively, for the SHP during the winter. Using data from 1961 to 1990, Klink (1999) calculated that the SHP has a mean winter wind direction which flows from the southwest to the northeast. The combination of historical and modeled data sets suggests that the single-Pecos-sourced sediments of Phase I likely represent a time period when the Laurentide Ice sheet was substantially diminished, resulting in more winds from the southwest to carry Pecos sand. Moreover, this style of southerly derived material from the Pecos River Valley likely extended back into the late Miocene as recorded in the upper part of the underlying Ogallala Formation on the SHP (Gustavson and Holliday, 1999). A sole source is in contrast to the mixed sediments of Phases II and III, both of which likely represent periods where a larger Laurentide ice sheet resulted in a stronger north to south wind, which would have carried northerly derived silt to the SHP (Stine et al., 2020).

Gustavson and Holliday (1999) hypothesized a minimum age of at least ~0.910 Ma for our Phase I strata based on: (1) the stratigraphic position below the consistently reverse polarity Paleosol 2, indicating a minimum age greater than ~0.773 Ma (Patterson and Larson, 1990; Channell et al., 2020) ; and (2) the presence of well-developed Stage III-IV calcic horizons, which require a minimum of ~50 ky to ~100 ky to develop (Bachman and Machette, 1977; Machette, 1985). Moreover, the minimal weathering intensities indicated by our data set imply a minimal degree of soil welding, suggesting that the calcic horizons of Phase I did not develop contemporaneously. With these admittedly rough age controls, we tentatively interpret the lack of glacial loess and arid conditions of Phase I to be the result of having occurred prior to the onset of strong, well-developed 100 ka climate cycles in North America. However, until better age control is established, ambiguity exists on whether this correlates to a period prior to the MPT (at a time prior to ~1.2 Ma) (Imbrie et al., 1993); or simply when the Laurentide ice sheet first demonstrated 100 ka cycles (at about 0.9 Ma) Balco and Rovey, 2010.

Using similar criteria as above, Phase II is interpreted to have occurred at about the time of the MPT (1.2 Ma–0.7 Ma). Marine isotope records from this period indicate the inception of 100 ka climate cycles as well as a general decreasing trend in stable isotope values, likely corresponding to a decreasing trend in global temperatures during this time period (Lisiecki and Raymo, 2005; Lowe and Walker, 2015). This implies that the onset of the MPT (1.2 Ma – 0.7 Ma) was a warmer time period than Post-MPT times (0.7 Ma – Modern) (Imbrie et al., 1993). On a regional scale, slightly warmer 100 k.y. glacial cycles may have resulted in different environments than colder counterparts in more recent times. If our initial MAT measurements prove to be correct than this could potentially provide an explanation for the change in precipitation in the SHP during the MPT. Rainfall can often result during weather fronts, which is when large hot and cold air masses interact (Barry and Chorley, 2010). Therefore, it is possible that the interaction between the colder air of the Laurentide ice sheet and the relatively warmer air of the SHP region could have resulted in an initial increase in precipitation during the MPT, although more sites and numerical models are needed in order to confirm this hypothesis. Alternatively, the increase in precipitation in the SHP during the MPT, could have been the result of either "squeezing" (Oster et al., 2015; Putnam, 2015) or "splitting" (COHMAP Members, 1988) of the westerlies jet stream, both of which have been cited as explanations for why other North American regions (i.e. Great Basin) were similarly more humid during glaciations (Putnam, 2015; Wang et al., 2021).

Finally, Phase III is interpreted to have occurred after the cessation of the MPT, and younger than ca. 0.773 Ma, when climate change was dominated by 100-ka cycles. Moreover, the lowering of MAT and MAP in this phase also agrees with post-MPT global climatic trends of lower global temperatures and more arid climates (Rea, 1994; Werner, 2002; Winkler et al., 2002; Martin, 2006; Sun et al., 2012; Yann et al., 2013; Lang et al., 2014). Assuming that future studies confirm our initial MAT results, then a regional decrease in annual temperature could provide a potential explanation for the increase in aridity. Colder air masses contain less moisture than their warmer counterparts, which results in less precipitation (Barry and Chorley, 2010). Therefore, it is possible that any weather front due to the interaction of Laurentide- and SHP-sourced air masses, could have resulted in less precipitation during Phase III than in Phase II, though once again confirmation of this hypothesis would require more sites and numerical models.

Despite the increase in aridity, climate models for the time of the LGM (Bromwich et al., 2004, 2005) have suggested that large post-MPT ice sheets would have resulted in relatively enhanced levels of precipitation for the SHP during the summer. Throughout the SHP and adjacent regions, increased seasonality is also evident in the proliferation of C4 plants, which preferentially develop in arid and semi-arid regions with wetter summers (Ehleringer et al., 1997; Huang et al., 2001; Edwards et al., 2010; Strömberg, 2011; Cotton et al., 2016; Green et al., 2017). Correlation of this numerical model and regional distribution of C4 plants with our observation of ultrafine SP/SSD magnetite in Phase III soils, could explain how precipitation became great enough in an otherwise arid environment to result in magnetic enhancement. Moreover, if Bromwich et al. (2004, 2005) ideas are indeed correct this would also support the hypothesis that the formation of magnetically enhancing, pedogenic magnetite is the result of increased seasonality as suggested by Balsam et al. (2004) and Zhang and Nie (2017).

CONCLUSIONS

Representative samples from all paleosols and the overlying Surficial Soil from the type-site of the BDF subjected to a range of both non-magnetic and magnetic experiments provide an improved understanding of the magnetic mineralogic cause of

magnetic enhancement and magnetic depletion within the formation profile, observations which might be applied to similar sites. Results show a relatively uniform mineralogy, where the magnetic signal is dominated by partially maghemitized magnetite grains, despite the fact that the magnetic mineralogy is dominated by hematite, potentially sub-micron in size, in terms of weight/volume percent. Moreover, the presence of fine-grained hematite within all the samples, regardless of weathering intensity, as reported by (Stine et al., 2020), implies that the intensity of the magnetic signal (χ, ARM, IRM) with that magnetic enhancement and magnetic depletion are competing processes during soil development of the BDF. The dominating process is related to weathering intensity, which in turn is tentatively interpreted to be caused by MAP.

For the BDF at its type section, we have identified three environmental phases (I-III) which we tentatively correlate to the Middle-Pleistocene transition (MPT), a time period when the frequency of glacial-interglacial cycles shifted from a ~41 k.y. cycle to a ~100 k.y. cycle, between about 1.2 and 0.7 Ma (Imbrie et al., 1993). Phase I represents a relatively arid environment which occurred prior to the onset of the MPT. During this phase the dominance of ~41-k.y cycles limited the growth of the Laurentide ice sheet, which allowed southwest to northeast winds to carry Pecos river sands to the SHP. Coarse magnetite grains were carried with the Pecos sands and preserved by the arid environment, resulting in a relative preservation of the magnetic signal.

Phase II represents a relatively subhumid to semiarid environment, which occurred during the onset of the MPT. During this phase the onset of ~100-k.y. cycles allowed for the expansion of the Laurentide ice sheet. The presence of the ice sheet so far south resulted in stronger to south winds which deposited newly created loess onto the SHP, where it mixed with Pecos sands. An increase in precipitation levels resulted in the dissolution of eolian magnetic material and thus magnetic depletion. Though the source of this precipitation increase is difficult to explain, we tentatively propose that it is higher regional mean annual temperatures (MAT) and the larger Laurentide ice sheet. Nevertheless, the high error bars of our MAT calculations implies that future research should attempt different methods in order to determine MAT and confirm or deny our results.

Finally, Phase III represents a semiarid to arid environment, which occurred after the MPT was completed and ~100-k.y. glacial-interglacial cycles dominated. Phase III is similar to Phase II, in that it is a mix of Pecos river sands and northern loess, likely due to the enhanced Laurentide ice sheet. Phase III represents a relatively intermediate level of precipitation; in that it is less than Phase II but greater than Phase I. This moderate level of precipitation resulted in the pedogenic neoformation of ultrafine SP and SSD magnetite which enhanced the magnetic signal.

The results of this research show that the magnetic signal of the SHP is the result of a complicated interaction between changing provenance and precipitation levels. Therefore, we recommend that, at least for the SHP, a holistic approach be taken in reconstructing paleoenvironment which incorporates rock-magnetic, geochemical, and microscopy observations.

DATA AVAILABILITY STATEMENT

The raw data supporting the conclusions of this article will be made available by the authors, without undue reservation.

AUTHOR CONTRIBUTIONS

All rock-magnetic data, including the SEM observations were collected by JS, all geochemical (oxide and trace element) and textural data was collected by HB. All geochemically based climofunctions were calculated by HB. JS and JG wrote and edited the manuscript with regards to the rock-magnetic data and interpretation JS and DS wrote and edited the manuscript with regards to the Geologic, sedimentologic, and paleoenvironmental background information. JS, JG, and DS wrote and edited the final to the final discussion sections. **Figures 1–4**, and **Figures 15** were created and edited by JS, HB, and DS. **Figures 4–14** were created and edited by JS and JG.

FUNDING

Research funding for JS includes: the Geological Society of America for Graduate Research Awards No. 11267-16 and No.12277-18, the Dr. Oscar Wilhelm Memorial Student Research Fund at the University of Texas at Dallas, and the Visiting Fellowship Awarded by the Institute for Rock Magnetism (IRM) at the University of Minnesota in October, 2018. The visiting fellowship awarded by IRM allowed for Travel and use of their rock-magnetic instrumentation. HB student research grant from the Southwest Section of the American Association of Petroleum Geology. Dr. JG Faculty Start-up support provided by the University of Texas at Dallas Dr. DS Faculty Start-up support provided by Texas Tech University.

ACKNOWLEDGMENTS

JS thanks the Geological Society of America for Graduate Research Awards no.11267-16 and no.12277-18. JS also acknowledges support awarded through the Dr. Oscar Wilhelm Memorial Student Research Fund at The University of Texas at Dallas (UTD). JS also would like to thank, Leah Thompson and Dr. Ignacio Pujano at UTD for all their help in preparing specimens and interpreting data from the Scanning Electron Microscope. JS would also like to thank the Institute for Rock Magnetism (IRM) at the University of Minnesota for awarding him a visiting fellowship in October, 2018. The visiting fellowship allowed JS to utilize their rock-magnetic instrumentation. The authors would also like to thank Joshua Feinberg (IRM), Dario Bilardello (IRM), and Bruce

Moskowitz (IRM) for providing valuable insight on the interpretation of the low-temperature data gathered at the IRM. The IRM is a US National Multi-user Facility supported through the Instrumentation and Facilities Program of the National Science Foundation, Earth Sciences Division, and by funding from the University of Minnesota. HB appreciates the student research grant provided by the Southwest Section of the American Association of Petroleum Geology. JG and DS acknowledge faculty start-up support from UTD and Texas Tech University, respectively. We would also like to thank our three reviewers for their many helpful suggestions.

SUPPLEMENTARY MATERIAL

The Supplementary Material for this article can be found online at: https://www.frontiersin.org/articles/10.3389/feart.2021.601401/full#supplementary-material

REFERENCES

Achakulwisut, P., Anenberg, S. C., Neumann, J. E., Penn, S. L., Weiss, N., Crimmins, A., et al. (2019). Effects of Increasing Aridity on Ambient Dust and Public Health in the U.S. Southwest under Climate Change. *GeoHealth* 3, 127–144. doi:10.1029/2019gh000187

Ao, H., Dekkers, M. J., Roberts, A. P., Rohling, E. J., An, Z., Liu, X., et al. (2017). Mineral Magnetic Record of the Miocene-Pliocene Climate Transition on the Chinese Loess Plateau, North China. *Quat. Res.* 89, 619–628. doi:10.1017/qua.2017.77

Armstrong-Altrin, J. S., Nagarajan, R., Madhavaraju, J., Rosalez-Hoz, L., Lee, Y. I., Balaram, V., et al. (2013). Geochemistry of the Jurassic and Upper Cretaceous Shales from the Molango Region, Hidalgo, Eastern Mexico: Implications for Source-Area Weathering, Provenance, and Tectonic Setting. *Comptes Rendus Geosci.* 345, 185–202. doi:10.1016/j.crte.2013.03.004

Bachman, G. 0, and Machette, M. N. (1977). Calcic Soils and Calcretes in the Southwestern United States. Available at: https://pubs.usgs.gov/of/1977/0794/report.pdf (Accessed April 2, 2021). doi:10.3133/ofr77794

Balco, G., and Rovey, C. W. (2010). Absolute Chronology for Major Pleistocene Advances of the Laurentide Ice Sheet. *Geology* 38, 795–798. doi:10.1130/G30946.1

Balco, G., Rovey, C. W., and Stone, J. O. H. (2005). The First Glacial Maximum in North America. *Science* 307, 222. doi:10.1126/science.1103406

Balsam, W., Ji, J., and Chen, J. (2004). Climatic Interpretation of the Luochuan and Lingtai Loess Sections, China, Based on Changing Iron Oxide Mineralogy and Magnetic Susceptibility. *Earth Planet. Sci. Lett.* 223, 335–348. doi:10.1016/j.epsl.2004.04.023

Balsam, W. L., Ellwood, B. B., Ji, J., Williams, E. R., Long, X., and el Hassani, A. (2011). Magnetic Susceptibility as a Proxy for Rainfall: Worldwide Data from Tropical and Temperate Climate. *Quat. Sci. Rev.* 30, 2732–2744. doi:10.1016/j.quascirev.2011.06.002

Barry, R. G., and Chorley, R. J. (2010). *Atmosphere, Weather, and Climate*. 9th ed. New York: Routledge: Taylor & Francis Group.

Batchelor, C. L., Margold, M., Krapp, M., Murton, D. K., Dalton, A. S., Gibbard, P. L., et al. (2019). The Configuration of Northern Hemisphere Ice Sheets through the Quaternary. *Nat. Commun.* 10, 1–10. doi:10.1038/s41467-019-11601-2

Berger, W. H., and Jansen, E. (1994b). in *The Polar Oceans and Their Role in Shaping the Global Environment*. Editors O. M. Johannessen, R. D. Muench, and J. E. Overland. 1st ed. (Washington D.C.: American Geophysical Union). doi:10.1029/GM085

Berger, W. H., and Jansen, E. (1994a). Fourier Stratigraphy: Spectral Gain Adjustment of Orbital Ice Mass Models as an Aid in Dating Late Neogene Deep-Sea Sediments. *Paleoceanography* 9, 693–703. doi:10.1029/94PA01454

Bhattacharya, T., Tierney, J. E., Addison, J. A., and Murray, J. W. (2018). Ice-sheet Modulation of Deglacial North American Monsoon Intensification. *Nat. Geosci.* 11, 848–852. doi:10.1038/s41561-018-0220-7

Bhattacharya, T., Tierney, J. E., and DiNezio, P. (2017). Glacial Reduction of the North American Monsoon via Surface Cooling and Atmospheric Ventilation. *Geophys. Res. Lett.* 44, 5113–5122. doi:10.1002/2017GL073632

Bird, A., Millar, I., Rodenburg, T., Stevens, T., Rittner, M., Vermeesch, P., et al. (2020). A Constant Chinese Loess Plateau Dust Source since the Late Miocene. *Quat. Sci. Rev.* 227, 106042. doi:10.1016/j.quascirev.2019.106042

Bloemendal, J., King, J. W., Hall, F. R., and Doh, S.-J. (1992). Rock Magnetism of Late Neogene and Pleistocene Deep-Sea Sediments: Relationship to Sediment Source, Diagenetic Processes, and Sediment Lithology. *J. Geophys. Res.* 97, 4361–4375. doi:10.1029/91JB03068

Bomar, G. W. (1983). *Texas Weather*. First. Austin, TX: University of Texas Press.

Broccoli, A. J., and Manabe, S. (1987). The Effects of the Laurentide Ice Sheet on North American Climate during the Last Glacial Maximum. *Gpq* 41, 291–299. doi:10.7202/032684ar

Bromwich, D. H., Toracinta, E. R., Oglesby, R. J., Fastook, J. L., and Hughes, T. J. (2005). LGM Summer Climate on the Southern Margin of the Laurentide Ice Sheet: Wet or Dry?*. *J. Clim.* 18, 3317–3338. doi:10.1175/JCLI3480.1

Bromwich, D. H., Toracinta, E. R., Wei, H., Oglesby, R. J., Fastook, J. L., and Hughes, T. J. (2004). Polar MM5 Simulations of the Winter Climate of the Laurentide Ice Sheet at the LGM*. *J. Clim.* 17, 3415–3433. doi:10.1175/1520-0442(2004)017<3415:PMSOTW>2.0.CO;210.1175/1520-0442(2004)017<3415:pmsotw>2.0.co;2

Channell, J. E. T., Singer, B. S., and Jicha, B. R. (2020). Timing of Quaternary Geomagnetic Reversals and Excursions in Volcanic and Sedimentary Archives. *Quat. Sci. Rev.* 228, 106114. doi:10.1016/j.quascirev.2019.106114

Chaparro, M. A. E., Moralejodel, M. d. P. P., Böhnel, H. N., and Acebal, S. G. (2020). Iron Oxide Mineralogy in Mollisols, Aridisols and Entisols from Southwestern Pampean Region (Argentina) by Environmental Magnetism Approach. *Catena* 190, 104534. doi:10.1016/j.catena.2020.104534

Chebykin, E. P., Edgington, D. N., Grachev, M. A., Zheleznyakova, T. O., Vorobyova, S. S., Kulikova, N. S., et al. (2002). Abrupt Increase in Precipitation and Weathering of Soils in East Siberia Coincident with the End of the Last Glaciation (15 Cal Kyr BP). *Earth Planet. Sci. Lett.* 200, 167–175. doi:10.1016/S0012-821X(02)00588-5

Chen, L. M., Zhang, G. L., Rossiter, D. G., and Cao, Z. H. (2015). Magnetic Depletion and Enhancement in the Evolution of Paddy and Non-paddy Soil Chronosequences. *Eur. J. Soil Sci.* 66, 886–897. doi:10.1111/ejss.12281

Chepil, W. S. (1957). Dust Bowl: Causes and Effects. *J. Soil Water Conservation* 12, 108–111.

Chlachula, J., Evans, M. E., and Rutter, N. W. (1998). A Magnetic Investigation of a Late Quaternary Loess/palaeosol Record in Siberia. *Geophys. J. Int.* 132, 128–132. doi:10.1046/j.1365-246x.1998.00399.x

Chlachula, J., and Little, E. (2011). A High-Resolution Late Quaternary Climatostratigraphic Record from Iskitim, Priobie Loess Plateau, SW Siberia. *Quat. Int.* 240, 139–149. doi:10.1016/j.quaint.2011.01.045

Chlachula, J., Rutter, N. W., and Evans, M. E. (1997). A Late Quaternary Loess - Paleosol Record at Kurtak, Southern Siberia. *Can. J. Earth Sci.* 34, 679–686. doi:10.1139/e17-054

Chlachula, J. (2003). The Siberian Loess Record and its Significance for Reconstruction of Pleistocene Climate Change in north-central Asia. *Quat. Sci. Rev.* 22, 1879–1906. doi:10.1016/S0277-3791(03)00182-3

Clark, P. U., Archer, D., Pollard, D., Blum, J. D., Rial, J. A., Brovkin, V., et al. (2006). The Middle Pleistocene Transition: Characteristics, Mechanisms, and Implications for Long-Term Changes in Atmospheric pCO2. *Quat. Sci. Rev.* 25, 3150–3184. doi:10.1016/j.quascirev.2006.07.008

Clark, P. U. (2012). Ice Sheets in Transition. *Science* 337, 656–658. doi:10.1126/science.1226335

Coe, R. S., Singer, B. S., Pringle, M. S., and Zhao, X. (2004). Matuyama-Brunhes Reversal and Kamikatsura Event on Maui: Paleomagnetic Directions, 40 Ar/ 39 Ar Ages and Implications. *Earth Planet. Sci. Lett.* 222, 667–684. doi:10.1016/j.epsl.2004.03.003

COHMAP Members (1988). Climatic Changes of the Last 18,000 Years: Observations and Model Simulations. *Science* 241, 1043–1052. doi:10.1126/science.241.4869.1043

Condie, K. C. (1993). Chemical Composition and Evolution of the Upper continental Crust: Contrasting Results from Surface Samples and Shales. *Chem. Geology.* 104, 1–37. doi:10.1016/0009-2541(93)90140-E

Cornell, R. M., and Schwertmann, U. (2006). *The Iron Oxides: Structure, Properties, Reactions, Occurrences and Uses, 2nd, Completely Revised and Extended Edition*. 2nd ed. Heppenheim, Germany: Wiley.

Cotton, J. M., Cerling, T. E., Hoppe, K. A., Mosier, T. M., and Still, C. J. (2016). Climate, CO2, and the History of North American Grasses since the Last Glacial Maximum. *Sci. Adv.* 2, e1501346. doi:10.1126/sciadv.1501346

Crabtree, G. W. (2005). Dustfall on the Southern High Plains of Texas. Available at: https://ttu-ir.tdl.org/bitstream/handle/2346/1225/DustfallOnTheSouthernHighPlainsOfTexas.pdf?sequence=1 (Accessed April 2, 2021). doi:10.1002/0471718769

Cui, Y., Verosub, K. L., and Roberts, A. P. (1994). The Effect of Low-Temperature Oxidation on Large Multi-Domain Magnetite. *Geophys. Res. Lett.* 21, 757–760. doi:10.1029/94GL00639

Day, R., Fuller, M., and Schmidt, V. A. (1977). Hysteresis Properties of Titanomagnetites: Grain-Size and Compositional Dependence. *Phys. Earth Planet. Interiors* 13, 260–267. doi:10.1016/0031-9201(77)90108-X

de Grave, E., Barrero, C. A., da Costa, G. M., Vandenberghe, R. E., and van San, E. (2002). Mössbauer Spectra of α- and γ-polymorphs of FeOOH and Fe2O3 : Effects of Poor Crystallinity and of Al-For-Fe Substitution. *Clay miner.* 37, 591–606. doi:10.1180/0009855023740062

de Grave, E., and Vandenberghe, R. E. (1990). Mössbauer Effect Study of the Spin Structure in Natural Hematites. *Phys. Chem. Minerals* 17, 344–352. doi:10.1007/BF00200130

Dekkers, M. J. (1989a). Magnetic Properties of Natural Goethite-I. Grain-Size Dependence of Some Low- and High-Field Related Rockmagnetic Parameters Measured at Room Temperature. *Geophys. J. Int.* 97, 323–340. doi:10.1111/j.1365-246X.1989.tb00504.x

Dekkers, M. J. (1989b). Magnetic Properties of Natural Goethite-II. TRM Behaviour during Thermal and Alternating Field Demagnetization and Low-Temperature Treatment. *Geophys. J. Int.* 97, 341–355. doi:10.1111/j.1365-246X.1989.tb00505.x

Dunlop, D. J. (1986). Hysteresis Properties of Magnetite and Their Dependence on Particle Size: A Test of Pseudo-single-domain Remanence Models. *J. Geophys. Res.* 91, 9569. doi:10.1029/jb091ib09p09569

Dunlop, D. J. (1995). Magnetism in Rocks. *J. Geophys. Res.* 100, 2161–2174. doi:10.1029/94JB02624

Dunlop, D. J., and Özdemir, Ö. (1997). *Rock Magnetism: Fundamentals and Frontiers*. 1st Edn. Cambridge, United Kingdom: Cambridge University Press. doi:10.1017/CBO9780511612794

Dunlop, D. J., and Özdemir, Ö. (2018). Remanence Cycling of 0.6-135 Mm Magnetites across the Verwey Transition. *Earth Planets Space* 70, 164. doi:10.1186/s40623-018-0928-z

Dunlop, D. J. (2002a). Theory and Application of the Day Plot (Mrs/Ms versus Hcr/Hc) 1. Theoretical Curves and Tests Using Titanomagnetite Data. *J. Geophys. Res.* 107, 1–22. doi:10.1029/2001jb000486

Dunlop, D. J. (2002b). Theory and Application of the Day Plot (Mrs/Ms versus Hcr/Hc) 2. Application to Data for Rocks, Sediments, and Soils. *J. Geophys. Res.* 107, 1–15. doi:10.1029/2001jb000487

Dyke, A. S., Andrews, J. T., Clark, P. U., England, J. H., Miller, G. H., Shaw, J., et al. (2002). The Laurentide and Innuitian Ice Sheets during the Last Glacial Maximum. *Quat. Sci. Rev.* 21, 9–31. doi:10.1016/S0277-3791(01)00095-6

Edwards, E. J., Osborne, C. P., Strömberg, C. A. E., Smith, S. A., Bond, W. J., Christin, P. A., et al. (2010). The Origins of C4 Grasslands: Integrating Evolutionary and Ecosystem Science. *Science* 328, 587–591. doi:10.1126/science.1177216

Egli, R. (2004). Characterization of Individual Rock Magnetic Components by Analysis of Remanence Curves, 1. Unmixing Natural Sediments. *Studia Geophysica et Geodaetica* 48, 391–446. doi:10.1023/B:SGEG.0000020839.45304.6d

Egli, R., Chen, A. P., Winklhofer, M., Kodama, K. P., and Horng, C.-S. (2010). Detection of Noninteracting Single Domain Particles Using First-Order Reversal Curve Diagrams. *Geochem. Geophys. Geosyst.* 11, a–n. doi:10.1029/2009gc002916

Egli, R. (2013). VARIFORC: An Optimized Protocol for Calculating Non-regular First-Order Reversal Curve (FORC) Diagrams. *Glob. Planet. Change* 110, 302–320. doi:10.1016/j.gloplacha.2013.08.003

Egli, R., and Winklhofer, M. (2014). "Recent Developments on Processing and Interpretation Aspects of First-Order Reversal Curves (FORC)," in *Natural Science Series,* Ученые заПиски КазанскоГо университета (Scientific Notes of the Kazan University). Available at: http://kpfu.ru/uz-rus/ns15614–53

Ehleringer, J. R., Cerling, T. E., and Helliker, B. R. (1997). C 4 Photosynthesis, Atmospheric CO 2, and Climate. *Oecologia* 112, 285–299. doi:10.1007/s004420050311

Eichler, C. (2020). Determining the Source of the Ogallala Formation: Sedimentary Petrology of the Ogallala Formation, Southern High Plains, West Texas and Eastern New Mexico. *Doctoral Dissertation*. Lubbock (TX): Tech University Geosciences Department.

Elderfield, H., Ferretti, P., Greaves, M., Crowhurst, S., McCave, I. N., Hodell, D., et al. (2012). Evolution of Ocean Temperature and Ice Volume through the Mid-pleistocene Climate Transition. *Science* 337, 704–709. doi:10.1126/science.1221294

Evans, M., and Heller, F. (2003). *Environmental Magnetism: Principles and Applications of Enviromagnetics*. 1st Edn. San Diego, CA: Elsevier Science.

Eyre, J. K., and Shaw, J. (1994). Magnetic Enhancement of Chinese Loess-The Role of γFe2O3? *Geophys. J. Int.* 117, 265–271. doi:10.1111/j.1365-246X.1994.tb03317.x

Fabian, K., McEnroe, S. A., Robinson, P., and Shcherbakov, V. P. (2008). Exchange Bias Identifies Lamellar Magnetism as the Origin of the Natural Remanent Magnetization in Titanohematite With Ilmenite Exsolution from Modum, Norway. *Earth Planet. Sci. Lett.* 268, 339–358. doi:10.1016/j.epsl.2008.01.034

Fabian, K., Shcherbakov, V. P., and McEnroe, S. A. (2013). Measuring the Curie Temperature. *Geochem. Geophys. Geosyst.* 14, 947–961. doi:10.1029/2012GC004440

Frey, P. A., and Reed, G. H. (2012). The Ubiquity of Iron. *ACS Chem. Biol.* 7, 1477–1481. doi:10.1021/cb300323q

Gehring, A. U., Fischer, H., Louvel, M., Kunze, K., and Weidler, P. G. (2009). High Temperature Stability of Natural Maghemite: A Magnetic and Spectroscopic Study. *Geophys. J. Int.* 179, 1361–1371. doi:10.1111/j.1365-246X.2009.04348.x

Geiss, C. E., and Zanner, C. W. (2006). How Abundant Is Pedogenic Magnetite? Abundance and Grain Size Estimates for Loessic Soils Based on Rock Magnetic Analyses. *J. Geophys. Res.* 111, a–n. doi:10.1029/2006JB004564

Ginoux, P., Prospero, J. M., Gill, T. E., Hsu, N. C., and Zhao, M. (2012). Global-scale Attribution of Anthropogenic and Natural Dust Sources and Their Emission Rates Based on MODIS Deep Blue Aerosol Products. *Rev. Geophys.* 50, 3005. doi:10.1029/2012RG000388

Green, J. K., Konings, A. G., Alemohammad, S. H., Berry, J., Entekhabi, D., Kolassa, J., et al. (2017). Regionally strong Feedbacks between the Atmosphere and Terrestrial Biosphere. *Nat. Geosci* 10, 410–414. doi:10.1038/ngeo2957

Gustavson, T. C., and Holliday, V. T. (1999). Eolian Sedimentation and Soil Development on a Semiarid to Subhumid Grassland, Tertiary ogallala and Quaternary blackwater Draw Formations, Texas and New Mexico High plains. *J. Sediment. Res.* 69, 622–634. doi:10.2110/jsr.69.622

Guyodo, Y., LaPara, T. M., Anschutz, A. J., Penn, R. L., Banerjee, S. K., Geiss, C. E., et al. (2006). Rock Magnetic, Chemical and Bacterial Community Analysis of a Modern Soil from Nebraska. *Earth Planet. Sci. Lett.* 251, 168–178. doi:10.1016/j.epsl.2006.09.005

Guyodo, Y., Mostrom, A., Lee Penn, R., and Banerjee, S. K. (2003). From Nanodots to Nanorods: Oriented Aggregation and Magnetic Evolution of Nanocrystalline Goethite. *Geophys. Res. Lett.* 30. 2003 Available at: http://doi.wiley.com/10.1029/2003GL017021 (Accessed February 7, 2021). doi:10.1029/2003gl017021

Haltia, E. M., and Nowaczyk, N. R. (2014). Magnetostratigraphy of Sediments from Lake El'gygytgyn ICDP Site 5011-1: Paleomagnetic Age Constraints for the Longest Paleoclimate Record from the continental Arctic. *Clim. Past* 10, 623–642. doi:10.5194/cp-10-623-2014

Hanesch, M., Stanjek, H., and Petersen, N. (2006). Thermomagnetic Measurements of Soil Iron Minerals: The Role of Organic Carbon. *Geophys. J. Int.* 165, 53–61. doi:10.1111/j.1365-246X.2006.02933.x

Harrison, R. J., and Feinberg, J. M. (2008). FORCinel: An Improved Algorithm for Calculating First-Order Reversal Curve Distributions Using Locally Weighted Regression Smoothing. *Geochem. Geophys. Geosyst.* 9, a–n. doi:10.1029/2008GC001987

Head, M. J., and Gibbard, P. L. (2005). Early-Middle Pleistocene Transitions: an Overview and Recommendation for the Defining Boundary. *Geol. Soc. Lond. Spec. Publications* 247, 1–18. doi:10.1144/GSL.SP.2005.247.01.01

Heider, F., Zitzelsberger, A., and Fabian, K. (1996). Magnetic Susceptibility and Remanent Coercive Force in Grown Magnetite Crystals from 0.1 μm to 6 Mm. *Phys. Earth Planet. Interiors* 93, 239–256. doi:10.1016/0031-9201(95)03071-9

Heller, F., and Tungsheng, L. (1984). Magnetism of Chinese Loess Deposits. *Geophys. J. Int.* 77, 125–141. doi:10.1111/j.1365-246X.1984.tb01928.x

Herron, M. M. (1988). Geochemical Classification of Terrigenous Sands and Shales from Core or Log Data. *J. Sediment. Petrol.* 58, 820–829. doi:10.1306/212f8e77-2b24-11d7-8648000102c1865d

Holliday, V. T., Hovorka, S. D., and Gustavson, T. C. (1996b). Lithostratigraphy and Geochronology of Fills in Small Playa Basins on the Southern High Plains, United States. *Bull. Geol. Soc. America* 108, 0953–0965. doi:10.1130/0016-7606(1996)108<0953:LAGOFI>2.3.CO;210.1130/0016-7606(1996)108<0953:lagofi>2.3.co;2

Holliday, V. T., Hovorka, S. D., and Gustavson, T. C. (1996a). Stratigraphy and Geochronology of Playa Fills on the Southern High Plains. *Geol. Soc. America Bull.* 108, 0953–0965. doi:10.1130/0016-7606(1996)108<0953:lagofi>2.3.co10.1130/0016-7606(1996)108<0953:lagofi>2.3.co;2

Holliday, V. T., Mayer, J. H., and Fredlund, G. G. (2008). Late Quaternary Sedimentology and Geochronology of Small Playas on the Southern High Plains, Texas and New Mexico, U.S.A. *Quat. Res.* 70, 11–25. doi:10.1016/j.yqres.2008.02.009

Holliday, V. T. (1997). Origin and Evolution of Lunettes on the High plains of Texas and New Mexico. *Quat. Res.* 47, 54–69. doi:10.1006/qres.1996.1872

Holliday, V. T. (1989). The Blackwater Draw Formation (Quaternary): A 1-4-plus-m.Y. Record of Eolian Sedimentation and Soil Formation on the Southern High Plains. *Geol. Soc. America Bull.* 101, 1598–1607. doi:10.1130/0016-7606(1989)101<1598:TBDFQA>2.3.CO;210.1130/0016-7606(1989)101<1598:tbdfqa>2.3.co;2

Hovorka, S. (1995). Quaternary Evolution of Playa Lakes on the Southern High Plains--A Case Study from the Amarillo Area, Texas. *Rep. Invest. – Univ. Tex. Austin, Bur. Econ. Geology.* 236, 1–52. doi:10.23867/ri0236d

Hrouda, F. (2011). Models of Frequency-dependent Susceptibility of Rocks and Soils Revisited and Broadened. *Geophys. J. Int.* 187, 1259–1269. doi:10.1111/j.1365-246X.2011.05227.x

Huang, Y., Street-Perrott, F. A., Metcalfe, S. E., Brenner, M., Moreland, M., and Freeman, K. H. (2001). Climate Change as the Dominant Control on Glacial-Interglacial Variations in C3 and C4 Plant Abundance. *Science* 293, 1647–1651. doi:10.1126/science.1060143

Hughes, P. D., and Gibbard, P. L. (2018). Global Glacier Dynamics during 100 Ka Pleistocene Glacial Cycles. *Quat. Res.* 90, 222–243. doi:10.1017/qua.2018.37

Imbrie, J., Berger, A., Boyle, E. A., Clemens, S. C., Duffy, A., Howard, W. R., et al. (1993). On the Structure and Origin of Major Glaciation Cycles 2. The 100,000-year Cycle. *Paleoceanography* 8, 699–735. doi:10.1029/93PA02751

Ishikawa, Y., and Akimoto, S. I. (1957). Magnetic Properties of the $FeTi0_3$-Fe_20_3 Solid Solution Series. *J. Phys. Soc. Jpn.* 12, 1083–1098. doi:10.1143/JPSJ.12.1083

Izett, G. A., Wilcox, R. E., and Borchardt, G. A. (1972). Correlation of a Volcanic Ash Bed in Pleistocene Deposits Near Mount Blanco, Texas, with the Guaje Pumice Bed of the Jemez Mountains, New Mexico. *Quat. Res.* 2, 554–578. doi:10.1016/0033-5894(72)90091-9

Jeleńska, M., Hasso-Agopsowicz, A., and Kopcewicz, B. (2010). Thermally Induced Transformation of Magnetic Minerals in Soil Based on Rock Magnetic Study and Mössbauer Analysis. *Phys. Earth Planet. Interiors* 179, 164–177. doi:10.1016/j.pepi.2009.11.004

Jennings, C. E., Aber, J. S., Balco, G., Barendregt, R., Bierman, P. R., Rovey, C. W., et al. (2013). "Mid-quaternary in North America," in *Encyclopedia Of Quaternary Science*. Editors S. J. Elias, G. J. Mock, D. M. Anderson, A. Beaudoin, H. H. Birks, E. Brook, et al. (Amsterdam, Netherlands: Elsevier Inc.), 180–186. doi:10.1016/B978-0-444-53643-3.00124-2

Jiang, Z., Liu, Q., Dekkers, M. J., Colombo, C., Yu, Y., Barrón, V., et al. (2014). Ferro and Antiferromagnetism of Ultrafine-Grained Hematite. *Geochem. Geophys. Geosyst.* 15, 2699–2712. doi:10.1002/2014GC005377

Jiang, Z., Liu, Q., Roberts, A. P., Barrón, V., Torrent, J., and Zhang, Q. (2018). A New Model for Transformation of Ferrihydrite to Hematite in Soils and Sediments. *Geology* 46, 987–990. doi:10.1130/G45386.1

Johnson, H. P., and Merrill, R. T. (1973). Low-temperature Oxidation of a Titanomagnetite and the Implications for Paleomagnetism. *J. Geophys. Res.* 78, 4938–4949. Available at: http://doi.wiley.com/10.1029/JB078i023p04938 (Accessed February 7, 2021). doi:10.1029/jb078i023p04938

Jordanova, N. (2016). *Soil Magnetism: Applications in Pedology, Environmental Science and Agriculture*. 2nd ed. San Diego, USA: Elsevier Science Publishing Co Inc. Available at: https://www.sciencedirect.com/book/9780128092392/soil-magnetism (Accessed February 7, 2021).

Kämpf, N., and Schwertmann, U. (1983). Goethite and Hematite in a Climosequence in Southern Brazil and Their Application in Classification of Kaolinitic Soils. *Geoderma* 29, 27–39. doi:10.1016/0016-7061(83)90028-9

Kandakji, T., Gill, T. E., and Lee, J. A. (2020). Identifying and Characterizing Dust point Sources in the Southwestern United States Using Remote Sensing and GIS. *Geomorphology* 353, 107019. doi:10.1016/j.geomorph.2019.107019

Karumuri, S. R., Kumar, A., Varma, M., Choudary, G., and Rao, K. H. (2009). Cation Distribution of Titanium Substituted Cobalt Ferrites. *J. Alloys Compd.* 488. doi:10.1016/j.jallcom.2009.08.086

Klein, C., and Dutrow, B. (2007). *Manual of Mineral Science*. 23rd ed.. Hoboken, NJ: John Wiley & Sons. Available at: https://books.google.com/books?id=kj5NuwEACAAJ.

Klink, K. (1999). Climatological Mean and Interannual Variance of United States Surface Wind Speed, Direction and Velocity. *Int. J. Climatol.* 19, 471–488. doi:10.1002/(SICI)1097-0088(199904)19:5<471::AID-JOC367>3.0.CO;2-X10.1002/(sici)1097-0088(199904)19:5<471::aid-joc367>3.0.co;2-x

Kravchinsky, V. A., Zykina, V. S., and Zykin, V. S. (2008). Magnetic Indicator of Global Paleoclimate Cycles in Siberian Loess-Paleosol Sequences. *Earth Planet. Sci. Lett.* 265, 498–514. doi:10.1016/j.epsl.2007.10.031

Kukla, G., Heller, F., Liu Xiu Ming, Xu Tong Chun, L. X., ChunSheng, X. T. L. T., and Sheng, A. Z. (1988). Pleistocene Climates in China Dated by Magnetic Susceptibility. *Geol.* 16, 811–814. doi:10.1130/0091-7613(1988)016<0811:PCICDB>2.3.CO;2.10.1130/0091-7613(1988)016<0811:pcicdb>2.3.co;2

Lagroix, F., and Guyodo, Y. (2017). A New Tool for Separating the Magnetic Mineralogy of Complex Mineral Assemblages from Low Temperature Magnetic Behavior. *Front. Earth Sci.* 5, 61. doi:10.3389/feart.2017.00061

Lagroix, F., Guyodo, Y., Till, J. L., and Naess, N. (2014). Magnetic mineral Separation: a Timeless challenge for an Experimental Rock Magnetist. Available at: https://ui.adsabs.harvard.edu/abs/2014EGUGA..16.3819L/abstract (Accessed February 7, 2021).

Lang, D. C., Bailey, I., Wilson, P. A., Beer, C. J., Bolton, C. T., Friedrich, O., et al. (2014). The Transition on North America from the Warm Humid Pliocene to the Glaciated Quaternary Traced by Eolian Dust Deposition at a Benchmark North Atlantic Ocean Drill Site. *Quat. Sci. Rev.* 93, 125–141. doi:10.1016/j.quascirev.2014.04.005

Lascu, I., and Feinberg, J. M. (2011). Speleothem Magnetism. *Quat. Sci. Rev.* 30, 3306–3320. doi:10.1016/j.quascirev.2011.08.004

Lattard, D., Engelmann, R., Kontny, A., and Sauerzapf, U. (2006). Curie Temperatures of Synthetic Titanomagnetites in the Fe-Ti-O System: Effects of Composition, crystal Chemistry, and Thermomagnetic Methods. *J. Geophys. Res.* 111, a–n. doi:10.1029/2006JB004591

Lee, J. A., Baddock, M. C., Mbuh, M. J., and Gill, T. E. (2012). Geomorphic and Land Cover Characteristics of Aeolian Dust Sources in West Texas and Eastern New Mexico, USA. *Aeolian Res.* 3, 459–466. doi:10.1016/j.aeolia.2011.08.001

Lee, J. A., Evan Moffett, K., Allen, B. L., Peterson, R. E., and Gregory, J. M. (1994). Environmental Controls on Blowing Dust Direction at lubbock, Texas, U.S.A. *Earth Surf. Process. Landforms* 19, 437–449. doi:10.1002/esp.3290190505

Lee, J. A., Gill, T. E., Mulligan, K. R., Dominguez Acosta, M., and Perez, A. E. (2009). Land Use/land Cover and point Sources of the 15 December 2003 Dust Storm in Southwestern North America. *Geomorphology* 105, 18–27. doi:10.1016/j.geomorph.2007.12.016

Lemmen, D. S., Duk-Rodkin, A., and Bednarski, J. M. (1994). Late Glacial Drainage Systems along the Northwestern Margin of the Laurentide Ice Sheet. *Quat. Sci. Rev.* 13, 805–828. doi:10.1016/0277-3791(94)90003-5

Lepp, H. (1975). *Geochemistry of Iron*. Stroudsburg, PA: Dowden Hutchinson & Ross Stroudsburg.

Levi, S., and Merrill, R. T. (1978). Properties of Single-Domain, Pseudo-single-domain, and Multidomain Magnetite. *J. Geophys. Res.* 83, 309. doi:10.1029/jb083ib01p00309

Li, J., Kandakji, T., Lee, J. A., Tatarko, J., Blackwell, J., Gill, T. E., et al. (2018). Blowing Dust and Highway Safety in the Southwestern United States: Characteristics of Dust Emission "Hotspots" and Management Implications. *Sci. Total Environ.* 621, 1023–1032. doi:10.1016/j.scitotenv.2017.10.124

Li, Y., Shi, W., Aydin, A., Beroya-Eitner, M. A., and Gao, G. (2020). Loess Genesis and Worldwide Distribution. *Earth-Science Rev.* 201, 102947. doi:10.1016/j.earscirev.2019.102947

Lisiecki, L. E. (2010). Links between Eccentricity Forcing and the 100,000-year Glacial Cycle. *Nat. Geosci.* 3, 349–352. doi:10.1038/ngeo828

Lisiecki, L. E., and Raymo, M. E. (2005). A Pliocene-Pleistocene Stack of 57 Globally Distributed Benthic δ18O Records. *Paleoceanography* 20, a–n. doi:10.1029/2004PA00107110.1029/2004pa001071

Liu, C., Deng, C., and Liu, Q. (2012). Mineral Magnetic Studies of the Vermiculated Red Soils in Southeast China and Their Paleoclimatic Significance. *Palaeogeogr. Palaeoclimatol. Palaeoecol.* 329-330, 173–183. doi:10.1016/j.palaeo.2012.02.035

Liu, Q., Banerjee, S. K., Jackson, M. J., Chen, F., Pan, Y., and Zhu, R. (2003). An Integrated Study of the Grain-size-dependent Magnetic Mineralogy of the Chinese Loess/paleosol and its Environmental Significance. *J. Geophys. Res.* 108, 2437. doi:10.1029/2002jb002264

Liu, Q., Deng, C., Torrent, J., and Zhu, R. (2007a). Review of Recent Developments in mineral Magnetism of the Chinese Loess. *Quat. Sci. Rev.* 26, 368–385. doi:10.1016/j.quascirev.2006.08.004

Liu, Q. (2004). Grain Sizes of Susceptibility and Anhysteretic Remanent Magnetization Carriers in Chinese Loess/paleosol Sequences. *J. Geophys. Res.* 109, B03101. doi:10.1029/2003jb002747

Liu, Q., Jackson, M. J., Banerjee, S. K., Maher, B. A., Deng, C., Pan, Y., et al. (2004a). Mechanism of the Magnetic Susceptibility Enhancements of the Chinese Loess. *J. Geophys. Res.* 109, 1–16. doi:10.1029/2004JB003249

Liu, Q., Jackson, M. J., Yu, Y., Chen, F., Deng, C., and Zhu, R. (2004b). Grain Size Distribution of Pedogenic Magnetic Particles in Chinese Loess/paleosols. *Geophys. Res. Lett.* 31, 1–4. doi:10.1029/2004GL021090

Liu, Q., Roberts, A. P., Torrent, J., Horng, C.-S., and Larrasoaña, J. C. (2007b). What Do the HIRM andS-Ratio Really Measure in Environmental Magnetism? *Geochem. Geophys. Geosyst.* 8, a–n. doi:10.1029/2007GC001717

Liu, Q., Yu, Y., Torrent, J., Roberts, A. P., Pan, Y., and Zhu, R. (2006). Characteristic Low-Temperature Magnetic Properties of Aluminous Goethite [α-(Fe, Al)OOH] Explained. *J. Geophys. Res.* 111, a–n. doi:10.1029/2006JB004560

Liu, X., Liu, T., Paul, H., Xia, D., Jiri, C., and Wang, G. (2008). Two Pedogenic Models for Paleoclimatic Records of Magnetic Susceptibility from Chinese and Siberian Loess. *Sci. China Ser. D-earth Sci.* 51, 284–293. doi:10.1007/s11430-007-0145-2

Liu, X., Liu, Z., Lü, B., Marković, S. B., Chen, J., Guo, H., et al. (2013). The Magnetic Properties of Serbian Loess and its Environmental Significance. *Chin. Sci. Bull.* 58, 353–363. doi:10.1007/s11434-012-5383-9

Liu, X. M., Hesse, P., and Rolph, T. (1999). Origin of Maghaemite in Chinese Loess Deposits: Aeolian or Pedogenic? *Phys. Earth Planet. Interiors* 112, 191–201. doi:10.1016/S0031-9201(99)00002-3

Liu, X. M., Xia, D. S., and Liu, T. S. (2007). Discussion on Two Models of Paleoclimatic Records of Magnetic Susceptibility of Alaskan and Chinese Loess (In Chinese). *Quaternary* 27, 210–220.

Liu, X., Shaw, J., Jiang, J., Bloemendal, J., Hesse, P., Rolph, T., et al. (2010). Analysis on Variety and Characteristics of Maghemite. *Sci. China Earth Sci.* 53, 1153–1162. doi:10.1007/s11430-010-0030-2

Liu, X., Shaw, J., Liu, T., Heller, F., and Yuan, B. (1992). Magnetic Mineralogy of Chinese Loess and its Significance. *Geophys. J. Int.* 108, 301–308. doi:10.1111/j.1365-246X.1992.tb00859.x

Löfverström, M., and Lora, J. M. (2017). Abrupt Regime Shifts in the North Atlantic Atmospheric Circulation over the Last Deglaciation. *Geophys. Res. Lett.* 44, 8047–8055. doi:10.1002/2017GL074274

Lowe, J., and Walker, M. (2015). *Reconstructing Quaternary Environments*. 3rd ed. London, United Kingdom: Routledge, Taylor & Francis Group.

Lowrie, W. (1990). Identification of Ferromagnetic Minerals in a Rock by Coercivity and Unblocking Temperature Properties. *Geophys. Res. Lett.* 17, 159–162. doi:10.1029/GL017i002p00159

Lu, S.-G., Zhu, L., and Yu, J.-Y. (2012). Mineral Magnetic Properties of Chinese Paddy Soils and its Pedogenic Implications. *Catena* 93, 9–17. doi:10.1016/j.catena.2012.01.002

Machette, M. N. (1985). Calcic Soils of the Southwestern United States. *Spec. Paper Geol. Soc. America* 203, 1–22. doi:10.1130/SPE203-p1

Maher, B. A., Alekseev, A., and Alekseeva, T. (2003a). Magnetic Mineralogy of Soils across the Russian Steppe: Climatic Dependence of Pedogenic Magnetite Formation. *Palaeogeogr. Palaeoclimatol. Palaeoecol.* 201, 321–341. doi:10.1016/S0031-0182(03)00618-7

Maher, B. A. (1986). Characterisation of Soils by mineral Magnetic Measurements. *Phys. Earth Planet. Interiors* 42, 76–92. doi:10.1016/S0031-9201(86)80010-3

Maher, B. A. (1998). Magnetic Properties of Modern Soils and Quaternary Loessic Paleosols: Paleoclimatic Implications. *Palaeogeogr. Palaeoclimatol. Palaeoecol.* 137, 25–54. doi:10.1016/S0031-0182(97)00103-X

Maher, B. A. (1988). Magnetic Properties of Some Synthetic Sub-micron Magnetites. *Geophys. J. Int.* 94, 83–96. doi:10.1111/j.1365-246X.1988.tb03429.x

Maher, B. A., MengYu, H., Roberts, H. M., and Wintle, A. G. (2003b). Holocene Loess Accumulation and Soil Development at the Western Edge of the Chinese Loess Plateau: Implications for Magnetic Proxies of Palaeorainfall. *Quat. Sci. Rev.* 22, 445–451. doi:10.1016/S0277-3791(02)00188-9

Maher, B. A. (2011). The Magnetic Properties of Quaternary Aeolian Dusts and Sediments, and Their Palaeoclimatic Significance. *Aeolian Res.* 3, 87–144. doi:10.1016/j.aeolia.2011.01.005

Maher, B. A., and Thompson, R. (1991). Mineral Magnetic Record of the Chinese Loess and Paleosols. *Geol* 19, 3–6. doi:10.1130/0091-7613(1991)019<0003:MMROTC>2.3.CO;210.1130/0091-7613(1991)019<0003:mmrotc>2.3.co;2

Maher, B. A., and Thompson, R. (1995). Paleorainfall Reconstructions from Pedogenic Magnetic Susceptibility Variations in the Chinese Loess and Paleosols. *Quat. Res.* 44, 383–391. doi:10.1006/qres.1995.1083

Maher, B. A., and Thompson, R. (1999). *Quaternary Climates, Environments and Magnetism*. 1st Edn (Cambridge, United Kingdom: Cambridge University Press).

Martin, H. A. (2006). Cenozoic Climatic Change and the Development of the Arid Vegetation in Australia. *J. Arid Environments* 66, 533–563. doi:10.1016/j.jaridenv.2006.01.009

Matasova, G. G., and Kazansky, A. Y. (2005). Contribution of Paramagnetic Minerals to Magnetic Properties of Loess-Soil Deposits in Siberia and its Paleoclimatic Implications. *Izvestiya, Phys. Solid Earth* 41, 81–89. Available at: https://www.researchgate.net/publication/287414681_Contribution_of_paramagnetic_minerals_to_magnetic_properties_of_loess-soil_deposits_in_Siberia_and_its_paleoclimatic_implications (Accessed February 7, 2021).

Matasova, G., Petrovský, E., Jordanova, N., Zykina, V., and Kapička, A. (2001). Magnetic Study of Late Pleistocene Loess/palaeosol Sections from Siberia: Palaeoenvironmental Implications. *Geophys. J. Int.* 147, 367–380. doi:10.1046/j.0956-540x.2001.01544.x

Mathé, P.-E., Rochette, P., Vandamme, D., and Fillion, G. (1999). Néel Temperatures of Synthetic Substituted Goethites and Their Rapid Determination Using Low-Field Susceptibility Curves. *Geophys. Res. Lett.* 26, 2125–2128. doi:10.1029/1999GL900424

Maxbauer, D. P., Feinberg, J. M., and Fox, D. L. (2016a). Magnetic mineral Assemblages in Soils and Paleosols as the Basis for Paleoprecipitation Proxies: A Review of Magnetic Methods and Challenges. *Earth-Science Rev.* 155, 28–48. doi:10.1016/j.earscirev.2016.01.014

Maxbauer, D. P., Feinberg, J. M., and Fox, D. L. (2016b). MAX UnMix: A Web Application for Unmixing Magnetic Coercivity Distributions. *Comput. Geosciences* 95, 140–145. doi:10.1016/j.cageo.2016.07.009

McClymont, E. L., and Rosell-Melé, A. (2005). Links between the Onset of Modern Walker Circulation and the Mid-pleistocene Climate Transition. *Geol.* 33, 389–392. doi:10.1130/G21292.1

McLennan, S. M. (1989). "Chapter 7. Rare Earth Elements In Sedimentary Rocks: Influence of Provenance and Sedimentary Processes," in *Geochemistry and Mineralogy Of Rare Earth Elements* (Washington D.C.: De Gruyter Mouton), 169–200. doi:10.1515/9781501509032-010

Meng, X., Derbyshire, E., and Kemp, R. A. (1997). Origin of the Magnetic Susceptibility Signal in Chinese Loess. *Quat. Sci. Rev.* 16, 833–839. doi:10.1016/S0277-3791(97)00053-X

Merrill, R. T. (1968). A Possible Source for the Coercivity of Ilmenite-Hematite Minerals. *J. Geomagn. Geoelec.* 20, 181–185. doi:10.5636/jgg.20.181

Morin, F. J. (1950). Magnetic Susceptibility ofαFe2O3andαFe2O3with Added Titanium. *Phys. Rev.* 78, 819–820. doi:10.1103/PhysRev.78.819.2

Mudelsee, M., and Schulz, M. (1997). The Mid-pleistocene Climate Transition: Onset of 100 Ka Cycle Lags Ice Volume Build-Up by 280 Ka. *Earth Planet. Sci. Lett.* 151, 117–123. doi:10.1016/s0012-821x(97)00114-3

Muhs, D. R., Bettis, E. A., and Skipp, G. L. (2018). Geochemistry and Mineralogy of Late Quaternary Loess in the Upper Mississippi River valley, USA: Provenance and Correlation with Laurentide Ice Sheet History. *Quat. Sci. Rev.* 187, 235–269. doi:10.1016/j.quascirev.2018.03.024

Muhs, D. R. (2018). The Geochemistry of Loess: Asian and North American Deposits Compared. *J. Asian Earth Sci.* 155, 81–115. doi:10.1016/j.jseaes.2017.10.032

Muhs, D. R. (2013). The Geologic Records of Dust in the Quaternary. *Aeolian Res.* 9, 3–48. doi:10.1016/j.aeolia.2012.08.001

Munroe, J. S., and Laabs, B. J. C. (2013). Temporal Correspondence between Pluvial lake Highstands in the Southwestern US and Heinrich Event 1. *J. Quat. Sci.* 28, 49–58. doi:10.1002/jqs.2586

Muxworthy, A. R., and Dunlop, D. J. (2002). First-order Reversal Curve (FORC) Diagrams for Pseudo-single-domain Magnetites at High Temperature. *Earth Planet. Sci. Lett.* 203, 369–382. doi:10.1016/S0012-821X(02)00880-4

Nagarajan, R., Armstrong-Altrin, J. S., Kessler, F. L., and Jong, J. (2017). "Petrological and Geochemical Constraints on Provenance, Paleoweathering, and Tectonic Setting of Clastic Sediments from the Neogene Lambir and Sibuti Formations, Northwest Borneo," in *Sediment Provenance: Influences On Compositional Change from Source to Sink*. Editor R. Mazumder (Amsterdam, Netherlands: Elsevier), 123–153. doi:10.1016/B978-0-12-803386-9.00007-1

Necula, C., Panaiotu, C., Schinteie, G., Palade, P., and Kuncser, V. (2015). Reconstruction of Superparamagnetic Particle Grain Size Distribution from Romanian Loess Using Frequency Dependent Magnetic Susceptibility and Temperature Dependent Mössbauer Spectroscopy. *Glob. Planet. Change* 131, 89–103. doi:10.1016/j.gloplacha.2015.05.009

Nesbitt, H. W., and Young, G. M. (1982). Early Proterozoic Climates and Plate Motions Inferred from Major Element Chemistry of Lutites. *Nature* 299, 715–717. doi:10.1038/299715a0

Newell, A. J., and Merrill, R. T. (2000). Nucleation and Stability of Ferromagnetic States. *J. Geophys. Res.* 105, 19377–19391. doi:10.1029/2000jb900121

Nie, J., King, J., and Fang, X. (2008). Late Pliocene-Early Pleistocene 100-ka Problem. *Geophys. Res. Lett.* 35, 1–4. doi:10.1029/2008GL035265

Nie, J., Song, Y., and King, J. W. (2016). A Review of Recent Advances in Red-Clay Environmental Magnetism and Paleoclimate History on the Chinese Loess Plateau. *Front. Earth Sci.* 4, 27. doi:10.3389/feart.2016.00027

Novlan, D. J., Hardiman, M., and Gill, T. E. (2007). A Synoptic Climatology of Blowing Dust Events in El Paso, Texas from 1932-2005. Available at: https://www.weather.gov/media/epz/research/elp07-2.pdf (Accessed April 2, 2021).

Nowaczyk, N. R. (2011). Dissolution of Titanomagnetite and Sulphidization in Sediments from Lake Kinneret, Israel. *Geophys. J. Int.* 187, 34–44. doi:10.1111/j.1365-246X.2011.05120.x

Ogg, J. G. (2020). "Geomagnetic Polarity Time Scale," in *Geologic Time Scale 2020*. Editors F. M. Gradstein, J. G. Ogg, M. D. Schmitz, and G. M. Ogg (Amsterdam, Netherlands: Elsevier), 159–192. doi:10.1016/b978-0-12-824360-2.00005-x

O'Reilly, W. (1976). Magnetic Minerals in the Crust of the Earth. *Rep. Prog. Phys.* 39, 857–908. doi:10.1088/0034-4885/39/9/002

O'Reilly, W. (1984). *Rock and Mineral Magnetism*. 1st ed. Boston, MA: Springer US. doi:10.1007/978-1-4684-8468-7

Orgeira, M. J., Egli, R., and Compagnucci, R. H. (2011). "A Quantitative Model of Magnetic Enhancement in Loessic Soils," in *The Earth's Magnetic Interior*. Editors E. Petrovský, E. Herrero-Bervera, T. Harinarayana, and D. Ivers (London, U.K.: Springer Netherlands), 361–397. doi:10.1007/978-94-007-0323-0_25

Oster, J. L., Ibarra, D. E., Winnick, M. J., and Maher, K. (2015). Steering of westerly Storms over Western North America at the Last Glacial Maximum. *Nat. Geosci.* 8, 201–205. doi:10.1038/ngeo2365

Özdemir, Ö., and Banerjee, S. K. (1984). High Temperature Stability of Maghemite (γ-Fe2O3). *Geophys. Res. Lett.* 11, 161–164. doi:10.1029/GL011i003p00161

Özdemir, Ö., Dunlop, D. J., and Berquó, T. S. (2008). Morin Transition in Hematite: Size Dependence and thermal Hysteresis. *Geochem. Geophys. Geosyst.* 9, a–n. doi:10.1029/2008GC002110

Özdemir, Ö., and Dunlop, D. J. (2010). Hallmarks of Maghemitization in Low-Temperature Remanence Cycling of Partially Oxidized Magnetite Nanoparticles. *J. Geophys. Res.* 115. doi:10.1029/2009jb006756

Özdemir, Ö., and Dunlop, D. J. (2014). Hysteresis and Coercivity of Hematite. *J. Geophys. Res. Solid Earth* 119, 2582–2594. doi:10.1002/2013JB010739

Parker, R. L., and Fleischer, M. (1968). *Geochemistry of Niobium and Tantalum A Review of the Geochemistry of Niobium and Tantalum and a Glossary of Niobium and Tantalum Minerals*. Washington, DC: U.S. Geological Survey. doi:10.3133/pp612

Patterson, P. E., and Larson, E. E., and (1990). "Paleomagnetic Study and Age Assessment of a Succession of Paleosols in the Type Section of the Blackwater Draw Formation, Northwestern Texas,," in *Geologic Framework and Regional Hydrology: Upper Cenozoic Blackwater Draw and Ogallala Formations, Great Plains*. Editors T. C. Gustavson (Austin, TX: The University of Texas at Austin, Buerau of Economic Geology), 234–244.

Peters, C., and Dekkers, M. J. (2003). Selected Room Temperature Magnetic Parameters as a Function of Mineralogy, Concentration and Grain Size. *Phys. Chem. Earth, Parts A/B/C* 28, 659–667. doi:10.1016/S1474-7065(03)00120-7

Petersen, N., and Vali, H. (1987). Observation of Shrinkage Cracks in Ocean Floor Titanomagnetites. *Phys. Earth Planet. Interiors* 46, 197–205. doi:10.1016/0031-9201(87)90182-8

Pluhar, C. J., and Kirschvink, J. L. (1991). Magnetostratigraphy and Clockwise Rotation of the Plio-Pleistocene Mojave River Formation, Central Mojave Desert, California. *Quarterly (San Bernardino County Museum Association)* 38, 31–42.

Prothero, D. R. (2011). Paleomagnetism, Magnetostratigraphy. *Encyclopedia Earth Sci. Ser. Part* 5, 925–933. doi:10.1007/978-90-481-8702-7_124

Putnam, A. E. (2015). A Glacial Zephyr. *Nat. Geosci.* 8, 175–176. doi:10.1038/ngeo2377

Raymo, M. E., Oppo, D. W., and Curry, W. (1997). The Mid-pleistocene Climate Transition: A Deep Sea Carbon Isotopic Perspective. *Paleoceanography* 12, 546–559. doi:10.1029/97PA01019

Raymo, M. E., Ruddiman, W. F., and Froelich, P. N. (1988). Influence of Late Cenozoic Mountain Building on Ocean Geochemical Cycles. *Geol.* 16, 649–653. doi:10.1130/0091-7613(1988)016<0649:IOLCMB>2.3.CO;210.1130/0091-7613(1988)016<0649:iolcmb>2.3.co;2

Raymo, M. E. (1994). The Himalayas, Organic Carbon Burial, and Climate in the Miocene. *Paleoceanography* 9, 399–404. doi:10.1029/94PA00289

Raymo, M. E. (1997). The Timing of Major Climate Terminations. *Paleoceanography* 12, 577–585. doi:10.1029/97PA01169

Rea, D. K. (1994). The Paleoclimatic Record provided by Eolian Deposition in the Deep Sea: The Geologic History of Wind. *Rev. Geophys.* 32, 159. doi:10.1029/93RG03257

Reeves, C. C., and Mahaney, W. C. (1976). "Quaternary stratigraphy and geologic history of Southern High Plains, Texas and New Mexico," in *Quaternary stratigraphy of North America*. Editor W. C. Mahaney (Stroudsburg, PA: Dowden, Hutchinson, & Ross), 213–234.

Retallack, G. J. (2005). Pedogenic Carbonate Proxies for Amount and Seasonality of Precipitation in Paleosols. *Geol* 33, 333–336. doi:10.1130/G21263.1

Roberts, A. P., Almeida, T. P., Church, N. S., Harrison, R. J., Heslop, D., Li, Y., et al. (2017). Resolving the Origin of Pseudo-single Domain Magnetic Behavior. *J. Geophys. Res. Solid Earth* 122, 9534–9558. doi:10.1002/2017JB014860

Roberts, A. P., Heslop, D., Zhao, X., and Pike, C. R. (2014). Understanding fine Magnetic Particle Systems through Use of First-Order Reversal Curve Diagrams. *Rev. Geophys.* 52, 557–602. doi:10.1002/2014RG000462

Roberts, A. P., Pike, C. R., and Verosub, K. L. (2000). First-order Reversal Curve Diagrams: A New Tool for Characterizing the Magnetic Properties of Natural Samples. *J. Geophys. Res.* 105, 28461–28475. doi:10.1029/2000jb900326

Robertson, D. J., and France, D. E. (1994). Discrimination of Remanence-Carrying Minerals in Mixtures, Using Isothermal Remanent Magnetisation Acquisition Curves. *Phys. Earth Planet. Interiors* 82, 223–234. doi:10.1016/0031-9201(94)90074-4

Rochette, P., and Fillion, G. (1989). Field and Temperature Behavior of Remanence in Synthetic Goethite: Paleomagnetic Implications. *Geophys. Res. Lett.* 16, 851–854. doi:10.1029/GL016i008p00851

Santana, G. P., Fabris, J. D., Goulart, A. T., and Santana, D. P. (2001). Magnetite and its Transformation to Hematite in a Soil Derived from Steatite. Available at: https://www.scielo.br/scielo.php?pid=S0100-06832001000100004&script=sci_abstract (Accessed February 7, 2021).

Scheinost, A. C., and Schwertmann, U. (1999). Color Identification of Iron Oxides and Hydroxysulfates. *Soil Sci. Soc. Am. J.* 63, 1463–1471. doi:10.2136/sssaj1999.6351463x

Scheinost, A. C. (2005). "Metal Oxides," in *Encyclopedia Of Soils in the Environment*. Editors J. L. Hatfield, D. S. Powlson, C. Rosenzweig, K. M. Scow, M. J. Singer, and D. L. Sparks (Charlottesville, VA: Elsevier Inc.), 428–438. doi:10.1016/B0-12-348530-4/00194-6

Schmieder, F., von Dobeneck, T., and Bleil, U. (2000). The Mid-pleistocene Climate Transition as Documented in the Deep South Atlantic Ocean: Initiation, Interim State and Terminal Event. *Earth Planet. Sci. Lett.* 179, 539–549. doi:10.1016/S0012-821X(00)00143-6

Schwertmann, U., and Cornell, R. M. (1991). *Iron Oxides in the Laboratory*. 2nd Edn. New York, NY: Wiley-Vch.

Schwertmann, U., Friedl, J., and Stanjek, H. (1999). From Fe(III) Ions to Ferrihydrite and Then to Hematite. *J. Colloid Interf. Sci.* 209, 215–223. doi:10.1006/jcis.1998.5899

Schwertmann, U. (1988). Occurrence and Formation of Iron Oxides in Various Pedoenvironments. *Iron in soils and clay minerals*, 267–308. doi:10.1007/978-94-009-4007-9_11

Schwertmann, U., and Taylor, R. M. (1972). The Transformation of Lepidocrocite to Goethite. *Clays and Clay Minerals* 20, 151–158. doi:10.1346/CCMN.1972.0200306

Schwertmann, U., and Taylor, R. M. (1989). "Iron Oxides," in *Minerals in Soil Environments*. Editors J. B. Dixon and S. B. Weed (Weinheim: John Wiley & Sons, Ltd), 379–438. doi:10.2136/sssabookser1.2ed.c8

Schwertmann, U. (1958). "The Effect of Pedogenic Environments on Iron Oxide Minerals," In *Advances in Soil Science* (Springer), 171–200.doi:10.1007/978-1-4612-5046-3_5

Schwertmann, U. (1971). Transformation of Hematite to Goethite in Soils. *Nature* 232, 624–625. doi:10.1038/232624a0

Sheldon, N. D., Retallack, G. J., and Tanaka, S. (2002). Geochemical Climofunctions from North American Soils and Application to Paleosols across the Eocene-Oligocene Boundary in Oregon. *J. Geology* 110, 687–696. doi:10.1086/342865

Singer, B. S. (2014). A Quaternary Geomagnetic Instability Time Scale. *Quat. Geochronol.* 21, 29–52. doi:10.1016/j.quageo.2013.10.003

Soil Survey Staff (1990). Keys to Soil Taxonomy. Available at: https://www.nrcs.usda.gov/Internet/FSE_DOCUMENTS/nrcs142p2_051857.pdf (Accessed February 7, 2021).

Song, Y., Shi, Z., Fang, X., Nie, J., Naoto, I., Qiang, X., et al. (2010). Loess Magnetic Properties in the Ili Basin and Their Correlation with the Chinese Loess Plateau. *Sci. China Earth Sci.* 53, 419–431. doi:10.1007/s11430-010-0011-5

Soreghan, G. S., Elmore, R. D., Katz, B., Cogoini, M., and Banerjee, S. (1997). Pedogenically Enhanced Magnetic Susceptibility Variations Preserved in Paleozoic Loessite. *Geol* 25, 1003–1006. doi:10.1130/0091-7613(1997)025<1003:PEMSVP>2.3.CO;210.1130/0091-7613(1997)025<1003:pemsvp>2.3.co;2

Stacey, F., and Banerjee, S. K. (1974). *The Physical Principles of Rock Magnetism*. Amsterdam: Elsevier Scientific Publishing Company.

Stine, J., Sweet, D. E., Geissman, J. W., Baird, H., and Ferguson, J. F. (2020). "Climate and Provenance Variation across the Mid-pleistocene Transition Revealed through Sedimentology, Geochemistry, and Rock Magnetism of the Blackwater Draw Formation, Southern High Plains, Texas, USA," in *Untangling the Quaternary Period—A Legacy Of Stephen C. Porter*. Editors R. B. Waitt, G. D. Thackray, and A. R. Gillespie (Geological Society of America). doi:10.1130/2020.2548(03)

Stober, J. C., and Thompson, R. (1979). Magnetic Remanence Acquisition in Finnish lake Sediments. Available at: https://academic.oup.com/gji/article/57/3/727/682760 (Accessed February 7, 2021).doi:10.3790/978-3-428-44398-7

Stober, J. C., and Thompson, R. (1977). Palaeomagnetic Secular Variation Studies of Finnish lake Sediment and the Carriers of Remanence. *Earth Planet. Sci. Lett.* 37, 139–149. doi:10.1016/0012-821X(77)90155-8

Stout, J. E. (2001). Dust and Environment in the Southern High Plains of North America. *J. Arid Environments* 47, 425–441. doi:10.1006/jare.2000.0732

Strangway, D. W., Honea, R. M., McMahon, B. E., and Larson, E. E. (1968). The Magnetic Properties of Naturally Occurring Goethite. *Geophys. J. Int.* 15, 345–359. doi:10.1111/j.1365-246X.1968.tb00191.x

Strangway, D. W., McMahon, B. E., Honea, R. M., and Larson, E. E. (1967b). Superparamagnetism in Hematite. *Earth Planet. Sci. Lett.* 2, 367–371. doi:10.1016/0012-821X(67)90158-6

Strangway, D. W., McMahon, B. E., and Honea, R. M. (1967a). Stable Magnetic Remanence in Antiferromagnetic Goethite. *Science* 158, 785–787. doi:10.1126/science.158.3802.785

Strömberg, C. A. E. (2011). Evolution of Grasses and Grassland Ecosystems. *Annu. Rev. Earth Planet. Sci.* 39, 517–544. doi:10.1146/annurev-earth-040809-152402

Sun, J., Lü, T., Zhang, Z., Wang, X., and Liu, W. (2012). Stepwise Expansions of C4 Biomass and Enhanced Seasonal Precipitation and Regional Aridity during the Quaternary on the Southern Chinese Loess Plateau. *Quat. Sci. Rev.* 34, 57–65. doi:10.1016/j.quascirev.2011.12.007

Tarling, D. H. (1983). *Palaeomagnetism: Principles and Applications in Geology, Geophysics and Archaeology*. 1st ed. New York: Springer Science & Business Media.

Tauxe, L., Bertram, H. N., and Seberino, C. (2002). Physical Interpretation of Hysteresis Loops: Micromagnetic Modeling of fine Particle Magnetite. *Geochem.-Geophys.-Geosyst.* 3, 1–22. doi:10.1029/2001GC000241

Tauxe, L. (2010). *Essentials of Paleomagnetism*. Berkely, CA: University of California Press. doi:10.1007/978-94-009-5955-2

Thompson, R., and Oldfield, F. (1986). *Environmental Magnetism*. 1st ed. London, United Kingdom: Springer Science & Business Media. doi:10.1007/978-94-011-8036-8

Torrent, J., Barrón, V., and Liu, Q. (2006). Magnetic Enhancement Is Linked to and Precedes Hematite Formation in Aerobic Soil. *Geophys. Res. Lett.* 33, L02401. doi:10.1029/2005GL024818

Torrent, J., Liu, Q., Bloemendal, J., and Barrón, V. (2007). Magnetic Enhancement and Iron Oxides in the Upper Luochuan Loess-Paleosol Sequence, Chinese Loess Plateau. *Soil Sci. Soc. Am. J.* 71, 1570–1578. doi:10.2136/sssaj2006.0328

Tziperman, E., and Gildor, H. (2003). On the Mid-pleistocene Transition to 100-kyr Glacial Cycles and the Asymmetry between Glaciation and Deglaciation Times. *Paleoceanography* 18, 1–8. doi:10.1029/2001pa000627

Ul-Hamid, A. (2018). *A Beginners' Guide to Scanning Electron Microscopy*. Cham, Switzerland: Springer International Publishing. doi:10.1007/978-3-319-98482-7

Vahle, C., Kontny, A., Gunnlaugsson, H. P., and Kristjansson, L. (2007). The Stardalur Magnetic Anomaly Revisited-New Insights into a Complex Cooling and Alteration History. *Phys. Earth Planet. Interiors* 164, 119–141. doi:10.1016/j.pepi.2007.06.004

Vandenberghe, R. E., Barrero, C. A., da Costa, G. M., van San, E., and de Grave, E. (2000). Mössbauer Characterization of Iron Oxides and (Oxy)hydroxides: The Present State of the Art. *Hyperfine Interactions* 126, 247–259. doi:10.1023/A:1012603603203

Verosub, K. L., Fine, P., Singer, M. J., and Tenpas, J. (1993). Pedogenesis and Paleoclimate: Interpretation of the Magnetic Susceptibility Record of Chinese Loess-Paleosol Sequences. *Geol.* 21, 1011–1014. doi:10.1130/0091-7613(1993)021<1011:PAPIOT>2.3.CO;210.1130/0091-7613(1993)021<1011:papiot>2.3.co;2

Verwey, E. J. W. (1939). Electronic Conduction of Magnetite (Fe3O4) and its Transition Point at Low Temperatures. *Nature* 144, 327–328. doi:10.1038/144327b0

Wang, H., Zhou, W., Shu, P., Hong, B., and An, Z. (2021). Two-stage Evolution of Glacial-Period Asian Monsoon Circulation by Shifts of westerly Jet Streams and Changes of North American Ice Sheets. *Earth-Science Rev.* 215, 103558. doi:10.1016/j.earscirev.2021.103558

Wang, P., Du, Y., Yu, W., Algeo, T. J., Zhou, Q., Xu, Y., et al. (2020). The Chemical index of Alteration (CIA) as a Proxy for Climate Change during Glacial-Interglacial Transitions in Earth History. *Earth-Science Rev.* 201, 103032. doi:10.1016/j.earscirev.2019.103032

Wang, S., Lin, S., and Lu, S. (2013). Rock Magnetism, Iron Oxide Mineralogy and Geochemistry of Quaternary Red Earth in central China and Their Paleopedogenic Implication. *Palaeogeogr. Palaeoclimatol. Palaeoecol.* 379-380, 95–103. doi:10.1016/j.palaeo.2013.04.010

Werner, M. (2002). Seasonal and Interannual Variability of the mineral Dust Cycle under Present and Glacial Climate Conditions. *J. Geophys. Res.* 107, 4744. doi:10.1029/2002JD002365

Wickert, A. D., Mitrovica, J. X., Williams, C., and Anderson, R. S. (2013). Gradual Demise of a Thin Southern Laurentide Ice Sheet Recorded by Mississippi Drainage. *Nature* 502, 668–671. doi:10.1038/nature12609

Wickert, A. D. (2016). Reconstruction of North American Drainage Basins and River Discharge since the Last Glacial Maximum. *Earth Surf. Dynam.* 4, 831–869. doi:10.5194/esurf-4-831-2016

Winkler, A., Wolf-Welling, T., Stattegger, K., and Thiede, J. (2002). Clay mineral Sedimentation in High Northern Latitude Deep-Sea Basins since the Middle Miocene (ODP Leg 151, NAAG). *Int. J. Earth Sci.* 91, 133–148. doi:10.1007/s005310100199

Yann, L. T., DeSantis, L. R. G., Haupt, R. J., Romer, J. L., Corapi, S. E., and Ettenson, D. J. (2013). The Application of an Oxygen Isotope Aridity index to Terrestrial Paleoenvironmental Reconstructions in Pleistocene North America. *Paleobiology* 39, 576–590. doi:10.1666/12059

Yu, Z., Wan, S., Colin, C., Song, L., Zhao, D., Huang, J., et al. (2018). ENSO-like Modulated Tropical Pacific Climate Changes since 2.36 Myr and its Implication for the Middle Pleistocene Transition. *Geochem. Geophys. Geosyst.* 19, 415–426. doi:10.1002/2017GC007247

Zan, J., Fang, X., Yan, M., and Li, B. (2017). New Insights into the Palaeoclimatic Interpretation of the Temperature Dependence of the Magnetic Susceptibility and Magnetization of Mid-late Pleistocene Loess/palaeosols in Central Asia and the Chinese Loess Plateau. *Geophys. J. Int.* 208, 663–673. doi:10.1093/gji/ggw419

Zhang, R., and Nie, J. (2017). Goethite Concentration Variations in the Red Clay Sequence on the Chinese Loess Plateau. *Geochem. Geophys. Geosyst.* 18, 4179–4185. doi:10.1002/2017GC007148

Zhi, Y., Jun, C., and Junfeng, J. (2000). 57Fe-Mössbauer Studies on Loess-Palaeosol Samples from the Luochuan Section, Loess Plateau of Central China. *Spectrosc. Lett.* 33, 833–846. doi:10.1080/00387010009350160

Zhou, L. P., Oldfield, F., Wintle, A. G., Robinson, S. G., and Wang, J. T. (1990). Partly Pedogenic Origin of Magnetic Variations in Chinese Loess. *Nature* 346, 737–739. doi:10.1038/346737a0

Zhou, W., van der Voo, R., Peacor, D. R., Wang, D., and Zhang, Y. (2001). Low-temperature Oxidation in MORB of Titanomagnetite to Titanomaghemite: A Gradual Process with Implications for marine Magnetic Anomaly Amplitudes. *J. Geophys. Res.* 106, 6409–6421. doi:10.1029/2000jb900447

Zhu, R. X., Matasova, G., Kazansky, A., Zykina, V., and Sun, J. M. (2003). Rock Magnetic Record of the Last Glacial-Interglacial Cycle from the Kurtak Loess Section, Southern Siberia. *Geophys. J. Int.* 152, 335–343. doi:10.1046/j.1365-246X.2003.01829.x

Conflict of Interest: The authors declare that the research was conducted in the absence of any commercial or financial relationships that could be construed as a potential conflict of interest.

Advantages of publishing in Frontiers

OPEN ACCESS
Articles are free to read for greatest visibility and readership

FAST PUBLICATION
Around 90 days from submission to decision

HIGH QUALITY PEER-REVIEW
Rigorous, collaborative, and constructive peer-review

TRANSPARENT PEER-REVIEW
Editors and reviewers acknowledged by name on published articles

Frontiers
Avenue du Tribunal-Fédéral 34
1005 Lausanne | Switzerland

Visit us: www.frontiersin.org
Contact us: frontiersin.org/about/contact

REPRODUCIBILITY OF RESEARCH
Support open data and methods to enhance research reproducibility

DIGITAL PUBLISHING
Articles designed for optimal readership across devices

FOLLOW US
@frontiersin

IMPACT METRICS
Advanced article metrics track visibility across digital media

EXTENSIVE PROMOTION
Marketing and promotion of impactful research

LOOP RESEARCH NETWORK
Our network increases your article's readership